Transformative Technologies for Future Nanomedicines CDT

Novel Devices for Evaluating Nanomedicine Biological Fate

Kiri Amabel Thornalley

A thesis submitted in fulfilment of the requirements for the degree of

Doctor of Philosophy

Strathclyde Institute of Pharmacy and Biomedical Sciences

University of Strathclyde

February 2024

Declaration

This thesis is the result of the author's original research. It has been composed by the author and has not been previously submitted for examination which has led to the award of a degree.

Signed:

Date:

Look Grandad!

I told you I was working hard at school.

In Loving Memory of my grandfather, Roger Thornalley

18th February 1935 - 17th July 2020

Contents

List of Tables

List of Figures

List of Equations

List of accompanying material not attached to this thesis

The following can be found on the University of Strathclyde KnowledgeBase at: https://doi.org/10.15129/0c656eea-2d11-4e79-abed-d792195f90fc.

- All data that underpins this thesis
- Companion App for Android, as .apk
- .stl and .mp4 files where the reader cannot or does not wish to download and install the .apk.

Using Augmented Reality

This thesis contains several figures (primarily those within chapters 3 and 4) that can be interacted with using augmented reality. Many of the results in this work are derived from simulations, which change over time and selecting stills to tell this entire story in 2D is often challenging. Augmented reality can be useful to improve the clarity of temporal data, as well as the understanding of 3D models.[1] As a consequence, augmented reality is being increasingly used in a number of areas, including education and interactive posters are becoming more popular.[2–7] The figures that can be viewed in this way will be accompanied by the following icon (**Figure 1.1**).

Figure 1.1: The icon used within this work to indicate the figure can also be viewed using augmented reality. Icon made by Freepik from www.flaticon.com

The augmented reality app has been created using Unity (2022.3.13f1, Unity Technologies) and Vuforia (10.18, PTC, Inc). These images consist of two parts – a static target image (these are the printed figures within this thesis) and the interactive overlay. LeanTouch (3.0.2, Carlos Wilkes) has also been used, to enable the reader to interact (*i.e.,* scale, rotate) the 3D geometries of interest in this work.

Installation of the mobile application

The .apk file is for android phones or tablets running Android 8.0 – “Oreo” or newer. The device will need to be set up to allow .apk files that did not originate from the Google Play store to be installed and run.

On installing the application, Android now prompts “Allow to take photos and record video” – the app requires access to the camera in order to ‘see’ and track the targets, without this permission the app will not function.

Where the reader does not wish to (or is unable to) install the app, the interactive components of this thesis (with the exception of Figure 1.2 – as this exists only to confirm the app is correctly installed and functional on the device) are also available as .mp4 files. There are also a set of .stl files, these can be viewed and interacted with using the 3D model viewer installed on Windows 10. The file name corresponds to the figure number given within the caption.

Figure 1.2: If the app Is correctly installed and ambient lighting conditions are adequate, then the robot in this figure should wave.

Troubleshooting

The printouts from many modern laser printers will give images a glossy sheen. Under normal ambient lighting conditions, this doesn’t impact the reliability of the tracking.[8] However, if the reader finds that the app doesn’t respond to a particular target image, then the lighting may well be the issue.

Abbreviations

Abbreviation	Meaning
ABC	ATP Binding Cassette
ABS	Acrylonitrile Butadiene Styrene
ADMET	Absorption, Distribution, Metabolism, Excretion, Toxicity
ADP	Adenosine Diphosphate
AMR	Antimicrobial Resistance
ATP	Adenosine Triphosphate
BALF	Bronchoalveolar Lavage Fluid
BBB	Blood-Brain Barrier
CAD	Computer aided design
CD	Circular Dichroism
CDX	Cell-derived Xenograft
CFD	Computational Fluid Dynamics
CFL	Courant-Friedrichs-Lewy
CVC	Central Venous Catheter
DARPA	Defence Advanced Research Projects Agency
DCS	Differential Centrifugal Sedimentation
DEM	Discrete Element Method
DLS	Dynamic Light Scattering
DTT	Dithiothreitol
EGFR	Endothelial Growth Factor Receptor
EMA	European Medicines Agency
EMT	Epithelial-mesenchymal Transition
EPR	Enhanced Permeation and Retention
ESKAPE	A group of pathogens particularly good at antimicrobial resistance
FBS	Foetal Bovine Serum
FCS	Fluorescence Correlation Spectroscopy
FDA	Food and Drug Administration
FDCA	Food, Drug and Cosmetics Act
FDM	Fused Deposition Modelling
FEM	Finite Element Method
FTIR	Fourier-transform Infrared Spectroscopy
FVM	Finite Volume Method
HDL	High Density Lipoprotein
HER	Human Epidermal Growth Factor Receptor
HER-2	Human Epidermal Growth Factor Receptor-2
HIV	Human Immunodeficiency Virus
IgG	Immunoglobulin G
ITC	Isothermal Titration Calorimetry
IV	Intravenous
LC-MS/MS	Liquid Chromatography Tandem Mass Spectrometry
LES	Large Eddy Simulation

LIGA	Lithographie, Galvanoformung, Abformung; German for Lithography, Electroplating, Moulding
MDR	Multi-drug Resistance
MEMS	Micro-electromechanical system
MINBE	Minimum Information about Nanomaterial Biocorona Experiments
MIRIBEL	Minimum Information Reporting In Bio–nano Experimental Literature
mm	Millimeter
MMP	Matrix Metalloproteinase Receptor
MPI	Magnetic Particle Imaging
MRI	Magnetic Resonance Imaging
mRNA	Messenger RNA
MST	Microscale Thermophoresis
mV	Millivolt
NC3R	National Centre for the Replacement, Refinement and Reduction of Animals in Research
NHP	Non-human Primate
NIH	National Institute of Health
NLC	Nanostructured Lipid Carrier
nm	Nanometre
PAGE	Poly(acrylamide) Gel Electrophoresis
PBS	Phosphate Buffered Saline
PBT	Polybutylene terephthalate
PC	Polycarbonate
PC1	Principal Component 1
PC2	Principal Component 2
PCA	Principal Component analysis
PCL	Poly(caprolactone)
PDE	Partial Differential Equation
PDMS	Poly(dimethylsiloxane)
PDX	Patient-derived Xenograft
PEG	Poly(ethylene glycol)
PETG	Poly(polyethylene terephthalate glycol)
PGA	Poly(glycolic acid)
PHSA	Public Health Service Act
PICC	Peripherally Inserted Central Catheter
PIVC	Peripherally Inserted Venous Cannula
PLA	Poly(lactic acid)
PLGA	Poly(lactic-co-glycolic acid)
PMMA	Poly(methyl methacrylate)
POTS	Postural Orthostatic Tachycardia Syndrome
PS	Polystyrene
PTA	Particle Tracking Analysis
PVDF	Poly(vinylidene difluoride)
QbD	Quality by Design
RBC	Red Blood Cells
RMM	Resonant Mass Measurement
SAM	Self-assembled Monolayer

SARS-COV-2	Severe Acute Respiratory Syndrome Coronavirus-2
SDS-PAGE	Sodium Dodecyl Sulfate Poly(acrylamide) Gel Electrophoresis
SEC	Size Exclusion Chromatography
SLA	Stereolithography
SLN	Solid-Lipid Nanoparticle
SLS	Selective Laser Sintering
SPIONS	Superparamagnetic Iron Oxide Nanoparticles
SPR	Surface Plasmon Resonance
SVC	Superior Vena Cava
TBST	A mixture of tris-buffered saline (TBS) and Polysorbate 20
TEM	Transmission Electron Microscopy
UKRI	UK Research and Innovation
UV	Ultraviolet
VAD	Vascular Access Device
VCAM-1	Vascular Cell Adhesion Molecule-1
VEGFR	Vascular Endothelial Growth Factor Receptor
WSR	Wall Shear Rate
WSS	Wall Shear Stress
µCP	Microcontact Printing
µTAS	Micro Total Analysis Systems

Acknowledgements

Dr Cameron Brown and Prof. Blair Johnston, thank you for encouraging every unhinged, slightly sleep-deprived idea I've ever had at 3am (*e.g.* the decision to use augmented reality to better display the results in Chapter 3), and for your unconditional, and utterly unwavering support. I will never have the words to express quite how grateful I am for everything.

Prof. David Smith, thank you for being mad enough to still believe I could, when everyone here thought I couldn't. Dr Izzy Jayasinghe, Dr Candice Majewski and Dr Leah Ridgeway, I'm not sure I would have got as far as even writing up this thesis without you three; I'd have quit first. Prof. Caroline Kamerlin, Prof. Rachel Oliver and Elli, thank you for figurately dragging me kicking and screaming through the preparation of what is now chapter 2 of this thesis. I will admit to now not remembering much of it, except the nightmares, and feeling so, so very frightened.

I have met far more members of staff in the Disability and Wellbeing service than I may originally have intended; you're all absolutely brilliant. Crystal, I don't think I would ever have come back from my suspension of studies, had you not been so willing to work in tandem with Rebecca. Andy, thank you for your kindness, patience and understanding. We got there eventually with the adjustments for my viva. Sonia, apologies for every supervision meeting you've sat through as notetaker, where you've had absolutely no idea what's going on. Your support has meant I could concentrate on following the conversation; instead of multitasking and taking utterly dreadful notes.

I also wish to thank Merrit Rothe, for her support with the Bradford Assay and Dr Zahra Rattray for the lyophilisation of nanoparticles in Chapter 2 of this thesis. I must also thank our wonderful collaborators at Malvern Panalytical, Liam Cole, Yu-Su Chen and Elise Guerini.

I am intensely grateful for the companionship and camaraderie from the utterly brilliant folks of Strathclyde UCU. The most rewarding part of strike action was not getting our supervisors their pensions back (although that was lovely), but the friends you meet whilst freezing to death on the picket. They know who they are; thank you for showing me what it means to stand up for what you believe in, there is power in a union.

Mr Francis Kataria, I think it's at least 80% my fault you're stuck with a PhD project that doesn't work. I owe you a drink when we're both finished.

Mr Chukwuebuka (Richard) Obiora, I did this for both of us.

Presentations and publications

Parts of this this work have been presented at the following conferences:

Royal Society of Chemistry, #RSCPoster, 3rd March 2020, Online *via* Twitter. (Poster Presentation) Won 2nd prize in Nanoscience category.

Royal Society of Chemistry - Analytical Biosciences Group, Early Career Researchers' Meeting 2020, University of Strathclyde, Glasgow, 5th-6th March 2020. (Oral Presentation)

The STEM Village, Webinar series, Online, 18th April 2020 (Oral presentation)

University of Strathclyde Doctoral Researchers' Group, Doctoral School Multidisciplinary Symposium, 26th May 2020, Online *via* Twitter due to COVID-19. (Poster Presentation)

Abstract

The formation of the protein (biomolecular) corona around nanoparticles is a phenomenon of high current interest in pharmaceutical sciences, as the composition of the protein corona is known to influence nanoparticle biological fate. The protein corona can be modified by many physicochemical parameters, including the presence of fluid shear, leading to differences in both thickness and composition when results from static *in vitro* and dynamic *in vivo* studies are compared. This thesis considers the protein corona that develops around the biologically compatible poly (lactic-co-glycolic) acid (PLGA) nanoparticles following coincubation with biological media (foetal bovine serum, human serum) before moving on to study the physiological forces experienced by these nanoparticles *in vivo* immediately following the introduction into the body *via* several clinically used vascular access devices.

This work presents (for the first time) the use of resonant mass measurement to analyse protein corona formation around submicron polymeric nanoparticles and shows its use as an orthogonal method alongside particle tracking analysis. Computational fluid dynamics (CFD) has been used to study blood flow *in vivo*. Finally, the insights obtained here were then used as input parameters to guide the design and development of a 3D-printed microfluidic device capable of subjecting nanoparticles to physiologically relevant fluid shear. This device will give rise to a protein corona with a structure and composition more like that obtained *in vivo* without requiring animal-based pre-clinical studies.

In this work, it has been shown that there are statistically significant temporal, temperature and protein concentration effects on the composition of the protein corona around PLGA nanoparticles (0 vs 24hrs, $p=<0.001$, 25°C vs 37°C $p=0.02$, 10% FBS vs 20% FBS, $p=0.01$). With reference to previously published work, a combined CFD-DEM methodology has successfully been developed to study fluid flow and nanoparticle behaviour *in vivo*. Furthermore, additional insights were developed using principal component analysis to identify key physical parameters that influence protein corona formation. Finally, these were used to successfully develop a microfluidic device that is compatible with the manufacturing limits of fused deposition modelling and capable of replicating the physiologically relevant forces identified previously. Further study of this phenomenon would enable the data-driven prediction of nanoparticle characteristics from protein corona composition and/or biological fate, enhancing the translational success of novel nanotherapeutics from lab bench to patient bedside

“If you decide to follow me, I will take you to where I believe our knowledge has reached: up to the brink of that vast nocturnal and star-studded ocean of all that we still don’t know.”

Carlo Rovelli, The Order of Time.

Chapter 1 Introduction

1.1 Introduction

The protein corona is a layer of proteins (or other biomolecules) that are known to spontaneously form around nanoparticles following co-incubation in biological fluids.[9,10] This protein corona is believed to influence biocompatibility, pharmacokinetics, pharmacodynamics and consequently nanoparticle biological fate.[11–16] However, the relationship between physicochemical properties and composition of the protein corona around polymeric nanoparticles is understudied, and the protein corona is thought of as a contributing factor to the challenges seen within pharmaceutical sciences for the translation of novel nanotherapeutics from lab bench to patient bedside.[17–21] Furthermore, cell uptake studies are often undertaken under static conditions or in two dimensions (*i.e.,* cells are grown in Petri dishes, and the absence of complex mechanical, chemical and biological cues means these techniques often poorly capture the complex 3D structures and behaviour seen *in vivo*).[22,23] Where *in vivo* studies are used, these generally use rats or mice, and translational applicability of these studies is often lacking.[24] Despite this, Doxil (a PEGylated liposomal form of doxorubicin) was one of the first nanotherapeutics to obtain clinical approval from the Food and Drug Administration (FDA) in 1995.[25] Many other nanotherapeutics have since followed; more recently, two novel nanoparticle-based mRNA vaccines for SARS-COV-2 (COVID-19) have been developed and granted clinical approval.[26–30]

This work seeks further understanding of protein corona formation around poly(lactic-co-glycolic acid) (PLGA) nanoparticles following exposure to protein-rich media. Computational fluid dynamics (CFD) is used to create computational simulations providing further insight into fluid and nanoparticle behaviour *in vivo* before a microfluidic device is developed to subject PLGA nanoparticles to physiologically relevant fluid forces, enabling the influence of fluid shear on nanoparticles to be better explored. This thesis outlines (as far as the author is aware) the first use of resonant mass measurement for the *in situ* study of protein corona formation around submicron polymeric nanoparticles before extending this to be used as an orthogonal method alongside particle tracking analysis; the development of a coupled finite volume – Discrete element methodology to understand fluid and particle behaviour simultaneously through *in silico* simulations; followed by the design of a microfluidic device capable of subjecting nanoparticles to physiologically relevant shear rates, and consideration of the necessary attributes that influence the possibility for manufacturing this device by 3D printing.

In this thesis, it will be shown that resonant mass measurement and particle tracking analysis are suitable high-resolution methods by which protein corona formation around polymeric nanoparticles can be followed. Further, these techniques can be used in an orthogonal fashion to overcome the issues known to plague single-technique analysis. A combined finite-volume – discrete-element methodology can be used to study fluid behaviour as well as particle aggregation and agglomeration *in vivo*, before these results are used as target values for the design and development of a novel microfluidic device capable of subjecting nanoparticles to physiologically relevant shear stresses – therefore replicating the modifications in protein corona size and composition that would be seen *in vivo*.

Also, this work has the potential to alter how cell uptake studies are designed and undertaken – this work clearly shows the need for pre-screening of nanoparticles before any cell-based study to determine colloidal stability. Further, the microfluidic device would generate a protein corona around the nanoparticles consistent with their physiological composition, which may further alter apparent efficacy. Finally, these computational studies could easily be modified to match a specific patient, leading to advances in personalised and precision medicine and providing another pathway by which the aims of the 3Rs of biomedical research could be met.[31]

1.2 A Brief Review of the Literature

This section will give a very brief overview of the literature; a significantly more detailed review of the necessary concepts and relevant literature is provided at the beginning of each section of this thesis.

The idea of a spontaneously forming protein or biomolecular corona around nanoparticles is not new – the phenomenon itself has been known since the 1960s and given the name protein corona by Cedervall *et al*. in 2007.[32,33] Since then, it has been found that this corona does not solely contain proteins; other

biomolecules are also found within, and current understanding suggests lipids may also play an important role in dictating eventual biological fate.[34–36] The protein corona is traditionally represented as consisting of two parts: the hard (tightly bound) and soft (loosely bound) corona.[37,38] They are often shown as two separate and distinct layers, but recent experimental work suggests this may not reflect reality.[39,40] The nanoparticle-protein corona complex and its incubation medium often need to be separated to analyse the protein corona around nanoparticles. The tightly-bound hard corona usually stays mostly intact, but the soft corona is currently considered to be rather difficult to analyse and its isolation is the target of much current work.[18,20,41] The concept of the absorbome was introduced in 2012 by Walkey and Chan.[42] They presented a list of 125 proteins commonly found within the protein corona and developed on various types of nanoparticles.[42] An analogous list of the proteins found within the soft corona is (as yet) unavailable.

Several physicochemical characteristics of the “naked” nanoparticle (*i.e.,* nanoparticle before contact with protein-containing fluids) are known to influence protein corona formation – mainly its thickness and composition (summarised in **Table 2.1**). The protein corona composition can be further influenced by various aspects of the biological system in which the nanoparticles are found.[43–45] These parameters are termed the bio-nano interface by Mahmoudi and colleagues, and more recent studies have given rise to the idea of a personalised protein corona.[16,43,44,46,47] Consequently, there are a near-infinite number of possible combinations of physical and biological factors that will influence the protein corona formed around a particular nanoparticle *in vivo*.[48] Further, the abundance of a particular protein in plasma or another medium does not necessarily mean this is reflected in corona composition.[37,49] It is unsurprising that accurate prediction of protein corona composition around nanoparticles is challenging.

Being able to accurately predict protein corona composition, alongside knowledge of the contribution towards nanoparticle biological fate of each protein, would significantly impact the design and development of novel nanotherapeutics. As discussed previously, the ‘naked’ nanoparticle's identity and physicochemical attributes impact the protein corona's composition, and the composition of the protein corona influences nanoparticle biological fate. If it were possible to reverse engineer this process, *i.e.,* have a desired target tissue, lifetime, *etc.*, identify the necessary protein corona and consequently the exact ‘naked’ nanoparticle required to achieve this, this would trigger a paradigm shift within pharmaceutical sciences.

This thesis does not consider the plethora of other clinically relevant nanoparticles and stops short of manufacturing the microfluidic device designed in **Chapter 5**; therefore, its utility for studying protein corona formation under dynamic conditions is not evaluated experimentally here. These limitations are a direct consequence of the COVID-19 pandemic on this project.

1.3 Mind the Gap

The protein (biomolecular) corona is known to influence nanoparticle biological fate. As mentioned previously, accurate prediction of the composition of protein coronae from first principles is challenging. This issue is then further exacerbated by the fact attempting to remove nanoparticles from their co-incubation fluid – to enable *ex-situ* analysis – further changes the protein corona; weakly bound proteins (soft corona) are often disturbed and then removed *via* the more commonly used nanoparticle recovery methods.[17,18,20,42] Therefore, new *in situ* analysis methods are of interest, particularly those that are not ensemble methods and are instead capable of high-resolution nanoparticle-by-nanoparticle analysis.[17,50]

Due to these challenges in separating nanoparticles and co-incubation fluid, few studies have considered the protein corona around biologically compatible polymeric nanoparticles – magnetic nanoparticles are often favoured due to their ease of separation.[11] Even fewer studies consider the influence of fluid shear *in vivo* as an explanation for the challenges in translation from pre-clinical animal research to that in humans. Only a handful of such studies consider polymeric nanoparticles.[51–55] Consequently, further work on fluid shear's role in determining protein corona composition on polymeric nanoparticles (and in particular PLGA) *in vivo* is required. Furthermore, this work would also contribute to increasing the available data on protein corona composition around nanoparticles and enable machine learning approaches to predict the composition from a set of known parameters. Wang *et al.* have previously shown that such an approach would be feasible.[56]

Additionally, there have been several high-profile instances where results of clinical trials in animals and those in humans wildly diverge, and many studies show that animal pre-clinical testing is often a poor predictor of toxicity in human trials.[24] Even though animal-based pre-clinical testing is a legal requirement for almost all regulatory bodies (as of December 2022, the FDA is now a notable exception), there is increasing pressure from consumers to move away from such testing and towards *in silico* or other methods (*e.g.,* human-on-chip).[57–60] However, such technologies are still in their infancy and not necessarily ready for clinical use.

1.4 Aims and Objectives

Several groups have made repeated calls in the literature to now move towards understanding protein corona formation when the nanoparticle formulation of interest is subject to flow.[34,53,61] This thesis makes steps towards achieving this aim of developing a better understanding of protein corona formation under dynamic conditions.

This thesis will show the development of a novel, high-resolution analytical method by which nanoparticles can be studied; computational fluid dynamics studies to understand the forces at work on PLGA nanoparticles *in vivo*; using microfluidics to subject the nanoparticles to physiologically relevant shear

rates and thus, this device could be used to accelerate the understanding of fluid shear *in vivo* on protein corona formation.

1.5 Methodology

To complete these objectives, this thesis presents a combination of experimental and theoretical work as well as an extensive literature review. PLGA nanoparticles (with and without PEGylation) are analysed at baseline, as well as following coincubation with protein-rich media (foetal bovine serum (FBS)) (**Chapter 2**). Resonant mass measurement and particle tracking analysis are used to understand protein corona effects on nanoparticle physicochemical characteristics as a function of time, temperature and protein concentration under static conditions. **Chapter 3** and **Chapter 4** outline the development of a coupled finite-volume-discrete element method for studying fluid and nanoparticle behaviour *in vivo*. These computational studies then give rise to the parameters that influence the development of the microfluidic device designed and presented here. Further CFD simulations then confirm these forces can be replicated within the device. An extensive literature review then considers the possibility and practicality of 3D-printing this device using a biocompatible polymer, which could later be used for on-chip cell culture.

1.6 Main Findings

The main findings of this thesis are that resonant mass measurement and particle tracking analysis are shown to be suitable analytical methods for the analysis of polymeric nanoparticle protein corona formation in protein-rich media, in contrast to dynamic light scattering. They are then further shown to be suited for orthogonal analysis, which overcomes the issues associated with single-technique analysis.

A combined finite-volume – discrete element methodology is suitable for studying fluid behaviour and particle aggregation and can also be used to explore the forces present *in vivo*, where a series of vascular access devices (VADs) (*e.g.* peripherally inserted venous cannula) are of interest. Additional CFD simulations show that a microfluidic device can be designed to subject polymeric nanoparticles to physiologically relevant fluid shear.

Finally, the literature review in **Chapter 5** shows that this device theoretically could be 3D-printed using fused deposition modelling and the biocompatible polymer poly(lactic acid) in lieu of traditional soft lithographic techniques and manufacture using poly(dimethylsiloxane) (PDMS). Following further Principal Component Analysis (PCA), it is shown that the hydrodynamic environment of the devices accurately replicates that within the VADs studied earlier in this work.

1.7 Thesis Overview

Most of the research within this thesis was undertaken during the SARS-COV-2 (COVID-19) pandemic; consequently, this thesis includes both practical laboratory work and computational studies. Due to the wide range of topics under discussion in this work, there is no stand-alone literature review chapter.

Instead, this thesis is split into three distinct sections and each section follows a traditional thesis structure – including a separate literature review.

Part 1 (**Chapter 2**) of this thesis covers Nanomedicine, the protein corona and particle metrology. Part 2 (**Chapter 3** & **4**) considers computational fluid dynamics and the development of a combined CFD-DEM methodology for studying nanoparticle aggregation behaviour *in vivo*. Part 3 (**Chapter 5**) then covers the design and computational modelling of a microfluidic device and the consideration of pertinent factors for the 3D printing of the final device. The thesis is then drawn to a close (**Chapter 6**) with a discussion of the conclusions that can be drawn from the thesis as a whole, alongside potential areas suitable for further study, and consideration of how these results contribute to the strategic aims of both UK Research and Innovation (UKRI) and National Centre for the Replacement, Refinement and Reduction of Animals in Research (NC3R).

Part 1:
Nanomedicine, The Protein Corona and Particle Metrology

Chapter 2
The Evaluation of Protein Corona Effects on PLGA Nanoparticle Size Distribution

2.1 Introduction

This chapter begins with an extensive review of the literature concerning nanomedicines and the spontaneous formation of a layer of biomolecules, known as the protein corona, following the introduction of nanoparticles into any biological fluid (*e.g.,* blood, serum or plasma). This layer of biomolecules is known to impact nanoparticle biological fate and is a phenomenon of significant current interest. Once the concept of the protein corona has been introduced, the discussion then considers the impact of current *in vitro* and *in vivo* methods on the translation of promising novel nanotherapeutics from lab bench to clinical use.

The aims and objectives of this chapter are: to develop and optimise the methodologies for the novel analytical technologies of particle tracking analysis and resonant mass measurement for evaluating protein corona effects on nanoparticle characteristics; for the first time, to present size

distribution analysis of polymeric nanoparticles following co-incubation with protein-rich media *via* resonant mass measurement; to establish equilibrium parameters for protein corona formation around poly(lactic-co-glycolic acid) (PLGA) nanoparticles, and understanding the impact of incubation duration and temperature, serum origin and PEGylation on protein corona formation and its physicochemical characteristics.

The structure of this chapter following the literature review is then as follows: baseline analysis of particles in buffer conditions (phosphate-buffered saline (PBS)) to understand the impact of lyophilisation on particle size, polydispersity index and zeta potential; timepoint and titration studies to assess whether dynamic light scattering (DLS) is a suitable technique by which to follow protein corona formation *in situ*. Next, nanoparticles are co-incubated with protein-containing media to study protein corona formation and how physiochemical characteristics vary following exposure to biofluids. Particle tracking analysis (PTA) and resonant mass measurement (RMM) are used for the analysis of samples in PBS, foetal bovine serum (FBS), and human serum before discussing the new insights obtained regarding equilibrium parameters. The use of PTA and RMM as an orthogonal technique is discussed before conclusions, and further work brings this chapter to a close.

2.2 Literature Review

This is the first of three literature reviews in this thesis. As discussed previously, this thesis is split into three separate parts. The literature review in this part sets the scene for the entire thesis. It will begin with a broad introduction to nanomedicine, considering why nanomedicines are thought to be an improvement on other drug delivery methods, a brief overview of the most commonly used nanoparticles (inorganic, lipid, polymer) before the concept of the protein corona is introduced. Later, nanoparticle characteristics that impact protein corona formation *in vivo* are outlined in detail, before analytical methods suitable for measuring a range of physicochemical properties of the newly formed protein corona are considered. The final section of this literature review considers the difficulties in (lab) bench to clinical translation of novel nanotherapeutics, covering the challenges of predicting efficacy *in vivo*, as well as the role animal-based pre-clinical models have to play. To bring this literature review to a close, the limited current regulatory guidance for the evaluation of nanomedicines is reviewed.

2.2.1 An Introduction to Nanomedicine

Nanomedicine is the area of science which studies the application of nanotechnology to various clinical applications.[37] These clinical applications include diagnostics, medical imaging, and therapeutics.[62] The National Nanotechnology Initiative in the US defines nanotechnology as the study of materials and phenomena in the 1-100 nm size range.[63] However, some believe this upper limit is somewhat arbitrary, and altered physical and biological properties of materials can be observed up to several hundred nanometres in size. Examples of this include: the plasmon-resonance of gold nanoshells up to 150 nm in size; the enhanced circulation time of liposomes

between 150-200 nm, and the increased accumulation and permeation in tumours of nanoparticles between 100 and 400 nm in diameter.[64–66]

There is (as yet) no internationally agreed upon definition of what exactly is meant by nanomaterial and therefore nanomedicine,[67,68] with several bodies (National Institute of Health, European Science Foundation and the European Technology Platform) all having their own slightly different working definitions.[62,69] Surprisingly, the Food and Drug Administration (FDA) has no definition.[68] This lack of an agreed-upon definition leads to issues with the regulation of these products and likely impairs their development (discussed further in **section 2.2.9.2**).[68]

Many nanoparticle-based medicines now have clinical approval from various regulatory authorities around the world. In 2017, 50 nanoparticle-based therapeutics had clinical approval from the FDA.[70] Of these, therapeutics based around nanocrystals, liposomes and polymers were the most common.[70] By 2022, an additional 13 FDA-approved drugs have come to market (**Figure 2.1**).[71] Much of this increase is in lipid-based or liposomal nanoparticles; driven primarily by work within oncology, but also *via* the two liposomal mRNA vaccines granted Emergency Use Authorisation in 2020 for the prevention of SARS-COV-2.[28,29,72].

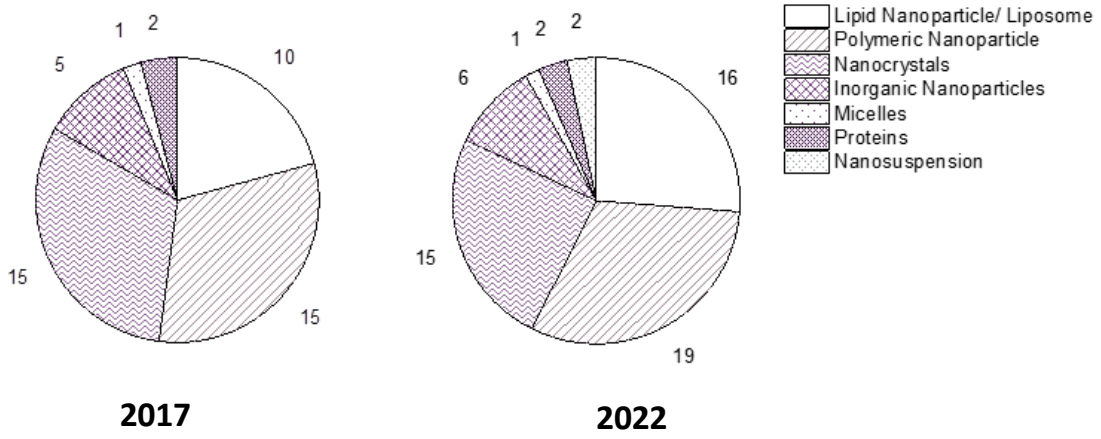

Figure 2.1: Types of nanoparticles in therapeutics licensed for clinical use in 2017 and 2022. Data from [70,71]

The number of nanoparticles in clinical trials is on the rise.[73] Between 2016 and 2019, 15 new nanoparticle technologies entered clinical trials.[27] Since 2019, a further 35 have entered clinical trials; most of these are mRNA-based vaccines, clearly exploiting the success of the mRNA-based vaccines for SARS-COV-2.[28]

The conversion of nanotherapeutics from clinical trial to clinical approval is low (6% for oncology-related nanotherapeutics and typically much lower for other indications, compared to other forms at 7.9%)[74–76] which suggests understanding of nanoparticle biological fate and their behaviour *in vivo* is still incomplete. Cabral and colleagues have recently proposed several strategies to improve the clinical translation of nanoparticles, these include overcoming

the mismatch between pre-clinical animal models and humans (discussed further in **section 2.2.9**), as well as controlling pharmacokinetics of the nanoparticle and associated drug payload.[77]

2.2.2 Nanomedicines as an Improved Drug Delivery Method

Nanoparticles can be used to enable targeted delivery of drug payloads, leading to altered biodistribution and biological fate, an increased therapeutic index and evading multi-drug resistance.

2.2.2.1 Altered Biodistribution

The methods by which nanoparticles can alter biodistribution can be classified as active or passive targeting. Passive targeting usually exploits the enhanced permeation and retention effect.[78] Active or ligand-mediated targeting decorates the nanoparticle with a range of ligands (*e.g.,* nucleic acids, peptides, sugars or antibodies) to use molecular recognition to target the nanoparticle to a chosen cell type (**Figure 2.2**).

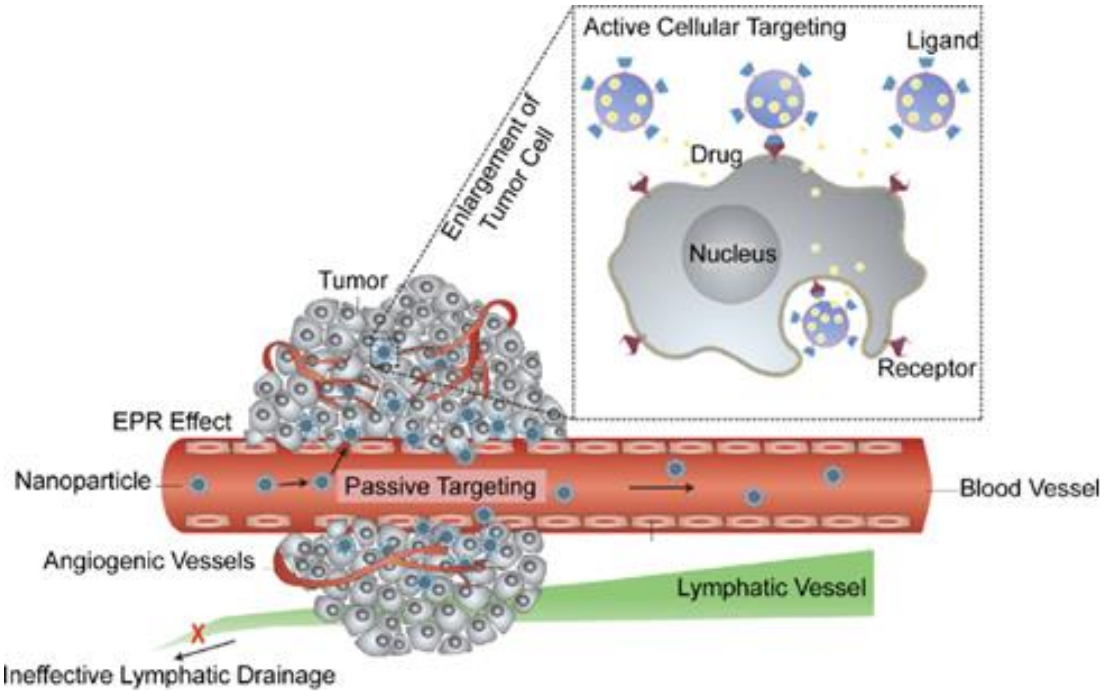

Figure 2.2: A schematic to show the wide variety of ways in which a nanoparticle carrying a chemotherapeutic payload can be targeted towards the cell type of interest. This also shows some of the inherent vulnerabilities of tumours – the development of new angiogenic vessels and their poor lymphatic drainage. Reproduced with permission from [79].

Passive Targeting

Passive drug targeting relies on one of the hallmarks of solid tumours – their rapid development of new blood vessels in a process known as angiogenesis. However, these new blood vessels are characteristically “leaky”, and are more permeable than capillaries elsewhere in the body.[80] Additionally, solid tumours have poor lymphatic drainage which then enables nanoparticles to preferentially accumulate in tumours, leading to the higher intratumoral concentrations seen by Matsumura and Maeda, and termed the enhanced permeation and retention effect (EPR).[78,80] This phenomenon was accepted

almost unequivocally by the community when originally hypothesised [81–83]; however, work more recently questions this and evidence suggests most nanoparticle entry into solid tumours is not *via* gaps between endothelial cells as originally hypothesised, but through active transport mechanisms.[84–88] Comparing and contrasting these two hypotheses in the context of novel nanotherapeutics is outwith the scope of this thesis, but has been undertaken in a recent review by Ngyuen *et al*.[88]

Passive targeting may also refer to the use of an inherent characteristic of the nanoparticle (*e.g.,* charge) as a way to preferentially target cells.[89] Simple electrostatics can then be used to bind cationic (positively-charged) liposomes; exploiting the overexpression of negatively-charged phospholipid headgroups on endothelial cells present in solid tumours.[90,91]

Active (Ligand-Mediated) Targeting

Active (ligand-mediated) targeting decorates the surface of the nanoparticle with a ligand; these ligands may be nucleic acids, peptides, sugars or antibodies.[89,92] Molecular recognition then occurs between this ligand and cell surface targets, which may be proteins, sugars or lipids (*i.e.,* all components of the cell surface membrane can be selected), enabling a chosen cell type to be targeted (**Figure 2.2**).[73] Active targeting can be broadly classified into three types, these include: angiogenesis-associated targeting, targeting to uncontrolled cell proliferation markers and tumour cell targeting.[89]

Angiogenesis-associated targeting is particularly desirable since it not only enables control over the size of the tumour, but also its metastatic ability.[89] The main angiogenesis-associated targets that have been explored include, the vascular endothelial growth factor receptors (VEGFRs)[93], αvβ3 integrins [94,95], matrix metalloproteinase receptors (MMPs)[96], and vascular cell adhesion molecule-1 (VCAM-1).[89] Additional advantages of this target include: the accessibility of the altered vasculature, therefore overcoming known issues with drug delivery into the centre of a solid tumour; the destruction of a small part of the vasculature causes death of a large part of the tumour; tumour type is unimportant, this method would work with any solid tumour, and finally, endothelial cells in the vasculature are unlikely to undergo phenotypic variation, so acquired drug resistance is only a minor concern.[97]

Cell proliferation markers are a potentially useful target, because many are overexpressed by a variety of different tumour cell types. The most common of these include human epidermal receptors (HER), transferrin and folate receptors.[89,92] Within the HER family, endothelial growth factor receptors (EGFR) and human epidermal receptor-2 (HER-2) are the most heavily researched receptors, as they are known to mediate an important cell growth and proliferation pathway.[89,98–100]

In some types of cancer, the tumour cells themselves overexpress certain cell surface targets. The most well-known of these is the use of Herceptin to target breast cancer cells which overexpress HER-2.[89] Cell type-specific targets also exist for lung (EGFR,[101] Interleukin-22R1,[102] and others), colorectal

(Endothelial protein C receptor,[103] muscarinic receptors[104]) and prostate cancers.[89,105]

Despite all of these possible methods by which to target unwanted cells, the rational design of nanomedicines that are capable of active targeting is not simple, as a variety of factors modify the efficacy of the system, including administration route and physiochemical properties of the nanoparticle. Finally on its journey through the bloodstream, the particle will acquire an outer shell of biomolecules known as the protein corona, which further modifies the final biological fate.[73] The physicochemical properties of nanoparticles, the protein corona and its impact of biological fate of nanomedicines will be discussed in more detail in **section 2.2.6**.

2.2.2.2 Modified Biological Fate

Nanoparticles, by virtue of their small size, have altered biological fate in comparison to small-molecule drugs. They are able to cross cell membranes and enter organs that larger molecules cannot (*e.g.,* blood-brain barrier).[106,107] Furthermore, they also develop a spontaneous coating of proteins (and other biomolecules, but these are not of interest here) known as the protein corona, on introduction into any biological fluid, which further modifies immune system response and organ distribution.[49] These parameters can be altered by adding various coatings to the 'naked' nanoparticle, and these coatings as well as the idea of a protein corona is discussed in further detail in **section 2.2.6**. Non-stealthed (*i.e.* uncoated) nanoparticles often reach increased concentrations where phagocytotic cell populations are high (*e.g.* liver).

2.2.2.3 Increased Therapeutic Index

The therapeutic index of a drug is frequently defined as a ratio between the highest exposure of the drug which does not result in toxicity and the exposure at which the desired effect occurs.[108] This is often expressed as the mathematical equation (**Equation 1**).

$$TI = \frac{TD_{50}}{ED_{50}} \quad (1)$$

Equation 1: Calculation of therapeutic index. TI = Therapeutic Index, TD_{50} = toxic dose in 50% of the population and ED_{50} is the effective dose in 50% of the population.

It might be expected that a large therapeutic index is always the target, but this is not always the case. For example, both warfarin (an anti-coagulant) and various lithium salts (for the treatment of Bipolar Disorder) have very low therapeutic indices, on the other hand, the antibiotic penicillin has a large therapeutic index (**Figure 2.3**).[108] Whether a narrow therapeutic index is acceptable depends on the illness that the new drug will treat, and the consequences of having no treatment at all.[108] Therefore, the treatment of particularly lethal forms of cancer such as lymphoma, using drugs with a narrow therapeutic window is considered to be acceptable, but for a simple headache, this is not the case.

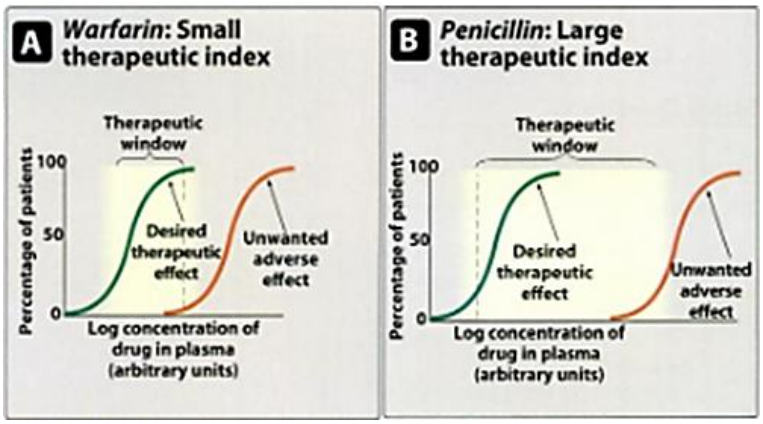

Figure 2.3: A comparison of the therapeutic indices of A) warfarin (an anticoagulant) and B) penicillin (a commonly used antibiotic). Plasma concentration (as a logarithmic scale) necessary to invoke the desired therapeutic response is shown in green, whilst the plasma concentration associated with unwanted adverse effects of the drug is shown in orange. From [108].

The therapeutic index of a drug can be improved in two ways through using nanoparticles. Firstly, by increasing the amount of drug internalised into a given cell; simply increasing extracellular drug levels is usually ineffective to induce any effect. [89] As already discussed (**section 2.2.2.1**), there are many ways in which nanoparticles can be targeted to a cell type of interest. This targeting increases the percentage of any administered drug reaching the area or cell type of interest (0.01 % of a given dose are internalised for ångström-sized particles, whilst for nanomedicines this increases to 1-5 %), so a smaller dose is required to obtain the same therapeutic effect.[109,110] Secondly, because the drug that is administered is targeted and the dose used is lower, plasma levels of the drug also remain low, since much less of the drug enters the systemic circulation, consequently, lowering the incidence of undesirable side effects and therapeutic index increases.[110]

2.2.2.4 Evading Multi-Drug Resistance

Nanomedicines can be used to avoid multi-drug resistance in cancer (anti-neoplastic resistance), where it is often responsible for the failure of chemotherapy in the treatment of breast, ovarian, lung and colorectal cancers, and also antimicrobial multidrug resistance (AMR).[92,111,112] The ESKAPE group (Enterococcus *faecium*, Staphylococcus *aureus*, Klebsiella *pneumoniae*, Acinetobacter *baumannii*, Pseudomonas *aeruginosa*, and Enterobacter *spp*.) is a group of dangerous pathogens, which are particularly good at MDR.[112] Multidrug resistance occurs *via* three separate pathways: the inactivation of administered drugs; suppressing apoptosis (controlled cell death), and interfering with drug efflux.[111]

Inactivation of Administered Drugs

The tumour microenvironment is characterised by hypoxia and acidic pH.[113] This acidic pH then limits the cellular uptake of weakly basic drugs such as Doxorubicin.[92] Not only does the tumour microenvironment inhibit cellular uptake of some chemotherapeutics, there are other pathways through which cancer cells can render inactive any drugs which do manage to achieve cellular

uptake. Cancer cells are known to be able to downregulate proteins involved in phosphorylation (*e.g.,* as in acute myeloid leukaemia) as well as upregulating the activity of the glutathione-S-Transferrase family (GST). Downregulating phosphorylation proteins and enzymes in this pathway can render some chemotherapeutic drugs inactive.[114] The GST family conjugate glutathione to xenobiotic substances, to make them more water-soluble and easier to remove from the cell and are additionally implicated in suppressing apoptosis.[115] Yuan and colleagues have recently shown that copper nanoparticles enclosed in lipids are capable of binding GSH, and eventually causing cell death.[116]

Suppressing Apoptosis

Cells have two possible apoptosis pathways – one activated by cell death receptor signalling (extrinsic), and the other by intracellular signalling (intrinsic).[117] Both pathways result in the eventual release of caspases.[118] Apoptosis can be supressed by a range of apoptotic pathway defects. In cancer cells, it is commonly the intrinsic signalling pathway, which detects stress and DNA damage within the cell that is faulty.[117–119] As a consequence of the functional inactivation of p53 (a nuclear transcription factor), the cell cannot 'sense' DNA damage, and the cells continue to grow as apoptosis is not triggered, enabling DNA damage to be passed on to daughter cells.[120,121] Furthermore, some cancer cells may overexpress certain proteins which inhibit the function of caspases, providing another pathway by which apoptosis may be suppressed.[118,122] Despite all these potential pathways by which apoptosis may be supressed in cancer cells, it is possible for nanoparticles to induce caspase-mediated apoptosis.[123]

Overcoming Drug Efflux

Cancer cells can move drugs across cellular membranes *via* efflux pumps. ATP-binding cassette (ABC) transporters use the hydrolysis of adenosine triphosphate (ATP) as their energy source to move substrates across cell membranes.[124] Many different ABC transporters exist, and those most commonly implicated in multidrug resistance in cancer are the multidrug resistance protein 1 (MDR1, also known as P-glycoprotein or P-gp, also known as ABCC1.[125,126] ABCB1 is another ABC transporter, and can bind to a variety of drugs including several classes of chemotherapeutic agents – topoisomerase inhibitors, microtubule-targeted drugs and tyrosine kinase inhibitors and it is usually this protein implicated in MDR in cancer cells.[126]

There are two potential hypotheses which have previously been suggested as pathways by which nanoparticles can overcome drug efflux: the nanoparticle binds to the active site of the efflux pump and it is the nanoparticle which is then pumped out of the cell; or alternatively nanoparticle interferes with proton gradient within the cell, efflux pump now does not function and nothing is pumped out of the cell.[127]

2.2.3 Types of Nanomedicines

Various nanostructures have been used to date, to generate novel nanomedicines including inorganic nanoparticles[128], carbon nanotubes[129], dendrimers[130,131], self-assembling peptides[132–134], liposomes[135] and quantum dots[136]. In addition, DNA origamis[137,138], nanomachines and nanorobots[139–141] have also been explored for therapeutic applications. A comprehensive review of these nanostructures, has been undertaken by Farjadian *et al*.[142]

Only inorganic nanoparticles (gold, silver, iron), liposomes and polymer nanoparticles will be discussed in detail here, as these have clinical approval; the remainder are interesting but fall outside of the scope of this thesis.[143]

2.2.3.1 Inorganic Nanoparticles

Most common clinically used inorganic nanoparticles include gold and iron. They are employed for predominantly drug delivery and/or theragnostic applications (therapeutic and diagnostic functions contained within the same nanoparticle), because of their useful optical properties (in the case of gold nanoparticles) or magnetic properties.[26]

Gold Nanoparticles

Gold nanoparticles have been explored in the clinic for photothermal therapy and drug delivery.[144,145] Several reports highlight the importance of gold nanoparticles for high-sensitivity analysis of various biomolecules in complex fluids for diagnostic applications *e.g.,* within the rapid tests for SARS-COV-2 (COVID-19).[146,147]

Gold nanoparticles are easy to functionalise, and a wide range of functional groups (*e.g.* hydroxyl (OH), methyl (CH_3) and various aromatic groups) have been explored.[144,148] This is useful, because it enables the nanoparticles to be designed and tailored specifically for a particular function (*e.g.* decorated with specific ligands to target an overexpressed receptor).[149] The size and shape of these gold nanoparticles is also known to have a significant impact on their behaviour and biological fate.[150,151] A wide variety of different nanoparticle shapes have previously been synthesised; these include rods, stars and spherical nanoparticles.[151–153] Their unique optical properties derived from plasmon resonance make gold nanoparticles attractive for theranostic applications.[154,155]

Historically, a variety of synthetic methods have been used to generate gold nanoparticles.[156,157] Modifications on these earliest methods have generally been introduced to increase the colloidal stability of the resulting nanoparticle suspensions – aggregation is a known issue with their formation, particularly as particle size increases.[157,158]

Iron Nanoparticles

For clinical applications, the most commonly used iron oxides are magnetite (Fe_3O_4) and maghemite (γ-Fe_2O_3).[159,160] Iron oxide nanoparticles have been known to show toxicity both *in vitro* and *in vivo.*[70,109] However, the toxicity of nanoparticles can be modified by the addition of coatings, these coatings are

generally polymers, such as poly(ethylene glycol) (PEG).[109,161] The inherent toxicity of these iron nanoparticles could potentially be used instead of a drug payload.[109]

A variety of clinical uses are known for iron nanoparticles, including targeted delivery of drugs or biomolecules (*e.g.,* proteins and antibodies).[162] Iron nanoparticles are also used clinically for the treatment of iron deficiency anaemia in some cases.[163] Furthermore, their magnetic properties also make superparamagnetic iron oxide nanoparticles (SPIONs) useful as contrast agents for Magnetic Resonance Imaging (MRI), but also for the higher-resolution novel imaging method of Magnetic Particle Imaging (MPI).[164–167] These magnetic properties also enable SPIONs to be used alongside an external magnetic field to induce hyperthermia in malignant cells.[168–170]

There are many ways by which iron nanoparticles (and particularly SPIONs) can be manufactured.[171] The most popular methods are coprecipitation methods in solution or microemulsion, or partial oxidation of ferrous hydroxide gels.[171] Other methods are available.[172] The major drawback of these nanoparticles is that they are prone to agglomeration as a consequence of their magnetic properties and are air sensitive.[171]

2.2.3.2 Lipid-based Nanoparticles

Liposomes and solid lipid nanoparticles are both forms of artificial vesicles with a spherical shape, and each is capable of carrying a drug payload in several different ways (*e.g.,* inside the aqueous or solid core or conjugated to external phospholipids).[70,173]

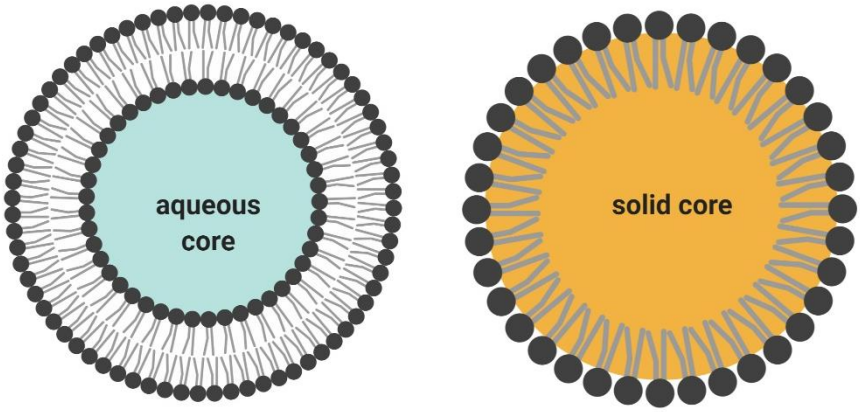

Figure 2.4: Liposomes and solid-lipid nanoparticles (SLNs) are both spherical forms of artificial lipid-based systems. Left: a simple liposome – phospholipid bilayer enclosing an aqueous core. Right: a solid-lipid nanoparticle – solid lipid core stabilised by surfactant and coated with an external layer of phospholipids. Figure created in Biorender.

<u>Liposomes</u>

Liposomes are small, artificial vesicles of spherical shape comprising of one or more phospholipid bilayers around an empty core, which range in size from thirty nanometres to several microns in diameter (**Figure 2.4**).[70,174] Liposomes are frequently used clinically for the treatment of cancer, and liposomal doxorubicin formulations represent some of the earliest nanomedicines to

receive FDA approval.[26] More recently, liposomal forms of amphotericin B have been developed, as well as two lipsome-based mRNA vaccines.[29,72,175] Their properties such as stimuli-responsiveness, size and eventual biocompatibility can be modified by changing lipid composition,[176,177] surface charge[178] and preparation method.[179] An extensive list of potential liposomal formulation methods is reported in detail by Akbarzadeh and coworkers.[179]

Solid Lipid Nanoparticles

Solid lipid nanoparticles (SLNs) consist of a solid lipid core stabilised by surfactants, that are solid at ambient (25°C) and physiological temperature (37°C).[180,181] A wide variety of lipids can be used for the solid core of these SLNs - triglycerides, fatty acids and steroids (*e.g.,* cholesterol).[182] The solid core is then coated with phospholipids (**Figure 2.4**), whose hydrophilic headgroups enable SLNs to be water soluble.[180] Nanostructured lipid carriers (NLC's) are often considered to be the "second-generation" of SLNs, but they will not be discussed here.[181,183] SLNs have shown promise for the treatment of many different cancer types, but are yet to progress beyond pre-clinical models into human trials.[94,184–187]. Furthermore. they are known to be prone to 'burst release' of their drug payload, and drug loading efficiency is also poor.[188] However, there are three ways by which a drug can be incorporated into an SLN, enabling control over drug release profile; i) through incorporating the drug into the solid solution, ii) by having a drug-free core, but a drug-enriched shell, iii) a drug-enriched core and drug-free shell.[173] If the drug is incorporated into the shell, then immediate release is observed, whilst if it is mostly concentrated in the core, then sustained or delayed release is seen.[189] Finally, unlike liposomes, even cationic SLNs have been seen to be well-tolerated in murine studies.[190] Mukherjee *et al.* outline an extensive list of possible methods for forming SLNs.[182]

2.2.3.3 Polymeric Nanoparticles

In this section, the clinical uses, physical properties, and manufacturing methods of most used biodegradable polymeric nanoparticles are considered. These polymers (poly(lactic acid), poly(ε-caprolactone) and poly(lactic-co-glycolic acid) all have similar degradation pathways and can undergo either chemical (acid-/base-catalysed hydrolysis, which is therefore influenced by environmental pH) or enzymatic hydrolysis. It has previously been reported that non-enzymatic hydrolysis is the dominant degradation pathway.[191] Polymeric nanoparticles and their starting polymers may be functionalized with the polymer poly(ethylene glycol) (PEG) and are generally termed PEGylated and non-PEGylated forms, depending on their stealthing status.[192,193] The impact of PEGylation on protein corona formation and eventual nanoparticle biological fate will be discussed further in **section 2.2.6.1**.

Poly(lactic acid)

PLA is a biodegradable polymer, whose monomers are the naturally occurring lactic acid. Lactic acid exists in two enantiomeric* forms, known as L-lactic acid and D-lactic acid.[194] PLA nanoparticles are mainly used clinically where extended-release is desirable and have been trialled as vaccine adjuvants.[193,195,196]

Both monomer molecular weight, as well as the choice of enantiomer/ ratio of L-PLA:D-PLA impacts the physical properties of the resulting polymer.[194] Increasing monomer molecular weight is known to slow degradation rate, as the polymer becomes more hydrophobic and hence absorbs less water.[197] Changing the enantiomer of lactic acid also modifies the crystallinity of the resulting polymer, where only L-lactic acid is used; the resulting polymer is crystalline, hydrophobic and subsequently takes a very long time to degrade; when only D-lactic acid is used, the resulting polymer is amorphous, and degrades much faster.[198] Manufacture of PLA nanoparticles can be split into four different types – emulsion-based, precipitation-based, direct compositing methods (*e.g.* spray drying) and newer methods such as microfluidics.[199]

Poly(ε-caprolactone)

Poly(ε-caprolactone) (PCL) is a synthetic, biodegradable hydrophobic polymer whose backbone is made of polyester linkages, which degrades slowly (over 3-4 years) in the presence of water.[200–202] Like other biodegradable polymers, clinically relevant uses of both the bulk polymer and nanoparticulate formulations are known. The bulk polymer is commonly used within tissue engineering and implantable devices, as mechanical properties are favourable for these applications.[191] PCL nanoparticles have been used as a drug delivery method and have frequently been trialled for treating brain tumours.[200,203] PCL is a semi-crystalline polymer (generally 50% crystalline) with a melting point of 60°C and a glass transition temperature (Tg) much lower than other biodegradable polymers of -60°C.[204] A wide variety of methods can be used to manufacture PCL nanoparticles, including nanoprecipitation, emulsification/ solvent evaporation and double emulsion methods; however, the choice of manufacturing method has been shown to impact final nanoparticle size and polydispersity.[200]

Poly(lactic-co-glycolic acid)

The remainder of this review of polymeric nanoparticles will focus on poly(lactic-co-glycolic acid) (PLGA) nanoparticles as they are used in this thesis. PLGA is a copolymer consisting of the monomers lactic and glycolic acid. This polymer is probably one of the most widely researched and, subsequently, most used biocompatible and biodegradable polymers.[205] As such, it is considered to be the gold standard for drug delivery systems, where controlled release of the drug payload is required.[205] Clinical uses for both bulk and microparticulate PLGA are known. There are a variety of uses of bulk

* Enantiomer – a pair of molecules that are mirror images of each other, but cannot be superimposed on top of each other *e.g.,* your hands.

PLGA with clinical approval; these include dissolvable stitches and prosthetics.[206,207] PLGA microparticles are used clinically as drug-delivery methods, such as Lupron Depot® for the treatment of advanced prostate cancer in men and endometriosis in women.[208] Nanoparticles have been tested for the extended release of an extensive range of novel drug cargoes, but not all of these have progressed from proof-of-concept or pre-clinical studies.[209,210] The relative proportions of lactic and glycolic acid and molecular weight of the monomers can be modified to tune the biodegradability and, therefore, lifetime of the overall polymer.[70,211] As the proportion of lactic acid increases, the polymer becomes more hydrophobic and degrades more slowly; the lifetime of this polymer can be as long as several years, depending on the exact molecular weight of the monomers and their proportions.[211,212] 50:50 PLGA (where equal amounts of both monomers are used) is known to have the shortest half-life *in vivo*, around 50-60 days, whilst 75:25 takes between four and five months to degrade.[213] Many methods exist for the synthesis of PLGA nanoparticles.[214] Most of these are based on the formation of various emulsions that may include electrospraying, nanoprecipitation and microfluidic methods.[215–217] Microfluidic methods are capable of producing PLGA nanoparticles with a diameter <100 nm and a narrow size distribution (polydispersity index (PDI) <0.2).[218,219]

Despite PLGA-based drug delivery methods being used in clinical practice, there are known experimental issues with utilising this polymer to develop novel nanomedicines.[208,213,220] An ideal nanomedicine formulation has the following properties: high encapsulation efficiency, high drug loading capacity, sustained and complete release of drug cargo and retains structural integrity.[213] However, meeting all of these parameters for PLGA-based nanomedicines is not always straightforward: to achieve target nanomedicine characteristics (*e.g.,* drug loading and encapsulation efficiency) is dependent on the chosen drug, the lactic acid: glycolic acid ratio of the polymer, as well as a chosen manufacturing process.[221] Drug loading is often impaired with PLGA nanoparticles. Pieper and Langer have previously reported a relationship between nanoparticle preparation technique, drug load and loading efficiency.[222] The double emulsion technique was significantly worse in terms of loading efficiency.[222] PLGA nanoparticles are also known to be prone to burst release of their drug cargo, but this is not unique to this polymer. Burst release refers to the rapid release into the bloodstream of surface adsorbed drug cargo, and it is often followed by a slower, more sustained period of drug release.[223] The presence and identity of the drug payload is also known to impact drug release kinetics through its dissolution and diffusion behaviour.[197,224] The physicochemical properties of the drug payload itself are also known to influence the precise drug release kinetics – it is suggested that both pH and drug solubility in water play an important role.[197,224] Complete release of protein-based cargoes is known to be impaired.[210,213]

Understanding the mechanism of drug release from PLGA-based systems is a complex process, and several mathematical models (e.g., chemical-potential-gradient model) are in current use – although detailed discussion of

their mathematics is outside the scope of this thesis.[224–226] The drug release kinetics of PLGA-based nanomedicines is intimately linked to the degradation of the polymer itself, but this is not the only parameter that influences drug release – polymer composition and its physiochemical characteristics, the drug payload and environmental factors all influence the eventual degradation rate of the polymer and therefore of drug release.[197] There are three known ways in which polymers can erode – surface (heterogeneous) erosion, bulk (homogeneous) erosion as well as autocatalysis (**Figure 2.5**).[197,205] PLGA undergoes hydrolysis in aqueous conditions, forming lactic and glycolic acids which are naturally occurring within the body, and are then metabolised *via* the Krebs cycle to give carbon dioxide and water.[212] Consequently, very little toxicity is associated with these nanoparticles and degradation products.[203]

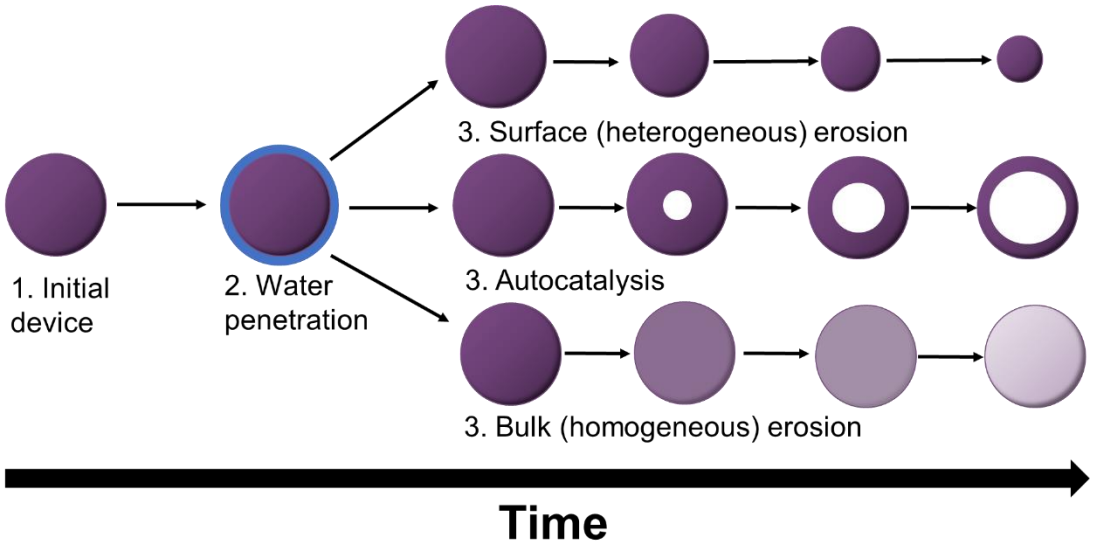

Figure 2.5: A schematic to show the 3 common degradation pathways of polymeric nanomedicines.1. The initial drug-loaded nanoparticle device is introduced into the bloodstream. 2. Water penetration occurs – this process may be negligible for some polymers. 3. Polymer degradation begins, and drug payload begins to diffuse out of the polymer. Adapted from [198,205]

Environmental parameters such as pH and fluid flow will impact polymer degradation. Results suggest that PLGA will degrade faster in either acidic or basic conditions than neutral ones – this would agree with the known mechanisms of acid- and base-catalysed ester hydrolysis.[227,228] Fluid flow has interestingly been demonstrated to slow the rate of polymer degradation; it has been suggested that the presence of fluid flow continually washes away acidic hydrolysis products and subsequently prevents (or at least reduces) autocatalysis.[229]

2.2.4 The Protein Corona

The idea of proteins being adsorbed onto the surface of nanoparticles was first suggested by Vroman in 1962, but calling this phenomenon a protein corona didn't occur until 2007, when the term was introduced by Cedervall and colleagues.[32,33]

2.2.4.1 What is the Protein Corona?

The protein corona is formed spontaneously when a ‘naked’ nanoparticle is introduced into any biological fluid.[9,10,37] Despite its name, it is not composed entirely of proteins, and it is already known that other biomolecules - for example, lipids - can be found within the protein corona.[34,35,39] These other biomolecules are, as yet, little understood, but current understanding suggests that lipids may be incredibly important for understanding nanoparticle biological fate.[36,37,55] Current understanding considers the corona to have two layers, the hard and soft corona (**Figure 2.6**), but these may not necessarily be two separate and distinct layers *in vivo*.[37,39,40]

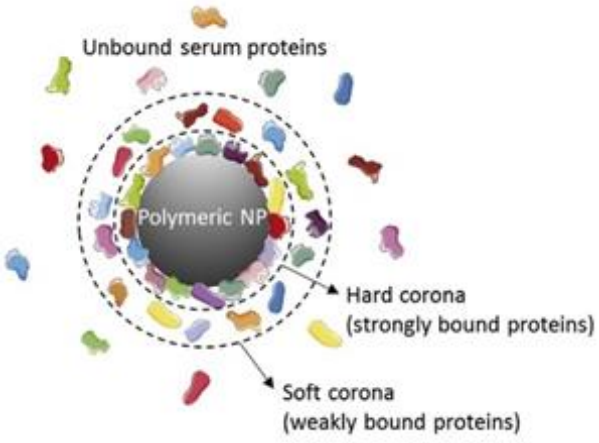

Figure 2.6: The 'hard' and 'soft' corona that develops around PLGA and other polymeric nanoparticles following incubation in biological fluids. Despite their portrayal in the literature, the hard and soft corona are not necessarily considered to be two separate and distinct layers. Reproduced with permission from Ndumiso *et al.,*[39]

The protein corona is known to significantly influence nanoparticles' eventual biological fate. The protein corona can mask any targeting moieties that may have been attached to the ‘naked’ nanoparticle to encourage the targeted uptake of nanoparticles, altering the biodistribution and pharmacokinetics of the drug payload.[10–12,37] The adsorbed proteins in the protein corona are capable of acting as opsonins – effectively biological markers which ‘flag’ the nanoparticle-protein corona complex for uptake and eventual destruction by macrophages and other cells capable of phagocytosis, impacting the circulation time of the nanoparticle.[13,230] This process of opsonisation can be controlled by coating the ‘naked’ nanoparticles with various stealth coatings, including poly(ethylene glycol), and this is discussed in more detail in **Section 2.2.6.1**. Finally, the protein corona is known to impact particle aggregation and particle agglomeration at physiological temperatures; this aggregation alters subsequent drug release.[15,231]

2.2.4.2 The Vroman Effect

Through time-evolution studies, the proteins in the protein corona are known to be in constant flux, and this evolution is controlled by the ‘Vroman effect’.[37] According to the Vroman effect, any currently adsorbed protein can desorb from the nanoparticle and be replaced by another protein of high affinity; this results in protein concentration remaining constant, but the exact composition

of proteins in the corona may change significantly over time.[37] However, some studies suggest that this effect may not be a wholly accurate description of what occurs during the development of the protein corona; Docter *et al.,* were able to show that for a select group of polystyrene nanoparticles, the composition did not change qualitatively, only quantitively – contradicting the Vroman effect.[232] Since then, a newer model of protein corona formation has been suggested, which has binding kinetics independent of the Vroman effect (**Figure 2.7**).[232]

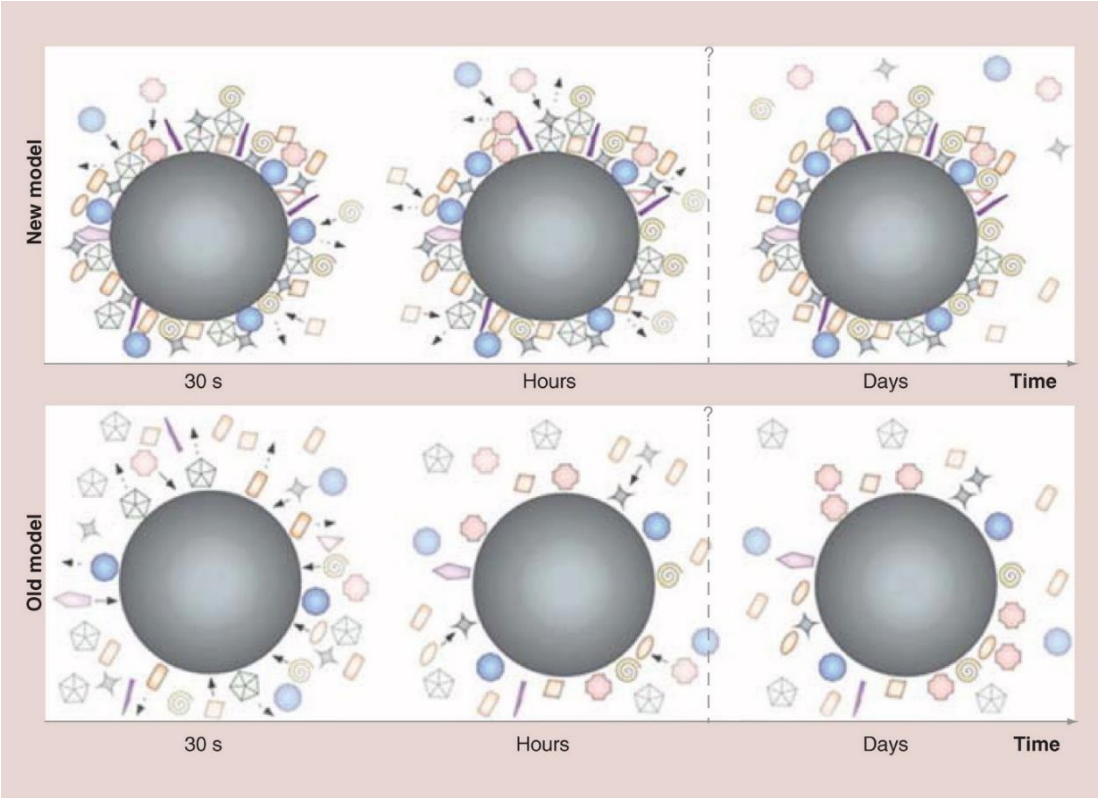

Figure 2.7: A schematic to compare the Vroman effect and the newer model proposed by Docter *et al*. to explain the formation of the protein corona and its compositional variation over time. New model (above): During the early phase, a complex corona is established. Over time the protein corona remains stable and shows quantitative, not qualitative changes in composition. Old model (below): A protein corona forms rapidly, comprised of low affinity, but highly abundant proteins. Over time, significant changes in composition occur, controlled by the Vroman effect. From [233].

2.2.4.3 Hard Corona

The hard corona is a tightly bound layer of proteins, which adheres strongly to the nanoparticle, with an exchange time on the order of hours.[37] The hard corona is considered to make up most of the protein corona.[37] When nanoparticles are incubated in human serum, the hard corona is known to frequently contain a small subset of proteins, including albumin, Immunoglobulin G (IgG) and fibrinogen, despite the complexity of human plasma.[129] This subset of proteins is not necessarily the most physiologically abundant proteins but rather the ones with the highest affinity.

Proteins in the hard corona are known to undergo a significant degree of conformational change on binding.[37] Since the protein corona is comprised of tightly bound, high-affinity proteins, this part of the corona is considered fairly stable - if the biological environment of the nanoparticle does not change.[9] However, even the slightest change in incubation media will cause changes in the hard corona, making analysis difficult.[9,234] Binding affinities of individual proteins to a given nanoparticle can be determined experimentally by several methods.[235] Broadly speaking, the kinetics of the formation of the hard corona have been determined that the binding constant K_{on} (adsorption) is much greater than K_{off} (desorption) and as such the proteins are tightly bound.[37] The general consensus in the literature is that the protein corona that forms around nanoparticles during *in vitro* studies is not necessarily representative of that which forms *in vivo*.[37,41] Firstly, many studies do not consider the impact of fluid flow on the composition of the protein corona – indeed, only a handful of such studies exist,[51,53,54,61,236] and most of these do not use polymeric nanoparticles.[52] Some *in vivo* studies suggest that the hard corona is enhanced in apolipoproteins – particularly apolipoprotein E. Still, caution must be taken with these assumptions since they are derived from murine studies.[237] The specific challenges associated with using preclinical animal models will be discussed further in section **2.2.9.1**.

2.2.4.4 Soft Corona

The soft corona is an external layer of proteins that interacts weakly with the hard corona, and the proteins involved in the soft corona are more loosely bound.[37,38] They have a much shorter residence time and adsorb and desorb much faster (on the order of minutes) than proteins in the hard corona.[20,37] The soft corona is also believed to form only a small proportion of the protein corona, and these proteins undergo low conformational change on binding.[1]

Computational studies have suggested that the soft corona is not a uniformly distributed sphere around the hard corona but is more a loosely defined layer associated with the nanoparticle.[238] As previously stated, the soft corona is formed of proteins which have only a loose association with the hard corona, and as such, it takes very little to dislodge the soft corona from the nanoparticle-protein corona complex; therefore, isolation and analysis are difficult. The soft corona is only accessible by *in situ* methods (*i.e.,* those that do not require a separation step from the biological fluid).[20] Only recently, have suitable *ex situ* techniques been developed.[18,20,41] As a consequence, the identity of the proteins within the soft corona and their role in determining the biological fate of any nanoparticle is very much unknown.[11,233] Where the soft corona has been studied from an analytical perspective, the impact of the soft corona on cellular uptake is somewhat inconclusive.[20,238] Since the proteins that make up the soft corona are only weakly associated with the hard corona through protein-protein interactions, it is not surprising that the binding constants for adsorption and desorption are expected to be approximately similar.[1]

2.2.5 Understanding the Dynamics of Protein Corona Formation

The formation of a protein corona can be separated into two stages: i) bare nanoparticle enters the bloodstream and initial corona formed, and ii) initial corona begins to evolve due to competition between proteins.[235] The formation of the hard corona is difficult to understand through experimental methods because of its speed, whilst the soft corona is challenging to isolate experimentally, and consequently, its composition and influence on nanoparticle biological fate is mostly unknown.[20,235,239]

In silico or mathematical models can provide unique insight into aspects of protein corona formation that are too complex or difficult to determine *via* experimental methods.[240] These mathematical models can also be used as a starting point from which experiments can be designed or evaluated.[235,240] At first, *in silico* modelling was popularised as a way to understand protein folding and protein-protein interactions, but has since been expanded to also model the adsorption of proteins onto bio- and nanomaterials.[42] Understanding how the protein corona changes over time is fundamental to being able to predict the biological fate of these nanoparticles, and therefore, to their future clinical applications.[241]

Dell'Orco *et al.*, and several other groups have used similar methods to develop a mathematical model of protein corona formation in a ternary system.[240,242,243] They have developed a model for the "metastable" spontaneous initial formation of the protein corona, as well as the stable equilibrium state of a nanoparticle introduced into a ternary system (human serum albumin, high density lipoprotein (HDL) and fibrinogen).[240,242,243] Dell'Orco *et al.*, developed the model first in 2010, but Sahneh and colleagues later extended to analytically describe the two equilibrium points in protein corona formation and simplified the model to create a "reduced complexity" form that runs much faster.[240,242] A version of this model including partial differential equations (PDEs) to study the influence of protein diffusivity as it tends to infinity has also been developed by Skakauskas and Katauskis.[243] Detailed discussion of the models is outside the scope of this thesis.

There are three ways in which the protein corona can be modelled computationally. These methods encompass both quantum mechanical methods as well as molecular dynamics (**Figure 2.8**). Quantum mechanical methods are highly accurate, but are too computationally demanding to be used for the modelling of protein adsorption.[42] On the other hand, molecular dynamics methods are less accurate, but are far less computationally demanding. All-atom and coarse-grained simulations can be combined to create multiscale simulations of protein adsorption.[42] The validity of the results obtained from computational studies depends on i) accurate modelling of the interactions in the system, ii) the water molecules and ions in the simulation being properly described and iii) sufficient sampling is carried out.[42]

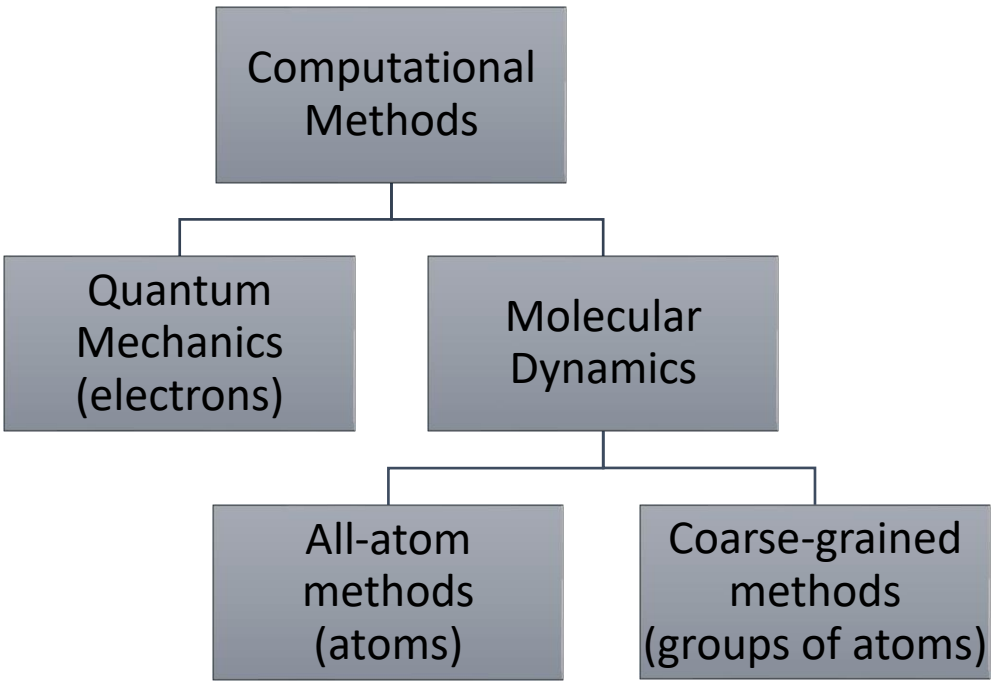

Figure 2.8: Illustrates the relationship between the computational methods currently used to model protein adsorption. Adapted from [235]

Vilaseca *et al.,* have shown that the Vroman effect can be understood computationally *via* molecular dynamics simulations.[244] Like other work discussed here, this also considers a ternary protein model (albumin, IgG and fibrinogen). Again, a coarse-grain simulation is used, since an all-atom simulation was simply too computationally demanding at the time to model much more than a few hundreds of nanoseconds.[244] It is now a decade since this work was published and it is likely still too computationally demanding to model protein corona formation in this way.

Vilanova *et al.* have undertaken a combined computational and experimental approach to better understand the dynamics of protein corona formation.[235] It is not unusual to carry out computational work in this way, (*i.e.,* to validate the results from models against experimental observations)†.[42,129,235] Experimental work used a three-component model plasma containing human serum albumin, transferrin and human fibrinogen, alongside silica nanoparticles.[235] Firstly, the affinities of each individual protein for the 'naked' silica nanoparticles was measured using Differential centrifugal sedimentation (DCS) and Microscale Thermophoresis (MST); the affinities were probed both in and out of solution.[235] These protein affinities, and other previously known parameters were used to define a coarse-grained model, which can mimic the adsorption of proteins for up to 10 seconds.[235] Theoretical predictions about the kinetics were then tested experimentally using fluorescence correlation spectroscopy (FCS), and the predictions about the relative abundances of proteins were determined experimentally using gel electrophoresis.

† This approach is often referred to as being *a posteriori*.

More recently, the application of machine learning to nanoparticles, protein corona formation and prediction of nanoparticle biological fate *in vivo* has been considered by some groups, and termed nanoinformatics.[56,245–247] The application of machine learning has been prompted by the explosion in the volume of published data concerning nanoparticles and nanomedicines.[248] A wide range of different machine learning algorithms have been used, and have been reviewed in detail by Lavanya and Sasipriya.[248] Maojo *et al.*, have previously suggested that useful applications of nanoinformatics can be classified in to three groups: imaging, modelling and data mining.[246] However, they note that one of the major difficulties with this work is the often poor quality of available data.[246] Lazarovits *et al.*, have been able to develop a supervised neural network that can interpret the temporal evolution of the protein corona and predicts nanoparticle biological fate by determining circulation half-life, and accumulation in both the spleen and liver.[245] Wang and colleagues, using a k-nearest neighbour network developed a structure-activity database for a library of gold nanoparticles, and predicted biological fate for a set of computationally designed nanoparticles and confirmed these results *via* experimental methods.[56]

2.2.6 Nanoparticle Characteristics That Impact Protein Corona Formation

The characteristics (*i.e.,* protein composition, corona thickness) of the spontaneously formed protein corona around nanoparticles in biological fluids is determined by a wide variety of factors (**Figure 2.9**).[43] These factors do not play an independent role on the resulting protein corona, but rather are interdependent.[48]

The properties of the biological fluid which nanoparticles are incubated in (*e.g.,* origin, temperature, concentration) are also known to influence the resulting protein corona, but these parameters are less well studied.[43,249,250]

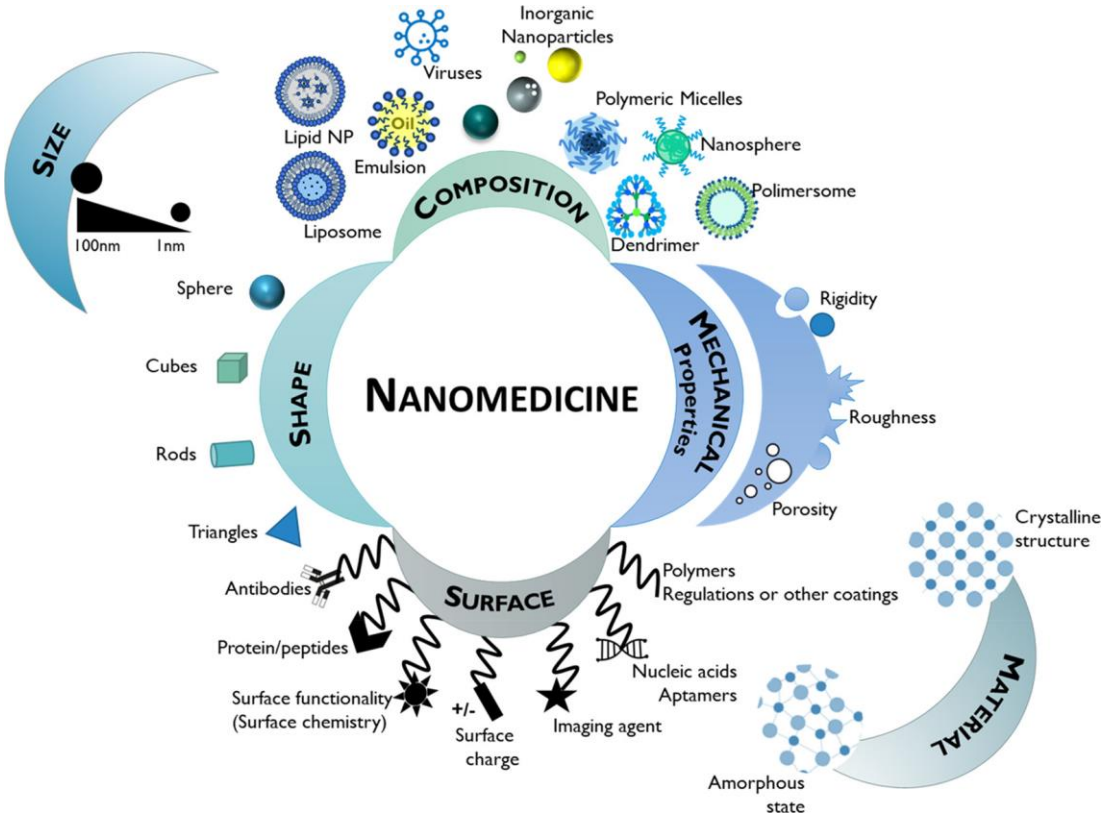

Figure 2.9: A variety of parameters will affect the protein corona formed on nanoparticle surfaces.These properties include the identity of the naked nanoparticle, its shape, size, and any surface modifications that may have been made. Reprinted with permission from Domingues et al., ACS Nano **2022**, 16 (7), 9994–10041. Copyright 2022 American Chemical Society.

2.2.6.1 Physiochemical Characteristics

The physicochemical characteristics of nanoparticles and their impact on protein corona formation is well understood and the influence of each characteristic is summarised in **Table 2.1**.

Table 2.1: A summary of nanoparticle physicochemical parameters documented to date and their effect on the developing protein corona.

Nanoparticle characteristic	Effect on protein corona	References
Size/ surface area	Size and surface area are inversely proportional, for a fixed mass or volume of nanoparticles. Increasing surface area (decreasing size) increases amount of protein adsorbed to the nanoparticle surface, and increases protein binding affinity, which influences composition.	35,251
Shape	Increased surface curvature leads to a thicker protein corona on spherical nanoparticles compared to flat surfaces (*e.g.,* nanorods). Increasing surface curvature decreases protein-protein interactions and fewer binding sites are available. Altering surface morphology (making the surface more curved) has also been shown to influence the secondary and tertiary structure of some proteins and encourage protein unfolding, leading to modified biological fate and immunological response.	252–254
Degree of aggregation/ agglomeration	Nanoparticle agglomeration (aggregation) affects particle size. The formation of a protein corona is also known to impact the colloidal stability of the nanoparticles, but the precise effect of protein corona formation on a specific nanoparticle is unclear. Situations where both an increase in colloidal stability and decreasing stability have been reported in the literature. Where stability increases, this is suggested to occur through steric stabilization *i.e.,* formation of a protein corona prevents nanoparticles contacting each other.	255–258
Chemical identity of 'naked' nanoparticle	The composition of the protein corona can be considered unique to each material.	37
Crystalline structure	Changing the degree of crystallinity of polymeric nanoparticles *via* heating modifies composition of the protein corona.	259
Surface coating (*e.g.,* stealth coatings – PEG)	Adding PEG radically alters the composition of the protein corona - significantly fewer of the proteins most closely implicated in the immune response (opsonins) are identified. The specific conformation of PEG may also alter the amount of protein that binds – a mushroom conformation of PEG will allow more protein to bind than a brush formation. Other stealthing agents, including ionic liquids have been studied.	11,260,261
Functional groups and targeting ligands (*e.g.,* antibodies)	Amine functionalized nanoparticles seen to adsorb a greater number of proteins and a greater number of complement proteins. Functionalization can increase nanoparticle aggregation.	262,263
Surface charge (zeta-potential), Charge density	Negatively charged nanoparticles bind more proteins with a pI>5.5, and the reverse is true for positively charged nanoparticles. Some of the most abundant proteins (*e.g.,* albumin) seem have binding affinities independent of surface charge. Increasing charge density increased total amount of adsorbed protein, with little effect on composition.	49,264,265
Hydrophilicity /hydrophobicity	Hydrophobicity affects both amount of protein adsorption and the composition of the protein corona. The protein corona of hydrophobic nanoparticles often contains more albumin than hydrophilic nanoparticles. Hydrophobic nanoparticles also tend to denature proteins to a greater extent than hydrophilic or neutral nanoparticles. Enhanced adsorption of proteins on hydrophobic nanoparticles also increases rate of opsonization and subsequent clearance.	49,266

Impact of the Protein Corona on Drug Release

Protein corona formation can subsequently alter drug release from nanoparticles. The rate of drug release is often much slower, and potentially, the entire drug payload is not released.[15] Furthermore, the protein corona will affect particle agglomeration, which then has an additional effect on the drug release profile. Drug release from agglomerates will occur at a different rate compared to individual nanoparticles, altering bioavailability.[267]

2.2.6.2 Biological Characteristics

It is not only the physicochemical characteristics of the nanoparticle that influences the formation of the protein corona around nanoparticles. The choice of biological medium, its concentration and any change in that medium, as well as incubation time and temperature, are capable of encouraging significant change in either density or composition of the protein corona.[42,249,250,268] It can also further be influenced by the manufacturing method of the nanoparticles as well as how nanoparticles are isolated from biological fluids following protein corona formation.[269–271]

Biological Medium

The choice of the biological medium affects not only the identities of the proteins present within the medium, but also the composition of the resultant protein corona. Several human-derived biological media have been studied in depth (human plasma, human serum, tumour interstitial fluid), to understand their composition and ascertain their impact on nanoparticle protein corona formation.[272–274] Nanoparticles incubated in plasma have been shown to adsorb more fibrinogen and those incubated in serum tend to adsorb more complement factors.[42] Whole blood has also been considered as an incubation medium, but blood plasma and serum are more commonly used in such studies.[274]

Blood plasma contains all components of whole blood, except for platelets, red and white blood cells. It contains several thousand different proteins, and the abundance of any given protein in human plasma is not necessarily reflected in the protein corona.[37,49] However, a subset of commonly found proteins in the hard corona has been identified (**Table 2.2**).[273] Walkey and Chan have presented a list of 125 proteins which are commonly found within the protein corona which develop on various types of nanoparticles, that they term the ‘adsorbome’.[42] They proposed that the protein corona is complex and no universal protein corona exists for all nanoparticles.[42] A common set of proteins commonly found within the soft corona is as yet unknown, but work to experimentally isolate and analyse the soft corona is ongoing.[18,20] Studies have also shown that the chosen anticoagulant for human plasma collection, influences final protein corona composition.[274,275]

Table 2.2: Top five most abundant proteins found in human plasma. From Leeman *et al.* [273]

Protein	Relative abundance (%)	Typical concentration ranges (mg mL^{-1})	Isoelectric point (PI)
Serum albumin	50-60	35-50	4.7
Immunoglobulin G (IgG)	-	10 [273]	6.6-7.2
Fibrinogen	-	2-4	5.8
Alpha-2-macroglobulin	3-5 [276]	~ 3	5.0-5.2 [276]
Immunoglobulin M (IgM)	-	1	4.5-6.5 [277]

In comparison to blood plasma, human serum has all coagulation factors removed.[42] The total protein concentration of human plasma and/or serum has been determined to be 60-80 mg mL^{-1}, and most of this is human serum albumin (50-60%), followed by immunoglobulins, of which immunoglobulin G (IgG) is the most abundant (~10 mg/mL).[273] Work by Ndumiso *et al.* with unmodified PVA-stabilised PLGA and PCL nanoparticles suggests that human serum has a comparatively lower binding affinity for PLGA nanoparticles, in comparison to PCL, and develops a much less complex corona.[39] The hard corona isolated from PLGA nanoparticles in this work is entirely composed of albumin.[39] This low protein binding affinity to PLGA may help explain the known biocompatibility of this polymer. These findings are very different to those obtained in Partikel *et al.*, but these differences are likely to be due to the significant changes in nanoparticle size (~400 nm vs 200 nm), zeta potential (-18 mV vs -40 mV), as well as experimental set up and subsequent human serum concentrations.[250]

Tumour interstitial fluid has also been studied and its composition in a variety of tumour types has been determined.[272] Tumour interstitial fluid (TIF) is the fluid which surrounds a tumour.[272] There are several known methods by which this fluid may be drained, and it is believed that it's composition may hold fundamental insights into tumour behaviour and progression.[272] Furthermore, the overexpression of some proteins within the interstitial fluid has enabled the development of nanoparticle-enabled serological tests for cancer.[278] More recently, its impact on protein corona formation and composition has been determined.[51] Braun and colleagues have previously reported that interstitial fluid encourages particle aggregation, as well as a significant change in protein corona composition – in their synthetic interstitial fluid, the authors saw significant protein loss. They believe the lack of protein within their interstitial fluid drives a concentration gradient which encourages protein dissociation.[51]

Incubation Time

Incubation time is known to influence the quantity of protein in the protein corona, but not its composition.[232] Barrán-Berdón *et al.* have previously shown that the protein corona is constantly evolving for up to an hour after first contact with a biological fluid.[268] Consequently, most protein corona studies incubate nanoparticles with the medium of interest for at least one hour – after which it is assumed that an equilibrium state is reached.[35].

Impact of Changes in Incubation Medium on Protein Corona Composition

If the incubation medium does not change, the composition of the protein corona is known to be stable, once an equilibrium state is reached. Where changes in these parameters occur, then differences in the protein corona can be detected. Here, the impact of: changing biological fluid origin; protein concentration; incubation temperature and the role of shear stress, methods of manufacture and isolation from incubation fluid following protein corona formation will be discussed.

Origin of Incubation Medium

Most studies investigating protein corona formation on nanoparticles have been performed using foetal bovine serum (FBS) as the incubation medium.[250,279] Unsurprisingly, these *in vitro* studies often differ from results obtained *in vivo*, making clinical translation of promising nanoparticles difficult (discussed further in section **2.2.8.2**). There are some similarities between the protein coronae that develop around nanoparticles irrespective of biological fluid origin (bovine vs human) *e.g.* the corona will primarily be composed of albumin.[275] However, there are also significant differences in the identities of the proteins detected within the corona, and little in the way of overlap between foetal bovine and human serum (summarised in **Figure 2.10**).

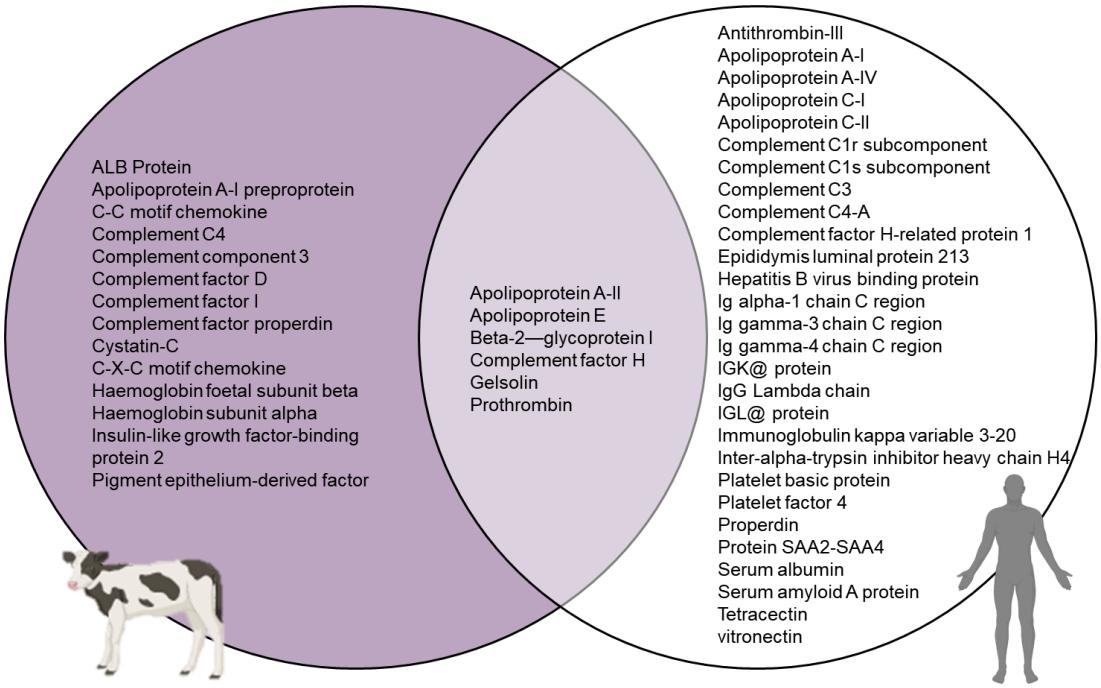

Figure 2.10: A comparison of the proteins identified *via* proteomics analysis in the protein corona which develops around PLGA nanoparticles in FBS and human serum. Only the proteins which were detected in all 3 runs have been included here. A much more consistent and complex protein corona develops when nanoparticles are incubated in human serum compared to FBS. Adapted from [250].

Furthermore, work has also studied the evolution of the protein corona as the nanoparticle completes its journey through the body. The protein corona that develops around a nanoparticle when incubated in bronchoaveolar lavage fluid (BALF), is unsurprisingly different to that when incubated in whole

blood/plasma/serum, including pulmonary surfactant associated proteins.[280] But as the corona evolves to reflect changing biological environment, some proteins from the initial corona that developed whilst surrounded by pulmonary surfactant still remain on the surface. This 'fingerprint' can then be used to determine the relative organ biodistribution of nanoparticles.[49,234,281]

Protein Concentration

It has been shown that the concentration of the medium in which protein corona studies are performed also influences certain properties of the protein corona. Partikel *et al.* showed that altering the amount of either human serum albumin or FBS will alter corona composition and thickness.[250] For the corona which develops during incubation in FBS, the composition remains fairly static irrespective of protein concentration and possibly suggests a threshold value beyond which increasing FBS concentration has limited effect, whilst for the protein corona that results from incubation in human serum is clearly dominated by albumin, but its composition becomes more complex as serum concentration increases.[250]

Incubation Temperature

Incubation temperature also modifies the protein corona. Mahmoudi *et al*. have demonstrated, using dextran coated SPIONs, that not only does incubation temperature affect the degree of protein coverage *i.e.* how complete is the protein corona, but it also influences the composition of the corona.[249] As temperature rises, the composition of the protein corona changes and begins to comprise of ever increasing numbers of positively-charged proteins.[249]

Shear Stress

Shear stress is beginning to be understood as a physiological parameter that may explain the difficulty in pre-clinical to clinical translation as seen and discussed previously.[52–54] What makes these studies different to the static conditions more routinely employed in protein corona studies, is that the nanoparticles are continually exposed to a fresh supply of incubation fluid and therefore of biomolecules.[51] Furthermore, the soft corona is comprised of only loosely-bound proteins, depending on the magnitude of the shear forces, these loosely-bound proteins could be removed, altering protein corona composition and therefore biological fate.[282] Pozzi *et al.,* show that not only do the identity of the proteins present within the corona vary depending on the presence of flow, but dynamic incubation conditions result in decreased levels of complement proteins.[53] These decreased levels of complement proteins then impact immune system response to these nanoparticles, possibly increasing their biological compatibility and circulation time. Braun *et al.,* showed that fluid shear also leads to greater amounts of protein being detected within the protein corona.[51]

Manufacturing Method

Previous work within the literature has suggested that manufacturing method may also influence the composition of the protein corona, however, this work considers microparticles, which are far larger than the nanoparticles studied

later in this chapter, so the results from Lück and colleagues may only be partially applicable.[259] They found spray dried PLGA microparticles developed a protein corona that was enriched in apolipoproteins; this was not the case for those formed by an water-in-oil double-emulsion method.

Isolation Method From Incubation Fluid Following Protein Corona Formation

The precise method by which nanoparticles are isolated from incubation fluid following protein corona formation is known to affect the analysis of the protein corona itself. A common protein precipitation method – using trichloroacetic acid in acetone is known to selectively remove albumin.[271] This is a protein that is frequently found in high-abundance. The influence of washing procedures, as well as a comparison of centrifugation parameters has been discussed in depth by Docter *et al*.[283] Despite this, no best practice methodology has - as yet - been implemented for the isolation of nanoparticles. Currently, the "best" isolation method (particularly for isolating liposomes) is somewhat controversial.[284,285]

2.2.6.3 Summary

In this and prior sections of the literature review, it has been shown that a wide variety of nanoparticles have clinical use, and an even greater range of physicochemical and biological factors will impact on the protein corona formed around them. It is known that the protein corona formed *in vitro* and that which forms *in vivo* differs significantly, but few studies have currently been undertaken to truly understand the impact of fluid flow on the size and composition of the protein corona.[51–55] Furthermore, only a handful of studies have been undertaken using polymeric nanoparticles to probe the impact of physicochemical parameters on the final protein corona that forms, and where they do exist, most of these use model polystyrene nanoparticles which find little in the way of clinical use.[11]

2.2.7 Analysis of the Protein Corona

Protein corona studies usually begin with the analysis of the 'naked' nanoparticle, prior to incubation in any biological medium. The parameters of interest in this context frequently include particle size, polydispersity and zeta potential (**Table 2.3**).[143]

Table 2.3: Analytical methods used to characterise 'naked' nanoparticles. † will give much smaller sizes than DLS and PTA as this technique does not measure particle size in solution.

Nanoparticle parameter	Analytical methods
Size	Dynamic light scattering (DLS), particle tracking analysis (PTA), transmission electron microscopy (TEM)†, resonant mass measurement (RMM)
Shape	Transmission electron microscopy
Zeta Potential	Electrophoretic Light Scattering, measured using the Zetasizer
Particle concentration	Resonant mass measurement, particle tracking analysis

The structure and composition of the protein corona can be measured in many different ways, depending upon the parameter(s) of interest (**Table 2.4**).[42,286]

The protein corona can be isolated and analysed either *in situ*, which gives the most relevant information, but the techniques which allow this are few in number and hence fewer parameters can be analysed, or *ex situ* which allows more parameters to be probed, but the process of isolation is known to disturb the composition of the protein corona.[42]

Table 2.4: A summary of the analytical methods commonly used to measure various parameters of a protein corona. From [42,287,288] Bold font highlights in situ analytical methods.

Corona parameter	Analytical Methods
Thickness	**Dynamic Light Scattering (DLS)**, **Differential centrifugal sedimentation (DCS)**, Size Exclusion Chromatography (SEC), **Transmission Electron Microscopy (TEM)**
Density	Colorimetric protein assays (*e.g.* Bradford Assay)
Identity and quantity of proteins	Poly(acrylamide) Gel Electrophoresis (PAGE), Liquid Chromatography tandem mass spectrometry (LC-MS/MS)
Conformation of bound proteins	Circular Dichroism (CD), fluorescence quenching, computational simulation, Fourier-transform infrared spectroscopy (FTIR)
Binding affinity	Size Exclusion Chromatography (SEC), **Surface Plasmon Resonance (SPR)**, Isothermal Titration Calorimetry (ITC).

Where *ex situ* techniques are chosen for analysis, the nanoparticles must first be isolated from the incubation medium. There are a wide range of isolation techniques that are currently used, each with its own relative merits. The most widely used method is to incubate nanoparticles in biological media, that are then recovered *via* centrifugation and ultrafiltration, followed by extensive washing to remove unbound proteins.[37] However, the many cycles of washing and centrifugation can lead to modifications in the protein corona.[9] Washing modifies the biological medium surrounding the nanoparticle; therefore, altering the composition of the protein corona, and centrifugation removes any weakly bound proteins *i.e.,* soft corona. Ultrafiltration and size exclusion chromatography may also be used as an isolation method and this is considered to disturb the protein corona to a lesser extent. However, due to ease of use and availability, centrifugation is still commonly used.[42]

Following isolation from the incubation medium, the individual proteins within the protein corona can be quantified and identified.[42] This is done using high temperatures, high salt concentrations, detergents or enzymes to denature the proteins; the proteins can then be separated by gel electrophoresis and identified by mass spectrometry.[42] A variety of other analytical techniques are also used to obtain more information about the protein corona,[289] but only the most frequently used: SDS-PAGE and Western Blotting (immunoblotting), liquid chromatography tandem mass spectrometry (LC-MS/MS), isothermal titration calorimetry, size exclusion chromatography, dynamic light scattering and the novel analytical techniques particle tracking analysis and resonant mass measurement are discussed in detail below.

2.2.7.1 SDS-PAGE and Western Blotting

Immunoblotting occurs in 6 stages, i) extraction and quantification of protein sample, ii) resolving the protein sample using SDS-PAGE, iii) transferring the separated proteins to a membrane, iv) blocking non-specific binding sites on the membrane, v) addition of antibodies, and vi) detection.[290]

Sodium dodecyl sulfate polyacrylamide gel electrophoresis (SDS-PAGE) is an analytical method capable of separating a complex mixture of proteins by their molecular weight. SDS-PAGE is a particularly popular technique as it is quick and cheap to run.[287] In SDS-PAGE the proteins first need to be denatured and negatively charged. This is accomplished by simply boiling them with a reducing agent such as Dithiothreitol (DTT) or 2-mercaptoethanol, and an anionic surfactant like sodium dodecyl sulfate (SDS).[287] Treating the proteins with SDS causes them to repel each other and therefore detach from the surface of the nanoparticle.[287] The proteins can then be loaded onto a polyacrylamide gel, and separated according to their electrophoretic mobility - their electrophoretic mobility is related to the size of the protein.[287] Used alongside Western Blotting, it is possible to detect very small (<1 ng) amounts of a particular protein.[14] The exact lower limits of detection depend on the stain that is used. The most common of these is Coomassie Blue (despite its lower detection limit of ~5 ng),[291] but chemiluminescent stains exist, which enable the identification of as little as a few attograms (10^{-18} g) of protein.[292]

Western Blotting gives a semi-quantitative method to analyse proteins. Once the proteins have been separated on the polyacrylamide gel, they can then be transferred to either a PVDF (poly(vinylidene difluoride)) or nitrocellulose membrane.[293] After transferring the proteins to the membrane, the membrane is then commonly blocked with 5% skimmed milk in TBST (a mixture of tris-buffered saline (TBS) and Polysorbate 20, also known as Tween 20), to prevent non-specific binding of the antibody that is added next.[293] The primary antibody is chosen to bind to one specific protein of interest; the secondary antibody often has a chemiluminescent component attached (*e.g.,* horseradish peroxidase) and the bound secondary antibody is then detected by developing photographic film.[293]

SDS-PAGE and Western Blotting have frequently been used to study the composition of the nanoparticle protein corona (**Figure 2.11**).[283] Once gel electrophoresis has been completed, each protein within the protein corona corresponds to a band within the gel. Known proteins can then be identified purely through their molecular weight following cross-reference to a protein ladder.[283] For example, albumin has a characteristic, frequently very intense, band at ~ 66 kDa.[250,274] Gel electrophoresis will also permit qualitative analysis of protein coronae, as compositional changes between them correspond to a differing pattern of protein bands in the gel. The identification of a singular unknown protein can be done *via* Western Blotting (immunoblotting) if a suitable primary and secondary antibody is chosen, but for the identification of many unknown proteins, then mass spectrometry is necessary.

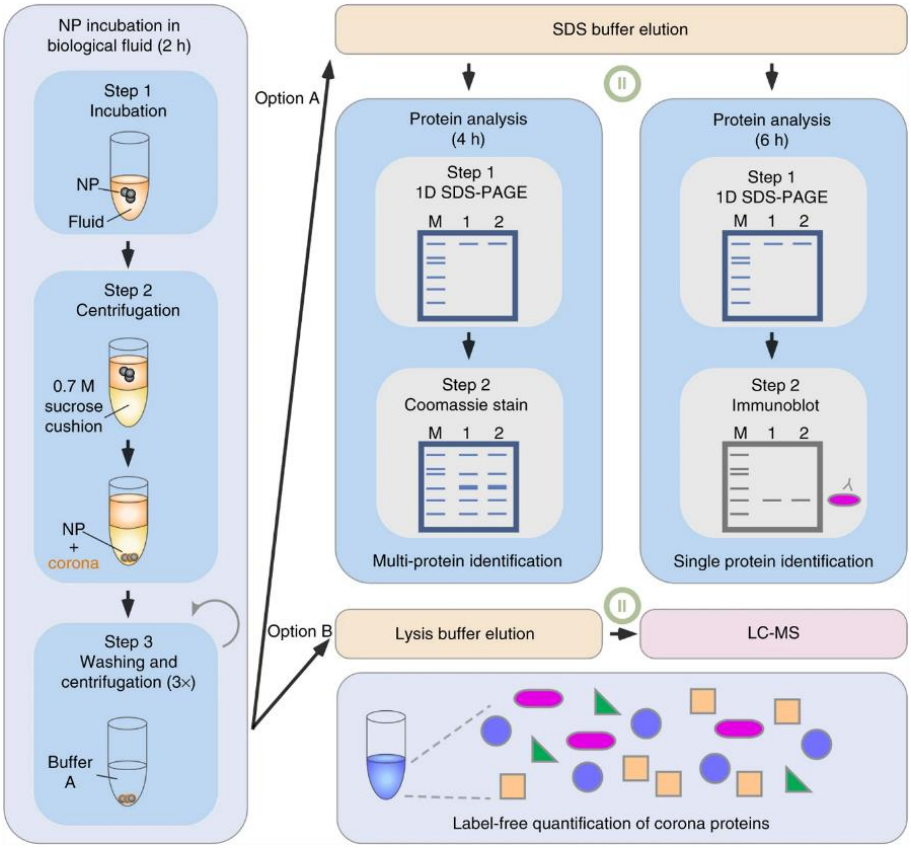

Figure 2.11: A schematic to illustrate the method used by Docter *et al.* to analyse the protein corona around polystyrene and silica nanoparticles. For both methods, the nanoparticles undergo three rounds of washing and centrifugation, final analytical process varies depending on the number of unknown proteins that need identification. Reproduced with permission from Springer Nature. From [283].

2.2.7.2 LC-MS/MS

Liquid chromatography tandem mass spectrometry (LC-MS/MS) is a powerful analytical technique, that can detect and identify the components of complex mixtures and is frequently used to undertake proteomics analysis (**Figure 2.11**).[294] LC-MS/MS relies on coupling mass spectrometers together in series, to analyse complex mixtures.[294] Liquid chromatography is first used to separate the components of the complex mixture, before they are passed to the first of two mass spectrometers for ionisation, producing precursor ions (**Figure 2.12**).[294] Between the first and second mass spectrometers is a series of mass filters, with a collision cell between them.[294] It is in this collision cell where the precursor ions are ionised for a second time, producing 'product ions', and it is these product ions which suggest the identity of the original analyte.[294]

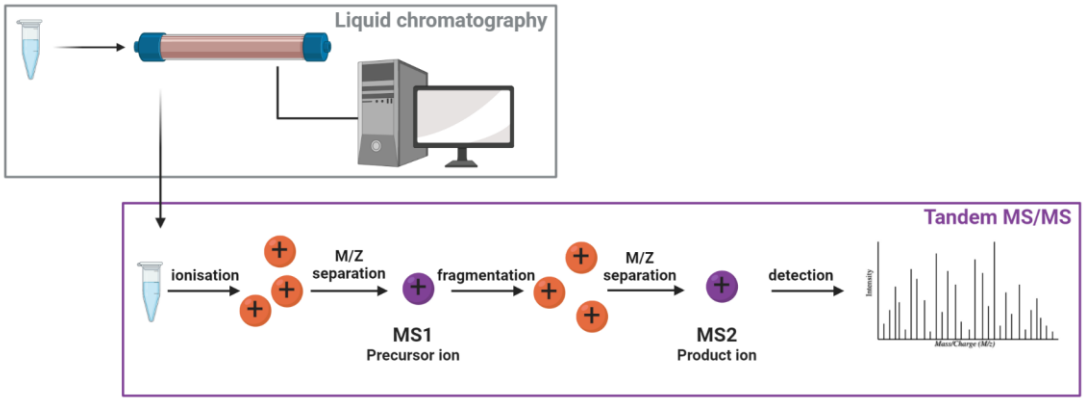

Figure 2.12: A schematic to illustrate the stages of LC/MS-MS analysis. The sample is first passed through liquid chromatography for analysis before being passed through two mass spectrometers where precursor and then product ions are produced. Figure created using Biorender.com

There are a variety of advantages that LC-MS/MS has over other analytical methods these include: superior selectivity, the ability to multiplex to identify and quantify several analytes simultaneously, as well as being less reliant on the quality of the liquid chromatographic separation.[294] Tandem mass spectrometry has superior selectivity of analytes compared to other methods, as it identifies each compound by a minimum of two different properties – the masses of their precursor and product ions.[294] If this is further coupled to liquid chromatography, then retention time by LC is also used to identify the analyte.[294]

Tandem mass spectrometry and LC-MS/MS have both been used during the workflow to analyse the protein corona that develops around nanoparticles.[250,283] Mass spectrometry is particularly useful for the simultaneous detection and identification of unknown proteins within the corona, as both the precursor and product ions can be used for identification (**Figure 2.12**). Following fragmentation, the resulting pattern of ions can then be cross referenced to one or more databases, to identify the original proteins within the sample.[295] A protein is generally considered to be present in the protein corona if there is 95% confidence over its identity.[39] This process tends to be more successful when the nanoparticles have been incubated in biological fluid of human origin, as these databases are more complete, but the same process is often successful with some fluids of bovine or murine origin (*e.g.* FBS). However, Ashkarran and colleagues note that interlaboratory consistency of LC-MS/MS for proteomics analysis is lacking, and therefore highlights the urgent need for a standardised and widely adopted workflow for protein corona analysis.[296]

2.2.7.3 Isothermal Titration Calorimetry

Isothermal Titration Calorimetry (ITC) is a useful analytical method if thermodynamic data of protein binding is required. The data that can be obtained from ITC includes: binding affinity, binding stoichiometry and enthalpy changes which occur during protein binding.[33,287] ITC works by titrating one reactant (usually the ligand) into another reactant under isothermal conditions

and measuring the temperature change that occurs after each addition of reactant.[297] More additions of reactant are performed until the temperature in the cell does not change *i.e.,* the target is saturated and no further ligand will bind.[297] The isotherm is then fitted to a mathematical equation and the thermodynamic parameters of the reaction can then be obtained. Detailed discussion of the mathematics involved in the fitting and subsequent analysis is out of scope for this review.[298,299] From the isotherm produced by ITC: enthalpy (ΔH), entropy (ΔS), heat capacity (C_p), binding affinity (K_d) and Gibbs free energy (ΔG) can all be derived.[297,299] K_d, ΔH and binding stoichiometry (n) are all simple to obtain from the binding isotherm. The remainder of these parameters can then be determined by rearranging the following equations (**Equation 2**).[39]

$$\Delta G = -RTlnK_d = \Delta H - T\Delta S \qquad (2)$$

Equation 2: Calculating thermodynamic parameters from Isothermal Titration Calorimetry. Where R= universal gas constant (8.314 J K^{-1} mol^{-1}), T= absolute temperature (in Kelvin).

2.2.7.4 Size Exclusion Chromatography

Size exclusion chromatography is a chromatographic method that separates particles based on their hydrodynamic volume.[300] The sample is dissolved into a suitable solvent, before being injected into a column packed with a stationary phase, which contains pores of a defined size.[300] Molecules that are too large for the pores of the stationary phase elute rapidly from the column, whilst those which are small enough to fit inside the pores take much longer to elute.[300]

Size exclusion chromatography is a popular analytical method, because of its speed.[300] However, SEC has been known to cause solubilisation of large aggregates due to dilution effects, and larger particles are trapped within the column and consequently often not characterised by this method.[301,302] Further disadvantages include that only a very limited size range can be explored with this method, therefore samples require pre-filtration.[301] Finally, the results from SEC are only accurate if confirmed by another, orthogonal method.[303]

SEC finds itself used within protein corona studies as a method to separate the nanoparticle-protein corona complex from unbound proteins, as a replacement for the centrifugation and repeated washing steps shown above (**Figure 2.11**), and then is often followed by membrane ultrafiltration to isolate nanoparticles and their protein corona.[55,237]

2.2.7.5 Dynamic Light Scattering (DLS)

Dynamic light scattering (DLS) is an ensemble technique which relies on backscattered light at 173°. Dynamic light scattering uses monochromatic light, shone into the sample. When this incident light has its path blocked by a particle, then it is scattered in all directions.[304] The intensity fluctuations of this scattered light can be measured, and used to determine the diffusion coefficient of the object causing the scattering. Hydrodynamic radius of the particle can then be calculated *via* the Stokes-Einstein equation (**Equation 3**).

$$D_T = \frac{K_B T}{6\pi\eta R_h} \quad (3)$$

Equation 3: Stokes-Einstein equation for calculating hydrodynamic radii of particles *via* dynamic light scattering. Where D_T = diffusion coefficient, K_B = Boltzmann constant, T = absolute temperature (in Kelvin), η = viscosity of the solvent and R_h = hydrodynamic radius.

As an *in situ* analysis method, it is particularly easy to use and requires little prior sample preparation. Dynamic light scattering has frequently been used within the literature to measure the size distribution of 'naked' nanoparticles before incubation with protein-containing media, but also to probe the changes in particle size distribution following treatment and subsequent protein corona formation.[17,250,305] Where DLS is used for the latter, the nanoparticles have frequently been recovered from serum before analysis. One of the major disadvantages of DLS, however, is that this is an ensemble method, so the results that are obtained can easily be skewed by the presence of a small amount of aggregates, or (as in this thesis) by excess unbound protein.[306,307] Furthermore, where so-called single large angle scattering-DLS is used, nanoparticle aggregates cannot be accurately sized or are subject to significant errors.[306]

2.2.7.6 Novel Analytical Techniques

Here, the newer and less-used analytical techniques of particle tracking analysis (PTA) and Resonant Mass Measurement (RMM) are introduced.

Particle Tracking Analysis

Particle tracking analysis, similar to DLS, relies on incident light passing through the sample and being scattered by particles undergoing Brownian motion (**Figure 2.13**). However, unlike DLS, this is not an ensemble method and can analyse each individual particle that is present within the sample, so results are less likely to be biased by the presence of agglomerates. The system does this by recording video footage as the particles pass by the detector.[308] This footage is subsequently used to detect the centre of each particle, perform frame-by-frame tracking and calculate the particle trajectory, which is later used to determine the diffusion coefficient.[308] Next, since sample temperature and solvent viscosity are known, the Stokes-Einstein equation (**Equation 3**) can be rearranged to give the hydrodynamic radius of each nanoparticle seen within the footage.

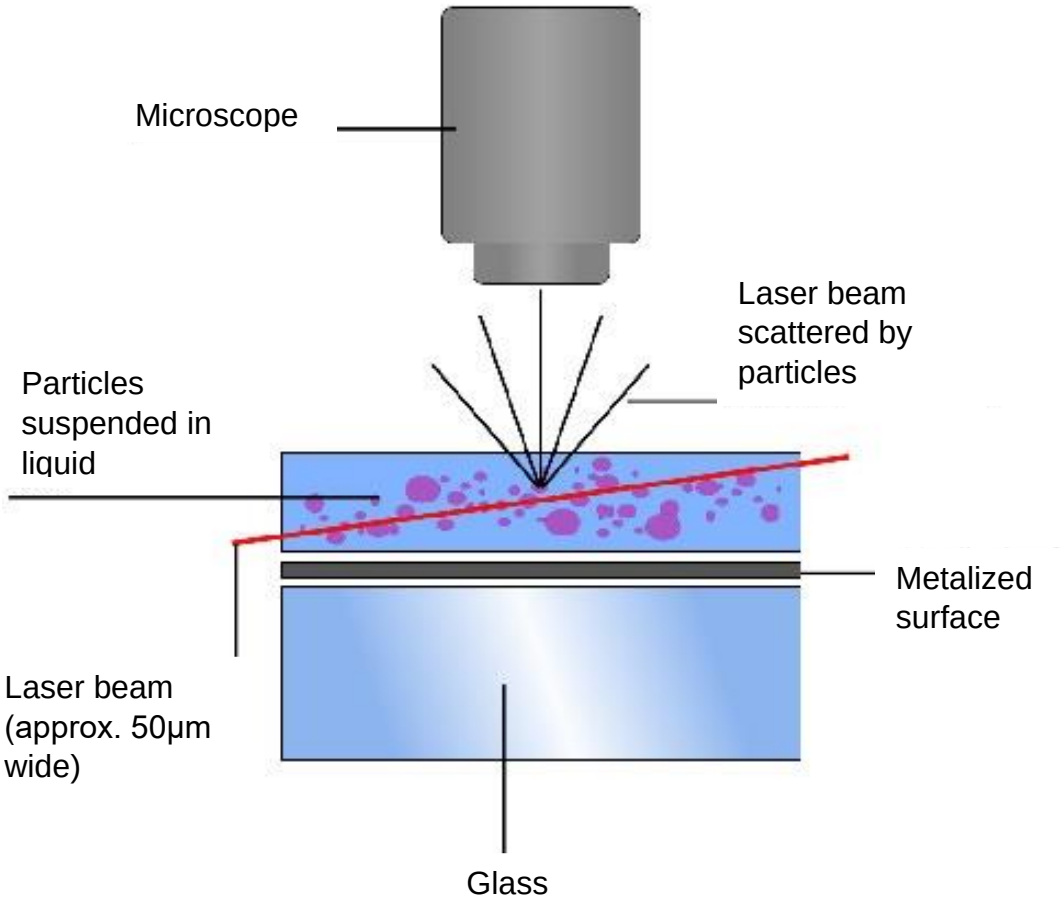

Figure 2.13: A schematic to show how particle tracking analysis (PTA) works. Light is shone through the sample and once the light hits a particle in solution, it is scattered. This light scattering is then detected. From [308]

Resonant Mass Measurement

Resonant mass measurement contains a microfluidic chip (**Figure 2.14**), containing a resonating cantilever, which resonates at a specific frequency (f).[309] For each particle passing through the sensor, the resonator's mass and resonance frequency momentarily increase, and the system measures the change in resonant frequency (Δf). The change in resonant frequency is then used to calculate the buoyant mass (M_B) of the particle passing over the resonating cantilever (**Equation 4**).[309] Once buoyant mass is known, both the 'dry' mass (M) of the particle and its diameter (D) can be calculated.[309] Further information regarding the underlying physical principles of resonant mass measurement is discussed by Nejadnik and Jiskoot.[310]

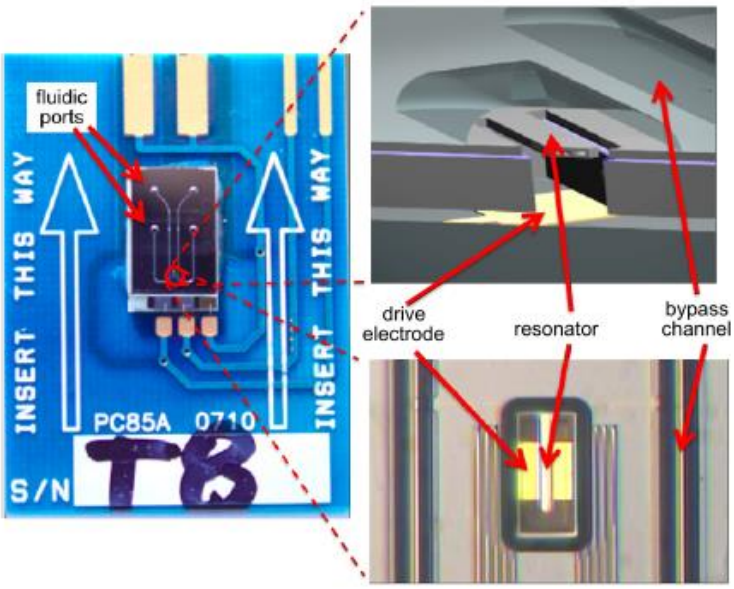

Figure 2.14: A representation of the Micro-Electro-Mechanical System (MEMS) sensor of the RMM system used in this work. Sample enters through the sample inlet port (top right), filling the bypass channel, before being pushed by the pressure differential across the chip over the resonator (centre) and exits the MEMS sensor via the sample waste port (bottom right) From [309]

$$M_B = \frac{\Delta f}{S}$$

$$M = \frac{M_B}{\left(\frac{1-\rho_f}{\rho_p}\right)} \qquad (4)$$

$$D = \left(\frac{6M}{(\pi\rho_p)}\right)^{\frac{1}{3}}$$

Equation 4: Calculating Buoyant mass, dry mass, and particle diameter *via* resonant mass measurement. Where M_B = buoyant mass, Δf = change in resonant frequency, S = sensitivity of the resonator, M = 'dry' mass, ρ_p and ρ_f = densities of the particle and of the surrounding fluid respectively.[309]

The advantage of using RMM and PTA for the analysis of nanoparticles is that both techniques require minimal sample preparation (*i.e.* nanoparticle recovery from serum), and can handle samples with a wide range of particle number concentrations (RMM target concentration for nano sensor: $2x10^8$ particles/ mL, PTA: $1x10^6$ – $1x10^9$ particles/ mL).[308,309] PTA can report particle size and number distribution, and sample concentration (particles/mL).[308] RMM provides particle diameter, (and of a sample, its distribution), particle mass, volume and surface area, particle density and sample concentration (particles/mL).[309] Both techniques can provide an insight into temporal effects of treatment with protein-containing media and their subsequent impact on nanoparticle physicochemical characteristics.

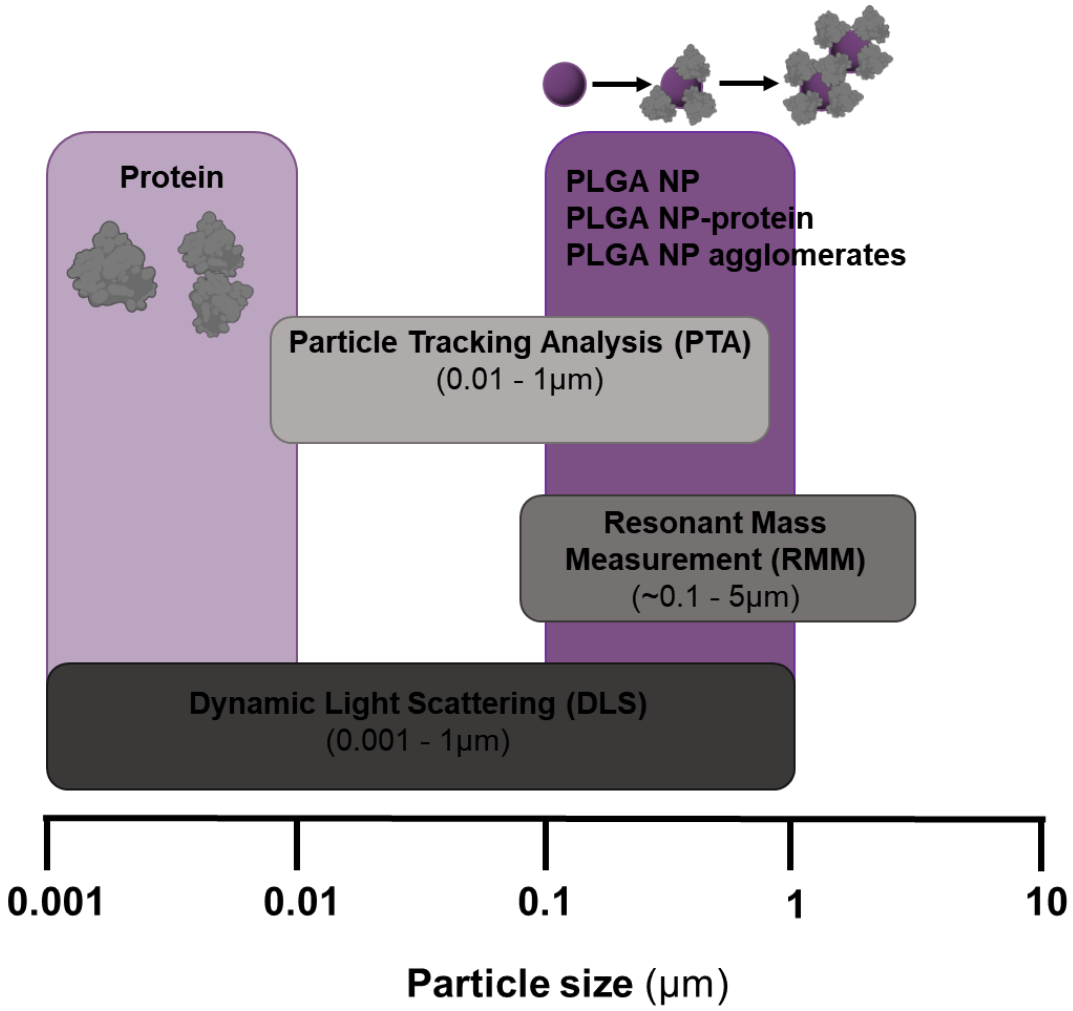

Figure 2.15: A comparison of the limits of detection of DLS, PTA and RMM as three orthogonal analytical techniques and their corresponding dynamic ranges. Particle size ranges shown are dependent on instrument settings and material characteristics of nanoparticles being measured. The size range in which serum proteins – as either monomers or larger aggregates - are found, is also shown.

Figure 2.15 shows the working range of RMM, PTA and DLS. There is a significant overlap between the size range in which the serum proteins can be found, and the lower end of the working range of both PTA and DLS. Less overlap occurs between the signal for proteins (< 10 nm) and RMM (> 100 nm). Unlike DLS, PTA is not an ensemble method, and the user can 'help' the software better differentiate between objects of interest (PLGA/PLGA-PEG nanoparticles with the newly developed protein corona) and bulk unbound serum protein, by altering a selection of camera settings during acquisition of the video footage and subsequent analysis.[311] Both the camera level and detection limit can be altered; altering the camera level (how close is the camera to the sample) before the acquisition of the video footage does enable the detection of smaller particles, as less scattered light is then required for the particle to be 'seen' by the camera, but it also has the ability to alter the apparent concentration of the sample, as more background 'noise' is also detected and considered to be particles of interest.[311] Increasing the detection

limit (amount of scattered light necessary for the nanoparticle to be 'seen') of the system then has the reverse effect.

In the final sections of this literature review, the *in vitro* and *in vivo* factors that hinder the clinical translation from promising candidate on the lab bench, through pre-clinical studies to clinical approval will be discussed.

2.2.8 Bench to Clinic Translation: Predicting the Efficacy of Nanomedicines *in Vivo*

There are a range of factors which hinder the accurate prediction of the efficacy of novel nanomedicines *in vivo*. These factors can broadly be categorised as physicochemical, biological and cell-related parameters.

2.2.8.1 Physicochemical Parameters

The physicochemical parameters of the nanoparticle that influence protein corona formation and therefore biological fate have already been discussed in detail in **section 2.2.6.1**. Here, the impact of manufacturing processes and analytical methodologies used for nanomedicine evaluation are considered.

Impact of Manufacturing Processes on Nanoparticle Attributes

Manufacturing processes are known to influence certain characteristics of the naked nanoparticles. These parameters include: size distribution and it's reproducibility and colloidal stability of the naked nanoparticle.[43,110] Furthermore, drug delivery platforms that require time-consuming or technically complex synthetic routes are often difficult to manufacture at scale.[110]

One of the key quality attributes for a novel nanomedicine is the existence of a manufacturing method that enables the nanoparticles to be made at scale, and the product to be consistently high-quality and lack significant batch-to-batch variation over a range of key attributes (*e.g.,* size distribution).[110,312] Luxenhofer has previously reviewed the known batch-to-batch variation in a range of polymers, and considers whether this natural variation needs not to be quashed, but rather embraced instead.[312] There are a wide range of possible manufacturing methods by which PLGA nanoparticles can be formed, and emulsion-based methods are generally the most popular as a consequence of their simplicity, but are not generally amenable to industrial-scale manufacture.[313] Scale-up causes various formulation parameters (*e.g.,* stirring rate) to change, and these have been shown to influence the physicochemical properties of the resulting nanoparticles.[314]

The stability of the PLGA nanoparticles is another factor impairing their translation to the clinic, however, clinical uses of PLGA microparticles are known, therefore it must be possible for these issues to be overcome, however these are typically intramuscular formulations.[315] Colloidal stability is dictated primarily by surface charge.[316] As discussed previously, some formulations of PLGA begin to degrade in an aqueous environment within 15 days, this gives the drug formulation an incredibly short shelf-life. Methods such as freeze-drying have been used previously to extend the shelf-life of these

nanoparticles, but they are still moisture-sensitive and may not enable the nanoparticles to be stored indefinitely.[317]

Analytical Methodologies for Nanomedicine Evaluation

Cytotoxicity of nanoparticles is modified by protein corona formation.[37] However, *in vitro* toxicity assays were not developed for use with nanoparticles, and their results may not be valid for reflecting the *in vivo* toxicity. Furthermore, known issues with interlaboratory consistency concerning analysis of nanoparticles is also discussed here.

The two most commonly used toxicity assays are MTS and Comet assays.[43] Both of these were developed in the 1980's, and were never designed to be applied to the study of nanoparticle toxicity.[318,319] Consequently, it is not surprising that known interactions between some types of nanoparticles and these cell proliferation assays (and a wide range of others) occur, leading to false negative/ false positive results.[320,321] Furthermore, Ong *et al.,* highlights that where these assays are used to determine nanoparticle toxicity, the researchers overwhelmingly seem unaware of the potential for interactions between the nanoparticles under study and their chosen assay.[322] This likely explains the apparent difficulty in reproduction of toxicological results within the literature, impairing clinical translation. Previous studies have considered the adaptations that may need to be made to common toxicological assays to account for interference by nanoparticles.[323]

One of the biggest issues with interlaboratory consistency of nanoparticle analysis and subsequently nanomedicine development, is that there is currently no set list of analyses that need to be carried out, nor is there consensus over what data must be reported for cell or animal based studies used to understand the toxicity and biological effect of these novel drugs.[324] Furthermore, it was not until 2018 before the first attempts were made by Faria and co-workers to introduce a framework for reporting data within this space. These guidelines are now known as the MIRIBEL (Minimum Information Reporting In Bio–nano Experimental Literature) guidelines.[325] A year later, Chetwynd and colleagues built upon MIRIBEL to introduce MINBE (Minimum Information about Nanomaterial Biocorona Experiments).[326,327] MINBE consists of two parts: a checklist of considerations for experimental design and a framework for reporting data in published literature, to give the minimum data necessary to accurately replicate the experimental work. Repeated calls have been made within the literature to increase compliance with these reporting frameworks, but uptake has been slow.[43] Also, the lack of standardised, internationally agreed upon methodologies for analysis further contributes to the lack of interlaboratory consistency (between two or more laboratories).[328] Montoro Bustos *et al.,* have additionally previously shown that intralaboratory consistency (*i.e.,* between workers within the same lab) is greater than interlaboratory consistency.[328] Work has been undertaken to develop standardised methodologies for a variety of analytical methods, including PTA, RMM and DLS.[329–334]

2.2.8.2 Biological Parameters

Protein corona formation is known to dictate biological activity of the nanoparticle, and *in vitro* performance can differ significantly from *in vivo* behaviour.[286] Here, the influence of coincubation in plasma vs serum, the concept of a personalised protein corona and interindividual variation is examined.

Plasma vs Serum

Isolated plasma and human serum are often used as model biological media instead of human blood.[42] However, neither is a true replica; plasma is enzymatically inactive and human serum does not contain coagulation factors.[42] The differences between them and their effect on the composition of the developing protein corona have been discussed previously in **section 2.2.6.2**. In this section, the use of animal plasma and serum on the development of a protein corona and its impact on immunological response *in vivo* will be considered.

Solorio-Rodriguez *et al*. have studied the differences in the composition of the protein corona after incubation in either human or murine (mouse) plasma.[335] What this paper does not explicitly mention, is the origin of the human plasma. We are told that they are volunteer donors, but no information is given regarding their age, sex or ethnicity. Considering that the murine plasma used is from male mice, the assumption can be made that these human donors are likely to also be male. They found 316 identified proteins are common to both the murine and human plasma-derived protein coronae, but when the most abundant proteins are considered, few are common between them.[335] The most commonly identified proteins in each corona are summarised in **Table 2.5**.

Table 2.5: A summary of the most common proteins identified in the protein corona by Solorio-Rodriguez *et al.* From [335]. There is little overlap between the most abundant proteins in human plasma and murine plasma.

Human plasma	Percentage abundance (%)	Murine plasma	Percentage abundance (%)
Albumin	10.00	Albumin	10.00
Immunoglobulins	7.00	serine protease inhibitor A3K	5.88
actin cytoplasmic 1	3.46	serotransferrin	5.29
haemoglobin subunit beta	1.56	alpha-1-antitrypsin 1–2	3.55
serotransferrin,	1.44	haemoglobin subunit beta	3.00
ficolin-3	1.38	fibrinogen gamma chain	2.65
complement C3	1.30	Fibrinogen beta chain	2.56
apolipoprotein A-1	1.29		

These results also highlight an important explanation for why nanomedicines may appear biologically compatible in animal models, but fail in human trials. Immunoglobulins and complement factors are found in such low abundance in the murine model, that immunological responses may well be unseen in mice, and then become apparent in human trials.[335]

Personalised Protein Corona

The concept of a personalised protein corona was introduced in 2014 by Hajipour and colleagues.[46] It was already known that the concentration and conformation of proteins in human plasma can be modified in various pathological states (*e.g.,* cancer, obesity, type 2 diabetes).[336–338] Therefore, it was hypothesised by the authors that this should also lead to alterations in the composition and conformation of identified proteins within the protein corona. In comparison to protein coronae from assumed healthy controls of both sexes, this hypothesis was confirmed.[46] This idea of the altered protein corona within pathological states has since been exploited to enable the development of nanoparticle-enabled blood tests to detect early-stage cancers.[278,339]

Further work has shown that age, sex and ethnicity are also capable of influencing the composition of the developing protein corona.[38,46,47,340] A more recent review from Liu *et al.,* outlines a far greater list of physiological, pathological and lifestyle factors that may alter protein corona composition, and suggests that it is the protein corona that needs to be carefully designed, rather than the 'naked' nanoparticle.[341]

Interindividual Variation

There is a wide range of work within the literature on interindividual variability as it pertains to the response to a given drug.[342–348] This work often focuses on interindividual variation in cytochrome levels (*e.g.,* CYP450; as one of the most important enzymes for drug metabolism).[346,348] Work has also been done to consider the seasonal and circadian variation in several cytokines – as it pertains to the increase in symptoms for inflammatory autoimmune conditions such as rheumatoid arthritis and interindividual variation with the immune system.[349]

2.2.8.3 Cell-related Parameters

These cell-related parameters are some of the least studied parameters for predicting nanoparticle biological fate and efficacy *in vivo.*[43,350] These parameters include: cell type, cell sex, passage number, cell cycle position, whether the cell has undergone the epithelial-mesenchymal transition (EMT) and briefly considering the impact of static cell culture methods.

Cell Type

Varying cell type can lead to differing responses to the same nanoparticle.[351] There are a range of ways cells can internalise nanoparticles (*e.g.,* phagocytosis, caveolae- and clathrin-mediated endocytosis), but not all of these pathways are available for every cell type – hepatocytes, for example, cannot internalise nanoparticles *via* caveolae-mediated endocytosis; caveolin-1 is poorly expressed in this cell type.[350] Response to nanoparticle uptake depends on cell size (and therefore cell cycle position).[43]

Cell Sex

The influence of sex‡ on cell behaviour is well known.[352,353] So too is the impact of sex in clinical studies.[354,355] The influence of cell sex is now considered such an influential parameter in predicting clinical efficacy, that the use of both sexes for *in vivo* experiments is now mandatory in pre-clinical research for several funding bodies including the National Institute of Health (NIH) in the US, as well as UK Research and Innovation (UKRI) in the United Kingdom.[356,357] However, it is only recently that studies to understand sex differences in the physiological response to nanoparticles have been undertaken, and where these studies exist, most of these are murine studies on metal nanoparticles.[358–361] A single study considers the impact of sex-based differences on the effects of polymeric nanoparticles.[362] The sex-linked physiological differences and their impact on nanoparticles *in vivo* has been reviewed by several groups.[363,364]

Passage Number

Passage number may have an impact on cell responses to nanoparticle uptake, but this is often not recorded.[43] Some cell lines *i.e.,* immortalised cell lines can be passaged indefinitely, however most non-cancer cells cannot, and there is a limit of 50 doublings (Hayflick limit) beyond which, the cells enter a state known as replicative senescence, where they stop growing.[365,366] Overpassaged cells are likely to lead to experimental results that cannot be replicated, as the more times the cells are passaged, the more likely it is that their behaviour begins to diverge from that of the original cell line.[43,367]

Cell Cycle Position

The role of cell cycle position on nanoparticle uptake has previously been controversial.[368–370] Rees and co-workers have shown that nanoparticle uptake is increased when cells are in the G2 stage of the cell cycle, clarifying why nanoparticle uptake is usually seen to be heterogenous within a sample.[371] The nanoparticles themselves can also interfere with the cell cycle and potentially induce apoptosis.[372]

EMT Transition

The epithelial-mesenchymal transition (EMT) is particularly important when the efficacy of novel nanoparticles as chemotherapeutics is considered. EMT is a key step in malignant cells becoming capable of undergoing metastasis.[23,43] Malignant cells have unique properties whilst in this state, and it is often difficult to encourage tumour cells to undergo this transition in static 2D culture methods.[23,43]

Static Cell Culture Methods

Conventional cell culture methods are problematic. They are easy and cheap to perform, but static culture methods lack the complex mechanical, chemical and biological cues necessary to encourage cells to adopt their complex *in vivo*

‡ Sex refers to biological attributes of humans and animals, including physical features, chromosomes, gene expression, hormones, and anatomy The terms sex and gender might be used interchangeably, but they do have different meanings.

structures.[22] The issues associated with 2D cell culture methods will be discussed in further detail in the literature review for Part Three of this thesis.

2.2.9 Pre-clinical Models: Do They Translate to *in vivo* Fate in Humans?

Pre-clinical testing is an important stage of drug development. Here, potential drug candidates are screened for toxicity, pharmacokinetics and pharmacodynamics, and efficacy *via* a range of animal models.[373] Animal-based pre-clinical testing is still mandatory for most regulatory bodies prior to the beginning of human trials. Rodent and non-rodent trials are required, irrespective of where the trials take place, the so-called "The two species requirement".[57–59] However, work is ongoing to consider whether single-species testing would be possible.[374]

2.2.9.1 Pre-clinical Models

A wide-range of pre-clinical models are in use. The use of zebrafish, mouse and non-human primate models for both immunological and tumour-bearing models are considered. An extensive study evaluating the immunological differences between human, mouse and several non-human primates has been undertaken by Bjornson-Hooper *et al*.[373] In the UK, as a consequence of the Animals (Scientific Procedures) Act 1986, Zebrafish embryos are considered a "non-protected species", as long as they are not modified and then permitted to reach the final one-third of gestation; mice and non-human primates are considered protected species.[375]

Zebrafish

Zebrafish (*Danio rerio*) are a popular tropical fish, and have in recent years become an important animal model for understanding the function of the immune system. They were first used by Streisinger *et al*. in 1981 to study neuronal development.[376] Since then, a variety of studies have used zebrafish to study everything from innate immune system response, to the development of Alzheimer's Disease.[377–379]

The immune system response of zebrafish, is remarkably similar to responses observed in mammals or in cell culture.[377,380] Zebrafish are particularly useful models for studying immune system response to acute and chronic infection and novel nanoparticles, because adaptive immunity doesn't occur until between week three and week six post-fertilisation.[377,381] It is this gap which makes zebrafish such an attractive model, because it is possible to thoroughly probe the innate immune system response, without complication of the T- cell and B-cell responses of adaptive immunity. Furthermore, their offspring are transparent, which provides opportunities for real-time visualisation of the immune response which is impossible in other animal models.[377] Adult zebrafish also possess a variety of useful properties including: small size, relatively rapid life cycle, ease of breeding, and a growing list of molecular tools for the study of infectious diseases.[381]

Using immunodeficient zebrafish, Yan *et al*. were able to engraft several different types of cancer cells into these zebrafish, and then, because of the

larvae being transparent, observe the behaviour of the cancer cells.[379] Liu and Leach have reviewed the use of genetically modified zebrafish for the development of cancer models.[382] A wide variety of such models have been used previously; they have been used to understand the role of p53, a tumour supressing protein in the development of cancers, but also to obtain further information on the development of skin and pancreatic cancers, as well as identify new genes responsible for the growth of more aggressive forms of malignant melanoma.[382,383] Surprisingly, the tumours grown in these animals are histologically very similar to the analogous tumours that grow in humans.

Mouse (murine) Models

Mouse models are frequently used to test the efficacy and immunological response of novel drugs in humans, but the translation of these results from murine studies often falls short due to differences in the immune system of both species.[324,384–387] Consequently, “humanised mice” have been developed to address this shortcoming. These mice are immunodeficient by nature, and may have been engrafted with a humanised immune system (as is of interest here), or other human genes, cells or tissues.[388]

As discussed previously, the translational applicability of murine studies is often lacking. One such issue is due to the differences in the composition of the protein corona (**section 2.2.8.2**). Further issues with murine studies have been outlined at length by Mestas and Hughes as well as Zschaler *et al*.[384,385] The differences between the immune system in mouse and human include: far more lymphocytes found in mice, human expression of IgG receptors that mice do not and differences in T-cell development and regulation.[384] Adaptive and innate immunity also vary.[384,385] As a consequence of the poor translational applicability of murine studies regarding immune system response to novel drugs, humanised mouse models have been developed. Humanised mice were initially developed in 1988, following the discovery of a spontaneous mutation in a commonly-used strain of laboratory mice.[389,390] They are often used to study antiretroviral drugs and the development of Human Immunodeficiency virus (HIV).[391] These humanised mice show some similarities to the human immune system *e.g.* certain types of T-cells.[390]

A range of tumour-bearing mouse models have been used to study oncogenesis and the efficacy of novel chemotherapeutics. These include Xenograft models (where human tissues are transplanted into immunodeficient mice) and spontaneous oncogenesis models. Two distinct types of xenograft models have been developed with immunodeficient mice. They may either be mice inoculated with human-derived cancer cell lines (cell-derived xenograft (CDX)), or patient-derived samples of tumours are implanted into the mice (patient-derived xenograft (PDX) models.[392,393] One disadvantage of these xenograft models is that they all use immunodeficient mice, limiting their translational applicability.[393] PDX models are useful, and many studies show their translational value in successfully identifying clinically effective novel drugs in humans.[394,395] However, Jackson and Thomas note that these models certainly are not perfect, are often biased towards more

aggressive tumours as these are easier to propagate and ethical concerns exist – pain relief may not be given due to fears of this confounding results and few studies have assessed objective markers of pain in mice.[396–398] They make calls for non-animal experiments using human tissue to come into common practice.[396] It is also possible to study tumour growth and other aspects of their behaviour in spontaneous oncogenesis models.[392] These models involve the transplantation of healthy human cells that have tumour suppression genes switched off, or oncogenes overexpressed. They recapitulate the change in human cells from normal to pathological states.[392] Finally, humanised mice with human immune systems can also be used for investigating various forms of cancers, an extensive overview is given by Tian *et al*.[392] Further issues with the use of murine models for cancers is that young mice are frequently used, these poorly mimic the older, obese human population who frequently develop cancers.[399,400]

Non-human Primates

Non-human primates (NHPs) refer to the animals of the order Primates, *e.g.* great apes and monkeys, but not humans (**Table 2.6**). They are also some of the most controversial animal models used in biomedical research; the controversy frequently stems from their similarity to ourselves.[401] Some have suggested that NHPs should not be used at all for clinical studies, because of the small, but significant biological differences that exist, and instead such studies should be carried out on small groups of humans.[402] This seems rational, but is forbidden by the Nuremberg Code[§], which defines a set of ethical principles for human experimentation.[403]

Experiments on great apes have been *de facto* banned within the United Kingdom since 1997, as the Home Office simply do not grant project licenses for such work. They have been legally banned in EU member states since 2013, although a loophole does exist that would permit such work in the extreme scenario of a novel disease being discovered where no other animal model, or alternative method would be a suitable human mimic.[404]

[§] The Nuremberg Code states the following "… 3. The experiment should be so designed and based on the results of animal experimentation and a knowledge of the natural history of the disease or other problem under study, that the anticipated results will justify the performance of the experiment."

Table 2.6: A summary of non-human primate species that have historically been used for biomedical research in the United Kingdom. Adapted from [401]

Great Apes	
Chimpanzees	Not since 1986
Bonobos	
Gorillas	
Orangutans	
Old World Monkeys	
Macaques	
Baboons	Not since 1998
Prosimians	
Lemurs	Not since 1991
New World Monkeys	
Marmosets	
Tamarins	
Capuchins	
Squirrel Monkeys	

Non-human primates are the closest related animals, so it would be expected that the immune system is likely to be the most like that in humans. This closeness between NHPs and humans means there is greater validity for the application of these results to humans, than can be obtained with other pre-clinical models *e.g.* mice.[402] The immune system of the Rhesus macaque is well-studied and frequently used for immunology studies, but it is the adaptive rather than innate immunity that is better understood.[405,406] Many of the viruses known to infect humans also infect NHPs, and it is for this reason that they are often useful animal models, particularly for the development of vaccines.[406] However, they are not perfect replicas for the human immune system. Genome-wide sequencing has previously highlighted three changes, which likely explain why humans are much more susceptible to HIV/AIDS compared to other primates.[407] On the other hand, there are many respiratory infections that primates are more susceptible to than humans.[408]

For tumour-bearing models, the most common hosts are chimpanzees, baboons, gorillas, macaques, squirrel monkeys and marmosets.[409] It has been shown previously that every human cancer gene has an orthologue in NHPs.[410] For as yet unknown reasons, NHPs in captivity have surprisingly low levels of spontaneous cancers, and for this reason have been less useful as tumour models.[411,412]

Summary

If these animal-based pre-clinical models are so poor at predicting the efficacy of novel nanotherapeutics in humans, what should be done? Moreno and Pearson have previously suggested the following steps need to be taken to help prevent the attrition of drugs through the drug development pipeline: i) better pre-clinical drug development to identify the least toxic and most efficacious drugs, this could be done through identification of relevant tumour targets, and genotyping to identify the population in which the drug is likely to be most effective (discussed further in **section** Error! Reference source not found.); ii) better pre-clinical models need to be developed. The current models

show poor correlation between performance in the model and efficacy in phase II trials. New models would better capitulate the important parameters of tumour biology and their microenvironment, more successfully than current models, microfluidic or "lab-on-a-chip" devices could be used to accomplish this objective and is discussed further in **Section** Error! Reference source not found., iii) finally Moreno and Pearson also highlight ways in which trial design could be modified, so that the least successful drug(s) could be dropped from the trial at a much earlier stage.[413]

In addition to the very questionable validity of pre-clinical models and the impact this has on clinical trials – significant injury or death of human participants and discovering the drug has no effect, or an entirely different effect in humans compared to those observed in preclinical models. There has also been the introduction of the "3 R's of animal research".[31,414] These were first proposed by Russell and Burch in 1959. The aims of the 3R's are: to replace the use of animals in research; reduce the number of animals used within clinical trials, and refine techniques to minimise pain, suffering and distress of the animals which cannot be replaced.[31] Significant progress on the implementation of the 3R's has been made. The European Pharmacopeia is taking significant steps towards having completely phased out the rabbit pyrogen test by 2026,[415] the FDA (Food and Drug Administration) Modernization Act 2.0, signed late December 2022, no longer mandates the use of animal-based pre-clinical studies,[416] The National Centre for the Replacement, Refinement and Reduction of Animals in Research (NC3R's) in the UK, will no longer fund any project looking at reducing animal use nor those investigating refinement of current techniques.

2.2.9.2 Regulatory Guidance on Nanomedicine Evaluation

One of the biggest challenges in pre-clinical to clinical translation is the lack of specific published regulations for nanomedicines. Currently none exist.[13,45,68] There are however national and international efforts ongoing in an attempt to rectify this.[13] As a consequence of having no regulatory framework for nanomedicines, it may be that in one country they are considered medicines, in another a medical device and thus have differing standards they must meet before being granted clinical approval.[68] Unsurprisingly, novel nanomedicines are considered slightly differently by both the FDA and European Medicines Agency (EMA). A more detailed discussion of the issues with regulatory guidance for nanomedicines has been undertaken by several groups.[68,417]

FDA

The FDA currently has no specific regulatory framework for nanomedicines.[418] They have, however published a draft guidance document on the use of nanotechnology in medicinal products.[419]

The Food and Drug Administration regulate drugs and other medical devices under two distinct and separate statutes of US Law. These are the Food, Drug and Cosmetics Act (FDCA) which handles chemically-synthesised drugs and medical devices and the Public Health Service Act (PHSA) which deals with

biologically derived medicinal products.[418] These classifications are particularly problematic for novel nanomedicines, as it is possible for them to come under both statutes. Therefore, they are reviewed by the FDAs Office of Combination Products and then assessed by the nanoparticle's primary mode of action, whether that is as a drug, a biologic or as a device.[420]

EMA

In comparison to the FDA, the European Medicines Agency has published comparatively more regulatory guidance regarding nanomedicines, in the form of "reflection papers".[421–424] They have also began to consider how regulatory frameworks would handle a new generation of nanomedicine, but also how to regulate the introduction of so called "nanosimilars".[425]

2.3 Chapter Aims and Objectives

In this chapter, *in situ* characterisation methods will be used to understand the impact of protein corona formation on PLGA and PLGA-PEG nanoparticles. Previous studies have shown that *ex situ* characterisation results in the loss of the loosely-bound 'soft corona' around nanoparticles, and protein corona formation is known to have a significant influence on nanoparticle biological fate.[17–21]

This aim will be achieved by completing the following objectives:

1. Optimise protocols and methodology for evaluating protein corona effects on nanoparticle physiochemical properties *via* RMM and PTA.

Protocols will be developed and optimised to evaluate the use of RMM and PTA for the *in situ* measurement of protein corona effects on nanoparticle size under conditions where protein concentrations are biologically relevant (*e.g.* cell culture studies where media is supplemented with 10% FBS).

2. Establish incubation durations in serum and their impact on PLGA/PLGA-PEG characteristics as measured by RMM, DLS and PTA.

A series of timepoint experiments will be performed using PLGA/PLGA-PEG nanoparticles to understand the influence of incubation time, temperature, serum origin and impact of PEGylation on protein corona formation around PLGA nanoparticles. The physicochemical characteristics will be analysed *via* RMM, PTA and DLS (as appropriate).

2.4 Materials and Methods

2.4.1 Materials

Human serum [H4522] was purchased from Sigma Aldrich (Gillingham, UK), foetal bovine serum was purchased from Thermo Fisher (Invitrogen). Both were centrifuged to remove any insoluble particles or large agglomerates. Bradford assays were used to determine total protein concentration of Human serum (~70 mg mL^{-1}) and FBS (33 mg mL^{-1}). Phosphate-buffered saline (PBS) was purchased from Sigma Aldrich and used as per manufacturer's instructions. Bradford Assay kit [23246] and stock BSA [23209] were purchased from Thermo Fisher and used as per manufacturer's instructions. 100 nm PLGA and PLGA-PEG nanoparticles were purchased from Nanovex (Asturias, Spain), and lyophilized in-house before long-term storage at -80°C.

2.4.2 Methods

2.4.2.1 Lyophilisation of PLGA and PLGA-PEG Nanoparticles

PLGA and PLGA-PEG nanoparticles were lyophilised in-house by Dr Zahra Rattray. No further experimental details are available.

2.4.2.2 Preparation of Stock Solutions and Samples

On the day of experiments, nanoparticles were removed from -80°C storage and allowed to reach ambient temperature. 1 mg of 100 nm PLGA nanoparticles were resuspended at a concentration of 1 mg mL^{-1} in ultrapure water and sonicated for 60 seconds. The nanoparticle solution was aliquoted and further diluted to give a final concentration of 0.1 mg mL^{-1}. These were then frozen at -20 °C for long term storage. Defrosted aliquots were kept at 5 °C for up to 5 days, before being discarded. Stock solutions of serum (FBS or human serum) were prepared by diluting serum with ultrapure water to obtain necessary concentrations (20, 40, 80 % v/v FBS, and 1, 10 % v/v human serum). Such solutions were then stored at 5 °C for up to 5 days, before being discarded.

Each sample was prepared, to give a final nanoparticle concentration of 0.01 mg mL^{-1}. Samples were incubated between 0 and 24 hours (0, 2, 4, 24 hours), in temperature-controlled rooms at either ambient (25 °C) or physiological (37 °C), with gentle end-over-end rotation provided by a tube rotator, to prevent sedimentation effects on protein corona formation. Following incubation, samples were placed on ice, and analysed immediately.

2.4.2.3 Quantification of Protein Concentration in Serum via Bradford Assay

Total protein concentration of the sera used in this work was quantified *via* Bradford assay, this is an adaptation of the method given by the manufacturer.[426] These assays were performed by Miss Merrit Rothe.

A suitably sized aliquot of Bradford reagent was prepared and permitted to warm to ambient temperature for 30 minutes before the assay was undertaken. Bovine serum albumin (BSA) standards were prepared in the same buffer as the unknown samples, following the guidelines given in **Table 2.7**.

Table 2.7: Composition of each sample included in the Bradford Assay

Sample	Volume of diluent (µL)	Volume (µL) and source of BSA	Final concentration (µg mL^{-1})
A	0	300 of stock	2000
B	325	325 of stock	1000
C	325	325 of sample B	500
D	325	325 of sample C	250
E	325	325 of sample D	125
F	325	325 of sample E	62.5
G	400	0	0 *i.e.* Blank

10 µL of sample/known standard was pipetted into each well of a 96 well plate. Each sample and known standard was measured in triplicate. 300 µL of Bradford reagent was introduced into each well. Plates were incubated for up to 5 minutes. Absorbance was measured at 600 nm.

Data Analysis

Absorbance of the blank (Sample G) was removed from all readings. A protein standard curve (concentration of known standard vs. absorbance at 600nm) is plotted for each plate. Protein standard curve can then be used to determine protein concentrations of unknown samples (**Appendix D**).

2.4.2.4 Particle Tracking Analysis

PTA measurements were performed using an NTA system (NS300, Malvern Panalytical, Malvern, UK), fitted with a 488 nm laser. Using a syringe driver, where flow rate was set to 50 (arbitrary units), a 1 mL syringe was used to load the samples into the system. Three captures each of 60 seconds duration were obtained and averaged for each sample. Camera settings were manually chosen to keep them constant for each set of samples – changing camera level and/or detection limit has previously been shown by Gross *et al.* to alter apparent nanoparticle size.[311] The camera settings are shown in **Table 2.8**.

Table 2.8: Camera setting for Particle Tracking Analysis

Protein source	Camera Level	Detection limit
1x PBS	14	3
FBS	11	13
Human Serum	5	15

Detection limits were chosen such than < 5 'false particles' per frame were identified. These are instances where background noise has been erroneously tracked as particles.[427] Between samples, the system was flushed with PBS buffer to remove residual particles and to prevent cross-contamination between samples.

2.4.2.5 Dynamic Light Scattering

Dynamic light scattering measurements were performed using a Zetasizer Nano-ZS (Malvern Panalytical, Worcestershire, UK) equipped with a 633 nm He-Ne laser. All measurements were performed in triplicate and samples were dispersed in ultrapure water and measured at ambient temperature (25 ℃)

using the non-invasive backscatter (173°) setting, to rule out particle agglomeration following lyophilisation and storage.

This system was additionally used with electrophoretic mobility scattering to measure zeta-potential. In this case, samples were suspended in ultrapure water and transferred to a folded capillary cell [DTS1070] for analysis.

2.4.2.6 Resonant Mass Measurement

Resonant mass measurement was undertaken using the Archimedes system (Malvern Panalytical Malvern, Worcestershire, UK), fitted with a nano sensor. Detection limit of the system was set at 0.01 Hz; corresponding to a lower particle size limit of 136 nm. Prior to analysis, the system was calibrated using 508 nm polystyrene latex particles (Malvern Panalytical) and 100% Deuterium oxide (D_2O) (Sigma Aldrich) for bulk sensitivity calibrations. For samples containing FBS, the density of the medium was determined using a value of 1.2 mg mL^{-1} for FBS and 0.998 mg mL^{-1} for water, such that 10% FBS has a density of 1.02 mg $mL^{-1.}$ The negative buoyancy setting and density of PLGA (1.30 g cm^{-3}) was used for all measurements. As with the method reported by Krueger *et al.*, the system was considered to be clean if Milli-Q water could be run through the system for 5 minutes with fewer than five particles being detected.[333] All samples were measured in triplicate. Analysis was performed using V1.21 of the Archimedes software.

2.4.2.7 Statistical Analysis

Statistical analysis was performed using Origin 2019b. Three-way ANOVA or paired t-tests were used as appropriate to explore the relationship between nanoparticle attributes (*e.g.,* size, dry mass) and incubation parameters. A $P < 0.05$ was considered statistically significant. R^2 values reported for experiments where the limits of RMM were considered.

2.5 Results and Discussion

Particle size is well-recognised as a key characteristic which impacts nanoparticle-biological interactions and subsequent biological fate.[49,428] Therefore, understanding colloidal stability of nanoparticles following dispersion in protein-containing media is a important step in the design and process development of novel nanotherapeutics.

This section begins with baseline characterisation of 100 nm PLGA/PLGA-PEG nanoparticles following in-house lyophilization for long-term storage. Experiments were performed to first assess whether DLS is suitable for analysis of nanoparticle suspensions in protein-rich media, before using the newer and higher-resolution particle metrology techniques of particle tracking analysis (PTA) and resonant mass measurement (RMM). Finally, RMM and PTA were used to study the possibility of orthogonal methods for assessing protein corona effects on nanoparticle size distributions.

2.5.1 Baseline Analysis of Nanoparticles

The PLGA and PLGA-PEG nanoparticles used within this work were characterised before incubation with protein-containing media (FBS and human serum). **Table 2.9** summarises the characteristics of the PLGA and PLGA-PEG nanoparticles used, as determined by the manufacturer. Mean particle size and polydispersity index were measured *via* DLS, whilst zeta potential was measured by M3-PALS (Mixed Measurement Mode Phase Analysis).

Table 2.9: A summary of characteristics of PLGA and PLGA-PEG nanoparticles before modification. These values are obtained directly from the manufacturer (Nanovex) and errors were not provided.

Nanoparticle identity	Mean particle size (nm)	Polydispersity Index (PDI)	Zeta potential (mV)
PLGA	106.7	0.039	-31.2
PLGA-PEG	103.5	0.110	-30.0

However, these nanoparticles were received suspended in ultrapure water. This is problematic, as PLGA nanoparticles can undergo degradation *via* several pathways, including hydrolysis, and therefore are only suitable for storage in this state for short time periods (< 60 days).[317,429] To enable long-term storage, these nanoparticles were subject to lyophilisation (also known as freeze-drying or cryodessication) and changes in particle size and other physicochemical characteristics are known to be possible.[429] Consequently, in-house analysis *via* DLS, NTA and RMM was performed to determine particle size, polydispersity index and zeta potential following lyophilisation.

Table 2.10: Baseline characterisation of 100nm PLGA and PLGA-PEG nanoparticles (0.01 mg mL^{-1} in ultrapure water, n = 3) following lyophilization to enable long-term storage. Mean particle size, PDI and Zeta potential were measured by DLS, PTA and RMM. Errors are given as standard deviation.

Nanoparticle identity	Particle size (nm)			Polydispersity index (PDI)		Zeta potential (mV)
	Z-ave size (DLS)	RMM	PTA	DLS	RMM	DLS
PLGA	135 ± 3.6	121 ± 5.1	106 ± 35.6	0.05 ± 0.03	0.056 ± 0.003	-21.8 ± 2.0
PLGA-PEG	140 ± 0.9	120 ± 1.2	108 ± 26.7	0.08 ± 0.02	0.066± 0.0011	-15.4 ± 1.2

In comparison to the characteristics reported in **Table 2.9**, the process of lyophilisation alters nanoparticle physiochemical characteristics. Comparing Z-average particle size as measured *via* DLS pre- and post- lyophilisation, changes in particle size are seen for both PLGA and PLGA-PEG (106.7 to 135 nm) and (103.5 to 140 nm) respectively. Even though changes in nanoparticle size are observed, size ratio (ratio of particle size pre- and post-lyophilisation) does not diverge from 1, suggesting lyophilisation was successful and nanoparticles have not been subjected to stresses that would encourage aggregation. The polydispersity index of these samples is comparatively less impacted by lyophilisation and remains < 0.1 in each case, indicative of monodisperse samples, which further suggests successful lyophilisation. Zeta potential as measured *via* electrophoretic light scattering is also altered by the process of lyophilisation, decreasing by approximately 10 mV in each case, but even following lyophilisation, both samples are moderately negatively charged. It is suggested that the change in zeta potential is an effect of the interaction between cryoprotectant (sucrose) used during the process and the nanoparticle surface.[429] The change in zeta potential may influence both formation and exact composition of the protein corona.[265,430]

The analytical techniques used here and later on in this chapter include DLS, RMM and PTA. These techniques have been chosen for a number of reasons: all three techniques are capable of nanoparticle analysis *in situ* so require no separation of the nanoparticles from their incubation medium, making them much easier to use; DLS is a commonly-used particle sizing technique, so it was considered to be sensible to use this – at least for baseline analysis where the nanoparticles were suspended in non-protein containing media; PTA is a much newer technique capable of high-resolution, particle-by-particle analysis, whilst RMM is not an optical method, but is capable of high-resolution analysis. These three techniques rely on two different physical principles for their analysis. Both DLS and PTA rely on light scattering as particles move due to Brownian motion. Particle size (hydrodynamic particle radius) in both cases is defined by Stokes-Einstein equation (**Equation 3**), and therefore can be directly compared. On the other hand, RMM does not rely on light scattering, but instead on the change in resonant frequency of the resonator within the

MEMS chip within the device. It does not give hydrodynamic particle radius, instead gives buoyant mass which is a measure of the difference between the particle density and that of the carrier fluid. If it is assumed the object causing the change in resonant frequency is spherical, then particle diameter can be calculated. Therefore these techniques can be used in an orthogonal fashion.

Reasonable agreement can be seen between the particle sizes reported *via* DLS, RMM and PTA (**Table 2.10**). The larger particle size as reported *via* RMM compared to DLS and/or PTA is expected. The lower detection limit of RMM (~135 nm) is higher than that of DLS and PTA and consequently, this would be expected to increase apparent particle size, since the smallest particles cannot be seen *via* RMM. Furthermore, polydispersity index as measured *via* DLS and RMM agree within error in each case. In summary, all three techniques used here (DLS, RMM and PTA) are suitable for baseline characterisation; however, this is not the case once the polymeric nanoparticles have been co-incubated with protein-containing media.

2.5.2 Dynamic Light Scattering

Dynamic light scattering is a popular analytical technique frequently used for the size analysis of nanoparticle suspensions. Much of its popularity comes from its simplicity and lack of necessary sample preparation *i.e.* it permits analysis *in situ*.

2.5.2.1 Timepoint Experiment

For this set of experiments, only PLGA nanoparticles (final concentration 0.01 mg mL^{-1} co-incubated in 10 % or 20 % FBS (3.3 mg mL^{-1} and 6.6 mg mL^{-1} protein respectively - determined by Bradford assay, see **Appendix D**) were used. These experiments were performed to assess whether DLS could be used to probe changes in z-average particle size as a function of incubation time and temperature. Z-average particle size, peak 1 and peak 2 data *via* DLS can be found for this data set and those in 10% FBS at 37 °C and 25 °C in **Appendix A**.

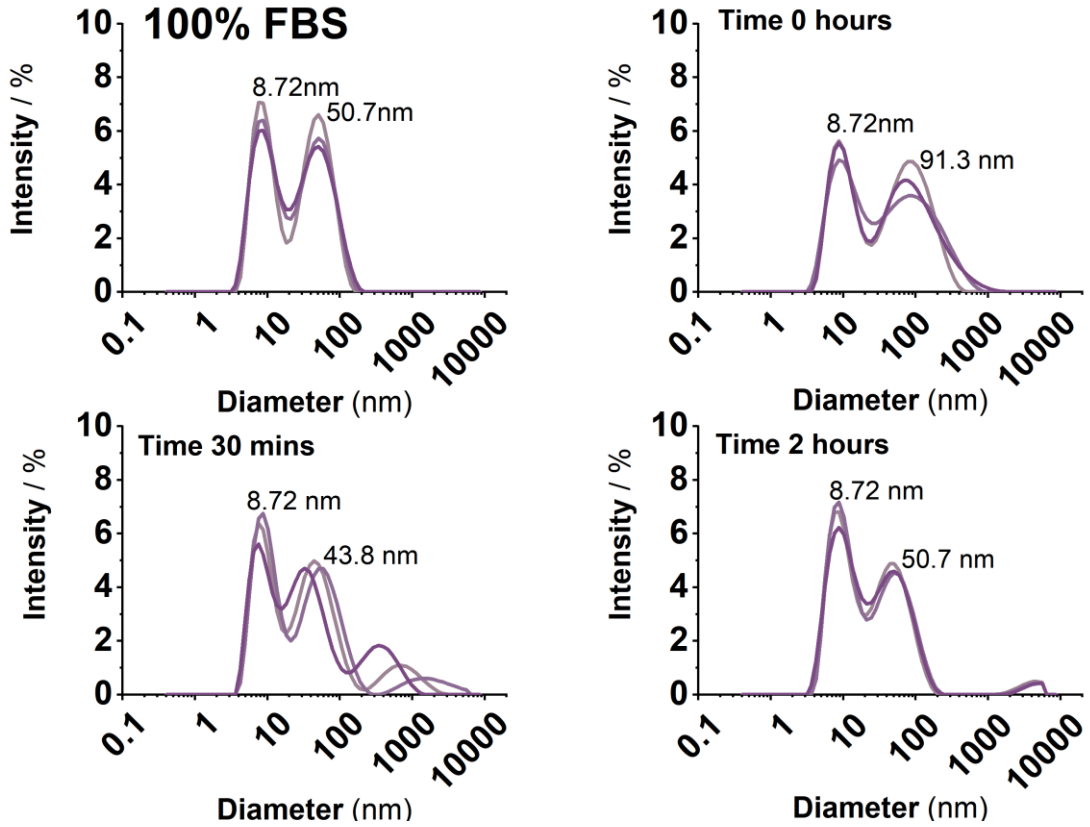

Figure 2.16: Intensity size distribution for 100 nm PLGA nanoparticles in 20 % FBS, at 37 °C with incubation times between 0 and 2 hours. 100% FBS used as control. DLS did not resolve any changes in particle size. Each coloured trace represents a single repeat. All samples were measured in triplicate.

Using DLS, it was not possible to resolve two clear peaks corresponding to FBS and PLGA nanoparticles (**Figure 2.16**). It was also not possible to resolve two clear peaks where the incubation medium contains 10 % FBS (*e.g.* cell culture experiments) (**Appendix A**). Therefore, it was also not possible to detect changes in particle size because of protein corona formation. These observations are consistent with those previous assessments in the literature in which DLS analysis of the protein corona is performed.[431] It is suggested that the ensemble nature of particle size distribution determination *via* DLS, detects the most abundant component within the sample (*i.e.,* FBS) and is therefore unable to resolve the presence of 100 nm PLGA nanoparticle occurring at a much lower abundance.[431]

Resolution of clear peaks corresponding to FBS and PLGA was challenging, even under conditions where these peaks should be clear and easily resolved. Therefore, titration experiments were undertaken to see if clear peaks could be resolved when the incubation medium contains a lower concentration of protein.

2.5.2.2 Titration Experiment

These experiments were conducted to determine a concentration of FBS where both PLGA nanoparticles and protein peaks could be resolved. PLGA

nanoparticles were incubated in varying concentrations of FBS (0.02 %-100 %), corresponding to 0.006 mg mL^{-1} - 33 mg mL^{-1} protein respectively.

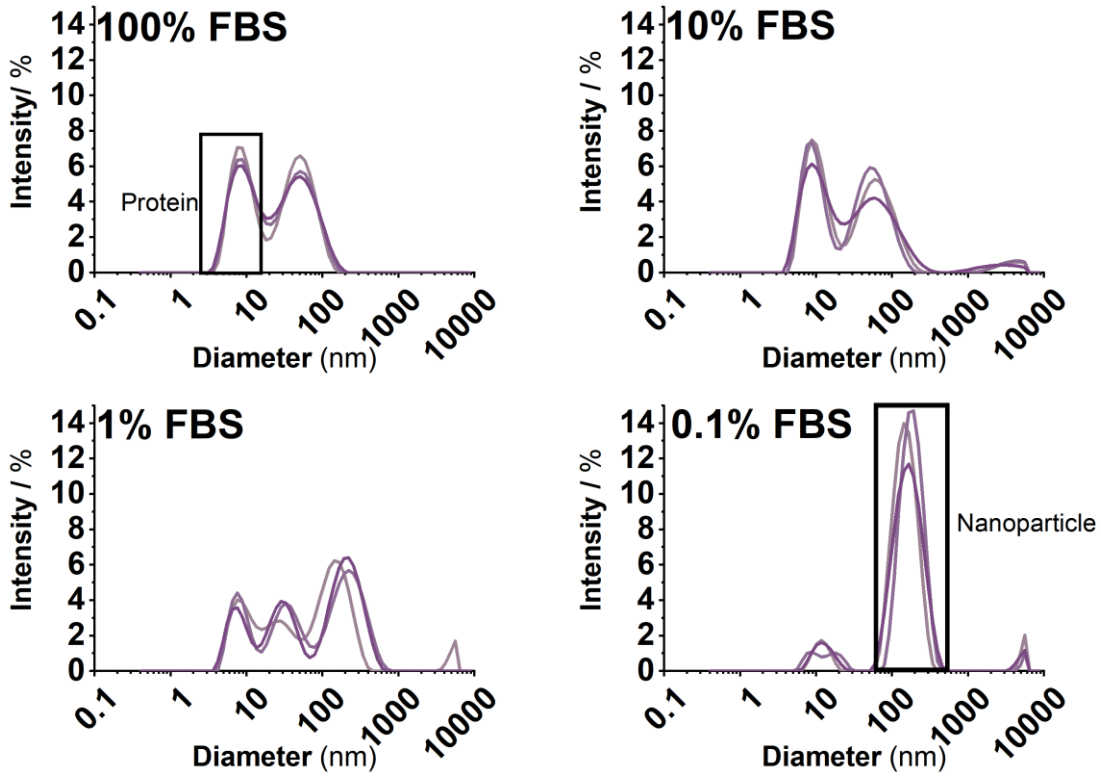

Figure 2.17**:** Intensity distributions for the incubation of PLGA nanoparticles in varying concentrations of foetal bovine serum (FBS). 100% FBS used as control. The concentration at which both components were able to be resolved via DLS significantly differs to physiologically-relevant values. Only 0.1 %, 1 %, 10 % and neat FBS are shown (n= 3), the remainder of this data set can be found in **Appendix B**. Peaks corresponding to FBS and 100 nm nanoparticles have been highlighted to show the approximate necessary concentration at which both components can be seen.

The intensity-based size distributions (**Figure 2.17**), show that to observe a clear and well resolved peak for PLGA nanoparticles, a 0.1 % concentration of FBS is required. These values are outside physiological parameter ranges and therefore do not represent biologically-relevant conditions for *in vitro* assessment of protein corona formation. A similar experiment was performed in which PLGA nanoparticles were incubated in human serum, and the same results were obtained *i.e*. that the target sample protein concentrations needed to resolve both protein and nanoparticle peaks are significantly lower than physiological values (**Appendix C**). The data obtained from performing experiments at such low serum concentrations would not be physiologically relevant and of limited use in terms of mimicking *in vivo* relevant conditions.

Both sets of experiments undertaken here show that the low resolution of DLS limits it's use as a technique for the measurement of protein corona effects on nanoparticle size distributions *in situ* where physiologically-relevant levels of protein (*e.g.* cell culture studies) are used. Therefore, higher-resolution 'particle-by-particle' analysis are required. Consequently, further analysis will

be undertaken using both particle tracking analysis and resonant mass measurement.

2.5.3 Particle Tracking Analysis

Particle tracking analysis was used to measure the variation of PLGA and PLGA-PEG nanoparticle physicochemical characteristics following incubation with serum as a function of incubation time, temperature, protein source and its concentration. The incubation time beyond which nanoparticle size remains constant (equilibrium conditions) was also determined.

Samples were firstly incubated in phosphate buffered saline to determine the impact of incubation time, temperature and nanoparticle identity, but also to assess the impact of gentle end-over-end rotation on PLGA nanoparticle aggregation. If significant aggregation had been seen over short time points, then it could be determined that the nanoparticles were subject to too much shear under these conditions, this was not observed. Later PLGA and PLGA-PEG nanoparticles were incubated with 10 % and 20 % FBS (3.3 and 6.6 mg mL^{-1} protein respectively), as well as 1 % human serum (0.7 mg mL^{-1}). A higher concentration (10 %) of human serum (~ 7 mg mL^{-1}) was attempted for a single sample, but was unsuccessful and not explored further.

2.5.3.1 Control Samples in PBS

PLGA and PLGA-PEG nanoparticles were incubated in phosphate buffered saline (PBS) for between 0 and 24hrs. These samples were used as controls (relative to serum-treated samples) to assess whether nanoparticle size changes, when incubated at ambient and physiological temperature, and exposed to a medium lacking protein (*i.e.* buffer conditions).

At 0 hours, the distribution is unimodal, with a mean particle diameter 116 -124 nm, for all four samples (**Figure 2.18**). By 24 hours, a multimodal distribution is observed, with a corresponding reduction in particle number concentration.[**] This suggests the presence of particle agglomerates within the samples. These effects are more pronounced under physiologically-relevant temperature (37 °C) conditions.

As PBS contains no proteins, the size change cannot be due to developing a protein corona. Therefore, what these results show is the expected solution-phase behaviour of polymeric (or indeed any) nanoparticle, and the effect of the end-over-end rotation (implemented during incubation to reduce sedimentation of nanoparticles), on particle size distribution.[432] Nanoparticles are known to aggregate in solution, as a way of lowering their surface free energy, and in a solid-liquid colloid the solid particles will not stay suspended in solution indefinitely.[433] It is then the formation of aggregates which leads to

[**] This is an interdisciplinary project and as such, is likely to be of interest to researchers from a number of different fields. From a Chemistry and (Chemical) Engineering perspective, concentration typically refers to molar concentration, or otherwise mass per volume *e.g.,* g L^{-1}. For Pharmacy, however, concentration is often particle number per volume e.g., particles/mL. For the avoidance of ambiguity, where particle number per volume is used, this will be referred to as particle number concentration.

the decrease in particle number concentration seen here, and in all other samples studied in this work (**Figure 2.19**).

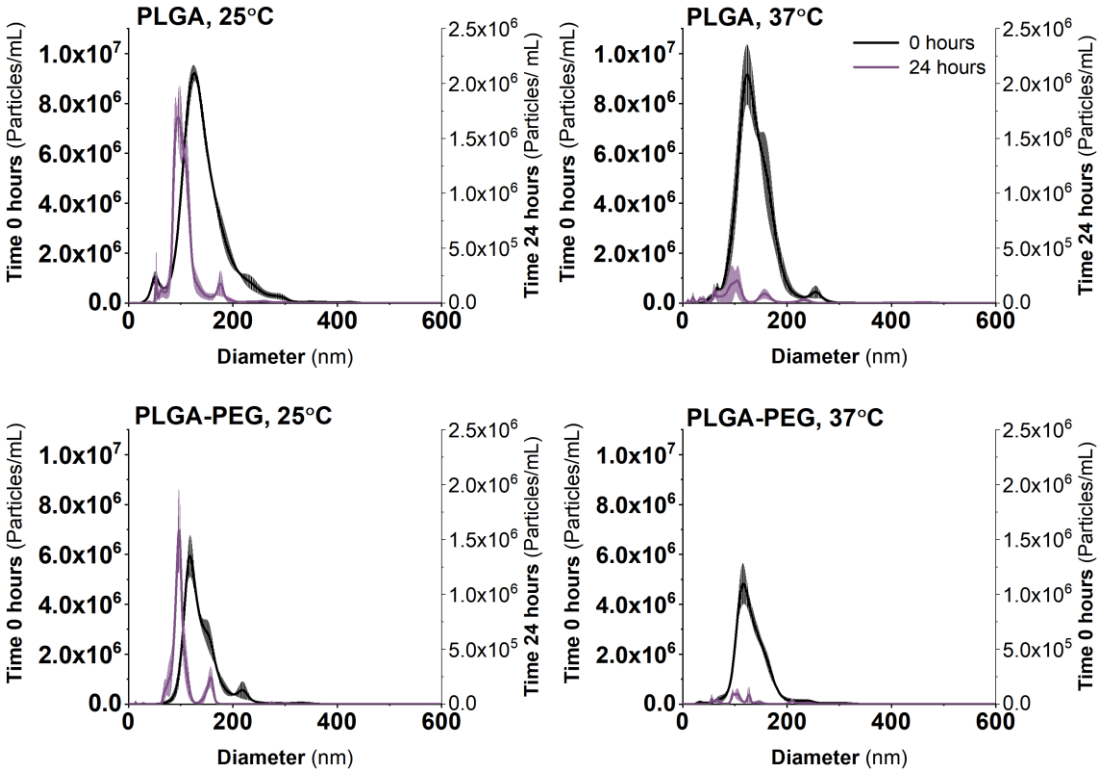

Figure 2.18: The effect of incubation time, temperature and particle identity on particle agglomeration in PBS, as determined *via* particle tracking analysis. These graphs show a significant decrease in particle number concentration with incubation time. Three-way ANOVA was used to determine statistically significant ($P < 0.05$) incubation parameters. No statistically significant parameters were found.

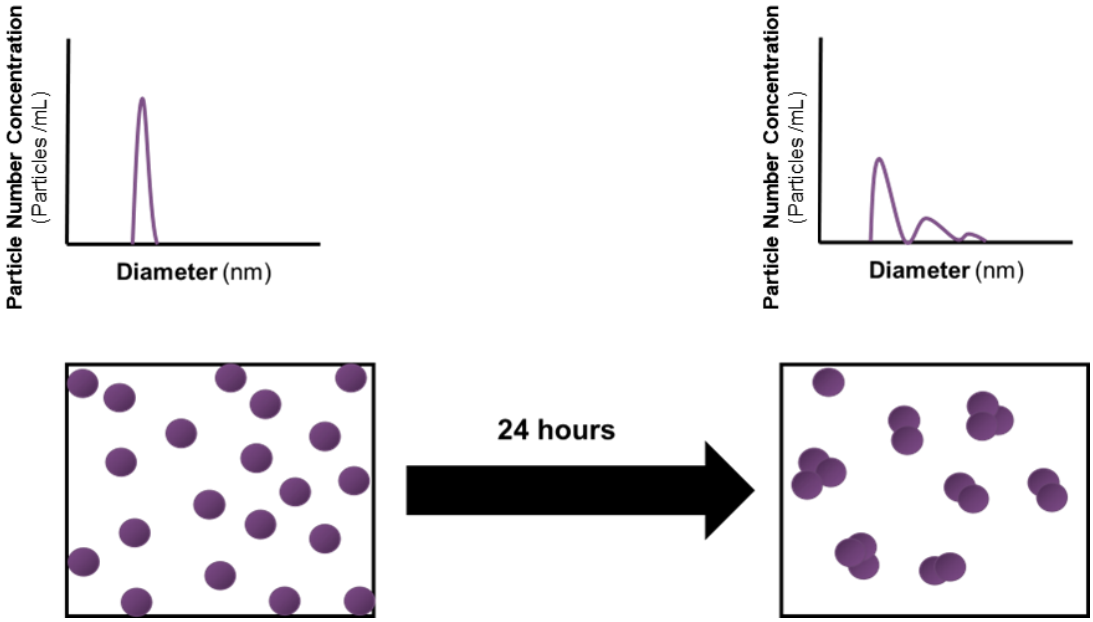

Figure 2.19: An illustration to explain the impact of particle aggregation on particle number concentration and why this falls dramatically as incubation time increases. Each square contains 20 particles. Left hand square represents the sample at time 0 hours, right hand square after 24 hours.

2.5.3.2 Samples in FBS

PLGA and PLGA-PEG samples were incubated in 10 % and 20 % FBS, ~3.3 mg mL^{-1} and 6.6 mg mL^{-1} protein content, respectively to evaluate temporal effects of PLGA nanoparticle treatment with serum, and subsequent effects on nanoparticle characteristics (size and particle number concentration).

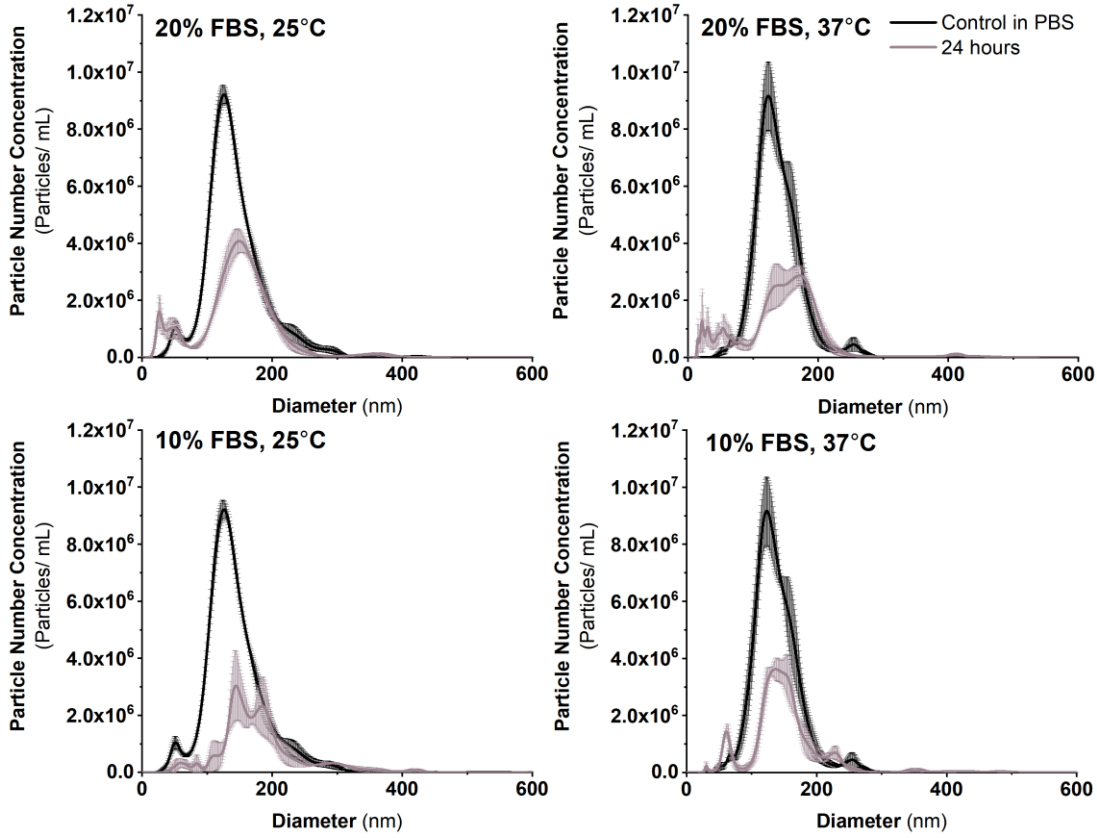

Figure 2.20: The effect of incubation time, temperature and FBS concentration on PLGA nanoparticle size distributions measured by PTA (n=3). The number concentration of PLGA nanoparticles decreases significantly with incubation time. A three-way ANOVA was used to identify statistically significant ($P < 0.05$) incubation parameters The results obtained are as follows: incubation time (0 vs 24 hours) ($p=0.12$), incubation temperature (25°C vs 37°C) ($p=0.654$) and protein concentration (10% vs 20% FBS) ($p= 0.013$).

Figure 2.20 shows how the particle size distribution of PLGA nanoparticles changes as a function of time, incubation temperature and FBS concentration. There is comparatively little change in the samples between 0 and 24 hours where incubation temperature is 25°C, but as with the samples in PBS (**Figure 2.18**), the formation of larger agglomerates can be seen. Where the incubation temperature is 37°C, a greater decrease in particle number concentration, particularly at 150 nm can be seen; this implies the formation of larger aggregates in these samples. These findings (*i.e.* particle agglomeration and increase in particle size following protein corona formation) are consistent with previous reports in the literature.[260,433]

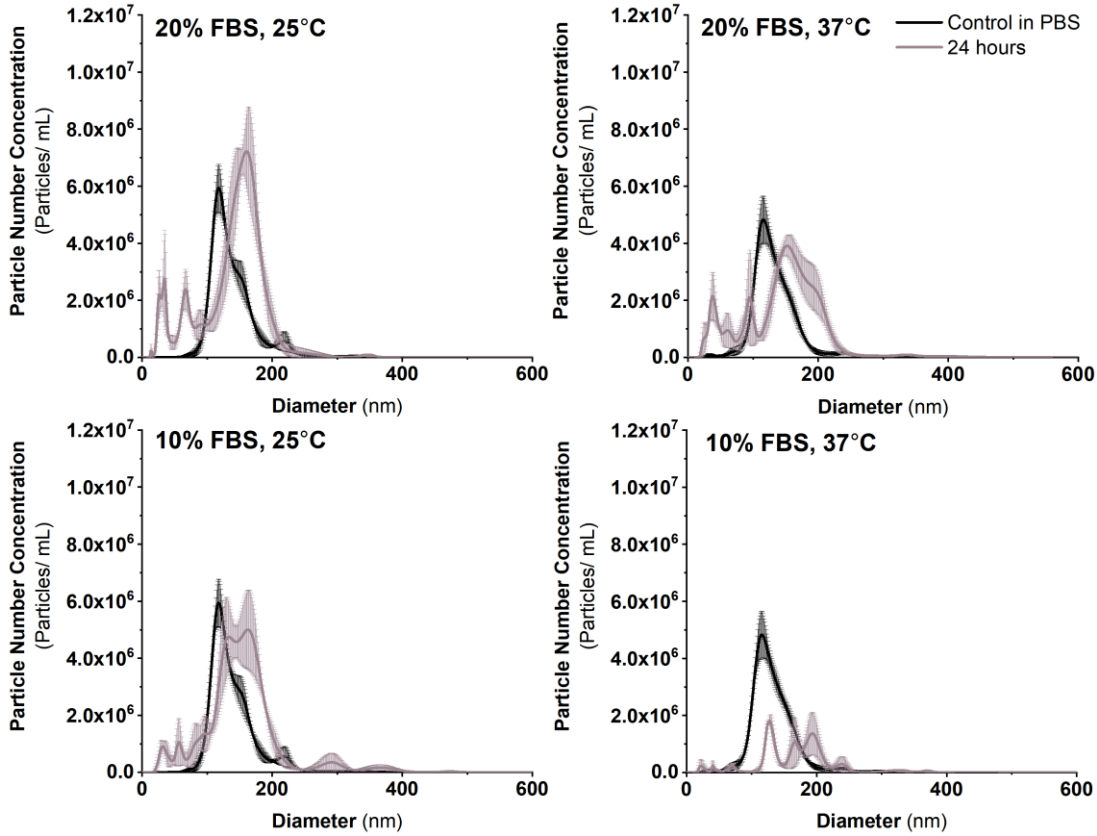

Figure 2.21: The effect of incubation time, temperature, and concentration of protein on particle agglomeration of PLGA-PEG in FBS as measured by PTA (n=3). Particle number concentration corresponding to PLGA nanoparticles decreases significantly with incubation time and as a function of FBS concentration. A three-way ANOVA was used to identify statistically significant ($P < 0.05$) incubation parameters. The results obtained are as follows incubation time (0 vs 24 hours) ($p=0.61$), incubation temperature (25°C vs 37°C) ($p = <0.001$) and protein concentration (10% vs 20% FBS) ($p= 0.002$). Via paired t-test, there was no statistically significant difference between PLGA and PLGA-PEG found ($p = 0.49$).

Figure 2.21 shows how the particle size distribution of PLGA-PEG changes as a function of time, incubation temperature and FBS concentration. There is comparatively minor change in the samples at 10% FBS (~3.3 mg mL^{-1} protein content) between 0 and 24 hours at an ambient incubation temperature (25°C), but the formation of larger agglomerates can be seen. A more pronounced effect on particle number concentration is seen when the particles were incubated at the highest FBS concentration (~6.6 mg mL^{-1} protein content) and at physiological temperature.

When samples of PLGA and PLGA-PEG in comparable incubation conditions are compared, it can be seen than PEGylation impairs the formation of nanoparticle aggregates, as would be expected, since the largest aggregates in the PLGA-PEG samples are smaller than those where the PEGylation is absent. The remainder of this data set for both PLGA and PLGA-PEG nanoparticles can be found in **Appendix F**.

2.5.3.3 Samples in Human Serum

Since this work considers the *in situ* analysis of nanoparticles in protein-rich media, and how serum origin influences protein corona composition, samples were also co-incubated in human serum and analysed *via* PTA. Human serum is the fluid that remains once clotting factors have been removed from human plasma.[434] A single sample of 100 nm PLGA nanoparticles was attempted in (10 % v/v) human serum (~7 mg mL^{-1}) (**Figure 2.22**). The excess, unbound protein (here human serum) as well as the nanoparticles themselves both scatter light, making it challenging for the operator to differentiate between the two and determine the necessary camera settings required for successful analysis. As a consequence, these conditions were not attempted further. Later work from other groups has since shown that these coincubation conditions may have successfully been explored if the fluorescence mode had been used alongside fluorescently-labelled PLGA/ PLGA-PEG nanoparticles.[435]

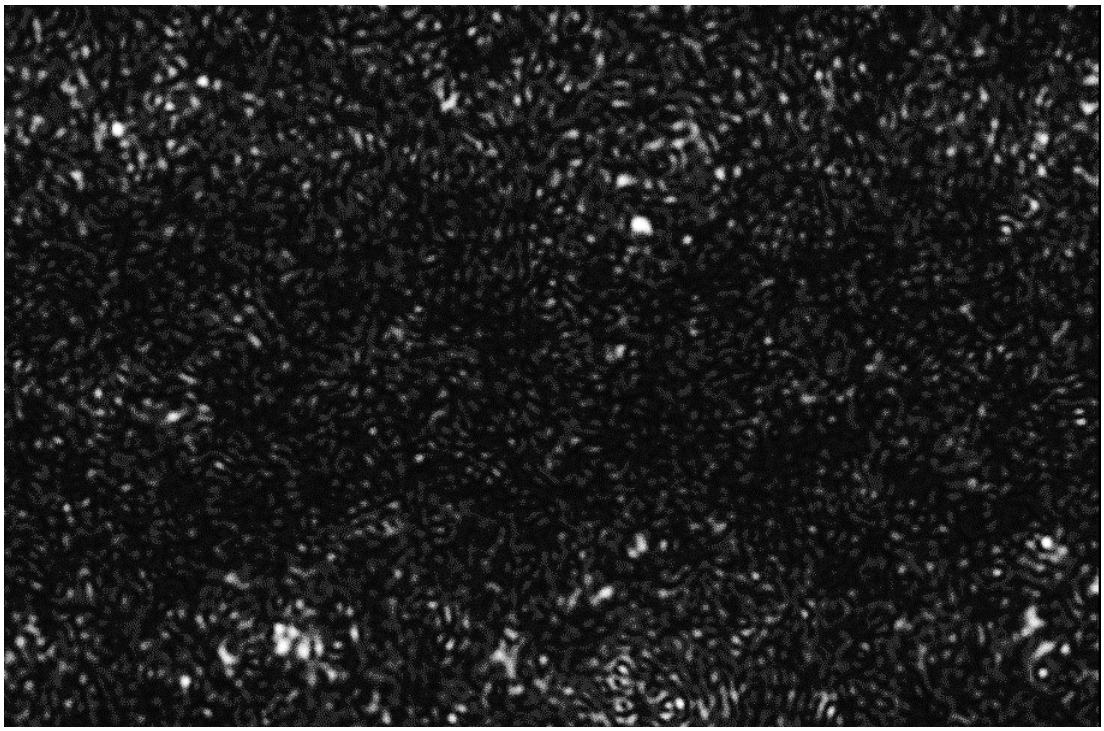

Figure 2.22: *In situ* analysis of nanoparticles in protein-rich media *via* PTA is problematic. A single snapshot of 100 nm PLGA nanoparticles in 10 % human serum - note the significant difficulty in identifying PLGA nanoparticles from unbound protein. For this reason, these conditions were not studied further.

Despite the difficulties reported with samples co-incubated in 10 % human serum, a set of samples were successfully analysed following coincubation in 1 % human serum (0.7 mg mL^{-1}) for between 0 – 2 hours (**Figure 2.23**).

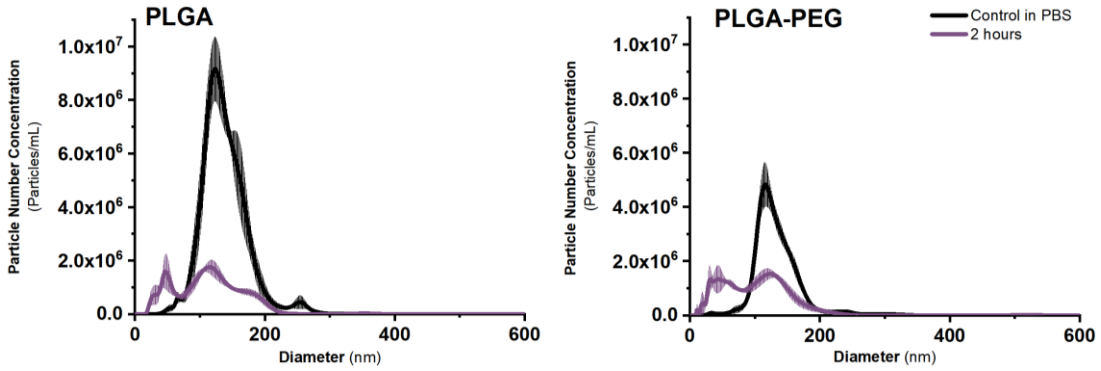

Figure 2.23: The effect of incubation time on PLGA and PLGA-PEG size distributions following co-incubation with 1 % v/v human serum at 37 °C as measured by PTA (n=3). Statistically significant ($P < 0.05$) incubation parameters were not found via paired t-test.

Both treated PLGA and PLGA-PEG nanoparticles show a clear decrease in particle number concentration with time, and an increase in particle size accompanied with a broadening of size distribution. D50 for both samples control - 133.2 nm, PLGA - 112.9 nm, PLGA-PEG - 117.7 nm. Largest particle size: control - 255 nm, PLGA - 353 nm, PLGA-PEG - 407 nm.

Particles in the 300-400 nm size range emerged for both PLGA and PLGA-PEG nanoparticles following treatment, which suggests that PEGylation does not completely prevent particle agglomeration resulting from the formation of a protein corona. At 1 % human serum (0.7 mg mL^{-1} protein content), these protein concentrations are significantly lower than physiological values (60-80 mg mL^{-1} protein content), so the insights gained here may not be accurate representations of the biological environment these nanoparticles would experience *in vivo*.

2.5.3.4 Equilibrium Parameters Determined via PTA

For samples incubated in protein-containing media, we can show *via* PTA that particle size remains constant after two hours, and this would agree with much of the previous work in the literature concerning the formation of nanoparticle protein corona.[240,242] Apparent particle size does appear to fall once incubation duration reaches 24 hours, but this is likely to be related to the impact of incubation duration on nanoparticle aggregation and the subsequent fall in the number of discrete PLGA particles present in the sample (**Figure 2.19**), and particle diameter is then skewed in these samples by the presence of excess, unbound protein. These results then suggest that nanoparticle behaviour in serum is subject to a two-stage process. The results at 25 °C are subject to only protein adsorption (and therefore protein corona formation), whilst those samples incubated a physiological temperature undergo not only protein corona formation, but also the formation of larger particle aggregates.

2.5.3.5 Limitations of this Method

One significant limitation of PTA is that like DLS, it also relies on light scattering because of the Brownian motion of particles. This technique is higher-resolution and less prone to the errors in particle size measurement introduced

by the presence of excess unbound protein in samples, but its utility is limited for turbid samples, where background noise is high.

Furthermore, PTA often disregards true particles in error – relies heavily on the experience and expertise of the user to accurately identify suitable camera settings (*e.g.* threshold values). This limitation becomes more significant when samples are suspended in protein-heavy solutions and/or are turbid and therefore PTA is more likely to underestimate sample concentration, limiting the utility of this technique for *in situ* analysis of samples treated at physiologically relevant protein concentrations. Therefore, these observations have informed the rationale for considering the utility of RMM within this work.

2.5.4 Resonant Mass Measurement

In earlier sections, findings from the application of DLS and PTA to the characterization of PLGA and PLGA-PEG nanoparticles treated with serum were presented. DLS was unable to resolve PLGA nanoparticles from bulk protein within the solution. Due to the optical principles of PTA, neat serum conditions could not be used to assess protein corona formation effects on nanoparticle characteristics. Therefore, RMM, a technique using buoyant mass measurement, was used as an orthogonal approach, as this technique relies on a non-optical method and therefore should theoretically be compatible with protein-heavy and potentially turbid samples.

For the first time, the application of RMM in profiling the impact of protein corona formation on PLGA nanoparticle physiochemical characteristics is presented. Since this is a novel application for this particle metrology technique, the experimental limits of the technique will first be determined, before presenting physicochemical analysis analogous to that previously reported for PTA.

2.5.4.1 Determining the Experimental Limits of RMM for Nanoparticle Physicochemical Characteristics.

As RMM is a novel technique for the analysis of nanoparticle protein coronae, and little work exploring this currently exists within the literature, this section begins by finding the experimental limits of this technique. First, is there a relationship between nanoparticle concentration in mg mL^{-1} and that measured *via* RMM, and secondly does increasing nanoparticle concentration impact apparent particle size? Later, the consequences of increasing protein concentration in the coincubation fluid is also assessed.

Relationship Between Sample Concentration and Particle Number Concentration Determined by RMM

Figure 2.24 shows a linear relationship between nanoparticle concentration in mg mL^{-1} and particle number concentration (particles mL^{-1}) measured *via* RMM. As concentration of the prepared sample in mg mL^{-1} increases by a factor of 10, so too does number concentration, in particles mL^{-1}. It is known that to afford the high-resolution analysis of this technique, particle number concentration is limited to ~ 10^8 particles mL^{-1}. For the PLGA nanoparticles in this work, 0.1 mg mL^{-1} is approaching this limit, and therefore where more

concentrated solutions are used, particles do not pass through the resonator alone. At the other extreme, the most dilute samples that can be analysed *via* RMM is then controlled by analysis time – the more dilute the sample, the longer it will take to reach the 300 particle limit beyond which the size distribution is considered reliable.[436] Here, analysis time was limited to < 15 minutes for each sample, limiting concentration to ~ 0.01 mg mL^{-1}.

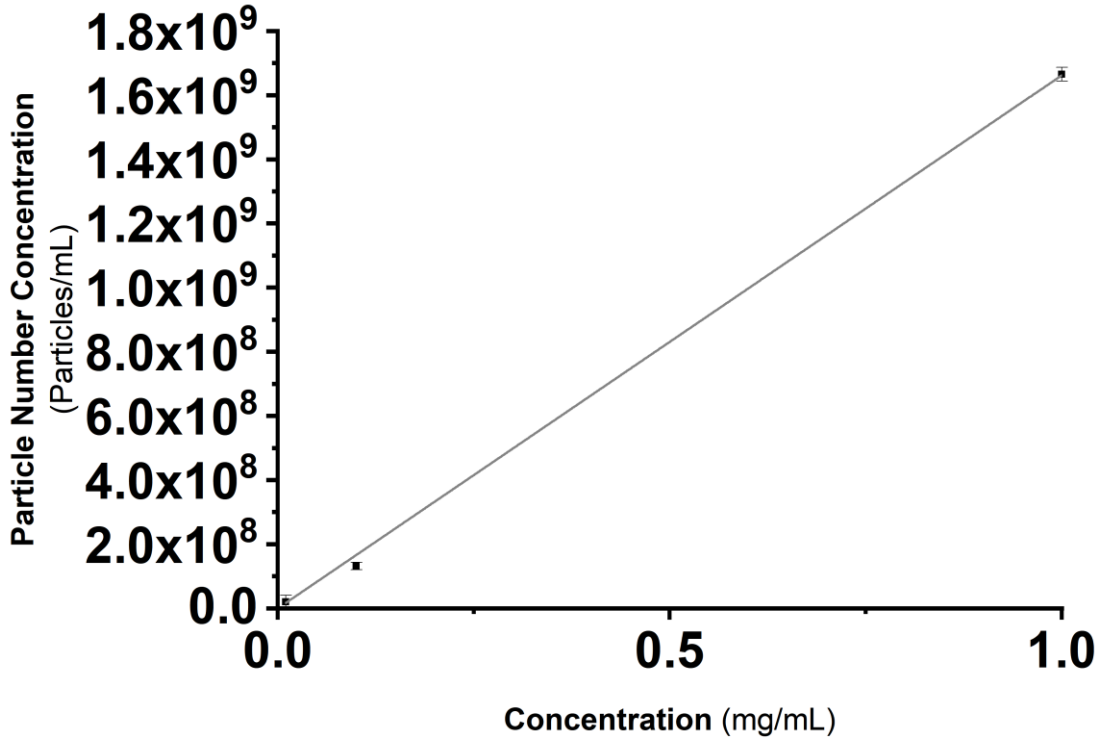

Figure 2.24: Relationship between concentration of PLGA (mg mL^{-1}) vs particle number concentration reported *via* RMM n= 3. Errors are given ± standard deviation.. R^2 = 0.99

Relationship Between Sample Concentration and Apparent Particle Size

Figure 2.25 shows increasing particle concentration in mg mL^{-1} has an impact on apparent particle size of the samples under test. It is also noted that coincidence (how frequently do two or more particles pass over the resonator simultaneously) rises as concentration increases, irrespective of particle size (**Table 2.11**). This is then known to impact apparent particle size, in line with previous work.[436] However, a detailed understanding of why coincidence impacts particle size is, as yet, unknown.

Table 2.11: A comparison of sample concentration, particle diameter and coincidence. PLGA nanoparticles suspended in ultrapure water, n=3. Errors given as standard deviation. ††

Concentration (mg mL^{-1})	Mean Particle Diameter (nm)		Coincidence (%)	
	100 nm	200 nm	100 nm	200 nm
0.01	146.0 ± 12	365.7 ± 4.0	23.3 ± 1.2	1.0 ± 0
0.1	161.3 ± 12	374.7 ± 2.1	30.0 ± 1.0	11.7 ± 1.2
1	191.5 ± 27	480.0 ± 1.0	33.0 ± 0	28.0 ± 0

†† These results are unfortunately complicated further by the introduction of another user, and therefore slightly altered system set up.

The manufacturer advises that sample coincidence <10 % is required for reliable particle size distributions. Here, a number of samples are seen to have coincidence values >10%, potentially leading to unreliable particle size distributions and therefore unreliable average particle diameter.

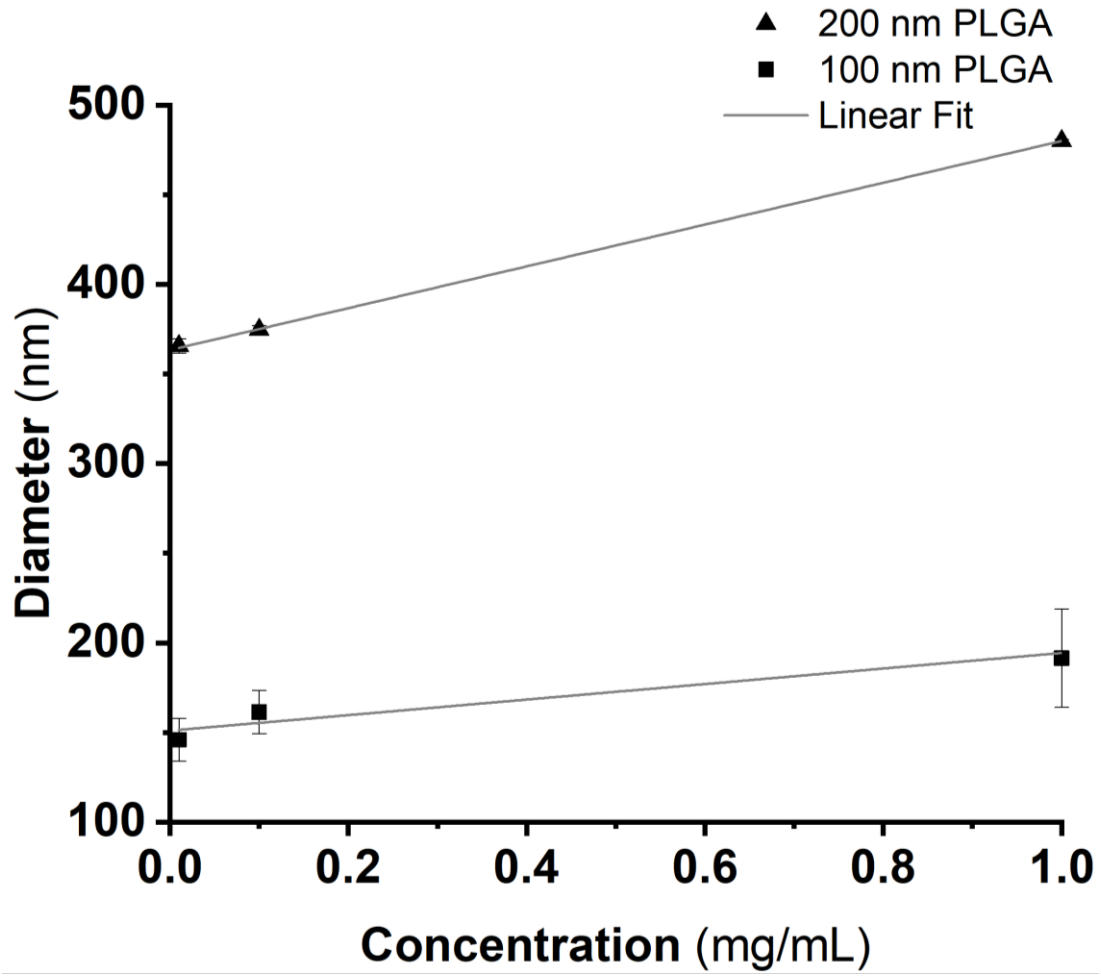

Figure 2.25: Increasing nanoparticle concentration affects mean particle size. Samples are PLGA suspended in ultrapure water (n=3) Errors are given ± standard deviation. $R^2 = 0.51$.

Furthermore, the point sensitivity of the sensor in use, and therefore limit of detection (LOD) – the smallest sized particles that can be detected drifts during this study (not shown), which may explain some degree of the increase in particle size as the samples become more concentrated. This drift in LOD then impacts apparent particle size of the samples, since the smallest particles now cannot be seen and as such average particle size is biased by the absence of these smallest particles.

Relationship between Protein Concentration in Coincubation Fluid and Nanoparticle Size

Since RMM is not an optical method, and is also capable of the analysis of mixed samples (*i.e.* particles of both positive and negative densities), it was of interest to see how this particular particle metrology technique handles protein-rich carrier fluids. Samples using 200 nm PLGA nanoparticles were prepared as previously described, but alternatively were suspended in much higher

levels of FBS – up to 80 % FBS (~26.4 mg mL^{-1} protein concentration). We also see that the coincidence (the frequency with which two or more particles pass through the resonator simultaneously) of these samples rise as protein concentration of the incubation medium is increased (**Table 2.12**). Manufacturer advises coincidence < 10 % to obtain accurate size distributions.

Table 2.12: A comparison of incubation medium and average coincidence values. 0.01 mg mL^{-1} 200 nm PLGA nanoparticles n=3, errors given as standard deviation.

Incubation medium	Coincidence (%)
PBS	10.7 ± 2.1
10 % FBS	23.0 ± 1.0
40 % FBS	25.6 ± 1.5
80 % FBS ‡‡	38.3 ± 1.5

Increasing protein concentration of incubation medium leads to an increase in formation of the larger > 300 nm aggregates (**Figure 2.26**). This agrees with previously reported studies.[437] Furthermore, it suggests the impact of incubation in protein-rich media does not equally impact the entire population, as there are still significant numbers of ~ 200 nm nanoparticles present in the sample, even despite incubation in 40 % FBS for 24 hours. It would be expected that the impact of the increased protein content in the medium would be most pronounced with these samples.

Following the studies by which the analytical limits of this technique had been explored, samples were prepared as previously described and analysis of these samples was also performed using RMM.

‡‡ This sample is not shown in Figure 2.26. This sample was only incubated at 25 °C.

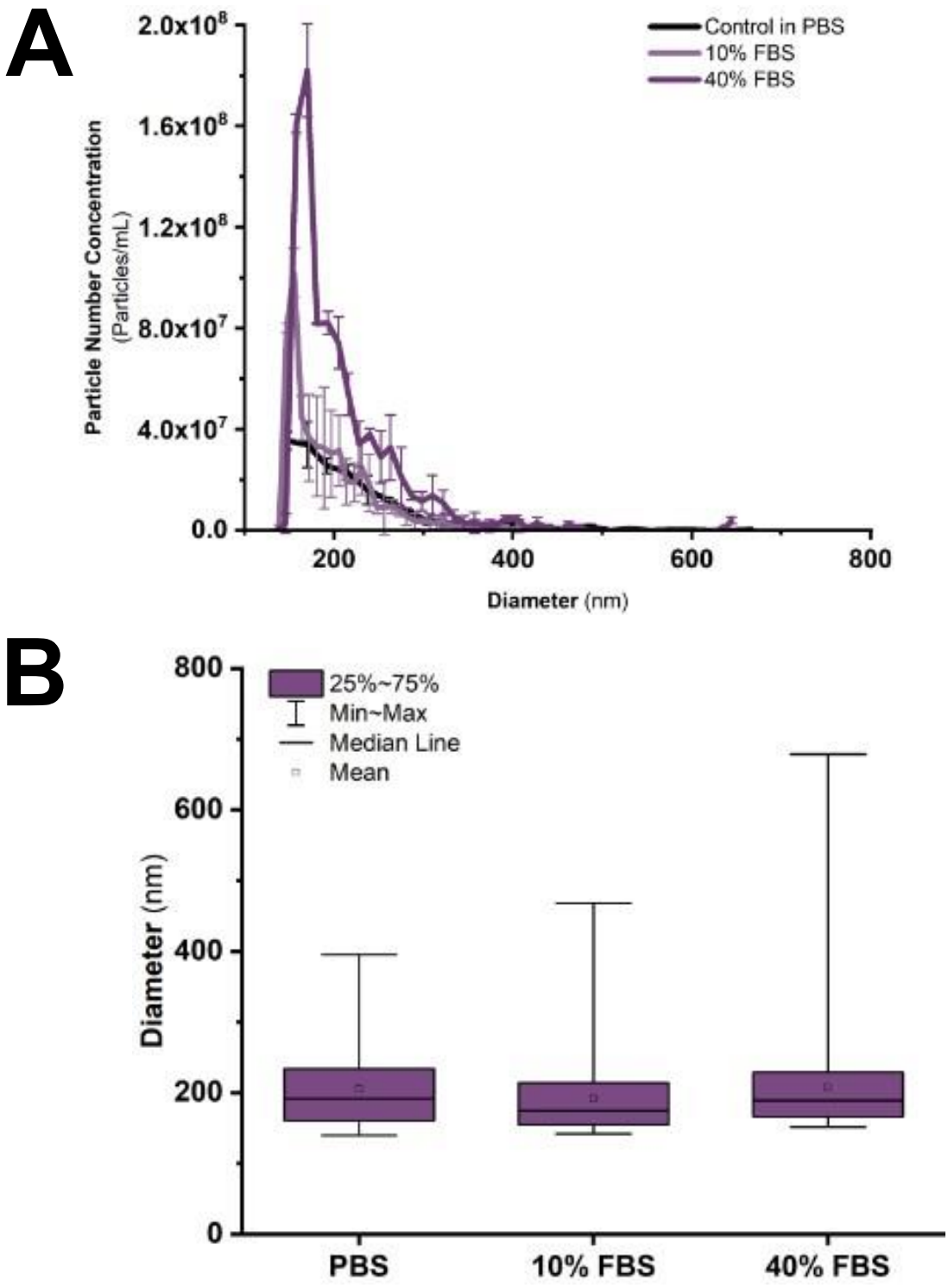

Figure 2.26: 0.01 mg mL^{-1} 200 nm PLGA nanoparticles co-incubated in PBS, 10% and 40% FBS, 37 °C, 24 hours, n=3 and errors are given as standard deviation. A) Particle size distribution as obtained via RMM. B) Box plot to better enable the comparison of nanoparticle size as a function of protein content in incubation medium, suggests protein content impacting the population unequally.

2.5.4.2 Samples in FBS

PLGA and PLGA-PEG samples were incubated in 10% and 20% FBS (~3.3 mg mL^{-1} and 6.6 mg mL^{-1} protein content, respectively) to evaluate temporal effects of PLGA nanoparticle treatment with serum, and subsequent effects on nanoparticle characteristics (size and particle number concentration).

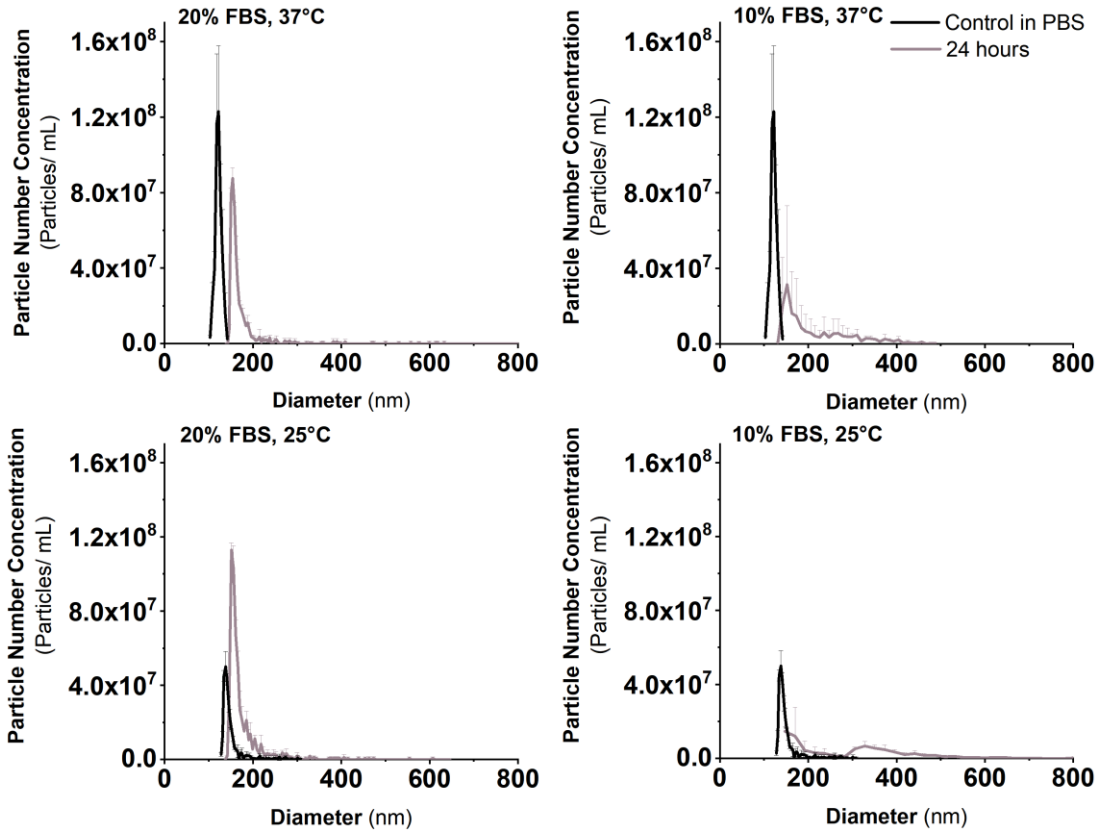

Figure 2.27: The effect of incubation time, temperature and FBS concentration on PLGA nanoparticle size distributions measured by RMM. (n=3). The number concentration of PLGA nanoparticles decreases significantly with incubation time. A three-way ANOVA was used to identify statistically significant ($P < 0.05$) incubation parameters. The results obtained are as follows: incubation time (0 vs 24 hours) ($p = < 0.001$), incubation temperature (25°C vs 37°C) ($p=0.02$) and protein concentration (10% vs 20% FBS) ($p= 0.01$).

Control samples in PBS are unimodal (average diameter: 137 nm, 121 nm at 25 °C and 37 °C respectively)[§§]. A clear shift in both nanoparticle size distribution and number concentration can be seen following incubation in FBS, and this impact particularly on nanoparticle size distribution is strongest with the sample incubated in 20 % FBS at 37 °C (**Figure 2.27**). The samples co-incubated in 20 % FBS develop much larger aggregates than those in less concentrated solutions of FBS.

[§§] LOD set lower for 37 °C sample, hence lower apparent average diameter.

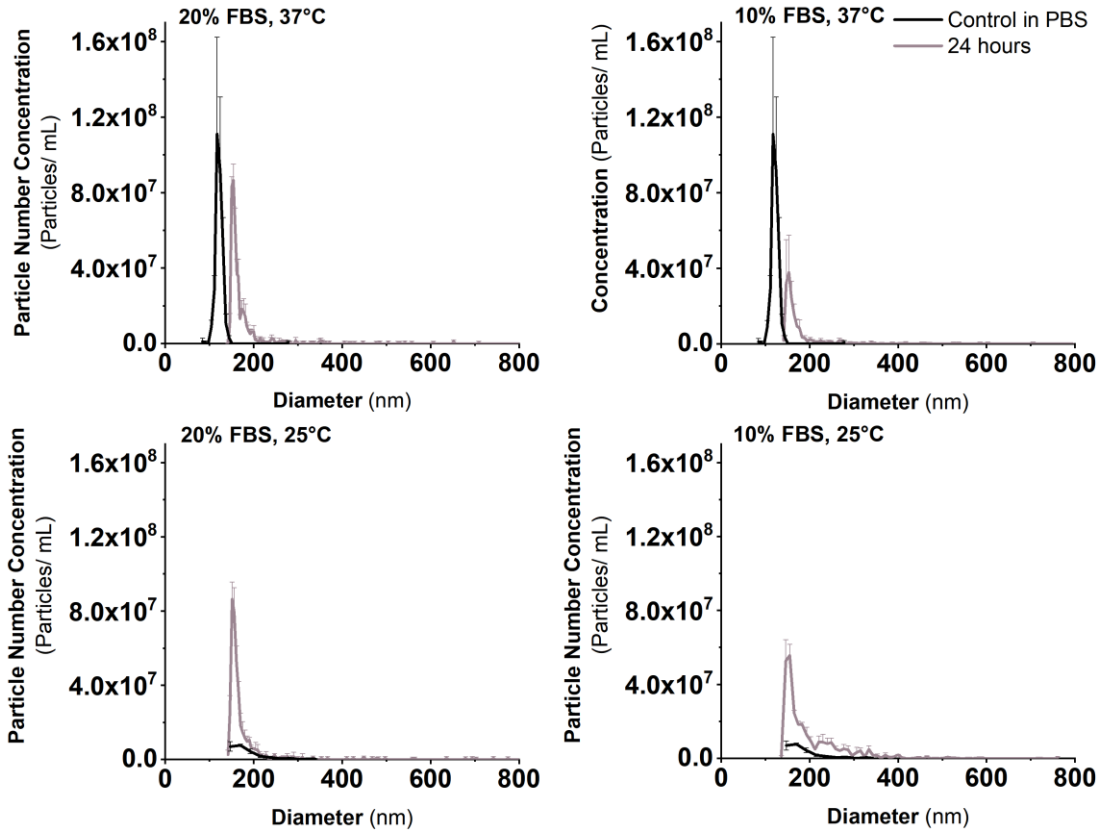

Figure 2.28: The effect of incubation time, temperature and FBS concentration on PLGA-PEG nanoparticle size distributions measured by RMM. (n=3). The number concentration of PLGA-PEG nanoparticles decreases significantly with incubation time. A three-way ANOVA was used to identify statistically significant ($P < 0.05$) incubation parameters. The results obtained are as follows: incubation time (0 vs 24 hours) ($p = <0.0001$), incubation temperature (25°C vs 37°C) ($p = <0.0001$) and protein concentration (10% vs 20% FBS) ($p = 0.011$).

Control samples in PBS are unimodal (average diameter:150 nm, 121 nm at 25 and 37 °C respectively).Following 24 hours of incubation in protein-containing media, the impact of incubation parameters are less clear to observe with these samples using PLGA-PEG nanoparticles (**Figure 2.28**). However, for the samples at 37 °C, a clear decrease in particle number concentration and shift in size distribution can be seen, which is again indicative of nanoparticle aggregation behaviour. For the samples in 20 % FBS, there is also a difference in the size of the largest aggregates that can be seen.

When the impact of these incubation parameters is compared between PLGA and PLGA-PEG nanoparticles, PEG-ylation does not completely prevent the formation of a protein corona, and therefore subsequent nanoparticle aggregation, as larger aggregates are still observed in these samples. However, these aggregates are smaller (243 nm) than those where the PEGylation is absent (250 nm). The remainder of the data set for both PLGA and PLGA-PEG nanoparticles can be found in **Appendix I**.

2.5.4.3 Dry Mass

As discussed previously (**Equation 4**), resonant mass measurement can also determine the "dry mass" of a particle when both buoyant mass (wet mass) and the density of the carrier fluid are known. In this context, dry mass is the mass of the particle, minus any mass from adsorbed carrier fluid.[309] RMM will only calculate this value, when a single object (single particle or aggregate of particles) passes over the resonator at any given time; where multiple objects do this simultaneously, these particles are considered coincident and are not analysed.

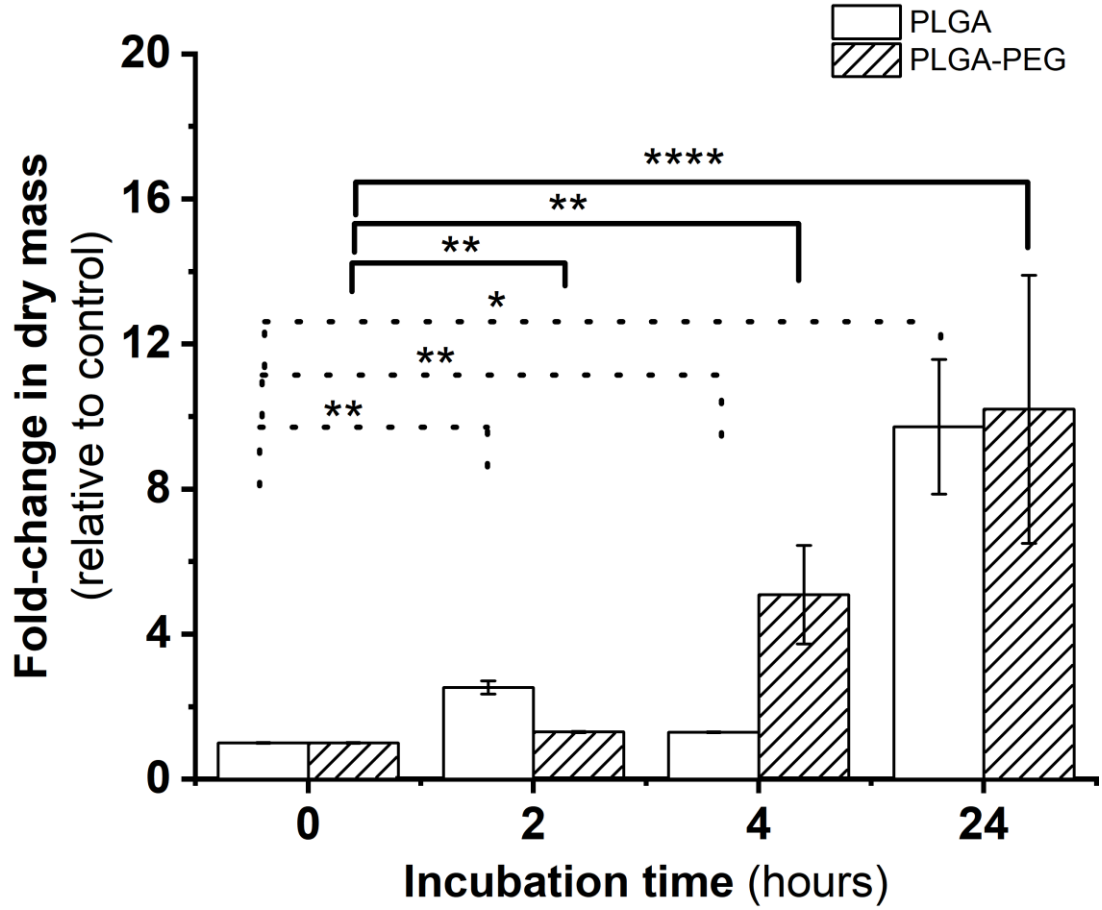

Figure 2.29: The impact of incubation time on mean particle dry mass relative to control. PLGA and PLGA-PEG nanoparticles treated in 10% FBS (n=3). Errors are given as standard deviation.* represents P<0.05, **< 0.01, ***<P0.001 and *** P<0.0001 as determined by paired t-test. The same analysis has been undertaken for samples incubated in 20 % FBS and similar results are seen (**Appendix K**).

Samples were prepared as previously described and **Figure 2.29** shows changes in mean particle dry mass following incubation with media containing 10% FBS for various incubation durations (2 – 24 hours). The mean particle dry masses in each case are normalised against those for the corresponding nanoparticle coincubated in PBS, as such the values for both control samples are 1. Here, smaller increases in mean particle mass are seen on comparison between control samples (in PBS) and those incubated in FBS for 2 hours, (PLGA 2.5-fold increase, PLGA-PEG 1.3-fold increase relative to control) than is seen when comparing control samples with those incubated with FBS

between 4 (PLGA 1.3-fold increase, PLGA-PEG 5.1-fold increase relative to control) and 24 hours (PLGA 9.7-fold increase, PLGA-PEG 12.5-fold increase relative to control). If these changes in mean particle dry mass were indicative of aggregate and/or agglomeration formation, then mean particle dry mass (relative to control) would be expected to be at least a 2.0-fold change, indicating that two particles had formed a single aggregate that RMM has successfully analysed. This has not been seen at the earlier timepoints, thus, these results suggest that two different processes are at play. The smaller increases in mean particle dry mass that are seen at shorter durations (< 4 hours) are most likely to be suggestive of protein adsorption on the nanoparticle surface, as protein adsorption (and therefore protein corona formation) is an instantaneous process and these changes in mass are smaller for PLGA-PEG than PLGA.[438] It is already known that PEGylation has some ability to delay the process of protein adsorption (and therefore protein corona formation) around polymeric nanoparticles.[225,260] Protein corona formation is likely to then influence nanoparticle behaviour at subsequent timepoints, as this is known to impact a wide range of nanoparticle physicochemical characteristics including zeta potential.[438] Where the larger changes in mean particle dry mass (greater than individual particle mass) are observed within this study (timepoints of 4 hours or greater), these results are then suggestive of nanoparticle agglomeration, where many nanoparticles stick together. These results additionally show, that the extent of protein-particle and particle-particle interactions is not identical across a sample, which may have consequences for later nanoparticle aggregation following exposure to protein-rich media and/or depot formation in target organs *in vivo*.

2.5.4.4 Limitations of This Method

One of the most significant limitations of this technique is its novelty. It has not necessarily been well adopted in the literature for analysis of sub-micron sized particles, and to the best of our knowledge, this is the only RMM set up within Scotland, therefore obtaining interlaboratory consistency is challenging. We have also seen issues of intra-laboratory consistency (*i.e.,* the impact of changing to a much more experienced user on the LOD of the system, and therefore on the data obtained). As yet, no standardised methodology has been developed via NCL or EU-NCL.[427,439] Where interlaboratory standardisation studies have been attempted within the literature, these studies have frequently focussed on much larger particles (*i.e.* > 1 µm).[334,440]

Also, accurate evaluation of protein corona formation around PLGA(-PEG) particles below 100 nm diameter is likely to be difficult with the current set-up for the Archimedes system (LOD 0.01 Hz = 125-136 nm, depending on the point sensitivity of the sensor in use). At the other end of the size scale, it is advised that particles >1 µm are not analysed with the nano sensor.[309]

2.5.5 Orthogonal Analysis of PLGA and PLGA-PEG Samples via PTA and RMM

As discussed previously, none of the analytical techniques on offer provide a perfect method by which to study the physicochemical characteristics of

polymeric nanoparticles *in vitro.* Each technique has its own set of limitations; however, if we use two or more techniques to characterise the same sample – or technical replicates of a sample, some of these limitations can be overcome. Where this multi-technique methodology is used, and the techniques chosen rely on different fundamental physical principles, the analysis is considered 'orthogonal'. Such orthogonal analyses are now required in the development of novel biotherapeutics, to facilitate FDA and/or EMA approval.[441–443]

Here, data obtained *via* RMM and PTA will be analysed simultaneously. Particle diameter and calculated sample concentration of control samples or those in ultrapure water will both be discussed here, before showing the promise this technique has for samples where protein corona formation is of interest, before summarising the limitations of this novel orthogonal method.

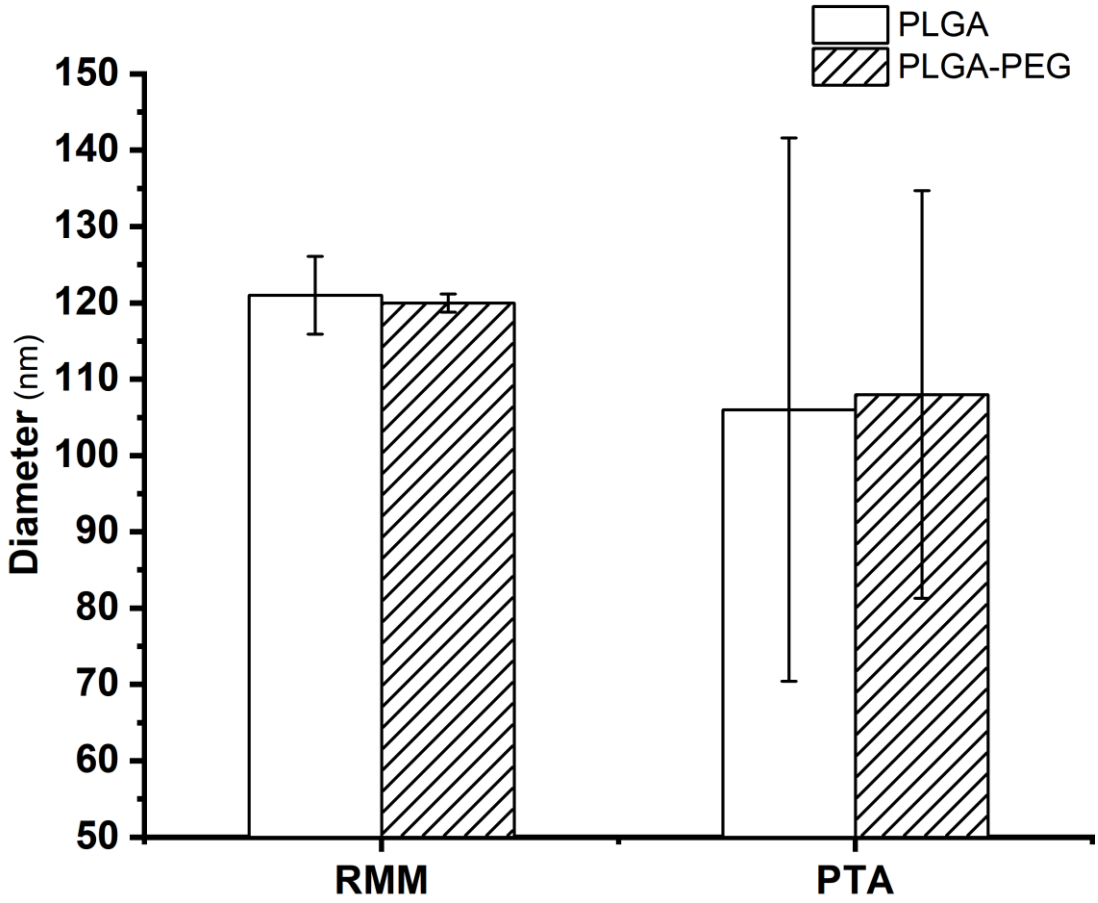

Figure 2.30: Baseline characterisation of 0.01 mg mL^{-1} PLGA/PLGA-PEG nanoparticles suspended in ultrapure water, n= 3 and errors given as standard deviation. **N.B.** detection limit is much lower for RMM in comparison to PTA.

In **Figure 2.30**, it can be seen that mean particle diameter is much smaller for PLGA and PLGA-PEG nanoparticles *via* PTA (106, 108 nm respectively), in comparison to RMM (120, 121 nm), despite these samples being technical replicates of each other. These results would arise from the differences in detection limit between the two techniques. The detection limit for RMM is higher than PTA (125 nm vs ~50 nm) and therefore the particle size distribution for this technique is likely to be biased upwards, since the smaller particles that

only PTA can see, are not included when average diameter is calculated. Additionally, **Figure 2.30** also shows that errors are much larger for PTA. It is suggested these differences in the size of the error arises from the differences in the underlying physical principles of these techniques – PTA is an optical technique which depends on light scattering, whilst RMM is not.

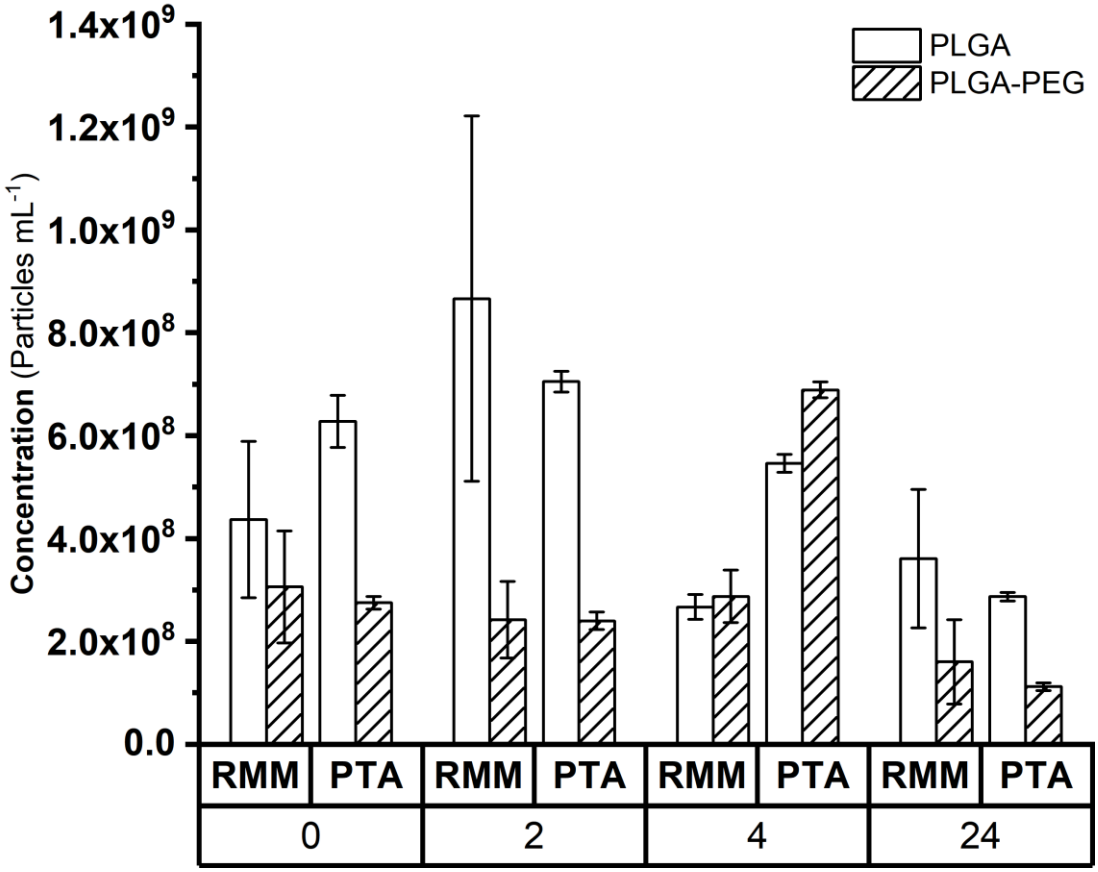

Figure 2.31: Sample particle number concentrations vary as a function of incubation time and analytical method. Sample at t0 is PLGA/PLGA-PEG nanoparticles suspended in ultrapure water as control. Samples at 2, 4, and 24 hrs are incubated in 10 % FBS. In each case n= 3, and errors are given as standard deviation.

From **Figure 2.31**, it can be noted that there are differences in particle number concentration when measured *via* PTA and RMM, again despite these samples being technical replicates of each other. It is suggested that these differences arise from the thresholding procedure implemented *via* PTA, which removed some true particles – considering them to be background protein and therefore not of interest. These particles were then not included when particle number concentration was calculated. This effect becomes significant when protein-rich biofluids are used as the incubation medium.

When the data obtained *via* both RMM and PTA is considered simultaneously, this disparity in particle number concentration when analysis method is varied, is also seen in **Figure 2.32**.

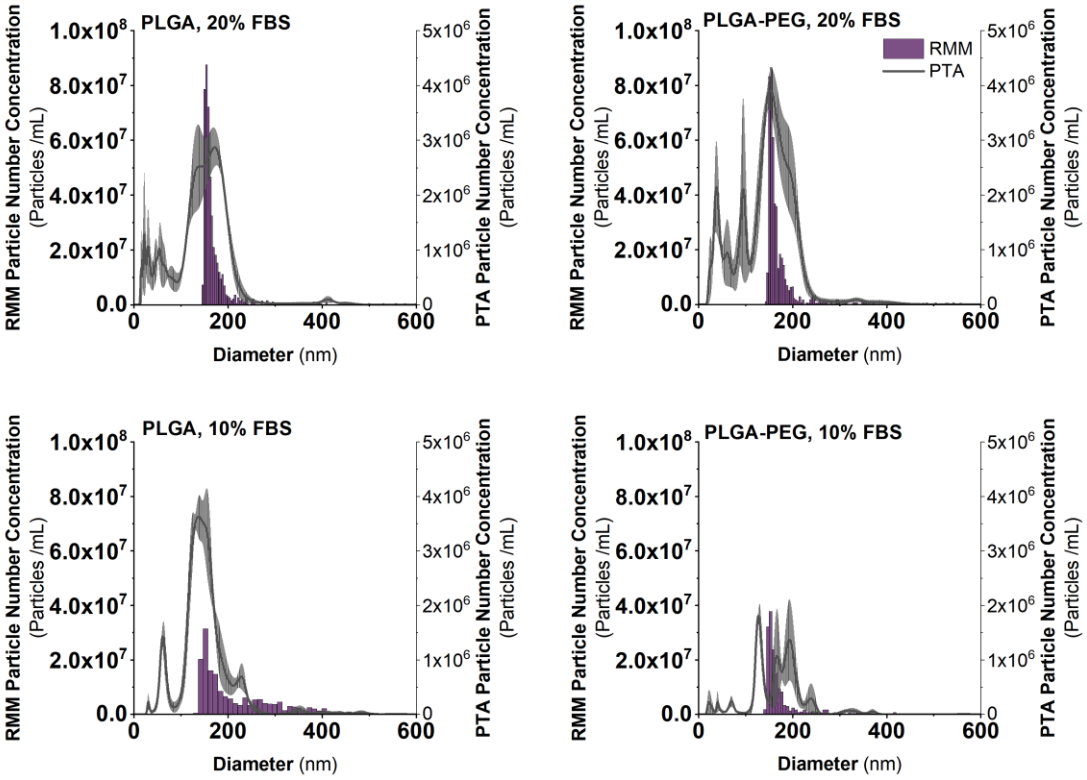

Figure 2.32: A comparison of PLGA and PLGA-PEG nanoparticle size distributions measured by RMM and PTA (n=3). Incubation time and temperature are 24 hours at 37°C for each sample. On visual inspection, good agreement in size distribution irrespective of methodology used, but clear differences in particle number concentration between methods. A one-sample t- test was used for each plot to confirm that sample means were not statistically different between methods.

However, if the particle size distribution is considered, then good agreement is seen between methods – PTA can see much smaller particles < 100 nm, that the current RMM set up cannot identify. Despite these differences, PTA and RMM can be said to cross-validate each other, as the results obtained for particle number concentration agree within error, and any variation in average particle size between analysis methods was not considered to be statistically significant (**Appendix L**).

2.5.5.1 Limitations of This Method

One limitation of this method is the analyte particle concentrations that can be studied using these techniques. To enable the single particle resolution afforded by these techniques, maximum PLGA nanoparticle concentration needs to be ~< $1x10^8$ particles mL^{-1}. The particle concentration limit for both these techniques are dependent on nanomaterial composition (*e.g.,* density for RMM) and optical (*i.e.*, refractive index for PTA) properties of the analyte.

Furthermore, using PTA and RMM orthogonally will not permit the resolution of nanoparticle protein corona formation at t= 0, in a solution which contains proteins. Protein corona formation is a spontaneous process, which occurs too rapidly to be seen by either technique. Our understanding of these earliest moments of corona formation rely on computational modelling, rather than experimental results.[235,240,242,268]

2.6 Conclusions

In this chapter, the particle metrology techniques of dynamic light scattering, particle tracking analysis and resonant mass measurement were introduced. Experiments were undertaken to assess the utility of dynamic light scattering for the *in situ* analysis of nanoparticle size distribution effects following protein corona formation. These experiments showed that two clearly resolved peaks were not seen unless a protein concentration of 0.03 mg mL^{-1} (0.1% FBS) was used. This is well below the physiologically relevant protein concentrations of 77 mg mL^{-1} for human serum and also below the 3.3 mg mL^{-1} where cell culture media is supplemented with 10% FBS. This is in line with previous results.[431] Hence, it was decided that this technique would not be pursued further, since the results obtained would neither be useful for elucidating the phenomenon of protein corona formation around PLGA nanoparticles *in vivo*, nor would it lead to further understanding of PC formation in commonly performed nanoparticle-cell uptake studies.

The higher-resolution techniques of particle tracking analysis and resonant mass measurement were then used for evaluating protein corona effects on nanoparticle physiochemical characteristics. This was firstly done by developing a methodology by which RMM could be used to undertake such studies, as this is the first time this technique has been applied to study protein corona formation effects on polymeric nanoparticles. Next, these higher-resolution particle metrology methods were individually applied to study physiochemical changes following protein corona formation under ambient (25 °C) and physiological temperatures (37 °C), as a function of incubation duration and serum concentration and origin. Findings show, that protein concentration has an impact on nanoparticle physiochemical properties over time. PLGA nanoparticle agglomeration occurs much more slowly when buffer conditions (PBS) or lower levels of FBS (10 %) are used as the incubation medium. Since physiological concentrations of proteins are significantly in excess of this, it would be sensible to suggest that changes in nanoparticle size will be much more rapid than those reported here, and are consistent with previously reported studies in which medium and protein concentration-dependent effects have been observed for the formation of protein coronae around nanoparticles.[35,237,444] Finally, dry mass changes were used to probe the origins of nanoparticle size change as a function of time. This study shows that initially, nanoparticle size change is related to the spontaneous formation of the protein corona (*i.e.* adsorption of proteins to the nanoparticle surface). At later timepoints *(i.e.* 24 hours), these surface-adsorbed proteins increase the likelihood for particle-particle agglomeration and aggregate formation. Finally, RMM and PTA were considered as an orthogonal method for the sizing and study of sub-micron particles *in situ*, and results show that despite differences in absolute values, that there is good agreement between both methods.

The results in this chapter show, that methods relying on optical principles (*i.e.* PTA and DLS) are prone to background noise contributions from the

incubation media (unbound protein). This effect is more pronounced with DLS, since it is an ensemble method and size measurements are dependent on the intensity of scattered light. This introduces the potential for biasing effects of co-incubation with protein towards larger agglomerates or detecting dominant species within the sample (*i.e.* protein contained within the incubation medium), and therefore slight changes in particle size are particularly difficult to determine. This work has also developed a novel methodology by which orthogonal analysis of protein corona formation around nanoparticles can be studied *in situ*, without the need of recovery methods, which are known to contribute to variations in the protein corona through the removal of the more loosely bound 'soft corona', and changes in the medium in which the nanoparticles are suspended.[234] Moreover, the use of orthogonal analysis overcomes the issues associated with single measurement techniques and therefore increases the range of potential analytical methods for the analysis of increasingly complex biotherapeutics, including nanoparticles.

2.7 Appendices

A. Dynamic Light Scattering - Timepoint Experiment

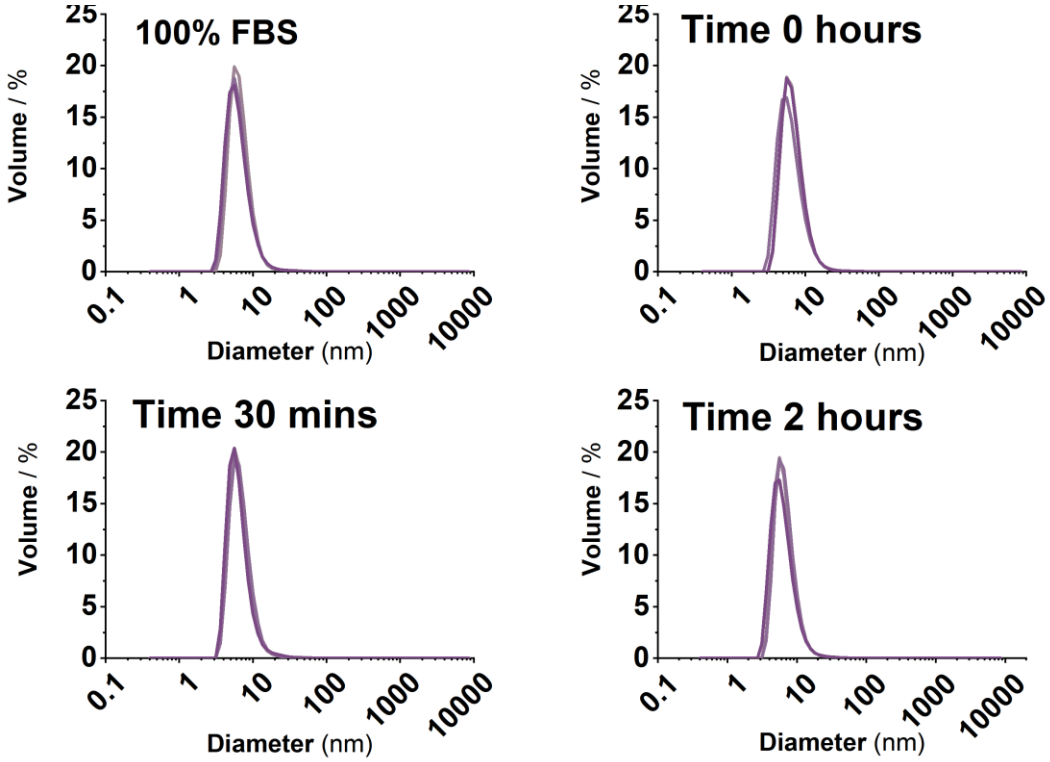

Volume distribution 100 nm PLGA nanoparticles in 20% FBS, at 37°C with incubation times between 0 and 2 hours. Any changes in particle size were not resolved by DLS. Each coloured trace represents a single repeat. All samples were measured in triplicate.

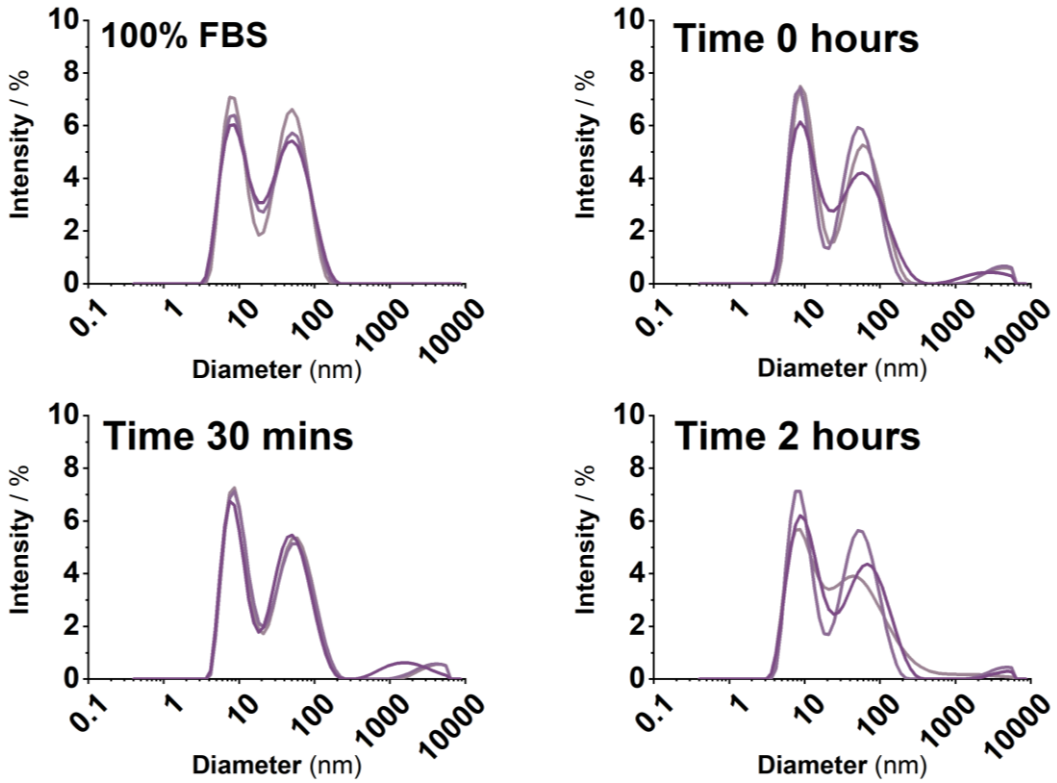

Intensity distribution 100 nm PLGA nanoparticles in 10% FBS, at 37°C with incubation times between 0 and 2 hours. Each coloured trace represents one repeat, samples measured in triplicate.

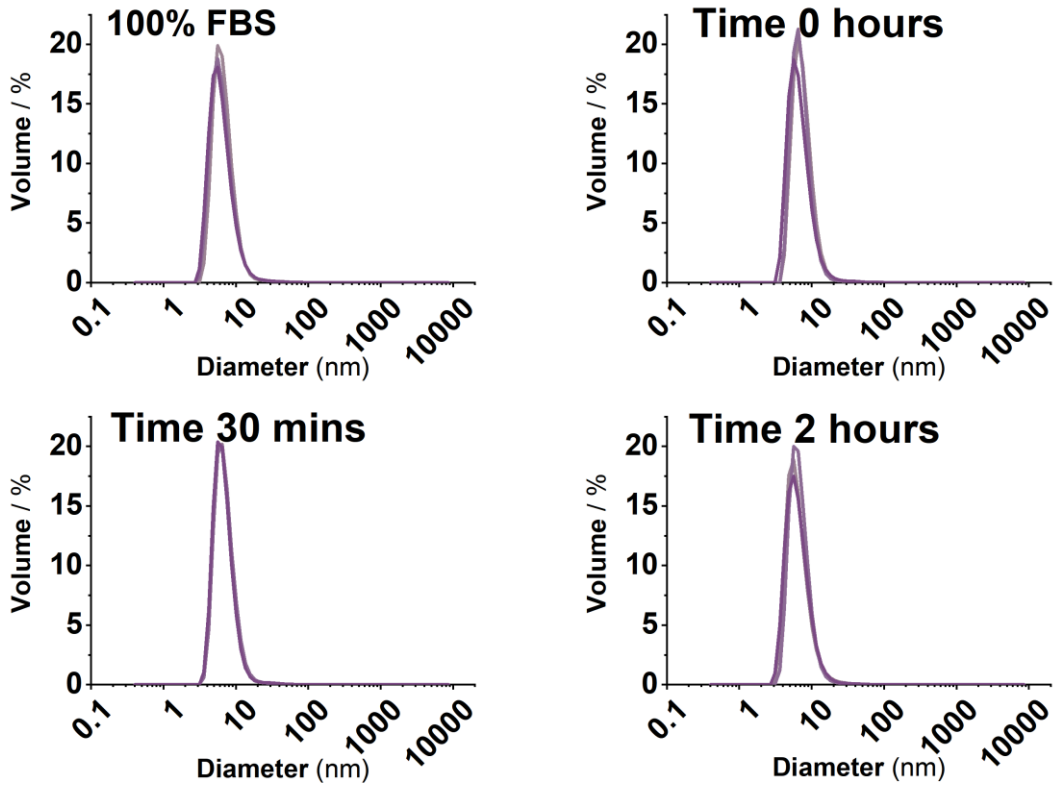

Volume distribution 100 nm PLGA nanoparticles in 10% FBS, at 37°C with incubation times between 0 and 2 hours. Each coloured trace represents one repeat, samples measured in triplicate.

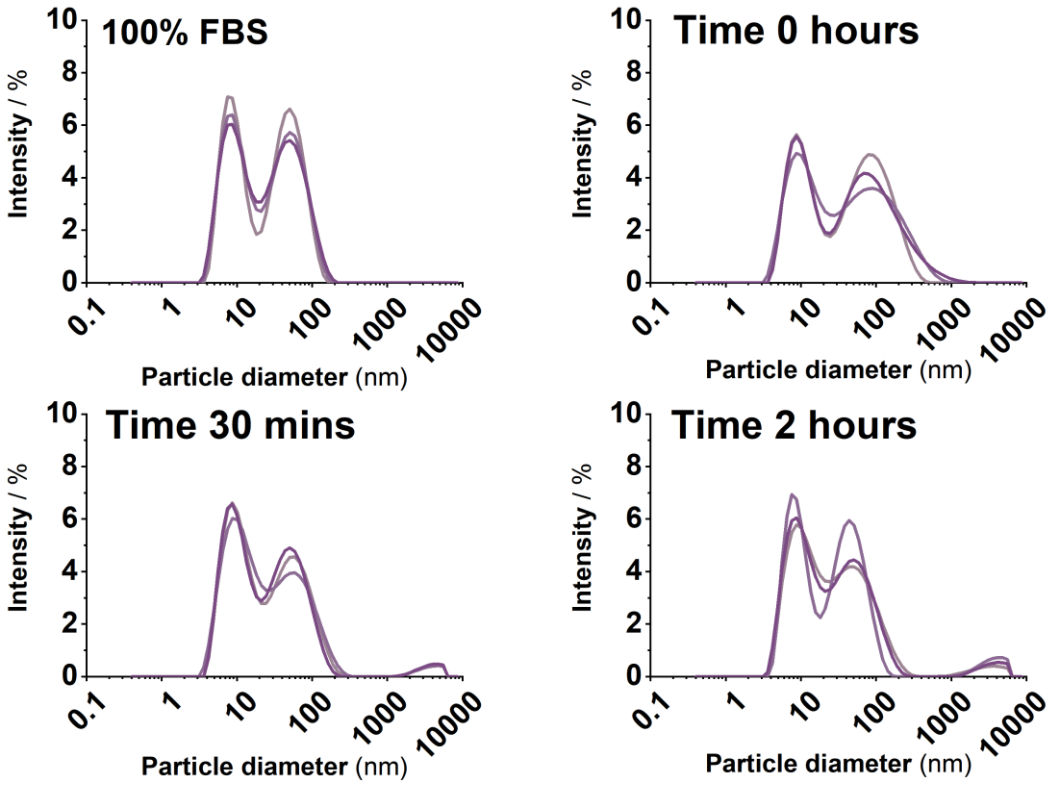

Intensity distribution 100 nm PLGA nanoparticles in 20% FBS, at 25°C with incubation times between 0 and 2 hours. Each coloured trace represents one repeat, all samples measured in triplicate.

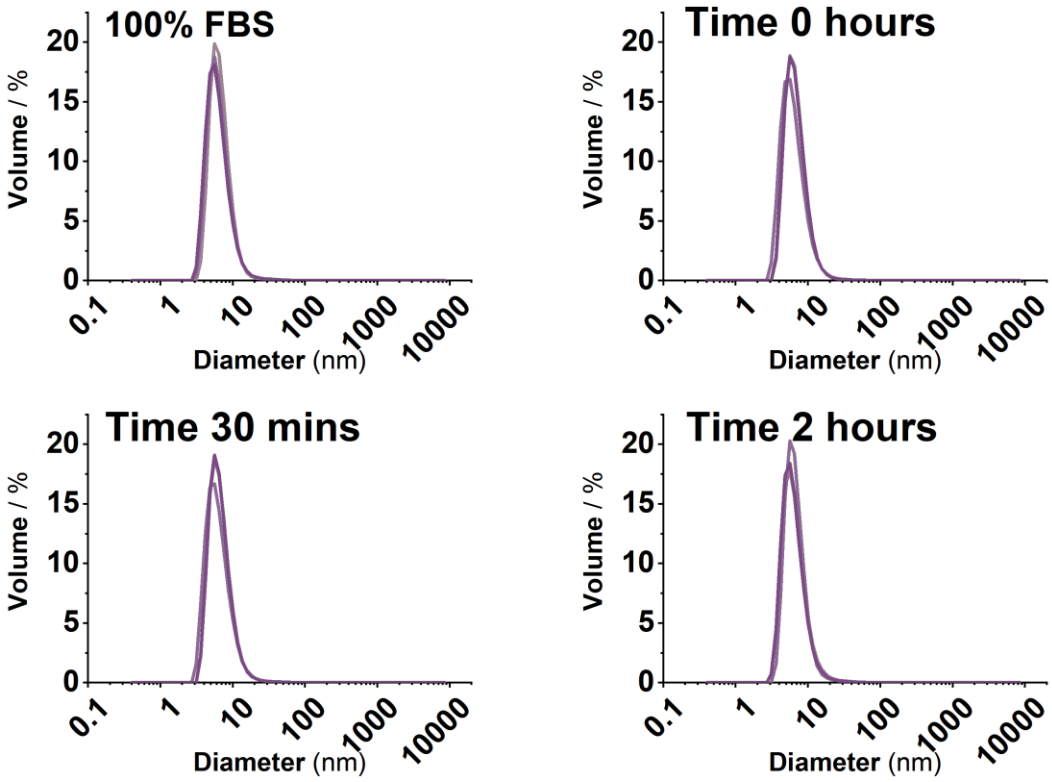

Volume distribution 100 nm PLGA nanoparticles in 20% FBS, at 25°C with incubation times between 0 and 2 hours. Each coloured trace represents one repeat, all samples measured in triplicate.

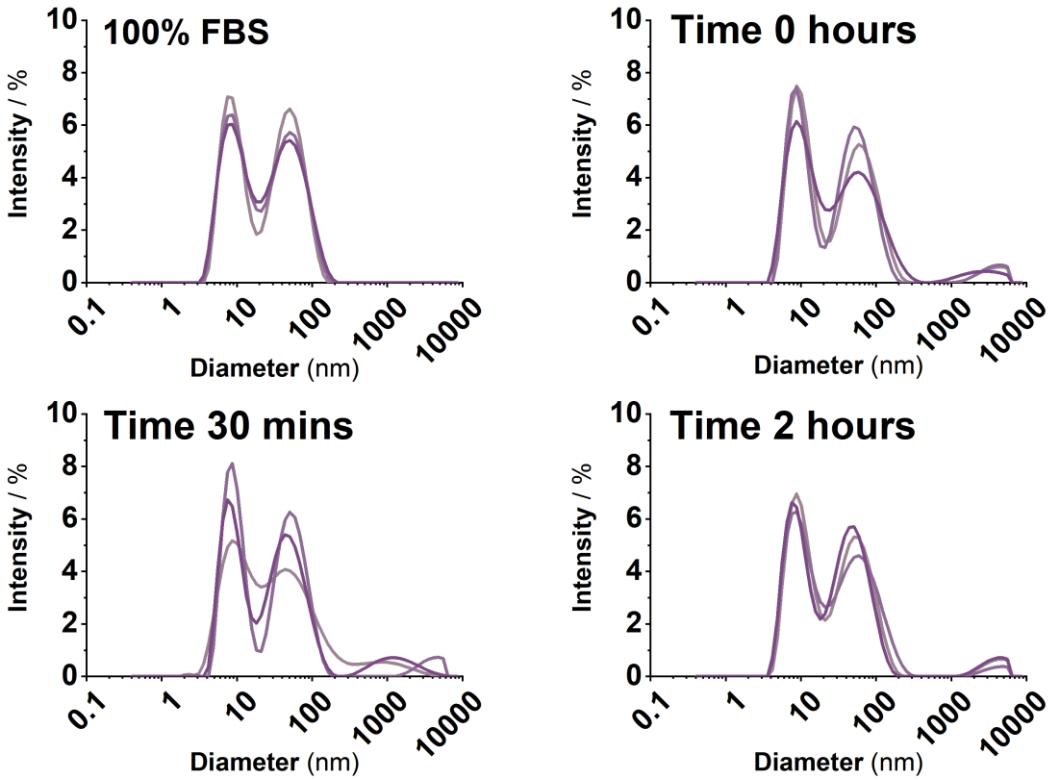

Intensity distribution 100 nm PLGA nanoparticles in 10% FBS, at 25°C with incubation times between 0 and 2 hours. Each coloured trace represents one repeat, all samples measured in triplicate.

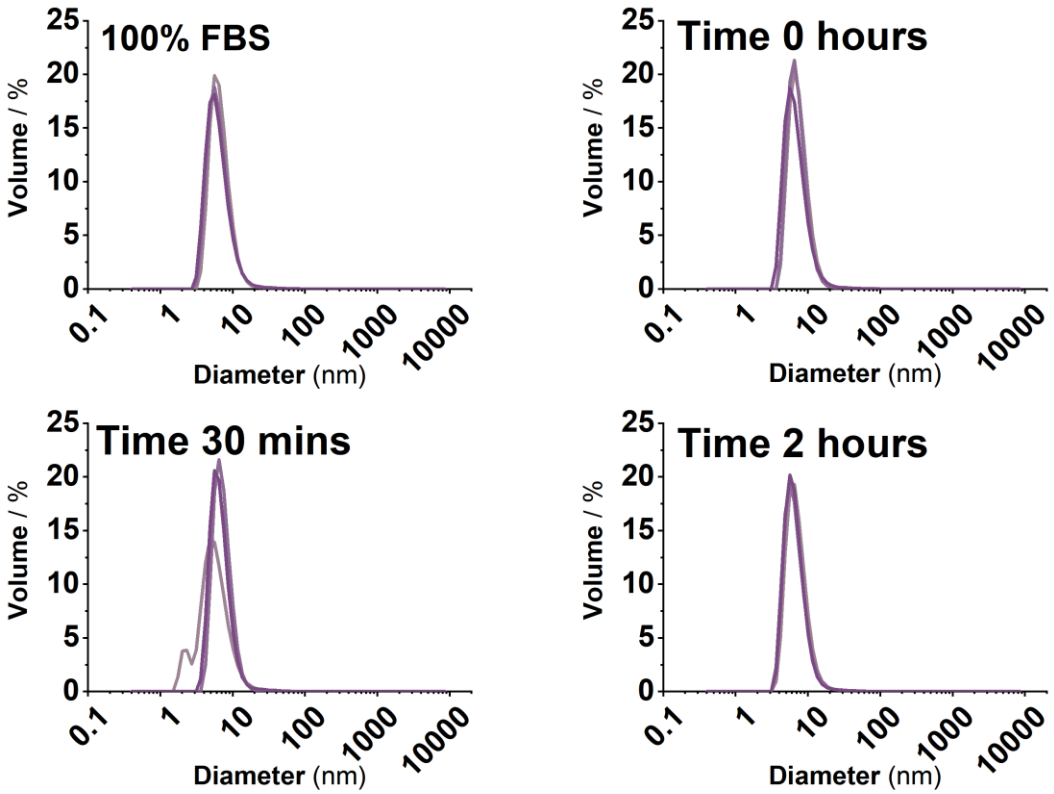

Volume distribution 100 nm PLGA nanoparticles in 10% FBS, at 25°C with incubation times between 0 and 2 hours. Each coloured trace represents one repeat, all samples measured in triplicate.

Z-average, peak 1 and peak 2 data for timepoint experiments with 100 nm PLGA nanoparticles and 10/20% FBS. Each sample has been measured in triplicate.

Sample Name	Z-Ave/ nm	PDI	Peak 1 / nm	Peak 2 / nm
100% FBS 1	15.99	0.445	52.98	9.31
100% FBS 2	15.82	0.441	55.86	10.27
100% FBS 3	15.88	0.445	54.58	9.687
0mins 10% FBS 1	18.46	0.48	68.97	10.4
0mins 10% FBS 2	18.25	0.478	61.01	9.795
0mins 10% FBS 3	18.16	0.479	11.45	75.4
0mins 20% FBS 1	21.12	0.558	101.8	10.95
0mins 20% FBS 2	21.69	0.507	133.3	12.45
0mins 20% FBS 3	22.17	0.516	136.1	11.02
30mins 10% FBS 25c 1	18.41	0.488	74.94	10.87
30mins 10% FBS 25c 2	17.62	0.464	58.13	9.561
30mins 10% FBS 25c 3	17.83	0.474	53.38	9.324
30mins 20% FBS 25c 1	16.51	0.478	10.57	63.53
30mins 20% FBS 25c 2	16.71	0.437	12.62	73.19
30mins 20% FBS 25c 3	16.28	0.466	10.49	58.09
30mins 10% FBS 37c 1	17.57	0.465	63.53	9.991
30mins 10% FBS 37c 2	17.68	0.466	63.38	10.17
30mins 10% FBS 37c 3	18.14	0.483	57.04	9.294
30mins 20% FBS 37c 1	17.57	0.531	53.83	9.391
30mins 20% FBS 37c 2	17.46	0.527	65.1	10.15
30mins 20% FBS 37c 3	17.7	0.537	41.03	8.958
120mins 10% FBS 25c 1	17.75	0.462	60.54	10.37
120mins 10% FBS 25c 2	17.02	0.498	68.61	10.41
120mins 10% FBS 25c 3	17.43	0.458	53.18	9.374
120mins 10% FBS 37c 1	17.51	0.463	164.5	10.73
120mins 10% FBS 37c 2	16.75	0.495	61.53	9.755
120mins 10% FBS 37c 3	17.01	0.504	11.22	79.23
120mins 20% FBS 25c 1	17.36	0.443	11.92	66.89
120mins 20% FBS 25c 2	16.91	0.441	48.98	9.368
120mins 20% FBS 25c 3	16.38	0.477	10.6	60.01
120mins 20% FBS 37c 1	15.62	0.449	10.36	54.92
120mins 20% FBS 37c 2	15.66	0.449	10.44	59.88
120mins 20% FBS 37c 3	15.67	0.448	10.64	56.86

B. DLS Titration Experiment – Foetal Bovine Serum

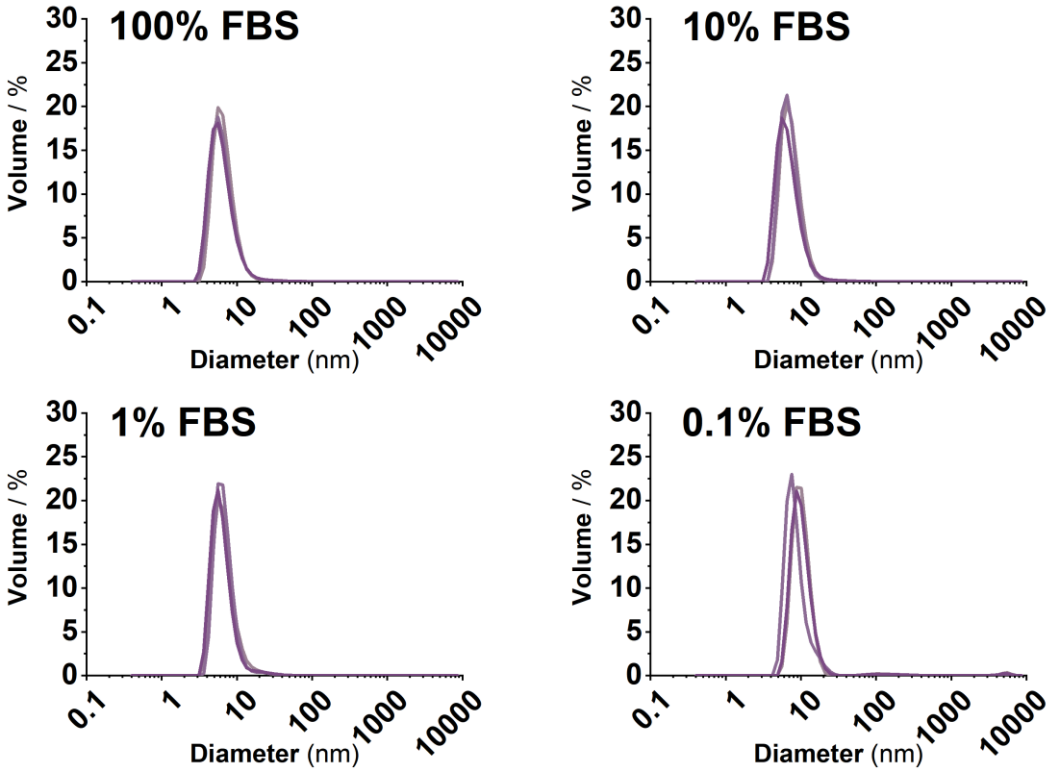

Volume distributions for the incubation of PLGA nanoparticles in varying concentrations of foetal bovine serum (FBS). The concentration at which both components were able to be resolved significantly differs to physiologically-relevant values. Only 0.1%, 1%, 10% and neat FBS are shown (n=3).

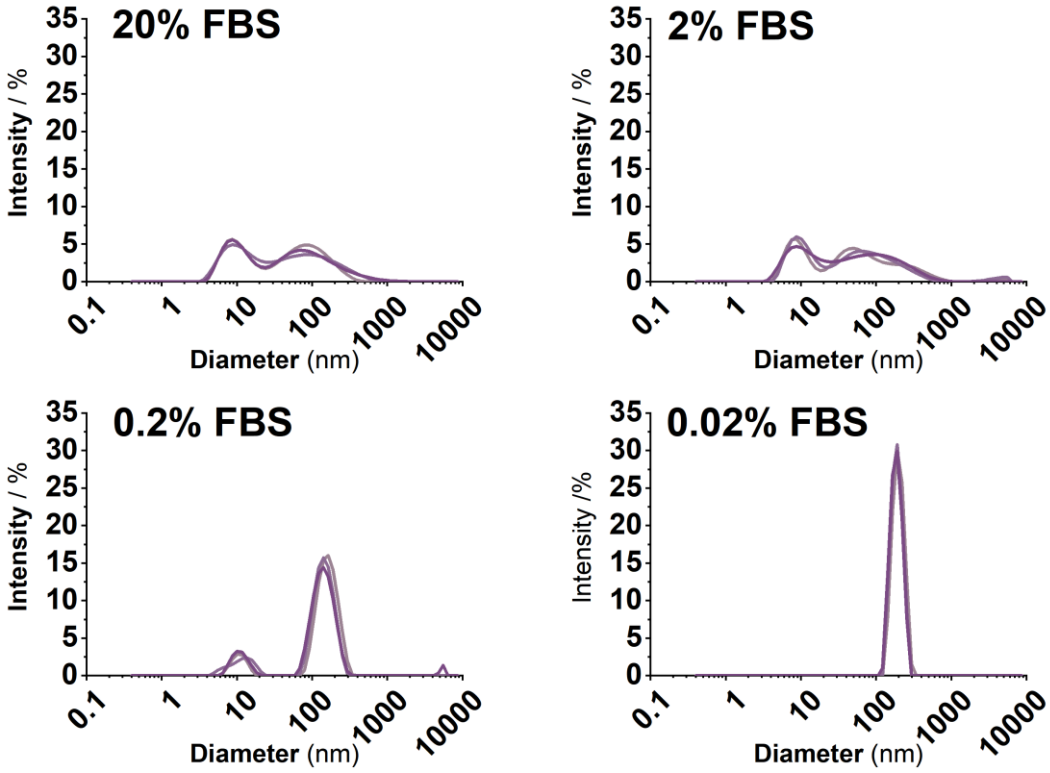

Intensity distributions for the incubation of PLGA nanoparticles in varying concentrations of foetal bovine serum (FBS). Concentration necessary to see both components is significantly different to physiological values. Each coloured trace represents one repeat, all samples measured in triplicate.

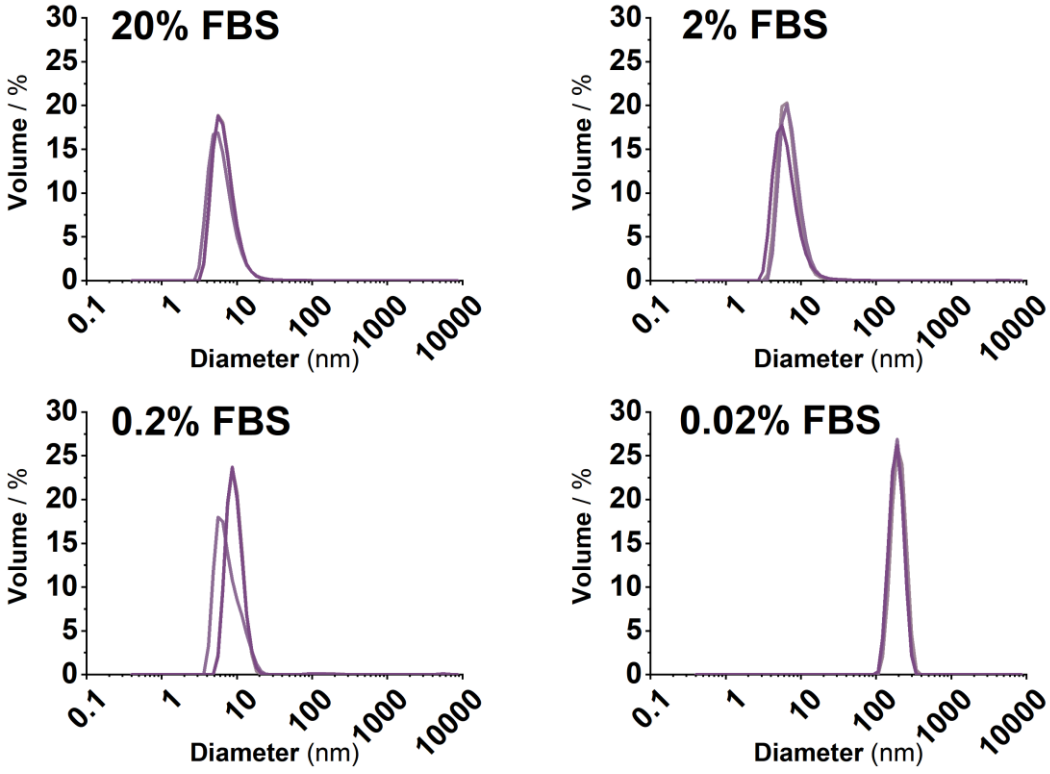

Volume distributions for the incubation of PLGA nanoparticles in varying concentrations of foetal bovine serum (FBS). Each coloured trace represents one repeat, all samples measured in triplicate.

Z-average, peak 1 and peak 2 values for 100nm PLGA titration experiments with decreasing amounts of FBS. All samples have been measured in triplicate.

Sample Name	Z-Ave/ nm	PDI	Peak 1/ nm	Peak 2/ nm
100% FBS 1	15.99	0.445	52.98	9.31
100% FBS 2	15.82	0.441	55.86	10.27
100% FBS 3	15.88	0.445	54.58	9.687
100nm PLGA in 10% FBS 1	18.46	0.48	68.97	10.4
100nm PLGA in 10% FBS 2	18.25	0.478	61.01	9.795
100nm PLGA in 10% FBS 3	18.16	0.479	11.45	75.4
100nm PLGA in 20% FBS 1	21.12	0.558	101.8	10.95
100nm PLGA in 20% FBS 2	21.69	0.507	133.3	12.45
100nm PLGA in 20% FBS 3	22.17	0.516	136.1	11.02
100nm PLGA in 2% FBS 1	21.95	0.673	130.7	9.412
100nm PLGA in 2% FBS 2	22.75	0.529	112	10.63
100nm PLGA in 2% FBS 3	23.05	0.532	133.1	11.64
100nm PLGA in 1% FBS 1	31.96	0.716	150.8	9.298
100nm PLGA in 1% FBS 2	28.72	0.881	238.7	37.9
100nm PLGA in 1% FBS 3	29.36	0.897	222.8	31.53
100nm PLGA in 0.2% FBS 1	94.99	0.699	165.4	10.8
100nm PLGA in 0.2% FBS 2	109.1	0.396	148.1	11.81
100nm PLGA in 0.2% FBS 3	93.09	0.528	146.3	11.13
100nm PLGA in 0.1% FBS 1	116	0.579	155.2	11.98
100nm PLGA in 0.1% FBS 2	139.3	0.384	188	17.38
100nm PLGA in 0.1% FBS 3	114.1	0.489	174.8	12.79
100nm PLGA in 0.02% FBS 1	235.4	1	198.3	0
100nm PLGA in 0.02% FBS 2	224.8	1	189.9	0
100nm PLGA in 0.02% FBS 3	218.7	1	187.4	0

C. DLS Titration Experiment - Human Serum

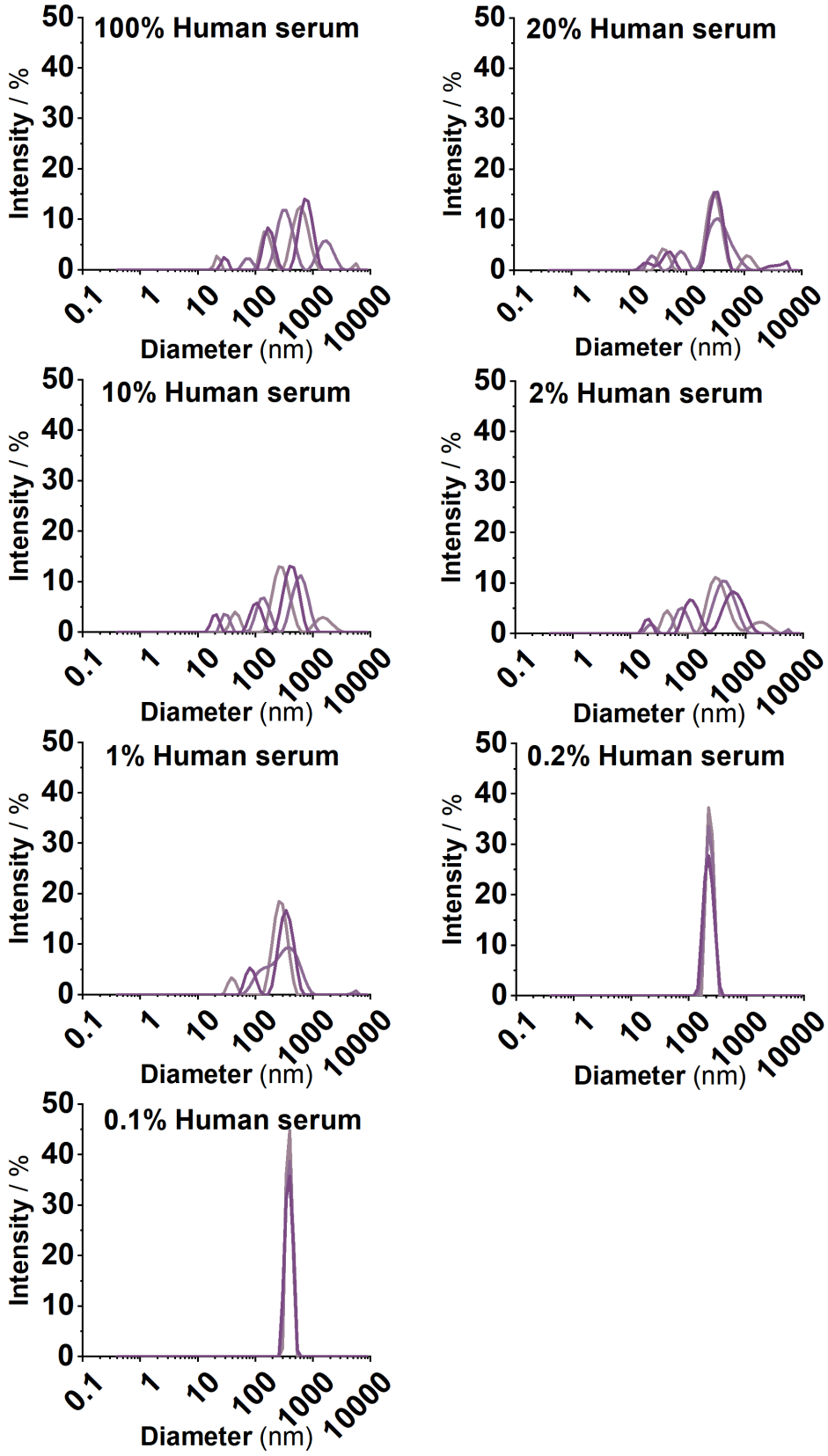

Intensity distributions for the incubation of PLGA nanoparticles in varying concentrations of human serum; concentration necessary to see both components is significantly different to physiological values. Each coloured trace represents one repeat, all samples measured in triplicate.

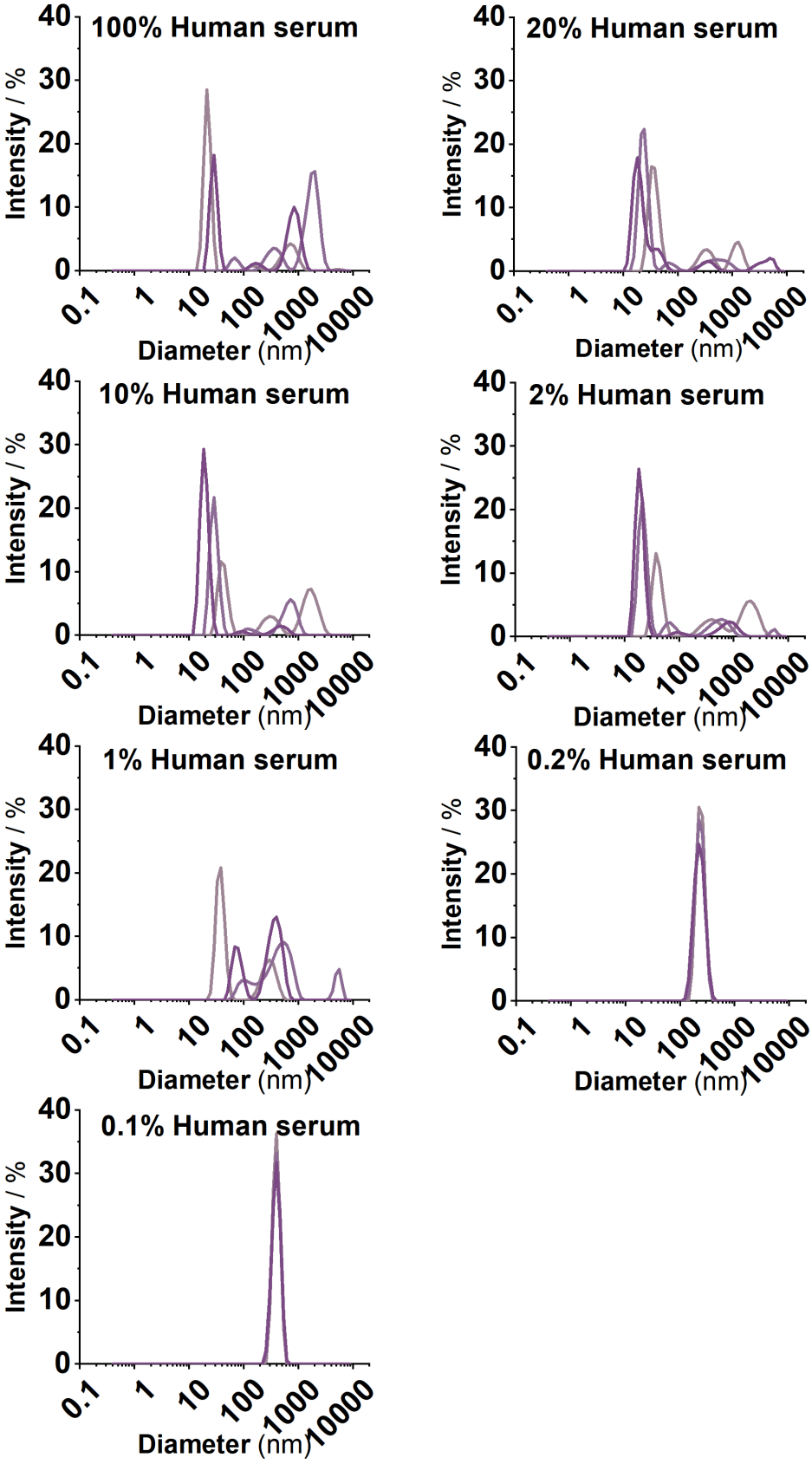

Volume distributions for the incubation of PLGA nanoparticles in varying concentrations of human serum; concentration necessary to see both components is significantly different to physiological values. Each coloured trace represents one repeat, all samples measured in triplicate.

Z-average, peak 1 and peak 2 data for titration experiments between 100nm PLGA nanoparticles and human serum. All samples measured in triplicate.

Sample Name	Z-Ave / nm	Peak 1 / nm	Peak 2 / nm
neat human serum 1	284.4	630.5	155.8
neat human serum 2	259.2	336.8	1719
neat human serum 3	263	773.5	173.6
100nm PLGA in 20% human serum 1	150.6	312.4	40.22
100nm PLGA in 20% human serum 2	178.1	413.6	81.25
100nm PLGA in 20% human serum 3	138.5	333.3	47.38
100nm PLGA in 10% human serum 1	171.7	290.8	1579
100nm PLGA in 10% human serum 2	159.9	616.4	138.3
100nm PLGA in 10% human serum 3	158	428.1	104.8
100nm PLGA in 2% human serum 1	183.8	358.3	43.81
100nm PLGA in 2% human serum 2	175	463.5	78.93
100nm PLGA in 2% human serum 3	160.9	670.2	121.1
100nm PLGA in 1% human serum 1	203.9	275.7	39.54
100nm PLGA in 1% human serum 2	194	325.4	5231
100nm PLGA in 1% human serum 3	195.8	349.5	83.2
100nm PLGA in 0.2% human serum 1	237.1	233.8	0
100nm PLGA in 0.2% human serum 2	224.6	228.8	0
100nm PLGA in 0.2% human serum 3	219.1	223.8	0
100nm PLGA in 0.1% human serum 1	373.6	386.1	0
100nm PLGA in 0.1% human serum 2	362.9	386.5	0
100nm PLGA in 0.1% human serum 3	362.8	381.7	0

D. Protein Content of Serum via Bradford Assay.

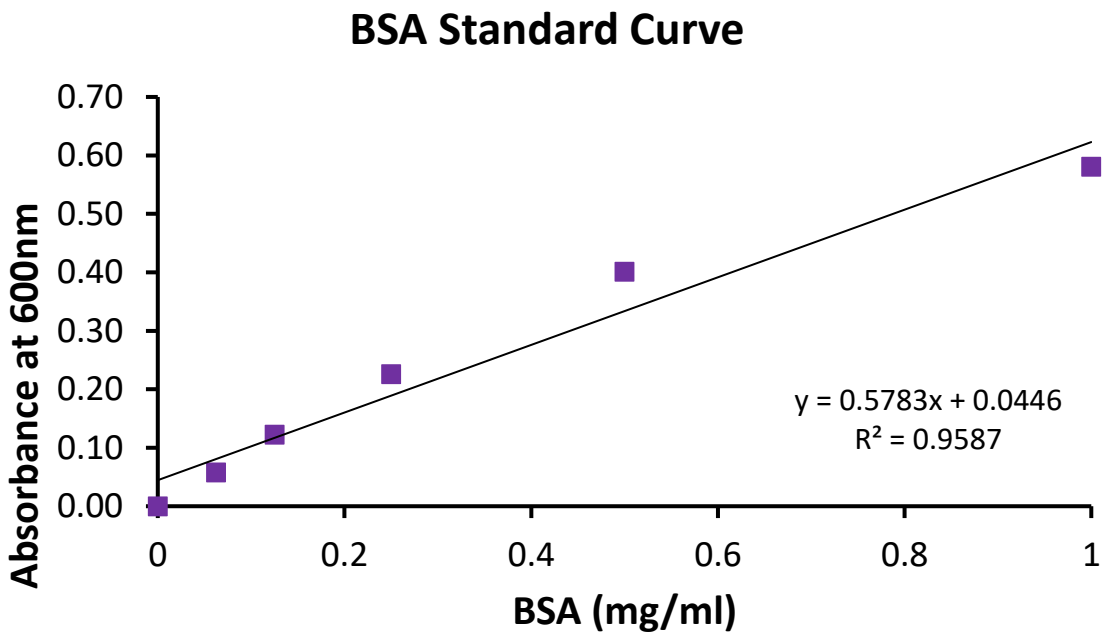

Average protein content (FBS) = ~33 mg mL^{-1}

Average protein content (Human serum) = 77 mg mL^{-1}

Calculations shown overleaf.

BSA Standard Measurement

BSA Standard mg/ml	Absorbance 600nm
0	0.5056
0	0.5030
0	0.5040
0.0625	0.5666
0.0625	0.5697
0.0625	0.5500
0.125	0.6407
0.125	0.6197
0.125	0.6194
0.25	0.7352
0.25	0.7336
0.25	0.7218
0.5	0.8976
0.5	0.8984
0.5	0.9193
1	1.1247
1	1.0337
1	1.0967

Average

BSA Standard mg/ml	Absorbance 600nm
0	0.5042
0.0625	0.5621
0.125	0.6266
0.25	0.7302
0.5	0.9051
1	1.0850

Subtraction of blank

BSA Standard mg/ml	Absorbance 600nm
0	0.0000
0.0625	0.0579
0.125	0.1224
0.25	0.2259
0.5	0.4009
1	0.5808

FBS Measurement

Dilution	Absorbance 600nm
1 in 50	0.8398
1 in 50	0.9143
1 in 50	0.9477
1 in 100	0.7818
1 in 100	0.8326
1 in 100	0.8250

Average

Dilution	Absorbance 600nm
1 in 50	0.90061667
1 in 100	0.81312563

Subtraction of blank

Dilution	Absorbance 600nm
1 in 50	0.39638
1 in 100	0.30889

Calculated concentration

Dilution	concentration mg/ml
1 in 50	30.41
1 in 100	45.70

Human serum Measurement

Dilution	Absorbance 600nm
1 in 100	0.8425
1 in 100	0.9474
1 in 100	0.9181
1 in 200	0.8345
1 in 200	0.7924
1 in 200	0.8302

Average

Dilution	Absorbance 600nm
1 in 100	0.90266711
1 in 200	0.81902598

Subtraction of blank

Dilution	Absorbance 600nm
1 in 100	0.39843
1 in 200	0.31479

Calculated concentration

Dilution	concentration mg/ml
1 in 100	61.18
1 in 200	93.44

E. Particle Tracking Analysis - Control Samples in PBS

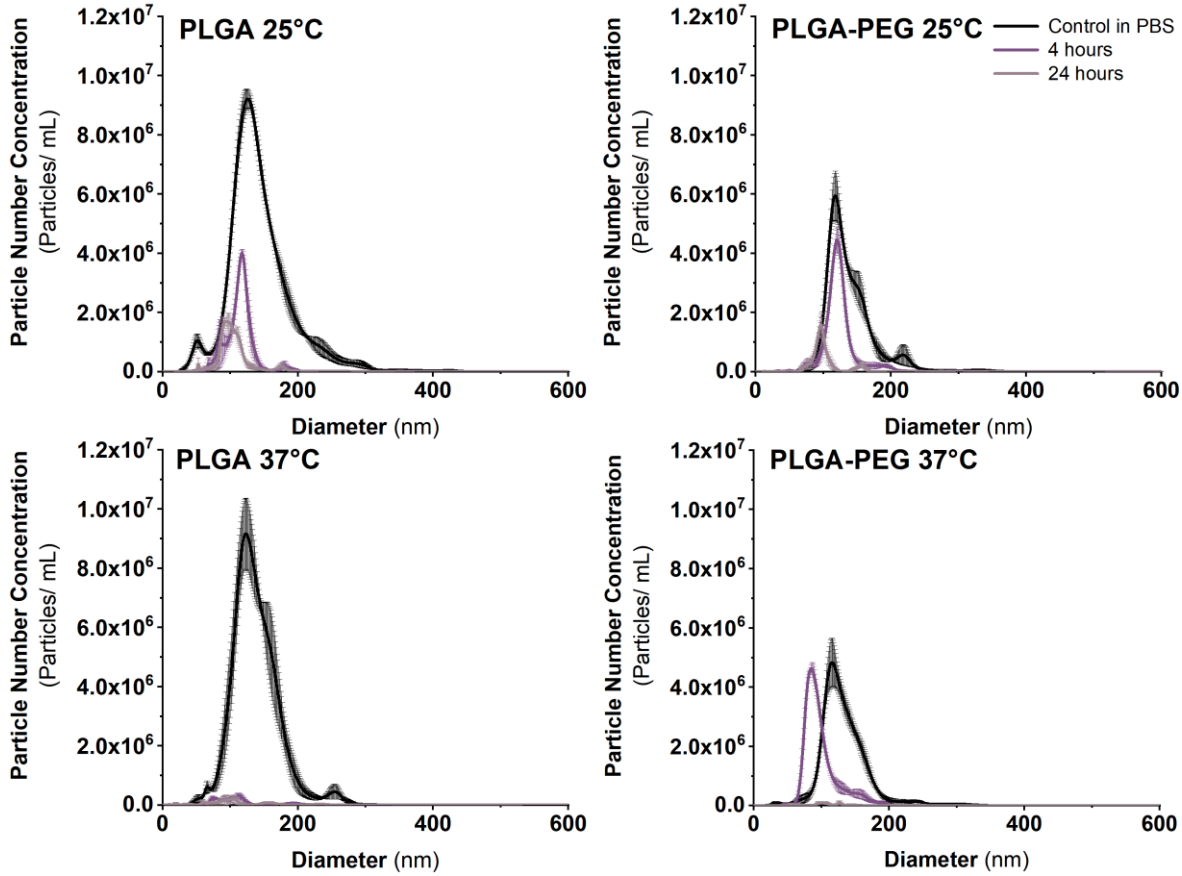

The effect of incubation time, temperature on particle agglomeration of PLGA and PLGA-PEG in PBS, measured by particle tracking analysis. Each sample was measured in triplicate.

F. Particle Tracking Analysis - Samples in FBS

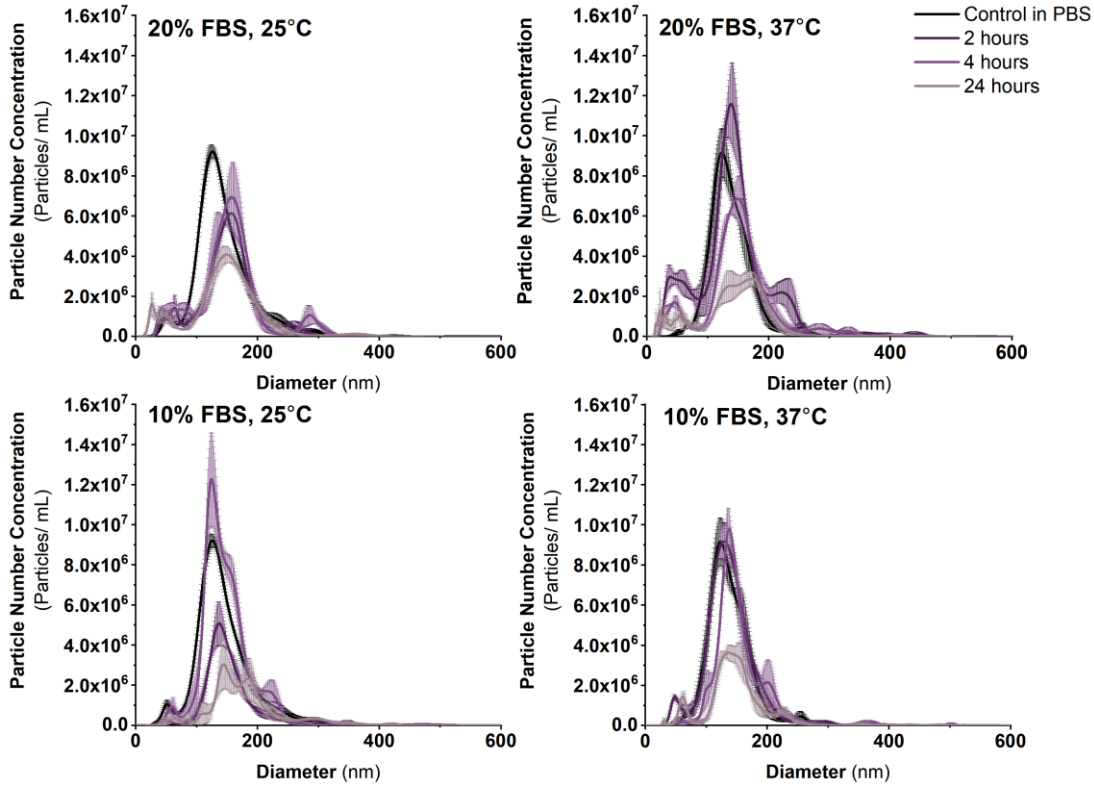

The effect of incubation time, temperature, and concentration of protein on particle agglomeration of PLGA in FBS. It can clearly be seen from these graphs that as incubation time increases, that concentration of particles decreases significantly.

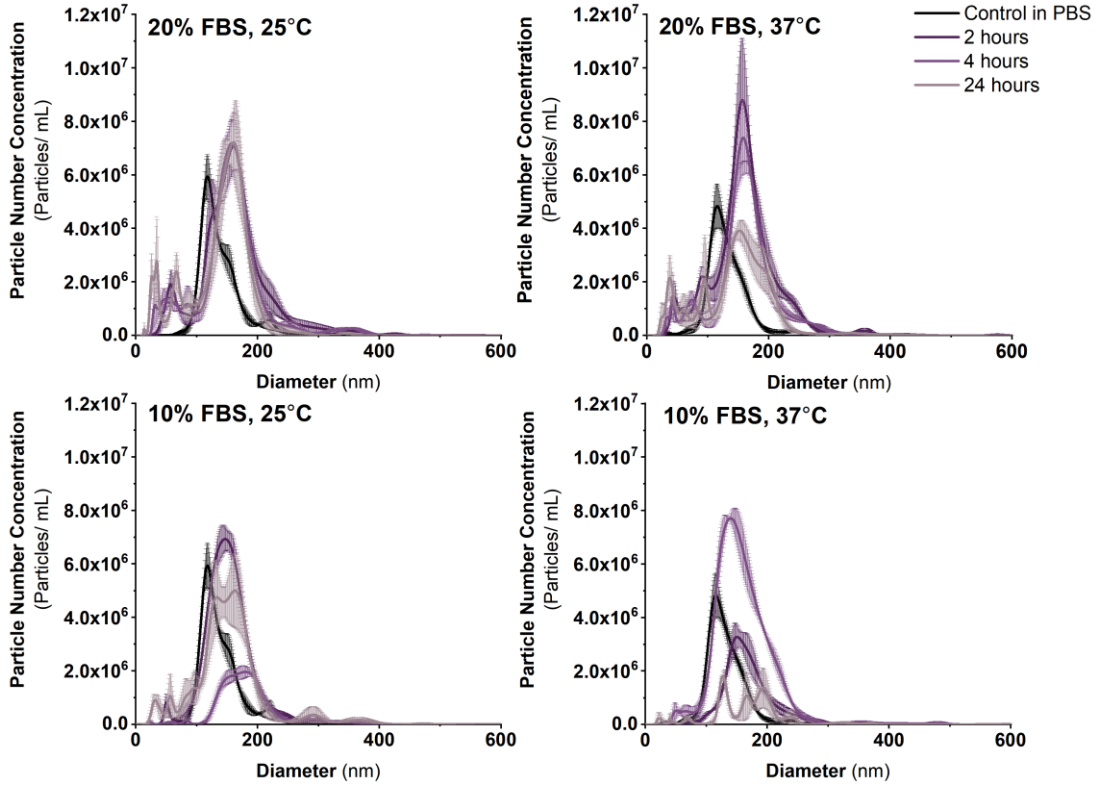

The effect of incubation time, temperature, and concentration of protein on particle agglomeration of PLGA-PEG in FBS. It can clearly be seen from these graphs that as incubation time increases, that concentration of particles decreases significantly.

Particle Count

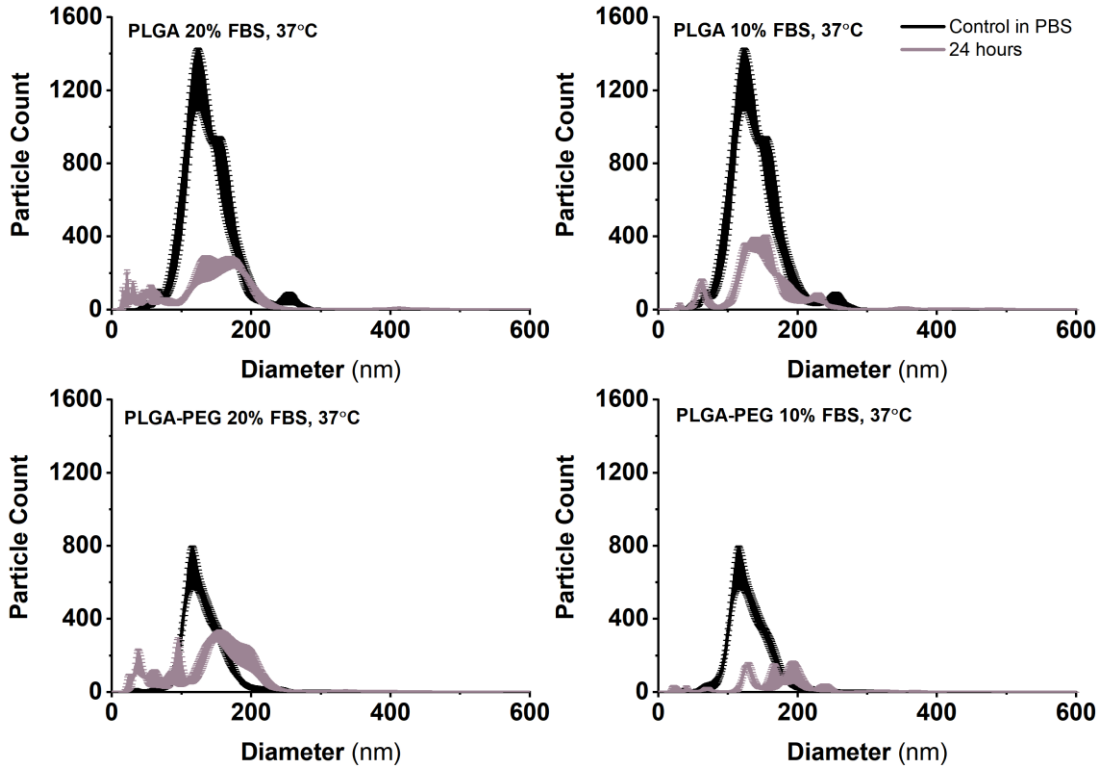

The effect of incubation time, temperature, nanoparticle identity and concentration of protein on particle agglomeration. It can clearly be seen from these graphs that as incubation time increases, that concentration of particles decreases significantly.

Sample ID	Particles per frame	Total Frames	Total particles in sample	Concentration (particles/mL)	Sample volume	Conversion factor
PLGA_PBS_25c	59.2	1498	88681.6	7.12E+08	1.25E-04	8028.72
PLGA_PBS_37c	57.9	1498	86734.2	6.28E+08	1.38E-04	7240.51
PLGA_20FBS_25c_24h	17.1	1498	25615.8	3.96E+08	6.47E-05	15459.21
PLGA_20FBS_37c_24h	18.9	1498	28312.2	3.14E+08	9.02E-05	11090.63
PLGA_10FBS_25c_24h	16.3	1498	24417.4	2.51E+08	9.73E-05	10279.55
PLGA_10FBS_37c_24h	18.9	1498	28312.2	2.87E+08	9.86E-05	10136.97
PEG_PBS_25c	29.2	1498	43741.6	3.10E+08	1.41E-04	7087.08
PEG_PBS_37c	26	1498	38948	2.75E+08	1.42E-04	7060.70
PEG_20FBS_25c_24h	26.4	1498	39547.2	5.45E+08	7.26E-05	13781.00
PEG_20FBS_37c_24h	20.9	1498	31308.2	3.96E+08	7.91E-05	12648.44
PEG_10FBS_25c_24h	24.8	1498	37150.4	4.72E+08	7.87E-05	12705.11
PEG_10FBS_37c_24h	6	1498	8988	1.12E+08	8.03E-05	12461.06

G. Particle Tracking Analysis – Samples in Human Serum

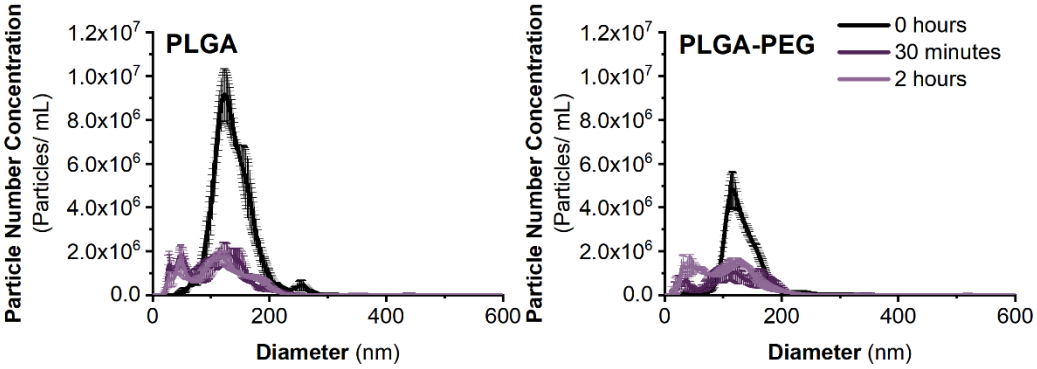

The effect of incubation time on PLGA and PLGA-PEG agglomeration and particle number concentration in 1 % human serum at 37°C, measured via particle tracking analysis. Each sample is measured in triplicate.

H. Particle Tracking Analysis – Statistical Analysis

Samples in PBS

Overall ANOVA

	DF	Sum of Squares	Mean Square	F Value	P Value
Group	1	882.09375	882.09375	2.04447	0.172
Time	1	577.22042	577.22042	1.33785	0.26439
Temp	1	21.09375	21.09375	0.04889	0.8278
Group * Time	1	194.37042	194.37042	0.4505	0.51167
Group * Temp	1	122.85375	122.85375	0.28474	0.60094
Time * Temp	1	82.51042	82.51042	0.19124	0.66773
Group * Time * Temp	1	165.90042	165.90042	0.38451	0.54393
Model	7	2046.04292	292.29185	0.67746	0.68901
Error	16	6903.26667	431.45417	0	0
Corrected Total	23	8949.30958	0	0	0

At the 0.05 level, the population means of **Group** are **not significantly** different.
At the 0.05 level, the population means of **Time** are **not significantly** different.
At the 0.05 level, the population means of **Temp** are **not significantly** different.
At the 0.05 level, the population means of **Group * Time** are **not significantly** different.
At the 0.05 level, the population means of **Group * Temp** are **not significantly** different.
At the 0.05 level, the population means of **Time * Temp** are **not significantly** different.
At the 0.05 level, the population means of **Group * Time * Temp** are **not significantly** different.

Samples in FBS

PLGA

Overall ANOVA

	DF	Sum of Squares	Mean Square	F Value	P Value
FBS Conc	1	354.97042	354.97042	7.78415	0.01311
Time	1	122.85375	122.85375	2.69406	0.12023
Temp	1	9.50042	9.50042	0.20833	0.65421
FBS Conc * Time	1	9.75375	9.75375	0.21389	0.64996
FBS Conc * Temp	1	135.85042	135.85042	2.97907	0.1036
Time * Temp	1	808.52042	808.52042	17.73006	6.63474E-4
FBS Conc * Time * Temp	1	342.77042	342.77042	7.51662	0.01448
Model	7	1784.21958	254.88851	5.58946	0.00213
Error	16	729.62667	45.60167	0	0
Corrected Total	23	2513.84625	0	0	0

At the 0.05 level, the population means of **FBS Conc** are **significantly** different.
At the 0.05 level, the population means of **Time** are **not significantly** different.
At the 0.05 level, the population means of **Temp** are **not significantly** different.
At the 0.05 level, the population means of **FBS Conc * Time** are **not significantly** different.
At the 0.05 level, the population means of **FBS Conc * Temp** are **not significantly** different.
At the 0.05 level, the population means of **Time * Temp** are **significantly** different.
At the 0.05 level, the population means of **FBS Conc * Time * Temp** are **significantly** different.

PLGA-PEG

Overall ANOVA

	DF	Sum of Squares	Mean Square	F Value	P Value
FBS Conc	1	1392.32667	1392.32667	14.21044	0.00168
Time	1	27.30667	27.30667	0.2787	0.6048
Temp	1	2890.815	2890.815	29.50438	5.53872E-5
FBS Conc * Time	1	469.935	469.935	4.79627	0.04368
FBS Conc * Temp	1	1066.66667	1066.66667	10.88667	0.00452
Time * Temp	1	1056.02667	1056.02667	10.77807	0.00468
FBS Conc * Time * Temp	1	2517.40167	2517.40167	25.69323	1.13931E-4
Model	7	9420.47833	1345.78262	13.7354	1.08653E-5
Error	16	1567.66667	97.97917	0	0
Corrected Total	23	10988.145	0	0	0

At the 0.05 level, the population means of **FBS Conc** are **significantly** different.
At the 0.05 level, the population means of **Time** are **not significantly** different.
At the 0.05 level, the population means of **Temp** are **significantly** different.
At the 0.05 level, the population means of **FBS Conc * Time** are **significantly** different.
At the 0.05 level, the population means of **FBS Conc * Temp** are **significantly** different.
At the 0.05 level, the population means of **Time * Temp** are **significantly** different.
At the 0.05 level, the population means of **FBS Conc * Time * Temp** are **significantly** different.

Samples in human serum

t-test

Descriptive Statistics

		N	Mean	SD	SEM	Median
"D50"		3	111.6	4.41362	2.5482	111.2
		3	112.13333	6.71218	3.87528	110.2
	Difference	3	-0.53333	2.48462	1.4345	0.8
	Overall	6	111.86667	5.08907	2.07761	110.7

Test Statistics

t Statistic	DF	Prob>|t|
-0.37179	2	0.74574

Null Hypothesis: mean1-mean2 = 0
Alternative Hypothesis: mean1-mean2 <> 0
At the 0.05 level, the difference of the population means is NOT significantly different from the test difference(0).

Two-way ANOVA also used for these samples and no statistically significant incubation parameters were found.

Overall ANOVA

	DF	Sum of Squares	Mean Square	F Value	P Value
Group	1	20.02083	20.02083	0.31443	0.59033
Incubation time	1	90.20083	90.20083	1.41664	0.26808
Interaction	1	73.5075	73.5075	1.15446	0.31395
Model	3	183.72917	61.24306	0.96184	0.45635
Error	8	509.38	63.6725	--	--
Corrected Total	11	693.10917	--	--	--

At the 0.05 level, the population means of **Group** are **not significantly** different.
At the 0.05 level, the population means of **Incubation time** are **not significantly** different.
At the 0.05 level, the interaction between **Group** and **Incubation time** is **not significant**.

I. Resonant Mass Measurement – Samples in FBS

PLGA

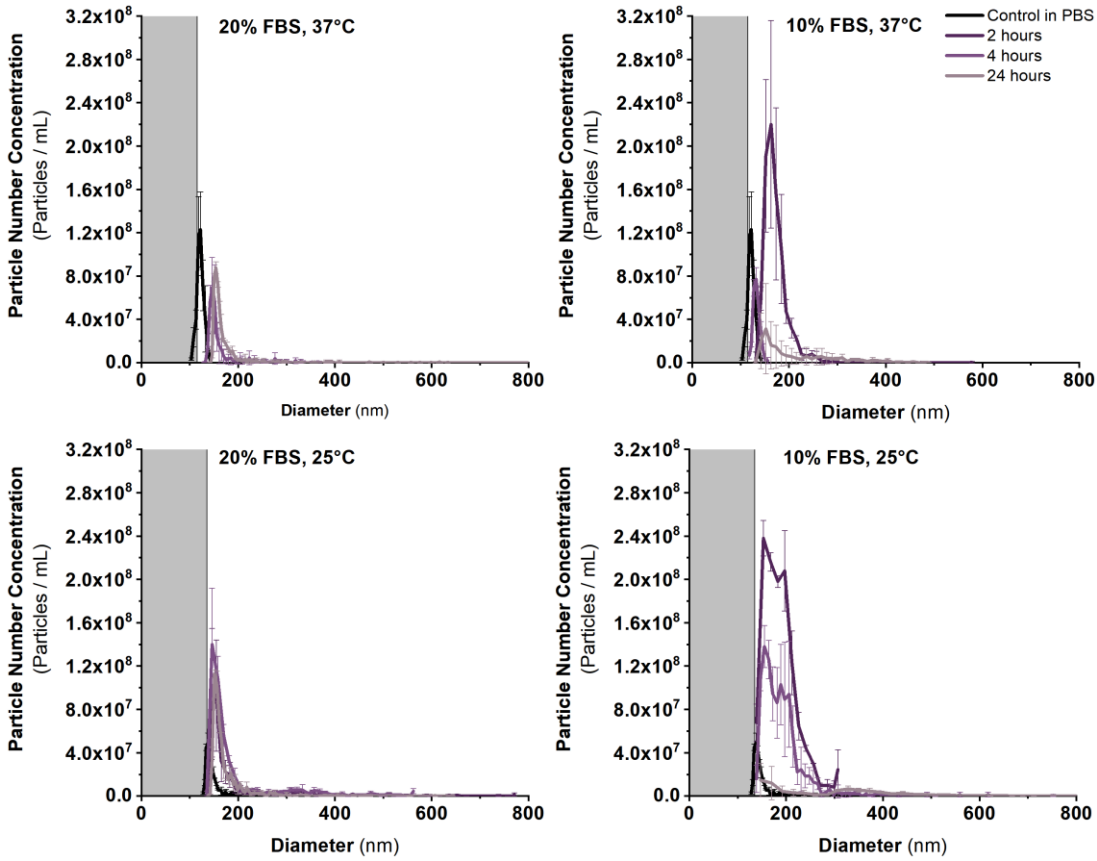

The effect of incubation time, temperature and FBS concentration on PLGA nanoparticle size distributions measured by RMM. (n=3). The concentration of PLGA nanoparticles decreases with incubation time.

PLGA-PEG

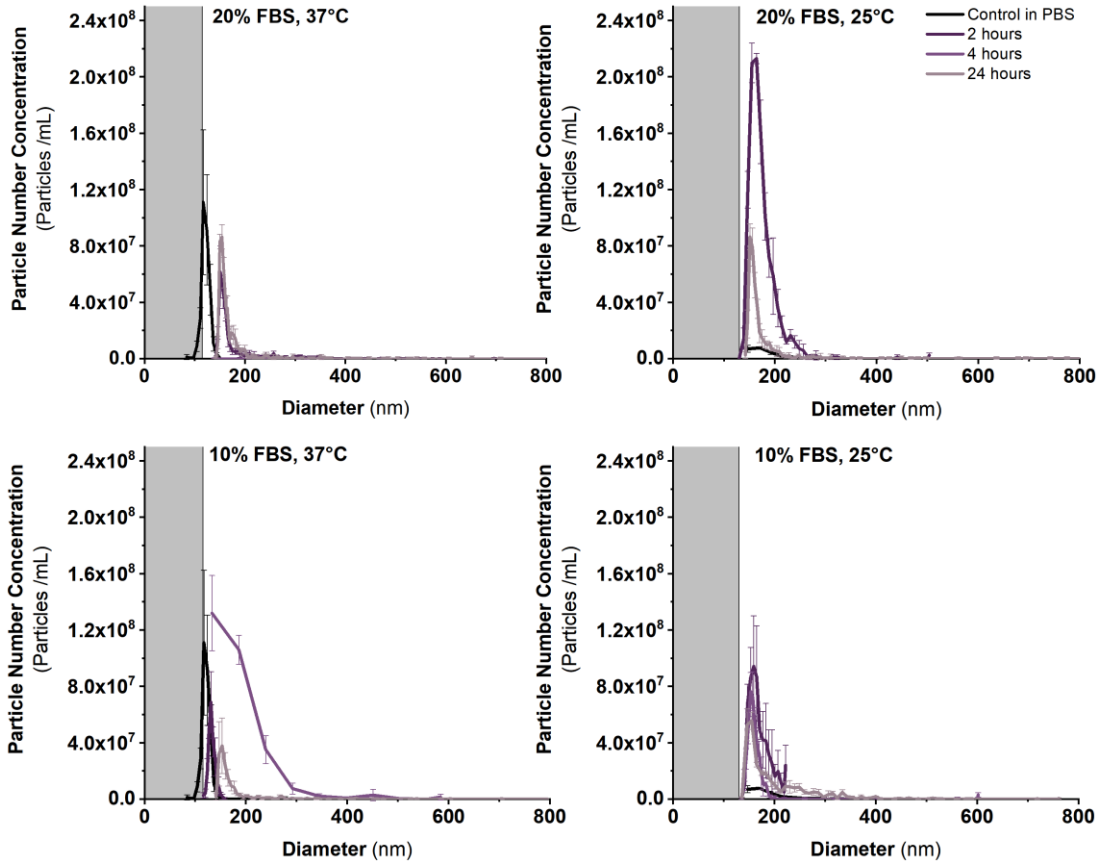

The effect of incubation time, temperature and FBS concentration on PLGA-PEG nanoparticle size distributions measured by RMM. (n=3). The concentration of PLGA-PEG nanoparticles decreases with incubation time.

J. Resonant Mass Measurement – Statistical Analysis

Samples in FBS

PLGA

Overall ANOVA

	DF	Sum of Squares	Mean Square	F Value	P Value
FBS Conc	1	10463.8032	10463.8032	8.44064	0.01033
Time	1	29577.3667	29577.3667	23.85861	1.65311E-4
Temp	1	8018.70484	8018.70484	6.4683	0.0217
FBS Conc * Time	1	10463.8032	10463.8032	8.44064	0.01033
FBS Conc * Temp	1	3806.46094	3806.46094	3.07049	0.09886
Time * Temp	1	1542.567	1542.567	1.24431	0.28112
FBS Conc * Time * Temp	1	3806.46094	3806.46094	3.07049	0.09886
Model	7	67679.16683	9668.4524	7.79907	3.52905E-4
Error	16	19835.09707	1239.69357	0	0
Corrected Total	23	87514.2639	0	0	0

At the 0.05 level, the population means of **FBS Conc** are **significantly** different.
At the 0.05 level, the population means of **Time** are **significantly** different.
At the 0.05 level, the population means of **Temp** are **significantly** different.
At the 0.05 level, the population means of **FBS Conc * Time** are **significantly** different.
At the 0.05 level, the population means of **FBS Conc * Temp** are **not significantly** different.
At the 0.05 level, the population means of **Time * Temp** are **not significantly** different.
At the 0.05 level, the population means of **FBS Conc * Time * Temp** are **not significantly** different.

PLGA-PEG

Overall ANOVA

	DF	Sum of Squares	Mean Square	F Value	P Value
FBS Conc	1	62.69434	62.69434	8.21049	0.01122
Time	1	1524.661	1524.661	199.67066	1.86446E-10
Temp	1	4895.4697	4895.4697	641.11409	2.45359E-14
FBS Conc * Time	1	62.69434	62.69434	8.21049	0.01122
FBS Conc * Temp	1	60.6426	60.6426	7.9418	0.01237
Time * Temp	1	2706.6132	2706.6132	354.45993	2.42451E-12
FBS Conc * Time * Temp	1	60.6426	60.6426	7.9418	0.01237
Model	7	9373.4178	1339.05969	175.36418	6.4837E-14
Error	16	122.17407	7.63588	0	0
Corrected Total	23	9495.59186	0	0	0

At the 0.05 level, the population means of **FBS Conc** are **significantly** different.
At the 0.05 level, the population means of **Time** are **significantly** different.
At the 0.05 level, the population means of **Temp** are **significantly** different.
At the 0.05 level, the population means of **FBS Conc * Time** are **significantly** different.
At the 0.05 level, the population means of **FBS Conc * Temp** are **significantly** different.
At the 0.05 level, the population means of **Time * Temp** are **significantly** different.
At the 0.05 level, the population means of **FBS Conc * Time * Temp** are **significantly** different.

K. Resonant Mass Measurement – Dry Mass

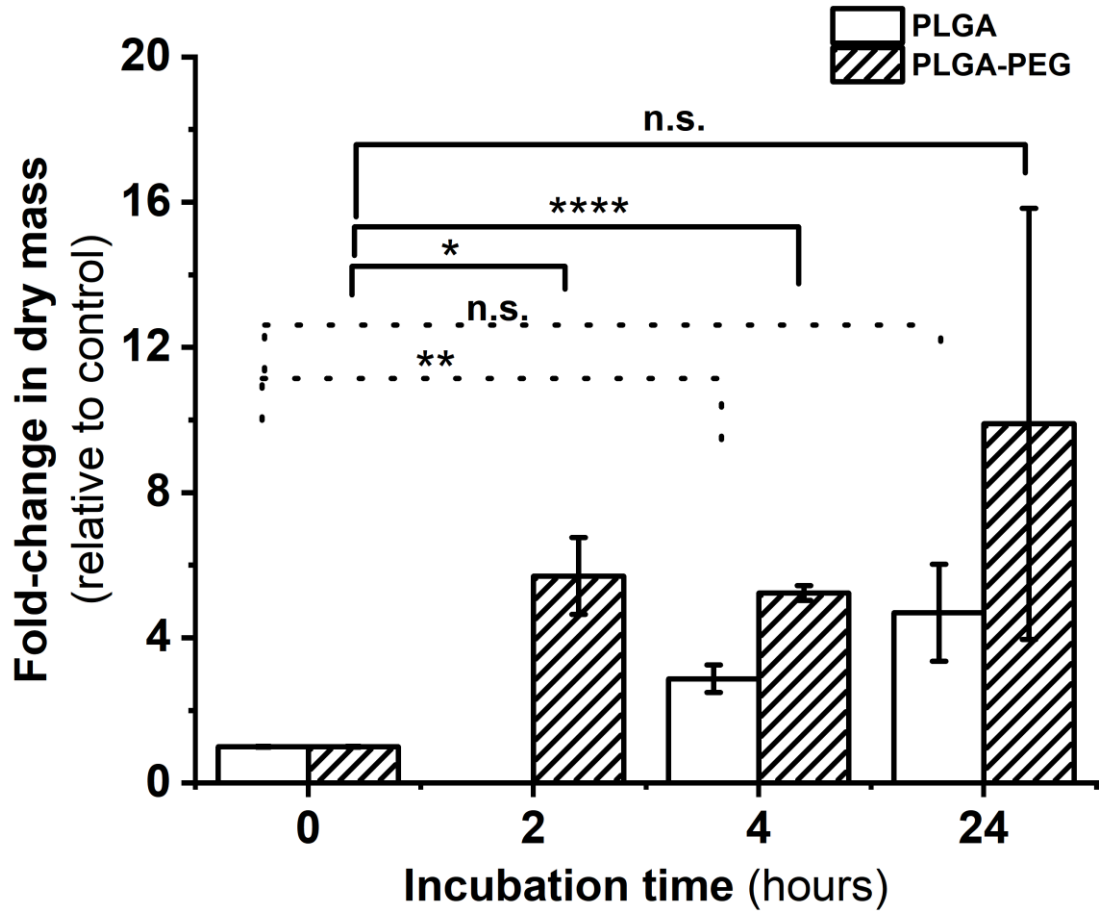

The impact of incubation time on mean particle dry mass relative to control (nanoparticles suspended in PBS). PLGA and PLGA-PEG nanoparticles treated in 20% FBS (n=3). No samples were analysed for PLGA nanoparticles in 20% FBS following 2 hours of coincubation. Errors are given as standard deviation.

10% FBS, 37°C

PLGA	Particle dry mass				Fold-change in mass				
Incubation time (hours)	Average particle dry mass (g)			Average particle dry mass (g)	Fold-change in mass relative to control			Average fold-change	Error
CONTROL	1.22E-15	1.21E-15	1.26E-15	1.23E-15	0.99	0.98	1.02	1.00	0.01
2	3.49E-15	2.72E-15	3.13E-15	3.11E-15	2.84	2.21	2.55	2.53	0.18
4	1.6E-15	1.62E-15	1.55E-15	1.59E-15	1.30	1.32	1.26	1.29	0.02
24	7.7E-15	1.27E-14	1.55E-14	1.20E-14	6.26	10.30	12.60	9.72	1.85

PLGA-PEG	Particle dry mass				Fold-change in mass				
Incubation time (hours)	Average particle dry mass (g)			Average particle dry mass (g)	Fold-change in mass relative to control			Average fold-change	Error
CONTROL	1.2E-15	1.23E-15	1.24E-15	1.22E-15	0.98	1.01	1.01	1.00	0.01
2	1.6E-15	1.62E-15	1.55E-15	1.59E-15	1.31	1.32	1.27	1.30	0.02
4	9.5E-15	4.87E-15	4.25E-15	6.21E-15	7.77	3.98	3.47	5.08	1.36
24	1.48E-14	1.88E-14	1.24E-14	1.53E-14	12.10	15.34	10.14	12.53	1.52

20% FBS, 37°C

PLGA	Particle dry mass				Fold-change in mass				
Incubation time (hours)	Average particle dry mass (g)			Average particle dry mass (g)	Fold-change in mass relative to control			Average fold-change	Error
CONTROL	1.22E-15	1.21E-15	1.26E-15	1.23E-15	0.99	0.98	1.02	1.00	0.01
2					0.00	0.00	0.00	0.00	0.00
4	3.17E-15	2.97E-15	4.46E-15	3.53E-15	2.57	2.42	3.62	2.87	0.38
24	8.98E-15	3.5E-15	4.85E-15	5.77E-15	7.29	2.84	3.94	4.69	1.34

PLGA-PEG	Particle dry mass				Fold-change in mass				
Incubation time (hours)	Average particle dry mass (g)			Average particle dry mass (g)	Fold-change in mass relative to control			Average fold-change	Error
CONTROL	1.2E-15	1.23E-15	1.24E-15	1.22E-15	0.98	1.01	1.01	1.00	0.01
2	9.56E-15	5.76E-15	5.61E-15	6.98E-15	7.82	4.71	4.58	5.70	1.06
4	5.95E-15	6.47E-15	6.79E-15	6.40E-15	4.86	5.29	5.55	5.23	0.20
24	2.66E-14	5.18E-15	4.51E-15	1.21E-14	21.77	4.23	3.69	9.90	5.94

L. Orthogonal Analysis

Control in PBS

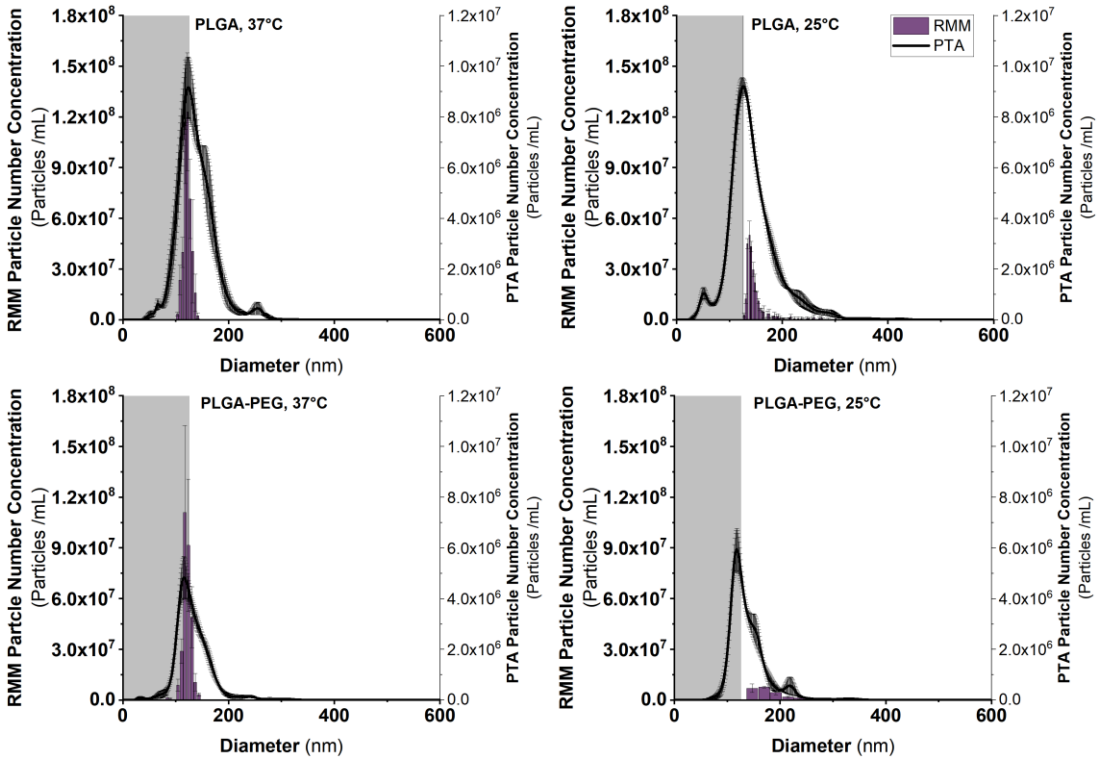

A comparison of PLGA and PLGA-PEG nanoparticle size distributions measured by RMM and PTA (n=3). Each sample has been coincubated in PBS. On visual inspection, generally good agreement in size distribution irrespective of methodology used, but clear differences in sample concentration between methods.

Samples in FBS

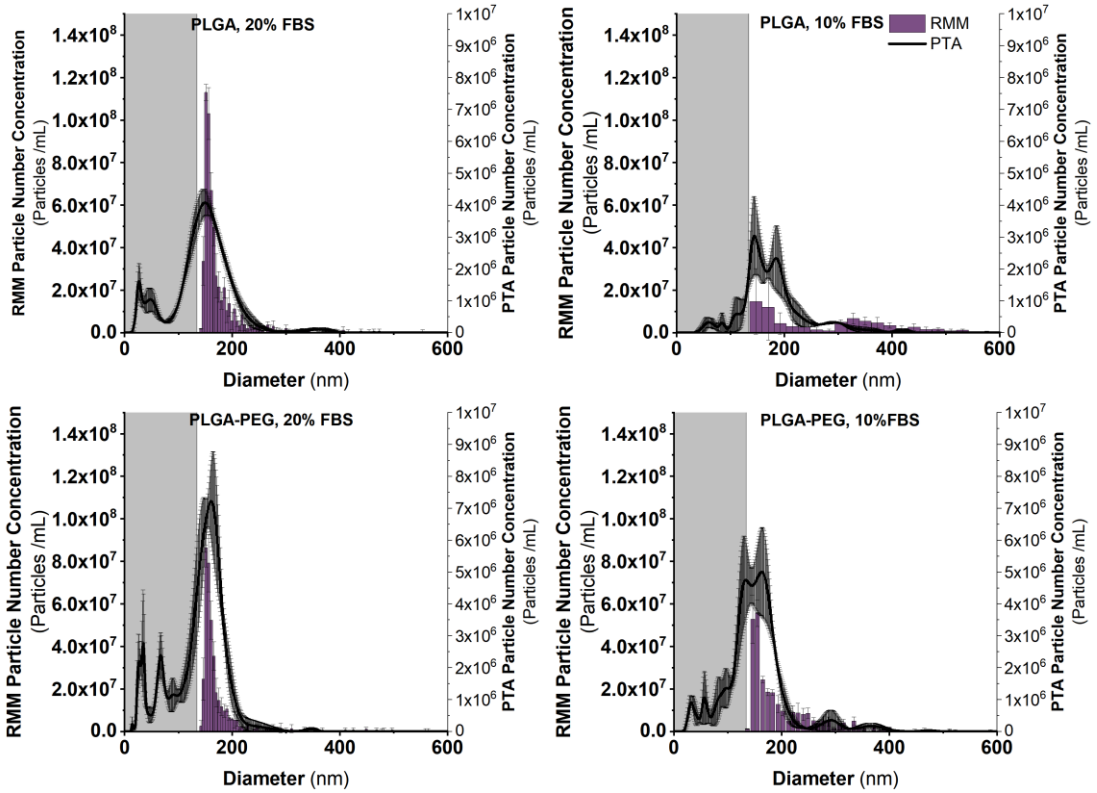

A comparison of PLGA and PLGA-PEG nanoparticle size distributions measured by RMM and PTA (n=3). Incubation time and temperature are 24 hours at 25°C for each sample. On visual inspection, generally good agreement in size distribution irrespective of methodology used, but clear differences in sample concentration between methods.

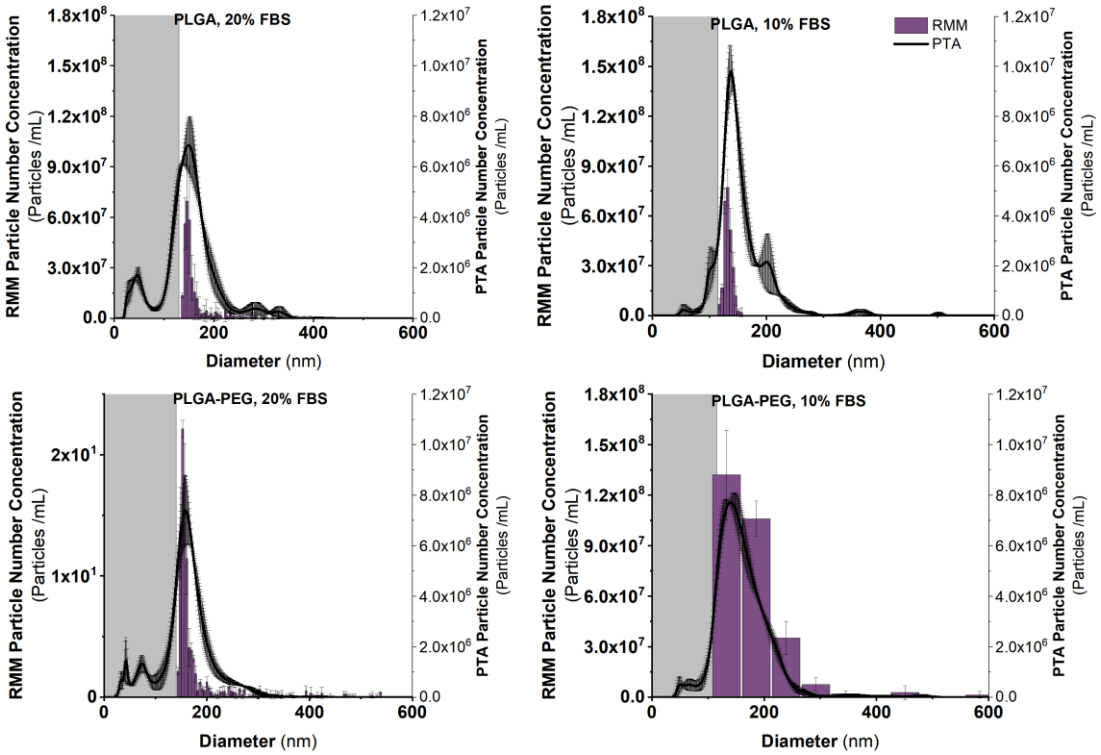

A comparison of PLGA and PLGA-PEG nanoparticle size distributions measured by RMM and PTA (n=3). Incubation time and temperature are 4 hours at 37°C for each sample. On visual inspection, generally good agreement in size distribution irrespective of methodology used, but clear differences in sample concentration between methods.

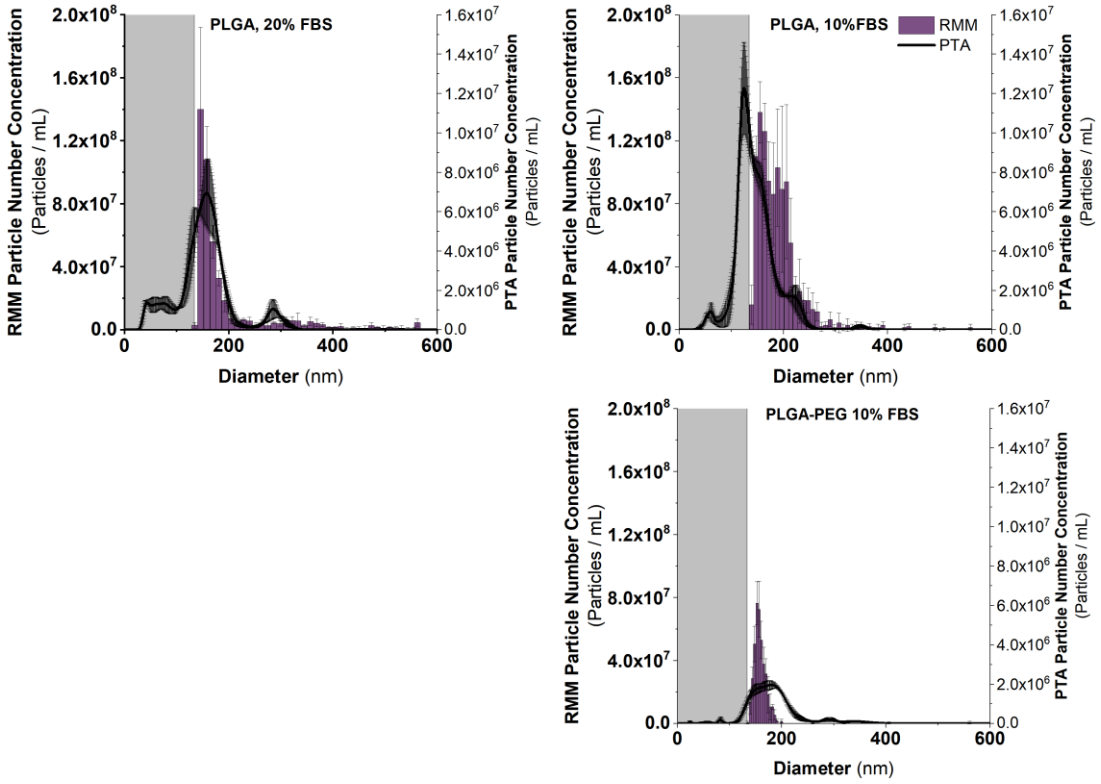

A comparison of PLGA and PLGA-PEG nanoparticle size distributions measured by RMM and PTA (n=3). Incubation time and temperature are 4 hours at 25°C for each sample. PLGA-PEG in 20% FBS is missing. On visual inspection, generally good agreement in size distribution irrespective of methodology used, but clear differences in sample concentration between methods.

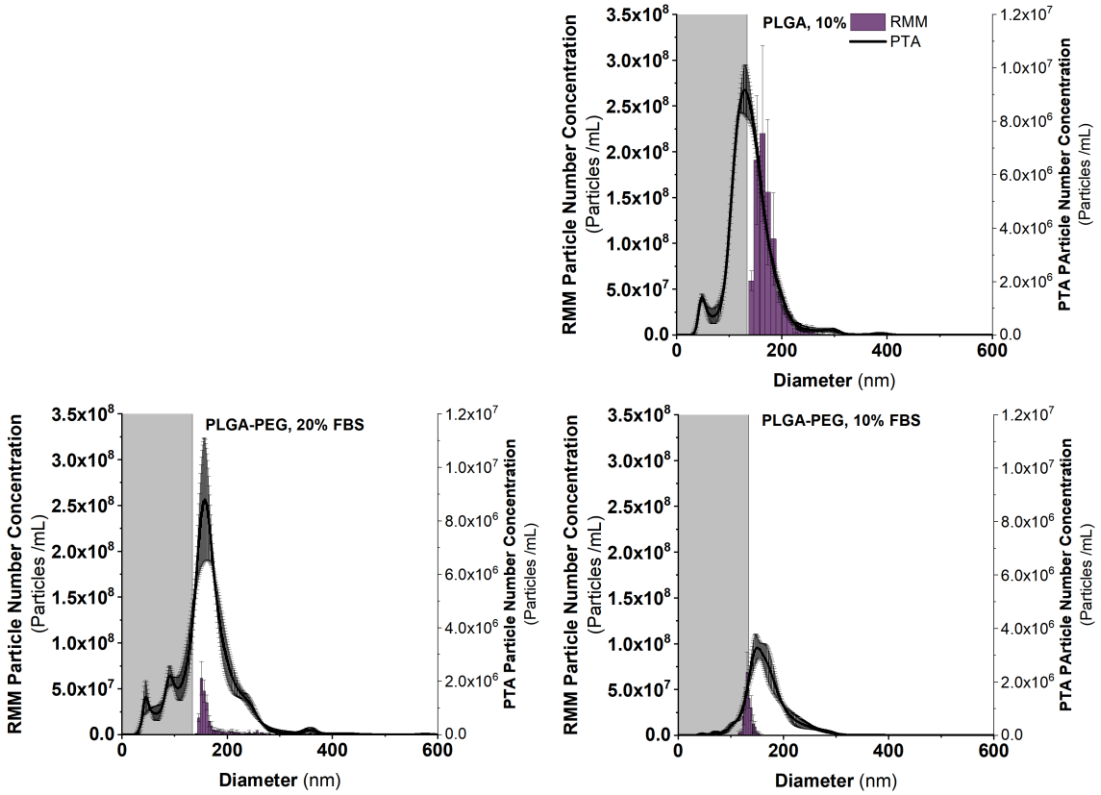

A comparison of PLGA and PLGA-PEG nanoparticle size distributions measured by RMM and PTA (n=3). Incubation time and temperature are 2 hours at 37°C for each sample. PLGA in 20% FBS is missing. On visual inspection, generally good agreement in size distribution irrespective of methodology used, but clear differences in sample concentration between methods.

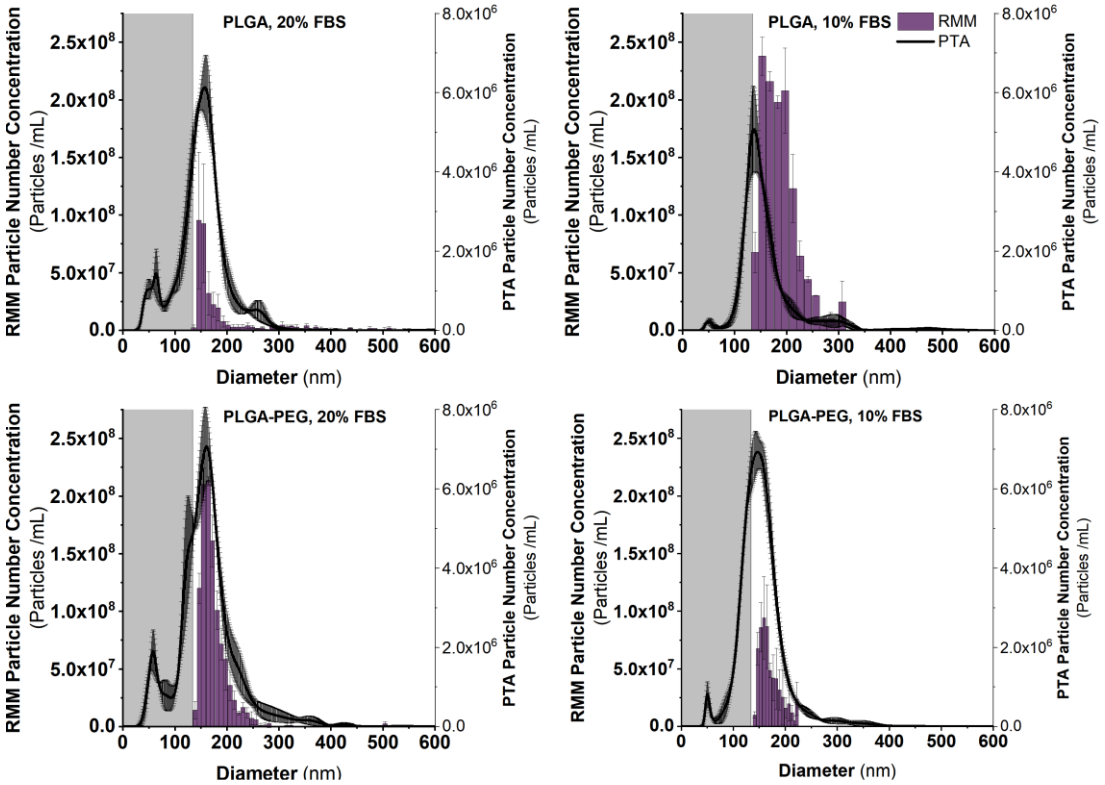

A comparison of PLGA and PLGA-PEG nanoparticle size distributions measured by RMM and PTA (n=3). Incubation time and temperature are 2 hours at 25°C for each sample. On visual inspection, generally good agreement in size distribution irrespective of methodology used, but clear differences in sample concentration between methods.

M.Orthogonal Analysis – Statistics

PLGA, 20% FBS, 37°C

Descriptive Statistics

		N	Mean	SD	SEM	Median
"D50"		3	151.3	5.24595	3.02875	152.1
		3	158.79667	1.3091	0.75581	158.43
	Difference	3	-7.49667	4.59061	2.65039	-5.61
	Overall	6	155.04833	5.34355	2.18149	156.905

Test Statistics

t Statistic	DF	Prob>|t|
-2.82851	2	0.10557

Null Hypothesis: mean1-mean2 = 0
Alternative Hypothesis: mean1-mean2 <> 0
At the 0.05 level, the difference of the population means is NOT significantly different from the test difference(0).

PLGA-PEG, 20% FBS, 37°C

Descriptive Statistics

		N	Mean	SD	SEM	Median
"D50"		3	151.26667	4.73744	2.73516	149.1
E		3	158.24333	0.34501	0.19919	158.24
	Difference	3	-6.97667	4.46363	2.57708	-8.8
	Overall	6	154.755	4.86077	1.9844	157.3

Test Statistics

t Statistic	DF	Prob>|t|
-2.7072	2	0.11365

Null Hypothesis: mean1-mean2 = 0
Alternative Hypothesis: mean1-mean2 <> 0
At the 0.05 level, the difference of the population means is NOT significantly different from the test difference(0).

PLGA, 10% FBS, 37°C

Descriptive Statistics

		N	Mean	SD	SEM	Median
"D50"		3	145.4	0.98489	0.56862	145.1
		3	191.94333	44.04553	25.4297	175.67
	Difference	3	-46.54333	44.86583	25.9033	-30.57
	Overall	6	168.67167	37.76607	15.41793	152.425

Test Statistics

t Statistic	DF	Prob>|t|
-1.79681	2	0.2142

Null Hypothesis: mean1-mean2 = 0
Alternative Hypothesis: mean1-mean2 <> 0
At the 0.05 level, the difference of the population means is NOT significantly different from the test difference(0).

PLGA-PEG, 10% FBS, 37°C

Descriptive Statistics

		N	Mean	SD	SEM	Median
"D50"		3	164.8	21.55017	12.442	164.7
E		3	158.35	5.64457	3.2589	156.57
	Difference	3	6.45	20.92227	12.07948	0.03
	Overall	6	161.575	14.52547	5.93	160.62

Test Statistics

t Statistic	DF	Prob>|t|
0.53396	2	0.64677

Null Hypothesis: mean1-mean2 = 0
Alternative Hypothesis: mean1-mean2 <> 0
At the 0.05 level, the difference of the population means is NOT significantly different from the test difference(0).

Part 2: Computational Fluid Dynamics

Chapter 3
Developing a Combined Computational Fluid Dynamics and Discrete Element Method Approach to Model Nanoparticle Behaviour *in vivo.*

3.1 Introduction

In **Chapter 2**, an extensive literature review of the current knowledge on a selection of nanoparticles as well as the phenomenon known as the protein (or biomolecular) corona was presented. Experimental studies were then undertaken to analyse poly(lactic-co-glycolic acid) nanoparticles at baseline and following coincubation in protein-rich media; develop, optimise and present for the first time a methodology suitable for the analysis of sub-micron nanoparticles using Particle Tracking Analysis and Resonant Mass Measurement as stand-alone and orthogonal techniques and finally, to

understand the influence of time, temperature and protein origin and concentration on protein corona formation under “static” conditions.

In this section of the thesis, fluid and particle behaviour *in vivo* will be studied using *in silico* models. These models will enable physiologically relevant parameters to be derived and then later used in **Chapter 5** for the development of a microfluidic device. In this chapter, a combined Computational Fluid Dynamics (CFD) and Discrete Element Method approach will be developed to model fluid and nanoparticle behaviour *in vivo*. The methodology developed here will be benchmarked against two previously published papers by Tan *et al*., and Barber *et al*.[445,446]

This chapter begins with a literature review introducing the relevant anatomy and physiology for this section of the thesis, the vascular access devices studied in **Chapter 4** are also introduced here. The literature review then introduces a more detailed discussion of the impact of fluid flow on nanoparticles. Finally, computational fluid dynamics is introduced – including Discrete Element Method and Finite Volume method, before a rationale for the selection of a coupled finite volume-discrete element method is provided. Next, the chapter outlines the iterative process by which this model was developed, before validation against two previously published papers and CFD best practice was performed. Finally, the consequences for the quality by digital design paradigm for novel nanotherapeutics is considered before limitations of the model, conclusions and further work bring this chapter to a close.

3.2 Literature Review

This is the second of three literature reviews in this thesis. The literature review here introduces the necessary concepts for Part 2 of the thesis (*i.e.,* this and the following chapter). This literature review begins with an introduction of human anatomy and physiology. These concepts include: the vascular tree; what role the blood vessels play in maintaining homeostasis and what happens when they are faulty; introducing some of the most common venous access devices that are in clinical use, before discussing Virchow’s triad as an explanation for the failure of vascular access devices (VADs) *in vivo* and the formation of venous thrombosis. The discussion then considers in greater detail, the impact of fluid flow on nanoparticles. Finally computational fluid dynamics (CFD) is introduced. A selection of common methods and applications are discussed, before justification for the selected methodologies in this work is given. A brief introduction to haemodynamics can be found in **Appendix A**.

3.2.1 Understanding Human Anatomy and Physiology

Human physiology is the study of how the human body works, and anatomy concerns its structure.[447] These two components are almost inseparable, for it is only possible for the human body to function in the way that it does, because of the way it is structured.[447] Primarily, the body wishes to maintain homeostasis, where physiological parameters remain within a pre-defined range. This is only possible because of a wide range of hormones that act on

various tissues and organs. Transporting these from one place to another is *via* blood flow, making the blood vessels and the other components of the circulatory system (*e.g.,* heart) one of the most important organ systems within the body.[447]

3.2.1.1 The Vascular Tree

The vascular tree refers to the continually branching pattern of blood vessels as they decrease in size. Blood vessels can be classified into five separate groups, these are: arteries, arterioles, capillaries, venules, and veins. Arteries and arterioles are the largest of these in the 'arterial tree' and are often described as bifurcating vessels as they branch off into smaller arteries and arterioles before becoming capillaries and the capillary beds. Venules and veins are conversely described as being converging vessels which increase in size to return blood to the heart.[448]

Arteries can further be classified into elastic and muscular arteries.[448] The elastic arteries are the larger of the two, with internal diameters between 1-2.5 cm in size. These elastic arteries are frequently those found closest to the heart (*e.g.* the aorta), as their high composition of elastic connective tissues enables them to maintain a relatively constant pressure, despite the peristaltic pumping motion of the heart.[449] The higher muscle content in the muscular arteries (*e.g.* femoral or cardiac arteries) – internal diameter 0.3 mm -1 cm – improves their ability to alter blood pressure and therefore rate of blood flow.[449] Arterioles are the smallest type of artery, with an internal diameter of 0.01 mm, and these arterioles control blood flow into capillaries.[448] Capillaries are the smallest blood vessels in the human body, with vessel walls comprised of only a single endothelial cell and often only a few microns in diameter.[450] These capillaries then form networks of capillaries known as capillary beds. Capillary beds are networks of capillaries that supply blood flow to organs, supplying oxygen and removing metabolic waste.[448] Veins and venules have much thinner walls than arteries since they return low pressure blood to the heart. The largest veins the body have an internal diameter comparable to that of the elastic arteries (~ 2 cm).[451] Venules are commonly only 8-10 micron in diameter and come together to form veins.[448]

3.2.1.2 Composition of Human Blood Vessels

When viewed as a tubular cross-section, blood vessels are composed of three distinct layers, known as the tunica intima, tunica media and adventitia (or tunica externa) respectively (**Figure 3.1**).

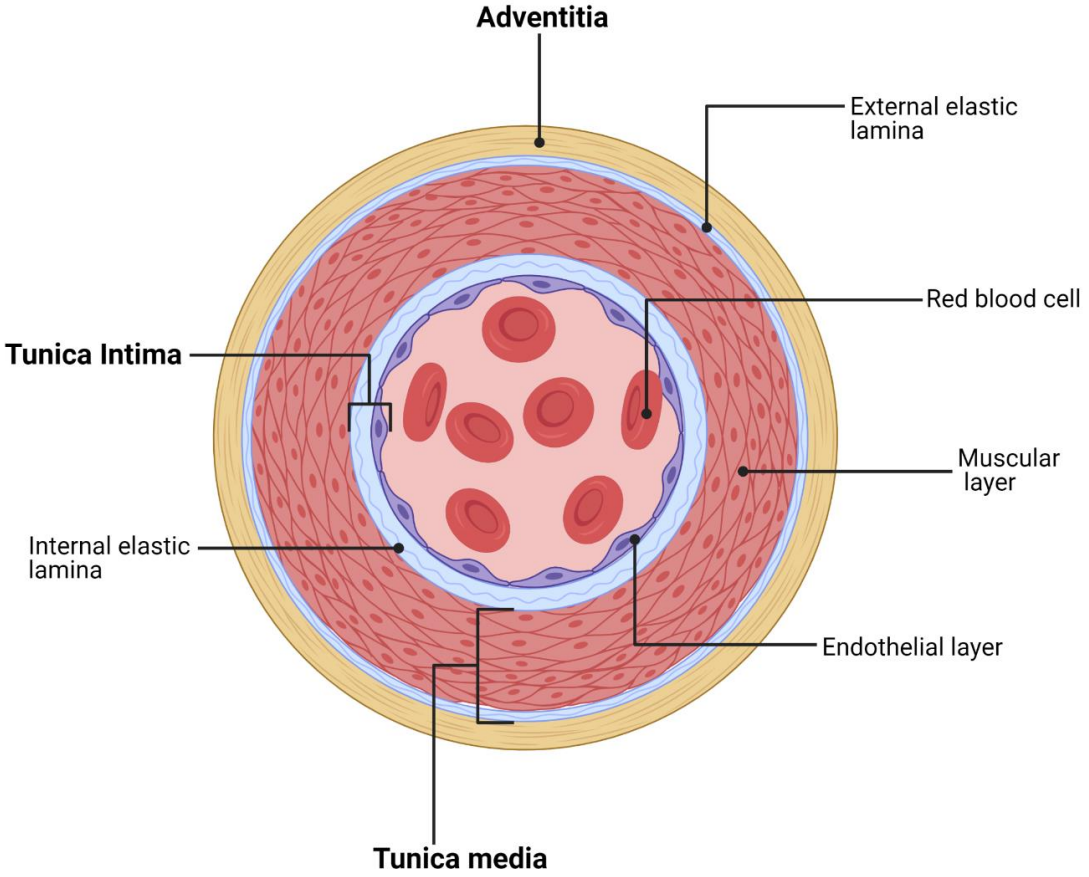

Figure 3.1: A tubular cross-section of a muscular artery. Note the presence of elastic laminae. Created using BioRender.com.

Each of these three layers contribute to the structure and mechanical properties of blood vessels. The tunica intima is the innermost layer of a blood vessel; it is a thin layer of endothelial cells attached to a network of collagen known as the basement membrane, which functions as a barrier between blood flow and extravascular tissues.[452] The tunica media provides much of the contractile ability of blood vessels, due to its concentric layers of smooth muscle cells embedded in a extracellular matrix of collagen and elastin.[452] These properties are much more apparent in arteries, where greater pulsatile flow is observed, than in arterioles and capillary beds. Finally, the adventitia is the outermost layer and was historically believed to be responsible for much of the structural integrity of blood vessels, since as it is composed of fibroblasts in a collagen-based matrix, alongside bundles of collagen running in the direction of the blood vessel's major axis (*i.e.* along its length).[452,453] In most arteries, these three layers are separated from each other by elastin laminae, but these laminae are not present in smaller blood vessels, where they innervate non-expandable tissues (*e.g.* the brain).[452]

3.2.1.3 Physiological Role of Blood Vessels

As discussed previously, blood vessels are fundamentally important for the delivery of oxygenated blood to organs and tissues and the removal of metabolic waste, but they also play a significant role in maintaining homeostasis in terms of blood pressure and therefore of blood flow rate in

vessels, as these two parameters are considered proportional to each other (discussed further in **section 3.7.1.1**). This role of controlling blood pressure and therefore rate of fluid flow is attributed primarily to arterioles, which are innervated by the autonomic nervous system, and their composition includes layers of collagen.[454] Consequently, both autonomic nervous system dysfunction and/or connective tissue disorders can be implicated in a variety of circulatory disorders including Postural Orthostatic Tachycardia Syndrome (POTS) and Raynaud's Phenomenon.[454]

3.2.1.4 Anatomy of the Upper Limb

The anatomy of the upper limb (hand, wrist, forearm, upper arm) is far more complex than is examined here. Only the vascular system is in scope for this work (**Figure 3.2**), and the bones, muscles and nerves are not dealt with here.

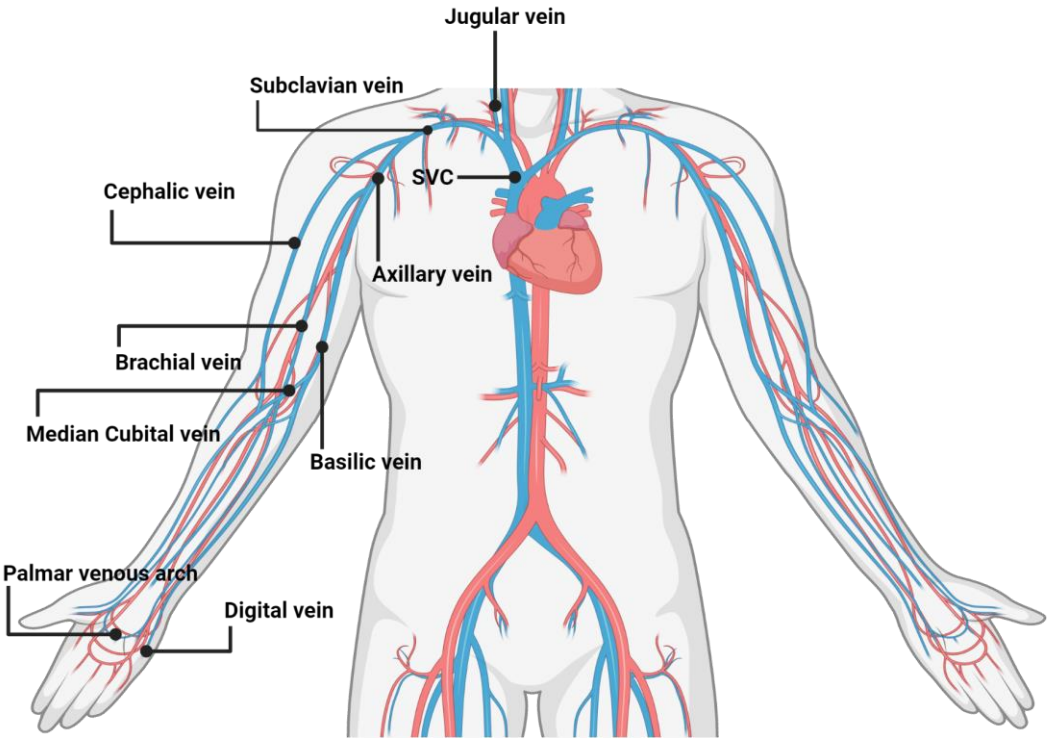

Figure 3.2: Veins in the upper limb. Created with BioRender.com

The axillary and cephalic veins are two separate branches of the subclavian vein. The axillary vein branches further at the level of the first rib to become the basilic and brachial vein, before continuing down the upper arm. At the anterior cubital fossa, (the interior of the elbow), the median cubital vein is found. The median cubital vein is a branch which connects the basilic and cephalic veins. This is also a common site for venepuncture as this is a superficial vein, found close to the skin. The basilic and cephalic veins continue down the forearm, and at the wrist become the palmar venous arch and later, the digital veins of the fingers.

Defining Position

In this section, standard anatomical position and its associated terminology is introduced. This nomenclature is used primarily in **Chapter 4**. Standard

anatomical position, which for humans is standing upright, facing with the feet pointing forward, the palms of the hands facing forward, and the thumbs pointed laterally (away from the body) (**Figure 3.3**).[455]

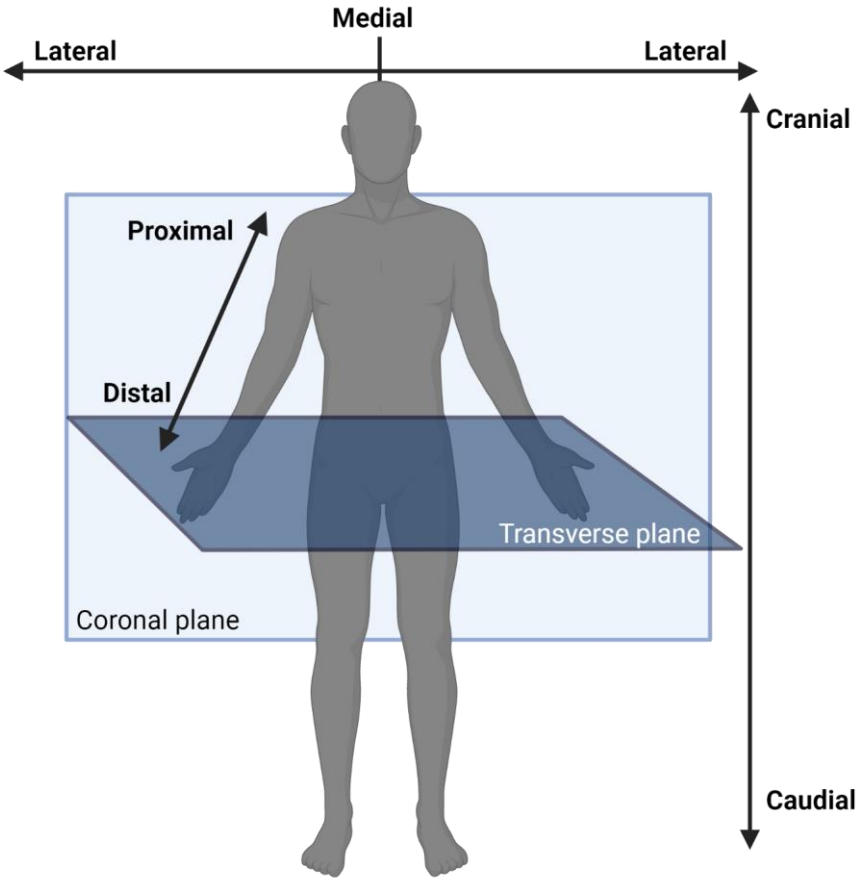

Figure 3.3: Standard anatomical position. Created with BioRender.com

When the terms left or right are used, these refer to the left and right sides of the individual or bone being studied, rather than the perspective of the viewer.[455] A range of anatomical planes of reference are used, as well as a set of directional terms – the full set are not defined here (**Table 3.1**).

Table 3.1: Anatomical planes of reference and directional terms. From [455]

Planes of reference	Sagittal	A plane through the body from front to back that divides the body into left and right halves; also called midsagittal, median, or midline. Not shown in Figure 3.3
	Coronal	A plane at right angles to the sagittal plane that divides the body into front and back halves; also called frontal
	Transverse	A plane through the body perpendicular to the sagittal and frontal planes; also called horizontal
Directional terms	Medial	Toward the midline of the body
	Lateral	Away from the midline of the body
	Proximal	Closest to an articular point; nearest the axial skeleton
	Distal	Farthest from an articular point; away from the axial skeleton
	Cranial	Up, or toward the head; also called superior
	Caudial	Down, or away from the head; also called inferior

3.2.2 Vascular Access Devices

Vascular access device (VAD) refers to any device used to obtain venous access (*e.g.* a cannula) and can be categorised into peripherally (outside of the chest or abdomen) or centrally inserted devices (**Figure 3.4**).[7] The peripheral vascular system refers to all blood vessels that exist within the body, outside of the chest and abdomen.[8] These peripheral veins are some of the most common entry routes for intravenous (IV) delivery of fluids or therapeutic molecules.[9]

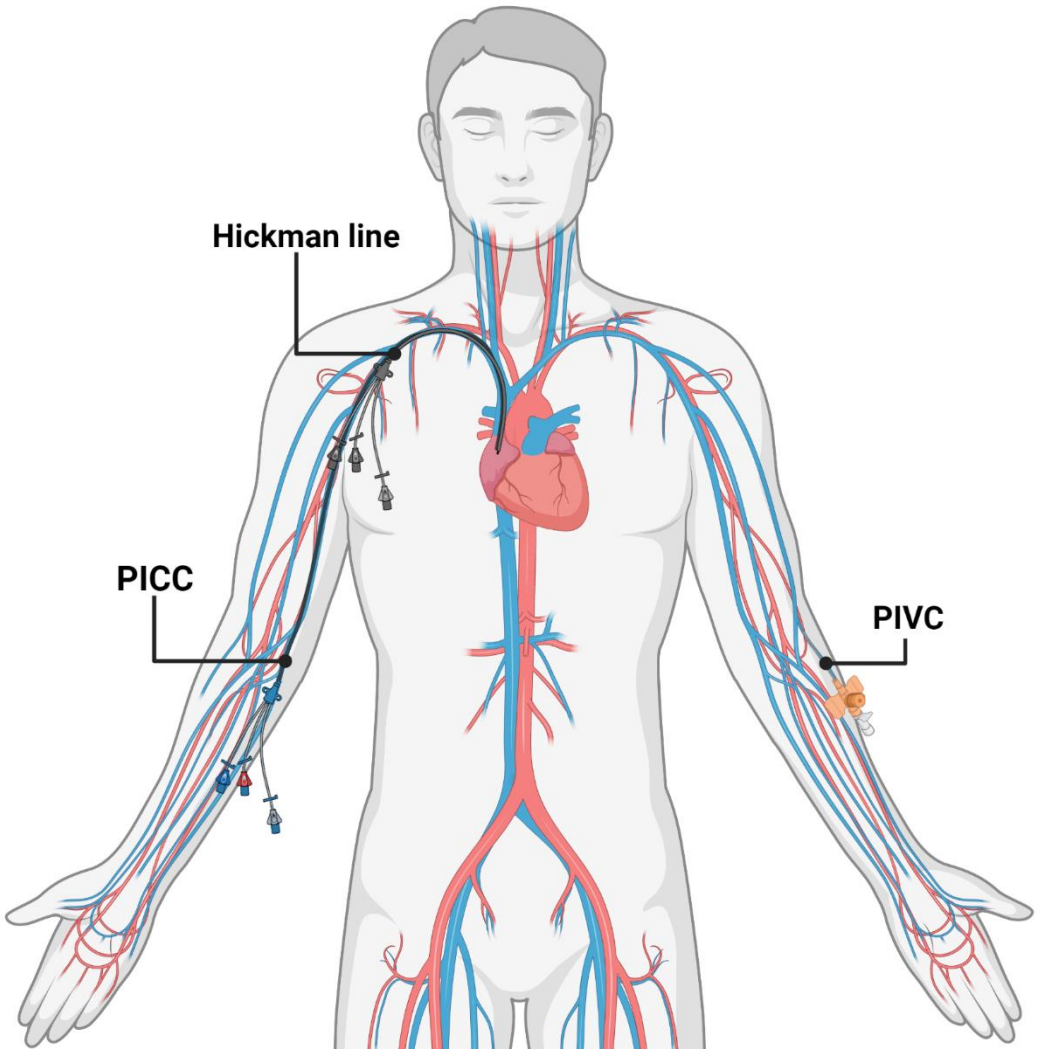

Figure 3.4: Many different vascular access devices are in common clinical use. This figure shows the usual entry locations of the venous access devices (VADs) studied in this work. PICC – peripherally inserted central catheter, PIVC – peripherally inserted venous cannula. Created with BioRender.com

3.2.2.1 Peripherally Inserted Venous Cannula (PIVC)

A peripherally inserted venous cannula is inserted into a vein in the arm or hand (frequently either the inside of the elbow (median cubital vein); the wrist (cephalic or basilic veins) or the back of the hand (metacarpal or dorsal arch), due to their ease of access and, compared to other sites, lack of impairment on patient mobility, although these can also be inserted into several veins in the feet.[456] The cannula consists of a stainless-steel needle (trocar) of varying length and internal diameter, and a colour-coded plastic cap to enable rapid, accurate identification and selection of an appropriately-sized cannula, depending on entry point, therapeutic use and required flow rate.[457] These colours are set by an ISO standard, and therefore standardised across manufacturers (**Table 3.2**).

Table 3.2: Colour-coding for identification of hypodermic needles as given by ISO 6009:2016.

Colour	Size (G)	External Diameter (mm)	Flow rate (ml/min^{-1})
Yellow	24	0.7	20
Blue	22	0.9	36
Pink	20	1.1	60
Green	18	1.3	90
Grey	16	1.8	180
Orange	14	2.1	240

However, peripheral entry may not always be desirable. PIVC often do not remain patent (functional) for extended periods of time, despite frequent flushing and the most used sites are often subject to significant movement which tends to encourage the cannula to fail. The PIVC then needs to be resited. VAD choice can further be influenced by the behaviour of the drug being administered (*e.g.* propensity towards causing extravasation, where the therapeutic agent leaks into surrounding tissues, whether it is a known vesicant or irritant)[458] and the quality of venous access in the patient, particularly when IV access has previously been frequently required, or if long-term access is likely to be clinically necessary (*e.g.* IV chemotherapy).[459,460] In this case, two types of central venous catheter may be used, known as PICC or Hickman lines.[460]

3.2.2.2 Peripherally Inserted Central Catheter (PICC)

A Peripherally inserted central catheter (PICC) is a thin flexible tube that is inserted into a vein in the upper arm - the right basilic vein is often the vein of choice due to its size, ease of access and simplicity of its route to the intended destination - and then guided through the circulatory system into the superior vena cava (SVC), directly above the heart.[460] Since the tip of the catheter ends in a much larger vein than a PIVC, this method of IV entry is accommodating of much higher flow rates, and a PICC is considered to be patent much longer than a PIVC.[460]

3.2.2.3 Hickman Line (Skin-tunnelled Central Venous Catheter)

Hickman lines or skin-tunnelled central venous catheters are large bore silicone lines often with multiple lumen, which enables different fluids to be given simultaneously.[460] These skin-tunnelled lines are inserted directly into the jugular or subclavian vein and then advanced such that the tip of the catheter again ends in the SVC. The exit point for these lines is often on the chest wall (skin tunnelling not shown in **Figure 3.4**).

3.2.2.4 Summary

In summary, it has been shown that there are many similarities between the VADs considered here (**Table 3.3**). There are additional forms of gaining central venous access, such as implantable ports, but these are outside the scope of this project and therefore will not be discussed here.

Table 3.3: A comparison of vascular access devices of interest in this work.

Vascular access device	External diameter (mm)	Flow rate (ml/ min^{-1})
PIVC	0.7-2.1	20-240
PICC	1.7 mm	20
CVC	3.3	Up to 300

3.2.2.5 Virchow's Triad as an Explanation of VAD Failure

Virchow's Triad refers to the 3 broad parameters known to influence the formation of venous thrombosis (**Figure 3.5**). These three parameters are: endothelial damage; haemodynamic changes in blood flow (*e.g.,* stasis), and hypercoagulability of blood components. Each of these three parameters can feasibly be studied *via in silico* models through studying wall shear stress, residence time and aggregation behaviour. Virchow's triad is often used as an explanation of the factors that influence VAD failure.[461]

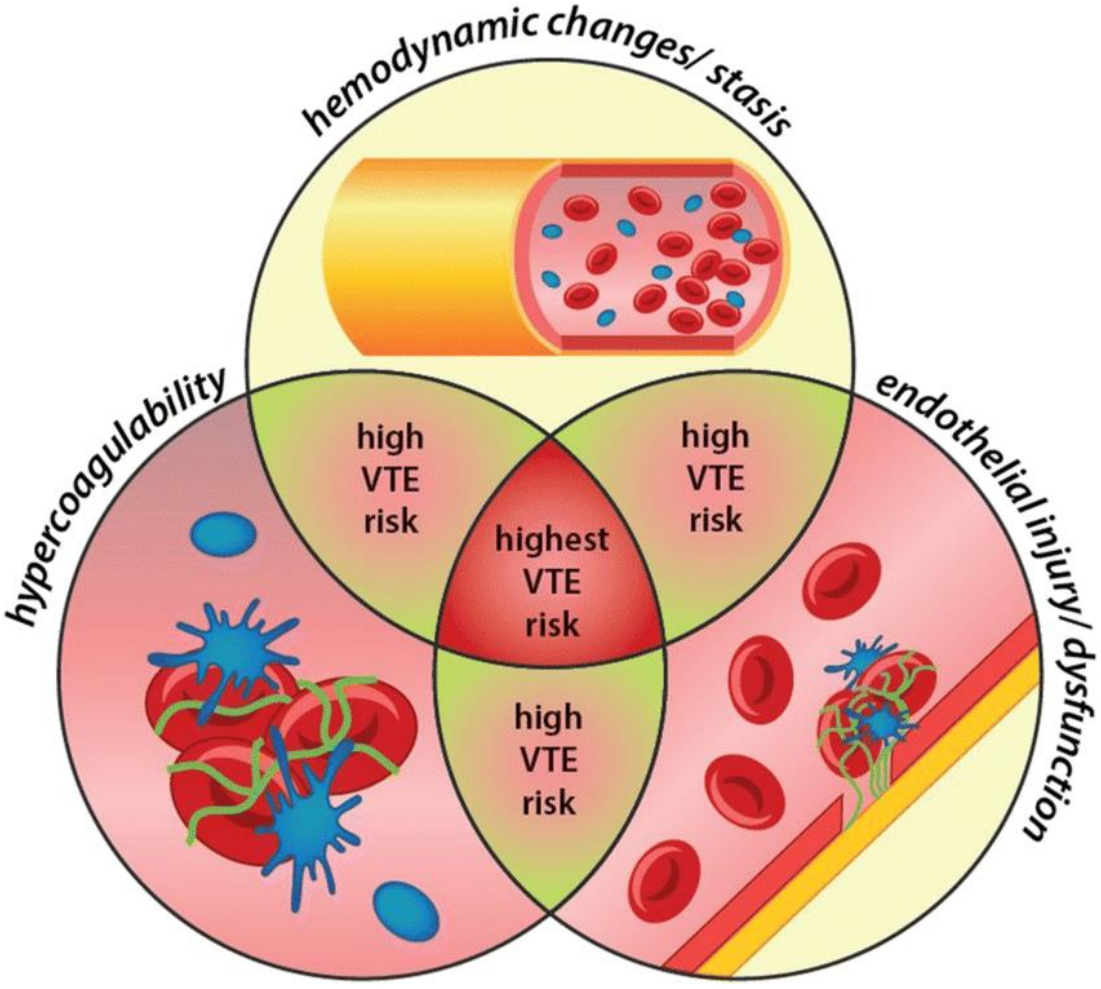

Figure 3.5: A schematic to show the factors implicated in Virchow's triad. Reproduced with permission from Springer Nature. From [462]

Mechanism of Venous Thrombosis

The formation of a blood clot (thrombus) is the final stage following a cascade of processes. This cascade begins with endothelial damage, where the cell membrane bursts, releasing haemoglobin into blood plasma. It is not the

release of haemoglobin itself that encourages the activation of platelets *in vivo*, but the release of a co-occurring enzyme, Adenosine diphosphate (ADP).[463] Activated platelets then excrete thrombin, which recruits other circulating platelets and eventually leads to thrombus (blood clot) formation.[464,465] A detailed discussion of the platelet aggregation cascade, and the interplay between platelet behaviour, the complement system and coagulation cascade are outwith the scope of this thesis.[466,467]

3.2.2.6 Impact of Fluid Flow on Nanoparticles

As discussed in the previous chapter, fluid flow (and therefore shear stress) has an impact on nanoparticle behaviour *in vivo*. These impacts include altering nanoparticle localisation[468–470], influencing cellular uptake[471–473] and contributing to particle deformation. Shear stress has also previously been investigated as a trigger for drug release. Further, some work has previously studied particle aggregation of polymeric nanoparticles under flow – but these studies primarily use polystyrene nanoparticles which find little clinical use. Clinical applicability and necessity of these studies is shown in work on monoclonal antibodies under flow, by Willis and colleagues.[474]

Nanoparticle Localisation

The influence of fluid flow on nanoparticle localisation has previously been studied, particularly to understand margination of nanoparticles within blood vessels – for uptake through the vascular endothelium is necessary for the eventual therapeutic effect of drug-carrying nanoparticles.[470]

Stephanou notes that the commonly-chosen mathematical model (as a Newtonian fluid) for many simulations of whole blood is far too simplistic and much of the fluid behaviour is subsequently lost.[469] In this paper, they do introduce a new mathematical model for the behaviour of blood at the nanoscale (in this work termed a nanofluid), which would be particularly useful for studies considering drug-loaded nanoparticles in capillaries (and capillary beds), however this was derived in MATLAB and is yet to be implemented into CFD software.[469]

Müller and colleagues have undertaken *in silico* studies in two and three-dimensions and their results show that larger particles are more likely to undergo margination than smaller particles *i.e.*, that micron sized particles perform better than sub-micron, but also that solid, rigid particles are more successful than soft, deformable particles.[470]

Gomez-Garcia *et al*., studied the process of margination (and later cellular uptake) using a combination of *in vivo* zebrafish studies*, in vitro* studies with human cells and computational fluid dynamics.[468] They have determined that short-term (<24 hour) studies *in vitro* study margination only, and are not long enough to encourage the shear-dependent phenotypic variation in cells that influence cellular uptake of nanoparticles.[468] They show nanoparticle localisation is inverse to shear stress, and highest accumulation of nanoparticles occur where fluid flow is disturbed in some way.[468] Later, *in vitro*

studies show that shear-induced phenotypic variation encourages nanoparticle uptake.

Cellular Uptake of Nanoparticles

Samuel and colleagues have previously used a commercially available microfluidic chip to determine the parameters that control nanoparticle uptake.[471] Like Gomez-Garcia, phenotypic variation induced by the application of shear stress is observed, and they further report that some shear stress is necessary for nanoparticle uptake into vascular endothelium.[471] However, they also show that increasing shear stress leads to decreasing particle uptake in untreated cells.

Fede *et al*., use a homemade microfluidic device to undertake much the same study as Samuel *et al.*, only this time it is gold nanoparticles that are the nanoparticle of interest.[472] Microfluidic devices and CFD modelling is again used by Zukerman *et al.*, to study functionalised polystyrene nanoparticles, whilst Freese and colleagues consider the influence of cyclic stretch and pulsatile flow on uptake of silica nanoparticles.[473,475]

Deformation of Particles

Fluid flow and subsequent shear rates have also previously been shown to encourage deformation of particles.[476,477] Buxton shows that fluid shear is capable of deforming polymer nanoparticles, both stretching and/or squeezing them, which potentially leads to the expression of any encapsulated liquid. Park and co-workers designed a range of novel polymeric microparticles and subjected them to fluid shear.[477] They found that the greater the void region within the shape, the more deformable these microparticles.[477]

Shear-triggered Drug Release

Since fluid flow can encourage deformation of particles, as well as alter polymer degradation, it is unsurprising that this behaviour has been exploited for shear-triggered drug release.[478,479]

Klein *et al*., as well as Beard *et al.*, have previously reported shear-induced drug release for both liposomes as well as nanoparticle aggregates, with higher shear rates encouraging significantly higher rates of drug release.[480,481] The Wyss Institute have then developed this technology further, for shear triggered release of clot busting drugs and/or chemotherapeutics.[482]

Polymeric Particle Aggregation under Flow

Aggregation behaviour of polymeric nanoparticles under flow has also previously been studied. The stability of PLGA and PLGA-PEG nanoparticles in electrolyte solutions has previously been determined by Saha and colleagues.[483] They show low concentrations of electrolytes are sufficient to rapidly encourage aggregation of PLGA nanoparticles, but that PEGylation is significantly robust to prevent electrolyte-triggered aggregation.[483] Bannon *et al.*, undertook a similar study using Nanoparticle Tracking Analysis, this time using polystyrene nanoparticles in whole plasma, and again show that aggregation behaviour depends on electrolyte concentration and

nanoparticles are less likely to undergo aggregation in these more physiologically relevant conditions if they are PEGylated.[435] These results likely have implications for the behaviour of PLGA nanoparticles *in vivo*.

Finally, it has been shown previously, that similar studies considering the impact of flow on aggregation behaviour are also useful for monoclonal antibody-based biologics (*e.g.* Adalimumab), under the Quality by Design (QbD) paradigm of drug development.[474]

3.2.3 Introduction to Computational Fluid Dynamics

Computational fluid dynamics (CFD) has become a more effective tool, as computers themselves have become more powerful. It is now possible to computationally model situations that would take much longer *via* experimental means, or would be impossible to do in this way.[484] Computational fluid dynamics is a numerical method that relies on computers to solve partial differential equations (PDEs), that describe the Navier-Stokes equations for compressible and incompressible flows.[485] CFD calculations usually take a system to be studied and express it as a series of conditions that describe the geometry of interest, the physical properties of the fluid to be studied and a set of both boundary conditions (*e.g.* no-slip as described in **Section 3.7.1.2**) and initial conditions (*e.g.* fluid velocity).[485]

CFD can be used in any context where the movement of fluid flow is of interest, and these applications span from aeronautics and modelling air flow (a plethora of such studies appeared during the ongoing COVID-19 pandemic, to provide an evidence base for the social distancing and other guidelines implemented by most governments)[486–489], to combustion[490] and biological applications such as modelling blood flow within arteries.[491–493] However, CFD is certainly not perfect, and care must be taken with interpreting the results obtained from these methods. There are several well-known sources of error inherent in these calculations including: discretisation error – which is intrinsic to all numerical methods, and the potential that the real-world behaviour of the system is of a complexity such that it cannot be perfectly described by current scientific theories.[485]

3.2.3.1 Discrete Element Method

The discrete element method is a numerical method which predicts the mechanics (*i.e.,* motion, velocity) of individual particles and was first proposed by Cundall in 1979, but the actual physical basis of this method is much older.[494–496] The physics which underpins this method mostly concerns the velocity, current position and motion of particles.[496] DEM considers the forces exerted by neighbouring particles or boundaries *via* a contact model, applies Newton's second law[***] to calculate particle velocity and particle rotation, then the new position of the particle is calculated.[496] Furthermore, this method relies on the assumption that the particles in this problem are spherical, as these are

[***] Newton's Second Law $F = ma$

the easiest shapes to model mathematically, and are less computationally demanding as the orientation of the particle does not need to be considered.[496]

Justification for Selecting this Method

Key advantages of this technique include its ability to give much more detailed information regarding the flow and movement of granular materials than would otherwise be possible using experimental methods, since the movement of individual particles can be followed.[496] With this numerical method, particles can be modelled as either hard spheres, where the particles are rigid and contact is instantaneous, like snooker balls, or can be modelled as soft spheres where particle-particle contact is lasting and multiple contacts between particles are possible.[496] It is for this reason that DEM can be used to model the formation of aggregates and agglomerates of nanoparticulate matter.[497,498] However, there are significant disadvantages inherent to this method. DEM is computationally demanding, which then limits the number of particles that can be modelled and/or limits the complexity of the system under investigation.[499] Additionally, this method alone is not capable of modelling particle-fluid interactions and requires the use of another method.[500,501]

3.2.3.2 Finite Volume Method

The physics which underpins time and space-dependant phenomena are often described by partial differential equations (PDEs) that are too complex to be solved analytically. Therefore, numerical methods like FVM are used to simplify, generate less complex (often integral forms of the original differential equation) and solve these to give approximate solutions.[502] Consequently, the outputs from these analyses are only ever approximate and the variation between reality and the solutions provided *via* FVM will depend on the exact input parameters, the discretization method and any approximations invoked to simplify the problem at hand.

The history of the finite volume method can be traced back to the early 1970's, when a new method to simplify PDEs where a non-rectangular geometry is involved, which the Finite Difference Method finds problematic, was introduced by McDonald in 1971.[503]

The finite volume method is underpinned by Gauss' divergence theorem - it is effectively integration by parts in three dimensions. Gauss' theorem states that any change in a closed volume can be calculated by first solving the equation for a small volume and then summing this over the entire quantity. This enables us to swap between surface (2D) integrals and volume integrals in 3-dimensions, often simplifying the calculations that need to be solved.

Justification of Selecting this Method

The finite volume method is one of the most popular CFD methods, and several commercially available CFD solvers use this method.[502] Its popularity arises from the fact FVM, unlike other methods, does not require the shapes of the cells to be consistent across the entire geometry. It is possible to adapt them (*e.g.* make them smaller and therefore obtain a higher resolution) at locations of interest.[502] This method is also considered to be robust, and can

handle solutions which contain discontinuities, if a suitable mesh is chosen.[502] Furthermore, it has also been shown to be significantly more computationally efficient than the Finite Element Method (FEM).[504] However, this method has known difficulties with modelling granular materials, due to the lack of reliable constitutive laws which underpin the analysis.[499] Therefore, we have chosen not to apply either DEM or FVM alone.

3.2.3.3 A Coupled Finite Volume-Discrete Element Method Approach for Modelling Nanoparticles in Biological Fluids

It is becoming increasingly common to apply several CFD methods simultaneously to model ever more complex systems.[505–507] As discussed previously, the finite volume method uses a continuum approach to model the carrier fluid, and does this well, but models particulate matter poorly. In contrast, DEM models particulate matter well, but cannot model particle-fluid interactions.[500,501] Clearly, neither technique alone adequately models the conditions we wish to study. However, if these two techniques are used together, then each technique can be employed to model only the components that they model well. This approach is termed coupled CFD-DEM and is commonly used for computational modelling of particulate suspensions.[505,508–510] The CFD and DEM can be coupled in one or both directions.[505,510] Here, because particulate volume is comparatively low, only one-way coupling of CFD to DEM is needed, as fluid flow impacts behaviour of the particulate matter, but the reverse is not also true.

3.2.3.4 Other CFD Methods Not Used Within This Work

The discrete element, finite element and finite volume methods are not the only CFD methodologies that could have been applied to this work. Here, the Lattice Boltzmann, Large Eddy Simulation (LES) and population balance methods will be studied, and their advantages, disadvantages and common applications outlined.

<u>Lattice Boltzmann Method</u>

The Lattice Boltzmann method is derived from two different models of Lattice Gas automata, separately pioneered by Hardy, Pomeau and de Pazzis as well as Frisch, Hasslacher and Pomeau.[511–513] The models differ by the shapes of their lattices. More recent developments enable this method to be used to model particle-laden flows.[514,515]

Lattice Boltzmann methods can be very rapid ways of solving the Navier-Stokes equation for incompressible flows, and are compatible with parallel computing.[515] However, the biggest disadvantage of this technique is that the lattice must remain uniform over the entire domain; areas of higher mesh density are not possible.[515]

<u>Large Eddy Simulation</u>

Large Eddy simulation (LES) is a mathematical model in CFD for modelling turbulence in fluid flows, initially proposed in 1963 by Smagorinsky for the modelling of atmospheric air currents.[516]

These simulations are efficient at modelling turbulent flows, at the expense of solving the Navier-Stokes equations at the smallest length scales and therefore near-wall effects cannot be resolved using this method.[517]

Population Balance Methods

Population balance methods split a polydisperse group of particles into size groups and then solves the necessary equations for each group.[518] They are particularly useful for the simulation of polydisperse particulate flows.[519]

3.2.3.5 Introducing Pathlines, Streaklines and Streamlines

Path-, streak- and streamlines are all useful ways of visualising the movement of fluids or particles and will be used later in this thesis.[520] For steady flow, streamlines, pathlines and streaklines all coincide.[520]

Pathline

A pathline is mathematically defined as the path traced by a single particle during a specified period. For steady flow, the pathline of every particle will be the same.

Streaklines

Streaklines are the output of a continuous stream of particles. For unsteady flow, these may not be the same as pathlines.[520]

Streamlines

Streamlines always run parallel to the velocity vector at a given moment in time.[520] These are a way of visualising fluid flow.

3.2.3.6 CFD Studies of Biomedical Devices

As outlined previously, CFD is a numerical methodology through which the movement and behaviour of fluid flows can be simulated *in silico*. In recent years, there has been a significant increase in the use of CFD for biomedical applications.[521] This has been used for a wide range of applications including to evaluate novel drug delivery platforms (as attempted in this thesis), through to the more commonly seen uses of cardiovascular studies to understand blood flow in vessels and organs (*e.g.* placenta[522]), enable surgical planning, and the development of new biomedical devices.[521,523]

In biomedical CFD research, the two largest areas of study are cardiovascular flows *i.e.* blood flow within vessels and organs, and the design and development of new biomedical devices.[521] Here, a selection of papers covering CFD studies of vascular access devices and/or blood flow *in vivo* will be discussed. The three vascular access devices of interest in this work are PIVC, PICC and CVCs.[524,525] Piper *et al.*, were particularly interested in studying the mechanistic parameters that influence the failure of peripherally inserted cannulae.[524] They studied a range of parameters including PIVC size in relation to that of the vessel, insertion angle, flow rate and also of tip position in reference to the endothelium of the inner wall. This work shows that, wall shear stress and damage to blood cells (haemolysis) can be influenced by flow rate and to a lesser extent, insertion angle of the PIVC itself.[524] They go on to suggest that it may be clinically sensible to propose maximum infusion rates

for PIVC to limit damage to the endothelium and thrombus formation (and later VAD failure).[524] Nifong and McDevitt studied the ratio between catheter external diameter and vessel size.[525] Like Piper and colleagues, they also show that increasing occlusion of the blood vessel, leads to a decrease in blood velocity, and that this decrease is statistically significant ($p < 0.0001$).[525] A large body of work also exists studying arteriovenous fistulae; these are (usually) surgically created connections between arteries and veins.[526]. Of particular interest is the study of haemodynamics to understand the underlying pathophysiology when this is unsuccessful.[527] As well as the haemodynamic behaviour of several types of haemodialysis catheters. Many studies consider the size, shape and orientation of lumen on the sides of these catheters, to enhance blood flow without excessively increasing fluid shear.[528–530]

3.2.3.7 CFD Workflow

In the work presented here, this combined approach permits the behaviour of nanoparticles *in vivo* (*e.g.,* aggregation and agglomeration) to be modelled, alongside understanding the behaviour of the carrier fluid (blood). The physiological process under study is the introduction of 100 nm PLGA nanoparticles into the human bloodstream, as if these were drug-carrying chemotherapeutics. Like DEM or FVM alone, the combined approach uses much the same workflow. This is to define the geometry of the problem, define a geometric mesh, set boundary conditions (*e.g.* no-slip condition at the wall), set initial conditions (*e.g.* pressure), running the calculations and then post-processing of this data to enable visualisation (**Figure 3.6**).

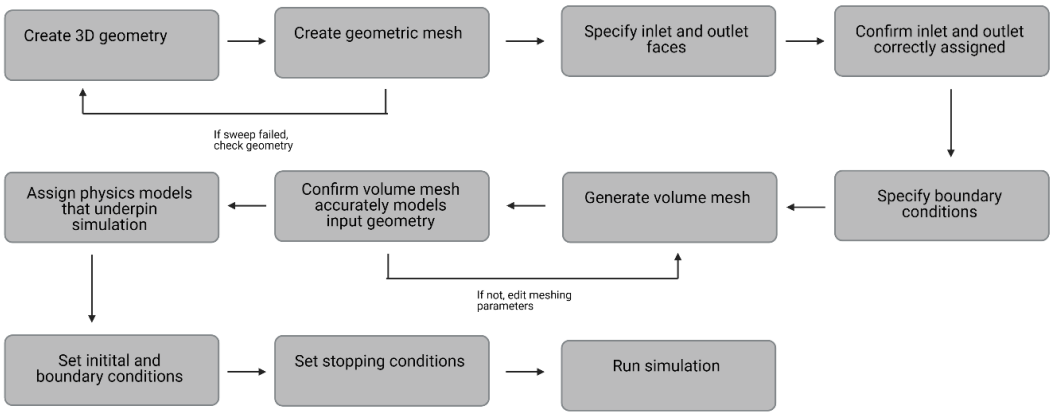

Figure 3.6: A summary of the workflow implemented in STARCCM+ for the simulations discussed in this work.

3.3 Chapter Aims and Objectives

It is already known that fluid flow *in vivo* has a significant impact on protein corona formation, but few studies have considered how this occurs and the consequences of this.[52] Where studies have been undertaken, these often use polystyrene nanoparticles, which find little clinical use.[52] Here, the impact of blood flow on PLGA nanoparticles will be modelled, which are in widespread clinical use because of the well-known safety profile and known biocompatibility of this particular polymer - both lactic and glycolic acids are naturally occurring within the human body.[203,212] Furthermore, experimental methods of modelling haemodynamics, whereby *in vivo* studies have been performed, have revealed that it is difficult to accurately measure wall shear stress within 0.2 micron (200 nm) of the vessel wall.[531] This may not sound problematic if larger blood vessels (*e.g.,* arteries and the aorta) are considered, but this limitation is significant when capillaries and capillary beds are the blood vessels of interest.

The aim of this work is to study the aggregation and agglomeration behaviour of PLGA nanoparticles on exposure to physiologically relevant fluid flow patterns and shear rates. Earlier work shows that nanoparticles are known to undergo aggregation once exposed to biological fluids to reduce surface free energy.[532,533] If these clusters of nanoparticles become too large, then their efficacy as a method by which chemotherapeutics can be administered *in vivo* may be affected, as there is also a size limit to the enhanced retention and permeation effect for tumour cells.

This aim will be achieved by completing the following objectives:

1. Undertake a literature review to gather necessary physiological parameters (*e.g.*, vessel length, diameter). The result of this is reported in **Appendix C**.

   The literature review will be undertaken using the search functionality provided by Web of Science, and the resulting data compiled into a spreadsheet for ease of access.

2. Develop a suitable workflow and methodology for studying this behaviour using STARCCM+, a commercially available CFD solver.

   This will be done by first using simplified geometries to undertake mesh independence studies to assess whether the volume meshes deliver results that balance both accuracy and computational demand. Then these parameters will be used to replicate two previously published studies of increasing complexity to confirm that the model does function correctly, the methodology is robust, and the results obtained are accurate.

3. Using the data collected in #1, and methodology developed in #2, create scaled models where only Finite Volume Method is used to model fluid flow.

An iterative approach to the development of the models will be used due to their complexity. Such approaches facilitate troubleshooting the software and/or the simulation itself.

4. Extend previously created models to use a coupled CFD-DEM approach to model both fluid flow and nanoparticle aggregation and agglomeration behaviour.

   The models produced in #3 will be extended by the addition of the Discrete Element Method to the physics continuum within the model, this will allow nanoparticle behaviour to be studied.

By the end of this work, a coupled CFD-DEM approach will have been developed that permit both fluid and nanoparticulate behaviour to be studied. The robustness of the methodology and accuracy of the results will be assessed by comparison to previously published studies (Tan *et al*., Barber *et al*.).[445,446] This methodology will then be used in **Chapter 4** to understand fluid shear on PLGA nanoparticles *in vivo* – as if they were administered *via* one of the vascular access devices discussed earlier.

3.4 Materials and Methods

The computational models presented in this chapter were simulated using STARCCM+ (Siemens PLM, Version 2021.2.1), a commercially available CFD solver.

As this model is complex, it was decided that an iterative approach was to be used, where the model would only be extended and made more complex once the earlier iteration had successfully been completed. Initially, a wholly-CFD model was developed, which represented only the geometry of the situation at hand and the behaviour of blood flow. Later, the model was extended using DEM and nanoparticulate behaviour studied using a Lagrangian multiphase model, which enables coupling between CFD and DEM.

3.4.1 Input Geometry

Input geometries were created in Solidworks 2019 (Dassault Systémes/ Solidworks Corporation), before being imported into STARCCM+. For initial testing, a singular cylindrical capillary with dimensions 50 x 2500 μm was created. A more complex bifurcation geometry, previously published by Tan *et al.* was also created.[445] This was a symmetrical bifurcation with inlet diameter 20 μm and outlet diameter 10 μm. Finally, a symmetric, asymmetric and T-junction geometries were created, mimicking those geometries studied by Barber *et al.*[446] The iterative development of the geometry as the problem becomes more complex, is detailed in **Appendix A.**

3.4.2 Mesh Development

A mesh convergence study was performed on the initial volume mesh of the singular capillary to refine it. A polyhedral mesh was used, as this allows faster convergence of the result compared to a comparable tetrahedral mesh.[58] Prism layer mesher was employed to increase the resolution at the walls of the blood vessels; a comparatively high number of prism layers were used to adequately resolve the viscous behaviour of the fluid phase. Mesh size was decreased to affect an increase in the number of cells in the geometry with each repeat. Next, these meshing parameters were applied to a more complex geometry, previously published by Tan *et al*., as it was necessary to determine whether the mesh required further refinement at bifurcations.[56] Consequently, these refined parameters were used to create the geometric mesh for all geometries studied in this work, as this mesh balances both accuracy of the result with computational demand (**Table 3.4**).

Table 3.4: Final meshing parameters used to create the volume mesh following mesh convergence studies.

Group	Mesher
Surface mesher	Surface remesher
Core volume mesher	Polyhedral mesher
Optional volume mesher	Generalised cylinder mesher
Optional boundary layer mesher	Prism layer mesher
Refining the mesh	
Base size	2.0×10^{-5} m
Number of prism layers	6
Prism layer stretching	1.5
Prism layer total thickness	33.33 (relative to base)
Refining the bifurcations	
Base size	1.5×10^{-6} m
Number of prism layers	6
Prism layer stretching	1.5
Prism layer total thickness	33.33 (relative to base)

3.4.3 Defining Boundaries

Once the mesh of the geometry had been rendered, inlets, outlets and walls were defined to set the boundaries of the problem.[534]

Table 3.5: Boundary conditions implemented in STAR CCM+. Boundary type is described in the STARCCM+ jargon.[535] **Note: The boundary conditions for solid phase are not implemented in the wholly CFD model.**

Physical Boundary	Phase	Boundary Type
Inlet	Liquid	Inlet
	Solid	Phase impermeable
Outlet	Liquid	Pressure outlet
	Solid	Phase impermeable
Wall	Liquid	Wall “no-slip”
	Solid	wall

3.4.4 Physics Continua and Input Parameters

Physics models are predetermined ways of describing spatial orientation of the volume mesh, defining whether the solution is steady or transient in nature, as well as describing the composition and behaviour of fluid flow within the simulation. Some optional models consider the effects of certain forces such as gravity, others impact the way the solvers function and therefore can be selected in order to refine the accuracy of the solution and/or aid its convergence.

Since the Reynolds number for this capillary model is 0.005, fluid flow is considered under the laminar regime. The physics models selected in STARCCM+ for the initial capillary geometry are summarised below (**Table 3.6**).

Table 3.6: Physics models selected in STARCCM+ for the initial model of a singular capillary. They are described in the STARCCM+ terminology.

Group box	**Physics model**
Space	Three dimensional
Time	Steady
Material	Liquid
Flow	Segregated flow Gradients (selected automatically)
Equation of state	Constant density
Viscous regime	Laminar

These selected physics models mean that the equations for the conservation of mass, energy and momentum were sequentially solved (**Equation 5-7**). STARCCM+ has the capacity to use a number of techniques to model fluids, including Volume of Fluid (VOF) and single phase, The VOF form of the equations are given here, even though this methodology is not used within this work. It is, however, facile to transition between VOF and single phase. In the volume of fluid method, epsilon (ε), can take any value between 0 (cell is completely empty of fluid) and 1 (cell is completely full of fluid). In the single phase method, epsilon can only equal 1.

$$\frac{\partial(\rho_f\,\varepsilon_f)}{\partial t} + \nabla.\left(\rho_f \varepsilon_f \vec{u}\right) = 0 \tag{5}$$

Equation 5: Conservation of mass. Where ρ_f = fluid density, ε_f = volume fraction of the fluid in the cell t= time and $\vec{u}$ = average velocity of the fluid phase.

$$\frac{\partial(\rho_f\,\varepsilon_f C_{p,f} T_f)}{\partial t} + \nabla.\left[\vec{u}\rho_f\,\varepsilon_f C_{p,f} T_f\right] = \nabla.\left(\varepsilon_f k_f \nabla T_f\right) + E_f \tag{6}$$

Equation 6: Conservation of energy. Where $C_{p,f}$ is the specific heat capacity of the fluid, T_f is the temperature of the fluid, k_f is the thermal conductivity of the fluid, E_f = net rate of heat transfer.

$$\frac{\partial(\rho_f\,\varepsilon_f)}{\partial t} + \nabla.\left(\rho_f \varepsilon_f \overrightarrow{uu}\right) = -\frac{1}{\rho}\nabla\rho - \nabla.\vec{\tau}_f + \rho_f \varepsilon_f g - \vec{F} \tag{7}$$

Equation 7: Navier-Stokes equation for conservation of momentum. Where τ_f is the fluid phase stress tensor, g is gravity and F is the volumetric mean of all the forces acting on the particle from the surrounding fluid.

The input parameters for this initial model are summarised in **Table 3.7**. Carreau-Yasuda fluid model implemented here to accurately capture the pseudoplastic behaviour of whole blood.[536] Typically, these simulations would be simplified by assuming that blood behaves as a Newtonian fluid.

Table 3.7: Input parameters for the initial capillary model. These material properties are used throughout this study.

			Units	Ref
Material properties (liquid, whole blood)	Density (ρ)	1050	kg m^{-3}	536
	Zero shear viscosity (η_0)	0.056	Pa s	
	Infinite shear viscosity (η_∞)	0.0035	Pa s	
	Relaxation time (λ)	3.313	s	
	Power constant (n)	0.3568	-	
	Yasuda exponent (a)	2.0	-	
Initial conditions	Velocity (v)	$5x10^{-5}$	m s^{-1}	

3.4.5 Dimensional Scaling

Dimensional scaling was used in these models for several reasons. These simulations seek to understand the aggregation and agglomeration of drug-loaded nanoparticles, such as chemotherapeutics *e.g.,* doxorubicin. When dosed by bodyweight, a standard dose of doxorubicin for a 70kg person would be not more than 168 mg of doxorubicin; assuming a particle diameter between 100-200 nm, this corresponds to significantly more than a million particles.[537–539] Attempting to model this number of particles is far too computationally demanding.

Secondly, there are a subset of differential equations, known as Stiff equations. These equations are those for which an explicit method of obtaining a solution does not work, and the timesteps necessary to solve such equations using an implicit method are unacceptably small, limiting the physical time that can be reasonably modelled.[62] However, these problems can be overcome if the model is scaled in some way (**Table 3.8**). The behaviour of the nanoparticles can be understood when far fewer particles are modelled within the system, and parameters can be changed to increase the timestep used to solve these stiff equations. It has previously been shown that if certain parameters are maintained as constant values, then other parameters may be scaled by factor k, which is the ratio between original and scaled particle diameter.[540–542] In depth derivations of necessary dimensionless parameters *e.g.,* Reynolds number *via* Buckingham Pi theorem is given in **Appendix C**. Other input parameters for the scaled model can be found in **Appendix C**.

Table 3.8: A comparison of original and scaled model parameters. Parameters in bold font are those which must be kept constant.

Parameter	Original	Scaled model	Units
Number of particles	$9.88x10^{17}$	1000	-
Scaling factor	1	10	-
Particle diameter (d_p)	$1x10^{-7}$	$1x10^{-6}$	m
Particle density (ρ_p)	1300	1062	kg m^3
Liquid density	1050	1050	kg m^{-3}
Liquid viscosity	0.0035	0.0035	m^2 s^{-1}
Liquid velocity	$5.00x10^{-4}$	$5x10^{-5}$	m s^{-1}
Reynolds number	0.001	0.001	-
Diameter-to-length ratio	50	50	-

3.4.6 Setting Stopping Criteria

Before the simulation can be run, conditions under which the simulation is stopped must be set, otherwise the simulation would run indefinitely. Where simulations are considered steady, then the stopping criteria is simply the number of iterations of the calculation the simulation must complete. For our simulations, they are considered complete after 1000 iterations. Where simulations are considered transient in nature (*e.g.,* implicit unsteady solvers are employed), then stopping criteria may become more complex. In these cases, the simulations consider the number of both inner (substeps) and outer iterations that have been calculated, and the physical time that has been covered.

3.4.7 Coupling CFD and DEM

Once the wholly CFD model had been successfully set up and simulations completed, the model was then further modified to additionally use DEM to enable the behaviour of nanoparticles to be accurately modelled. Therefore, physics continua were changed and the Lagrangian multiphase, Discrete Element Model and multiphase interaction models were selected (**Table 3.9**).

Table 3.9: Modified physics continuua for the coupled CFD-DEM model.

Group box	Physics model
Space	Three dimensional
Time	Implicit unsteady
Material	Liquid
Flow	Segregated flow Gradients (selected automatically)
Equation of state	Constant density
Viscous regime	Laminar
Optional models	Lagrangian multiphase Discrete element model (DEM) Multiphase interactions (selected automatically)

3.4.7.1 Defining the Solid Phase

Next, physics models and material properties of the nanoparticulate matter were defined (**Table 3.10**). The optional models of Residence Time and Passive Scalars have been implemented in this work to allow the collisions between nanoparticles to be studied. The passive scalars can be considered as tracer dyes within the simulation. They play no role in modifying the physics but enable parameters like residence time to be found. Using the methodology of Usune *et al.*, Young's modulus has been set to 1/1000 of the known literature value (2.43 GPa), such that a larger timestep may be employed in the simulation and a shorter physical time is possible. [543,544] This study reports that no significant effect on aggregation behaviour is observed by employing this modification.[544] Poisson's ratio for PLGA chosen as 0.4 due to lack of available data.[†††]

[†††] Poisson's ratio can be found for other polymers. Are typically between 0.3 and 0.5.

Table 3.10: Input parameters to define the solid phase of the coupled CFD-DEM model.

Group box		**Physics model**	
Particle type		DEM particles Pressure gradient force (selected automatically)	
Particle shape		Spherical particles	
Material		Solid	
Equation of state		Constant density	
Optional Models		Residence Time Passive Scalar	
Input parameters – Lagrangian phase			
Solid (PLGA) – material properties			Ref
	Density	1062 kg m^3	
	Poisson's ratio	0.4	
	Young's modulus	2.43 Pa‡‡‡	[543,544]
Wall – material properties	Density	1300 kg m^3	[545]
	Poisson's ratio	0.49	[545]
	Young's modulus	910 Pa	[544,545]

3.4.7.2 Defining the Sources of DEM Particles

The sources of DEM particles (*e.g.,* PIVC) were defined within the model by creating injectors. The injector defines position, direction, and the rate by which the particles are introduced into the continuous (fluid) phase.[535] Implementing the skin function alters the frequency with which the software runs contact detection between particles. With the skin function in use, contact detection is only ran if the particle has moved a distance greater than or equal to that of the skin thickness. This theoretically should make the simulation less computationally intensive, as contact detection will be invoked less frequently.

Table 3.11: Using injectors. The input parameters given here are calculated in Appendix C.

Properties	**Values**
Lagrangian phase	PLGA Nanoparticle
Type	Surface injector
Inputs	Inlet
Input parameters	
Retain injected particles	Enabled
Random injection	Enabled
Particle diameter	$1x10^{-6}$ m
Velocity	$8x10^3$ m s^{-1}
Skin	$1x10^{-7}$ m

3.4.7.3 Multiphase Interactions

Multiphase interactions are, as the name suggests, interactions between two or more phases within the simulation. Here, multiphase interactions were

‡‡‡ 1/1000 of 2.43 GPa is not 2.43 Pa. This value should be 2.43 kPa, but has been incorrectly implemented in the model.

created to model nanoparticle-nanoparticle interactions, as well as nanoparticle-wall interactions and are summarised in **Table 3.12**.

Table 3.12: Defining multiphase interactions for the CFD-DEM model. * Applied to nanoparticle-nanoparticle interactions only.

Group box	Physics model
Phase interaction topology	DEM Phase Topology
DEM Contact model	Hertz-Mindlin Rolling resistance (selected automatically)
Optional models	Artificial viscosity Linear cohesion Parallel bonds * Passive Scalar Transfer *

Hertz-Mindlin contact model chosen since it is the standard model within DEM to model interactions between particles.[535] The Hertz-Mindlin model calculates the normal repulsive force $F_{nr,}$ and these interactions between particles are considered to be elastic.[497,546] Rolling resistance model takes into account the impact of rotation on these interactions.[547] Artificial viscosity model chosen to help prevent two possible outcomes from occurring.[535] These outcomes are the model overpredicting particle overlap between colliding particles, which then results in either inaccurate results; and physically impossible results *e.g.* particles pass through walls. Linear cohesion model chosen to improve modelling of intermolecular attraction forces (Van der Waals forces) between particle surfaces, enabling nanoparticle aggregation and agglomeration to be shown.[548] Multiplication model blending factor F in the linear cohesion model is set to 1.5 by default to mimic Johnson-Kendall-Roberts (JKR) model (**Equation 8**).

$$F_{\text{cohesion}} = R_{min} W \pi F \quad (8)$$

Equation 8: Johnson-Kendall Roberts model where R_{min} = minimal radius of the surfaces in contact, W = work of cohesion F = multiplication model blending factor. 1.5 for JKR model. 2 for DMT model.

This is one of two models available to simulate Van der Waals forces (intermolecular attraction).[535] The difference between them is the size of the area where this force is in effect. JKR model needs direct contact between particles, whilst Derjaguin, Muller, and Toporov model (DMT) operates over a larger area. The JKR model is implemented by default in STARCCM+.[535] The frictional coefficients between nanoparticle-nanoparticle and nanoparticle-wall interactions are assumed as 0.1 because of the lack of available data.[544] Implementing parallel bonds for nanoparticle-nanoparticle interactions allows the formation of aggregates and larger agglomerates from colliding particles following their injection into the geometry to be studied. Applying passive scalar transfer in this simulation enables parameters like residence time of particles to be determined.

3.4.7.4 Selecting the Timestep for an Implicit Unsteady Method.

Implicit solutions are those which calculate the solution at the current time, and at a future timepoint. Therefore, they are more computationally demanding than explicit methods; however, they are considered both more stable and more accurate, if the equation at hand is considered "stiff" (**Section 0**).[549]

Introducing and Using the Courant Number

The Courant number is a unitless value which enables the necessary time step of a simulation to be calculated as a function of mesh size and flow velocity (**Equation 9**). It is known to be linked to Courant-Friedrichs-Lewy (CFL) stability condition.[550]

$$C = \frac{U\Delta t}{\Delta h} \tag{9}$$

Equation 9: Calculating Courant number. Where U = flow velocity, Δt = time step of the simulation, Δh = size of mesh cell

The exact choice of timestep matters for two reasons. One: for the stability of the discretisation scheme and the second because of the physical meaning of the timestep. Ideally, a timestep should be selected such that courant number remains less than one, and therefore, the information does not travel further than a single cell within that time (**Figure 3.7**). If the selected timestep is too large, the information (in this case, the distance a nanoparticle travels) moves too far in each time step and potentially leads to the simulation calculating results that are inaccurate, or otherwise physically impossible.

Time integration schemes must obey CFL conditions. If CFL > 1 then the simulation is likely unstable, may fail to converge and produce results which are inaccurate or worse, do not represent a physical possibility. Implicit schemes, like implicit unsteady time regime used here, are intrinsically stable and so are less dependent on the CFL condition being strictly followed.

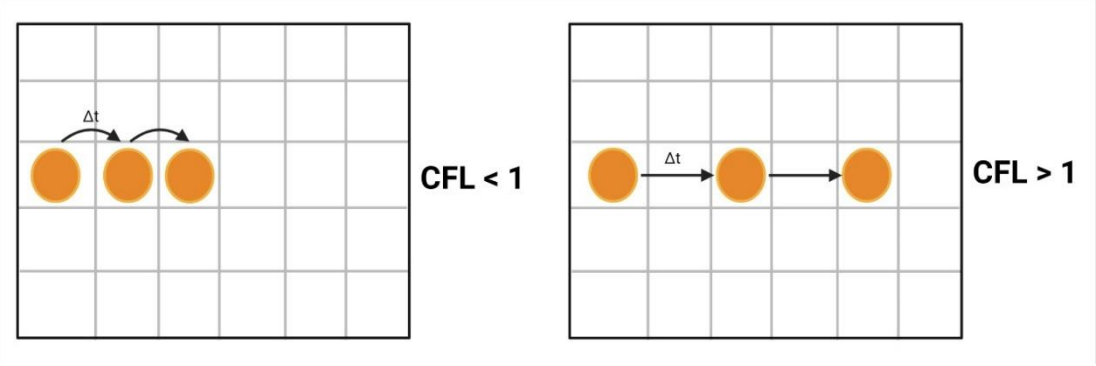

Figure 3.7: The Courant-Friedrichs-Lewy stability condition determines the stability of a computational simulation. Where CFL > 1, the nanoparticle skips mesh cells during the duration of a timestep and is more likely to fail to converge and/or produce results that are not permitted by currently known physics. Where CFL < 1, the nanoparticle visits each cell in turn, and the simulation is likely to converge and give physically probable results.

In terms of the physics of interest, the timestep must be selected such that all the physics of interest can be resolved. Any parameter that changes faster than the chosen timestep will not be represented within the simulation.

Particle Response Time

The particle response time gives the time required for the particle to reach 63% of free-stream velocity.[551] Where τ_p is much less than 1, then the particle will move approximately with the fluid.

$$\tau_p = \frac{\rho_p \, d_p^2}{18\mu_f} \tag{10}$$

Equation 10: Calculating particle response time. Where ρ_p is particle density, d_p is diameter of the particle and μ_f is fluid velocity.

For the scaled nanoparticles in this work, τ_p is shown to be 7.38x10^{-9} s, and therefore, the particle will move approximately with the same velocity as the fluid.

Maximum Allowable Timestep for Fluid – Courant Number

Rearranging **Equation 9** to give the following (**Equation 11**) enables the maximum allowable timestep for the fluid phase to be calculated.

$$\Delta t_f = \frac{C\Delta h}{U_f} \tag{11}$$

Equation 11: Calculating maximum allowable timestep of the fluid phase as a function of Courant number, fluid velocity and mesh density. Where C is courant number, Δh is mesh density and U_f is fluid velocity.

For the mesh density determined earlier for the bifurcations within the more complex geometries (1.5x10^{-6} m), the maximum possible timestep for the fluid phase is then 1.31x10^{-4} s.

Maximum Allowable Timestep for Particle – Rayleigh Criteria

Thus, from **Equation 12**, χ is then 0.94. Poisson's ratio of 0.4 chosen due to lack of available data for PLGA.

$$\chi = 0.1631v + 0.8766 \tag{12}$$

Equation 12: Calculating χ as a function of Poisson's ratio (v).

Using **Equation 13**, the maximum allowable timestep for the particulate phase is 1.98x10^{-9} s.

$$\Delta t_p = \frac{\pi R_p}{\chi} \sqrt{\frac{\rho}{G}} \tag{13}$$

Equation 13: Rayleigh criteria for calculating critical timestep. Where R_p = radius ρ = density, G = shear modulus.

The chosen timestep for the simulation will be somewhere between that for the solid (1.98x10^{-9} s) and the fluid phase (1.31x10^{-4} s). It also must be smaller than the particle response time calculated previously (7.38x10^{-9} s).[552] The

numbers obtained here are unsurprising and are broadly in agreement with those expected by Norouzi and co-workers.[552] Therefore, the timestep selected for this simulation is $7x10^{-9}$ seconds.

Stopping criteria change once implicit unsteady regime is selected. Implicit unsteady regime necessary to enable CFD-DEM coupling, as these are transient solutions. Once this alteration in simulation setup is performed, the stopping criteria then change from a simple number of iterations of the calculation – *c.f.* steady time regime, to a set of stopping criteria that are much more complex; relying on the physical time that is simulated and/or number of iterations of the calculation.

3.5 Results and Discussion

Since the creation of these models arises from an iterative method, where the model was extended or otherwise changed following each successful set of calculations, the results and the discussion of these will occur simultaneously.

Firstly, it will be shown how both meshing parameters and results from this *in silico* study have been validated through mesh independence studies and by comparison with known experimental data. It will be followed by discussion of the CFD model, and the behaviour of the carrier fluid, before considering the other information gained by coupling CFD and DEM on the behaviour of nanoparticulate matter *in vivo*. Finally, the inherent limitations of this model which occur through the assumptions used and/or the CFD solver itself will be discussed, as well as develop an understanding of what these results imply in terms of applying Quality by Design to the development of novel nanotherapeutics.

3.5.1 Mesh Independence Study

To assess the extent to which the results of the simulation depend on the mesh itself, a mesh independence study was carried out using the initial geometry replicating a singular capillary. This study enables a mesh density to be found, that strikes a balance between accuracy and the resolution of the resulting data, and computational demand. Maximum centreline velocity of the capillary has previously been calculated as $1.00\ x10^{-4}$ m s^{-1} (**Appendix B**). For the sake of speed and ease of set up, this mesh independence study uses water as the carrier fluid.

Residuals measure how much the equation changes between iterations. For a steady-state simulation, the calculation is considered to have successfully converged once residuals fall below $1\ x10^{-4}$.

Table 3.13: Results obtained from mesh independence study.

Number of cells	Maximum velocity (m s^{-1})	Residuals
7872	1.00 $x10^{-4}$	6.44 $x10^{-5}$
10220	9.98 $x10^{-5}$	1.63 $x10^{-5}$
16512	9.99 $x10^{-5}$	1.48 $x10^{-6}$
40638	1.00 $x10^{-4}$	8.63 $x10^{-8}$
76500	9.99 $x10^{-5}$	1.03 $x10^{-3}$
97812	9.93 $x10^{-5}$	2.58 $x10^{-6}$
98098	1.00 $x10^{-4}$	7.52 $x10^{-7}$
98670	9.94 $x10^{-5}$	2.31 $x10^{-6}$
735852	9.66 $x10^{-5}$	1.20 $x10^{-5}$

The results of this mesh independence study (**Table 3.13, Figure 3.8**) show that as mesh density increases, the results obtained from the simulation begin to converge on the expected (*i.e.* calculated) value. Once the mesh contains more than 98,000 cells, there is minor change seen in the values obtained for maximum velocity of the fluid, despite a significant increase in mesh density (from ~98,000 to >700,000 cells). It is also noted in this figure that the densest mesh gives a maximum velocity much lower than even the coarsest mesh assessed in this study.

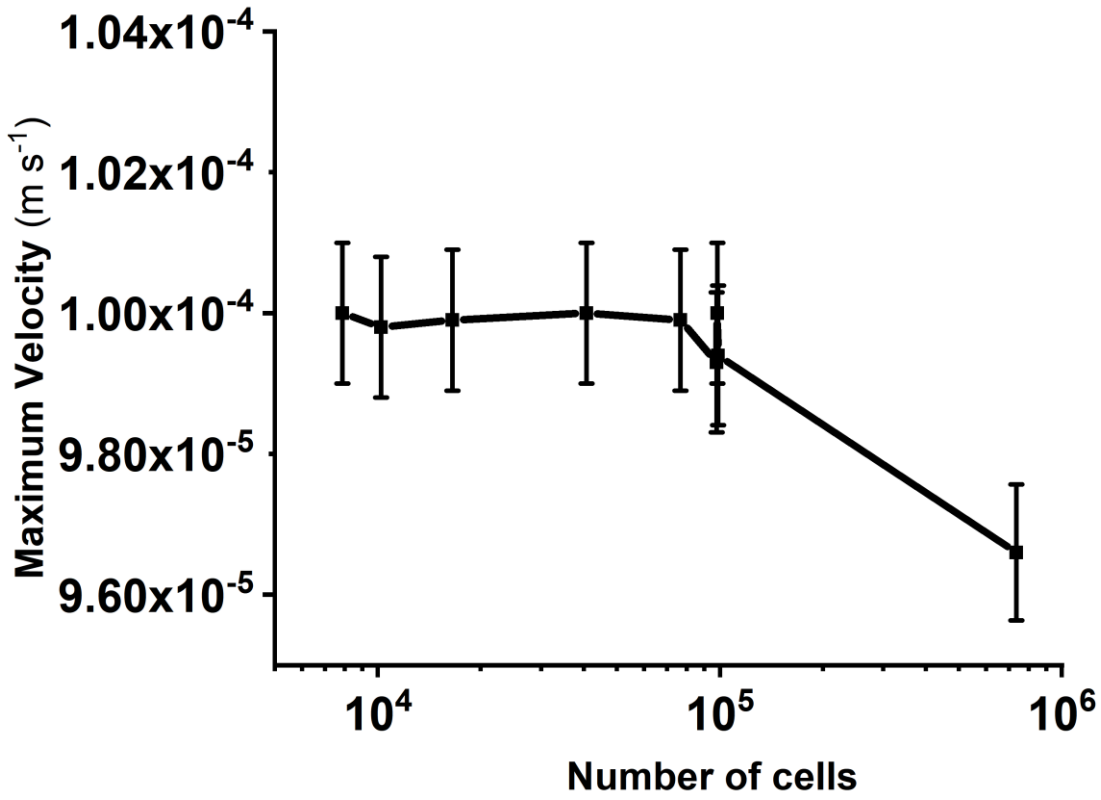

Figure 3.8: Mesh independence studies enable the least dense (and therefore computationally least intense) mesh to be chosen that does not compromise the accuracy of the result. Results of mesh convergence study from the original capillary geometry are shown. The mesh containing ~98,000 cells is the coarsest mesh that gives independent results. Error bars ±1% of the value used to help identify where mesh-independence occurs.

This was an unexpected result, but can easily be rationalised. Steady time regimes are much more reliant on the CFL condition being obeyed, whilst the

implicit unsteady regime used in the more complex simulations is comparatively more robust. Consequently, where this densest mesh is used, each cell is $2x10^{-6}$ m. The timestep size and input velocity then give a Courant number >1. Here, the CFL condition is not obeyed, and the simulation is unstable, leading to these unexpected results.

In this case, it has been decided that the mesh containing ~ 98,000 cells is the first one that gives independent results, because the result obtained for maximum velocity changes little, despite significant increases in mesh density. This gives a base size of $4.0\ x10^{-5}$ m for the mesh itself. This mesh is likely to be adequate for much of the more complex geometries employed later in this study. It does look like a coarser mesh with a base size of $8.0\ x10^{-5}$ m would also be suitable, however a mesh this coarse struggles to accurately resolve both the shape of the cylindrical capillary and of the more complex bifurcation geometry used later.

3.5.1.1 Assessing Generated Mesh Quality

The quality of the generated mesh can be assessed by looking at cell quality, skewness angle of the cells themselves and the degree to which the volume of one cell differs from its neighbours.

Cell Quality

Cell quality is a measure of how uniform are the cells that make up the mesh (**Table 3.14**). A perfect cell has a cell quality of 1.0. Ideally, the bulk of the cells within the mesh should have a cell quality rating of 0.5 or more.[535] Bad cells are those where quality is less than $1.0x10^{-5}$.[535] Such cell quality values suggest that the cells within the mesh vary significantly in size, shape and volume. All cells in this mesh have a cell quality of 1.0.

Table 3.14: Cell quality measures the uniformity of a simulated mesh. Cell quality for the simple capillary model used within this chapter. All cells are seen to have a cell quality of 1.0.

Cell quality	Number of cells
≤ 0.50	0
≤ 0.60	0
≤ 0.70	0
≤ 0.80	0
≤ 0.90	0
≤ 0.95	0
≤ 1.00	98098

Skewness Angle

Skewness angle measures the angle between a face normal and the vector that connects the centre of two neighbouring cells.[535] This shows whether the cells on either side are formed such that diffusion of quantities is possible without the quantities becoming unbounded.[535] A perfectly orthogonal mesh will have a skewness angle of 0°. Bad cells are those with a skewness angle greater than 85°, and skewness angles > 90° generally lead to issues with solution convergence.[535] As can be seen from **Table 3.15**, there is almost no skewness within the mesh which captures the fluid volume.

Table 3.15: Maximum skewness angles detected for each of the geometry parts in the original capillary geometry.

Geometry part	Maximum skewness angle (°)
Inlet	5.310
Outlet	5.310
Fluid	0.599

Volume Change

Volume change describes the ratio of a cells volume compared to that of its largest neighbour (**Table 3.16**).[535] A value of 1 is a good cell, as this shows that the cell concerned has a volume equal to or larger than that of its neighbours.[535] Cells where the volume change is < 0.01 are considered bad cells – large increases in volume from one cell to another may lead to inaccuracies in results and instability in the solvers.[535]

Table 3.16: Volume change of cells within a mesh is a proxy measure of the accuracy of the results it will generate. All cells within this mesh have a volume change > 0.01.

Volume change	Number of cells
<0.01	0
<0.1	0
<1	98098

Based on this mesh independence study, a base size of 2.0 $x10^{-5}$ m was selected. The volume mesh generated was then further evaluated in terms of its quality, cell skewness and volume change. The mesh was found to be suitable for further analysis in each case.

3.5.2 An Additional Mesh Independence Study

Since the capillary geometry study does not consider the impact of bifurcations and any refinement of the mesh that these may require, a second mesh independence study was conducted, using an incrementally more complex geometry (**Figure 3.9**).

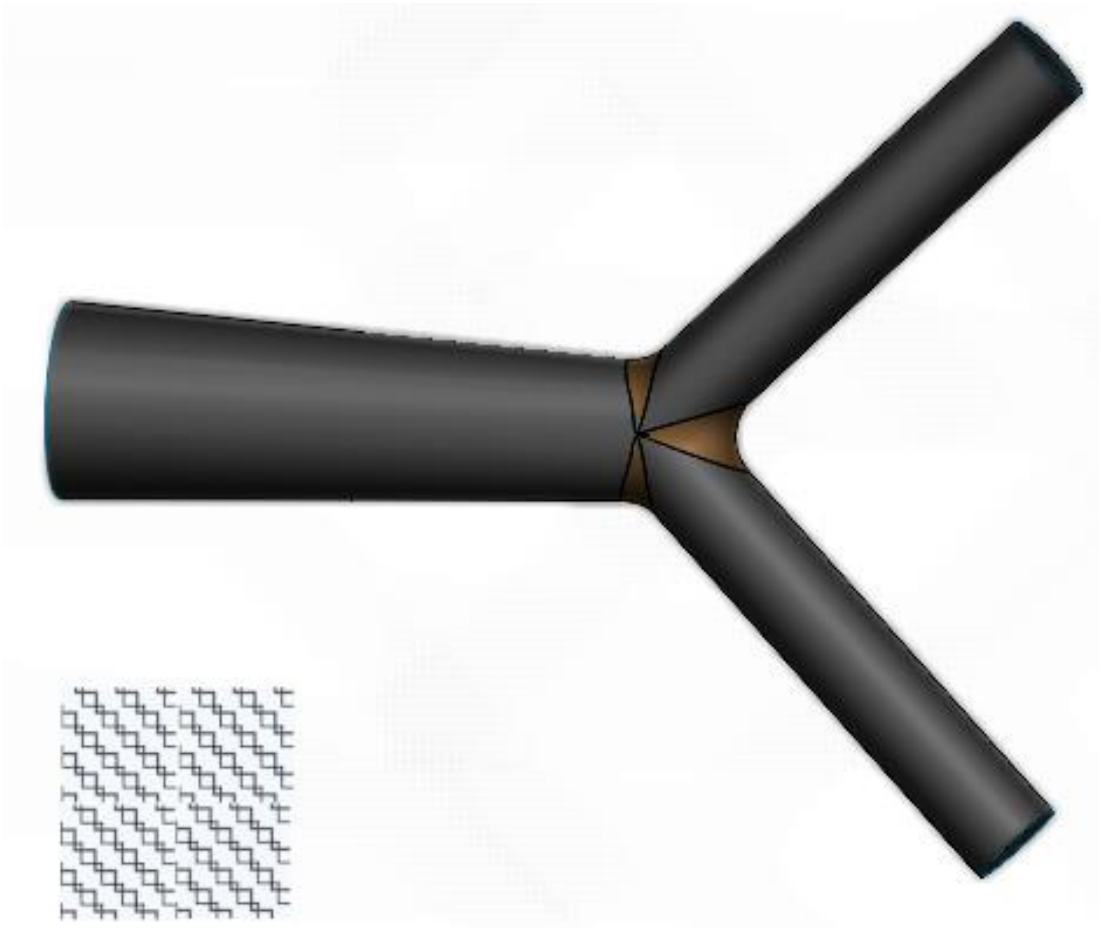

Figure 3.9: The more complex geometry used for the second mesh independence study. This is a 10x scaled version of the geometry originally published by Tan *et al*. Fillet is highlighted in orange. AR+

Here, only the mesh density of the fillet (highlighted in orange) was modified, since this is where more complex flow patterns are expected to occur within this geometry. Previous work within fluid dynamics has shown that bifurcations or other sudden changes in width or shape of pipe geometry can lead to areas of recirculation of flow.[553]

Table 3.17: Results obtained from mesh independence study, only the meshing density of the fillet is altered in this case. Residuals given as the continuity for each calculation.

Number of cells	Maximum velocity (m s^{-1})	Residuals
30627	5.00 $x10^{-4}$	2.66 $x10^{-7}$
31904	4.98 $x10^{-4}$	4.60 $x10^{-7}$
32183	4.96 $x10^{-4}$	3.95 $x10^{-7}$
32212	4.96 $x10^{-4}$	3.54 $x10^{-7}$
34659	4.95 $x10^{-4}$	2.92 $x10^{-7}$
36251	4.96 $x10^{-4}$	3.26 $x10^{-7}$

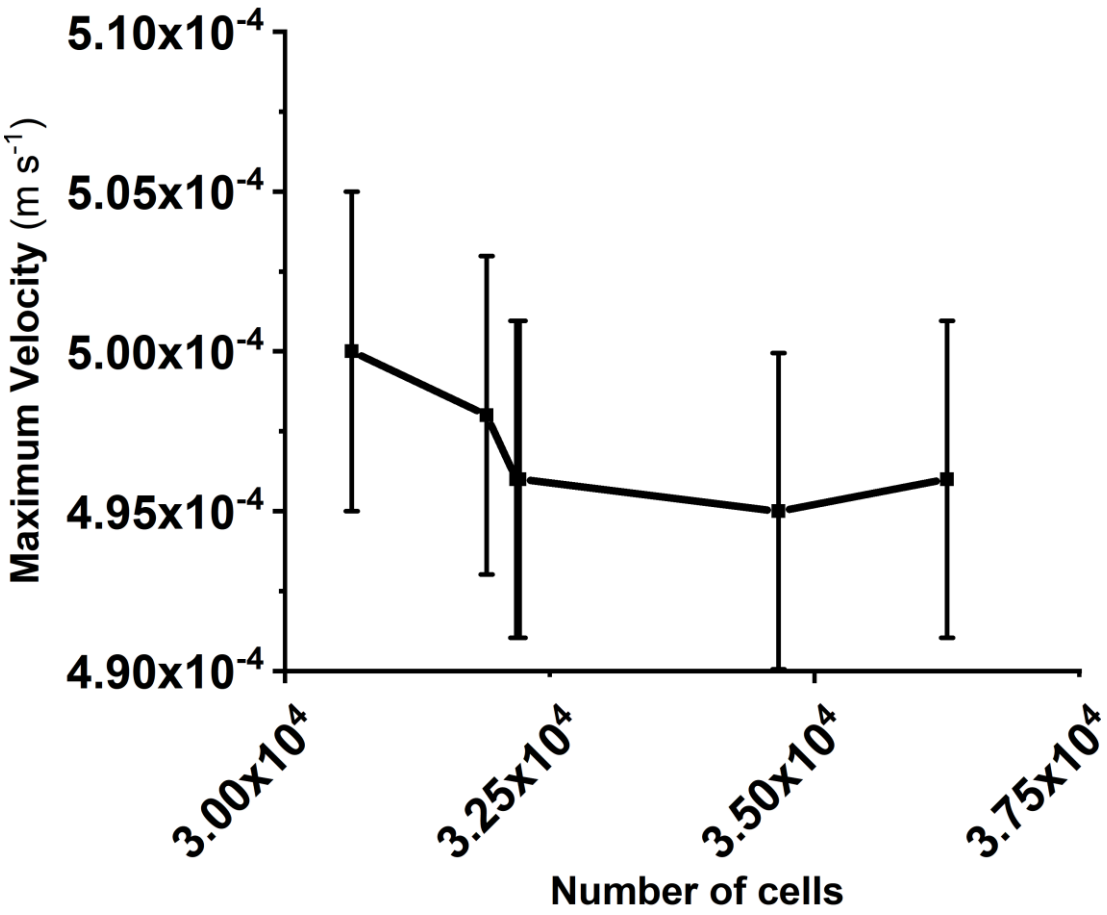

Figure 3.10: Mesh independence studies enable the least dense (and therefore computationally least intense) mesh to be chosen that does not compromise the accuracy of the result. Results of mesh convergence study from the more complex Tan geometry are shown. Increasing cell number arises from increasing numbers of cells within the fillet area defined previously. The mesh containing ~31,000 cells is the coarsest mesh that gives independent results. Error bars ±1% of the value used to help identify where mesh-independence occurs.

The results of this second mesh independence study (**Table 3.17)** shows that maximum fluid velocity is independent of mesh density once the geometry contains ~31,000 cells. This corresponds to a base size of the mesh of 1.5 $x10^{-6}$ m within the fillet area highlighted previously. Furthermore, it is known from earlier work, that the size of mesh cells must not be smaller than the size of nanoparticles used here.[552] As a consequence, for the refinement of the fillet area, the meshing density must not lead to a cell size < 1.0 $x10^{-6}$ m.

In conclusion, these mesh independence studies show that the mesh needs refining at bifurcations to accurately resolve fluid velocity, since the mesh density that leads to the results being independent of the mesh in this case is greater than that used for the bulk of the geometry (2.0 $x10^{-5}$ m). The assessment of the quality of this mesh can be found in **Appendix C**.

3.5.3 Validation of Model and Methodology Against Published Studies.

To validate the computational model created within this work, calculations were conducted to compare results obtained from this *in silico* study and two other previously published studies.

3.5.3.1 Tan et al.

The geometry previously reported by Tan *et al*. was used; this consists of one main vessel and two symmetric daughter vessels of smaller diameter. A horizontal cross section of this geometry is shown (**Figure 3.11**). Calculation set up was broadly as previously described for the coupled CFD-DEM model (**Section 3.4.7**). However, boundary conditions for the solid phase were set as open at the ends of the daughter vessels, which permits nanoparticles to exit the geometry to more closely mimic the published methodology. 200 particles of a size suitable to represent 100 nm PLGA particles were injected into the geometry. Calculations also show that nanoparticles will travel the entire length of the geometry in 1 second. The simulation has been set to model a time period slightly in excess of this (1.05 s), to accommodate “lazy” nanoparticles, which may take longer to exit the geometry.

There are differences between the work published by Tan and colleagues and the work undertaken here. Firstly, it is difficult to determine the precise method by which their calculations were performed, however, this is not an issue, since it is likely there are many ways by which this simulation could be performed. In this work, the calculations used a coupled CFD-DEM method. Furthermore, the published work also lacks details about both nanoparticle identity, but also that of the carrier fluid within the system. The assumption is made that the fluid is an incompressible Newtonian fluid. Here, PLGA nanoparticles of a size suitable to mimic 100 nm nanoparticles are used and the carrier fluid is blood plasma, modelled using the 5-parameter Carreau-Yasuda model, which allows a full description of the pseudoplastic behaviour of plasma to be included within the simulation. These alterations have the potential to lead to subtle differences between the two models. It would be expected that there would be variation between the models with respect to behaviour of both fluid and particle, and therefore of nanoparticle aggregation and agglomeration. As such, identical results between both models are not expected.

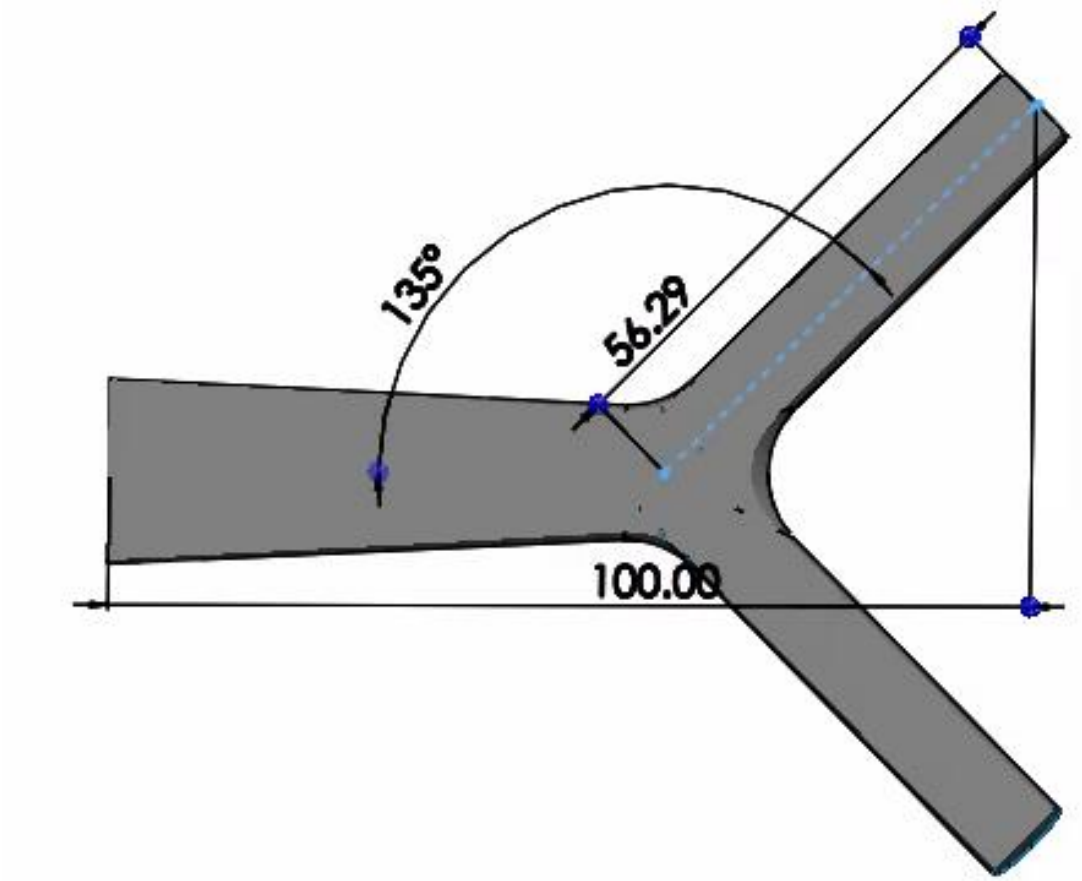

Figure 3.11: A representation of the 10x scaled version of the geometry used in this work.[445] Dimensions are given in micrometres.

Due to the complexity of the model, this has again been developed with an iterative approach. Initially, the model was studied purely as a CFD model, so fluid behaviour could be understood, before the model was made more complex by coupling between CFD-DEM to enable particle behaviour to be studied, and finally nanoparticle-wall interactions were added into the model to more closely mimic the study performed by Tan and colleagues. To visualise the results more easily, a planar slice of the geometry in the y-plane is presented in each case.

Fluid-only Model

Initially, just the fluid behaviour was of interest in this geometry. Streamlines were used to elucidate how the fluid moves within this geometry (**Figure 3.12**).Fluid flow enters *via* the inlet (far left of the geometry), flows in the x-direction and exits through one of the two available outlets *via* the daughter vessels. In the scalar scene (B), the no-slip boundary condition (and therefore zero fluid velocity) at the walls can also be seen. Finally, the cross-sections selected here, show the development of complex secondary flow fields as the slice being considered is closer to the bifurcation in the geometry. This mirrors the results obtained by Guha and colleagues on studying fluid flow within symmetric branching networks *in vivo*.[553]

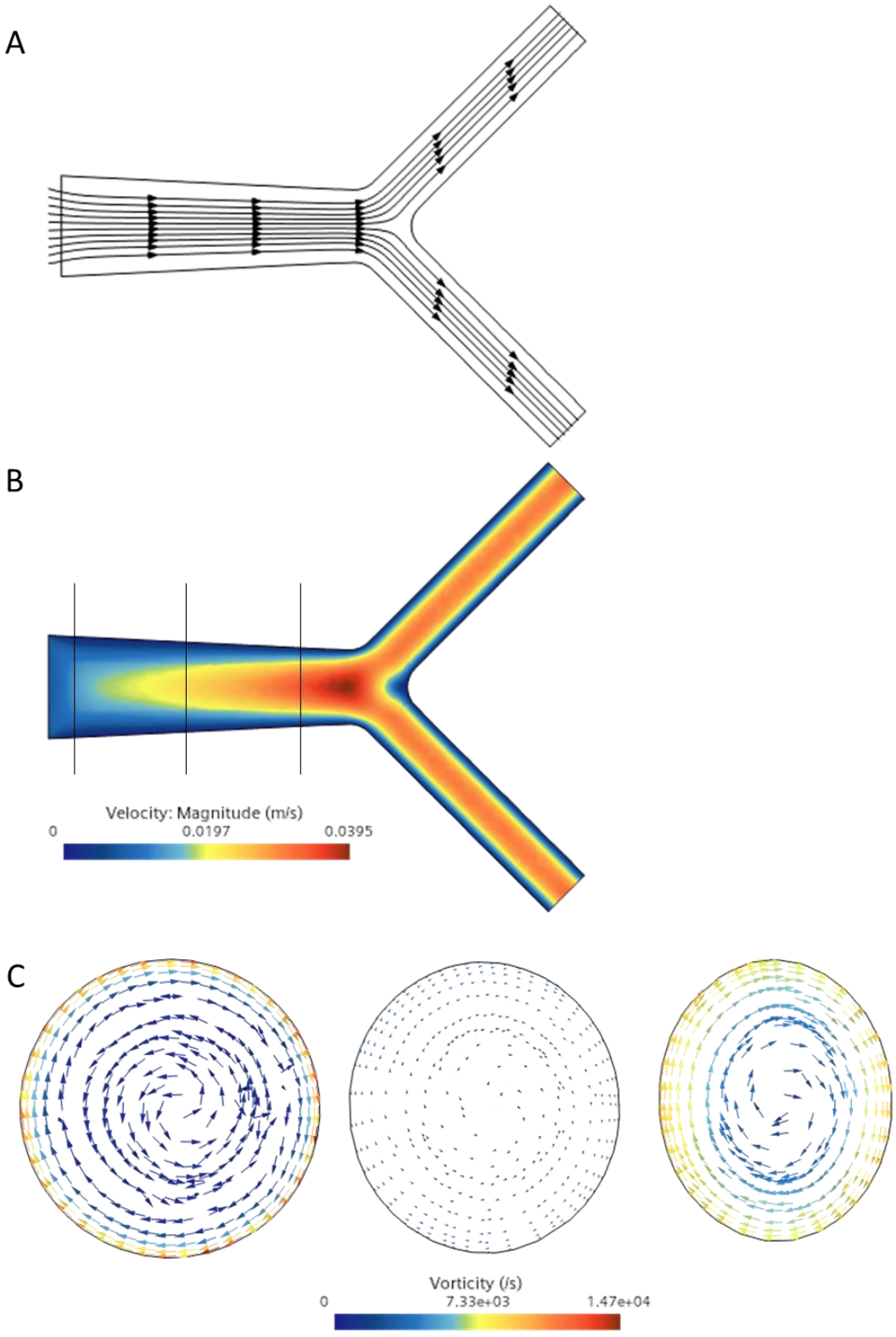

Figure 3.12: Fluid velocity changes as a function of vessel length. A) Plane section in Y-direction. Fluid enters from the inlet (far left) and exits through one of two outlets within the geometry. B) Fluid velocity increases as a function of vessel length. C) 3 arbitrarily chosen planar sections in the x-direction are shown. Shape changes along the X direction – vessel tapers slightly. Fluid flow becomes more complex as it travels further down the larger mother vessel.

Finally, this model can also be used to study the wall shear stress within the geometry (**Figure 3.13**). It can be shown that in the larger "mother" vessel, the wall shear stress is ~0.7 Pa, and is ~ 1.4 Pa at the fillet area[445] This paper gives wall shear rates of 200 s^{-1} and 400 s^{-1} at the bifurcation (analogous to the fillet area highlighted previously), which convert to 0.7 Pa and 1.4 Pa if the fluid is assumed to be blood plasma. This also provides more evidence to the assertions made previously, that dimensional scaling has been successfully applied – the models are dynamically similar.

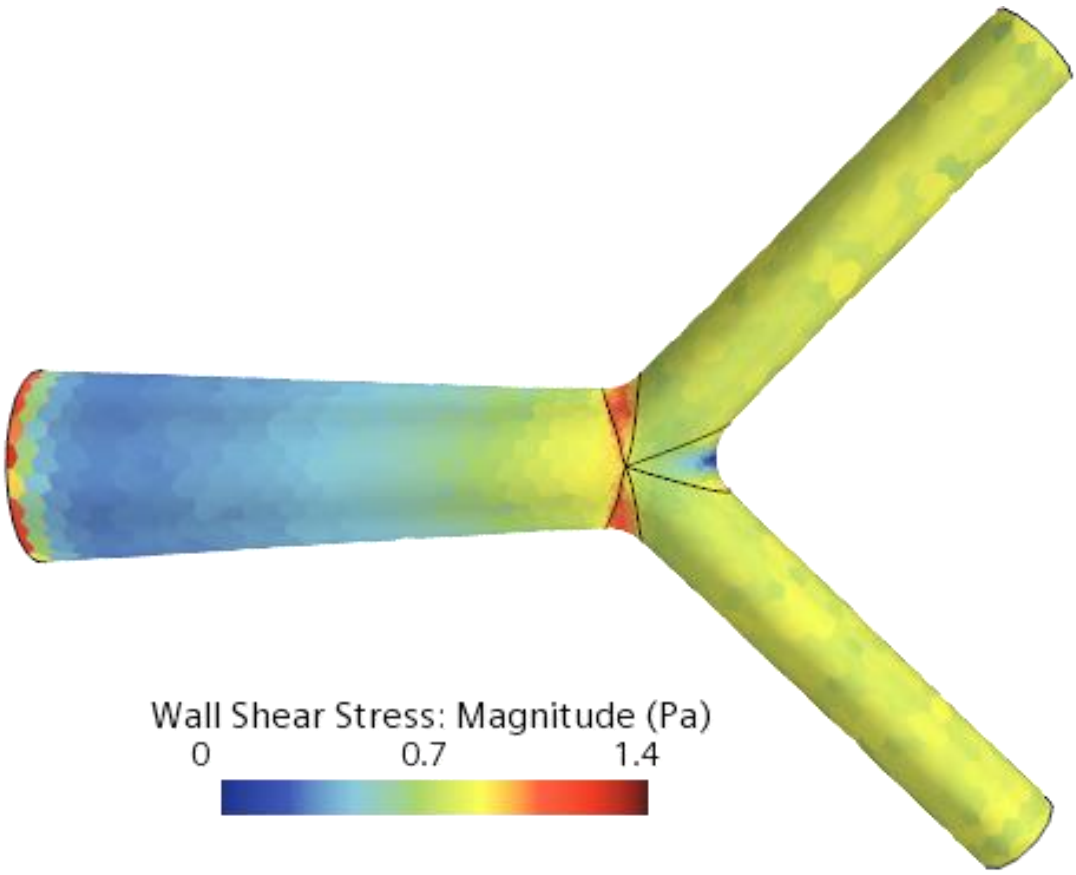

Figure 3.13: Wall shear stress agrees well with that expected from the original Tan *et al.* geometry. The similarity between the two models provides more evidence that dimensional scaling has successfully been applied to this larger scale model, since the forces within the models are considered dynamically similar.

Fluid and Particle Model

Once particles have been added to the model, and the simulation run, it is clear to see that the bulk of the nanoparticles injected into the geometry are attracted to the slowest moving areas at the bifurcation (**Figure 3.14**), or at the walls of the geometry. This is not dissimilar to those results published by Tan and colleagues, or those available within the area of vascular biology more widely, where low and/or oscillating wall shear stress has been previously implicated in the earliest stages of atherosclerosis.[554,555]

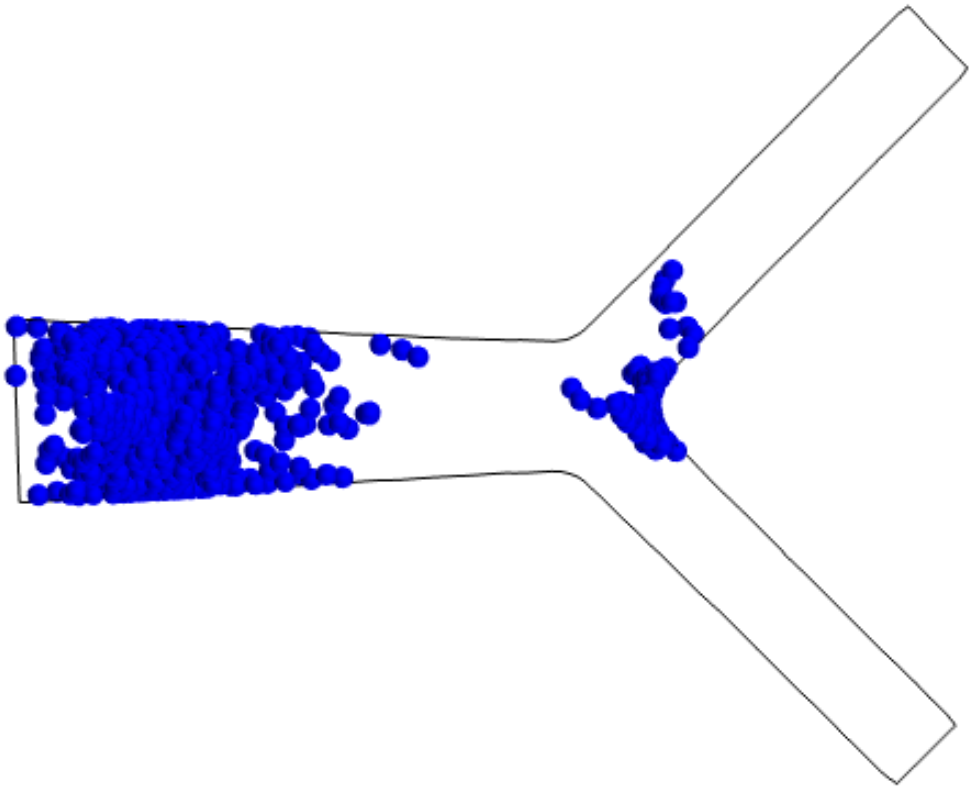

Figure 3.14: Particle density is highest where fluid velocity is low. Image shows nanoparticle position at the end of the simulation.

Complete Model

Wall interactions were added to this final version of the model to make it more closely replicate the results from the original Tan paper. Wall interactions are, as their name suggests interactions between the particles within the simulation and the boundaries of the geometry. Here, the same results as those given in the Tan paper are reported. Firstly, nanoparticle distribution will be discussed, before assessing impact of shear rate on nanoparticle binding. Finally, the utility of this model to understand the formation of nanoparticle aggregates and agglomerates *in vivo* will be considered.

It can be shown that nanoparticle binding density decreases at the bifurcation as wall shear stress and shear rate increase (**Figure 3.15**). This is unsurprising, as increasing fluid velocity reduces the probability that a collision between nanoparticle and vessel wall will result in bonding.[445] By applying the parallel bonds model, it is also possible to study nanoparticle aggregation behaviour (**Figure 3.16**). In this context nanoparticles, aggregates and agglomerates are defined as follows: nanoparticles are the primary particles in the nanoscale size range; aggregates are chemically bonded clusters of nanoparticles typically 200-300 nm in size and agglomerates are larger structures formed by groups of aggregates, which are held together by weaker forces *e.g.,* Van der Waals.[497]

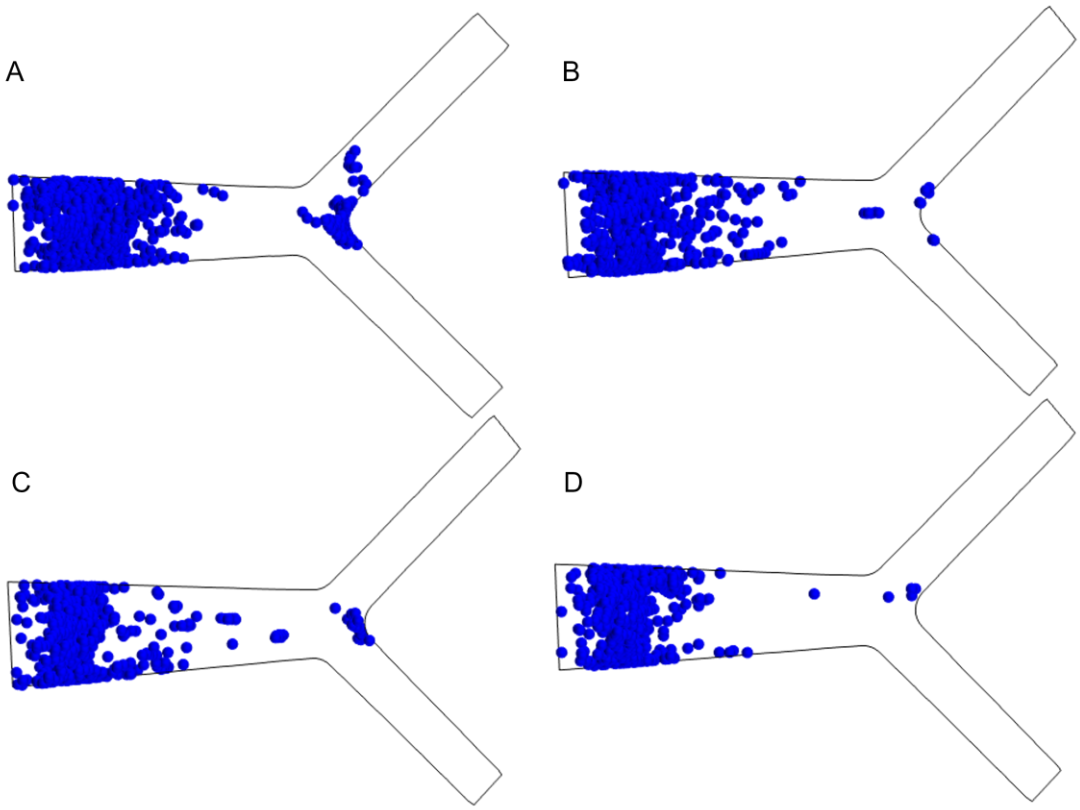

Figure 3.15: Nanoparticle density around the bifurcation decreases as shear rate and fluid velocity increase. Shear rate at bifurcation for each image is as follows: A) 400 s^{-1} B) 800 s^{-1} C) 1600 s^{-1} D) 2000 s^{-1}. Images show nanoparticle position at the end of the simulation.

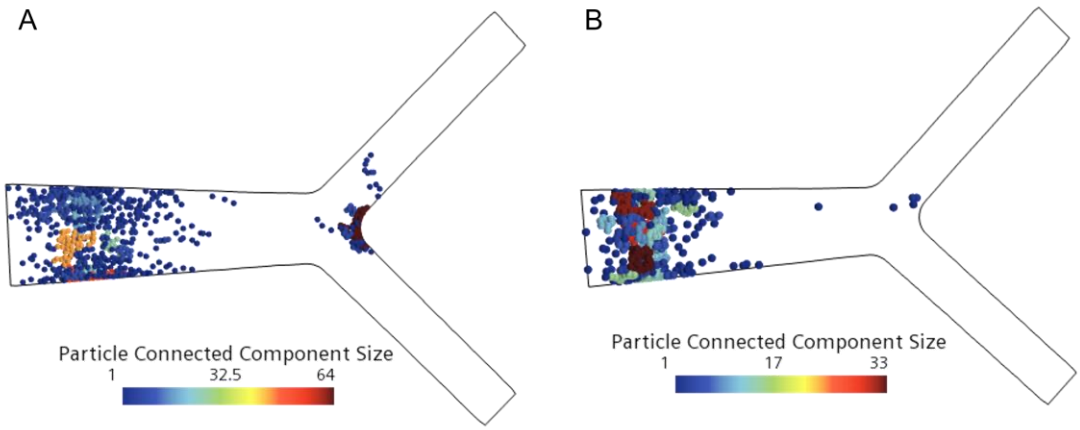

Figure 3.16: Nanoparticle aggregation behaviour can be studied with this model. A) Wall shear 400 s^{-1} at bifurcation. B) Wall shear stress 2000 s^{-1} at bifurcation. Images show nanoparticle position at the end of the simulation.

For both images (**Figure 3.16**), a mixture of both individual nanoparticles and larger clusters can be seen. The aggregates are largest where fluid velocity is lower. However, in B, where wall shear at the bifurcation is 2000 s^{-1}, additional distinct clusters can be seen. The clusters in this second case are significantly smaller in terms of the number of nanoparticles they contain, which further

suggests that the large aggregate in A is likely to be considered an agglomerate. The weaker forces which hold this agglomerate together are disrupted as fluid velocity increases.

3.5.3.2 Barber et al.

In this section, the developed methodology will be used to replicate the previously published study by Barber and colleagues. This paper considers partitioning of red blood cells (RBCs) into daughter vessels. A symmetric bifurcation (similar in shape and size to the Tan paper considered earlier) is used as a control geometry. Benchmarking against this paper enables fluid behaviour (as streamlines) and particle streaklines to be assessed.

Streamlines, streaklines and pathlines can be defined as follows. Streamlines are a way of visualising fluid flow. Streaklines are the output of a continuous stream of particles, whilst pathlines track the movement of a single particle. Pathlines are not shown here but are defined for the sake of completeness. For unsteady flow, pathlines and streaklines may differ. For steady flow, streamlines, streaklines and pathlines all coincide.

3 geometries are used within this paper: two bifurcations – symmetric and asymmetric and a T-junction. (**Figure 3.17**). In each case these are 10x models, and like the models studied previously, areas where fluid flow is likely to be more complex will be meshed at a higher density. Further details in **Appendix A**

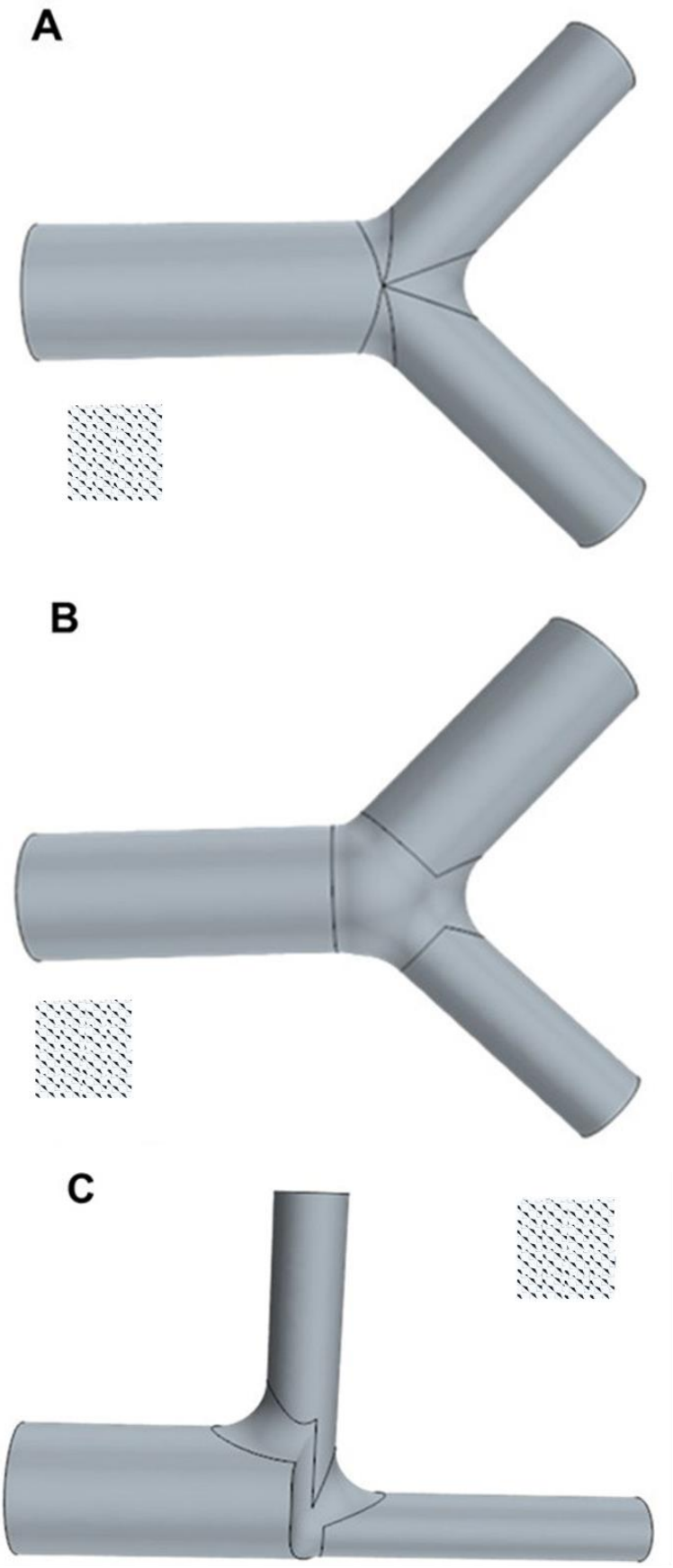

Figure 3.17: A summary of the three geometries explored within Barber *et al*. A) symmetric bifurcation - daughter vessels 40 μm diameter. B) Asymmetric bifurcation - daughter vessels 72.7 and 50.4 μm. C) T-junction - daughter vessels 40 μm in diameter. AR+

In this section each model will be discussed separately, first considering the behaviour of the fluid before considering the behaviour of the nanoparticles introduced into the model. Streamlines are obtained for each geometry by generating a 1x12 matrix giving 10 streamlines originating at the inlet of the mother vessel. The streaklines are then generated by using 4 injectors evenly spaced across the inlet of the mother vessel to introduce particles into the geometry. Using an even number of injectors and therefore obtaining an even number of streaklines (and streamlines) for each geometry makes any preference for one specific daughter vessel much easier to identify in the figures which follow.

Symmetric Bifurcation

As stated previously, the symmetric bifurcation has one mother vessel of larger diameter and two equally sized daughter branches. This symmetric bifurcation is used as the control geometry in this study. Streak and streamlines (**Figure 3.18, Figure 3.19**) clearly show that there is no preference for either daughter branch, and injected particles will be partitioned equally between both daughter vessels. When the streaklines are considered more closely, the particles injected closest to the centre of the mother vessel, where fluid velocity is highest, will reach the outlets of this geometry fastest. This is, perhaps, easier to see if **Figure 3.19** is viewed using augmented reality. These results closely match those previously reported by Barber and colleagues.

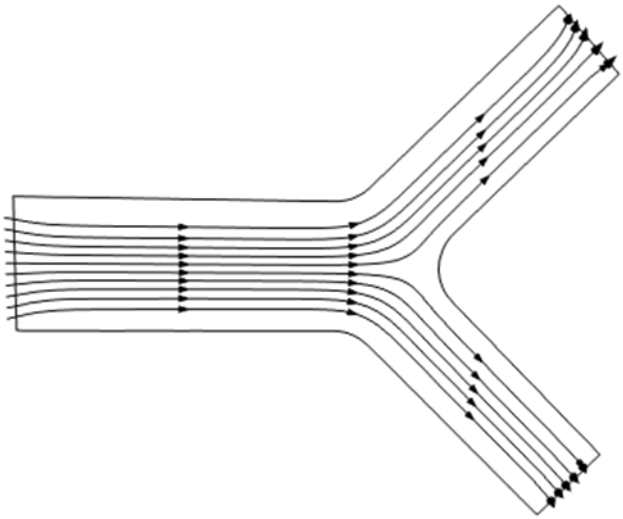

Figure 3.18: Symmetric bifurcation from Barber *et al*. No preference for either daughter vessel is seen *via* the streamlines used to visualise fluid behaviour in this geometry. This is as expected from previously published studies.

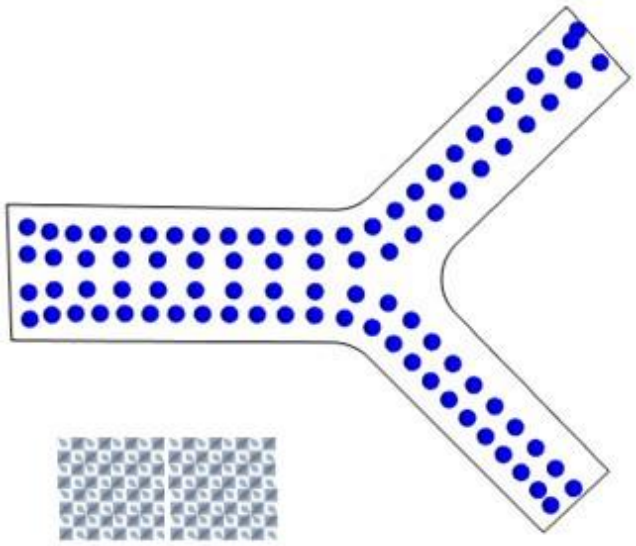

Figure 3.19: Symmetric bifurcation from Barber *et al*. Streaklines show no preference for either daughter branch and confirms the results obtained from the streamlines of fluid behaviour. AR+

Asymmetric Bifurcation

The asymmetric bifurcation has a similar geometry to the symmetric bifurcation presented earlier; however, the daughter vessels are of two different diameters (72.7 and 50.4 μm respectively). This asymmetry in the diameter and therefore fluid velocity then leads to an uneven partitioning of streamlines and particles between the two daughter vessels within this geometry (**Figure 3.20, Figure 3.21**).

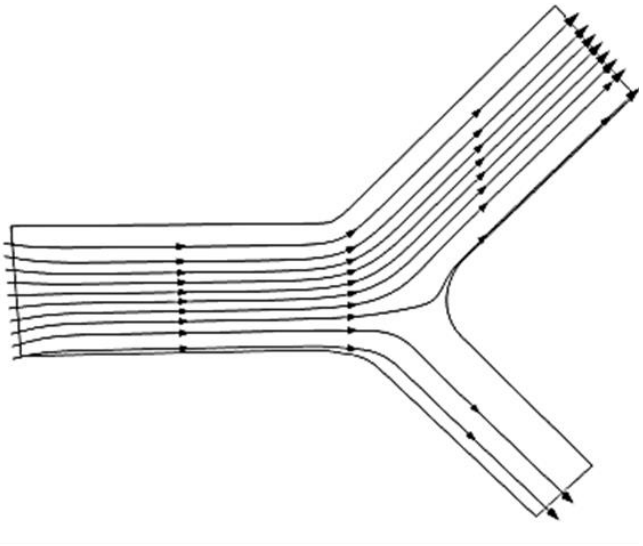

Figure 3.20: Asymmetric bifurcation from Barber *et al*. A clear preference for the larger of the two daughter vessels is observed.

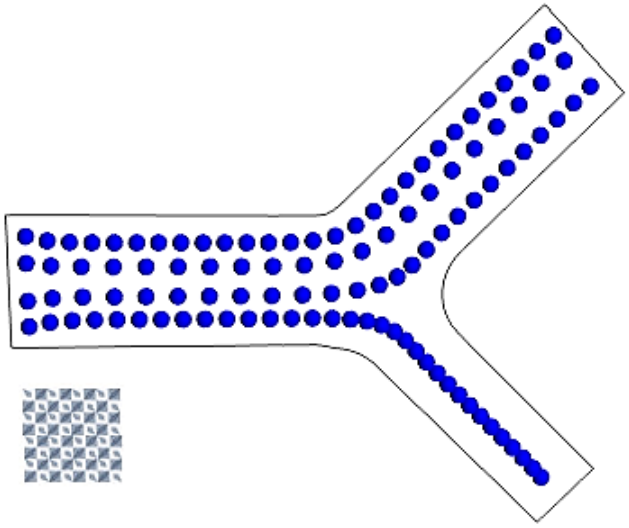

Figure 3.21: Asymmetric bifurcation from Barber *et al*. Streaklines show a clear preference for the larger of the two daughter branches. AR+

The particle streaklines shown in **Figure 3.21** make clear just how much slower fluid velocity is in the narrower daughter vessel – the slower the particles move, the closer together they appear. In this work, the particles are small relative to the overall geometry and the flow field, thus, they deviate little from the streamlines shown previously. The impact of the asymmetry in vessel diameter is then explained as fluid always follows the path of least resistance – the pressure drop between the geometry inlet and each outlet are slightly different to each other, despite the outlet boundary conditions being identical (pressure drop 19.71 Pa for the wider branch and 19.87 Pa for the narrower branch).

T-junction

The final geometry under study in this work is a T-junction. Like the symmetric bifurcation studied earlier, both daughter vessels are of the same diameter, and therefore, it would be expected that streamlines and therefore particle streaklines will partition themselves equally between both daughter vessels. These results are shown in **Figure 3.22**,**Figure 3.23**. Again, like the symmetric bifurcation, stream and streaklines are equally partitioned between both daughter branches and no preference for a particular branch is observed.

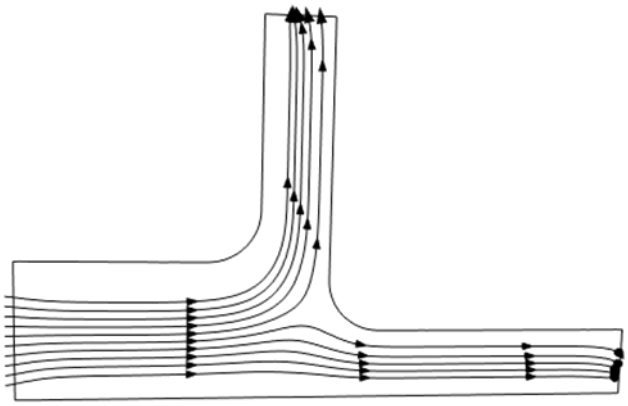

Figure 3.22: Streamlines showing fluid behaviour in the T-junction geometry. No preference for either daughter branch is observed, comparable to the results obtained for the symmetric bifurcation shown earlier.

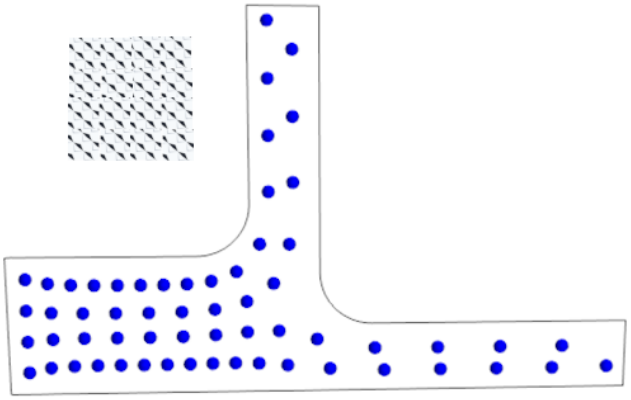

Figure 3.23: Streaklines for particle behaviour in the T-junction geometry. No preference for either daughter vessel is observed. AR+

If this geometry is compared with the symmetric bifurcation presented earlier, there is no significant difference in fluid or particle behaviour as a function of angle between the daughter branches (45° vs 90°). These results agree with those previously published within the literature.[446]

Summary

In summary, the results obtained using the combined CFD-DEM methodology developed in this chapter and the geometries reported previously by Barber *et al.*, it can be shown that for the symmetric bifurcation there is no preference for either daughter vessel – unsurprising as both vessels are identical in shape and size, and this geometry is therefore used as a control within the study. The asymmetric bifurcation where the daughter branches are of differing diameters shows very different results. Here, there is a clear preference for one daughter vessel over the other, and it is the smaller vessel which preferentially attracts the particles injected into the geometry. The T-junction geometry shows no preference for either daughter vessel – the same as the control geometry

(symmetric bifurcation). This geometry is particularly useful, as it reveals useful insights into the robustness of the methodology; it makes clear that the methodology is capable of handling extremes in geometry (90° angle between daughter vessels). Therefore, it can be shown that this methodology is robust, unaffected by the angle between daughter vessels and can study both fluid and particle behaviour simultaneously. This is then the rationale for applying this combined CFD-DEM methodology in the following chapter to understanding the behaviour of drug-loaded nanoparticles *in vivo* following intravenous administration.

3.5.3.3 What Do These Results Mean for Quality by (Digital) Design?

Quality by design (QbD) is a pharmaceutical development methodology, which first begins by considering key parameters of the final drug product. These parameters include safety, efficacy dosage form and the route by which the final drug will be given.[556,557] International harmonisation of these guidelines is ongoing.[558] The development of *in silico* models, such as those developed in this work play a fundamental role in QbD as it enables novel (nano)therapeutics to "fail faster and fail cheaper", *i.e.,* unsuccessful candidates are identified well before expensive stage I clinical trials commence. Additionally, *in silico* models have previously been used for various pharmacokinetic studies and could potentially be used for studying the efficacy of novel drugs in so-called "special populations" *e.g.,* paediatrics.[559]

3.5.3.4 Limitations of the Model

The models developed here are not perfect replicas of reality. There are many limitations which have been identified for this model. They concern the computational method that has been chosen (CFD-DEM); the assumptions implemented within the model to simplify it and simplify the calculations which need to be performed during the simulation, and finally limitations that are introduced through the chosen CFD solver.

<u>Limitations from Methodology</u>

Two well studied limitations exist for coupled CFD-DEM models, these are: the physical time that can be studied and the size of the problem that can be modelled.[75]

The physical time of the model is limited in two ways, by the stability conditions imposed on the solid phase (*i.e.,* particles) and the stability conditions imposed on the fluid phase. As discussed previously (**Section 3.4.7.4**), these stability conditions then apply limits on the size of the timestep used within the simulation; the smaller the timestep as determined by the Courant number and Rayleigh criteria, the shorter the physical time that can be modelled.

CFD-DEM models are well-known to be computationally demanding and therefore the size of the problem is also limited. Limits exist on both the total number of particles that the simulation can handle (generally fewer than 10^5) and also a limit to the size of the geometry concerned and/or density of the mesh, as there is a maximum total number of cells that are currently possible within these types of simulations.[75] To some extent, these limitations can be

overcome by running the simulation in parallel (*i.e.* on several processors simultaneously), but a point still exists where the computational demand of the simulation will exceed available computational resources.

Limitations Arising from Assumptions Used Within the Model

Several assumptions have been applied to these models. This model assumes the vessel walls are smooth. Owen and colleagues have previously shown that this assumption is not true *in vivo*, and that surface roughness affects fluid haemodynamics.[79] Also, these models do not consider the Fåhræus-Lindqvist effect. This effect describes the apparent change (decrease) in fluid viscosity of blood as vessel diameter decreases.

Limitations from the Software

Furthermore, additional limitations are introduced into this model by the CFD solver that has been chosen. A known limitation of the STAR-CCM+ software, is that it is not able to model so-called multiphase fluids. In the context of this study, this means that the computational simulation functions as if the PLGA nanoparticles were being introduced in a plasma-like carrier fluid. This does not reflect reality, where drug-loaded nanoparticles are frequently suspended in 0.9 % saline or 5 % glucose solutions.[80] These solutions have viscosities that are different to that of blood plasma, and thus fluid behaviour may vary from that seen within these models.[81,82] Recently published work suggests that this limitation of the model could be overcome with a coupled multiphase flow and DEM approach.[79]

3.6 Conclusions

A combined Finite Volume-Discrete Element Method has been developed for use with STARCCM+, a commercially available CFD-solver. The law of dynamic similarity and Buckingham Pi theorem have both been applied to create larger-than-life models of the geometries of interest.

First, a literature review was performed to gather necessary physiological parameters (*e.g.* vessel length, diameter.) as well as input parameters for simulations and properties of the VADs that will be studied in **Chapter 5**. This work is summarised in **Appendix E**.

Next, preliminary calculations using the data found for a generic capillary vessel were completed. Mesh independence studies were performed to balance accuracy of the results with computational demand of the simulations, and quantitative analysis of the generated volume mesh in terms of its quality, cell skewness and volume change was undertaken. The meshes were found to be suitable for further analysis in each case.

It was confirmed that the methodology functions correctly and is robust to changes in input geometry by running simulations which replicate previously published studies (Tan *et al.* and Barber *et al.*). Simulations were constructed and undertaken in an iterative manner due to their complexity. Fluid velocity, fluid shear and nanoparticle aggregation are the parameters of interest here, but streamlines, streaklines and pathlines have also been studied. The results

of these studies show that fluid and particle behaviour is not a function of angle between daughter vessels but does depend on vessel diameter – particles and streamlines preferentially choose the narrower of the two vessels, where such choice exists, otherwise they will be partitioned equally between both daughter vessels. Furthermore, these studies also show that the CFD-DEM methodology developed in this chapter is robust and can be adapted to any chosen geometry of interest. This developed methodology enables behaviour of the fluid and nanoparticle aggregation and agglomeration to be studied at will and can be modified to include any desired particle shape or size.

These *in silico* studies are useful when considering the nascent Quality by (digital) Design approach that is now beginning to find application within the development of novel pharmaceuticals, as these models would enable unsuccessful candidates to be identified well in advance of clinical trials. Finally, limitations of this study which arise from the methodology, model and chosen software have been discussed in detail.

3.7 Appendices

A. A Brief Introduction to Haemodynamics

Haemodynamics is, in its simplest form, the study of blood flow and blood pressure within the human body.[560] A complete discussion of this topic is well outside the scope of this thesis and therefore only the basics of haemodynamics necessary to contextualise the computational calculations discussed later, will be introduced here.

3.7.1.1 Ohm's and Poiseuille's Law

Blood flow is a function of pressure difference and resistance (**Equation 14**) and can be calculated using a modification of Ohm's law.[560]

$$Q = \frac{\Delta p}{R} \tag{14}$$

Equation 14: A modification of Ohm's law gives volume flow rate (Q) as a function of pressure difference and resistance. Where Δp = change in pressure and R= resistance of blood vessel

Poiseuille's law enables us to calculate Δp, the pressure differential between two ends of a pipe (in this context, a blood vessel), that results purely from the viscosity of the fluid; where the fluid is incompressible (*i.e.* not a gas), Newtonian and under a laminar flow regime (**Equation 15**). Equations **Equation 14** and **15** when used together also show that resistance is sensitive to change in blood vessel diameter.

$$\Delta p = \frac{8\mu L Q}{\pi R^4} \tag{15}$$

Equation 15: Poiseuille's law. Where μ = dynamic viscosity, L = length of pipe, Q = volumetric flow rate R = pipe radius.

Poiseuille's law has 4 important underlying assumptions. These are: viscosity of the fluid is constant; the tube is both cylindrical and rigid, length of tube is much greater than its diameter and flow is steady, non-pulsatile and non-turbulent. Many of these assumptions are violated when Poiseuille's law is applied to physiological blood flow.[560] In these cases, extended forms of Poiseuille's law can be used, such as the Darcy-Weisbach equation.[560]

3.7.1.2 Introducing Shear Stress, Shear Rate and Velocity Profiles

Shear stress, shear rate and the velocity profile of the fluid concerned are all intimately related to each other. In the circulation, blood flow is influenced by shear stress forces that occur at the walls of blood vessels; shear rate then considers how quickly these forces change between the wall and a point directly next to it and these factors then alter the velocity profile.[531]

<u>Shear Stress, Shear Rate and the No-slip Boundary Condition</u>

Shear stress is the force applied to a unit area that is created when a tangential force is applied to a surface (*e.g.,* blood flow against endothelium) (**Equation 16**). In other words, this is the force that the fluid applies to the surface and *vice versa*. In haemodynamics, this is often referred to as wall shear stress (WSS).

$$\tau = \frac{F}{A} \tag{16}$$

Equation 16: Shear stress (τ) is a function of force (F) applied to an area (A)

Wall shear stress has undergone significant study, as emerging evidence suggests that areas of blood vessels where WSS is low, or is oscillatory, are susceptible to the formation of atherosclerosis.[561,562]

Wall shear rate (WSR) then refers to how quickly the velocity of the fluid changes between a point on the vessel wall (where the velocity is zero, this is the source of the no-slip boundary condition commonly used in computational fluid dynamics) and a point directly next to it. WSR is measured in reciprocal seconds (s^{-1}) and is given by the equation below (**Equation 17**).

$$\gamma = \frac{4Q}{\pi R^3} \tag{17}$$

Equation 17: Wall shear rate (γ) is a function of volumetric flow rate and pipe radius where Q = flow rate and R = pipe radius

Simply, the no-slip boundary condition states that at a solid boundary, the fluid will have a velocity of zero.[563] The physical justification for this: that at a surface, adhesive (sticking) forces are greater than cohesive forces, therefore, for a viscous fluid, the velocity at a surface is zero, and therefore these particles do not move (slip).[563] In computational fluid dynamics, this boundary condition is the most commonly used version, as it accurately models what happens in most real-world situations, rather than it being an approximation to make the calculations less computationally demanding.[564]

Relationship between Flow Rate, Reynolds Number, Shear Stress and Velocity Profile

Reynolds number (R_e) of a fluid depends on flow rate, vessel diameter and several properties inherent to the fluid itself (**Equation 18**). When the fluid concerned is blood, the viscosity of blood at 37 °C is 0.0035 Pa s, the density is approximately 1060 kg m^3; the velocity of blood is then in m s^{-1} and the diameter of the blood vessel in metres, such that the Reynolds number is then a dimensionless quantity.[560]

$$R_e = \frac{\rho D v}{\eta} \tag{18}$$

Equation 18: Reynolds number where ρ the density of the fluid, D the diameter of the pipe, ν is the velocity of the fluid and η is fluid viscosity.

This equation dictates whether the fluid flow is considered laminar *i.e.,* the fluid moves in layers with no mixing between them, or in a turbulent fashion, where fluid from adjacent layers becomes mixed. For a cylindrical pipe, the commonly accepted critical Reynolds numbers are such, that if R_e is lower than ~2300, the fluid regime is considered laminar, and > 4000 the fluid is considered turbulent in nature. Between these numbers is a so-called “transition regime”.[565]

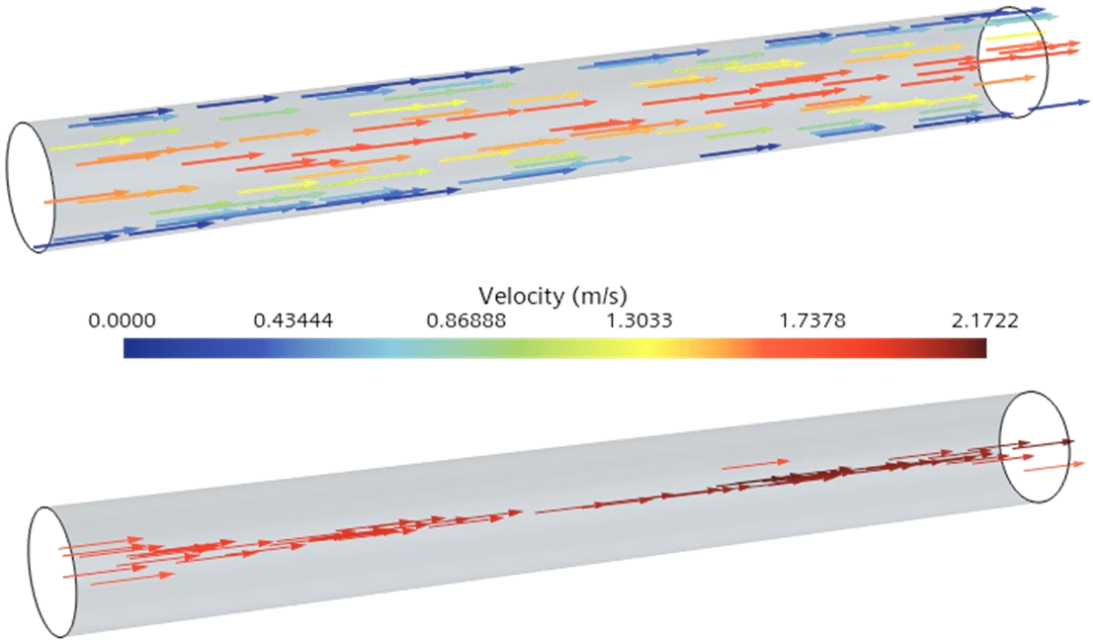

Figure 3.24: Reynolds number dictates fluid behaviour. In the vector image laminar flow (above) and turbulent flow (below) for a Newtonian fluid (water) flowing the positive x direction through a blood vessel 0.3 mm in diameter, as shown in the STAR CCM+ software. In the laminar regime, the no-slip boundary condition can clearly be seen.

The Reynolds number for the blood flow within a particular blood vessel varies depending on exact blood vessel under consideration; furthermore, the critical number where the transition from laminar to turbulent flow occurs will also vary and this is strongly influenced by the morphology of the blood vessel concerned. Narrowed (stenotic) or branched arteries will often encounter turbulent flow even at usual physiological blood velocity.[560] The Reynolds equation shows to a simple approximation that laminar flow is difficult to maintain where flow rate and therefore blood velocity is high.[560] Physiologic blood flow in arteries has been found by Saqr *et al.* to be turbulent, even when it is not associated with pathological changes within the artery itself.[566] In the microcirculation, because of the decrease in both blood velocity and vessel diameter, the blood flow tends to be laminar.[560]

As discussed previously, shear stress and shear rate are proportional to each other, and the constant of proportionality is then the viscosity of the fluid concerned. Shear rate being the rate of change of the velocity by which one layer of fluid passes over another, therefore shear rate and velocity profiles must also be mathematically related.[567] The speed of a fluid in a cylindrical pipe is not constant. At the walls, velocity of the fluid is zero, and the velocity of the fluid is greatest in the centre. Velocity profiles are therefore a graphical method to show the variation in fluid velocity as a function of distance from the wall.[531] Under a laminar flow regime, these velocity profiles are often parabolic, and are flattened in a turbulent regime (**Figure 3.25**).

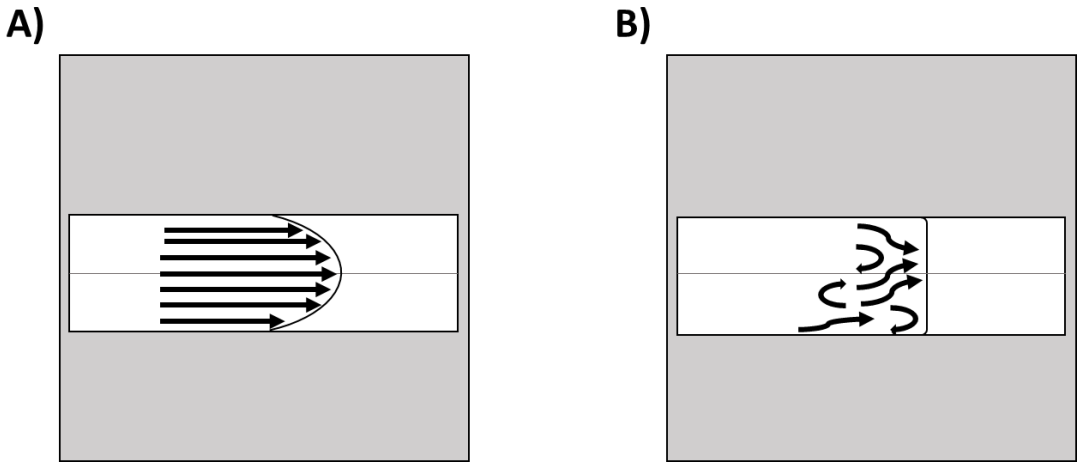

Figure 3.25: Shear rate and therefore fluid velocity affects the velocity profile of a fluid. Velocity profiles for a Newtonian fluid under a) laminar and b) a turbulent flow regime.

Entrance Lengths and "Fully Developed Flow"

The entrance length can be understood as the distance a fluid travels after entering a pipe (or any other enclosed space) before its flow is "fully developed".[568] When a fluid first enters a pipe, velocity is constant across the fluid.

As it continues further into the pipe, the impact of friction at the pipe walls begins to make its presence felt and fluid velocity begins to vary as a function of distance from the wall.[569] Fully developed flow is then when the velocity profile is no longer changing, and is usually parabolic in nature for a laminar regime (**Figure 3.25**).[570,571] The distance over which this continual change in velocity profile occurs, can be calculated in a laminar or turbulent flow regime.

$$L_e(laminar) = 0.05 R_e D \tag{19}$$

$$L_e(turbulent) = 4.4 D (R_e)^{\frac{1}{6}}$$

Equation 19: Entrance length as a function of pipe diameter and Reynolds number. Where R_e is the Reynolds number and D is diameter of the pipe.

The entrance lengths are greater in a laminar than in a turbulent flow regime, due to power term present in the calculation for turbulent flow, but detailed discussion of this is outside the scope of this report.

Understanding the nature of the fluid regime tells us how to proceed with calculations of fluid behaviour. If entrance length is much greater than the length of the blood vessel of interest, blood flow is never considered to be fully developed and this impacts on the calculations run later.

B. Input Geometries

This appendix details the development of each input geometry.

Cylindrical capillary geometry

Dimensions

Inlet/ Outlet: 50 μm

Length: 2500 μm

Geometry

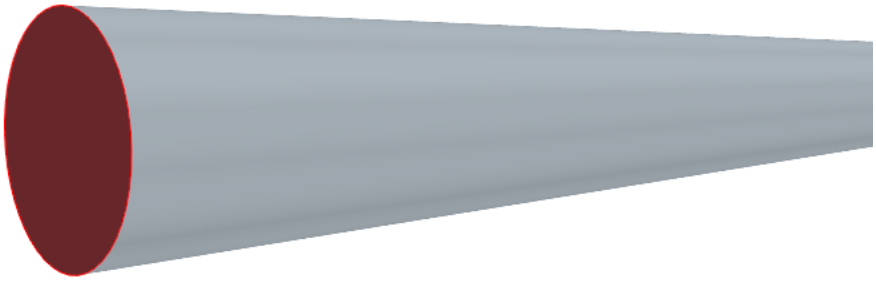

Mesh

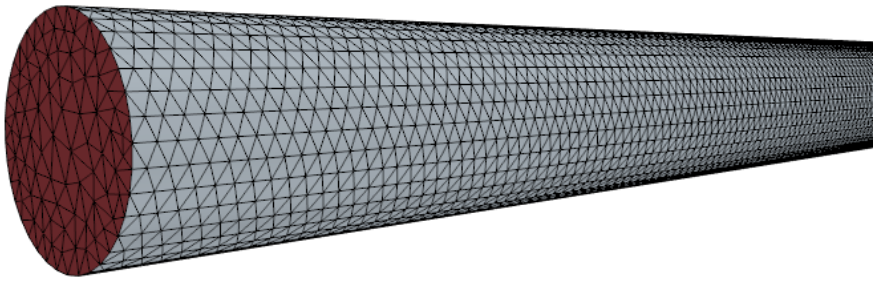

Simple bifurcation – Tan *et al.*

Dimensions

Inlet 20 μm

Outlet 10 μm

Length 100 μm

Geometry

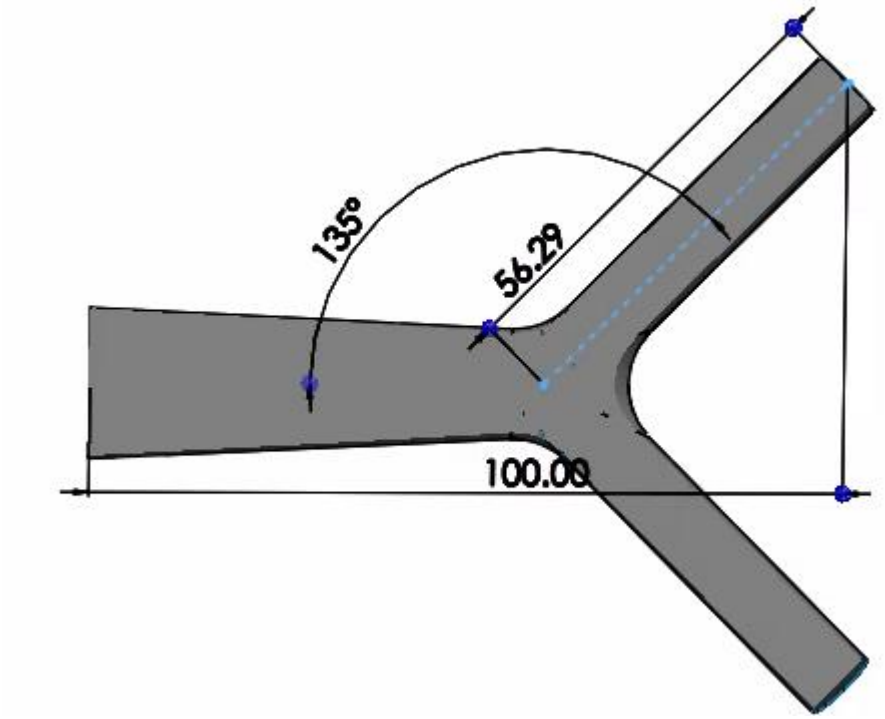

Mesh

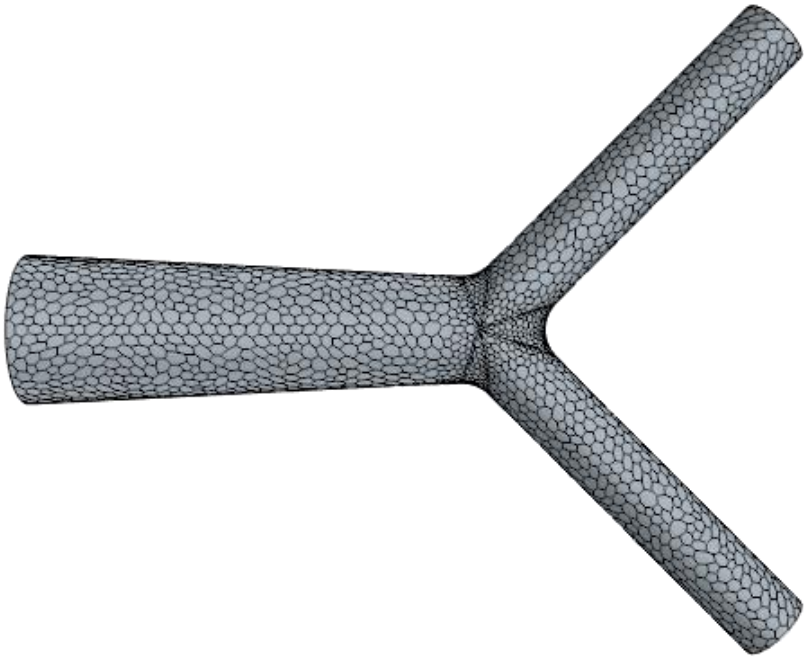

Barber et al

Dimensions

The dimensions of these figures are summarised in the table below.

Parameter	Symmetric	Asymmetric	T-junction
Q0	8 μm2s-1	8 μm2s-1	8 μm2s-1
Q1	2 μm2s-1	6.60 μm2s-1	2 μm2s-1
Q2	2 μm2s-1	3.17 μm2s-1	2 μm2s-1
W0 (mother vessel)	8 μm	8 μm	8 μm
W1 (daughter vessel)	4 μm	7.27 μm	4 μm
W2 (daughter vessel)	4 μm	5.04 μm	4 μm
Lv0	20 μm	20 μm	15 μm
Lv1 (daughter vessel)	20 μm	20 μm	20 μm
Lv2 (daughter vessel)	20 μm	20 μm	20 μm
β1	(π/4) 45°	(π/4) 45°	(π/2) 90°
β2	(π/4) 45°	(π/4) 45°	0°
r0	3 μm	3 μm	3 μm
r1	3 μm	3 μm	3 μm
r2	3 μm	3 μm	3 μm

Symmetric

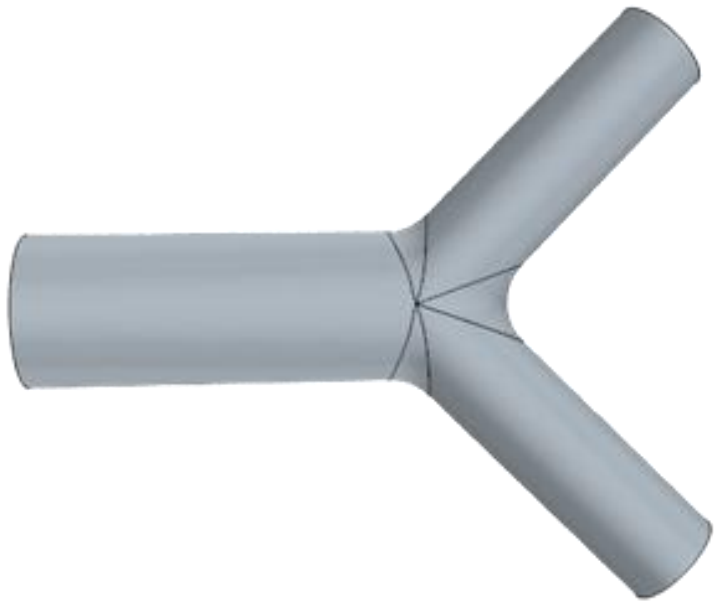

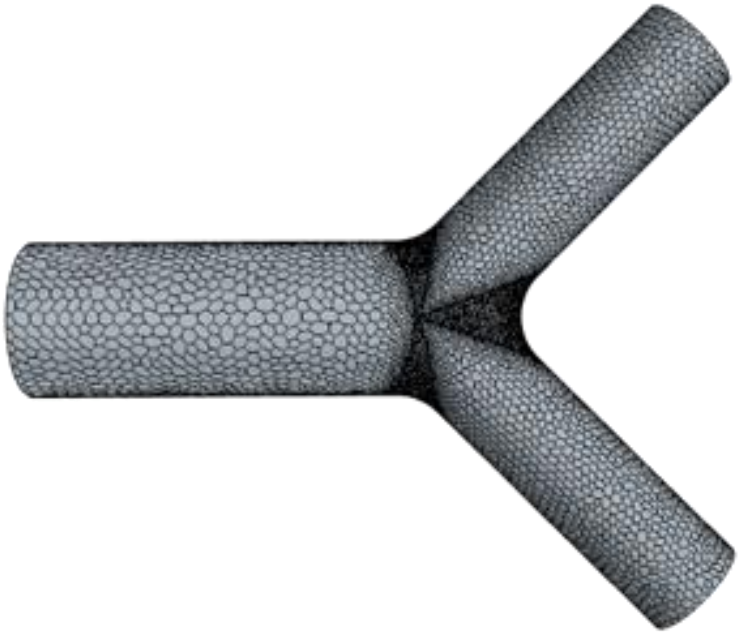

Asymmetric

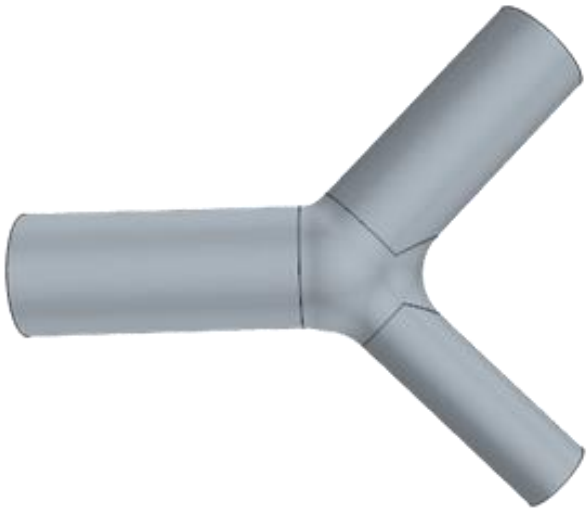

T-junction

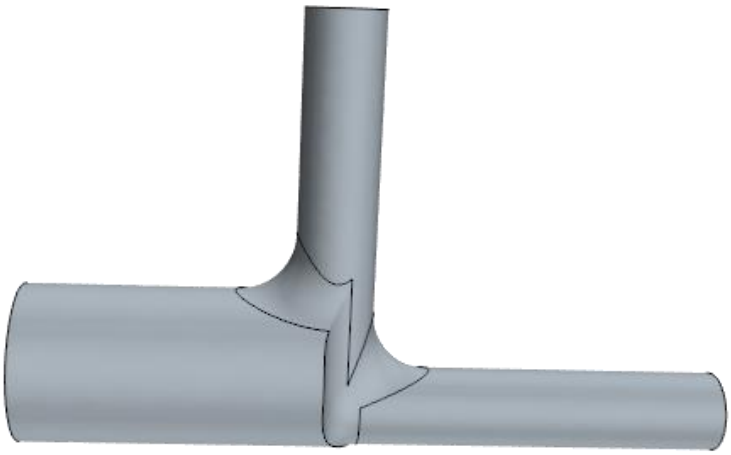

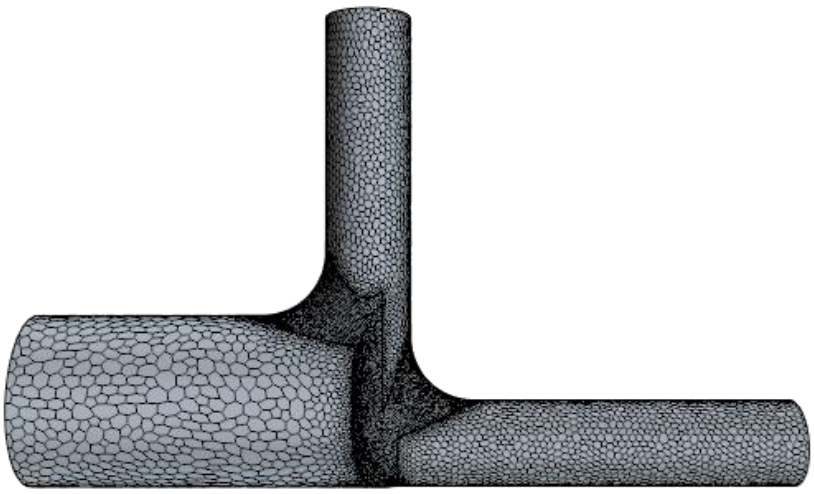

C. Assessment of Generated Mesh Quality

Tan et al., geometry

The quality of this generated mesh can be assessed in a quantitative fashion by looking at cell quality, skewness angle of the cells themselves and the degree by which the volume of one cell differs from its neighbours. Despite it being the fillet region that was of most interest within the mesh independence study, the quality of the entire mesh will be considered here.

Cell Quality

All cells within this volume mesh have a cell quality > 0.5. Therefore, it can be said that the mesh is of a sufficient quality to give accurate results (**Table 3.18**).

Table 3.18: Cell quality measures the uniformity of a simulated mesh. Cell quality for the Tan geometry used within this chapter. All cells are seen to have a cell quality of 1.0.

Cell quality	Number of cells
≤ 0.50	0
≤ 0.60	0
≤ 0.70	0
≤ 0.80	0
≤ 0.90	0
≤ 0.95	0
≤ 1.00	31904

Skewness Angle

In this case, the skewness angles of each part within the geometry are significantly higher than those in the initial capillary geometry, but none of these skewness angles are considered ‘bad’, nor do they (nor would they be expected to) lead to issues with convergence of the results for this more complex geometry (**Table 3.19**).

Table 3.19: Maximum skewness angles for each geometry part within the more complex Tan et al. geometry.

Geometry part	Maximum skewness angle (°)
Inlet	49.02
Outlet 1	73.90
Outlet 2	56.98
Fluid	9.79
Fillet	9.48

Volume Change

All cells have a volume change > 0.01 (**Table 3.20**). This suggests the results from this mesh will be accurate and the solver should be stable.

Table 3.20: Volume change of cells within a mesh is a proxy measure of the accuracy of the results it will generate. All cells within this mesh have a volume change > 0.01.

Volume change	Number of cells
<0.01	0
<0.1	2744
<1	29160

D. Dimensional scaling and Buckingham Pi theorem

This section introduces the role of dimensional scaling and dynamic similarity, as well as applying Buckingham Pi theorem to find the parameters which must be held constant to afford geometric, dynamic and kinematic similarity in the resulting scaled models.

Larger-than-life models are created in this work, since this affects the speed by which the calculations will be completed, but also enables improved spatial resolution of fluid behaviour. Buckingham Pi theorem is the process by which the non-dimensional parameters for this model can be found.

Law of dynamic similarity and its application

The law of dynamic similarity is a phenomenon where geometrically similar models (*i.e.,* different size, but same shape), with the same boundary conditions and dimensionless constants (*e.g.,* Reynolds number) will have identical fluid flows. The rationale for why Reynolds number must be held constant will be discussed later.

It can be shown that each of these three components are true for the scaled models that we are creating in this work.

Geometric similarity – same shape

It had been decided to create a 10x model, so vessel length and diameter were already known. It is common to see up to 8x models within the literature.[572,573] Scaling both by a factor of 10 means length-to-diameter ratio remains constant and therefore the model can be considered geometrically similar.

Dynamic similarity – same forces

It is already known that the carrier fluid for the scaled model will be the incompressible non-Newtonian fluid that is blood plasma. Fluid density (ρ) and dynamic viscosity (μ) were already known. Therefore, only inlet velocity is unknown. To obtain dynamic similarity in the model, Reynolds number must be equal to that of the original geometry *i.e.,* physiological values.

$$Re = \frac{\rho\, U_f D}{\mu}$$

This can be rearranged as follows to give U_f as a function of Reynolds number, fluid density, vessel diameter and dynamic viscosity.

$$U_f = \frac{Re\mu}{\rho D}$$

Dimensional analysis confirms the equation has been correctly rearranged, as U_f still has units of m s $^{-1}$.

Kinematic similarity – forces act in the same direction

Kinematic similarity is defined in fluid dynamics as the velocities of the fluid in both models being in the same direction and differing by a scale factor. Calculating maximum centreline velocity of both models shows kinematic similarity holds in this case. Calculating maximum centreline velocity in a straight pipe is given by the equation below.

$$U_{max} = 2xU_f$$

Applying the law of dynamic similarity

Applying the law of dynamic similarity enables the creation of models which differ from their size in real life, it is for this reason that it is frequently applied in other areas of engineering. and is particularly common within mechanics.[574,575] It has been introduced more recently in biomedical engineering, and often used where *in vivo* fluid dynamics are of interest.[576] These larger-than-life models have much improved spatial resolution of wall shear stress and fluid velocity, as they are not impacted by cardiac motion or respiration.[573,577] Therefore, it is then possible to measure fluid dynamics parameters in vessels that were previously too small to obtain satisfactory resolution.

Scaling non-Newtonian fluids

Applying dynamic scaling to non-Newtonian fluids such as blood has previously been studied.[572] In these cases, blood is often considered either as a 5-parameter Carreau-Yasuda fluid or is mimicked using the Sisko model.[578]

During the creation of scaled vascular models, and CFD vascular studies in general, it is usual for researchers to neglect the shear-thinning behaviour of blood and instead mimic the carrier fluid as a Newtonian fluid (*i.e.,* water).

Identifying necessary dimensionless constants

Buckingham Pi theorem is the process by which the appropriate non-dimensional parameters for a problem can be identified.[579,580]

The theorem uses the following definitions[580]:

n = the number of independent variables relevant to the problem

j = the number of independent dimensions found within the variables

j' = the maximum reduction possible in terms of the number of variables that must be considered simultaneously.

k = the number of independent Π terms that can be identified to describe the problem. k = n-j

Step 1: Identify variables involved in the problem

These variables are D, L ρ,u and μ

Step 2: Assign dimensions (MLTθ) to each of these variables.

Variable	Dimensions
Diameter	L
Length	L
Density	ML^{-3}
Velocity	LT^{-1}
Dynamic viscosity	$ML^{-1}T^{-1}$

Step 3. Calculating Pi products

In the first instance, assume j=j'.

From the dimensional analysis above, j'=3 (M,L and T). Therefore j=3.

The total number of independent Π terms is then k = 5-3 = 2.

Two independent Π terms will be found for this problem.

Step 4: Creating Pi products

We know from the above step that 2 independent Π terms will be found.

$$\Pi 1 = \frac{\rho u D}{\mu} = Re$$

The first independent term is the dimensionless value also known as Reynolds number.

The second is then:

$$\Pi 2 = \frac{L}{D}$$

Which is known as length-to-diameter ratio.

Pulling it all together – input parameters for capillary model

From this discussion above of the law of dimensional similarity and Buckingham Pi theorem, the necessary input parameters for the initial generic capillary geometry used in this work are given below (**Table 3.21**).

Table 3.21: Input parameters for scaled capillary model.

Parameter	Physiological values	Scaled model
Length (L)	2.50 $x10^{-4}$ m	2.50$x10^{-3}$ m
Diameter (D)	5.00$x10^{-6}$ m	5.00$x10^{-5}$ m
Inlet velocity (U_f)	5.00$x10^{-4}$ m s^{-1}	5.00$x10^{-5}$ m s^{-1}
Maximum centreline velocity (U_{max})	1.00$x10^{-3}$ m s^{-1}	1.00$x10^{-4}$ m s^{-1}
Fluid density (ρf)	1060 kg m^3	1060 kg m^3
Dynamic viscosity (μ)	0.0035 kg m^{-1} s^{-1}	0.0035 kg m^{-1} s^{-1}
Length to diameter ratio (L/D)	50	50
Reynolds number (R_e)	0.001	0.001

E. Literature Review

Author (Date)	Vascular site (Organ)	Diameter (μm)	Shear stress (τ Pa)	Blood Flow (μl/min), Mean and Standard Deviation	Comments	Methodology	Reference/ URL
Gilmore (2005)	Retina Arterioles	111.6		9.4 (SD 2.5)	This study measured the impact of oxygenation and hypoxia on arteriole parameters.	Canon laser blood flowmeter (Doppler)..	doi.org/10.1152/ajpheart.01037.2004
Hammes (2016)	Cephalic arch	2900	0.23-0.3 Pa	ND	22 patients all with advanced renal failure & are on dialysis. Parameters captured here are those taken "at mapping" i.e pre-AV fistual formation	BFV measured by doppler ultrasound. Venogram used to measure how big the vein is.	DOI:10.1371/journal.pone.015287
Klarhöfer (2001)	Aorta	10,000				Measured using MRI	
	finger (artery)	800-1800	ND	3000-26,000			
	Carotid artery		1.1-1.3pa				

Reneman (2008)	Brachial artery Femoral artery		0.4-0.5Pa 0.3-0.5 Pa		Suggests Poiseuille's law does not hold in vivo		10.1007/s11517-008-0330-2
Seymour (2019)	Abdominal aorta	7,700	0.19	876,000	**See table S1 from this paper**	Varies.	
	femoral artery	3,900	0.39	271,800			
	brachial artery	2,070	0.73	78,900			
	internal carotid	2,240	2.17	256,800			
	anterior cerebral	1,220	4.09	70,200			
	basilar	1,930	1.81	148,800			
	common carotid	3,290	1.19	485,400			
	vertebral	1,700	1.71	87,000			
	external carotid	2,080	1.55	163,200			
Suzuki (2020)	brachial artery	3720±450			Subjects for non-smoking cohort are all men.	Measured using doppler ultrasound. Doppler beam angle 60 degrees.	https://doi.org/10.14814/phy2.14369
Doriot (2000)	Coronary artery	2600-5000	0.68 Pa (SEM 0.027)	19400-123200		Intravascular flow wire + angiography to enable 3D reconstruction of arteries	doi:10.1097/00019501-200009000
Fung et al (1971)	Intestinal mesentary (capilliary bed)				The average length of a capillary is about 200-250 micron.		
Nasr (2012)	Radial artery (Arm)	male: 2690 female: 2430			Cadavers. Almost equal split between male/ female	Dissection. Measurements taken using vernier calipers and measuring strip	

Spivack (2012)	cephalic vein				Mean size decreases as distance from antecubital fossa (elbow) increases.	ultrasound	10.1016/j.ultrasmedbio.2011.11.008
	Great saphernous vein						
Planken (2005)	cephalic vein (at wrist)	1800				ultrasound	10.1093/ndt/gfi340
Irfan (2016)	cephalic vein (at wrist)	2800 (SD 1000)					10.1155/2016/8096473
	cephalic vein (at elbow)	3100 (SD 900)					
Mahler (2011)	basilic vein (at elbow)	5100 (SD 1300)				ultrasound	10.1186/1865-1380-4-53
Tenenbein (2006)	Internal jugular vein (left)	11200				ultrasound	Tenenbein, PK MD, FRCPC*; Godhke, B MD§; Britz, GW MD, MPH†; Sekhar, LN MD†; Lam, AM MD, FRCPC* † Internal Jugular Vein Diameter on Ultrasound Predicts Jugular Bulb Dominance, Journal of Neurosurgical Anesthesiology: October 2006 - Volume 18 - Issue 4 - p 304
	Internal jugular vein (right)	14800					
Zhu et al (2015)	Subclavian vein	9200				Ultrasonography	10.1016/j.jss.2015.02.063
Nazarin and Fosager (1995)	Brachiocephalic vein					Colour doppler sonography	10.1148/radiographics.15.6.8577962
Nadesan (2019)	SVC	2cm					10.1002/ca.23351
Shima (1996)	Median cubital vein	1.8mm				Japanese cadavers.	https://pubmed.ncbi.nlm.nih.gov/8938512/

	Size	External diameter (mm)	Internal diameter (mm)	Trocar length (mm)	Maximum flow rate ml/min	Reference
Peripherally inserted venous cannula	18G	1.3	0.9	32/45	90	https://www.terumo-europe.com/en-emea/products/surflo%E2%84%A2-i-v-catheter
	20G	1.1	0.8	32	60	
	22G	0.85	0.6	25	35	

	Size	Lumen	Length (cm)	External Diameter (mm)	Internal diameter (mm)	Maximum flow rate ml/min	Reference
Peripherally inserted central catheter	5F	Single		1.667	0.9		https://www.bd.com/en-us/products-and-solutions/products/product-page.9195118#specifications
	5F	Dual		1.667	0.9, 0.9		https://www.bd.com/en-us/products-and-solutions/products/product-page.1295108d#specifications
	5F	Treble		1.667	0.9,0.7,0.7		https://www.bd.com/en-us/products-and-solutions/products/product-page.1395108qd#specifications
Central Venous Catheter	9.6F	Single	90	3.1			https://www.bd.com/en-us/products-and-solutions/products/product-page.0600560#specifications
	10F	Triple	97	3.3	1.5,0.8,0.8		https://www.bd.com/en-us/products-and-solutions/products/product-page.0606560#specifications

Chapter 4
CFD-DEM Models of Clinically Relevant Venous Access Devices

4.1 Introduction

As discussed at the end of the previous chapter, the CFD-DEM methodology developed there will now be used to study the fluid and particle behaviour within three commonly used vascular access devices (VADs). These VADs are: a 20G peripherally inserted venous cannula (PIVC); a 10F peripherally inserted central catheter (PICC) and a 9.6F single lumen and the slightly larger 10F triple lumen Hickman line or central venous catheter (CVC).

In this chapter, several objectives will be established to enable the aim of this chapter to be met. These objective include: initially to develop CFD-only simulations where the VAD is considered firstly as an obstruction to blood flow before the simulations are further developed to infuse either 0.9% saline or 5% glucose down a single lumen of the device, this will enable fluid behaviour to be studied in detail, as well as to ascertain the influence of the carrier fluid on overall fluid velocity, residence time and wall shear stress. Once these simulations have been developed, it is then going to be possible to make these more complex by reintroducing the CFD-DEM approach developed in the

previous chapter. Here, nanoparticle behaviour and particle-related parameters (*e.g.,* particle shear stress) can now be determined *via in silico* studies. Particle shear stress is believed to be one of the key parameters to influence the physiochemical characteristics of the protein corona that develops *in vivo*, however few studies have so far considered the impact of fluid shear rate and particle shear stress on protein corona formation, and fewer still consider the protein corona around biocompatible polymeric nanoparticles. Finally, Principal Component analysis, as well as hierarchical clustering are implemented to simplify the data set, enabling key parameters for the development of the microfluidic device to be identified.

There is no literature review in this chapter, the literature review has been interwoven into that at the start of Part 2 of this thesis. In this chapter, the three VADs as detailed previously are studied. For each VAD, the structure is as follows, initially a mesh independence study is undertaken to determine the density of the mesh for both the blood vessel as well as VAD itself, that is necessary to balance result accuracy with computational demand. The quality of the resulting mesh is then analysed with the same methodology as the previous chapter. This is then followed by considering the VAD purely as an obstruction to blood flow in the vein. The simulation is then made more complex once multicomponent fluids are introduced and the VAD is now used for the infusion of fluid. Finally, the CFD-DEM methodology is implemented and now nanoparticle behaviour under flow can be studied. Once the simulations for this chapter are complete, two forms of unsupervised machine learning are implemented to simplify the data set, and enable further insights to be drawn from the data. The results of this chapter – summarised in **Section 4.4.4** – will then be used as input data for the design and development of a microfluidic device in **Chapter 5**.

4.2 Chapter Aims and Objectives

By the end of this chapter, a coupled CFD-DEM approach will have been used to study three different ways by which drug-loaded nanoparticles can be administered intravenously (*i.e.,* peripherally inserted venous cannula, Hickman and PICC lines). Once these models are complete, it will be possible to change the size and shape of nanoparticles that are introduced, to study any chosen nanoparticle. These studies can then be used to identify nanoparticles at risk of excessive aggregation and thus inform the design of novel nanotherapeutics.

This chapters aim will be achieved by completing the following objectives:

1. Create CFD-only models of the 3 VADs of interest for this chapter.

Initially, only the fluid behaviour in the geometry – with the VAD acting as an obstruction is of interest. Later, the complexity of the simulation will be further increased by introducing 0.9% saline into the simulation *via* the VAD under study.

2. Extend the models to use CFD-DEM, and therefore model fluid and nanoparticle behaviour simultaneously.

Once the impact of the VAD itself, and the impact of introducing 0.9% saline into the simulation has been studied, models will use CFD-DEM to model the impact of introducing 100 nm PLGA nanoparticles into the simulation.

3. Understanding the influence of several modifications on fluid behaviour and velocity *e.g.,* catheter tip shape, infusion fluid.

Lancet tip and lab tip needles will be studied using the PIVC model. 0.9% saline and 5% glucose are fluids with quite different viscosities; simulations will be performed to study their impact on fluid behaviour.

4. Develop an understanding of what these results mean in terms of the clinical use of VADs.

These results will be analysed for meaning in the context of Virchow's Triad and to begin to understand why ultrasound-guided IV insertion is known to be more prone to thrombosis, compared to "landmark-guided" methods.

4.3 Materials and Methods

The computational models presented in this chapter were simulated using STARCCM+ (Siemens PLM, Version 2022.1.1), a commercially available CFD solver. This is a more recent version of the software than that used with the models and benchmarking studies presented in the previous chapter. Only where physics models or other settings within the simulation set up diverge from those used previously will be discussed. Otherwise, much of the methodology developed in the previous chapter broadly still holds, and is duplicated in a brief format for the sake of completeness.

As this model is complex, it was decided that an iterative approach was to be used, where the model would only be extended and made more complex once the earlier iteration had successfully been completed. Initially, a wholly-CFD model was developed, which represented only the geometry of the situation at hand and the behaviour of blood flow. Later, the model was extended using DEM and nanoparticulate behaviour studied using a Lagrangian multiphase model, which enables coupling between CFD and DEM.

4.3.1 Input Geometries

Input geometries were created in Solidworks 2021 (Dassault Systemes/ Solidworks Corporation), before being imported into STARCCM+. Further details for each input geometry (PIVC, PICC, Hickman line) in this chapter can be found in **Appendix A**.

4.3.2 Mesh Development

Mesh convergence studies were used to confirm that the meshing parameters were appropriate to create a mesh of sufficient quality for further analysis. Cell quality, skewness angle of the cells themselves and the degree by which the volume of one cell differs from its neighbours was assessed. The vascular access device was meshed in each case with a denser mesh than the blood vessel. These mesh parameters are summarised in **Table 4.1**-**Table 4.3**.

Table 4.1: Final meshing parameters used to create the volume mesh following mesh convergence studies – PIVC model.

Group	**Mesher**
Surface mesher	Surface remesher
Core volume mesher	Polyhedral mesher
Optional boundary layer mesher	Prism layer mesher
Refining the mesh	
Base size	2.0 x10^{-4} m
Number of prism layers	6
Prism layer stretching	1.5
Prism layer total thickness	33.33 (relative to base)
Refining the VAD	
Base size	1.0x10^{-4} m
Number of prism layers	6
Prism layer stretching	1.5
Prism layer total thickness	33.33 (relative to base)

Table 4.2: Final meshing parameters used to create the volume mesh following mesh convergence studies – PICC line model.

Group	**Mesher**
Surface mesher	Surface remesher
Core volume mesher	Polyhedral mesher
Optional volume mesher	Generalised cylinder mesher
Optional boundary layer mesher	Prism layer mesher
Refining the mesh	
Base size	3.0 x10^{-4} m
Number of prism layers	6
Prism layer stretching	1.5
Prism layer total thickness	33.33 (relative to base)
Refining the VAD	
Base size	1.5x10^{-4} m
Number of prism layers	6
Prism layer stretching	1.5
Prism layer total thickness	33.33 (relative to base)

Table 4.3: Final meshing parameters used to create the volume mesh following mesh convergence studies – Hickman line model.

Group	**Mesher**
Surface mesher	Surface remesher
Core volume mesher	Polyhedral mesher
Optional volume mesher	Generalised cylinder mesher
Optional boundary layer mesher	Prism layer mesher
Refining the mesh	
Base size	3.0 x10^{-4} m
Number of prism layers	6
Prism layer stretching	1.5
Prism layer total thickness	33.33 (relative to base)
Refining the VAD	
Base size	1.5x10^{-4} m
Number of prism layers	6
Prism layer stretching	1.5
Prism layer total thickness	33.33 (relative to base)

4.3.3 Defining Boundaries

Once the mesh of the geometry had been rendered, inlets, outlets and walls were defined to set the boundaries of the problem.[534]

Table 4.4: Boundary conditions implemented in STAR CCM+. Boundary type is described in the STARCCM+ jargon [535] **Note: The boundary conditions for solid phase are not implemented in the wholly CFD model.**

Physical Boundary	Phase	Boundary type
Inlet	Liquid	Inlet
	Solid	Phase impermeable
Outlet	Liquid	Pressure outlet
	Solid	Phase impermeable
Wall	Liquid	Wall “no-slip”
	Solid	wall

4.3.4 Physics Continua and Input Parameters

Physics models are predetermined ways of describing spatial orientation of the volume mesh, defining whether the solution is steady or transient in nature, as well as describing the composition and behaviour of fluid flow within the simulation. Some optional models consider the effects of certain forces such as gravity, others impact the way the solvers function and therefore can be selected to refine the accuracy of the solution and/or aid its convergence.

4.3.4.1 Modelling VADs as an Obstruction in Blood Flow

Table 4.5 summarises the physics models employed in the wholly CFD model, where fluid behaviour is known to be within the laminar regime, and the only source of fluid is in the blood vessel *i.e.* the vascular access device is considered only as an obstruction to blood flow.

Table 4.5: Physics models selected in STARCCM+ where fluid behaviour is in the laminar regime.They are described in the STARCCM+ terminology.

Group box	Physics model
Space	Three dimensional
Time	Steady
Material	Liquid
Flow	Coupled flow Gradients (selected automatically)
Equation of state	Constant density
Viscous regime	Laminar
Optional Models	Gravity

The input parameters for the fluid phases used in this section are summarised in **Table 4.6**.

Table 4.6: Input parameters for the fluid phase, where the VAD is considered as only an obstruction to blood flow.

			Units	Ref
Material properties (liquid, whole blood)				
	Density (ρ)	1050	kg m^{-3}	524
	Dynamic viscosity (η)	2.78	Pa s	
Initial conditions				
Median Cubital Vein – inlet	Velocity (v)	0.11	m s^{-1}	581,582
Left brachiocephalic vein	Velocity (v)	0.48	m s^{-1}	583
Right brachiocephalic vein	Velocity (v)	0.84	m s^{-1}	

4.3.4.2 Modelling Multicomponent Fluids

Multicomponent fluids can be modelled using STARCCM+. In these simulations, this is used to model 0.9% saline or 5% glucose being infused into the system *via* the vascular access device. The simulations are set up as described by Piper and colleagues, this paper also influences the choice of turbulence model used within this work.[524] For the simulations where the fluid introduced *via* VAD is within the laminar regime, set-up stops after the viscous regime has been selected (**Table 4.7**). For the saline flush (300 mL min^{-1}), Mentor's Shear Stress Transport (SST) k-omega turbulence model is used in this case (and any other simulations known not to be in the laminar regime (*i.e.* R_e > 2300)).[524] The SST model combines both k-omega and k-epsilon turbulence models, such that k-omega is used at the wall and k-epsilon used for free stream turbulence.[584]

Table 4.7: Physics models selected in STARCCM+ to model multiphase fluids. Turbulent viscous regime chosen to model the 300mL min^{-1} infusion, otherwise, laminar is used.

Group box	**Physics model**
Space	Three dimensional
Time	Steady
Material	Multi-component liquid
Reaction regime	Non-reacting
Flow	Coupled flow Coupled species (selected automatically) Gradients (selected automatically)
Equation of state	Constant Density
Viscous Regime	Laminar / Turbulent Reynolds-Averaged Navier-Stokes (selected automatically)
Reynolds-Averaged Turbulence	k-omega Turbulence All y+ wall treatment (selected automatically) Wall Distance (selected automatically) SST (Menter) k-omega (selected automatically)
Optional Models	Gravity Passive Scalar

Next, the fluid phases (blood, 0.9% saline and 5% glucose) are defined (**Table 4.8**) – fluid density and viscosity are given in **Table 4.9**.

Table 4.8: Defining the fluid phases.

Group box	**Physics model**
Flow	Laminar
Material	Liquid
Equation of state	Constant density
Optional models	Passive scalar

Table 4.9: Input parameters and initial conditions for modelling multicomponent fluids.

			Units	Ref
Material properties (liquid, 0.9% m/v saline, 25°C)				
	Density (ρ)	1004.59	kg m^{-3}	585
	Viscosity (η)	0.00102	Pa s	586
Material properties (liquid, 5% m/v glucose, 20°C)				
	Density (ρ)	1017.50	kg m^{-3}	587
	Viscosity (η)	0.00114	Pa s	588
Initial conditions				
PIVC (10 mL min^{-1})	Velocity (v)	0.584	m s^{-1}	
PIVC (30 mL min^{-1})	Velocity (v)	1.75	m s^{-1}	
PIVC (60 mL min^{-1})	Velocity (v)	3.50	m s^{-1}	
Saline flush (300 mL min^{-1})	Velocity (v)	17.50	m s^{-1}	
PICC Line Single lumen (150 mL hr^{-1})	Velocity (v)	0.08	m s^{-1}	
PICC Line Single lumen (300 mL hr^{-1})	Velocity (v)	0.16	m s^{-1}	
PICC Line Single lumen (600 mL hr^{-1})	Velocity (v)	0.33	m s^{-1}	
PICC Line Single lumen (1185 mL hr^{-1})	Velocity (v)	0.65	m s^{-1}	
PICC Line Dual lumen (150 mL hr^{-1})	Velocity (v)	0.07	m s^{-1}	
PICC Line Dual lumen (300 mL hr^{-1})	Velocity (v)	0.13	m s^{-1}	
PICC Line Dual lumen (400 mL hr^{-1})	Velocity (v)	0.18	m s^{-1}	
PICC Line Dual lumen (547 mL hr^{-1})	Velocity (v)	0.24	m s^{-1}	
PICC Line Treble lumen (100 mL hr^{-1})	Velocity (v)	0.31	m s^{-1}	
PICC Line Treble lumen (150 mL hr^{-1})	Velocity (v)	0.46	m s^{-1}	
PICC Line Treble lumen (250 mL hr^{-1})	Velocity (v)	0.76	m s^{-1}	
PICC Line Treble lumen (280 mL hr^{-1})	Velocity (v)	0.85	m s^{-1}	
CVC Single lumen (50 mL min^{-1})	Velocity (v)	0.11	m s^{-1}	
CVC Single lumen (100 mL min^{-1})	Velocity (v)	0.22	m s^{-1}	
CVC Single lumen (150 mL min^{-1})	Velocity (v)	0.33	m s^{-1}	
CVC Single lumen (200 mL min^{-1})	Velocity (v)	0.44	m s^{-1}	
CVC Treble lumen (17 mL min^{-1})	Velocity (v)	0.57	m s^{-1}	
CVC Treble lumen (15 mL min^{-1})	Velocity (v)	0.49	m s^{-1}	
CVC Treble lumen (7 mL min^{-1})	Velocity (v)	0.23	m s^{-1}	
CVC Treble lumen (5 mL min^{-1})	Velocity (v)	0.16	m s^{-1}	

4.3.4.3 Tracking Fluid Residence Time

To track fluid residence time, the physics continua were modified to change the time regime to implicit unsteady, and Lagrangian multiphase model was also enabled to allow the introduction of Lagrangian particles into the system (**Table 4.10**). These Lagrangian particles were labelled as Residence Time and are massless, therefore behave like a tracer dye being introduced into the system. The particles are then monitored until they leave the domain.

Table 4.10: Modified parameters for the introduction of Lagrangian particles into the simulation to track fluid residence time.

Group box	Physics model
Particle type	Massless particles
Optional Models	Residence Time

Injectors are then defined to randomly introduce these particles (**Table 4.11**). Following the first timestep, particle flow rate was reduced to 0 – otherwise the simulation continues to introduce particles and the calculation progressively becomes increasingly computationally demanding. Altering the point inclusion

property from 1 to 0.1 additionally seems to help reduce the number of particles introduced into the system.

Table 4.11: Defining injectors for Lagrangian particles

Properties	**Values**
Lagrangian phase	Residence Time
Type	Part injector
Inputs	Needle Inlet, Blood Inlet
Input parameters	
Retain injected parcels	Enabled
Point Inclusion Probability	0.1
Particle flow rate	1000 /s

4.3.5 Coupling CFD and DEM

Once the wholly CFD model had been successfully set up and simulations completed, the model was then further modified to additionally use DEM to enable the behaviour of nanoparticles to be accurately modelled.

4.3.5.1 Modified Physics Continua

Therefore, physics continua were changed and the implicit unsteady time regime, Lagrangian multiphase and Discrete Element Model were selected (**Table 4.12**).

Table 4.12: Modified physics continua for the coupled CFD-DEM model. † if the wholly CFD model is in the turbulent regime, then this, and the other physics models outlined previously are used.

Group box	**Physics model**
Space	Three dimensional
Time	Implicit unsteady
Material	Multi-component liquid
Reaction regime	Non-reacting
Flow	Coupled flow Coupled species (selected automatically) Gradients (selected automatically)
Viscous regime	Laminar
Optional models	Lagrangian multiphase Discrete element model

4.3.5.2 Defining the Lagrangian Phase

Next, physics models and material properties of the nanoparticulate matter were defined (**Table 4.13**).

Table 4.13: Input parameters to define the solid phase of the coupled CFD-DEM model. For the stainless steel trocar used for the PIVC, the default settings within STARCCM+ are used.

Group box		**Physics model**	
Particle type		DEM particles Pressure gradient force (selected automatically)	
Particle shape		Spherical particles	
Material		Solid	
Equation of state		Constant density	
Optional particle forces		Drag force	
Optional Models		Two-way Coupling	
Input Parameters – Lagrangian Phase			
Solid (PLGA) – material properties			**Ref**
	Density	1062 kg m^3	
	Poisson's ratio	0.4	
	Young's modulus	2.43 Pa	[543,544]
Blood vessel – material properties	Density	1300 kg m^3	[545]
	Poisson's ratio	0.49	[545]
	Young's modulus	910 Pa	[544,545]
Needle – Material properties	Density	8055.0 kg m^3	
	Poisson's ratio	0.285	
	Young's modulus	1.93 $x10^{11}$ Pa	
Polyurethane	Density	1480 kg m^3	[589]
	Poisson's ratio	0.4	
	Young's modulus	7.6$x10^6$ Pa	[590]

4.3.5.3 Multiphase Interactions

Multiphase interactions are interactions between two or more phases. Here, the interactions can be classified as being between two liquid phases, or between two solid phases.

Defining Interactions Between the Liquid Phases

Interactions between blood and 0.9 % saline or 5 % glucose are managed automatically by STARCCM+.

Defining Interactions Between the Solid Phases

Interactions are defined between nanoparticles, and the nanoparticle-blood vessel and nanoparticle-VAD interaction are also defined.

Table 4.14: Defining multiphase interactions for solid phase in the CFD-DEM model. * applies to nanoparticle-nanoparticle interaction only.

Group box	**Physics model**
Phase interaction topology	DEM Phase Topology
DEM Contact model	Hertz-Mindlin Rolling resistance (selected automatically)
Optional models	Artificial viscosity Linear cohesion Parallel bonds* Passive Scalar Transfer* Particle-Wall link model

Next, blood vessel inlet is set using the composite method to be 100% blood, the VAD inlet is set to be either 100% saline or 100% glucose.

Defining the Sources of Particles

Finally, the source of nanoparticles is defined by using injectors. A plane is defined 0.1cm from the outlet of the VAD and this is used to both introduce the nanoparticles into the simulation, but also to reduce the real-world time and thus computational intensity of the simulation. The set up of this injector is like that defined earlier in **Table 4.11** – note the change in input as well as Lagrangian phase.

Table 4.15: Using injectors to introduce PLGA nanoparticles into the simulation.

Properties	**Values**
Lagrangian phase	PLGA Nanoparticle
Type	Part Injector
Inputs	Particle Inlet
Input parameters	
Retain injected particles	Enabled
Particle diameter	$1x10^{-6}$ m
Point Inclusion Probability	0.1
Particle flow rate	1000 /s

4.3.5.4 Setting Stopping Criteria

For steady simulations enough iterations is selected such that the residual falls < $1x10^{-3}$. In many cases, 1000 iterations is sufficient to have the residual fall well below this.

For simulations where the implicit unsteady time regime is used, stopping criteria were determined by the physical time the process of interest takes to occur (*e.g.,* for Lagrangian particles take to leave the domain). These simulations were permitted to iterate for as long as was necessary.

4.3.6 Unsupervised Machine Learning

Unsupervised machine learning methods were applied to the data to elucidate any clustering within, and to later identify variables that may be useful to target with the design of the microfluidic device. The methodology used here is similar to that published by Pereira Diaz *et al*.[591] Principal component analysis (PCA) and hierarchical clustering were used. PCA and hierarchical clustering were performed using Orange Data Mining (version 3.35.0, University of Ljubljana). Orange Data Mining is an open source data visualisation, machine learning and data mining toolkit written in Python, Cython, C++, and C. It effectively functions as a graphical user interface through which the user can interact with several popular python libraries including numpy, scipy and scikit-learn. The final, annotated, Orange workflow for this work is shown in **Figure 4.1**.

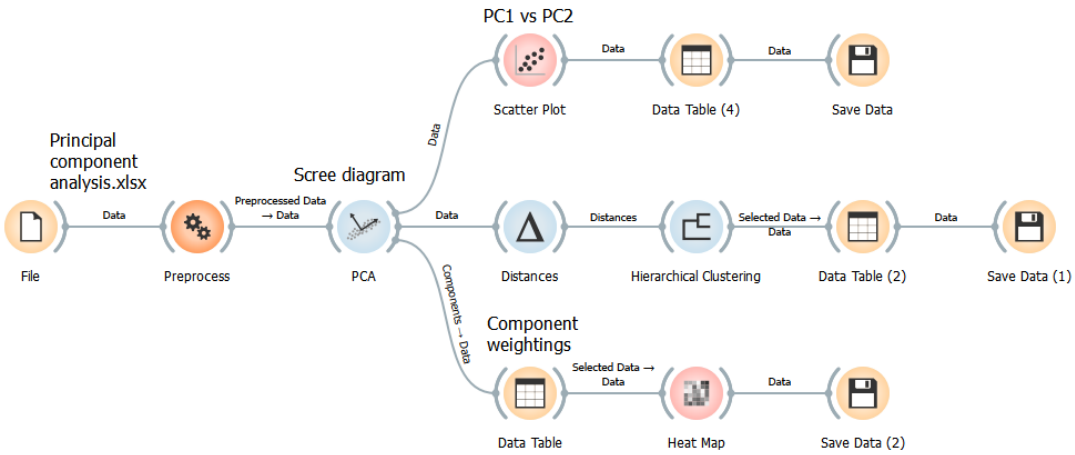

Figure 4.1: Final data analysis workflow as shown in Orange Data mining. Where necessary, 'widgets' have been annotated to show why exactly they have been used.

The preprocessing widget was used to give more control over how the data was processed prior to PCA being performed. Standardise to $\mu = 0$, $\sigma^2 = 1$ was selected. This method of standardisation is particularly suited for data sets where variables have varying units and/or different scales and is robust to outliers.

In the PCA widget, the option 'normalise variables' was additionally chosen. This means that any missing values are replaced by mean values and each column divided by its standard deviation.

Hierarchical clustering analysis was undertaken using Ward Linkage. This was specifically chosen since this methodology is less susceptible to noise, as well as outliers in the dataset. For this reason, it is often the preferred method of defining clusters in this type of analysis.

4.4 Results and Discussion

As a consequence of the complexity of the models used, an iterative approach is used where the simulation only becomes more complex once the previous iteration successfully completes. Such a methodology enables troubleshooting of the simulation when issues occur. Each geometry (PIVC, PICC, CVC) will be considered separately. Since the geometries for PICC and CVC are similar, the results for the CVC geometry are in **Appendix G**.

For each geometry, mesh independence studies will be undertaken to identify appropriate meshing parameters, that accurately resolve shape and fluid flow, without requiring excessive computational power (**Appendix B**). Next, the impact of inserting the vascular device *i.e.,* as an obstruction to blood flow *in vivo* will be studied, before studying the influence of infusing fluid (*i.e.* 0.9% saline, or 5% glucose). Finally, CFD-DEM will be employed to study the process of infusing drug-loaded PLGA nanoparticles. A summary of the input geometries used here can be seen in **Appendix A**.

4.4.1 Peripherally Inserted Venous Cannula (PIVC)

A peripherally inserted venous cannula consists of a stainless steel needle (trocar) of varying length and diameter, and a colour coded plastic cap which enables rapid identification and selection of an appropriately-sized cannula depending on entry point, necessary flow rate and therapeutic use.[457]

Here, it has been decided to introduce the PIVC into the median cubital vein – one of the most popular points of access for IV fluids, and venepuncture due to its ease of access as a 'superficial' vein; its positioning naturally anchors itself so is less likely to 'roll', and lack of impact on patient mobility.[456] It has been chosen to computationally model a "pink" cannula (20 G, maximum flow rate 67 mL min^{-1}), commonly used in inpatient settings for a wide variety of uses.[§§§]

4.4.1.1 Obstruction of Fluid Flow.

Initially, only the obstruction of fluid flow in the blood vessel has been studied. In these models, the trocar of the needle is considered a solid, cylindrical object. These simplified studies enable an understanding to be developed of why PIVC insertion can lead to thrombosis, even without the infusion of fluids and why they are removed as soon as they are no longer considered clinically necessary.[592]

Insertion Angle

Initially, the insertion angle of the PIVC was studied (**Figure 4.2**). This is similar to the work presented by Piper *et al.*, however, this study uses a quite different set of insertion angles (15 - 35°) compared to those (5 - 20°) chosen by Piper *et al.* in their 2018 study.[456,524] In that study, the authors study the insertion of a 20G cannula into the cephalic vein. Here, this study models the insertion of the cannula into the median cubital vein.

[§§§] This is also, coincidentally, the size of PIVC inserted into the author whilst admitted at the Glasgow Royal Infirmary, November 2021.

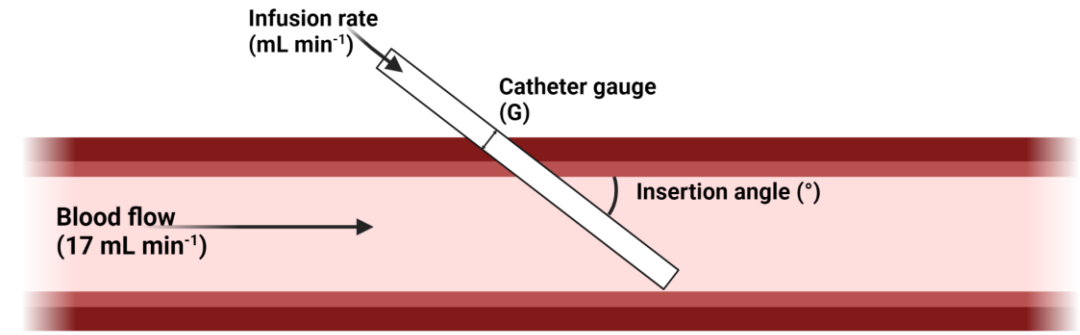

Figure 4.2: Schematic of the geometry used within this study. Adapted from Piper et al.[524] Created using Biorender.com.

For the three insertion angles studied here, the inlet velocity of the blood vessel is kept constant at 0.11 m s^{-1} (17 mL min^{-1}). A geometry with no needle inserted is used as the control. The maximum fluid velocity for each geometry is summarised in **Table 4.16**. A t-test was used to assess the statistical significance of these values. $P < 0.05$ is considered statistically significant. Fluid streamlines for each of the three geometries under study are shown in **Figure 4.3**.

Table 4.16: Summary of maximum fluid velocities for each of the input geometries studied in this section, compared to control.

Insertion angle (°)	Maximum fluid velocity (m s^{-1})	P-value
CONTROL	**0.202**	**-**
15	0.259	0.078
25	0.233	0.045
35	0.213	0.012

These results (**Table 4.16**) show maximum fluid velocity varies as a function of insertion angle. It is hypothesised that this inverse relationship between peak fluid velocity and insertion angle occurs because smaller angles of insertion lead to a greater length of needle being present in the vein. Therefore, more of the vein is occluded by the needle, and fluid velocity must then increase to maintain the same flow rate, since the blood vessel is now narrower. A t-test was used to assess whether these differences in fluid velocity were statistically significant, and found that the insertion of the needle does result in statistically significant changes in fluid velocity. Ohm's law also suggests that there is increased resistance at play, in the form of increased friction, therefore leading to an increase in the pressure drop across the geometry (**Table 4.17**).

Table 4.17: A comparison of the pressure drop across the geometry, relative to control.

Insertion angle (°)	Pressure (Pa)
15	96.3
25	79.4
35	72.7

Fluid Streamlines

Fluid streamlines are a way of visualising fluid flow. The shape of the streamlines shown in **Figure 4.3**, make it clear that the geometry has been created in such a way that it has been correctly understood by the software. (*i.e.,* that the needle is an obstruction in blood flow). There are disturbances in the shape of the streamlines as they pass over the surface of the needle. In each case, the streamlines before the needle geometry are clearly indicative of laminar flow – where fluids move in straight, parallel lines, and the flow behaviour quickly returns to this after the needle. For the needle inserted at 15°, this geometry has the largest areas of high velocity both before and after the needle, compared to other angles of insertion. In each case, a recirculation zone containing low velocity fluid can be observed at the tip.

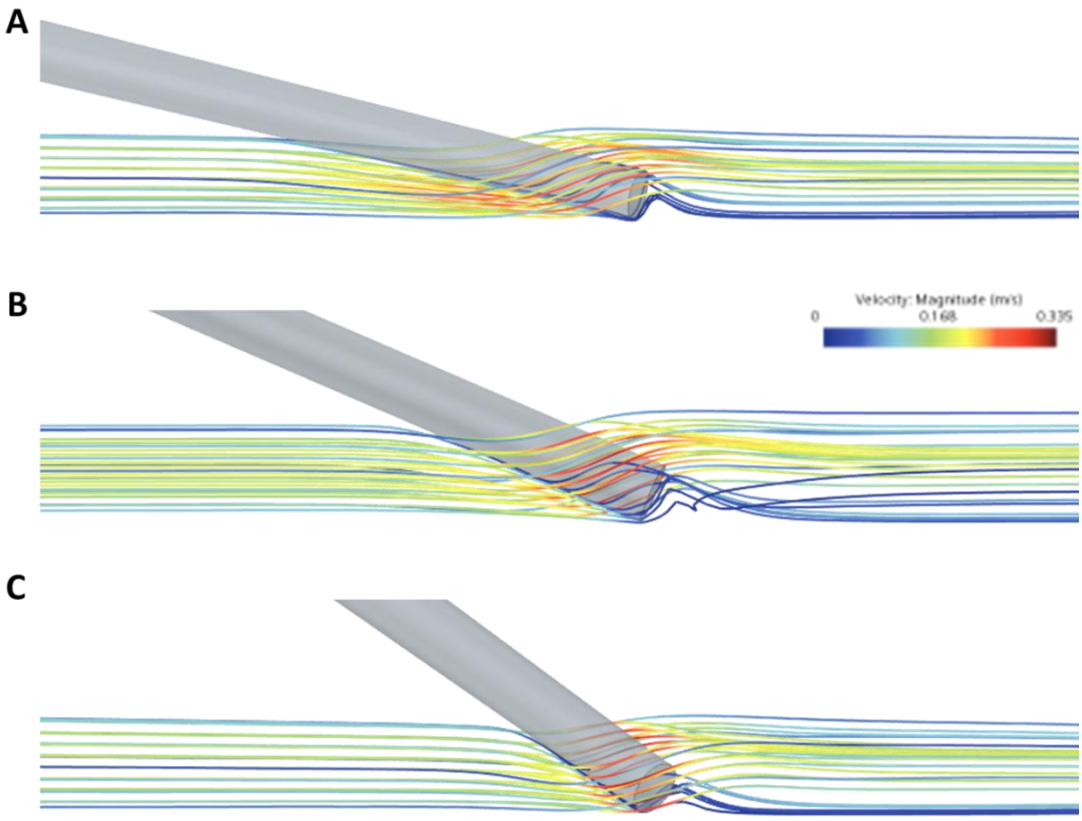

Figure 4.3: Fluid streamlines in the PIVC geometry as a function of needle insertion angle. Fluid flow is clearly disturbed near the needle and a small recirculation zone where fluid is locally of exceptionally low velocity can also be seen. A) 15 degrees B) 25 degrees C) 35 degrees.

Wall Shear Stress

For the control geometry (*i.e.* MCV only), wall shear stress is ~ 1.88 Pa throughout the geometry (not shown); this is consistent with previous studies.[593] In **Figure 4.4**, it is shown that wall shear stress is much higher around the insertion point of the needle, and that wall shear stress increases as needle insertion angle increases. This is the inverse to fluid velocity shown previously in **Figure 4.3**. In each case, the highest shear stresses are found where needle tip meets the vessel wall. This occurs because there is a very

narrow gap between the tip of the needle and vessel wall, for volume flow rate to be maintained here, fluid velocity must increase. Increased fluid velocity then leads to increased fluid shear and therefore friction applied at the vessel wall.

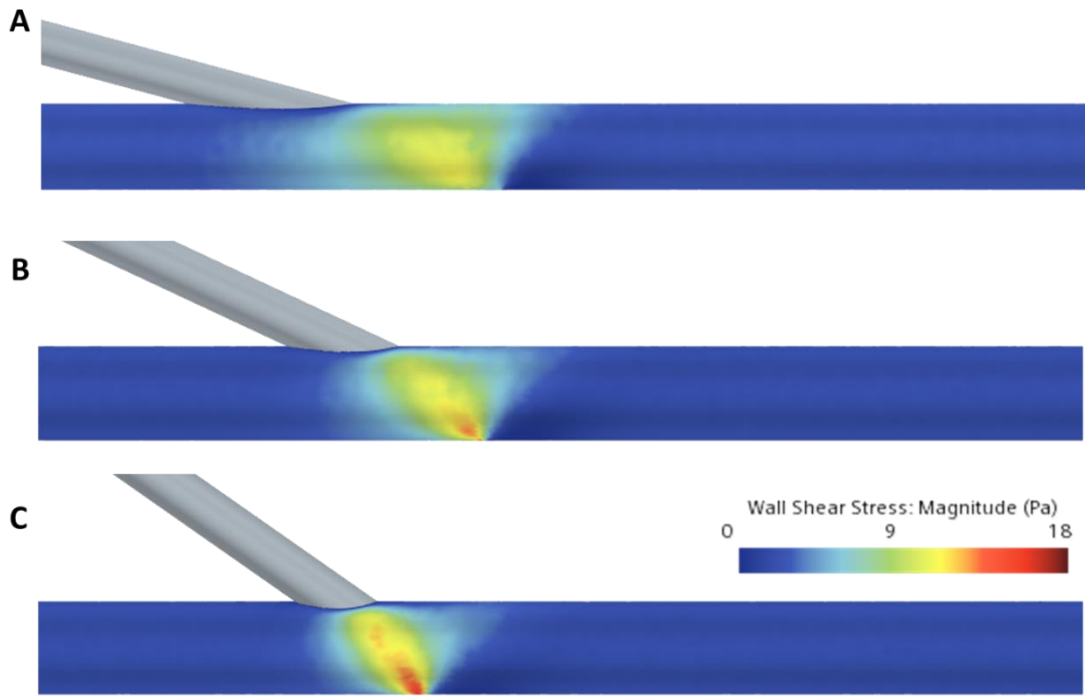

Figure 4.4: Wall shear stress varies as a function of insertion angle, the highest shear stresses in each case occur where the tip of the needle meets the vessel wall. A) 15 degrees, B) 25 degrees C) 35 degrees.

Summary

This study where the needle is simply considered as a solid object highlights the formation of a recirculation zone at the tip of the needle containing very low velocity fluid. Venous thrombosis is often triggered by stagnant fluid flow, which enables procoagulant factors, such as thrombin, to accumulate eventually leading to blood clot formation.[594] This blood clot (thrombus) can then lead to occlusion and failure of the PIVC, even in the absence of fluid being infused. It is for this reason, that PIVC are recommended to be removed as soon as they become clinically unnecessary.[460]

Needle Tip Shape

Previously, it has been shown that the angle of insertion impacts fluid velocity. Next, the influence of needle tip shape was considered. There is very limited work in the literature considering different needle tip shapes, or otherwise modifying the parameters of a PIVC (*e.g.* length and tip shape simultaneously, in order to modify fluid behaviour).[523,595] However, as far as the author is aware, this is the first time such studies have been undertaken, where only the shape of the tip of a PIVC is of interest, Here, two different tips are studied – Lancet point and lab point needles (**Figure 4.5**).

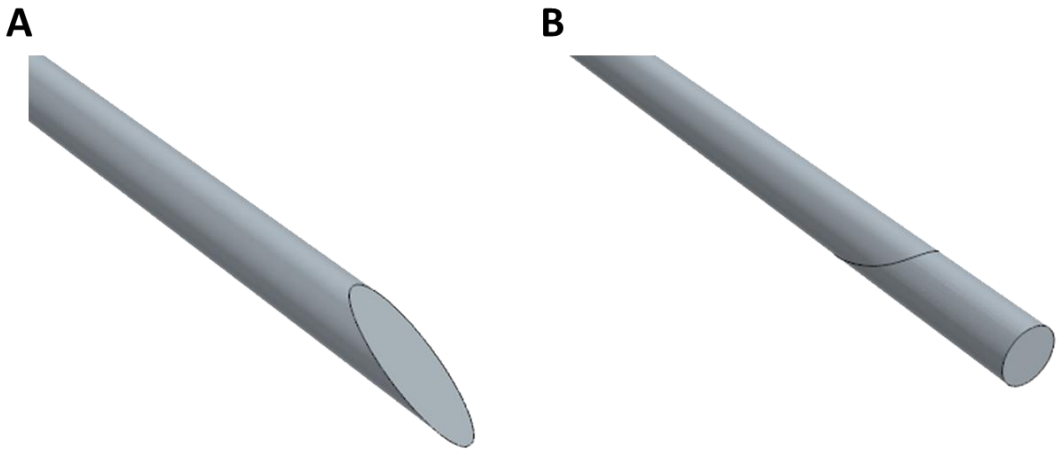

Figure 4.5: A comparison of needle tips studied in this work. A) Lancet point (15 degree bevel) B) Lab point (90 degree bevel)

A lancet point needle has a 15° bevel, whilst a lab point needle has no such bevel and instead has a 90° cut at its end. It was hypothesised that the lancet point needle would have a much more complex fluid pattern around the tip of the needle, compared to the lab point needle. Calculations were set up identical to those described in the previous section and fluid streamlines and velocity were studied (**Figure 4.6, Table 4.18**).

As predicted by Piper and colleagues, fluid streamlines (and therefore fluid flow) is much more complex around the tip of the bevelled needle (**Figure 4.6**). As discussed previously, for the lab point needle, fluid behaviour is clearly laminar proximal to the needle, disturbed over the needles surface and then quickly returns to laminar flow. For the bevelled lancet point needle, the fluid flow is again laminar until it almost reaches the needle. There is a clearly visible area of much higher velocity behind the needle, and in front of the bevelled face, an area of very low velocity. Visualising fluid velocity magnitudes as a vector quantity enables this zone to be identified as a recirculation zone (not shown).

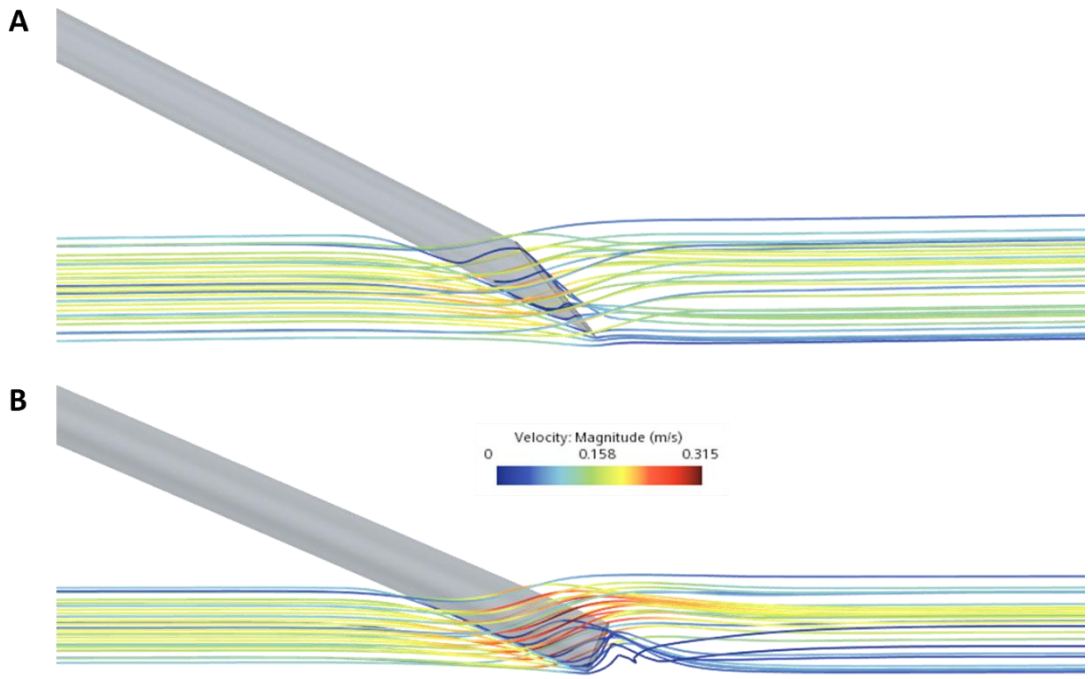

Figure 4.6: Fluid streamlines as a function of needle tip shape. The recirculation zone is much smaller for the angled Lancet point needle. A) Lancet point B) Lab point

Fluid velocities were then measured at a fixed point downstream from the proximal face of the needle (**Table 4.18, Figure 4.7**).

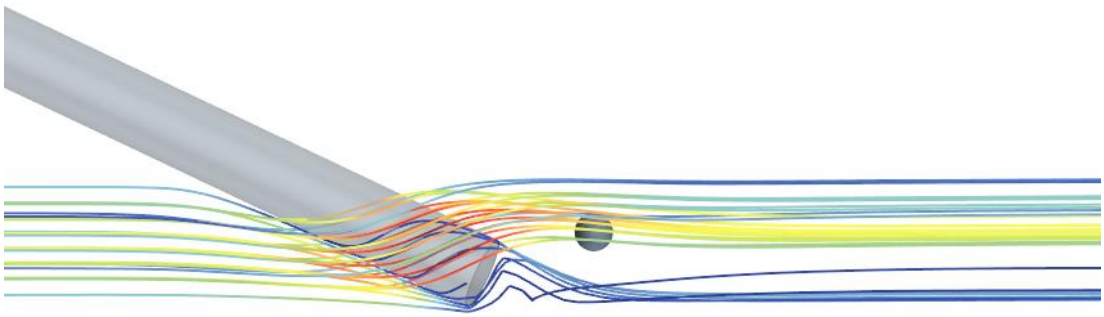

Figure 4.7: Positioning of point where fluid velocities were measured, relative to proximal face of the needle.

Table 4.18: A comparison of the fluid velocity at a set point downstream from the tip of the PIVC studied in this work.

Model	Fluid velocity (m s^{-1})
Lancet point	0.190
Lab point	0.221

4.4.1.2 Infusing Fluids via 20G Needle

Once the influence of introducing the PIVC into the MCV had been understood, the simulation was then made more complex by introducing a second fluid source into the model. Here, 0.9% saline and 5% glucose is infused into the model to simulate the administration of IV fluids – later this will be adapted to mimic the delivery of drug-loaded nanoparticles. The calculations presented

here only look at the introduction of 0.9% saline *via* cannula, but the results for glucose are similar and are available in **Appendix H**. Each simulation uses the same 25° geometry and 20 G cannula presented earlier, but a range of infusion rates are studied. 10-, 30- and 60-mL min^{-1} are chosen to cover the full range of flow rates typically used with this cannula. 300 mL min^{-1} is chosen to mimic a saline "flush" used to help prolong the patency of the PIVC.

First, flow rates in mL min^{-1} were converted to velocities for the needle assembly, and their corresponding Reynolds number was also calculated (**Table 4.19, Appendix C**). When a saline flush (flow rate 300 mL min^{-1}) is performed, the behaviour of the fluid is not within the laminar regime – R_e is well in excess of 2300.

Table 4.19: Calculating velocity and Reynolds number from flow rate where 0.9% saline or 5% glucose is used as the infusion fluid.

Flow rate (mL min^{-1})	Velocity (m s^{-1})	Reynolds number (saline)	Reynolds number (glucose)
10	0.584	346.83	314.31
30	1.75	1039.30	941.86
60	3.50	2078.61	1883.71
300	17.5	10,393.07	9418.57

Fluid Velocity and Streamlines

In this section, two distinct colour schemes are used to enable the origin of the streamline to be clearly seen. Furthermore, for the fastest inlet velocities, the difference between fluid velocity at the tip of the needle and fluid velocity in the vein, is difficult, if not impossible to visualise in any other way. Therefore, the fluid velocity in the vein is identified using the blue-red colour palette used earlier, and fluid streamlines originating from the infusion fluid are simply given as solid black lines (**Figure 4.8**). A second set of images have this colour scheme reversed.

Now, as infusion rate increases, a greater proportion of the blood flow in the vein distal to the needle is cleared by the incoming fluid. Where infusion flow rate is at or below 30 mL min^{-1}, a small recirculation area at the tip of the needle can be seen. This is not observed where flow rate is above 60 mL min^{-1}. This would agree with Doyle *et al*.'s work on a flow rate suitable to keep vein open (TKVO).[596] Areas of low velocity are observed at the non-slip boundaries at the vessel and needle walls. Furthermore, vein fluid velocity is slower proximal to the vein inlet, and incoming fluid increases this distal to the needle outlet. Where infusion rates are high, this increase in fluid velocity is significant. On the other hand, there is a local area of high velocity proximal to the needle, as seen previously in **Figure 4.3**.

If the colour scheme is then altered to highlight the infusion fluid, fluid velocity is comparatively high within the needle, the fluid leaves the needle and then rapidly loses momentum (**Figure 4.9**). This initially seems strange, however, can easily be explained by one of the basic laws of fluid dynamics. In a set volume with a constant density fluid, mass must be conserved (**Equation 5**).

So fluid flow into and out of the geometry must be equal. Therefore, the velocity of the fluid within the needle must decrease on entering the blood vessel, otherwise mass and therefore flow rate out of the geometry would increase over time; this is a physical impossibility.

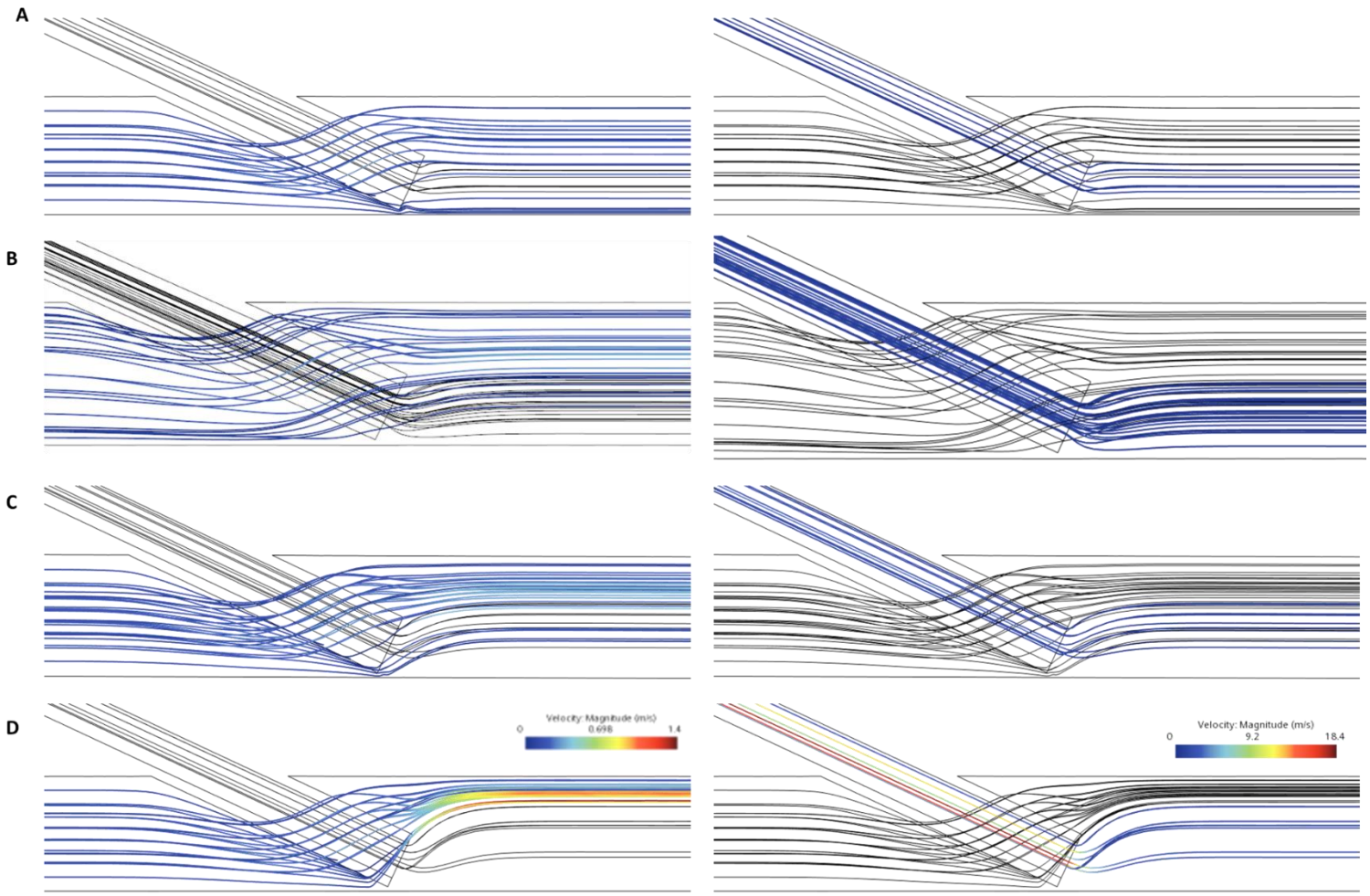

Figure 4.8: Fluid behaviour and fluid velocity vary as a function of flow rate. Left: fluid velocity in the vein geometry. Right: fluid velocity in the needle. A) 10 mL min^{-1} B) 30 mL min^{-1} C) 60 mL min^{-1} D) 300mL min^{-1}.

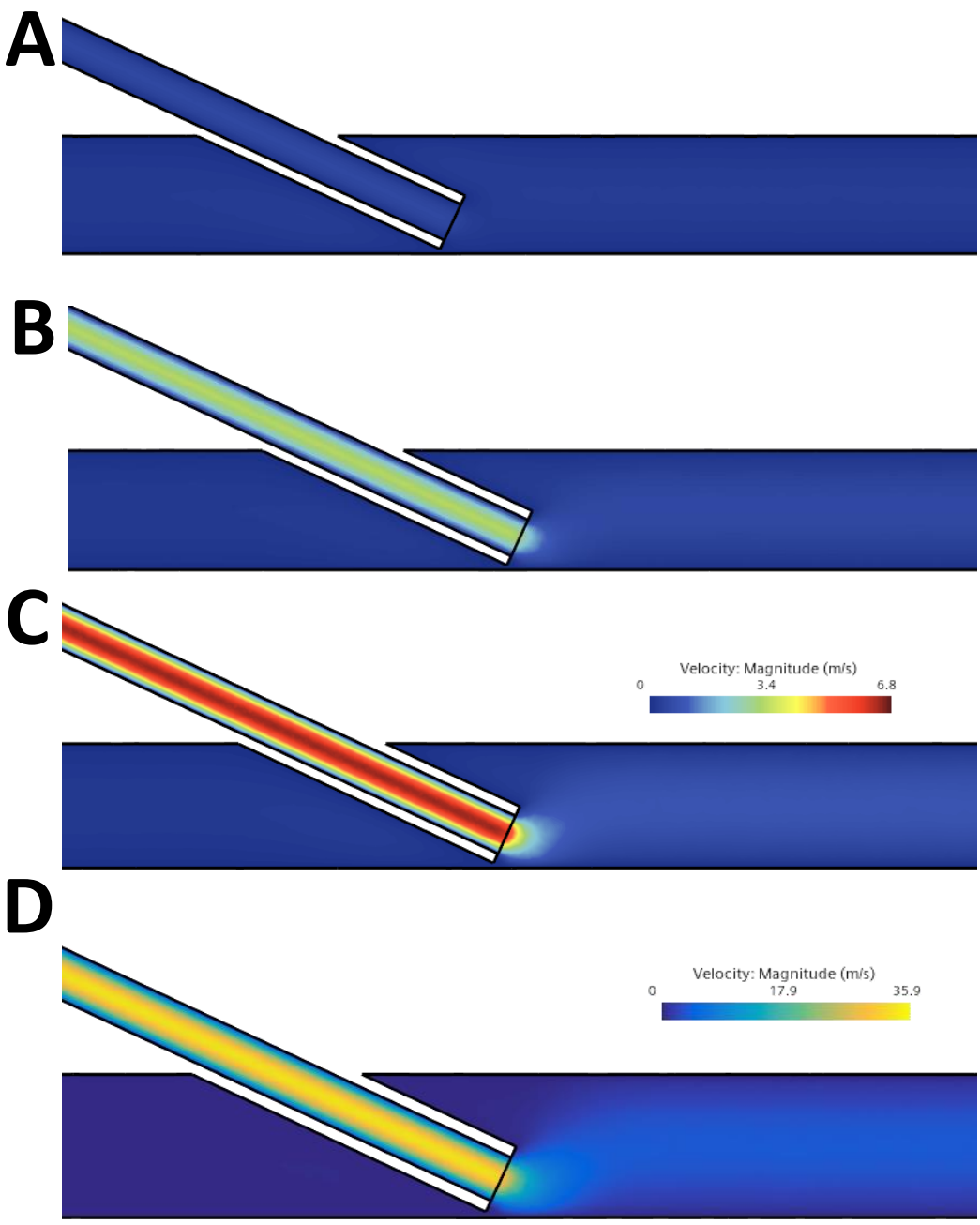

Figure 4.9: Fluid velocity, when the needle is used for the infusion of fluid. A) 10 mL min^{-1} B) 30 mL min^{-1} C) 60 mL min^{-1} D) 300mL min^{-1}.

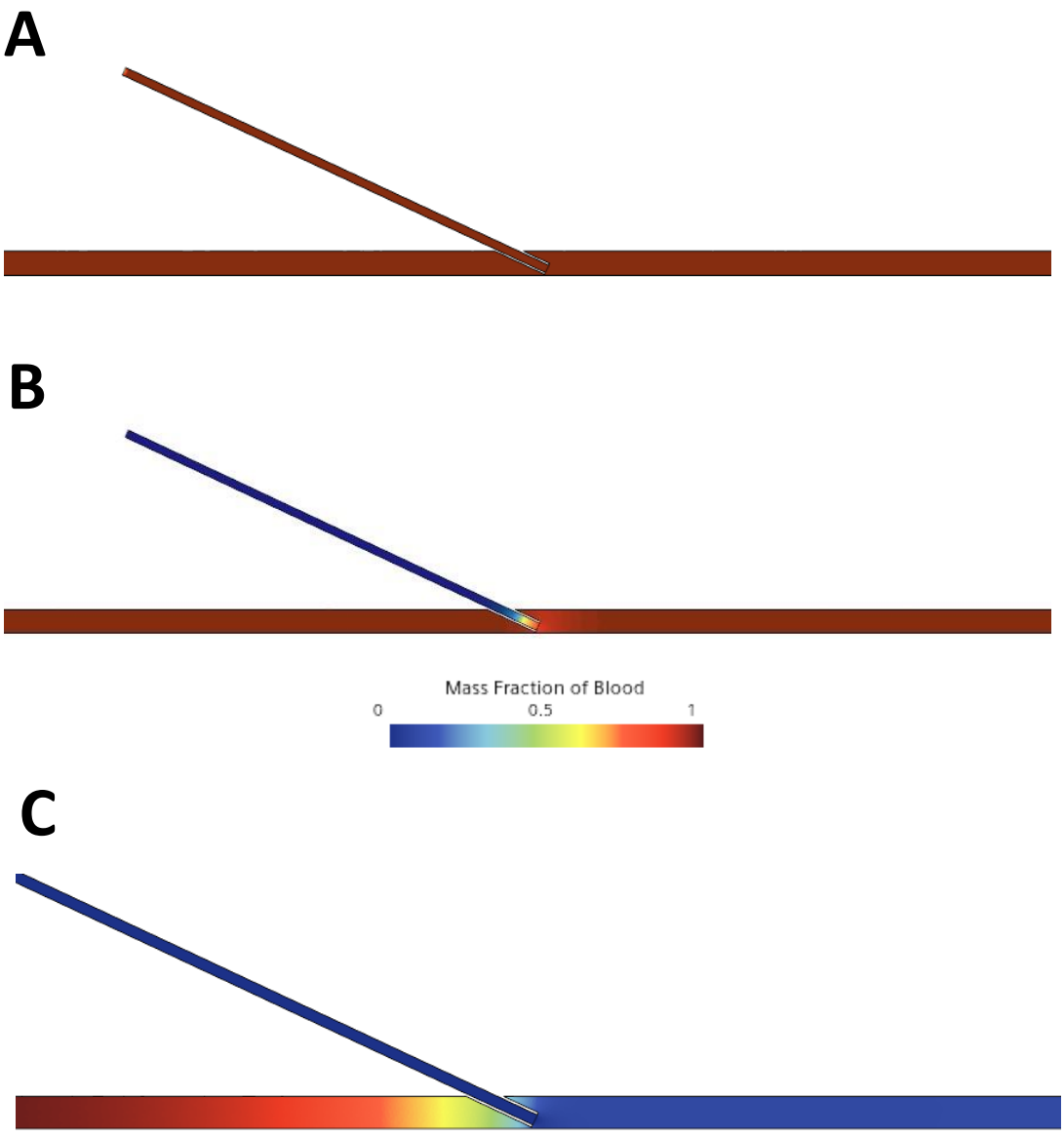

Figure 4.10: Mass fraction of blood in the median cubital vein varies as a function of infusion rate. A) No infusion B) 10mL min^{-1} c) 300mL min^{-1}. AR+

Mass Fraction of Blood

Mass fraction of blood has been investigated to understand the mixing of both blood and the infusion fluid. This gives a value between 0 and 1, where 1 is equal to 100% blood, and 0 is 100% saline.

Figure 4.10 shows three different flow rates (no infusion, 10 mL min^{-1} and 300 mL min^{-1}) and their impact on the composition of the fluid within both the needle and blood vessel. All the calculations in this study initially pass through a state where no infusion occurs. In this initial state, both the blood vessel and the needle are filled with blood. This represents the insertion of the cannula and the resulting “flashback”, where the needle fills with blood; no fluid is infused in this state. This figure additionally shows the composition of the fluid in the needle and blood vessel when fluid is infused at 10 mL min^{-1} and 300 mL min^{-1}. In each case, it can be seen that the needle is completely clear of blood, and

is wholly filled with 0.9 % saline, the blood vessel is partially cleared of blood both before and after the insertion point of the needle – this is perhaps easier to see where infusion rate is 300 mL min^{-1} – and this simulation can be explored further *via* augmented reality. This reflects the fluid streamlines shown previously in **Figure 4.8**. Additionally, the mixing area extends ~ 13 mm behind the needle, when the highest flow rate (300 mL min^{-1}) is used.

Residence Time

In this context, residence time is a measure of how long a fluid particle spends within the domain (*i.e.,* the geometry under study). Here, it has been measured using massless Lagrangian particles – these effectively function like a tracer dye. Particles were introduced at both the blood vessel and needle inlet and then followed until all particles had exited the domain (not shown), Data for the minimum (*i.e.,* first particle to escape) and maximum residence times for each flow rate can be found in **Appendix H**. These results show as infusion rate increases, both minimum and maximum residence times decrease.

Wall Shear Stress

Wall shear stress varies by an order of magnitude over the range of flow rates studied in this work (8,500 Pa – 70,000 Pa). These values are well over 100 times those shown in **Figure 4.4**. Again, the areas of peak wall shear stress are those directly adjacent to the needle outlet (**Figure 4.11**), and there is also an area of high wall shear either side of the needle, corresponding to where fluid velocity is highest. On the bottom face of the blood vessel, an area of locally very low wall shear stress can also be seen, this corresponds to the low velocity recirculation zone identified previously. Excessive wall shear stress is > 38 Pa. *In vivo* studies have previously shown that this is the critical shear stress, beyond which endothelial cells are damaged.[597] This area of 'excessive' wall shear stress is shown to extend the full length of the blood vessel that is modelled in this case, irrespective of infusion rate.

Summary

In summary, is has been shown that needle tip shape influences the fluid flow around the tip of the needle, impacting both the shape of streamlines, but also fluid velocity. When infusion of 0.9% saline is considered, it has been determined that its velocity is faster in the needle, but rapidly decreases once 0.9% saline and blood mix in the median cubital vein. Consistent with results previously obtained by Doyle and colleagues, an infusion flow rate > 30 mL min^{-1} is required to clear the low flow recirculation zone at the tip of the needle.[596] The mass fraction of blood within the geometry of interest has been investigated. The initial conditions where no infusion occurs represents insertion of needle and the resulting "flashback". Once fluid is infused *via* the needle, the proportion of blood remaining in vein after the needle is inversely proportional to infusion rate. Wall shear stress varies by an order of magnitude over the range of flow rates studied in this section. Observed shear rates are much larger than when needle is simply considered as an obstruction. Large areas on the vein have wall shear stress above the critical value (38 Pa), and thus would lead to damage of endothelial cells.[597]

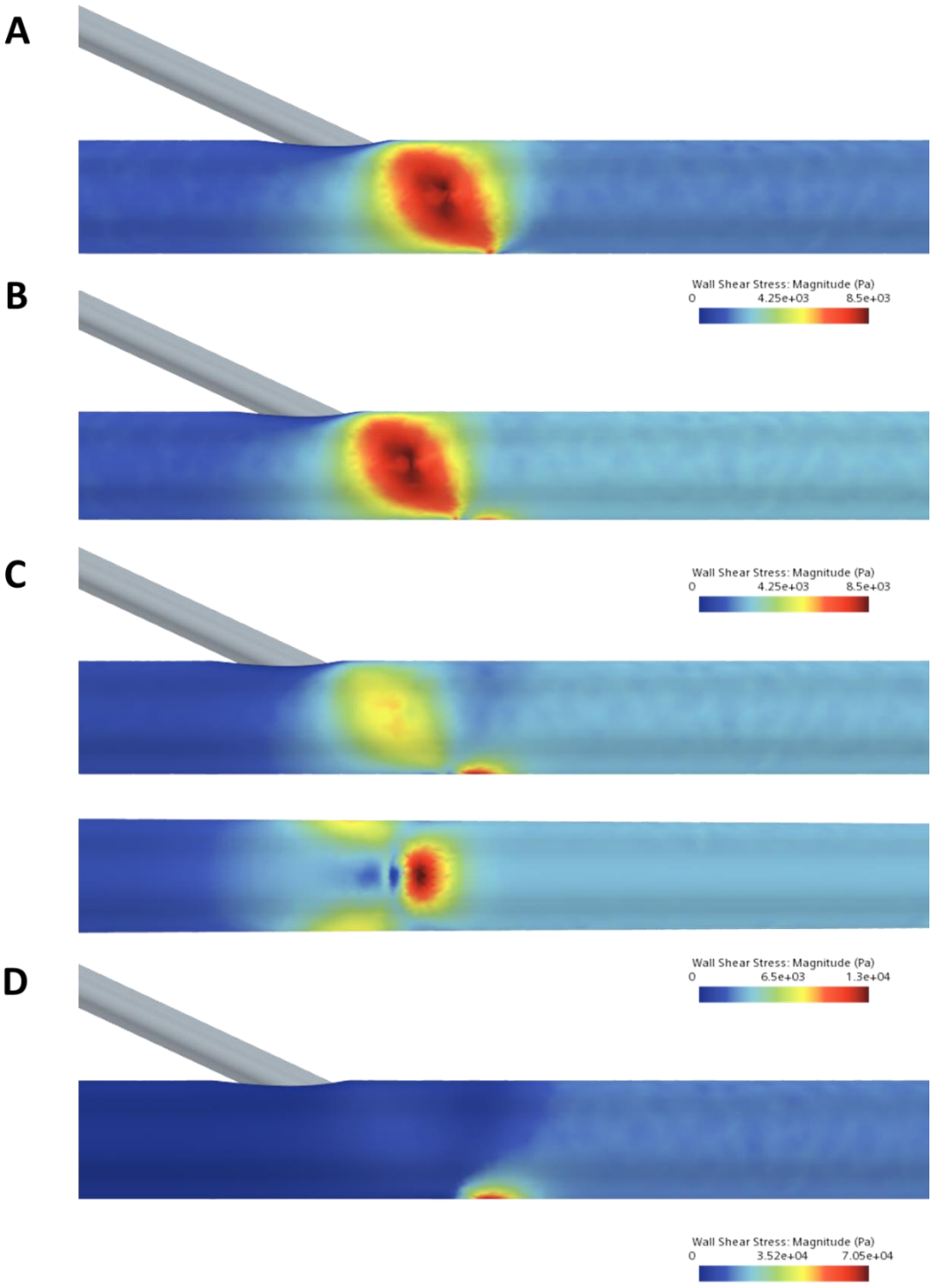

Figure 4.11: Wall shear stress varies as a function of infusion velocity. Infusion rates of 0.9% saline are as follows: A) 10mL min^{-1}, B) 30 mL min^{-1} C) 60 mL min^{-1} D) 300mL min^{-1}.

4.4.1.3 Damage Index as a Proxy Measure for Haemolysis and Thrombus Formation.

The damage index introduced here is used to measure the impact of the VAD on haemolysis. The magnitude, duration and nature (laminar or turbulent) of fluid flow is known to contribute to the damage caused to red blood cells and

their membranes, eventually resulting in haemolysis.[598] The absolute value of shear stress beyond which haemolysis occurs depends on exposure time.

The damage index (**Equation 20**) is calculated from the simulation by way of a passive scalar – these can be considered as tracer dyes that have no effect on the physics of the system.

$$D_I = (3.62x10^{-7})^{\frac{1}{0.785}}.\tau^{\frac{2.416}{0.785}} \quad (20)$$

Equation 20: Damage index. Where τ is wall shear stress.

The damage index is directly related to two quantities – fluid velocity and shear stress – by the Giersiepen – Wurzinger correlation.[598,599] A more detailed discussion of the implementation of the damage scalar and benchmarking against the Garon and Farinas paper to confirm set up in STARCCM+ is correct and the author has accurately understood the implementation of such is outlined in **Appendix D**.

The results provided by the damage index have previously been shown by Piper and colleagues to correlate well with lysis rates (*i.e.,* RBC damage) determined by experimental methods.[524] However, Yu, Engel and colleagues have previously reported that there are many haemolysis prediction models in current use for CFD, but large deviations in their predicted haemolysis rates are observed (often over several orders of magnitude), and depend significantly on chosen model and its parameters.[600] They show that parameters derived from the Giersiepen-Wurzinger correlation often overpredict haemolysis; however, those from Heuser and Opitz tend to underestimate haemolysis.[600] Despite these limitations of the haemolysis models, the results presented here are able to highlight combinations of infusion fluid and flow rate which may lead to cell lysis, encouraging thrombus formation and therefore lead to *in situ* failure of PIVC.

Table 4.20: Damage index as a function of infusion fluid identity and flow rate.

Flow rate (mL min^{-1})	**10**	**30**	**60**	**300**
0.9 % Saline	2.19	17.30	90.75	9691
5 % Glucose	2.23	17.72	94.27	9664

In this study, the damage indices (**Table 4.20**) have been obtained. From previous results, it has already been shown that increasing infusion rate increases wall shear stress (and by extension greater fluid shear). It has previously been reported that wall shear stresses above 150 Pa are associated with haemolysis.[601,602] Therefore, as fluid and wall shear stress increases, a higher proportion of red blood cells will undergo haemolysis. Because of the difficulty in implementing the damage scalar within STARCCM+, as well as the extent by which the results diverge on replication of the Garon and Farinas paper, as well as literature that shows interlaboratory comparison studies also highlight these challenges, the damage index was not implemented further in this work.

4.4.1.4 Summary

In this section, the results presented above will be summarised and impact of carrier fluid identity on fluid velocity, streamlines, residence times and wall shear stress will be compared. Later the damage index will be discussed. Finally, these results will be used to develop an understanding as to why ultrasound-guided IV access is more likely to result in PIVC insertion that fails, and what do these results tell us about Virchow's triad.

The results presented previously for mass fraction (**Figure 4.10**) show that for a given time, a greater proportion of blood is displaced when glucose is the infusion fluid, compared to saline. When wall shear stress is considered (**Figure 4.11**), wall shear stress is then slightly higher for glucose in comparison to saline, and therefore it is then unsurprising that the calculated damage index is then higher when glucose is used as the infusion fluid.

4.4.1.5 What Do These Results Tell Us in the Context of Virchow's Triad?

Virchow's triad refers to the three broad parameters (Stasis (residence times), vessel damage (WSS) and hypercoagulability (particle aggregation)) known to influence the formation of venous thrombosis.[461] It is thrombus formation that is frequently implicated in VAD failure. Here, it has been shown that both infusion fluid identity as well as infusion rate can influence at least two of these three parameters (stasis and vessel damage and it is likely they also impact particle aggregation). Further, these results additionally suggest insights into why Ultrasound guided venepuncture is more likely to fail.[603] These calculations show that prior PIVC use leads to endothelial damage and eventually gives rise to damaged superficial veins, that are no longer compressible and therefore not suitable for venepuncture and/or venous access. This damage then leads to the use of ultrasound guided methods to find and use deeper, less accessible veins.[603]

4.4.1.6 Nanoparticle Behaviour Under Flow

Now that the infusion of IV fluids (0.9 % saline and 5 % glucose) have been added to the model and understood, the final stage of this model is to add in the infusion of drug-loaded 100 nm PLGA nanoparticles *via* the 20G cannula modelled previously.

The set up for these simulations differs from those presented previously within this chapter. Here, implicit unsteady time regime is selected, as this enables the Discrete Element Method to be enabled within the simulation. Further details on the set up for these simulations is given in **section 4.3.5**. Despite the clinical process these simulations attempt to replicate *in silico*, the nanoparticles are not introduced *via* the needle inlet. A derived part was created to define a plane parallel to the needle outlet, 0.1 cm proximal to the needle outlet and this is then used as the part on which the nanoparticles are introduced. More control is achieved over the position of the injected nanoparticles. This decision has been made to speed up the calculation, as we are most interested in peak velocity and particle shear stress. This is not thought to affect the results obtained in this model, as the response time of

PLGA particles has previously been calculated (**Chapter 3**) and has found the be rapid *i.e.,* they will quickly respond to fluid flow.

300mL min^{-1} infusion rate is **not used** here, as these parameters are not clinically relevant for the infusion of drug-loaded nanoparticles. Therefore, only 10, 30 and 60 mL min^{-1} will be studied. For these simulations, only nanoparticle behaviour is of interest. Particle velocity and particle shear stress will be discussed and related to their impact on localisation of nanoparticles within blood vessels and later particle uptake into cells. Only the results for where the infusion fluid is glucose are shown here - the results where saline is used are available in **Appendix H**.

Particle Velocity

Particle velocity is a measure of how fast the particles within the simulation are moving. This depends on the weight and buoyancy of the particle as well as the drag force the particle is subject to. Since the particle is suspended in the fluid, and the previously calculated response time for these particles is known to be rapid, it is expected that the velocity of the particles will match that of the carrier fluid.

As expected, the particles rapidly adopt a parabolic shape with the fastest moving particles in the centre of the geometry. In these figures and the animation below, this gives rise to the appearance of several rows of particles all with similar speeds. Furthermore, particle velocity decreases on exiting the needle and entering the blood vessel (**Figure 4.12**).

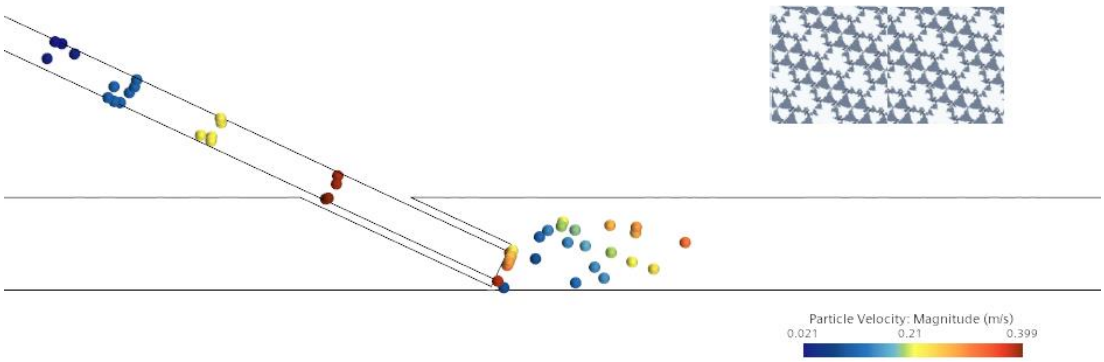

Figure 4.12: Particle velocity varies as a function of infusion rate and carrier fluid (glucose, 60mL min^{-1}). The particles rapidly show a decrease in velocity on entering the blood vessel. AR^{+}

Particle Shear Stress

Particle shear stress is a measure of (primarily) friction between the fluid and the particles suspended within it. It is this force which is believed to alter the composition of the protein corona around nanoparticles and it is for this reason that it will be one of the key parameters used within the development of the microfluidic device within the following chapter. Particle shear stress cannot be determined directly from STARCCM+. This parameter is not available by default in the software and must therefore effectively be installed by the user through a series of field functions (**Appendix F**).

Particle shear stress is shown in **Figure 4.13** to be a function of infusion rate. Maximum particle shear stress increases proportionally to infusion rate and therefore fluid velocity. The decrease in maximum particle shear stress seen for the fastest infusion rate corresponds with the particles beginning to leave the needle geometry (**Figure 4.14**).

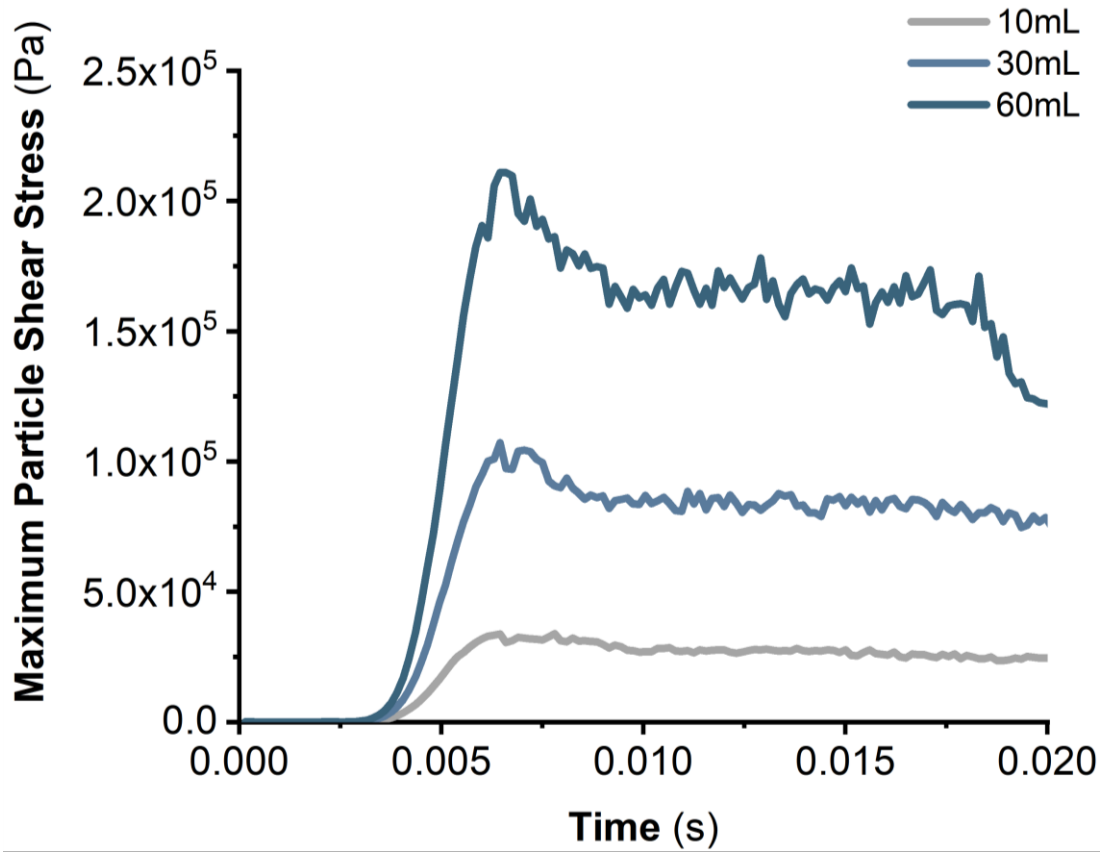

Figure 4.13: Particle Shear stress as a function of physical time. The decrease in maximum particle shear stress for the simulation where infusion rate is 60 mL min^{-1} corresponds to the particles beginning to exit the needle geometry. Here, only the results where glucose is used as the infusion fluid are shown, the results for saline are available in **Appendix H**.

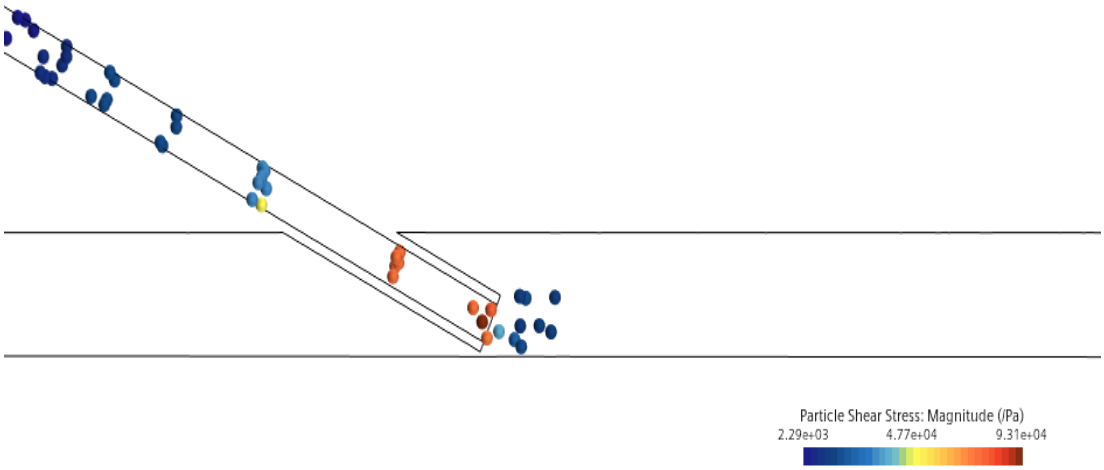

Figure 4.14: As particles leave the needle, particle shear stress (and velocity) fall rapidly. This effect is most pronounced where there is a significant difference between blood velocity and that of the infusion fluid.

As discussed previously, particle shear stress has been shown to alter protein corona composition around nanoparticles coincubated in biological fluids, influence the process of localisation of nanoparticles in blood vessels (margination) and of nanoparticle uptake by endothelial cells (and therefore particle uptake into tumours and apparent efficacy and/or cytotoxicity of novel nanotherapeutic drugs).[51,53,468,471]

However, these computational studies additionally highlight a significant gap within the literature. As far as the author is aware, few (if any) computational fluid dynamics studies of vascular access devices consider nanoparticle behaviour. Further work is required to confirm these results.

Summary

This final stage of this model has shown that it is possible to use a CFD-DEM approach to model the infusion of drug-loaded PLGA nanoparticles in IV fluids.

This methodology is now repeated for the remaining vascular access devices of interest in this work, before a PCA analysis is undertaken to simplify the data set that has been obtained and to identify similarities between the vascular access devices under study in this work.

4.4.2 Peripherally Inserted Central Catheter (PICC)

A peripherally inserted central catheter is a long (50-60cm), thin, flexible catheter usually made of polyurethane or silicone, typically inserted into the upper arm, and often referred to by their brand names (Hickman, Leonard, Broviac).[604,605]

The influence of PICC size and vessel diameter has been studied in detail by Nifong and McDevitt and will not be explored here.[525] Here, the power-injectable PICC lines from BD – specifically - a 5 Fr, single, double and triple lumen PICC will be modelled and the impact of moving from single, double to triple lumen has on fluid behaviour. In these simulations, the cannula is

assumed to be placed centrally in the left brachiocephalic vein, and that normal anatomy is present – common variations in the veins in the chest have been previously discussed by several groups.[606,607]

The model parameters for vessel size and fluid velocity are identical to those obtained by Peng *et al*. *via* computed tomography angiography and therefore are from a living patient, rather than a cadaver.[583] The models introduced and developed in this section consist of both brachiocephalic (innominate) veins, and the superior vena cava. It was decided to only model part of the veins concerned, to reduce the computational demand of the models. Calculations of entrance lengths were undertaken (**Appendix E**) to confirm that the length of the SVC that is modelled is sufficient (the entrance length is exceeded). Therefore, the shorter SVC that is measured here should have no significant impact on the results obtained.

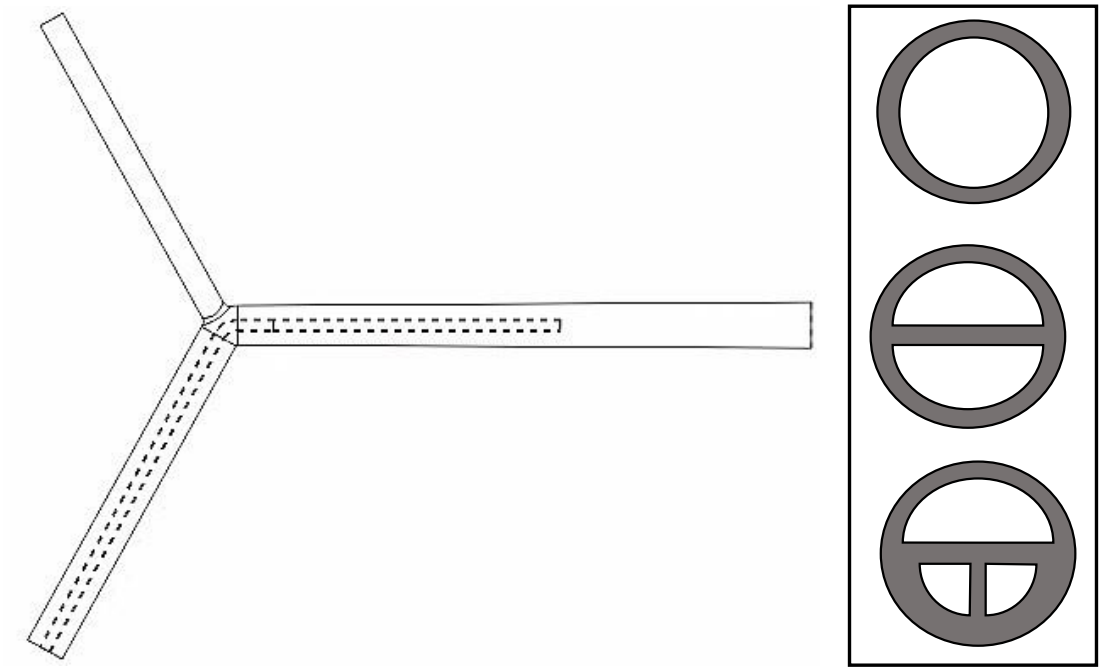

Figure 4.15: Outline of PICC line used within this work, showing the brachiocephalic veins and deliberately truncated SVC. Inset: cross sections of the single, double and triple lumen PICC lines used in this study.

4.4.2.1 Obstruction of Fluid Flow

Using the same approach as used and outlined previously for the 20G PIVC modelled earlier, the impact of inserting the PICC line will be studied. As a consequence of the fact all three PICC lines studied here have the same external diameter, only the single lumen geometry is used here. The inlet velocity of the left brachiocephalic veins is kept constant at 0.46 m s^{-1} and for the right brachiocephalic vein inlet velocity is 0.86 m s^{-1}. The outlet is set as a pressure outlet, at zero pressure. A copy of the geometry with no PICC line inserted will be used as a control. The fluid velocity observed at a set point within each geometry shown in **Figure 4.16** is summarised in **Table 4.21**. A paired t-test was again used to assess the statistical significance of any

change in maximum fluid velocity following the insertion of the PICC line that is being studied in this section.

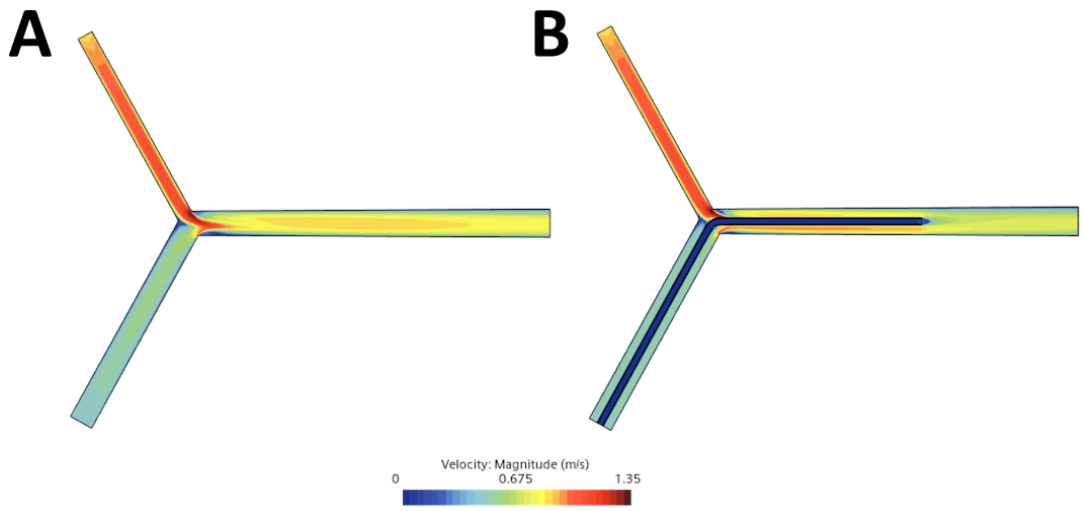

Figure 4.16: Fluid velocity in the right brachiocephalic vein is not impacted by the insertion of the PICC line. A) control B) following PICC line insertion.

In **Figure 4.16**, it can be seen that there is no difference in fluid velocity in the right brachiocephalic vein. Fluid velocity within the left brachiocephalic vein (where the PICC line is inserted) does appear to be slower. On joining the superior vena cava, the area of low fluid velocity decreases in size, and a band of increased fluid velocity appears below the PICC line. At the outlet of the PICC line, there is an area of very low flow, which is as expected considering the results shown earlier within this chapter. This area of comparatively low flow extends 0.003m distal to the outlet (not shown).

Table 4.21: A comparison of fluid velocity, a set distance downstream (0.015m) from the outlet of the PICC line, between the control geometry and that which has had the PICC line inserted. P <0.05 is considered statistically significant.

Geometry	Fluid velocity (m s^{-1})	p-value
CONTROL	0.840	-
With PICC line	0.715	0.051

Fluid Streamlines

Next, fluid streamlines were visualised to assess both the implementation of the geometry, and to see how fluid moves around this obstruction and to enable identification of any recirculation zones that may have developed, and therefore are present when the PICC line is not used for the infusion of fluids.

The beginnings of spiral flow can be seen most easily with the control geometry, particularly when streamline density is increased. The streamlines in this figure (**Figure 4.17**) show that the PICC line is understood by the software as representing an obstruction in fluid flow. When streamline density is increased, and the model viewed from inside the PICC line (not shown), no streamlines are seen, suggestive of the PICC line accurately being understood as an obstruction. Furthermore, the streamlines are seen to pass over the

surface of the PICC line. The areas of low fluid velocity are difficult to recognise in this figure, therefore, the vectors for fluid velocity were investigated in **Figure 4.18**, as these give both velocity and their direction, making recirculation zones easier to identify.

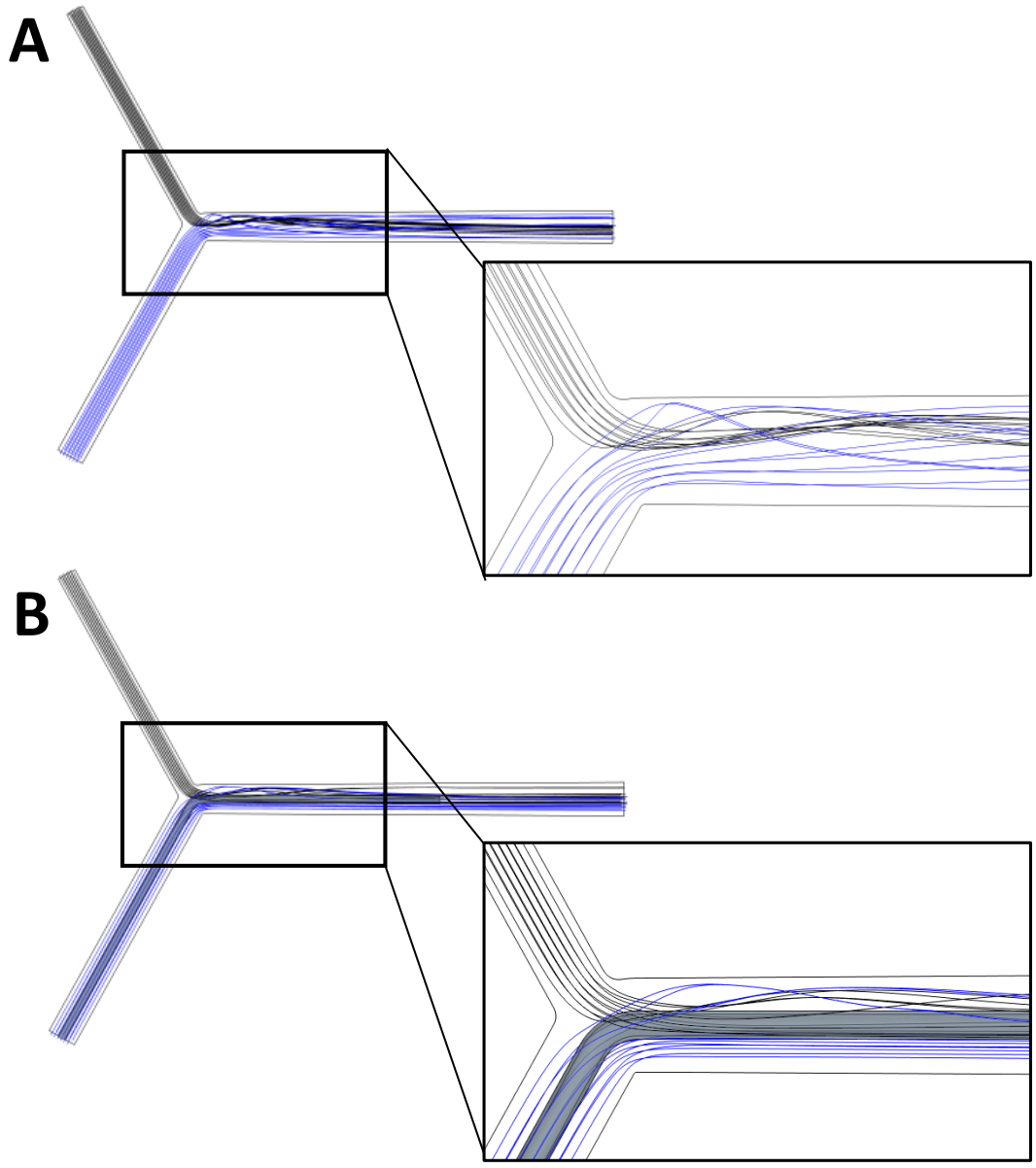

Figure 4.17: Fluid streamlines, as a planar section through the centre of the geometry, parallel to the x-axis. The PICC line is accurately simulated as an obstruction to fluid flow by the simulation. A) control geometry B) Following PICC line insertion. Two colours are used to represent the origin of each set of streamlines.

Recirculation zones are areas where fluid flow moves in the opposite direction from the bulk of the fluid. They are well understood in the classical problem of the backwards-facing step, and where vectors are visualised, frequently look like loops or swirls. In **Figure 4.16**, several areas of comparatively low fluid velocity were seen. These are: the junction where both brachiocephalic veins meet; within the superior vena cava, and finally at the outlet of the PICC line

when it is not used for the infusion of fluids. In **Figure 4.18**, it can be seen that these areas of low flow identified previously are indeed recirculation zones.

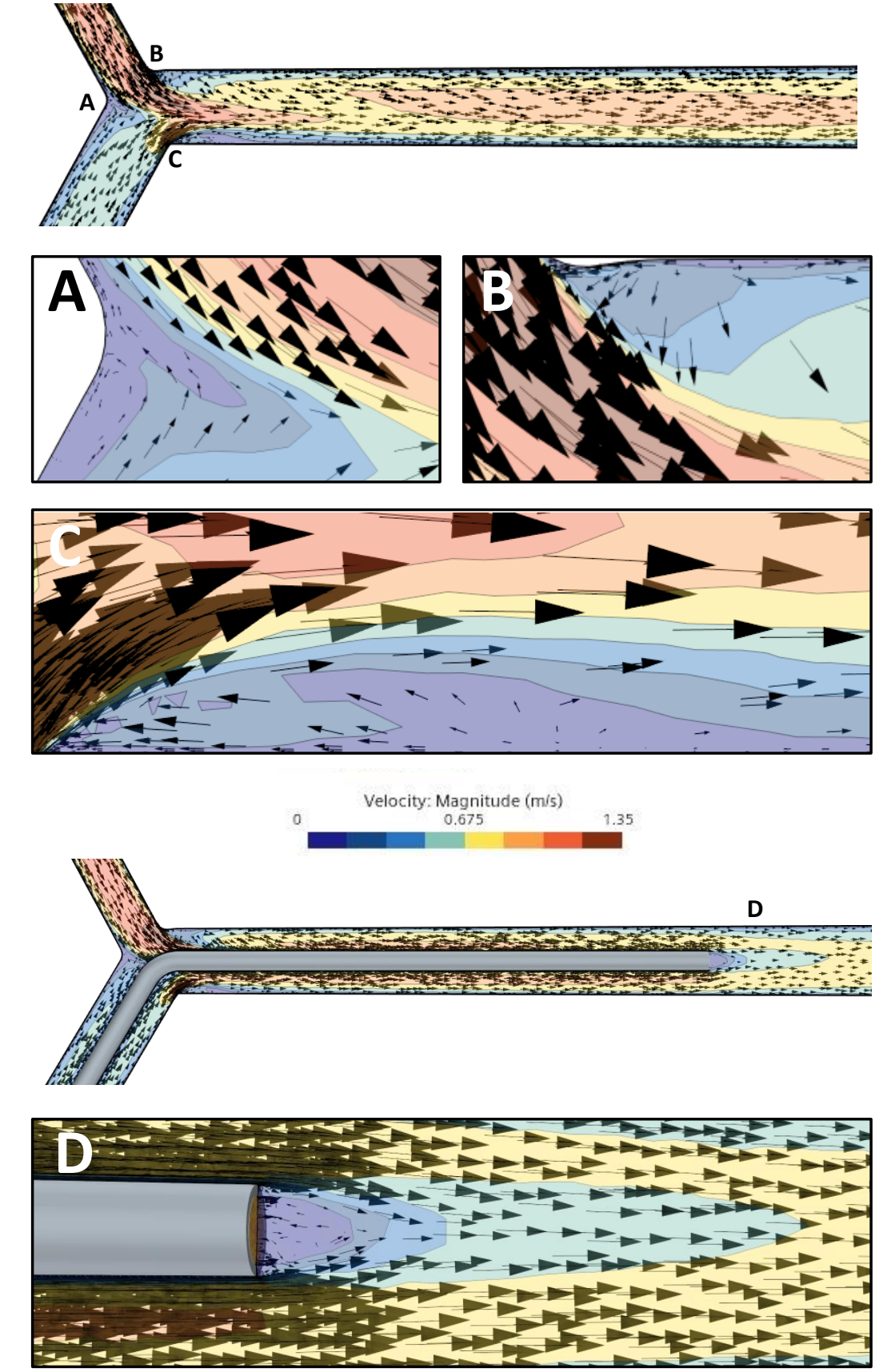

Figure 4.18: Vectors helping identify recirculation zones in the geometry.

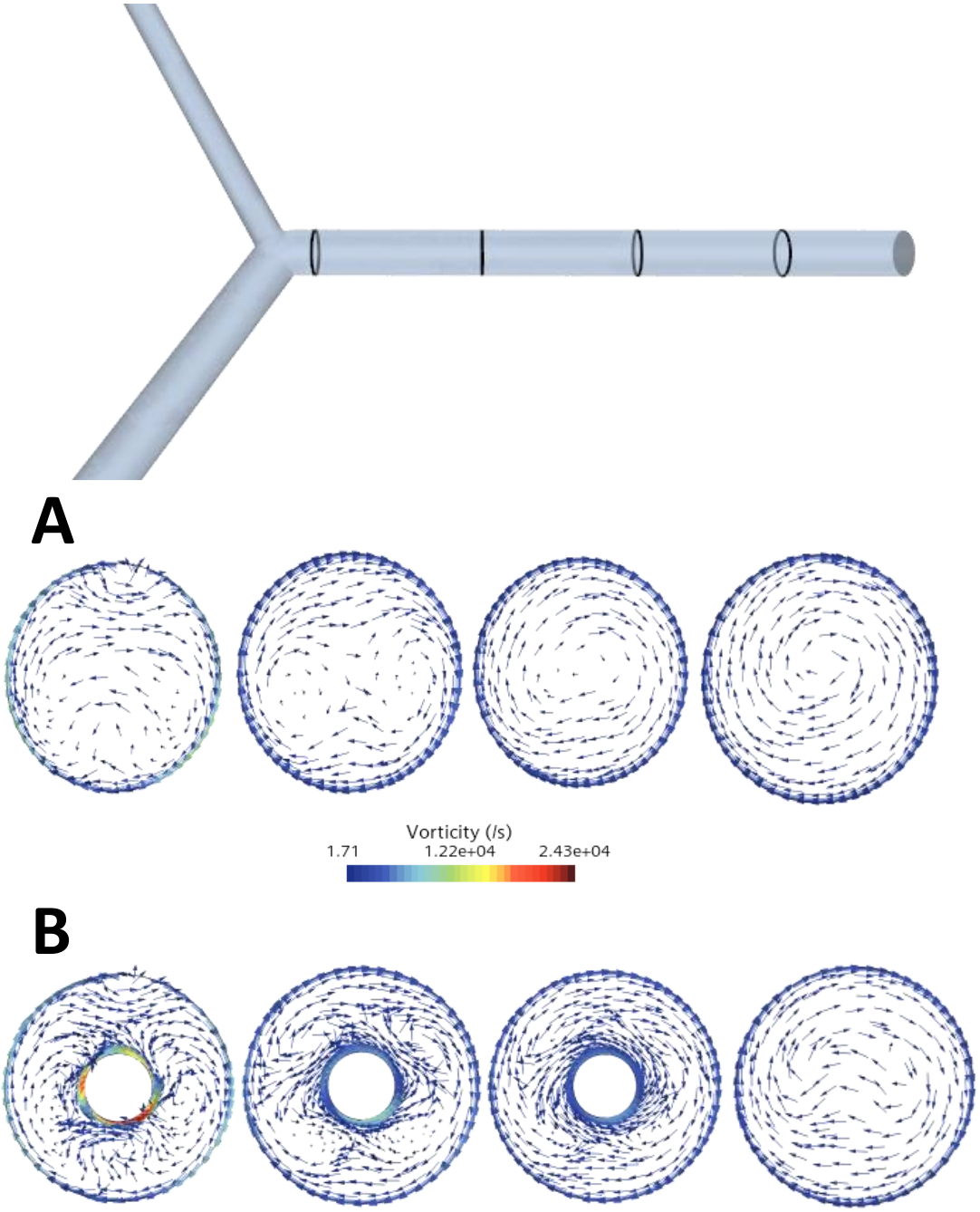

Figure 4.19: Cross-sectional slices of the control geometry show circular flow (A), this is lost on the insertion of the PICC line (B). Positioning of the first slice was chosen arbitrarily, the remaining 3 are 0.02 m apart, to cover the length of the SVC.

Finally, the spiral-like flow within the superior vena cava was studied in greater detail. This is easiest to visualise if the vorticity of the flow is studied (**Figure 4.19**). Vorticity is a microscopic measure of the rotation of any point within a fluid.[608] Any discussion of the mathematics involved is out of scope for this thesis.

In this figure. the first cross-sectional slice for the each set is significantly more complex than the remaining three. This is due to its position within the model of the superior vena cava. Here, blood flow from both brachiocephalic veins is mixing and this disturbs the spiral flow. In the control geometry, as the blood

travels further down the SVC, blood flow becomes more stable, adopts a laminar character and by the position of the final slice through the geometry, spiral flow has clearly been adopted. A clean spiral can be seen in this section (**Figure 4.19**). If the geometry following PICC insertion is considered, the fluid flow in the first section is much more chaotic and complex, this too is due to the mixing of blood flow from both brachiocephalic veins. However, as each slice is studied in turn, the same spiral pattern never develops in this geometry *i.e.,* shows a loss of circular flow, as reported previously by Peng *et al.*[583]

Wall Shear Stress

Wall shear stress is the force that a fluid applies against a surface (here – endothelium and PICC line). For the control geometry, average wall shear stress on the blood vessel is 2.74 Pa. Peak wall shear is 40 Pa, and is found where the three veins join.

Following the insertion of the PICC line, wall shear stress on the blood vessel increases to 3.61 Pa, as the space that the fluid can occupy decreases, and average wall shear stress on the PICC line itself is 4.66 Pa. Furthermore, areas of locally high and low shear can be seen. Areas of high shear exist where the three veins join, unsurprising considering the studies undertaken previously in this thesis. Furthermore, an area of exceptionally high shear (~50 Pa) can also be seen on the PICC line itself. This is in keeping with previous studies.[583]

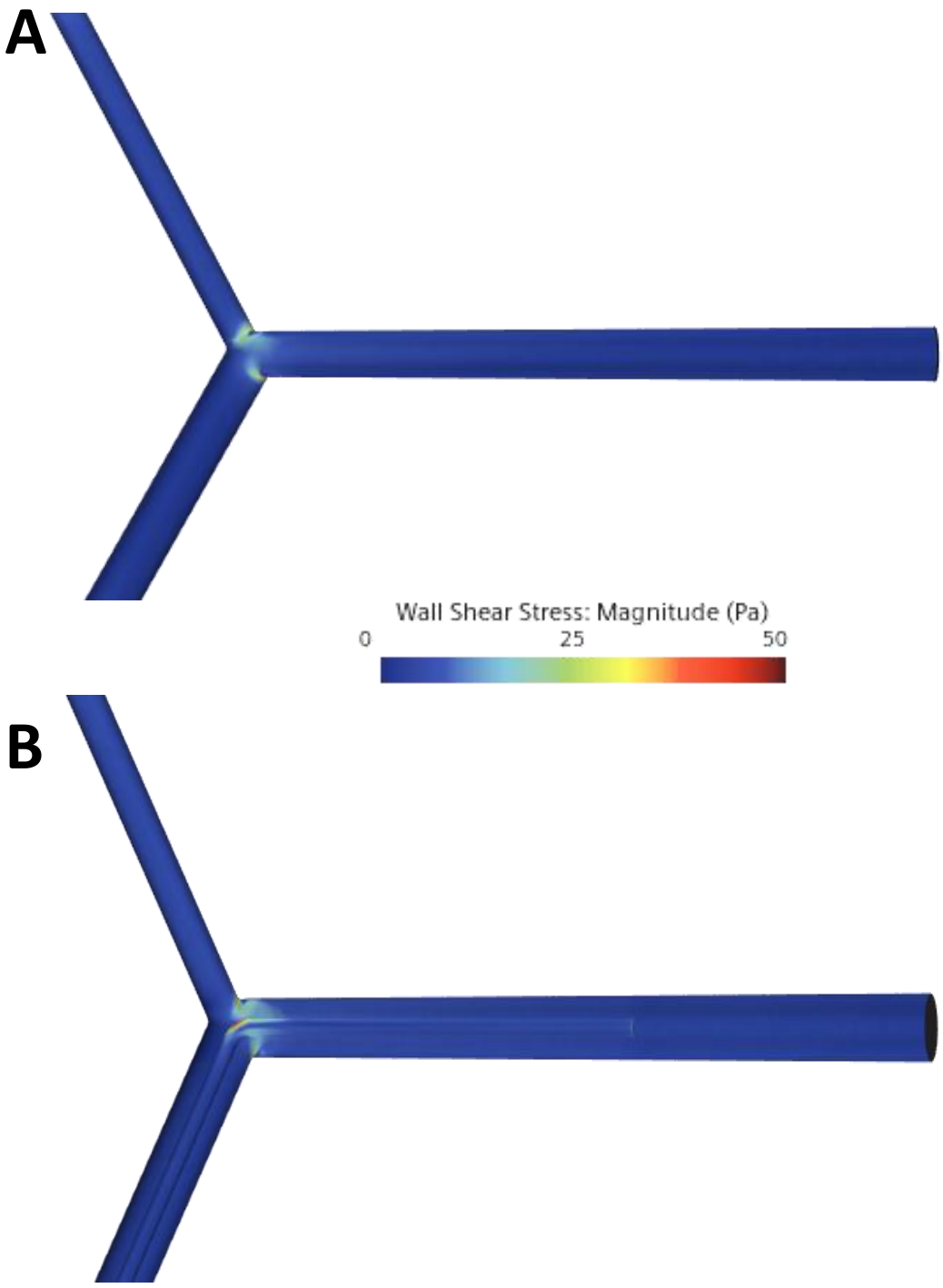

Figure 4.20: Wall shear stress A) Control. B) following PICC insertion.

4.4.2.2 Infusing Fluids via PICC Line

In this section, the impact of infusing fluid (0.9% saline) is considered. The results where 5% glucose is used as the infusion fluid can be found in **Appendix H**. A range of infusion rates will be used (**Table 4.22**).

Fluid velocity and streamlines will be considered first, followed by wall shear stress and then mass fraction of blood.

Fluid Velocity and Streamlines

Irrespective of infusion rate, infusion fluid, lumen shape and size, fluid behaviour is laminar (**Table 4.22**). For the multi-lumen devices used in this chapter, fluid will only be infused down the smallest available lumen. Calculations for this table are in **Appendix C**.

Table 4.22: Flow rates studied in the PICC geometries in this chapter.

	Flow rate (mL hr^{-1})	Velocity (m s^{-1})	Reynolds number (saline)	Reynolds number (glucose)
Single	1185	0.65	512.10	464.10
	600	0.33	260.00	235.63
	300	0.16	126.07	114.25
	150	0.08	63.03	57.12
Double	547	0.24	118.41	107.50
	400	0.18	88.80	80.49
	300	0.13	64.14	58.13
	150	0.07	34.54	31.30
Treble	280	0.85	252.82	229.11
	250	0.76	226.05	204.86
	150	0.46	136.82	123.99
	100	0.31	92.21	83.56

When using the PICC line to infuse fluids, large increases in infusion rate (150ml hr^{-1} to 1185 ml hr^{-1}) lead to comparatively slight changes in fluid velocity within the vein (**Figure 4.21**).

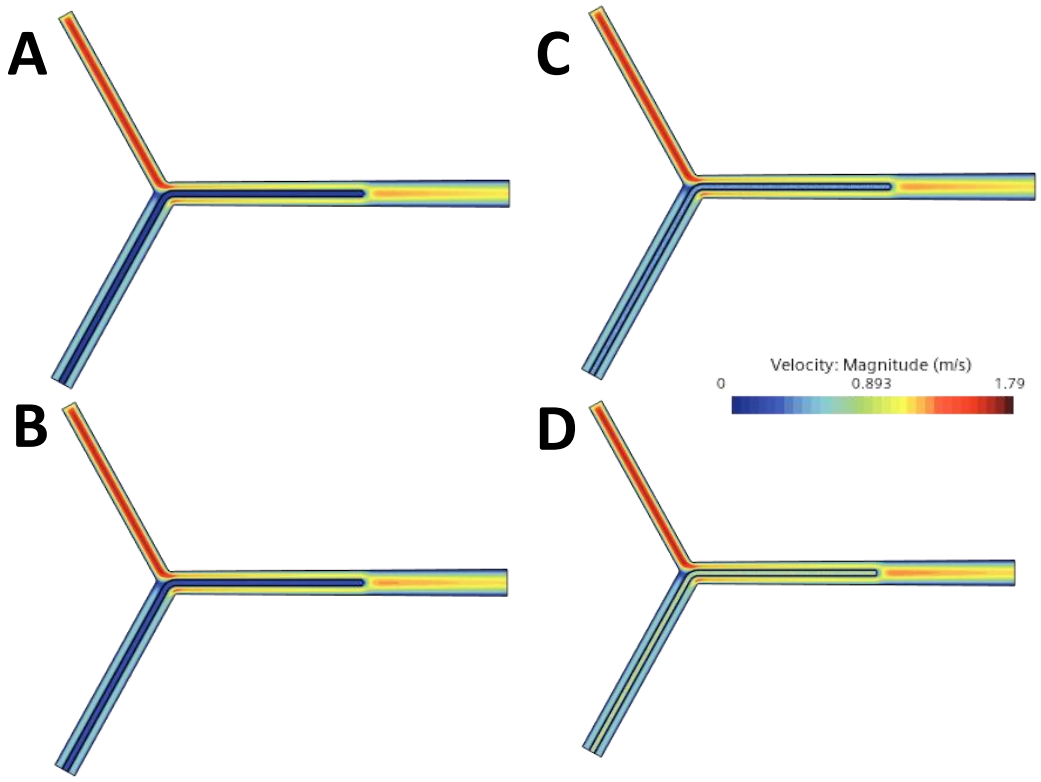

Figure 4.21: Large increases in infusion rate lead to comparatively slight changes in fluid velocity within the blood vessel. Infusion fluid: saline. A) 150 mL hr^{-1} B) 300 mL hr^{-1} C) 600 mL hr^{-1} D) 1185 mL hr^{-1}.

Furthermore, the thickness of the area of locally very low fluid velocity at the tip of the PICC line decreases, inversely as a function of infusion fluid velocity. This is easiest to see in the dual lumen geometry (**Figure 4.22**).

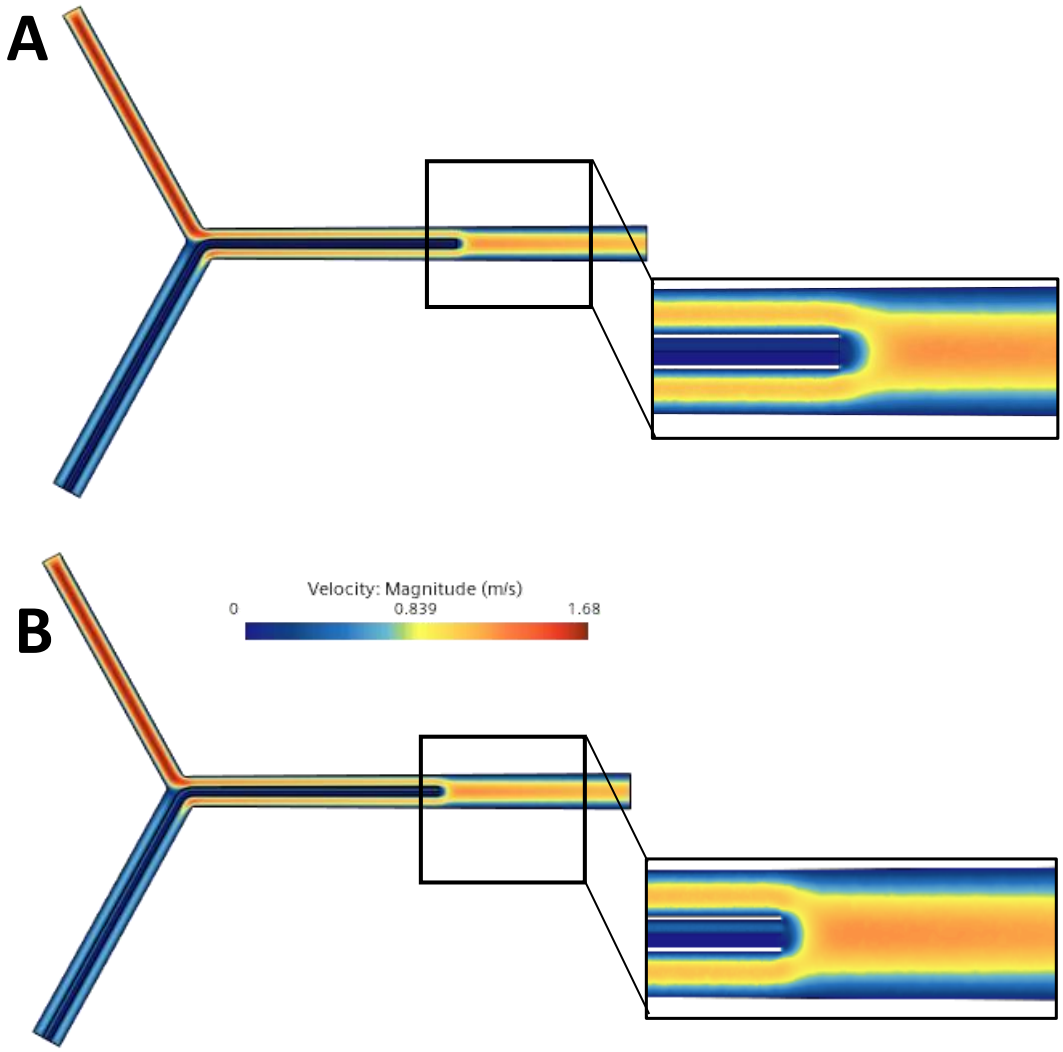

Figure 4.22: Fluid velocity as a function of flow rate. Substantial changes in infusion rate and therefore fluid velocity in the PICC line lead to slight changes in fluid velocity in the blood vessel. Infusion rates of saline in the dual lumen geometry are as follows: A) 150 ml hr^{-1} B) 547 ml hr^{-1} Inset: highlighting the size change of the localised area of low velocity at the tip of the PICC line.

Here, only the streamlines within the PICC line itself are of interest; the recirculation zones within the blood vessel have already been identified, shown and discussed previously (**Figure 4.17, Figure 4.18**). The streamlines at the end of the PICC line usually clearly visualise laminar flow (**Figure 4.23**) It is also interesting to note how the streamlines exit the PICC lines spread equally across the entire area of the outlet, but then are quickly concentrated into a narrow stream.

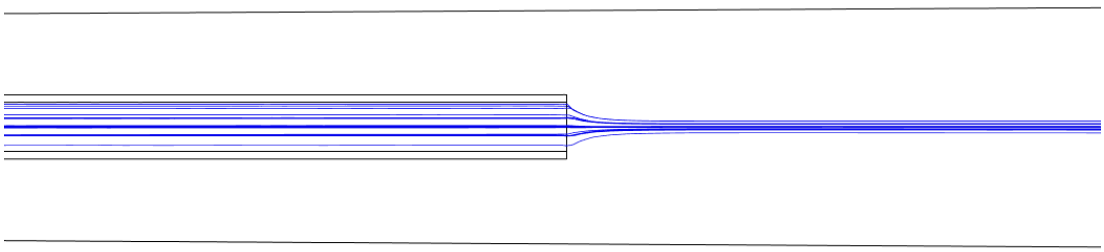

Figure 4.23: Laminar flow is clearly seen on visualisation of streamlines at the end of the PICC line. This behaviour occurs irrespective of flow rate.

However, we additionally see interesting behaviour of the streamlines immediately prior to the PICC outlet in the dual lumen geometry, which suggests the possibility of some sort of recirculation zone (**Figure 4.24**). Vectors were then visualised to help identify the nature, size and orientation of this recirculation zone (not shown).

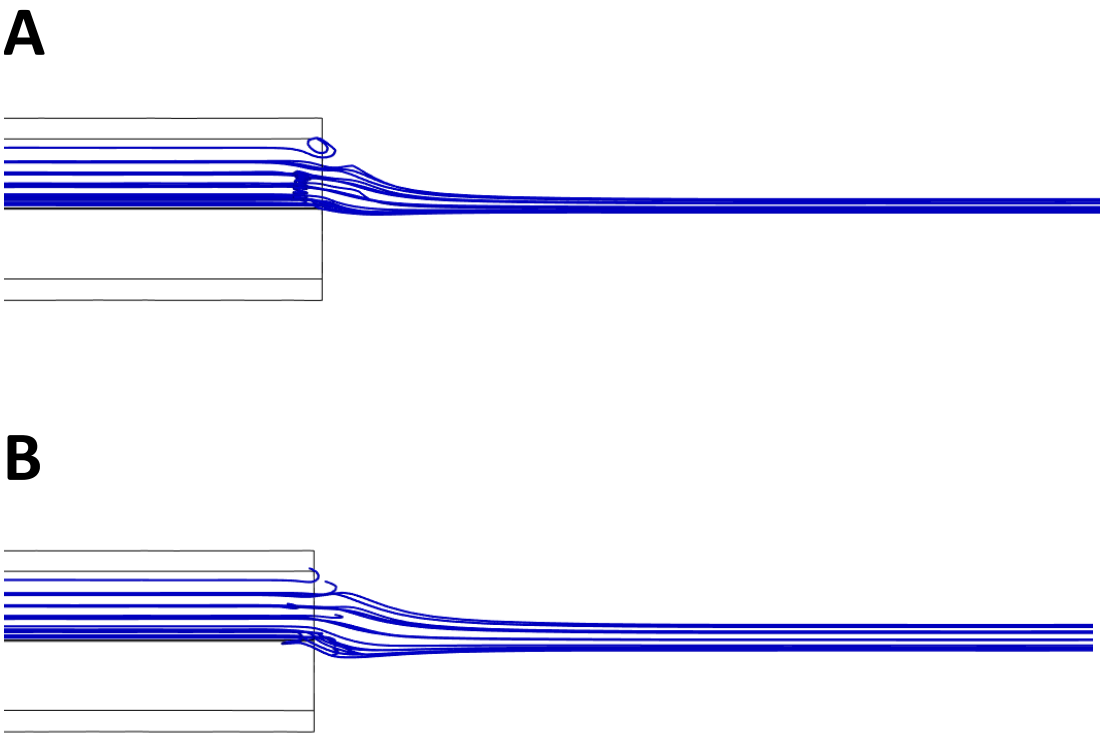

Figure 4.24: Visualisation of the streamlines at the exit of the dual lumen PICC line shows the focussing behaviour discussed earlier. Further, streamlines indicate the presence of a circulation zone. Infusion rates of saline are as follows: A)150 ml hr^{-1} B) 547 mL hr^{-1}.

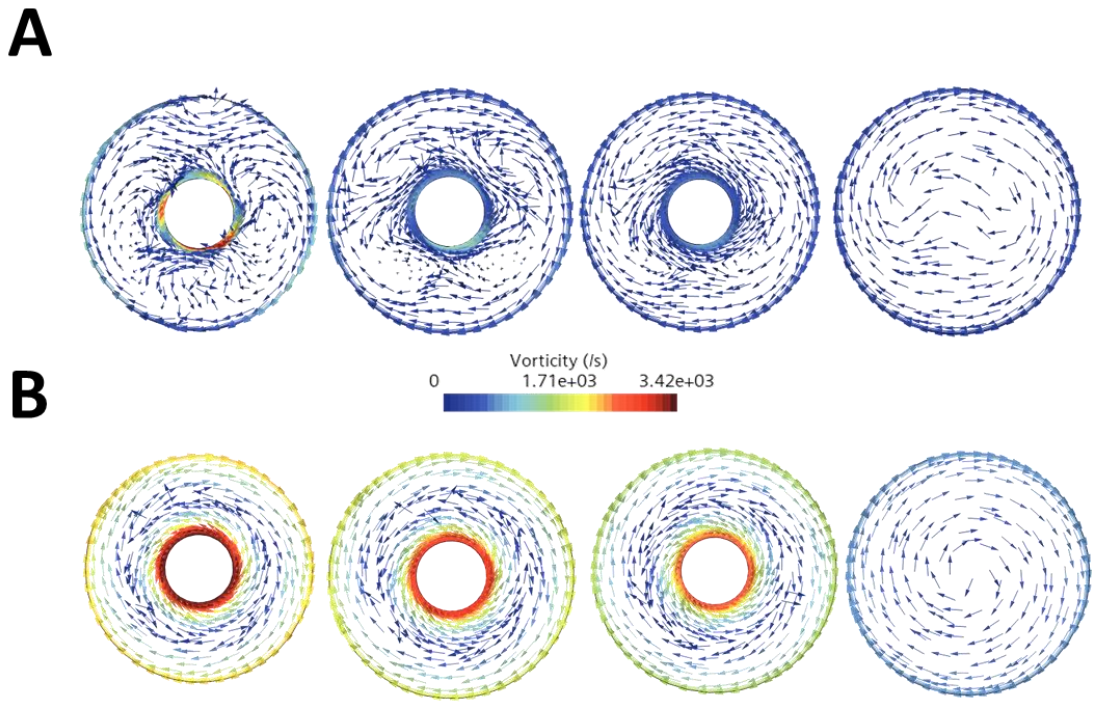

Figure 4.25: Cross-sectional slices of the geometry show circular flow is lost on the insertion of the PICC line (A). Spiral flow returns when the PICC line is used for the infusion of fluids (B). Positioning of the first slice was chosen arbitrarily, the remaining 3 are 0.02 m apart, to cover the length of the SVC.

Again, the circular flow of the geometry was assessed (**Figure 4.25**). As before, circular flow is disturbed by the insertion of the PICC line, but once the line is used for the infusion of fluids, the return of circular flow is seen in the final slice. This was unexpected, as similar studies from Peng *et al.*, do not study the forces present whilst the central line is being actively used for the infusion of fluids.[583] This result then highlights a further gap in the literature where additional studies would be necessary to confirm the results seen here.

Wall Shear Stress

Wall shear stress is a measure of the forces that the fluid exerts on the wall of the blood vessel and vice versa. In **Figure 4.26**, it is shown that there is almost no change of wall shear stresses within the domain, irrespective of infusion rate – this result is unsurprising considering those reported for fluid velocity in **Figure 4.21**. What is observed, however, are the same localised areas of high wall shear stress on the blood vessel geometry itself, as well as on the PICC line following insertion – as previously discussed in **Figure 4.20**. Furthermore, wall shear stress within the superior vena cava falls dramatically once the vessel is no longer obstructed by the PICC line, this is again in-keeping with previous results.

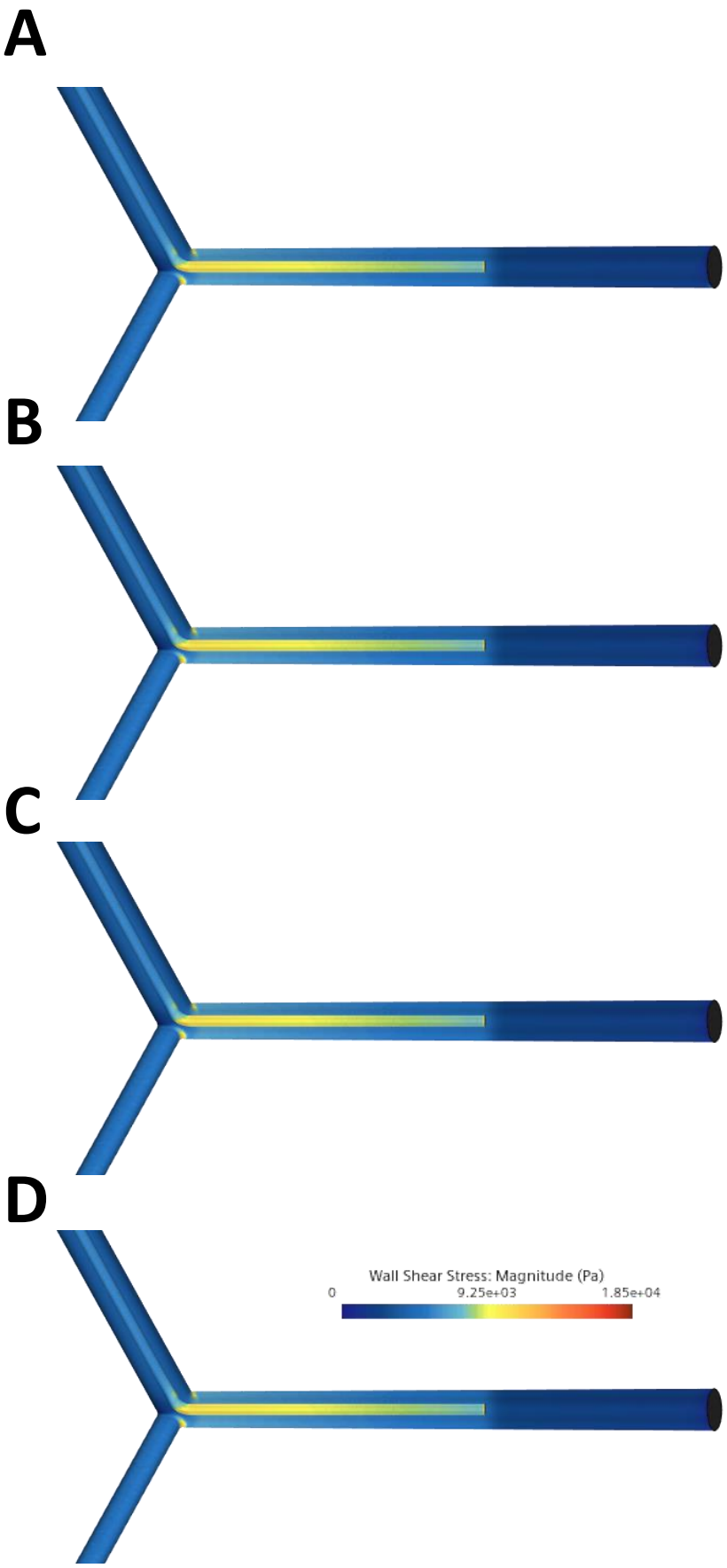

Figure 4.26: Wall shear stress varies as a function of infusion velocity. Infusion rates of 0.9% saline are as follows: A) 150 mL hr^{-1}, B) 300 mL hr^{-1} C) 600 mL hr^{-1} D) 1185mL min^{-1}.

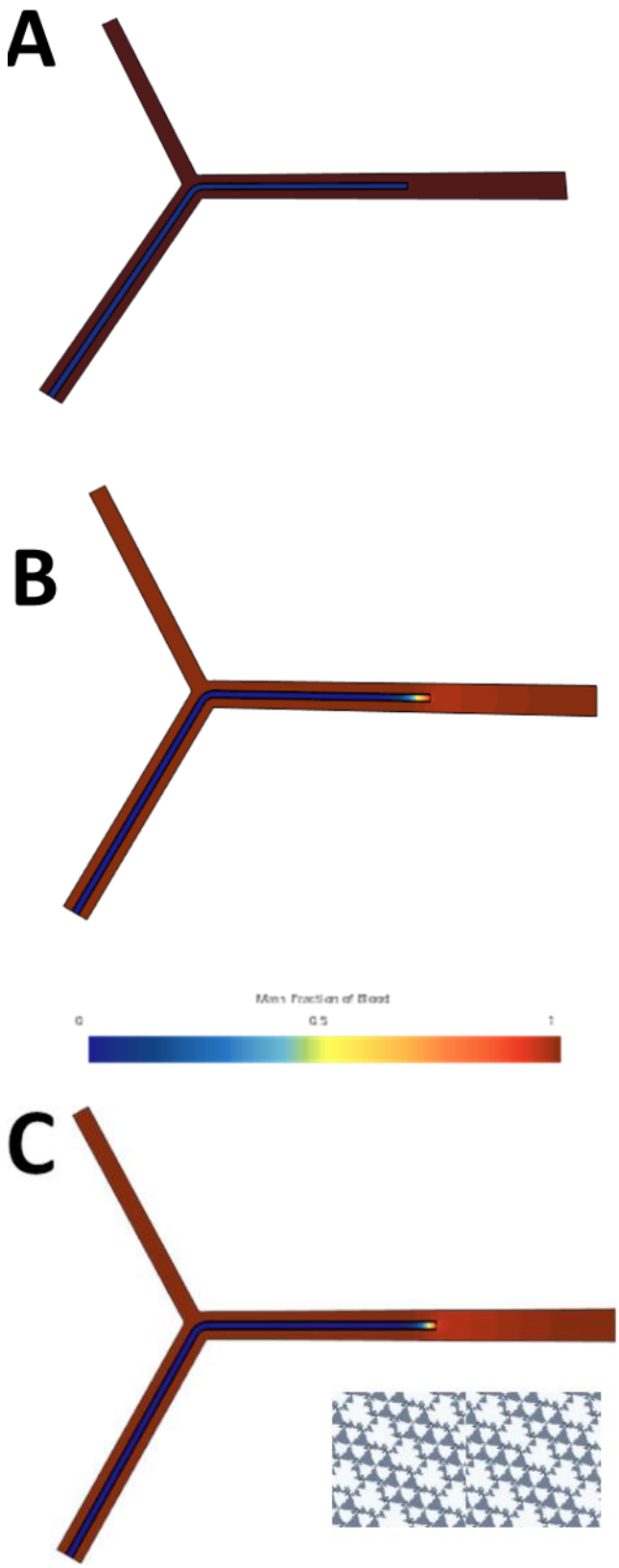

Figure 4.27: Mass fraction of blood. As infusion rate increases, a greater proportion of the blood vessel distal to the needle outlet is cleared of blood and replaced by 0.9% saline. A) No infusion B) 150mL hr^{-1} C 1185mL hr^{-1} **AR**$^{+}$

Mass Fraction of Blood

Mass fraction of blood has been investigated to understand the mixing of both blood and the infusion fluid. This gives a value between 0 and 1, where 1 is equal to 100% blood, and 0 is 100% infusion fluid. **Figure 4.27** shows the impact of infusion rate on mass fraction of blood after a set time (4 seconds). Like the results shown previously, an area at the tip of the PICC line is partially cleared of blood and replaced with infusion fluid. This is easier to see where infusion rate is 1185 mL hr^{-1} – and this simulation can be explored further *via* augmented reality. Like the PIVC geometry studied previously, there is a small amount of mixing of blood and infusion fluid proximal to the outlet.

Residence Time

Residence time is a measure of how long a fluid particle spends within the domain (*i.e.,* the geometry under study). Here, it has been measured using massless Lagrangian particles – these effectively function like a tracer dye. Particles were introduced at both the blood vessel and PICC inlet and then followed until all particles had exited the domain (not shown), Data for the minimum (*i.e.,* first particle to escape) residence times for each flow rate can be found in **Appendix H**. These results show as infusion rate increases, residence time decreases, corroborating those shown by the mass fraction of blood presented previously, since the greater the infusion rate, not only do particles introduced *via* the needle leave the domain faster, but blood is also cleared quicker and replaced by infusion fluid.

Summary

In this section, the results presented here have shown that the simulation accurately understands the PICC line is to be considered an obstruction to blood flow from the brachiocephalic (innominate) veins. This has been shown not only by an increase in peak fluid velocity as the blood vessel is occluded, but also a corresponding increase in wall shear stress. Assessing vorticity in fluid flow further shows that the spiral flow that is known to exist within the SVC is disturbed by the insertion of the PICC line, but returns when the line is used for the infusion of fluids.

There are a number of ways that this data can be applied in a clinical setting. This work reiterates the conclusions of Nifong and McDevitt, that fluid velocity and flow rate are significantly impacted by the insertion of a PICC line.[525] The altered fluid flow that occurs when a PICC line is inserted, can be reversed when it is used for the infusion of fluids, providing insight into why these VADs are patent for significantly longer than a PIVC (*i.e.,* the area of very low flow velocity is easily disturbed). Finally, for clinically complex patients who require long-term vascular access, computational simulations of their circulatory system could be constructed to find the most suitable combination of VAD and flow rate to prevent undesired effects *e.g.,* thrombus formation.

4.4.2.3 Nanoparticle Behaviour Under Flow

Where particles are infused, in a multi-lumen device, only one lumen is used. Where multiple lumen sizes are available, it has been decided that the smallest

of the available lumen will be used. The other lumen are assumed to be used for fluids. This assumption has been made to reduce the computational complexity of the simulation, even though this potentially diverges from how these central lines are used clinically – it is theoretically possible that multiple drugs could be infused simultaneously down multiple lumen devices. Set up for these CFD-DEM simulations is as described previously. Nanoparticles are introduced 0.1 cm parallel to the outlet, again, to reduce the real-world time that needs to be simulated.

For brevity, only the results for a single- and triple lumen device at their fastest infusion rates (and where the infusion fluid is saline) are shown here. The results for the remaining flow rates outlined previously, and/or those where glucose is the infusion fluid can be found in **Appendix H**. Here, only the nanoparticle behaviour is of interest. Particle velocity and particle shear stress will be studied in further detail, since fluid shear is known to play a significant role in influencing protein corona composition.

Single Lumen

Particle velocity is a measure of how fast the particles within the simulation are moving; this depends on several factors including mass and buoyancy of the particle as well as drag force. In this simulation, the particles rapidly adopt the expected parabolic shape, where the fastest moving particles are in the centre of the PICC geometry (**Figure 4.28**). As a consequence of the shape of this geometry, it gives rise to the apparent presence of several rows of particles all with similar velocities. Unlike the PIVC geometry studied earlier, particle velocity rises as the particles leave the PICC line and enter the blood vessel. This is as expected from the fluid velocity behaviour shown in **Figure 4.21**.

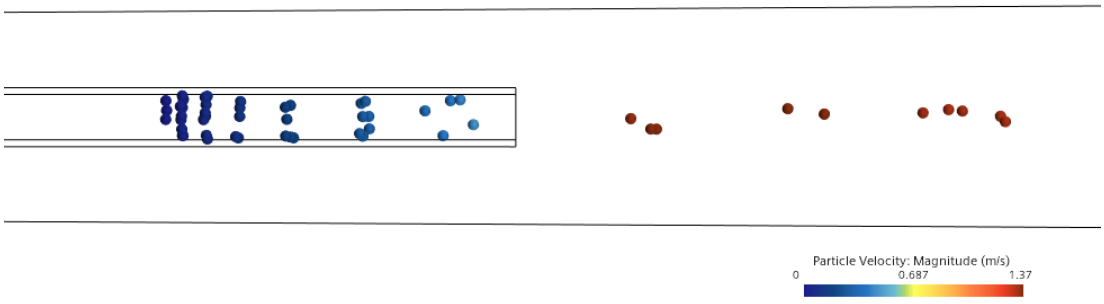

Figure 4.28: Particle velocity varies as a function of infusion rate and carrier fluid (saline, 547 mL hr^{-1}). The particles rapidly show an increase in velocity on entering the blood vessel.

Particle shear stress is a measure of friction between the fluid and the particles suspended within; this is believed to be one of the key forces responsible for altering the composition of the protein corona around nanoparticles and therefore is a key parameter for the microfluidic device developed in the following chapter. **Figure 4.29** shows a clear area of high particle shear immediately proximal to the PICC line outlet. Particle shear stress then falls once the nanoparticles have entered the bloodstream. Further, **Figure 4.30**

shows that the maximum particle shear stress is inversely proportional to input velocity.

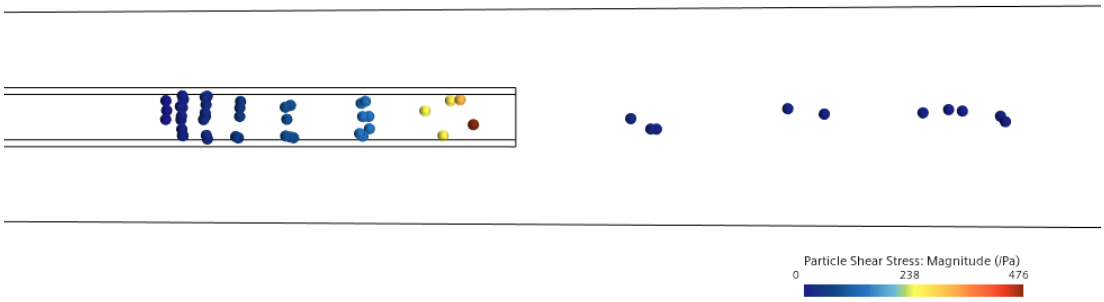

Figure 4.29: As particles leave the PICC line, particle shear stress falls rapidly, despite the increase in particle velocity.

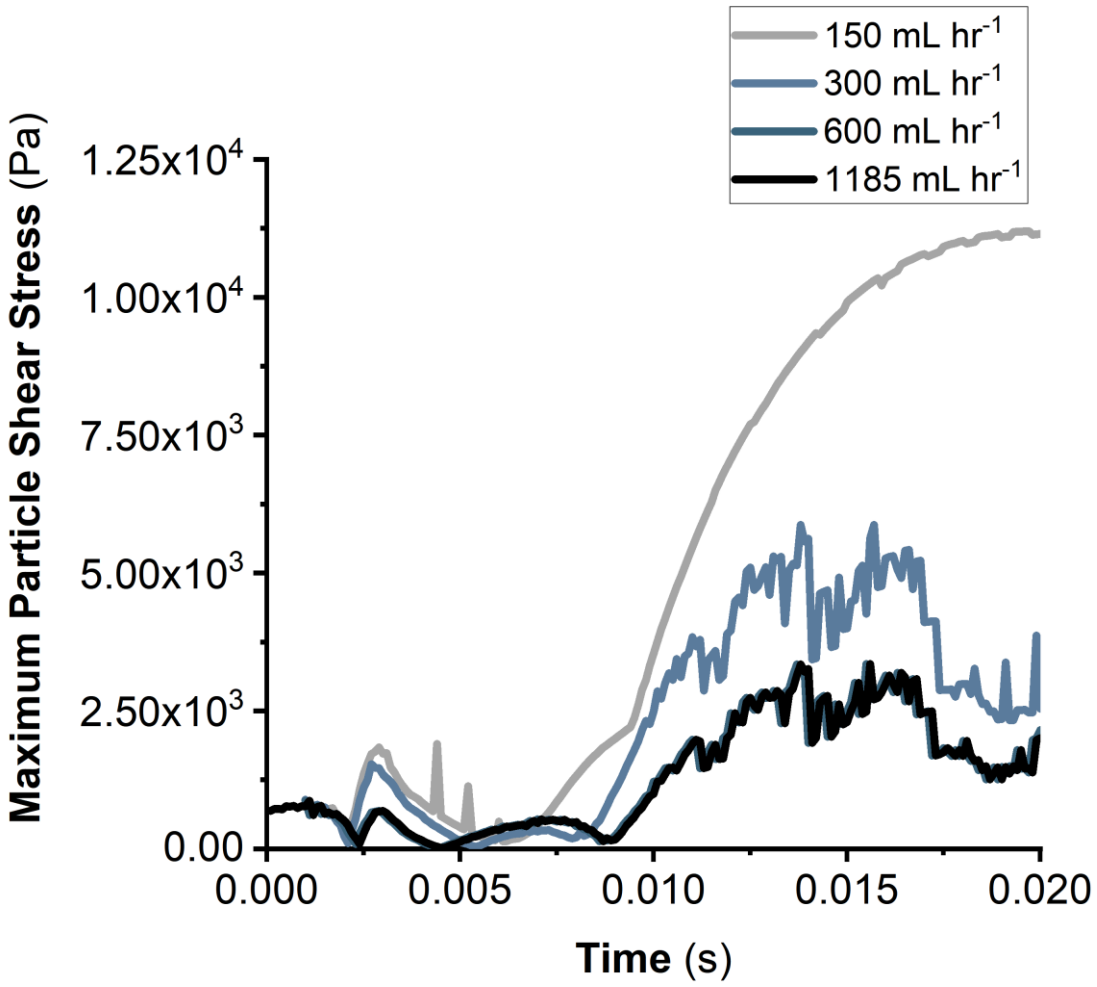

Figure 4.30: Particle Shear stress as a function of physical time. Here, particle shear stress is inversely proportional to fluid velocity. Here, only the results where saline is used as the infusion fluid are shown, the results for glucose are available in **Appendix H**.

Triple Lumen

The triple lumen PICC geometry has also been studied to determine the influence of infusion rate on particle velocity and particle shear rate with this geometry. **Figure 4.31**, like the single lumen geometry studied earlier, shows

that particle velocity increases on exiting the PICC line. Again, this is consistent with previously reported results on fluid velocity.

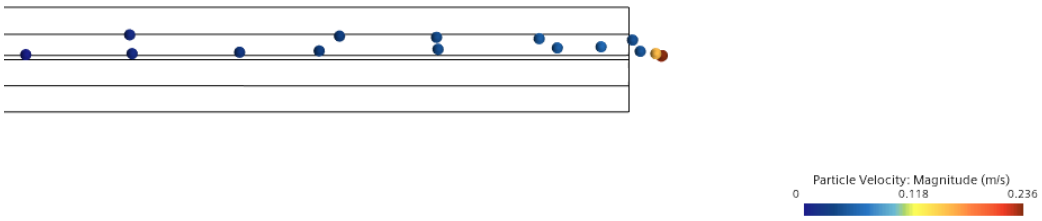

Figure 4.31: Particle velocity varies as a function of infusion rate and carrier fluid (saline, 280 mL hr^{-1}). The particles rapidly show an increase in velocity on entering the blood vessel.

Consistent with results for both the single lumen PICC line and PIVC geometries studied earlier in this work, particle shear stress is seen to be at its highest, immediately prior to exiting the VAD (**Figure 4.32**), and falls once the particles enter the blood vessel.

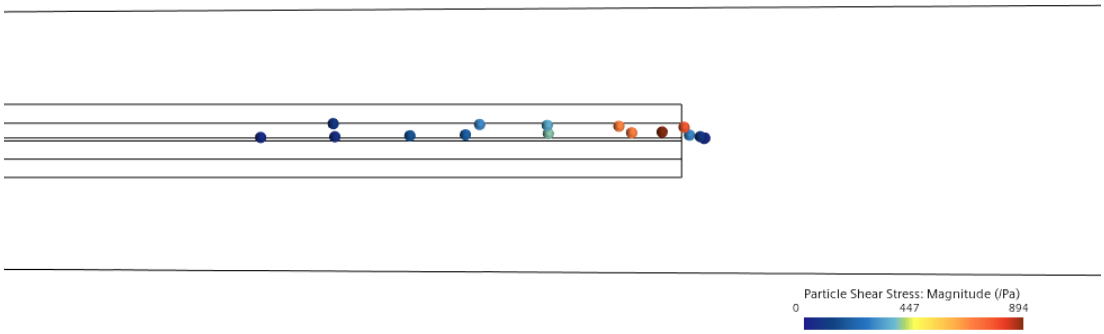

Figure 4.32: Particle shear varies as a function of infusion rate and carrier fluid (saline, 280 mL hr^{-1}). The particles rapidly show an increase in shear rate on approach to the exit of the PICC line.

In **Figure 4.33**, maximum particle shear stress is shown to vary proportionally to fluid velocity. Where particle shear stress begins to fall is consistent with particles beginning to leave the PICC line and enter the blood vessel.

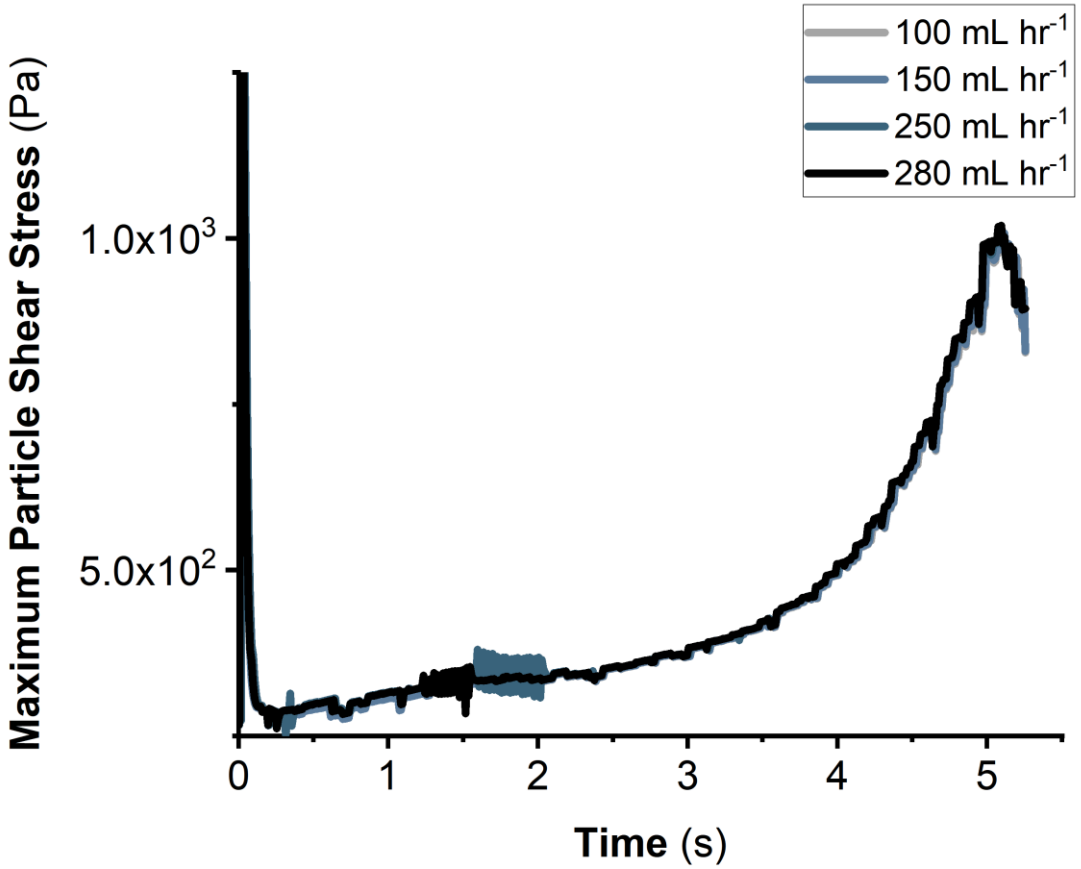

Figure 4.33: Particle shear stress as a function of time. In the triple lumen geometry, particle shear stress covers a small range and differences between various input velocities are challenging to see.

4.4.3 Principal Component Analysis

Principal component analysis (PCA) is a particularly important technique in the field of multivariate analysis. It enables a large dataset containing many variables to be compressed into a much smaller one, without losing any of the information contained within the original data set.[609] These new variables (principal components) are weighted averages of a suitable combination of the initial variables; since the weighting and the principal component are known, the original variables can be recovered.[609] Through a series of pre-processing steps, a complex multi-component data set can potentially be condensed into as few as two principal components – this is then easily plotted and understood. Furthermore, it enables comparisons to be made that may not be possible *via* univariate analysis. Detailed discussion of the complex mathematics which underpins this technique is outwith the scope of this thesis, but is discussed at length in the tutorial review from Bro and Schmilde.[609]

PCA is used here to initially determine if there is any similarity between the vascular access devices studied in this chapter. The data table used for PCA is given in **Appendix H**; the 15-dimensional space that would be necessary to plot all these variables is just far too complex to fathom. PCA can simplify this down to just two attributes (Principal Components) that can be plotted and more easily understood. Where the hydrodynamics of the simulations run previously are similar, they will appear as clusters. Additionally, the correlation matrix in **Appendix I**, shows significant correlation between a number of variables.

The data analysis here will be undertaken in a stepwise fashion, initially just considering fluid-related variables, particle-related variables and then both together. This methodology was chosen, since it was of interest to see whether the simulations needed to consider particle parameters, or if there was enough useful information when only fluid parameters are considered, such that these far more simple and therefore far faster simulations (in terms of both set up and running time) could be used instead. Scree plots are used in each case to determine the number of principal components necessary to explain a reasonable amount (~80%) of variance in the data. Once these principal components are identified, then the loadings of the initial variables can be explored. Further, the space that holds most of the simulations in this chapter is then explored; initially in terms of principal components, before relating these back to several parameters including average fluid shear stress (**Appendix J**). These newly calculated parameter values are then used as operating ranges for the microfluidic device developed in **Chapter 5**.

4.4.3.1 Analysis of Fluid-related Parameters

The first stage of the principal component analysis is to import the data. Next the PCA generates a scree diagram (**Figure 4.34**). This scree diagram consists of two lines, and shows the amount of variance explained in the data by each principal component (blue line), and how much variance is explained cumulatively by that number of principal components (black line). Here almost 91% of the variance can be explained by just two principal components; 96%

can be explained by 3. In this case, 2 principal components are more than adequate to condense the data set into something more manageable and easier to visualise (**Figure 4.36**).

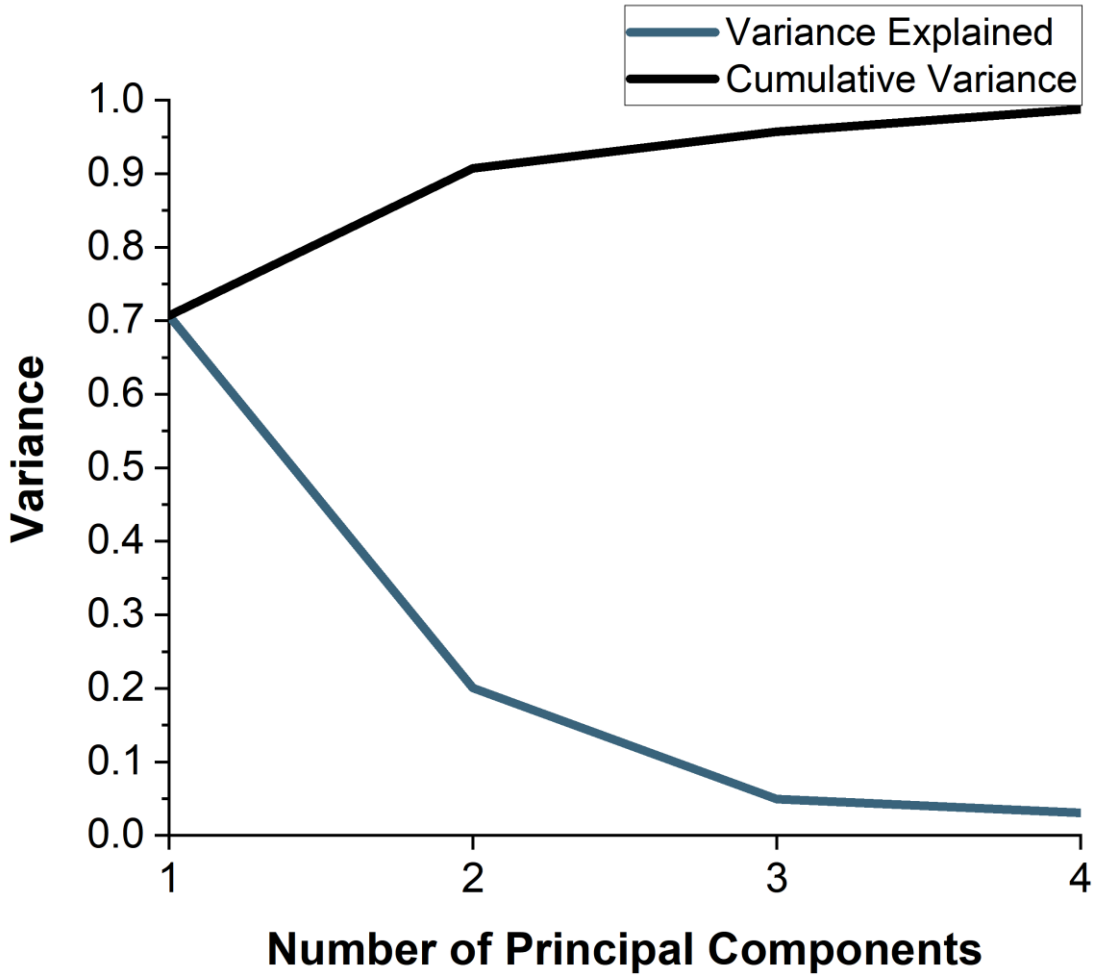

Figure 4.34: For the fluid-only parameters, two principal components are necessary to cover 90.7% of the variance in the data set. Variance explained cumulatively (black line), variance explained by each principal component (blue line).

These principal components consist of a weighted combination of the initial set of variables. For the fluid-only analysis, these weightings are given in **Table 4.23**, and are shown as a loadings plot in **Figure 4.35**.

Table 4.23: The weightings used for each factor to generate the principal components for the analysis of fluid-only parameters.

Factor	PC1	PC2
Input Velocity	0.40698	-0.00355
Maximum Velocity	0.41187	0.03494
Average Velocity	0.39091	-0.03377
Maximum Fluid Shear	-0.07007	0.71178
Average Fluid Shear	0.41488	0.02316
Maximum Wall Shear Stress	0.38705	0.23689
Average Wall Shear Stress	0.37437	0.21585
Minimum Fluid Residence Time	-0.21195	0.62270

The combinations of variables to make up each principal component can also be explored in further detail. The larger the **absolute value** of each variables weighting, the larger the contribution it makes to the principal component. Therefore, in **Figure 4.35**, it can be seen that PC1 is primarily composed from the variables related to fluid velocity as well as wall shear stress. PC2 on the other hand, is much more influenced by maximum fluid shear and minimum residence time.

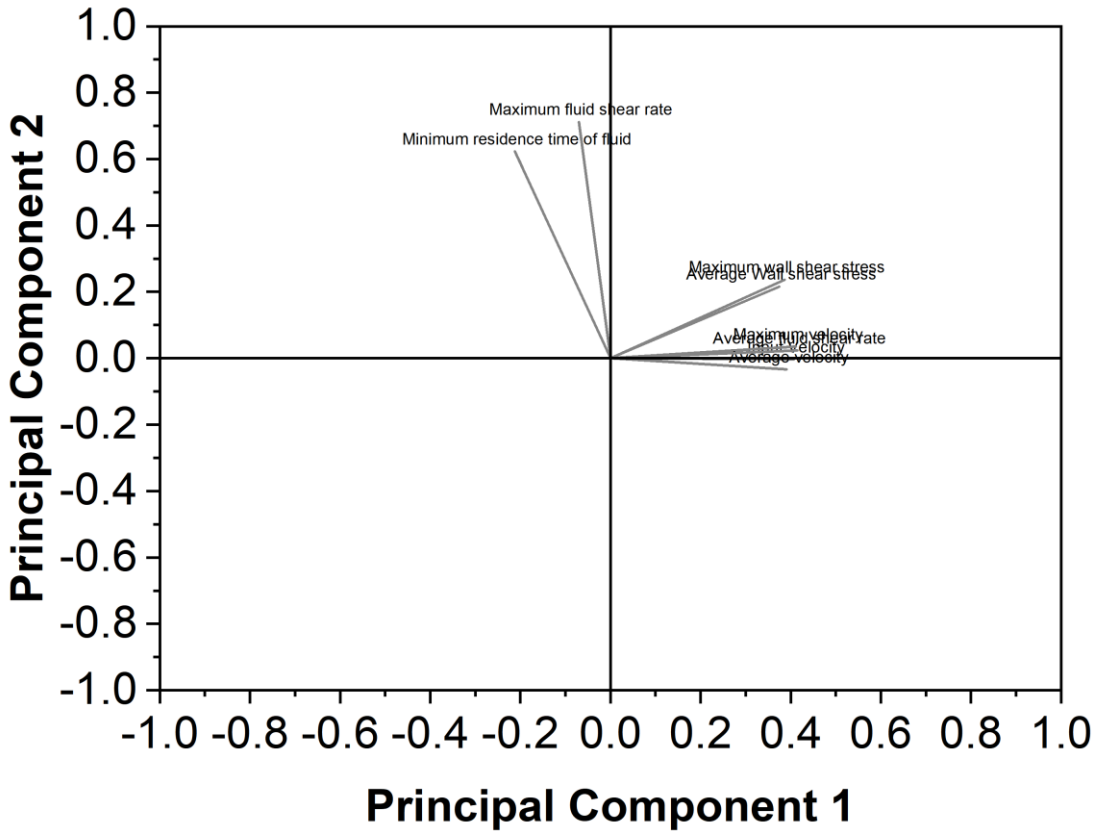

Figure 4.35 Loadings plot for fluid-only parameters. It is shown that PC1 is primarily composed from the variables related to fluid velocity as well as wall shear stress. PC2 on the other hand, is much more influenced by maximum fluid shear and minimum residence time.

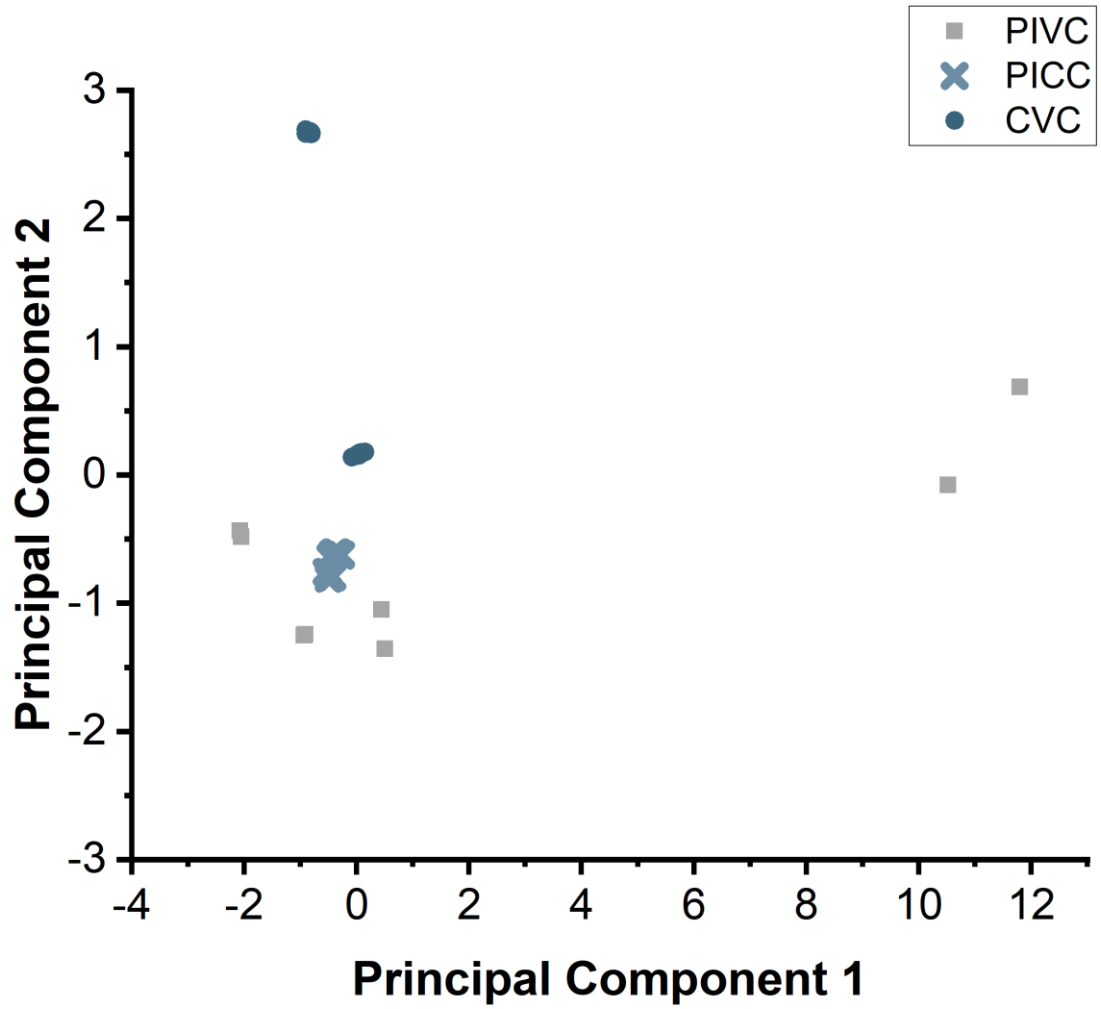

Figure 4.36: A scatter plot of PC1 vs PC2 for fluid-only parameters.

The PCA plot of the fluid-related parameters enable interesting insights into the data obtained so far in this work to be developed, which were not expected by the author (**Figure 4.36**). Considering that both PICC and CVC lines end within the SVC, overlap between these central lines would be unsurprising. This plot shows no overlap between the PICC and CVC lines studied in this work, when fluid-only parameters are considered.

The apparent outliers in the PIVC set correspond to those for the 300 mL min^{-1} "flushes". These simulations use far higher fluid velocities than the remainder of the set, which corresponds to higher fluid velocity, shear rate and shorter minimum residence time, leading to far larger values for PC1. Further, the wide range of input velocities used for this geometry give rise to the "stretched" appearance of the cluster.

4.4.3.2 Analysis of Particle-related Parameters

Analysis of the particle-related parameters alone was undertaken since it was of interest to determine whether fluid-only simulations would be adequate to obtain the necessary input parameters for the microfluidic device designed in **Chapter 5**, or if *in silico* studies of particle parameters were also required. Analysis has been undertaken in the same way as reported previously.

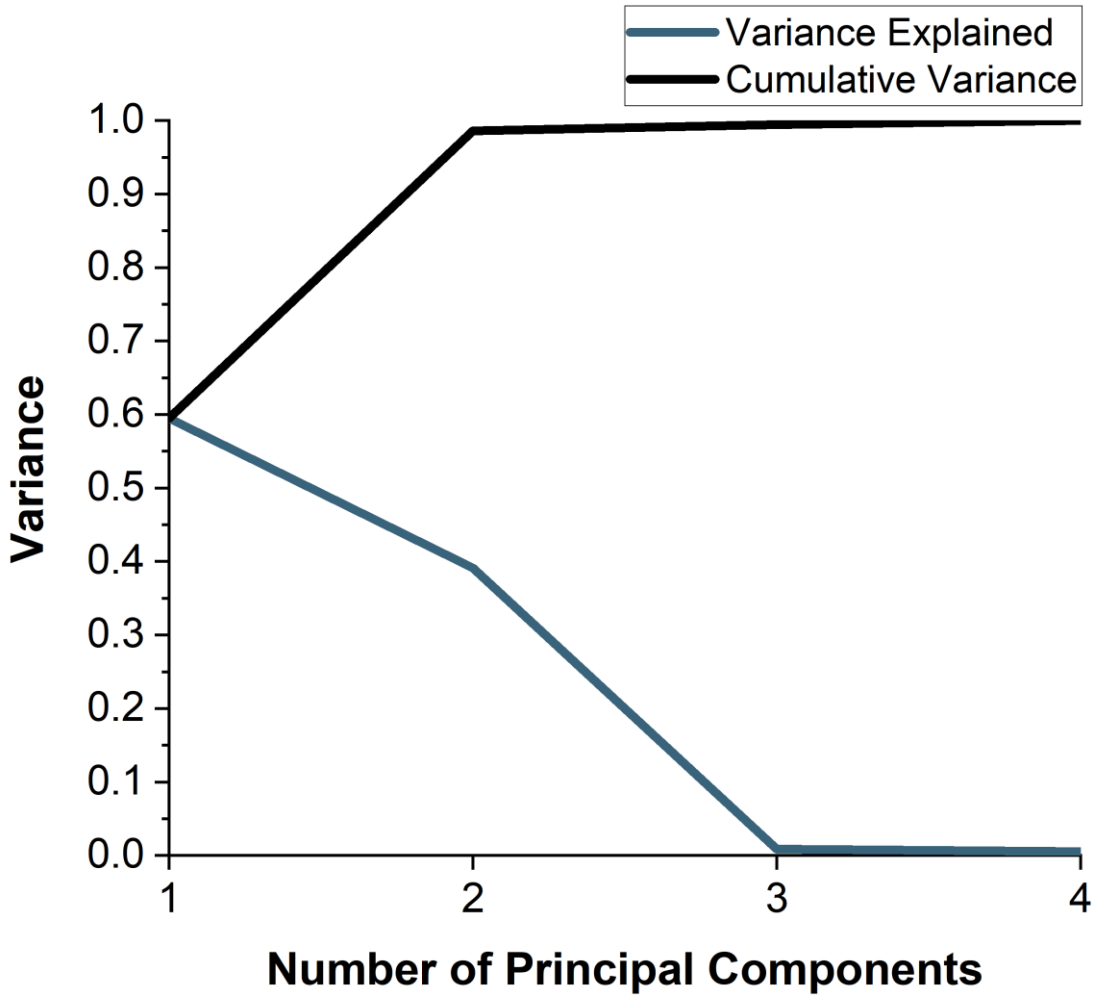

Figure 4.37: For the particle-only parameters, 2 principal components are necessary to cover 98.6% of the variance in the data set. Variance explained cumulatively (black line), variance explained by each principal component (blue line).

Like the fluid-only parameters reported earlier, only two principal components are required to explain >80% of the variance in the data set. Here (**Figure 4.37**) 98.6% of the variance can be explained by just two components. The weightings of each particle-related variable is given in **Table 4.24**, and shown as a loadings plot in **Figure 4.38**.

Table 4.24: The weightings used for each factor to generate the principal components for the analysis of particle-only parameters.

Factor	PC1	PC2
Maximum Particle Velocity	0.45393	0.56407
Average Particle Velocity	0.52996	0.4486
Maximum Particle Shear Stress	0.50612	-0.48986
Average Particle Shear Stress	0.50688	-0.48796

The combinations of variables for each principal component was then studied in further detail. From **Figure 4.38**, it is the absolute values of each variables weighting that is of interest. PC1 consists mostly of average particle velocity, whilst PC2 comprises mostly of maximum particle velocity. Particle shear stress-related variables are almost equally split over both principal components.

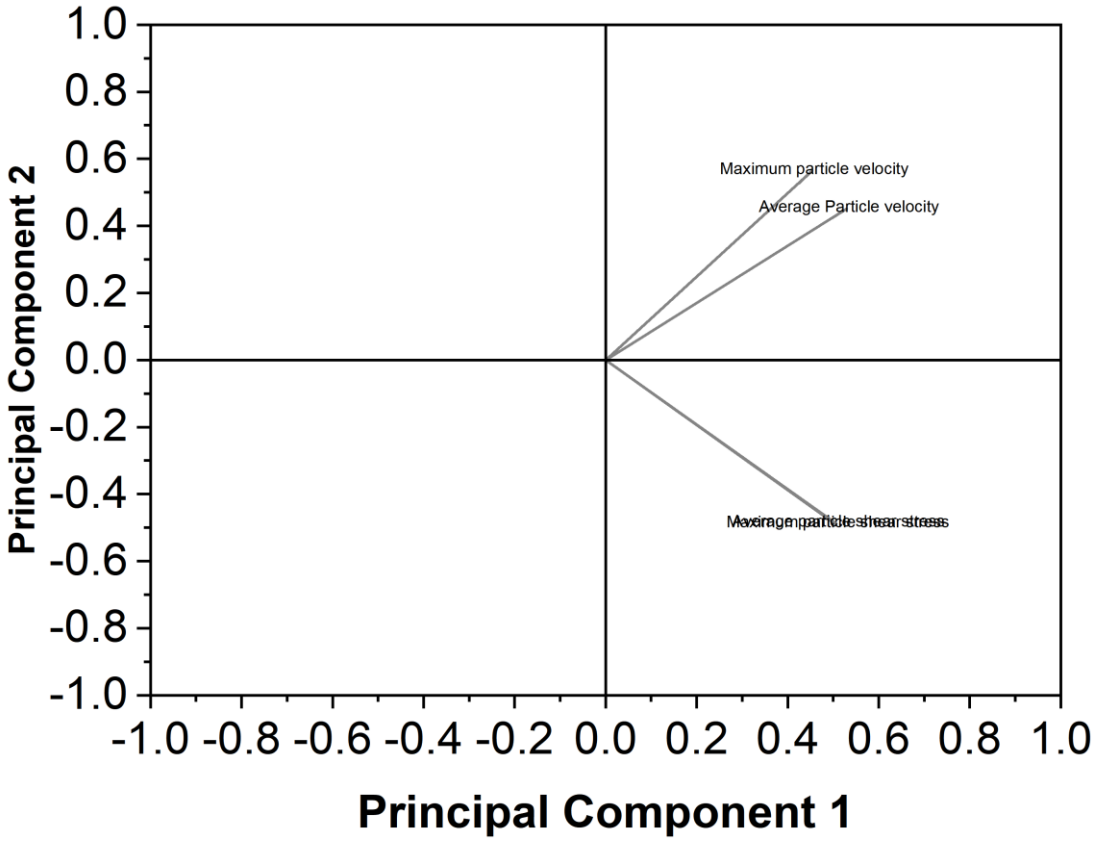

Figure 4.38: Loadings plot for particle-only parameters. It is shown that PC1 is largely comprised of average particle velocity, whilst PC2 is mostly maximum particle velocity. Particle shear stress-related variables are almost equally split over both principal components.

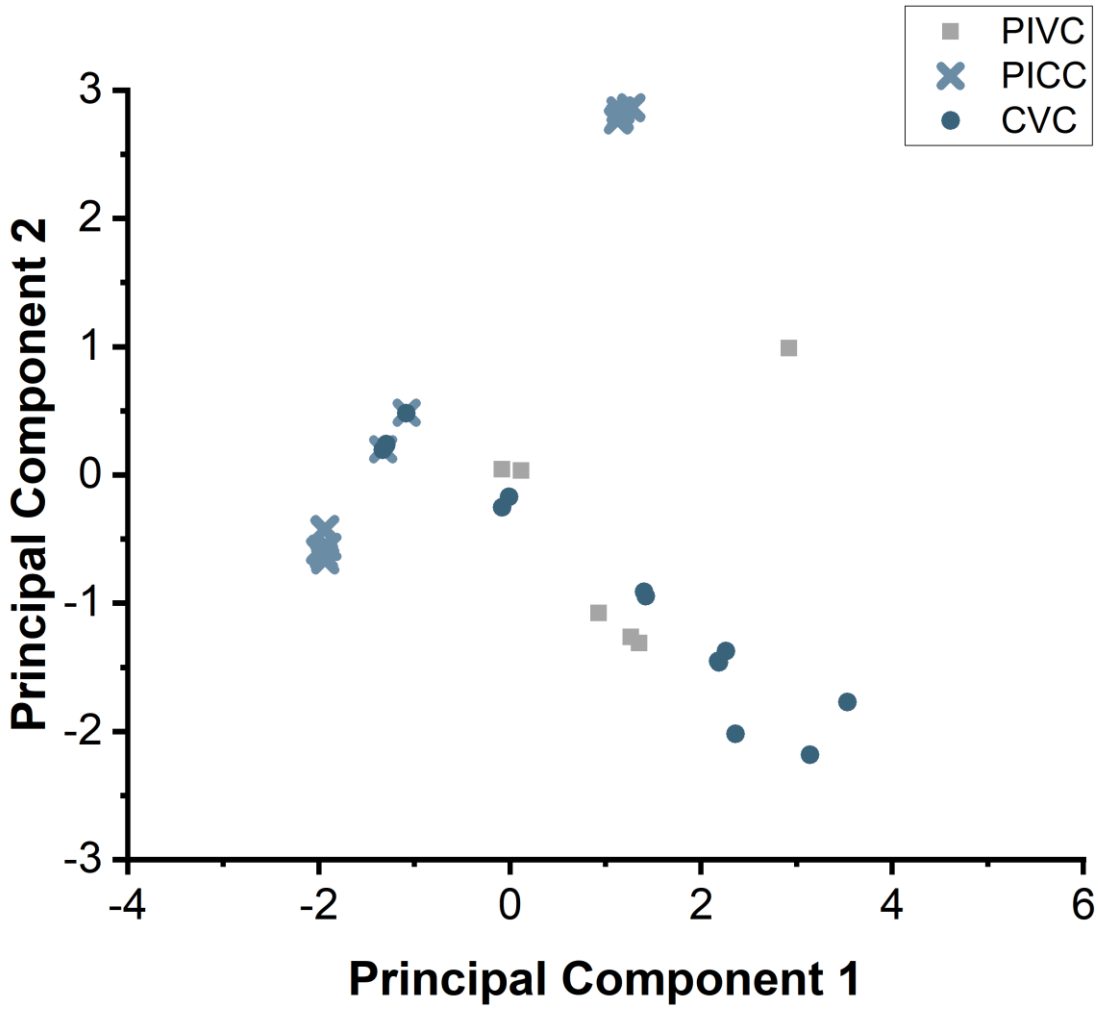

Figure 4.39: A scatter plot of PC1 against PC2 for the particle-only analysis. The PICC line geometries in this work appear to behave very differently to the others.

When the particle-only parameters are considered, the scatter plot of the first two principal components looks quite different to that for the fluid-only parameters (**Figure 4.39**). PC1 varies much less in this case, than it does in **Figure 4.36**, and all the data points seem to fit on the same line *i.e.,* that there is a stronger relationship between them. The small cluster of PICC-outliers where PC2 is approximately 3, has been probed in further detail, but a conclusive explanation as to why these points lie so far from the remainder of the data set has remained elusive. There appears to be no consistent infusion rate, infusion fluid nor geometry between all the points in this group.

4.4.3.3 Analysis of Fluid and Particle Parameters Together

Finally, fluid and particle parameters will be analysed together, to enable understanding to be gathered about the data set as a whole, and to determine whether particle-related parameters play a significant role in influencing the composition of principal components and therefore if these particle-related parameters are of interest as target input parameters for the microfluidic device developed in the following chapter. Analysis will be undertaken as outlined previously, but will then be followed by hierarchical clustering analysis to find the similarities between the simulations run in this chapter.

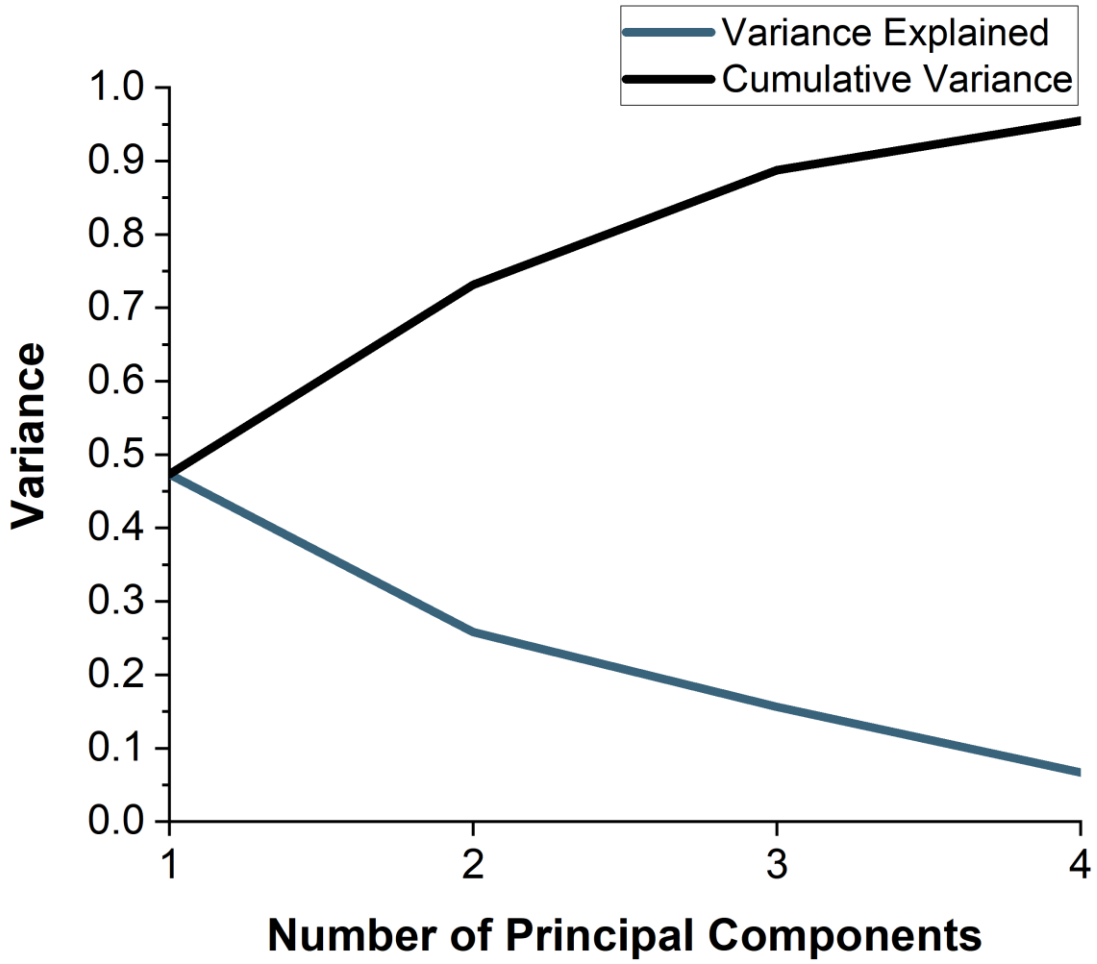

Figure 4.40: For the combined analysis, two principal components are necessary to cover 73.1% of the variance in the data set. Variance explained cumulatively (black line), variance explained by each principal component (blue line).

For the analysis of both fluid and particle parameters, the scree plot is shown in **Figure 4.40**. 2 Principal components are required to explain 73% of the variance in the data set and 88% by 3 – however 3 principal components are more challenging to visualise since this requires a 3D plot.

The two principal components which explain the greatest degree of variance in the data set can then be explored in further detail. The weightings for each variable are reported in **Table 4.25**, and shown by the loadings plot in **Figure 4.41**. In this figure, it is the absolute values of the weightings that are of interest; it can be shown that PC1 is heavily comprised of the fluid-related parameters of fluid velocity, average fluid shear rate and wall shear stress, whilst PC2 is mostly particle-related parameters. These weightings also further suggest that it is the fluid-related parameters that are more important than the particle-related ones, since PC1 represents a greater amount of variance in the data set than PC2.

Table 4.25: The weightings used for each factor to generate the principal components for the analysis of fluid and particle parameters.

Factor	PC1	PC2
Input Velocity	0.402748	0.088
Maximum Velocity	0.407357	0.098945
Average Velocity	0.394039	-0.0627
Maximum Fluid Shear	-0.08701	0.441783
Average Fluid Shear	0.411308	0.07846
Maximum Wall Shear Stress	0.381102	0.157642
Average Wall Shear Stress	0.372332	0.076507
Minimum Fluid Residence Time	-0.22322	0.317474
Maximum Particle Velocity	-0.01071	0.174458
Average Particle Velocity	-0.02147	0.274745
Maximum Particle Shear Stress	-0.0556	0.5299
Average Particle Shear Stress	-0.04979	0.508918

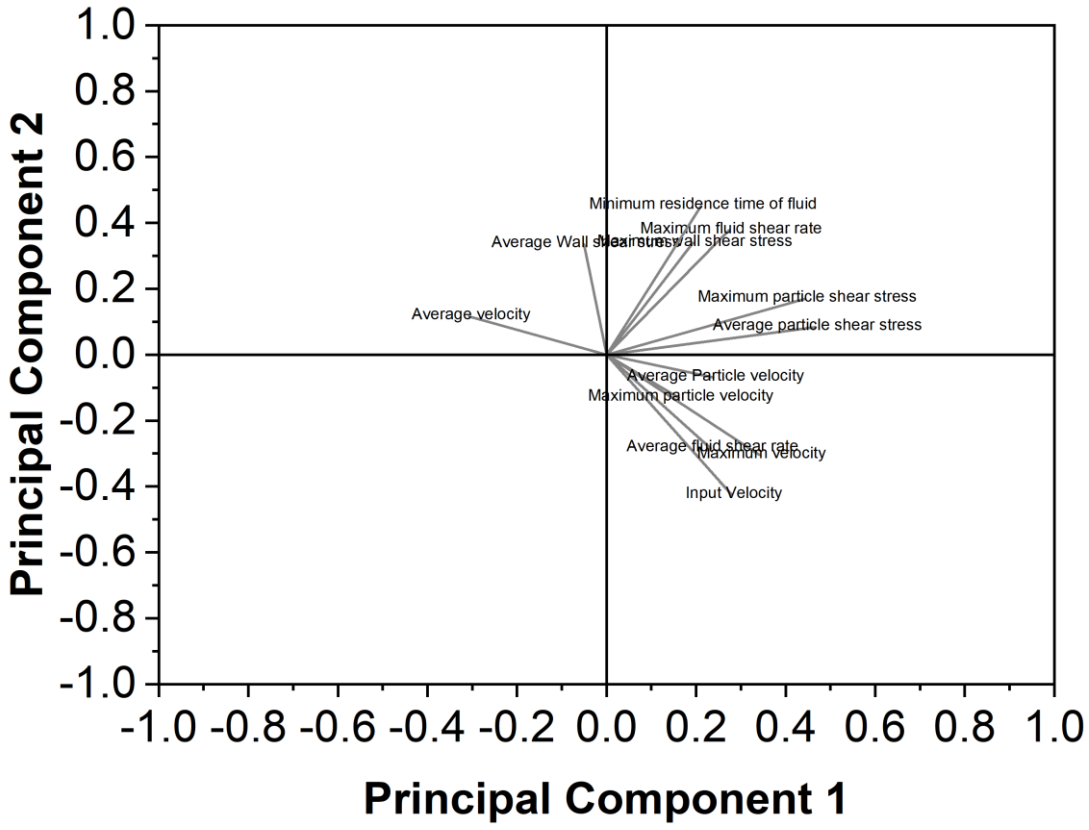

Figure 4.41: Loadings plot for the analysis of both fluid and particle-related parameters. It is shown that PC1 is largely comprised of fluid-related parameters, whilst PC2 is mostly particle-related parameters.

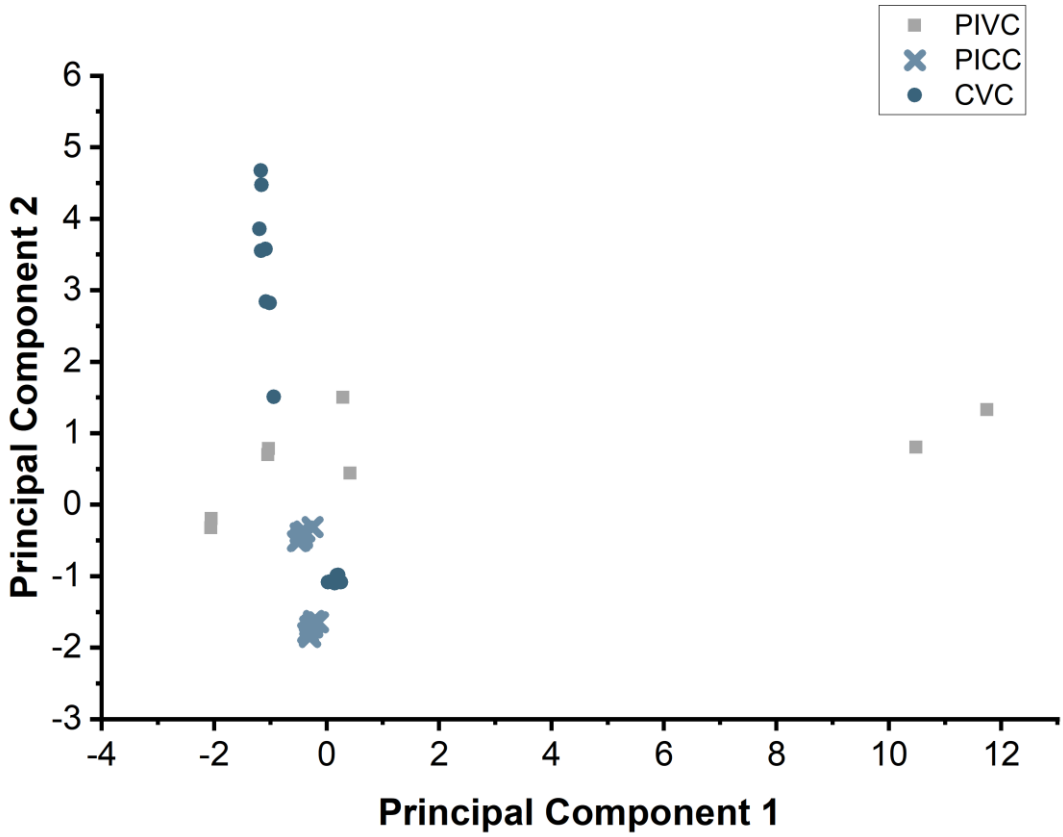

Figure 4.42: A scatter plot of PC1 against PC2 for the complete analysis. There is significantly more similarity between the PICC and CVC geometries once particle parameters are analysed. Two outliers from the PIVC set can clearly be seen, these are the 300mL min^{-1} 'flushes' discussed previously.

One of the most striking characteristics of the plot in **Figure 4.42**, is the similarity it has to the scatter plot for the fluid only parameters in **Figure 4.36**. However, in this case, there is a greater degree of overlap between PICC and CVC geometries in terms of the values of their principal components, which was not necessarily seen earlier. Furthermore, the clear outliers in this plot are the 300 mL min^{-1} "flushes" used with the PIVC geometry; the same as those highlighted previously.

Lastly, hierarchical clustering analysis was undertaken to explore the relationships between geometries in more detail. Hierarchical clustering analysis is an algorithm that groups similar objects (here these are the simulations and their different input parameters) into clusters. Each cluster is distinct from each other cluster; within each cluster however, the items are broadly like each other.

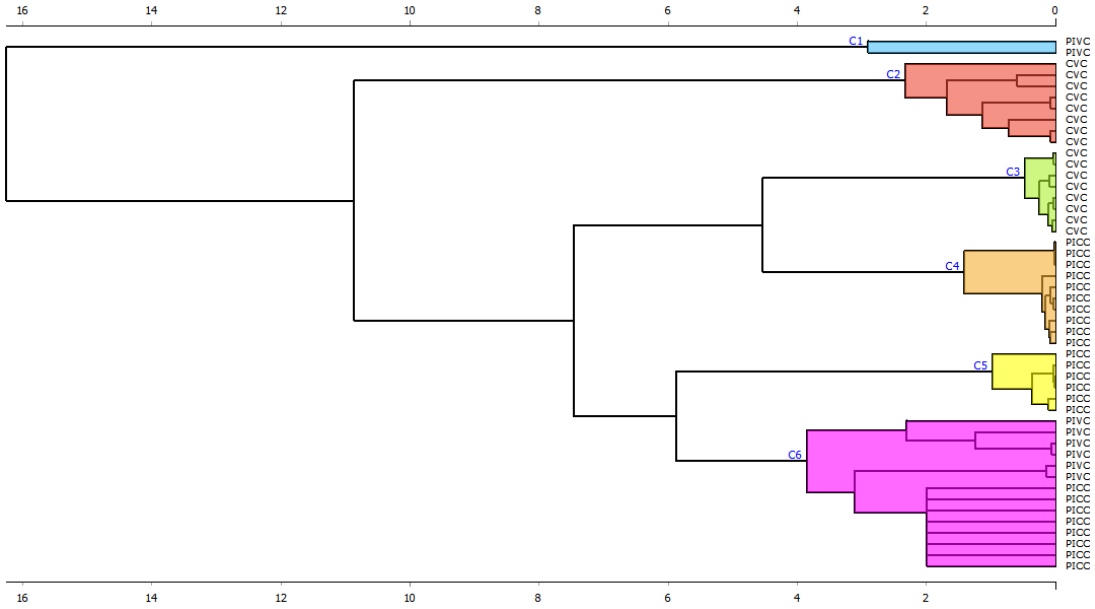

Figure 4.43: Dendrogram from hierarchical clustering analysis for the vascular access devices in this work. This dendrogram clearly shows 6 distinct clusters.

In **Figure 4.43**, it can clearly be shown there are 6 distinct clusters within this data set – C1 is a distinct PIVC only cluster, C2 and C3 are CVC only, C4 and 5 are PICC only, whilst C6 is a mixture of PIVC and PICC geometries.

The content of the C1 cluster being very separate from C6, where the remaining PIVC geometries are found is not surprising. C1 contains the 300 mL min^{-1} simulations that have consistently been seen to be outliers throughout this section, so it makes sense that these would cluster separately. It is interesting and unexpected that the dual lumen PICC lines and remaining PIVC geometries would cluster together in C6.

4.4.4 Summary

In this chapter it has been shown that a combined CFD-DEM methodology can be used to study nanoparticle and fluid behaviour through 3 different, commonly used, vascular access devices. This methodology has enabled flow rates to be correlated with fluid velocity, wall shear stress as well as particle shear rates and residence times. Wall shear stress has been seen to vary between 1949.63 and 14610.07 Pa, whilst fluid shear ranges between 598.30 and 9148.52 s^{-1} and particle shear rates between 7 and 453491.4 Pa.

Figure 4.42 shows the PCA plot for the simulations undertaken in this chapter. The overwhelming majority of the simulations output results that correlate to having principal components within a narrowly defined space. This space is where PC1 is between -2 and +1, and PC2 between -2 and +4. As mentioned earlier, principal components are weighted averages of a suitable combination of the initial variables; since both the weighting and principal components are known, this original variables can be recovered. This correlates to a space where average fluid shear and average particle shear rate ranges between

756.48 and 1749.34 s^{-1} and 149085.94 and 429037.20 Pa respectively (**Appendix J**).

The use of Principal Component Analysis here has enabled novel insights around the shear stresses and other forces that nanoparticles would be subjected to *in vivo* if they were given *via* one of the VADs discussed in this chapter. Since particle shear stress is a key factor for influencing nanoparticle biological fate through its impact on protein corona composition, these results will then be taken and used as ideal operating ranges of the microfluidic device, which should then cover the parameter space (as principal components), which has been outlined earlier in this chapter. Consequently, the input fluid velocity could be chosen so that the device can mimic any VAD, or alternatively if the necessary input parameters were known, any chosen blood vessel.

4.4.4.1 Limitations of These Models

There are several known limitations in the models developed in this work. These limitations mostly arise from the assumptions which have been implemented to simplify the calculations that need to be run. Firstly, input geometries are from idealised, generic geometries and are often from cadaverous studies, rather than live patients. Next, the physics continua used here assume that the walls of these bloods vessels are elastic, but are of fixed diameter. Therefore, vessel walls do not expand and contract in these simulations as they would *in vivo*, and this is likely to have a significant impact on the results obtained via simulation.[610] Finally, the way in which the damage index is calculated in this work is capable of overestimating haemolysis. It is well known that haemolysis damage indices calculated *via* the Giersiepen-Wurzinger correlation can overestimate the damage by up to an order of magnitude, since the exponents in the underlying equation mean it is possible for there to be circumstances in which the values are greater than 1/ 100%.[598,600]

4.5 Conclusions

In this chapter, the coupled CFD-DEM methodology developed in **Chapter 3** has been used in an iterative fashion, to study three different, commonly used vascular access devices (*i.e.,* peripherally inserted venous cannula, PICC and Hickman lines). This has enabled both fluid and nanoparticle behaviour to be determined simultaneously, as well as to determine particle-related factors such as particle shear stress. Furthermore, this work has highlighted the apparent paucity of data within the literature regarding particle shear stresses on nanoparticles when they are introduced into the bloodstream.

To achieve this aim, several objectives were set at the beginning of this work. Initially, the vascular access devices were developed as CFD-only simulations, since it was of interest to study how simply the insertion of the device alters blood flow in the vessels concerned. Later, these simulations were made more complex, by now using the VAD to introduce either of 0.9% saline, or 5% glucose. These two fluids are both common carrier fluids for many intravenously administered medications, but have quite different physical

properties in terms of density and viscosity and therefore the assumption was made that they would have quite different behaviour in these simulations. It was seen that wall shear stress and fluid velocity vary as a function of the chosen infusion fluid.

Once the fluid behaviour had been thoroughly investigated, the simulations were again made more complex by applying the full CFD-DEM methodology developed earlier. Particle behaviour could now be studied. Here, particle velocity and particle shear stress were two key parameters of interest since fluid shear rate (and therefore particle shear stress) are known to influence the physiochemical characteristics of the developing protein corona *in vivo*. Principal component analysis was used to simplify the data obtained from these simulations, from a 14-dimentional space, to a much simpler and easier to visualise and understand 2-D plot. Key parameters were then elucidated from this data and will be used as target operating ranges for the microfluidic device designed and simulated in the following chapter.

Furthermore, simulations also considered the influence of infusion fluid and catheter tip shape of fluid behaviour and therefore wall shear stress as well as what these results mean in the context of Virchow's triad and their use clinically.

In summary, this work is one of the first computational studies where multicomponent fluids and particle behaviour are studied simultaneously in the context of a vascular access device. Many studies exist within the literature where only fluid behaviour is of interest. The results obtained here regarding particle shear stresses could have a significant impact on the design and development of novel nanotherapeutics, since particle shear stress is known to influence protein corona composition, and therefore nanoparticle biological fate, but also likely influence the selection of the route by which they are given intravenously *e.g.,* if these simulations highlight that high particle shear is experienced by the nanoparticles whilst travelling through the VAD, and the delivery vehicle is known to be shear sensitive, with high shear encouraging aggregation, then this may determine that they are not suitable for PIVC. Several groups have previously investigated the influence of fluid shear on particle aggregation.[611–613]

4.6 Appendices

A. Input Geometries

PIVC

Insertion angle 15 °

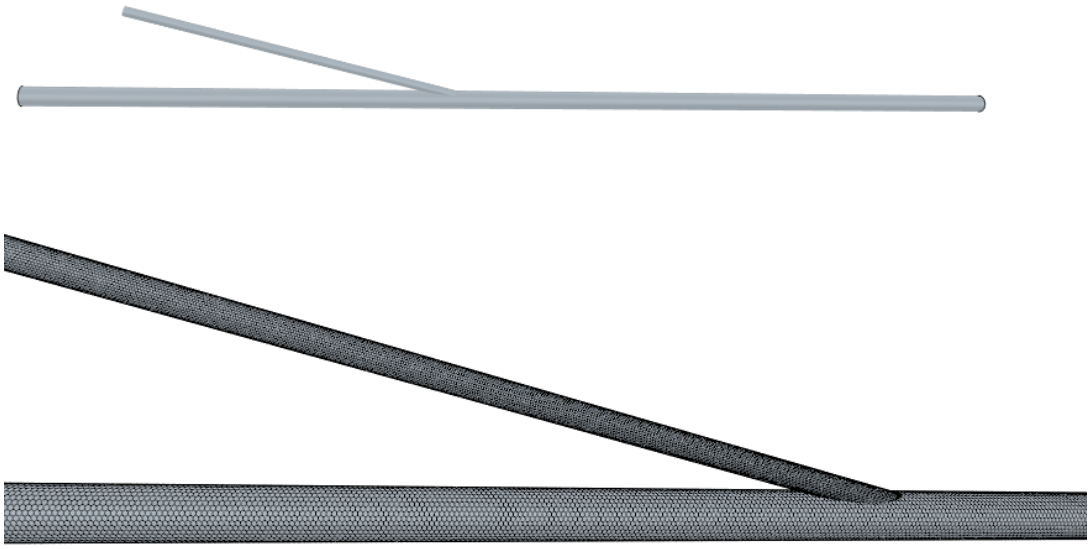

Insertion angle 25 °

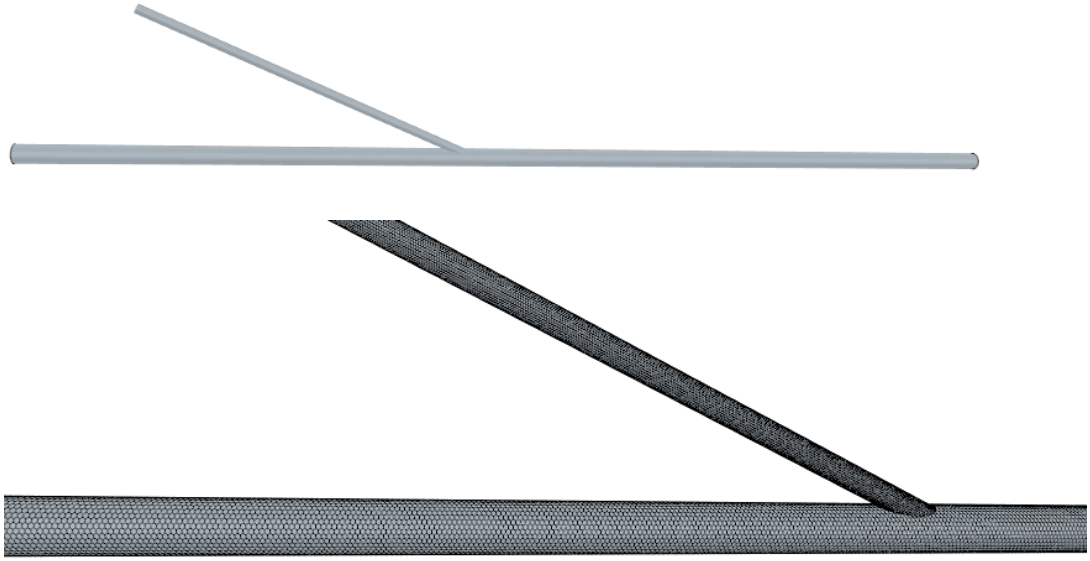

Insertion angle 35 °

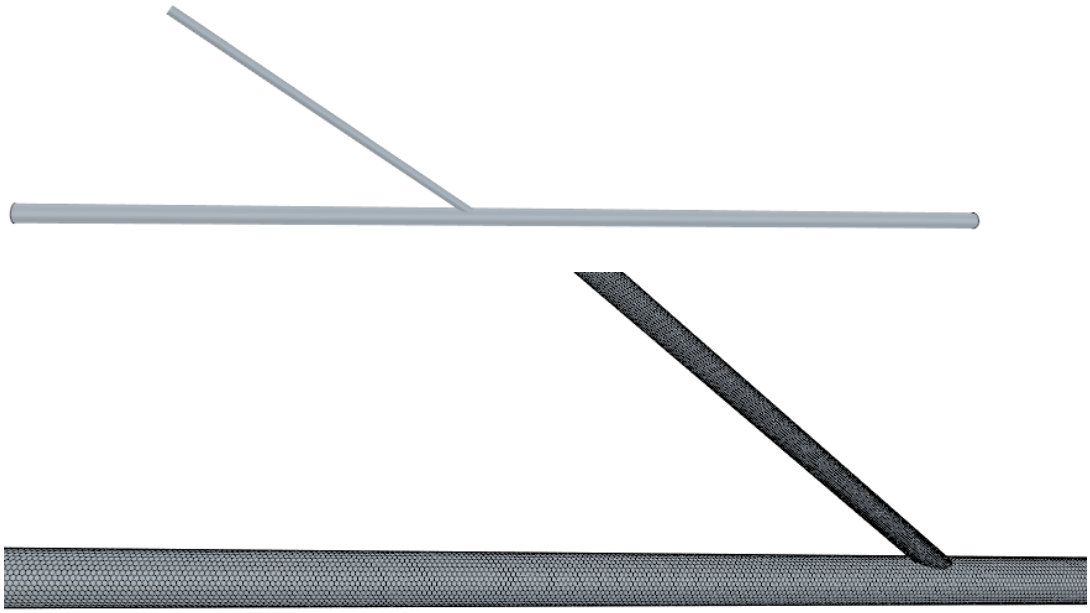

PICC

RBV – 3.6mm, LBV 5.5 mm SVC 6.4mm.

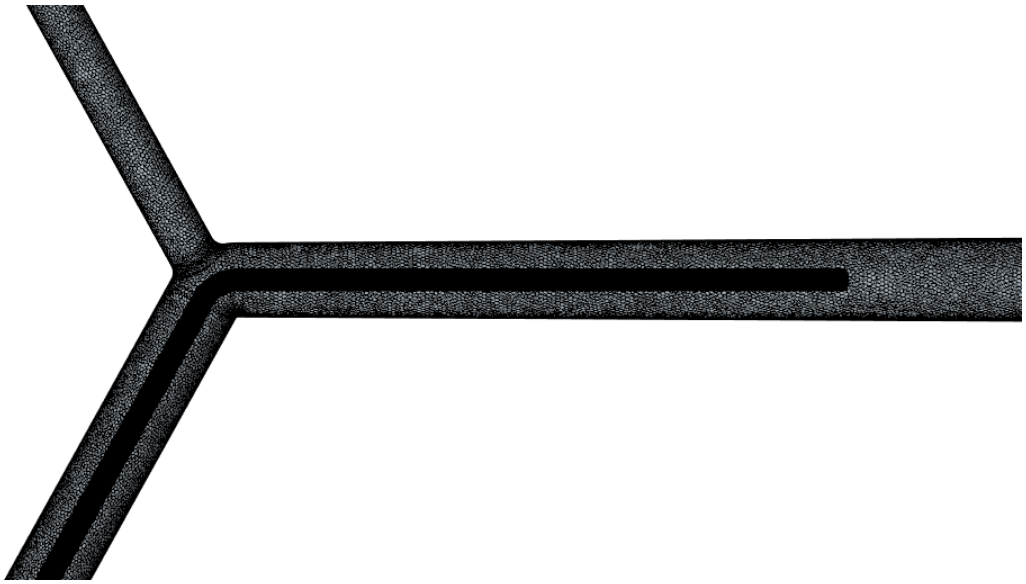

Hickman line

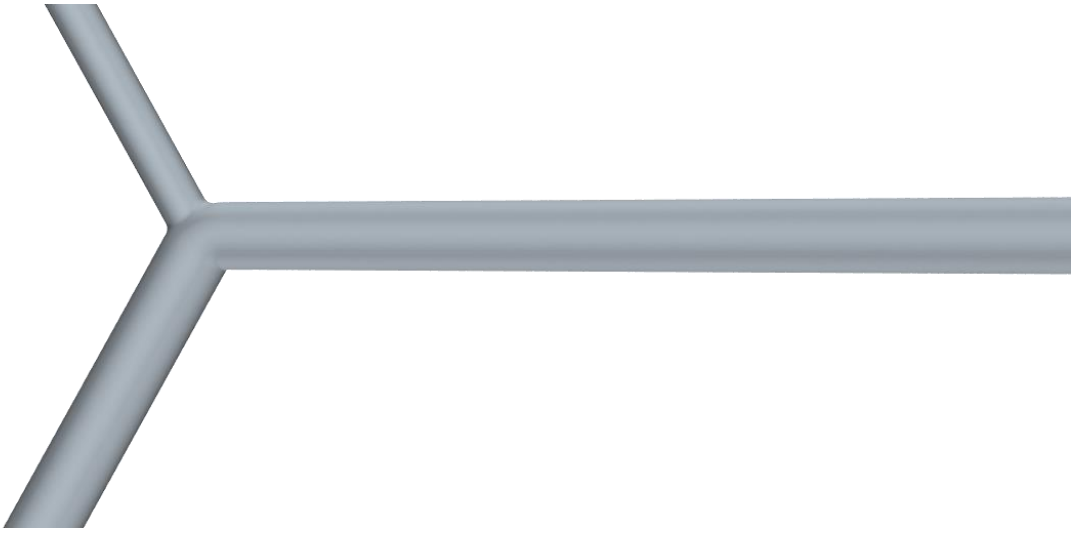

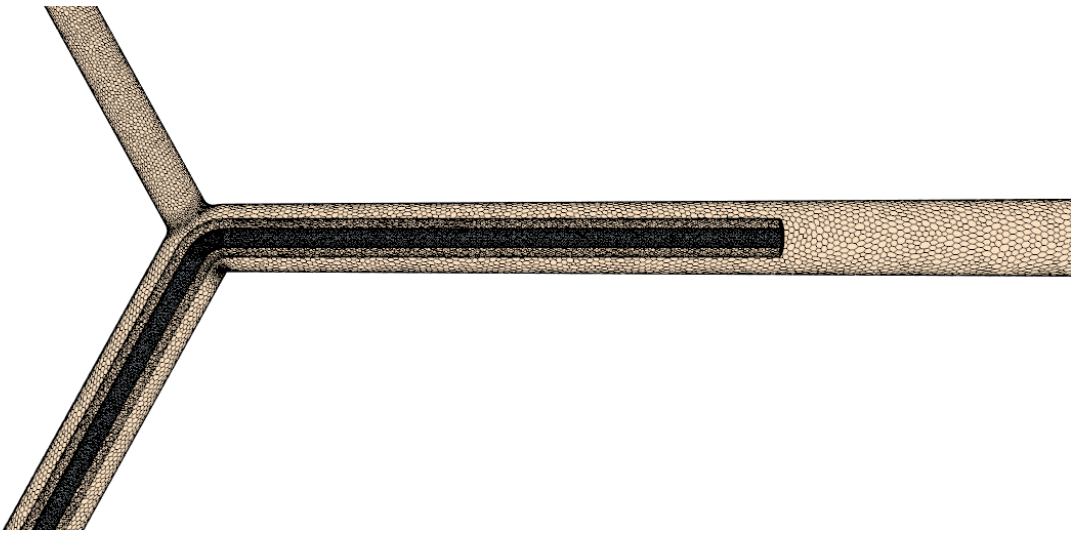

B. Mesh Independence Studies

PIVC

Input velocity for median cubital vein is 0.11 m s^{-1}. Calculated maximum velocity is then 0.22 m s^{-1}.

Results from mesh independence study. Needle assembly is meshed at 50% of base size.

Base size (m)	No. of cells	Max velocity (m s^{-1})	Residuals (as continuity)
5.0 $x10^{-3}$	26082	0.141	1.37$x10^{-3}$
9.0 $x10^{-4}$	320102	0.183	6.88$x10^{-5}$
5.0 $x10^{-4}$	389616	0.181	3.17$x10^{-4}$
2.0 $x10^{-4}$	393012	0.185	9.63$x10^{-6}$
1.0 $x10^{-4}$	1024417	-	-

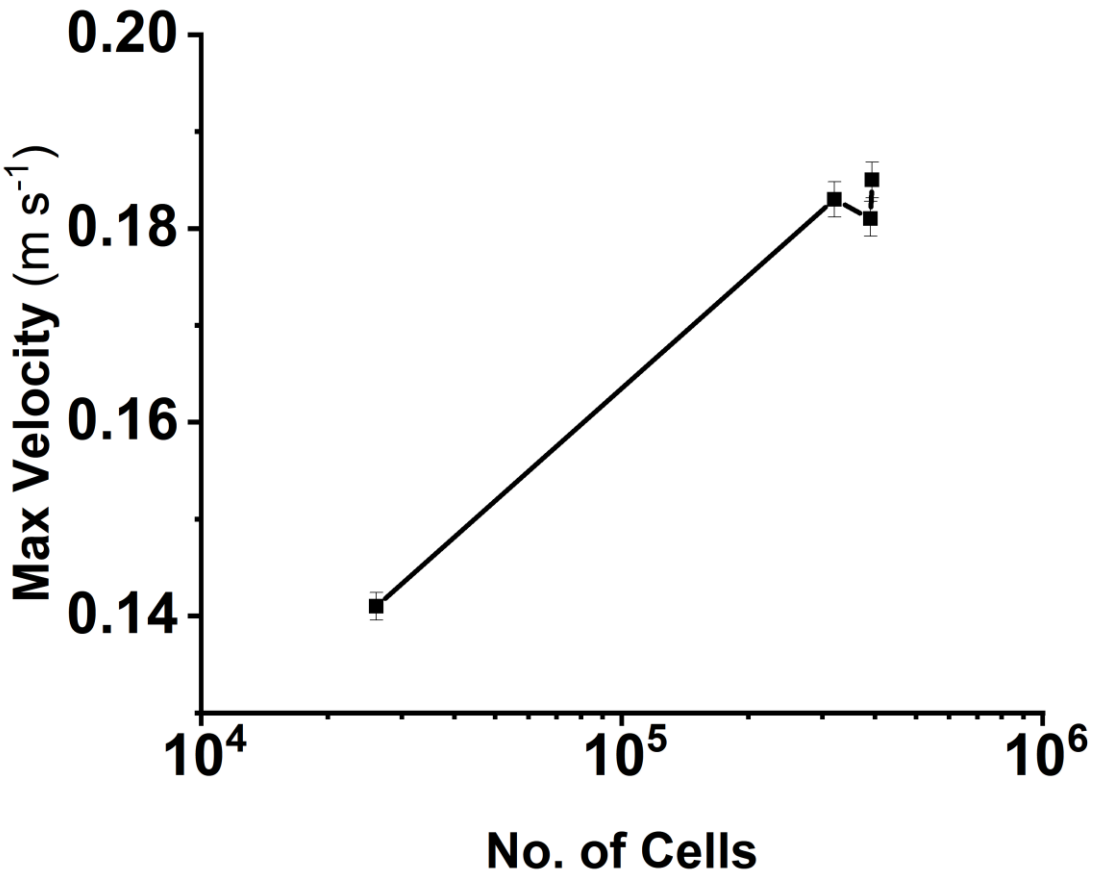

Cell Quality

Cell quality measures the uniformity of cells that make up the mesh (**Table 4.26**). A perfect cell has a cell quality of 1.0. Ideally, the bulk of the cells within the mesh should have a cell quality rating of 0.5 or more.[535] Bad cells are those where quality is less than 1.0$x10^{-5}$.[535] Such cell quality values suggest that the cells within the mesh vary significantly in size, shape and volume.

Table 4.26: Cell quality measures the uniformity of a simulated mesh. Cell quality for the PIVC model used within this chapter. All cells are seen to have a cell quality > 0.5.

Cell quality	Number of cells
≤ 0.50	0
≤ 0.60	0
≤ 0.70	0
≤ 0.80	0
≤ 0.90	0
≤ 0.95	0
≤ 1.00	393012

Skewness Angle

Skewness angle measures the angle between a face normal and the vector that connects the centre of two neighbouring cells (**Table 4.27**).[535] This shows whether the cells on either side are formed such that diffusion of quantities is possible without the quantities becoming unbounded.[535] A perfectly orthogonal mesh will have a skewness angle of 0°. Bad cells are those with a skewness angle greater than 85°, and skewness angles > 90° lead to issues with solution convergence.[535]

Table 4.27: Maximum skewness angles for each geometry part within the PIVC geometry.

Geometry part	Maximum skewness angle (°)
Blood vessel – wall	50.93
Blood vessel – inlet	41.22
Blood vessel – outlet	42.39
Needle	74.31

Volume Change

Volume change describes the ratio of a cell's volume compared to that of its largest neighbour (**Table 4.28**).[535] A value of 1 is a good cell, as this shows that the cell concerned has a volume equal to or larger than that of its neighbours.[535] Cells where the volume change is < 0.01 are considered bad cells – large increases in volume from one cell to another may lead to inaccuracies in results and instability in the solvers.[535]

Table 4.28: Volume change of cells within a mesh is a proxy measure of the accuracy of the results it will generate. All cells within this mesh have a volume change > 0.01.

Volume change	Number of cells
<0.01	0
<0.1	3280
<1	389732

In summary the results presented here show that the mesh generated here with a base size of 2 $x10^{-4}$ m for the blood vessel and 1 x 10^{-4} m for the needle, is of sufficient quality to be suitable for further analysis. No issues have been identified regarding cell quality, skewness angle nor volume change.

PICC

For this model an input velocity of 0.4 m s^{-1} has been set at both inlets (brachiocephalic/ innominate veins). Therefore, calculated peak fluid velocity is 0.8 m s^{-1}. Base size refers to the size of the cells used to mesh the blood vessel geometry. In each case is the PICC line meshed at a size half of this.

Table 4.29: Results from mesh independence study for PICC line

Base size (m)	No of cells	Max velocity (m s^{-1})	Residuals (as continuity)
5.0 x10^{-3}	228493	0.795	1.51x10^{-6}
1.0 x10^{-3}	258709	0.778	3.33 x10^{-6}
8.0 x10^{-4}	262483	0.782	1.81x10^{-3}
6.0 x10^{-4}	265526	0.784	2.17x10^{-6}
5.0x10^{-4}	273591	0.787	2.28x 10^{-6}
4.0 x10^{-4}	321717	0.794	2.35x10^{-6}
3.0 x10^{-4}	439225	0.815	3.40x10^{-6}
2.75 x10^{-4}	546042	0.810	2.77 x10^{-6}
2.50 x10^{-4}	674082	0.814	5.04x10^{-4}
2.0 x10^{-4}	991926	0.808	3.31x10^{-6}
1.0 x10^{-4}	4101695	0.792	2.98x10^{-6}

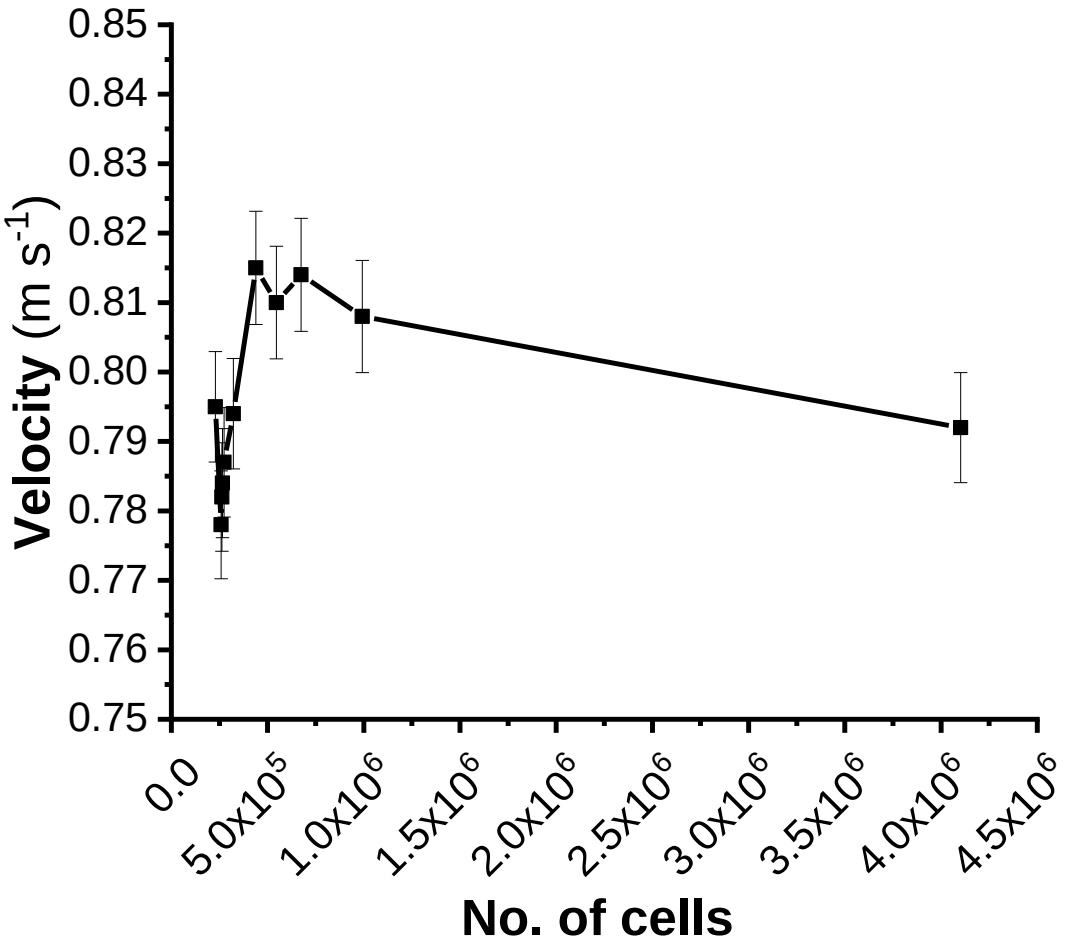

Cell Quality

Table 4.30: Cell quality measures the uniformity of a simulated mesh. Cell quality for the PICC model used within this chapter. All cells are seen to have a cell quality > 0.5.

Cell quality	Number of cells
< 0.50	0
< 0.60	0
< 0.70	0
< 0.80	0
< 0.90	0
<0.95	0
< 1.00	1569982

Skewness Angle

Table 4.31: Maximum skewness angles for each geometry part within the PICC line geometry.

Geometry part	Maximum skewness angle (°)
Blood vessel wall	6.01
Inlet 1	36.50
Inlet 2	29.27
Outlet	38.39
PICC line	42.32

Volume Change

Table 4.32: Volume change of cells within a mesh is a proxy measure of the accuracy of the results it will generate. All cells within this mesh have a volume change > 0.01.

Volume change	Number of cells
<0.01	0
<0.1	28254
<1	1541728

In summary, the results presented here show that the mesh generated here with a base size of $4x10^{-4}$ m for the blood vessel and $4x10^{-5}$ m for the PICC line, is of sufficient quality to be suitable for further analysis. No issues have been identified regarding cell quality, skewness angle nor volume change.

Hickman Line

Results from mesh independence study

Table 4.33: Results from mesh independence study for Hickman line.

Base size (m)	No of cells	Max velocity (m s-1)	Residuals (as continuity)
$5.0 x10^{-3}$	98933	0.785	-
$1.0 x10^{-3}$	695628	0.810	$2.59 x10^{-7}$
$8.0 x10^{-4}$	704387	0.818	$2.91 x10^{-7}$
$6.0 x10^{-4}$	709635	0.814	$3.02 x10^{-7}$
$5.0 x10^{-4}$	707502	0.806	$3.10 x10^{-7}$
$4.0 x10^{-4}$	848843	0.809	$3.74 x10^{-7}$
3.0x10-4	1127967	0.811	$4.90 x 10^{-7}$
$2.0 x10^{-4}$	2283585	0.810	$8.50 x10^{-7}$

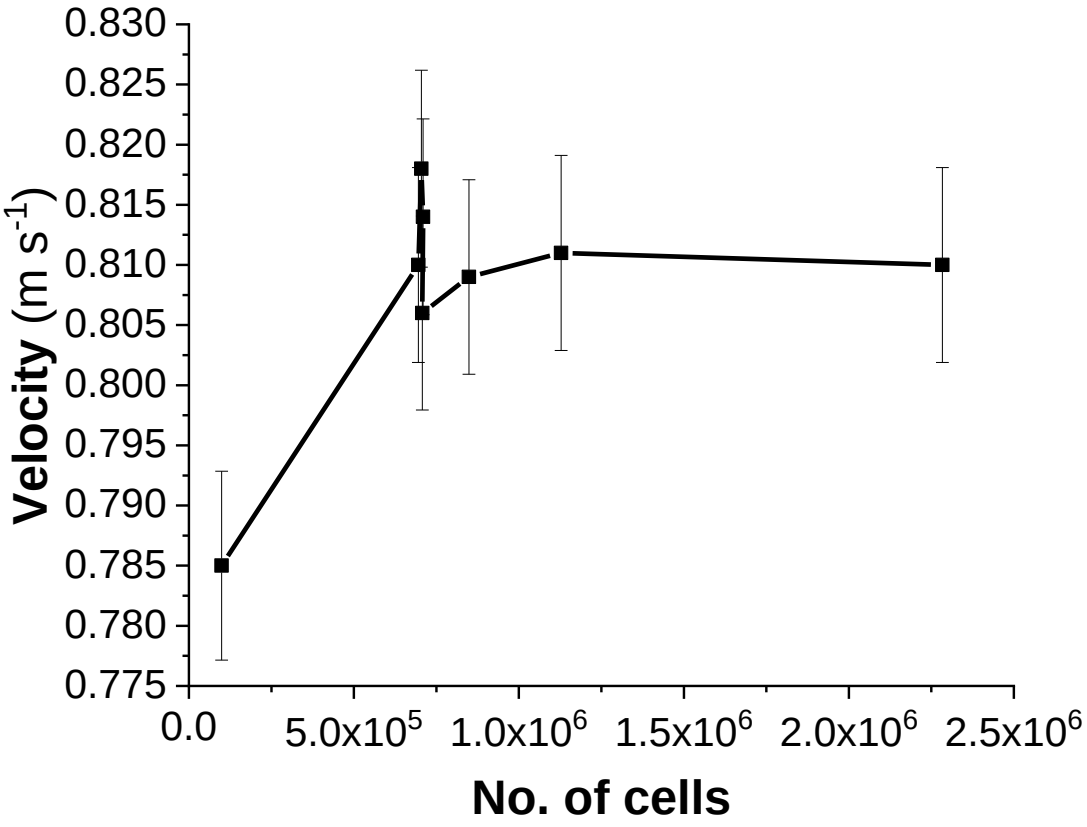

Cell Quality

Table 4.34: Cell quality measures the uniformity of a simulated mesh. Cell quality for the PIVC model used within this chapter. All cells are seen to have a cell quality > 0.5.

Cell quality	Number of cells
>0.80	0
>0.90	0
>0.95	0
1	707502

Skewness Angle

Table 4.35: Maximum skewness angles for each geometry part within the Hickman line geometry.

Geometry part	Maximum skewness angle (°)
Inlet 1	40.62
Inlet 2	41.54
Outlet	46.59
CVC	54.85

Volume Change

Table 4.36: Volume change of cells within a mesh is a proxy measure of the accuracy of the results it will generate. All cells within this mesh have a volume change > 0.01.

Volume change	Number of cells
<0.01	0
<0.1	16921
1	690581

In summary, the results presented here show that the mesh generated with a base size of 3 $x10^{-4}$ m for the blood vessel and 1.5 $x10^{-4}$ m for the Hickman line, is of sufficient quality to be suitable for further analysis. No issues have been identified regarding cell quality, skewness angle nor volume change.

C. Flow Rate to Inlet Velocity and Reynolds Number.

For a few of the blood vessels studied in this work, blood flow is often given as a flow rate, rather than as velocity.

Flow rate to inlet velocity

Necessary equations

$$Q = Av$$

$$v = \frac{Q}{A}$$

$$A = \pi r^2$$

Therefore,

$$Velocity = \frac{flow\ rate\ (L\ s^{-1}) x\ (m^3\ L^{-1})}{cross\ sectional\ area\ (m^2)}$$

Median cubital vein

Flow rate 17 mL min $^{-1}$ https://www.jstage.jst.go.jp/article/jpnwocm/25/3/25_576/_pdf

Diameter 1.8 mm

$$Velocity = \frac{2.83x10^{-4}\ (L\ s^{-1}) x\ 10^{-3} (m^3\ L^{-1})}{\pi (0.9x10^{-3})^2\ (m^2)}$$

$$Velocity = 0.11\ m\ s^{-1}$$

20 G cannula

internal diameter 0.603 mm

Flow rate (mL min^{-1})	Flow rate (mL s^{-1})	Flow rate (L s^{-1})
10	0.16	1.67x10^{-4}
30	0.5	5x10^{-4}
60	1	1x10^{-3}
300	5	5x10^{-3}

Using the same formula as above, the flow rates in mL min-1 become the following fluid velocities in m s^{-1}

Flow rate (mL min^{-1})	Fluid velocity (m s^{-1})
10	0.584
30	1.75
60	3.50
300	17.5

Input velocity to Reynolds number

$$R_e = \frac{\rho u L}{\mu}$$

Density kg m^{-3}		Viscosity Pa s	
0.9% saline	1004.59	0.9% saline	0.00102
5% glucose	1017.50	5% glucose	0.00114

The flow rates of the carrier fluids and their respective Reynolds numbers are outlined in the table below.

Flow rate (mL min^{-1})	Reynolds number – 0.9% saline	Reynolds number – 5% Glucose
10	346.83	314.31
30	1039.30	941.86
60	2078.61	1883.71
300	10393.07	9418.57

D. Implementation of Damage Scalar

The implementation of the damage scalar in these models to study the impact of the VAD on haemolysis of red blood cells is a multistep process. Here, the process by which these are set up in STARCCM+ will not be discussed in detail, but instead relate the walkthrough given by the STARCCM+ knowledgebase to the work published by Garon and Farinas.[598,614]

Step 1: Calculating fluid shear

The first step for the implementation of the damage scalar to measure damage index and thus the amount of haemolysis is to calculate fluid shear (τ). Activating the strain rate tensor modulus enables the field function below to be defined.

$StrainRate*$DynamicViscosity

Step 2: Creating the normalised damage index scalar D_I

This step uses equation 16 from Garon and Farinas, but additionally multiplies by fluid density to normalise the value. In this work, fluid density varies as blood mixes with the carrier fluid (saline/ glucose).

$$\frac{d}{dt}D_I = (3.62x10^{-7})^{\frac{1}{0.785}}\tau^{\frac{2.416}{0.785}}\rho = \sigma$$

Another field function is defined:

*pow(3.62e-7,(1/0.785)) * pow($Tau,(2.416/0.785)) * $Density*

Step 3: Volume integral of D_I

The following three steps outline the three reports that must now be created in STARCCM+ to calculate the damage index. First, generate a volume integral report to calculate average value of D_I over the entire volume mesh.

$$\int_v \sigma \, dV$$

Step 4: Average linear damage

This step calculates the product of the volume integral of D_I and the inverse of the flow rate (equation 25 from Garon and Farinas).

$$\overline{D_I} = \frac{1}{Q}\int_v \sigma \, dV$$

1/$QInReport*$VolIntReport

Step 5: Predicted level of haemolysis

This final step calculates (and later reports) equation 26.

$$D = (\overline{D}_I)^{0.785}$$

The report itself is defined as another field function outlined below.

Pow($AverageLinearDamageReport,0.785)

To then obtain the mean index of haemolysis (MIH) (equation 11 in the Garon and Farinas paper, but not reported by Piper et al.) the following is necessary, since what has been calculated previously is D(τ,t).

$$MIH = D_{(\tau,t)} x 10^6$$

Benchmarking against Garon and Farinas.

Benchmarking of the 16G cannula simulation in the Garon and Farinas paper and originally reported by De Wachter and colleagues is undertaken here, to confirm that the methodology for the damage index and conversion between damage index and normalised index of haemolysis is understood, before applying this methodology to the models in this chapter to calculate the damage index as reported by Piper *et al*.[524,598,615]

Geometry

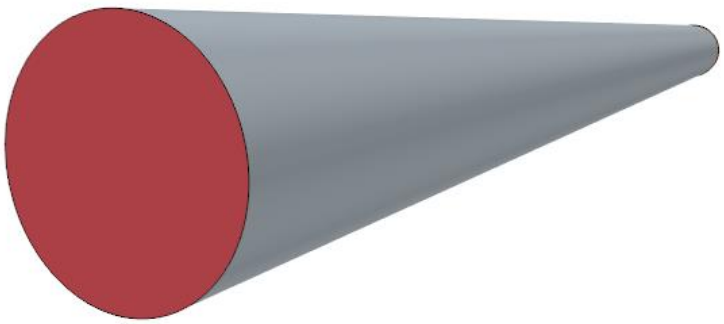

Mesh

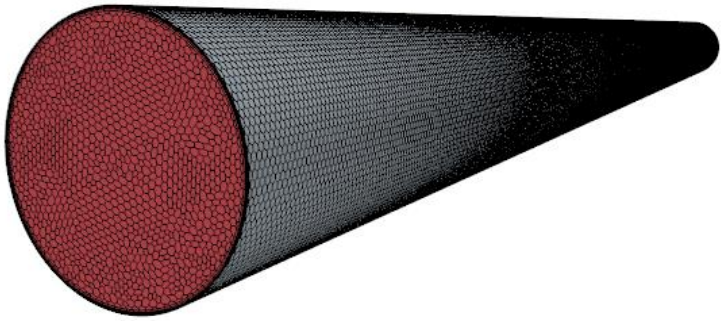

Mesh size chosen to give the same number of cells as reported by Garon and Farinas (647,569). Base size used 4.5×10^{-5} m.

Results

The simulation reports the damage index as 2.28×10^{-5} From equation 11, this gives the normalised index of haemolysis as 22.8.

E. Entrance Lengths, PICC and Hickman Line

Entrance lengths are the distance fluid flow must travel before the velocity profile stops changing. We calculate them here to confirm that a sufficient length of each vein within the model has been used, such that the truncation does not affect the results obtained within the model.

Different equations are used depending on the flow regime that is occurring.

$$L_e(laminar) = 0.05 R_e D$$
$$L_e(turbulent) = 4.4 D (R_e)^{\frac{1}{6}}$$

Entrance length as a function of pipe diameter and Reynolds number. Where R_e is the Reynolds number and D is diameter of the pipe.

First flow rates will be converted into fluid velocity in ms^{-1}, then Reynolds number will be calculated for each vein within the model, before this number can be plugged into one of the equations shown above.

$$R_e = \frac{\rho D v}{\eta}$$

Reynolds number where ρ the density of the fluid, D the diameter of the pipe, ν is the velocity of the fluid and η is fluid viscosity.

Entrance lengths

Left brachiocephalic vein

Diameter = 5.5 mm.

Flow rate = 10.86 mL s^{-1} fluid velocity = 0.45 m s^{-1}

Reynolds number

$$R_e = \frac{1050\ x\ 0.0055\ x\ 0.457}{0.0035} = 75.4$$

Entrance length

$$L_e(laminar) = 0.05\ x\ 75.4\ x\ 0.0055 = 0.021\ m$$

Right brachiocephalic vein

Diameter = 3.6 mm

Flow rate = 8.76 mL s^{-1} fluid velocity = 0.86ms^{-1}

F. Field Functions for Particle Shear Stress

Schiller-Naumann model has been implemented in STARCCM+ for the determination of the drag force experienced by the polymer nanoparticles. This equation is already within STAR CCM, as “Particle Schiller-Naumann drag coefficient”.

$$C_D = 24\,x\,\frac{1 + 0.15\,Re^{0.687}}{Re}$$

Drag coefficient, where R_e is Reynolds number.

The drag force experienced by the particles can be calculated using this drag coefficient along with the nanoparticle velocity (relative to the flow) using the following equation, where ν is the particle velocity and A is the reference area of the particles. This is available in STARCCM+ as particle drag force.

$$F_d = \frac{1}{2}\rho v^2 C_D A$$

Particle drag force, where ρ is particle density, ν particle velocity and A is reference area of the particle.

Finally, particle shear stress is then:

$$\tau = \frac{F_d}{A}$$

Shear stress (τ) is a function of force (F) applied to an area (A)

To calculate particle shear stress, a user-defined field function is used. This is implemented as $${ParticleDragForce}/${ParticleSurfaceArea}

G. Hickman Line

CVCs are often referred to *via* their brand names. Hickman and Leonard lines are similar, but Leonard lines have narrower internal lumen compared to a comparable Hickman line, and they will not be studied here. The influence of CVC size and vessel diameter has been studied in detail by Nifong and McDevitt and will not be explored here.[525] In this case, a 9.6 F, single lumen Hickman line and the slightly larger 10 F triple lumen Hickman line will be modelled (**Figure 4.44**).

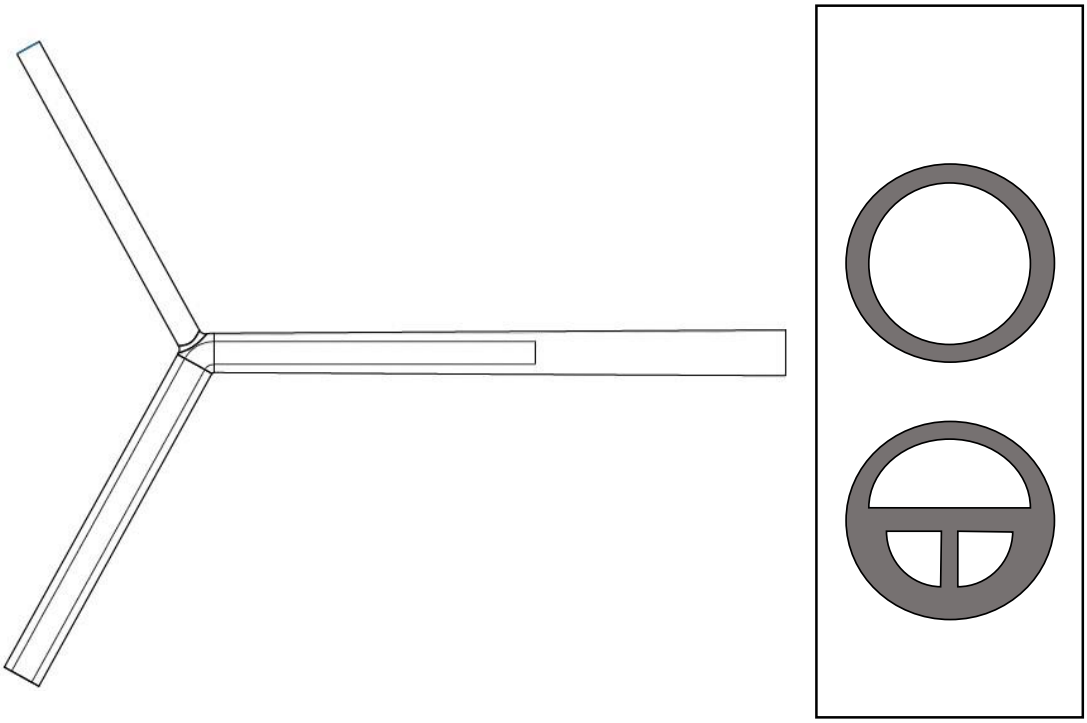

Figure 4.44: A cross section of the single and triple lumen Hickman line modelled in this study.

4.6.1.2 Obstruction of Fluid Flow Following Line Insertion

Initially, the Hickman line is considered just as an obstruction to the blood flow in the brachiocephalic vein and superior vena cava The inlet velocity of the left brachiocephalic veins is kept constant at 0.46 m s^{-1} and for the right brachiocephalic vein inlet velocity is 0.86 m s^{-1}. A copy of the geometry with no line inserted will be used as a control. The maximum fluid velocity observed for each geometry is summarised in Error! Reference source not found.. A paired t-test was again used to assess the statistical significance of any change in maximum fluid velocity following the insertion of the Hickman line that is being studied in this section. P <0.05 is considered statistically significant.

Table 4.37: A comparison of fluid velocity, a set distance downstream (0.015m) from the outlet of the Hickman line, between the control geometry and that which has had the line inserted.

Geometry	Fluid velocity (m s^{-1})	p-value
CONTROL	0.840	-
With Hickman line	0.753	0.034

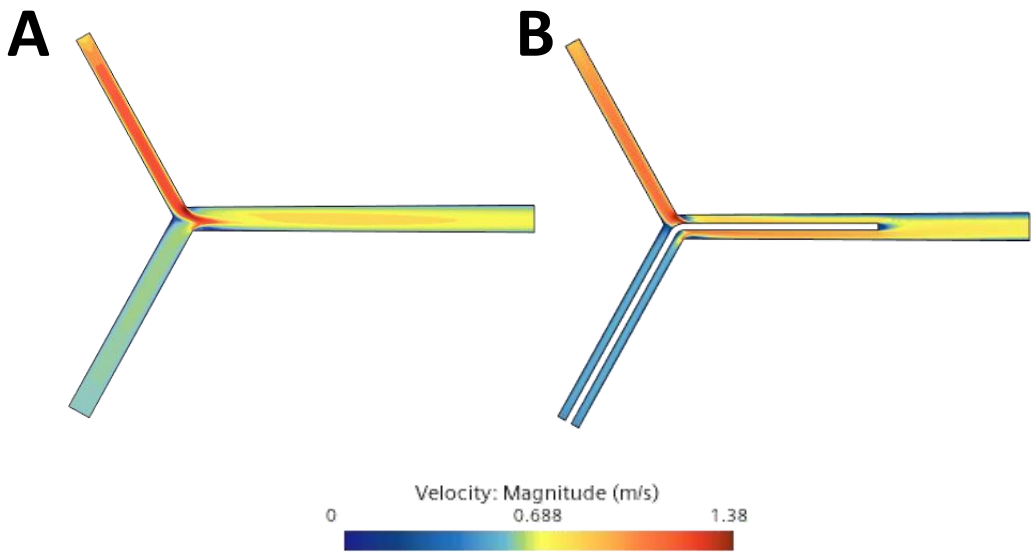

Figure 4.45: Fluid velocity in the right brachiocephalic vein is not impacted by the insertion of the Hickman line. A) control B) following Hickman line insertion.

Fluid velocity was studied in the geometry both before and after the insertion of the Hickman line (**Figure 4.45**). What is striking in this figure, is the development of an area of localised low velocity at the end of the Hickman line. Furthermore, there is also an apparent decrease in fluid velocity in the left brachiocephalic vein (where the Hickman line is inserted). There is also the formation of a band of low velocity fluid above the Hickman line.

Fluid Streamlines

Next, fluid streamlines were visualised to assess both how STARCCM+ understands the geometries imported from SolidWorks, but also to see how fluid moves around this obstruction and to enable identification of any recirculation zones that may have developed, and therefore are present when the line is not used for the infusion of fluids (**Figure 4.46**). The streamlines in this figure clearly show that the Hickman line is accurately modelled as an obstruction to fluid flow.

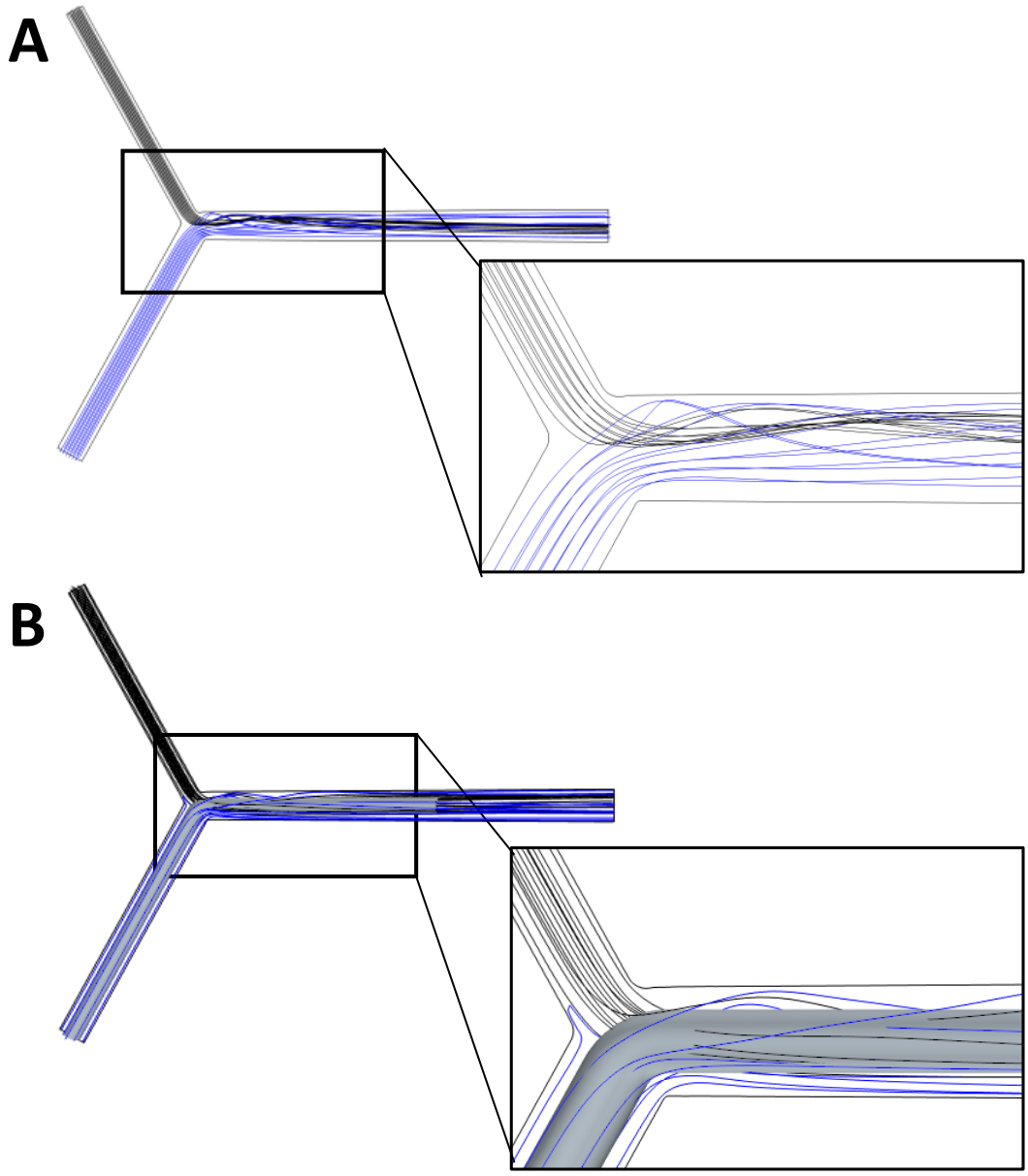

Figure 4.46: Fluid streamlines, as a planar section through the centre of the geometry, parallel to the x-axis. The Hickman line is accurately understood as an obstruction to fluid flow by the simulation. A) control geometry B) Following Hickman line insertion. Two colours are used to represent the origin of each set of streamlines.

When the vectors are studied (**not shown**), There are several recirculation zones that can be identified – these are identical to those shown earlier in (**Figure 4.18**), and discussed previously. At the tip of the Hickman line, there is a recirculation zone of 0.0015 m – not surprising considering results obtained earlier in this chapter, where fluid velocity is very low.

Vorticity

Like the cross sectional slices of the geometry shown for the impact of the insertion of a PICC line on the vorticity of the fluid, these cross sectional slices of the geometry involved here also show a loss of circular flow (**Figure 4.47**). The fluid behaviour shown in the first slice of each set is more complex than the others, since both brachiocephalic veins join the SVC immediately prior to

where this slice is taken. As the fluid progresses down the (truncated) SVC, the pattern becomes less complex, and spiral flow is clearly shown where the SVC is not partially occluded by the Hickman line (A). Where the Hickman line has been inserted, this spiral flow is not seen – consistent with the results presented previously for the PICC line.

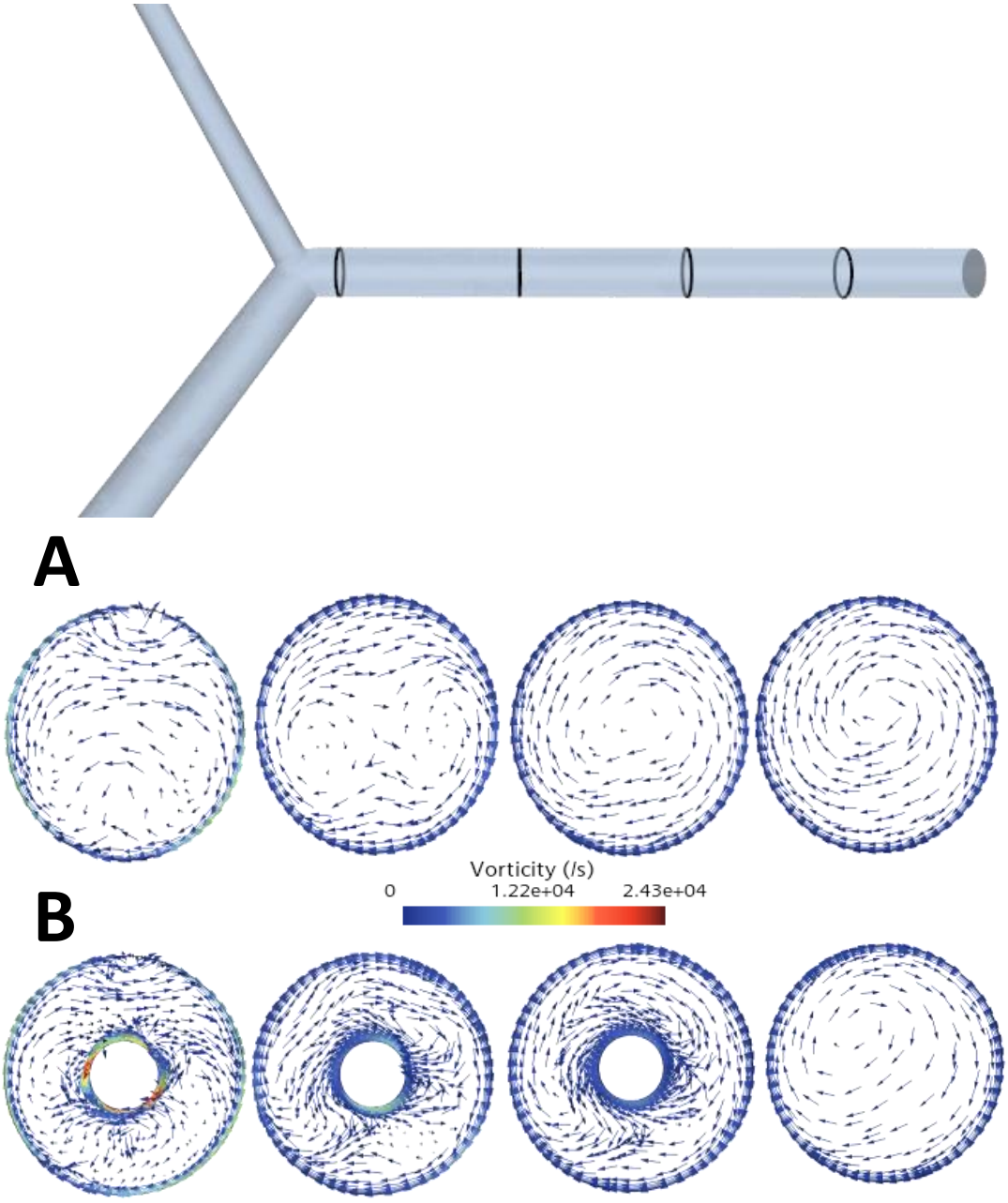

Figure 4.47: A) Cross-sectional slices of the control geometry show circular flow. This is lost on the insertion of the Hickman line (below). Positioning of the first slice was chosen arbitrarily, the remaining 3 are 0.02 m apart, to cover the length of the SVC.

Wall Shear Stress

Wall shear stress is the force that a fluid applies against a surface (here – endothelium and Hickman line). For the control geometry, average wall shear stress on the blood vessel is 2.74 Pa. Peak wall shear is 40 Pa, and is found

where the three veins join. Following the insertion of the Hickman line, areas of high and low shear can be shown (**Figure 4.48**). Wall shear stress of ~ 55 Pa is seen on Hickman line, at the point where both brachiocephalic veins join the SVC. This is even higher than the 40 Pa reported for the PICC line geometry. These results make sense when we consider that the Hickman line is of a larger diameter than the previously studied PICC line, therefore a greater proportion of the SVC is filled, and therefore to maintain the same volumetric flow rate through this narrower diameter, fluid velocity and therefore shear rate must increase.

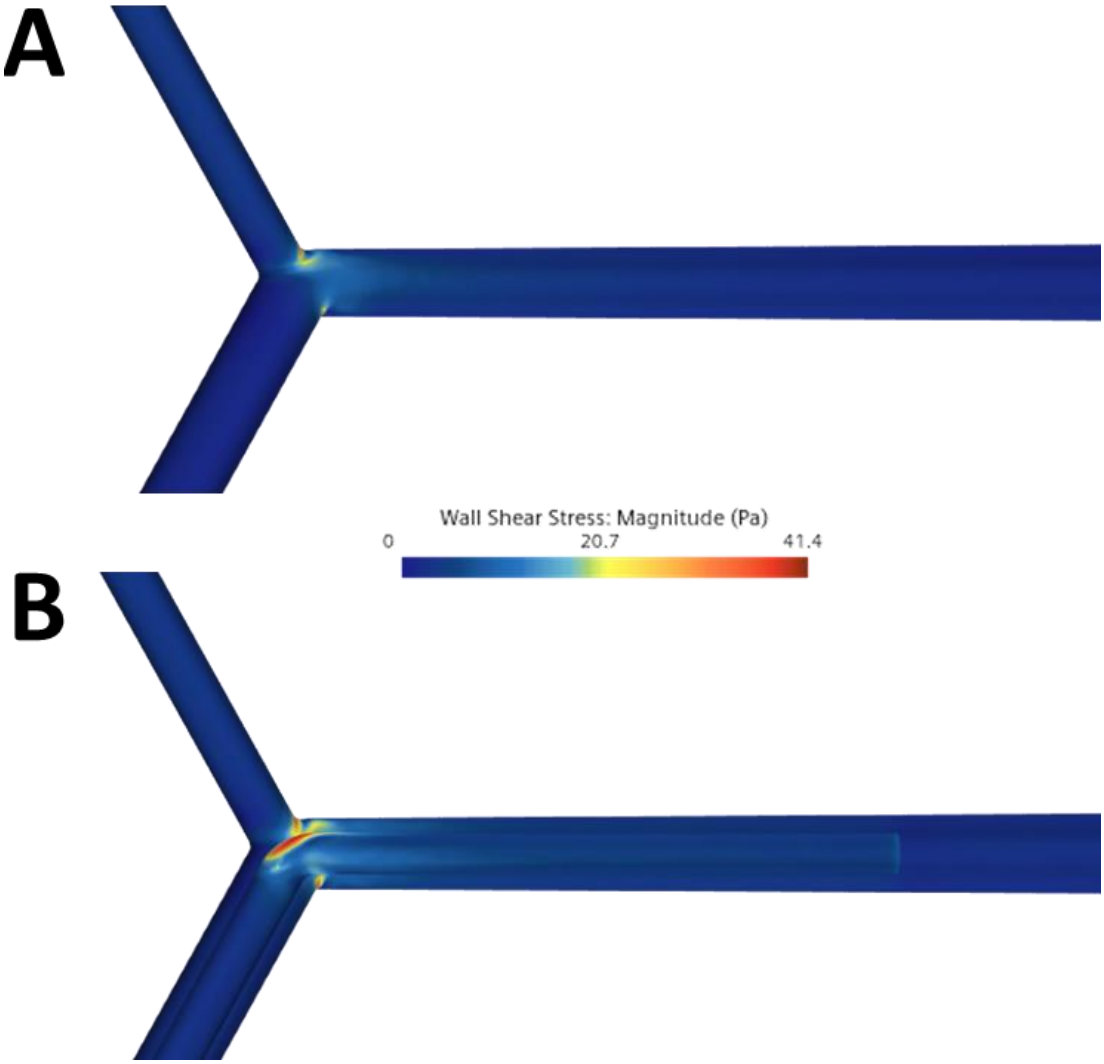

Figure 4.48: Wall shear stress A) Control. B) following Hickman insertion. The front face of this geometry is cut away to enable both Hickman line and blood vessel geometry to be visualised simultaneously.

4.6.1.3 Infusing Fluids via Central Venous Catheter

There are many combinations of parameters that could be studied here, due to their sheer number, only a selection of these will be studied (*i.e.,* fluid will only be infused down one lumen at a time, even when multiple lumen are available – even though this is known to diverge from how these vascular access devices are typically used clinically). Because of the similarity between the geometries under study, both will be considered simultaneously, where the results from both the single and treble lumen geometry are similar, then only the results from the single lumen will be reported. First fluid velocity and streamlines will be considered, followed by wall shear stress and mass fraction of blood.

Fluid Velocity and Streamlines

Simulations are set up as previously described. Maximum flow for the single lumen CVC used here has been taken from Berman *et al*.[616] Inlet velocity and Reynolds numbers have been calculated as previously described (**Table 4.38**).

Table 4.38: Flow rates and Reynolds numbers for the CVC geometry studied here.

	Flow rate (ml min^{-1})	**Velocity**	**Reynolds number (saline)**	**Reynolds number (glucose)**
Single Lumen	200	0.44	134.33	121.74
	150	0.33	100.75	91.30
	100	0.22	67.17	60.87
	50	0.11	33.58	30.43
Treble Lumen	17	0.57	705.0	639.3
	15	0.49	606.4	549.6
	7	0.23	284.7	258.0
	5	0.16	198.0	179.5

Fluid velocity was then studied following the infusion of fluid through the single lumen Hickman line geometry (**Figure 4.49**). The figure shows that even despite large increases in flow rate and therefore corresponding fluid velocity through the Hickman line, there is minor change in fluid velocity in the vein. This is again consistent with the results previously shown where the VAD is a PICC line

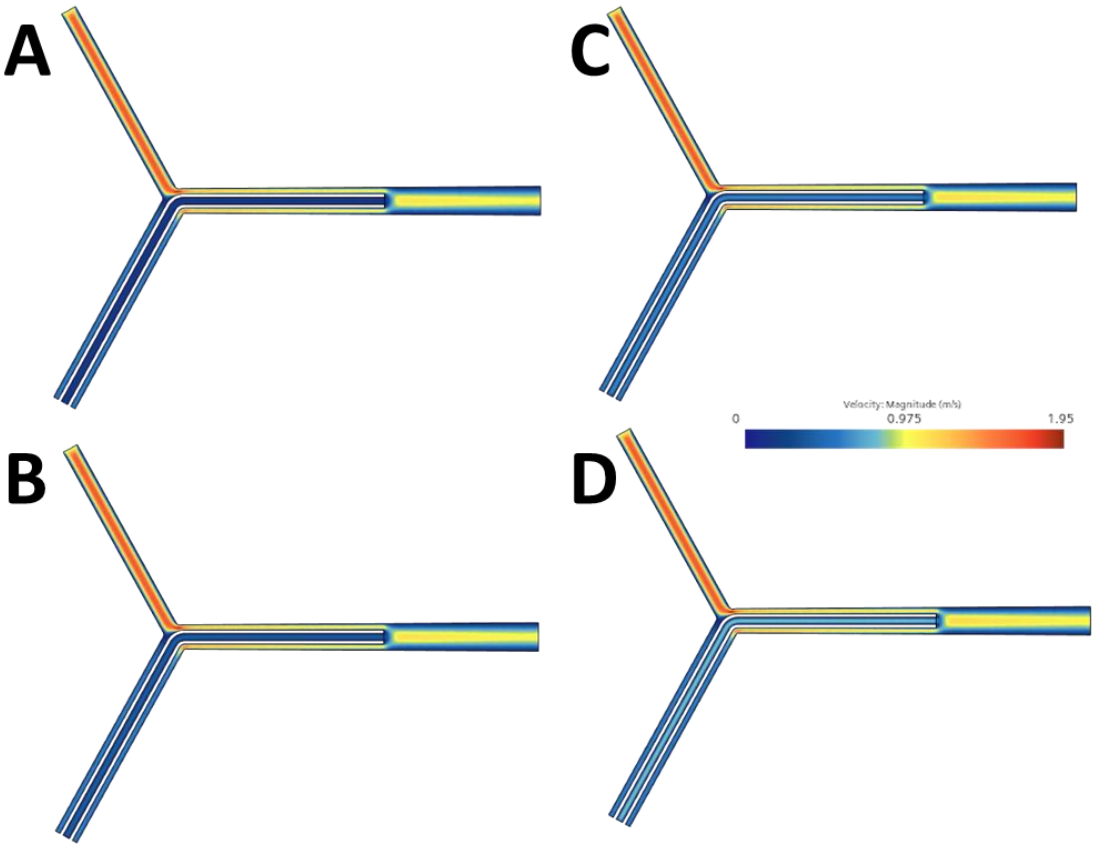

Figure 4.49: Fluid velocity as a function of flow rate. Large changes in infusion rate and therefore fluid velocity in the single lumen Hickman line lead to small changes in fluid velocity in the blood vessel.Infusion rates of saline are as follows: A) 50 ml min^{-1} B) 100 ml min^{-1} C) 150 mL min^{-1} D) 200 mL min^{-1}

The streamlines at the end of the Hickman line clearly visualise laminar flow (**Figure 4.50**). Again, the behaviour noted previously, where the streamlines exit spread equally across the entire area of the outlet, before quickly being concentrated into a narrow stream is observed.

Next, the streamlines for this geometry were visualised to better understand the behaviour of the fluid within the smallest lumen (Error! Reference source not found.). Within the smallest lumen in the triple lumen geometry studied in this section, the streamlines appear to behave very differently to other geometries in this chapter (**Figure 4.51**). Unlike the single lumen Hickman line studied earlier, it is apparent that the laminar flow and focussing behaviour of the streamlines following their exit from the VAD is not seen. Instead, both flow rates here show much more turbulent fluid behaviour, with the fastest infusion rate appearing to potentially indicate the presence of a recirculation zone immediately proximal to the outlet.

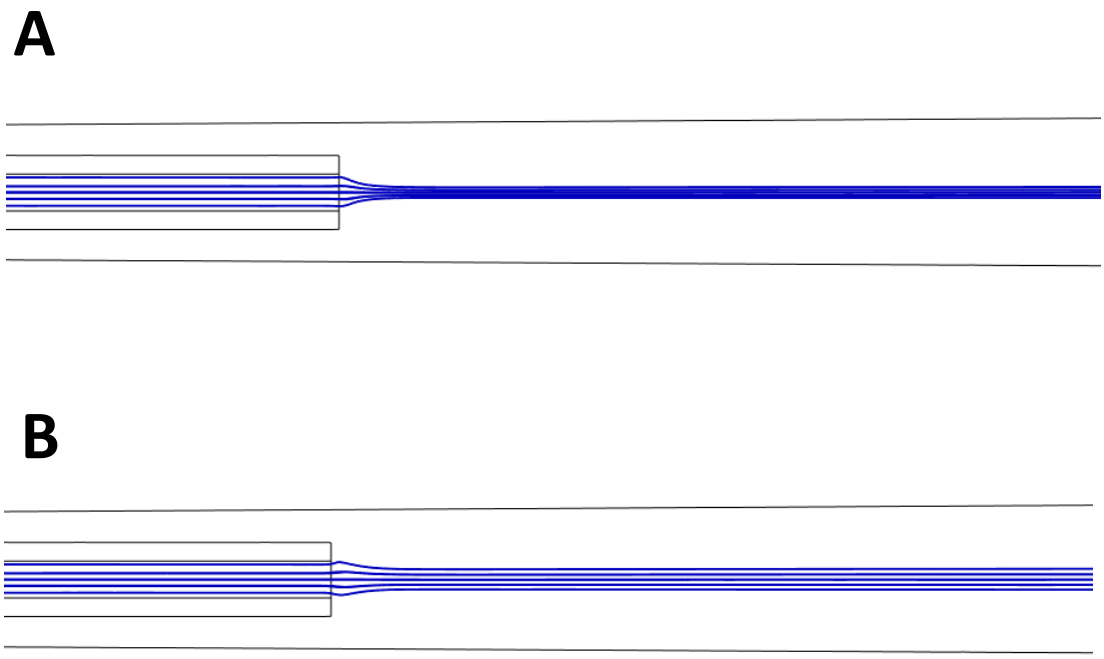

Figure 4.50: Laminar flow is clearly seen on visualisation of streamlines at the end of the Hickman line. This behaviour occurs irrespective of flow rate. A) 50 mL min^{-1} B) 200 mL min^{-1}

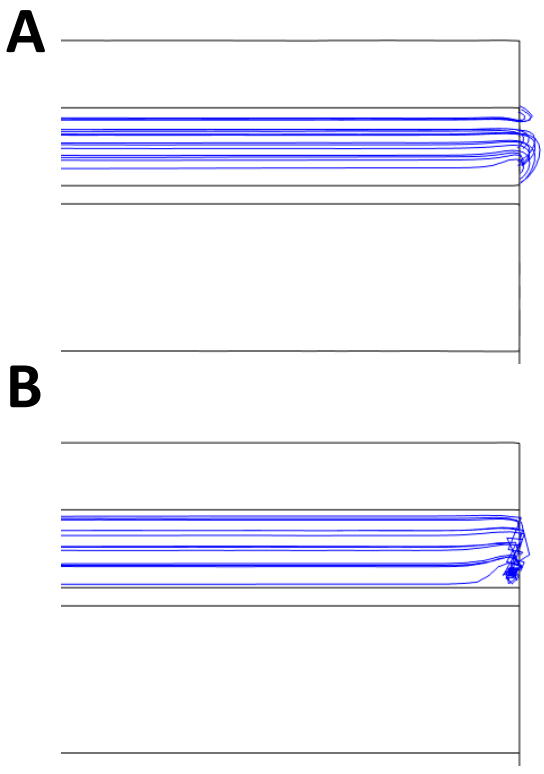

Figure 4.51: Streamlines for the triple lumen CVC geometry do not show the laminar flow and focussing behaviour reported earlier. Infusion rates of saline are as follows: A) 50 mL min^{-1} B) 200 mL min^{-1}

Finally, studying the possible return of spiral flow in the SVC was also of interest for this geometry (**Figure 4.52**). Spiral flow of the fluid in the superior vena cava is disturbed by the insertion of the Hickman line (A), leading to significantly more complex fluid behaviour in the final slice. Once the Hickman line is used for the infusion of fluids, the original spiral flow returns – this is most clearly seen in the final slice of the geometry.

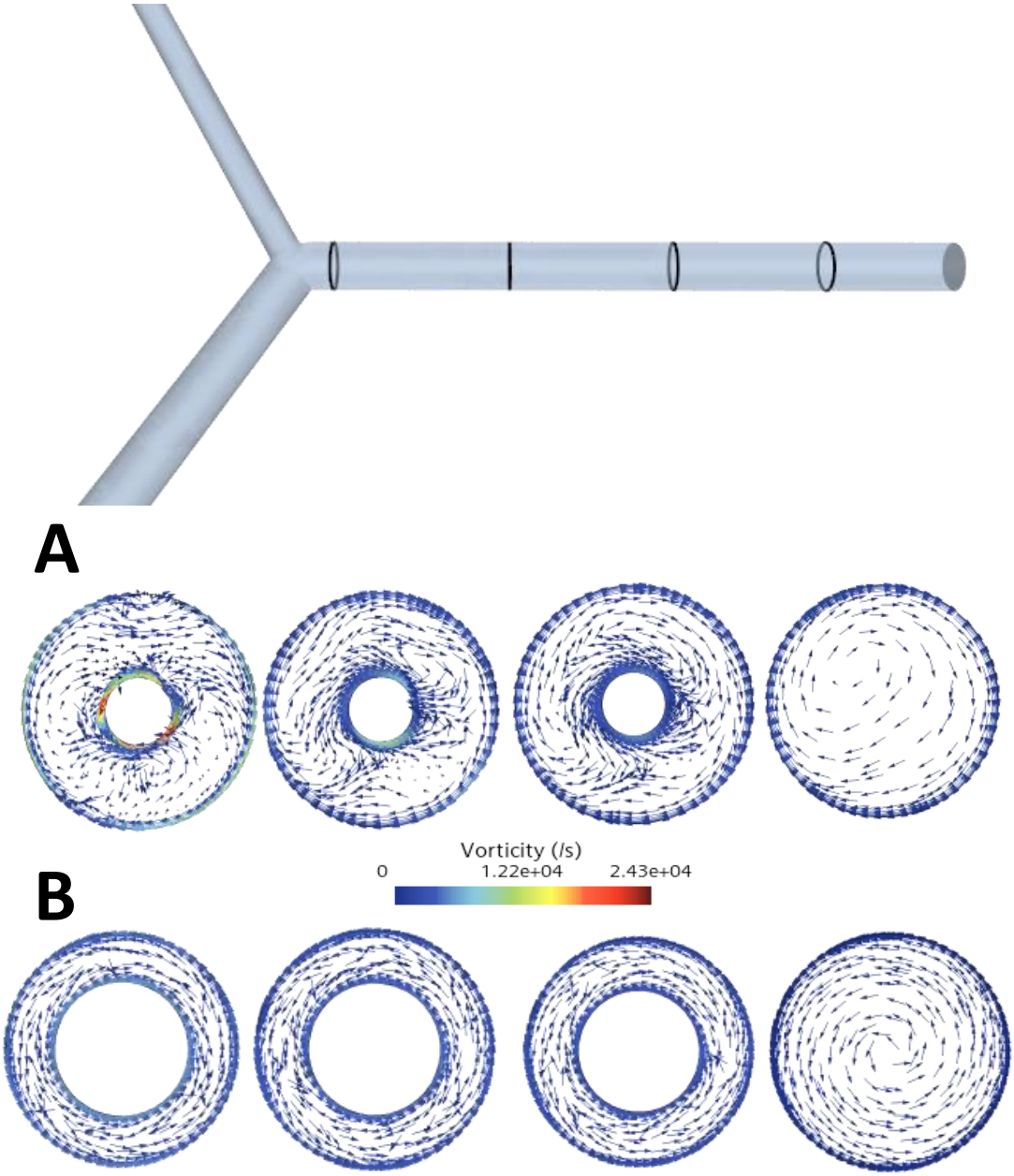

Figure 4.52: Cross-sectional slices of the geometry show circular flow is lost on the insertion of the Hickman line (A). Spiral flow returns when the Hickman line is used for the infusion of fluids (B). Positioning of the first slice was chosen arbitrarily, the remaining 3 are 0.02 m apart, to cover the length of the SVC.

Wall Shear Stress

Wall shear stress is a measure of the forces that the fluid exerts on the wall of the blood vessel and vice versa. In **Figure 4.53**, it is shown that there is almost no change of wall shear stress within the domain, irrespective of infusion rate – this result is unsurprising considering those reported for fluid velocity in **Figure 4.49**. What is observed, however, are the same localised areas of high wall shear stress on the blood vessel geometry itself, as well as on the Hickman line following insertion – as previously discussed in **Figure 4.48**. Furthermore, wall shear stress within the superior vena cava falls dramatically once the vessel is no longer obstructed by the Hickman line, this is again in-keeping with previous results.

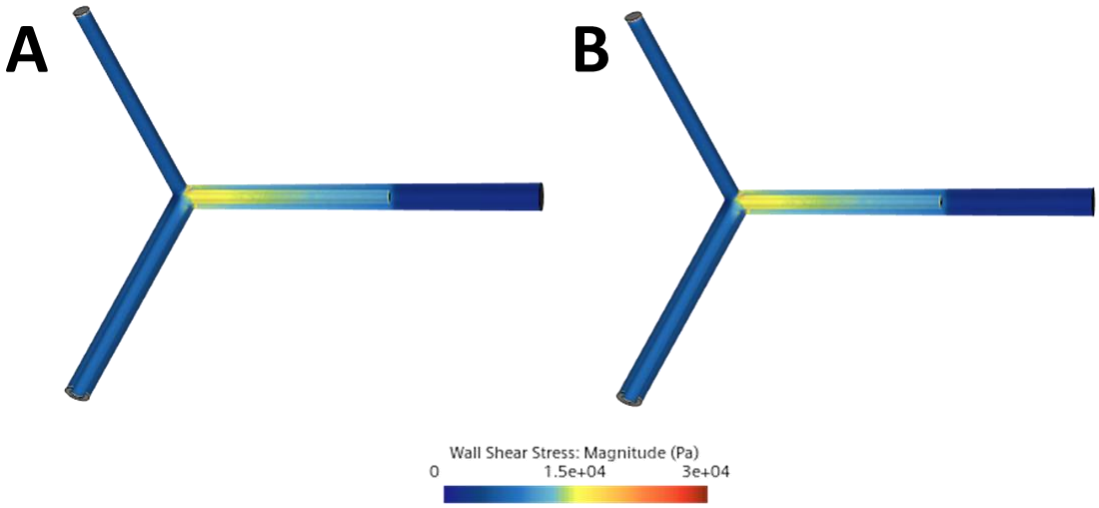

Figure 4.53: Wall shear stress varies as a function of infusion velocity. Infusion rates of 0.9% saline are as follows: A) 50 mL min^{-1} B) 200 mL min^{-1}

Mass Fraction of Blood

Mass fraction of blood (**Figure 4.54**) for the single lumen CVC geometry studied here shows that as infusion rate increases (and therefore fluid velocity through the Hickman line increases), a greater proportion of blood is cleared from the vein distal to the outlet; however the differences between 50 mL min^{-1} and 200 mL min^{-1} is somewhat challenging to see in this figure. These results also corroborate those shown in **Figure 4.49**, where increasing infusion velocity leads to almost negligible changes in fluid velocity in the vein.

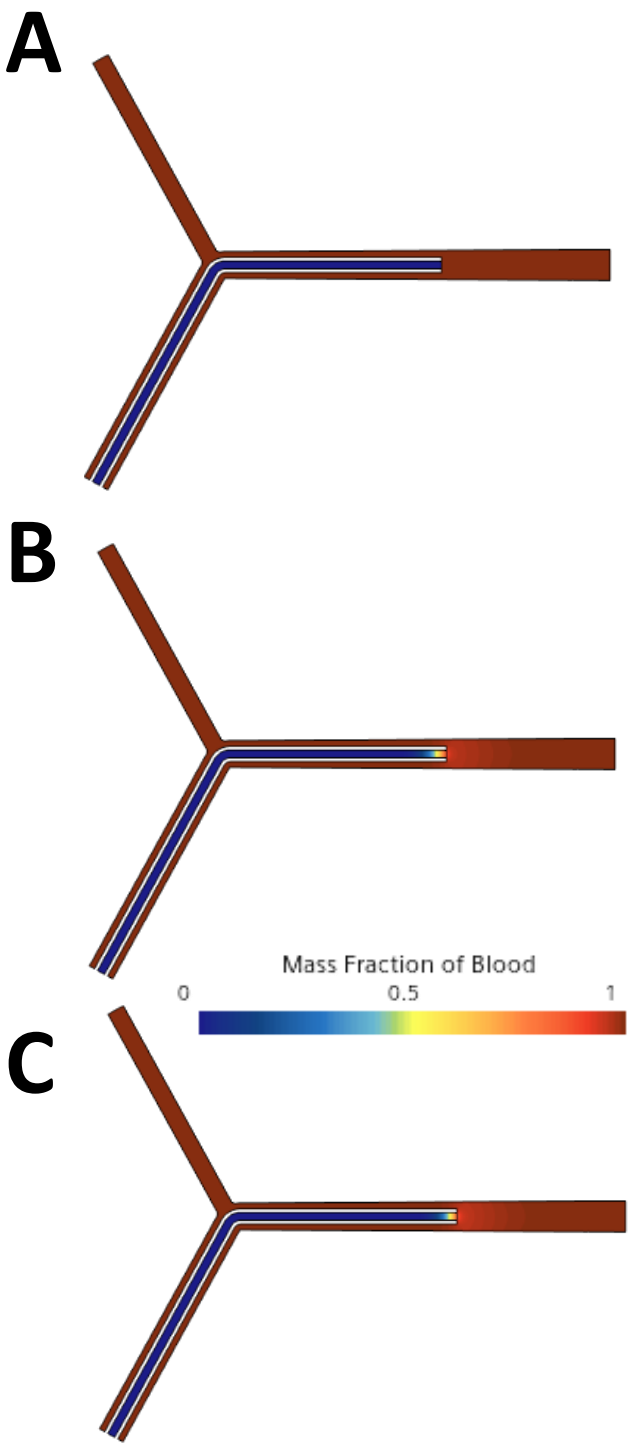

Figure 4.54: Mass fraction of blood. As infusion rate increases, a greater proportion of the blood vessel distal to the needle outlet is cleared of blood and replaced by 0.9% saline. A) No infusion B) 50 mL min^{-1} C 200 mL min^{-1}.

Residence Time

Residence time is a measure of how long a fluid particle spends within the domain (*i.e.,* the geometry under study), and was measured using the previously discussed method. Data for the minimum (*i.e.,* first particle to escape) residence times for each flow rate can be found in **Appendix H**. These results show as infusion rate increases, minimum residence times decrease,

corroborating those shown by the mass fraction of blood presented previously, since the greater the infusion rate, not only do particles introduced *via* the Hickman line leave the domain faster, but blood is also cleared quicker and replaced by infusion fluid.

4.6.1.4 Nanoparticle Behaviour Under Flow

In these simulations, where multi-lumen devices are used, the decision has been made that particles will be infused *via* one lumen only. In cases where there are multiple difference sized lumen available, it has been decided that the smallest of these will be used; the other lumen are assumed to be used for fluids. This assumption has been made to reduce the computational complexity of the simulation, even though this potentially diverges from how these central lines are used clinically – it is possible that multiple drug infusions would run simultaneously down multi-lumen devices. Set up for these CFD-DEM simulations is as previously described. Nanoparticles are introduced 0.1 cm parallel to the outlet, again, to reduce the real-world time that needs to be simulated.

Only the results for the single- and triple lumen device at their fastest infusion rates are shown here. The results for the remaining flow rates outlined previously, can be found in **Appendix H**.

Single Lumen

Particle velocity is a measure of how fast the particles within the simulation are moving. This depends on the weight and buoyancy of the particle as well as the drag force the particle is subject to. Since the particle is suspended in the fluid, and the previously calculated response time for these particles is known to be rapid, it is expected that the velocity of the particles will match that of the carrier fluid.

As a consequence of the shape of this geometry, the particles form several rows where they all have similar velocities (**Figure 4.55**). Unlike the PIVC studied earlier, the velocity of the particles are seen to increase in velocity on exiting the VAD and entering the blood vessel. This is consistent with the previously reported results for fluid velocity (**Figure 4.49**).

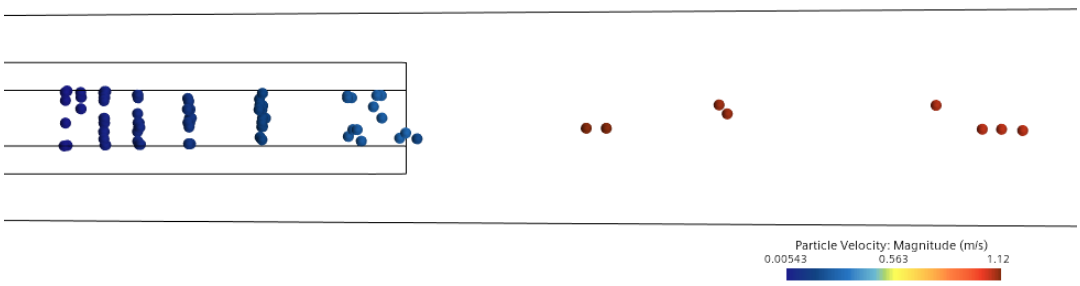

Figure 4.55: Particle velocity varies as a function of infusion rate and carrier fluid (saline, 200 mL min^{-1}). The particles rapidly show an increase in velocity on entering the blood vessel.

Particle shear stress is a measure of (primarily) friction between the fluid and the particles suspended within it. It is this force which is believed to alter the composition of the protein corona around nanoparticles and it is for this reason that it will be one of the key parameters used within the development of the microfluidic device within the following chapter. Consistent with previous results, it is shown by **Figure 4.56**, that as particles leave the CVC, particle shear stress increases.

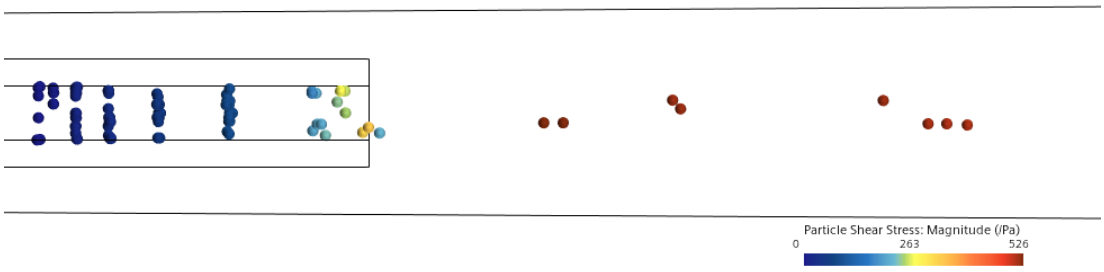

Figure 4.56: As particles leave the CVC line, particle shear increases.

Particle shear stress is shown in **Figure 4.57** to be a function of infusion rate. Maximum particle shear stress increases proportionally to infusion rate and therefore fluid velocity.

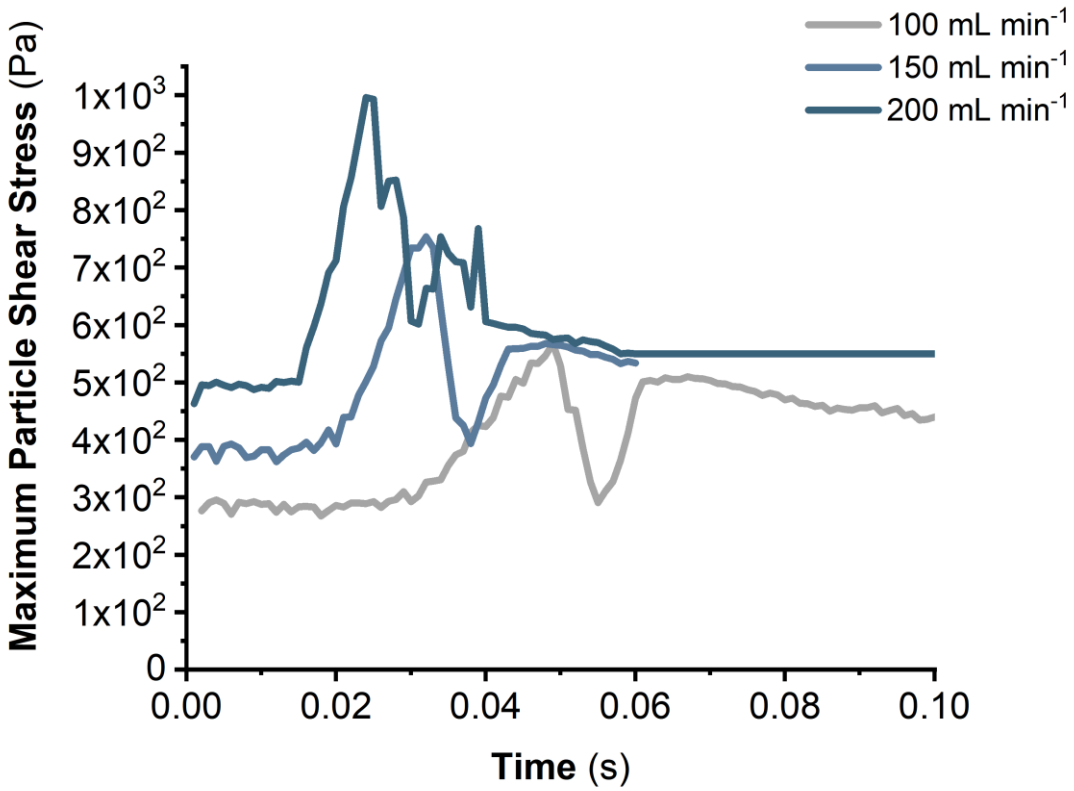

Figure 4.57: Particle shear stress as a function of time. As flow rate and fluid velocity increase, so too does maximum particle shear stress.

Treble Lumen

Like the analysis presented earlier, the triple lumen CVC geometry has also been studied in further detail to determine the influence of infusion rate on particle velocity and particle shear rate with this geometry. Particle velocity is shown in **Figure 4.58** to increase once particles reach the bloodstream. These results are consistent with both those for the single lumen geometry, as well as with the results for fluid velocity discussed previously.

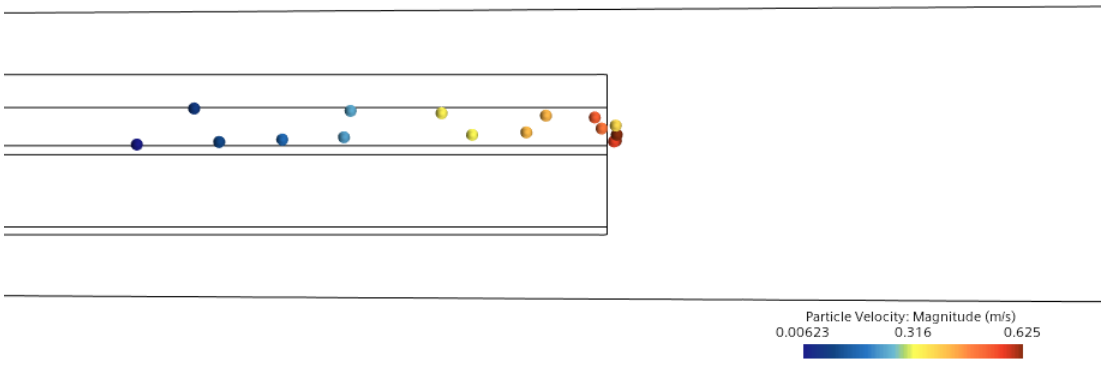

Figure 4.58: Particle velocity varies as a function of infusion rate and carrier fluid (saline, 17 mL min^{-1}). The particles rapidly show an increase in velocity on entering the blood vessel.

Consistent with the results for the single lumen CVC, particle shear stress is again shown to rise once the particles reach the blood stream (**Figure 4.59**).

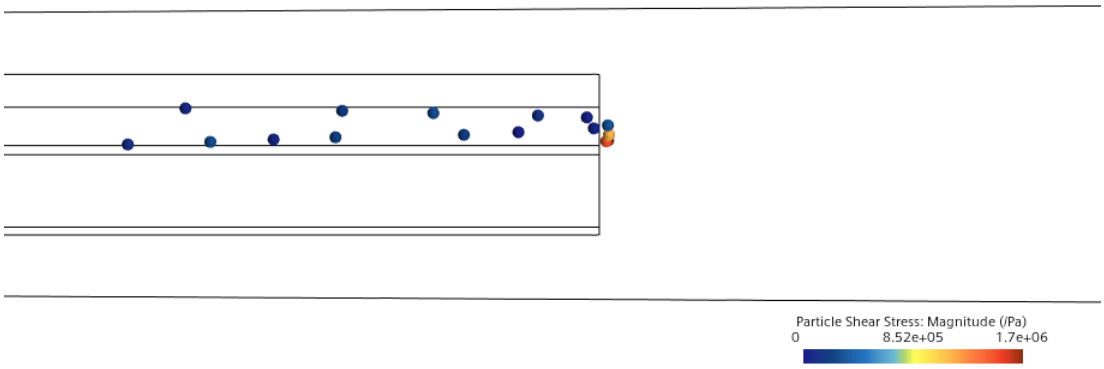

Figure 4.59: As particles leave the CVC line, particle shear increases

Particle shear stress is shown in **Figure 4.60** to be a function of infusion rate. Maximum particle shear stress increases proportionally to infusion rate and therefore fluid velocity.

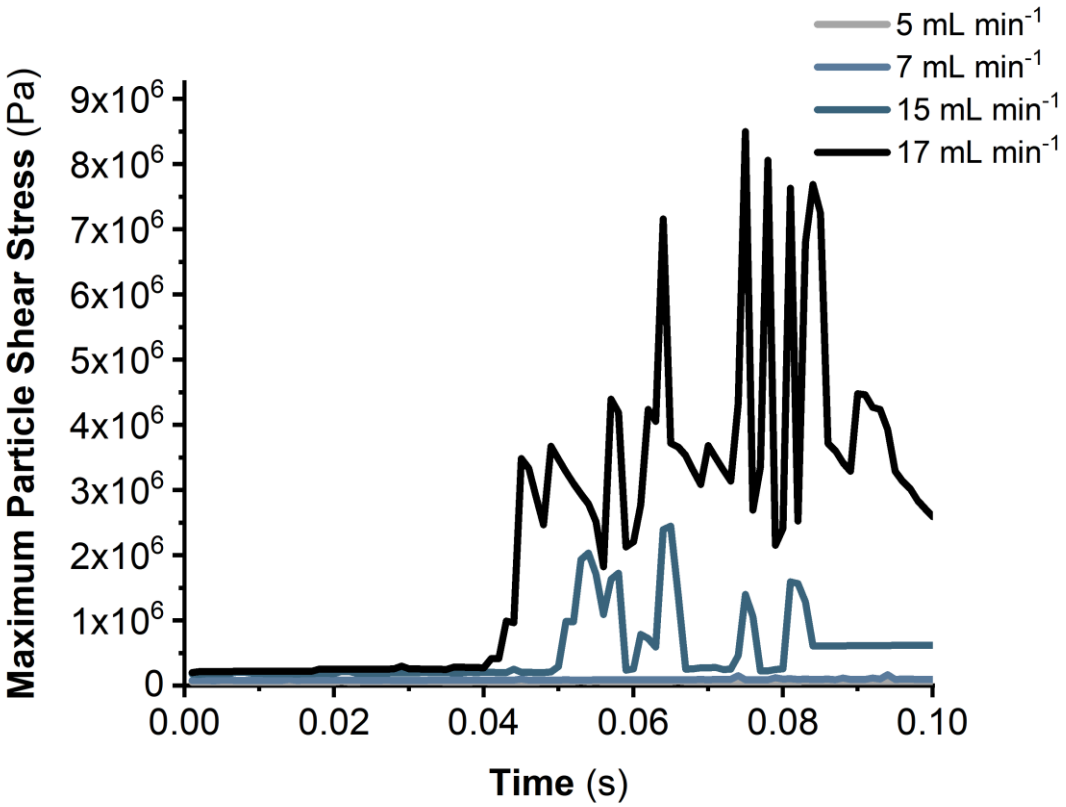

Figure 4.60: Particle shear stress as a function of time. As flow rate and fluid velocity increase, so too does maximum particle shear stress.

H. Data Table for Principal Component Analysis

VAD type	Lumen number	Infusion Fluid	Flow rate	Input Velocity (m s^{-1})	Maximum velocity (m s^{-1})	Average velocity (m s^{-1})	Maximum fluid shear rate (s^{-1})	Average fluid shear rate (s^{-1})	Maximum wall shear stress (Pa)	Average Wall shear stress (Pa)	Minimum residence time of fluid	Maximum particle velocity (m s^{-1})	Average Particle velocity (m s^{-1})	Maximum particle shear stress (Pa)	Average particle shear stress (Pa)
PIVC	Single	Glucose	10	0.58	1.13	0.16	9020.42	601.65	8500	1949.63	0.248	0.51	0.19	407449.70	94963.17
PIVC	Single	Glucose	30	1.75	3.44	0.27	24514.53	1179.77	13500	2837.34	0.129	0.45	0.20	856902.40	292908.50
PIVC	Single	Glucose	60	3.50	6.89	0.44	48573.85	2030.57	25800	4131.28	0.117	1.24	0.41	664672.20	265433.10
PIVC	Single	Glucose	300	17.50	33.95	1.82	146155.90	9140.02	80000	14516.25	0.015				
PIVC	Single	Saline	10	0.58	1.13	0.16	9020.43	598.30	8500	1948.85	0.254	0.48	0.18	341442.70	86405.82
PIVC	Single	Saline	30	1.75	3.40	0.27	14287.63	1170.37	12950	2820.42	0.131	0.44	0.19	830551.40	282881.50
PIVC	Single	Saline	60	3.50	6.88	0.43	28493.53	2005.61	25500	4043.04	0.080	0.41	0.19	686622.60	256155.90
PIVC	Single	Saline	300	17.50	36.20	1.81	146367.20	9148.52	138000	14610.07	0.020				
PICC	Single	Glucose	150	0.08	1.79	0.66	1037706.00	861.58	16000	4436.38	0.122	0.01	0.0001	10207.88	7165.29
PICC	Single	Glucose	300	0.16	1.79	0.66	1037706.00	876.43	19000	4435.64	0.122	0.01	0.01	16819.42	11091.59
PICC	Single	Glucose	600	0.33	1.79	0.67	1037706.00	900.03	19000	4437.17	0.122	0.02	0.02	36006.98	22012.62
PICC	Single	Glucose	1185	0.65	1.79	0.69	1037706.00	944.52	19000	4440.01	0.120	0.02	0.02	33267.64	16475.11
PICC	Single	Saline	150	0.08	1.79	0.66	1037706.00	863.27	18000	4434.36	0.122	0.03	0.02	22622.96	9325.25
PICC	Single	Saline	300	0.16	1.79	0.66	1037706.00	880.96	18500	4447.13	0.122	0.03	0.02	19356.23	11384.31
PICC	Single	Saline	600	0.33	1.79	0.67	1037706.00	904.55	18500	4448.30	0.121	0.04	0.03	23470.76	15124.93
PICC	Single	Saline	1185	0.65	1.79	0.69	1037706.00	949.04	18500	4450.50	0.120	0.03	0.03	11885.81	11885.81
PICC	Dual	Glucose	150	0.07	1.68	0.62	52870.01	810.50	18000	4660.93	0.168				
PICC	Dual	Glucose	300	0.13	1.68	0.63	52870.02	815.62	18000	4662.18	0.168				
PICC	Dual	Glucose	400	0.18	1.68	0.63	52870.02	820.00	18000	4662.95	0.168				
PICC	Dual	Glucose	547	0.24	1.68	0.63	52870.01	825.00	18000	4663.78	0.168				
PICC	Dual	Saline	150	0.07	1.68	0.63	52870.01	810.97	18000	4659.78	0.168				

PICC	Dual	Saline	300	0.13	1.68	0.63	52870.01	816.54	18000	4661.54	0.168				
PICC	Dual	Saline	400	0.18	1.68	0.63	52870.01	820.97	18000	4662.58	0.168				
PICC	Dual	Saline	547	0.24	1.68	0.63	52870.01	826.45	18000	4663.51	0.168				
PICC	Triple	Glucose	100	0.31	1.66	0.64	16769.50	816.17	17000	4636.89	0.166	1.22	0.45	754.10	202.44
PICC	Triple	Glucose	150	0.46	1.66	0.64	24197.65	818.73	17000	4636.97	0.166	1.26	0.41	873.55	218.31
PICC	Triple	Glucose	250	0.76	1.66	0.64	39973.46	823.73	17000	4637.04	0.166	0.06	0.04	954.71	454.33
PICC	Triple	Glucose	280	0.85	1.66	0.64	44705.45	825.34	17000	4637.10	0.166	1.22	0.45	783.52	211.90
PICC	Triple	Saline	100	0.31	1.66	0.64	16769.50	816.07	17000	4636.68	0.167	1.27	0.41	769.23	240.75
PICC	Triple	Saline	150	0.46	1.66	0.64	24197.04	818.59	17000	4636.78	0.167	1.27	0.41	773.97	242.56
PICC	Triple	Saline	250	0.76	1.66	0.64	39971.88	823.43	17000	4636.81	0.166	0.06	0.04	981.96	431.37
PICC	Triple	Saline	280	0.85	1.66	0.64	44703.50	824.97	17000	4636.86	0.166	0.06	0.04	957.64	462.86
CVC	Single	Glucose	200	0.44	1.95	0.66	13764.08	1167.32	30000	7277.41	0.24	0.28	0.12	484.54	110.48
CVC	Single	Glucose	150	0.33	1.95	0.65	13757.47	1147.82	29500	7273.85	0.24	0.43	0.13	615.74	233.26
CVC	Single	Glucose	100	0.22	1.95	0.65	13795.00	1129.29	29500	7275.46	0.24	0.43	0.13	1054.29	403.65
CVC	Single	Glucose	50	0.11	1.95	0.64	13789.08	1110.02	29000	7271.51	0.24	0.28	0.12	2067.51	610.78
CVC	Single	Saline	200	0.44	1.95	0.64	49660.70	1113.19	29500	6939.40	0.24	0.2817	0.1244	32.8141	7.0495
CVC	Single	Saline	150	0.33	1.95	0.64	49660.70	1090.76	29500	6871.09	0.24	0.2814	0.1243	371.0872	112.8124
CVC	Single	Saline	100	0.22	1.95	0.63	49660.70	1068.52	29500	6803.32	0.24	0.2811	0.1241	790.8918	237.0545
CVC	Single	Saline	50	0.11	1.95	0.63	49660.70	1046.29	29000	6734.92	0.24	0.2807	0.1239	1211.0580	361.3353
CVC	Triple	Glucose	17	0.57	2.31	0.49	3631552	906.87	30000	5665.74	0.33	0.56	0.27	1489335.00	453491.40
CVC	Triple	Glucose	15	0.49	2.31	0.49	3652101	900.84	30000	5625.89	0.33	0.47	0.24	1024002.00	202410.60
CVC	Triple	Glucose	7	0.23	2.3	0.49	3667271	879.83	30000	5486.40	0.33	0.47	0.24	1025191.00	208567.30
CVC	Triple	Glucose	5	0.16	2.29	0.49	3732859	874.01	30000	5447.24	0.33	0.62	0.17	1456748.00	354719.50
CVC	Triple	Saline	17	0.57	2.32	0.49	3715992	906.74	30000	5632.41	0.33	0.63	0.34	1703207.00	390349.10
CVC	Triple	Saline	15	0.49	2.32	0.49	3737539	900.84	30000	5597.35	0.33	0.50	0.26	1253939.00	306822.30
CVC	Triple	Saline	7	0.23	2.31	0.49	3736587	879.72	30000	5471.06	0.33	0.34	0.19	251832.50	141054.20
CVC	Triple	Saline	5	0.16	2.3	0.49	3734294	874.03	30000	5436.64	0.33	0.50	0.26	1248988.00	305964.80

I. PCA Correlation Matrix

	Input Velocity	Maximum velocity	Average velocity	Maximum fluid shear rate	Average fluid shear rate	Maximum wall shear stress	Average Wall shear stress	Minimum residence time of fluid	Maximum particle velocity	Average Particle velocity	Maximum particle shear stress	Average particle shear stress
Input Velocity	1	0.90578	-0.4072	-0.24808	0.80535	-0.11705	-0.38049	-0.39781	0.22367	0.23563	0.22036	0.37717
Maximum velocity	0.90578	1	-0.30574	-0.01498	0.91995	0.21548	-0.12416	-0.2261	0.1599	0.19952	0.34777	0.4933
Average velocity	-0.4072	-0.30574	1	-0.15021	-0.0671	0.2394	0.58285	-0.26335	-0.09663	-0.20056	-0.56669	-0.61544
Maximum fluid shear rate	-0.24808	-0.01498	-0.15021	1	-0.21835	0.50111	0.14119	0.67203	-0.05726	0.10595	0.75269	0.66917
Average fluid shear rate	0.80535	0.91995	-0.0671	-0.21835	1	0.34378	0.15263	-0.27608	0.07994	0.0748	0.10258	0.24464
Maximum wall shear stress	-0.11705	0.21548	0.2394	0.50111	0.34378	1	0.84857	0.63941	-0.08266	0.02558	0.35817	0.31272
Average Wall shear stress	-0.38049	-0.12416	0.58285	0.14119	0.15263	0.84857	1	0.45196	-0.12326	-0.09555	-0.08894	-0.15749
Minimum residence time of fluid	-0.39781	-0.2261	-0.26335	0.67203	-0.27608	0.63941	0.45196	1	0.01845	0.18054	0.5758	0.45879
Maximum particle velocity	0.22367	0.1599	-0.09663	-0.05726	0.07994	-0.08266	-0.12326	0.01845	1	0.95838	0.11289	0.12074
Average Particle velocity	0.23563	0.19952	-0.20056	0.10595	0.0748	0.02558	-0.09555	0.18054	0.95838	1	0.29396	0.29062
Maximum particle shear stress	0.22036	0.34777	-0.56669	0.75269	0.10258	0.35817	-0.08894	0.5758	0.11289	0.29396	1	0.96907
Average particle shear stress	0.37717	0.4933	-0.61544	0.66917	0.24464	0.31272	-0.15749	0.45879	0.12074	0.29062	0.96907	1

J. Converting Principal Components to Fluid and Particle Parameters

PCA is a dimensionality reduction method that maintains most of the initial input data. This means it is possible to move from principal components and their weightings, back to the initial input factors *i.e.,* the properties of the simulation (*e.g.* fluid shear). This methodology could be carried out on all 14 of the input factors, but here only maximum and average fluid shear rate and maximum and average particle shear stress are the parameters of interest. These factors have been determined from the weightings in **Figure 4.41**.

In this work, the values of the four factors outlined earlier, are of interest when PC1 has the values -2 and +1, and where PC2 is between -2 and +4.

Normalising the input data

A normalisation 'widget' was used, so that the precise normalisation methodology used by Orange could be a) identified and b) controlled by the user.

Normalisation was performed such that $\mu = 0$, $\sigma^2 = 1$.

Calculating factors from principal components

There are 4 points (-2,-2), (+1, -2), (-2 +4) and (+1,+4) that outline the space where most of the points lie. The normalised values are given in **Table 4.39**.

Table 4.39: Normalised values outlining the parameter space where the bulk of the simulations in this chapter fall following PCA analysis.

Principal components	Maximum fluid shear rate (s^{-1})	Average fluid shear rate (s^{-1})	Maximum particle shear stress (Pa)	Average particle shear stress (Pa)
(-2,-2)	0.931658952	-0.513359814	-2.104826112	-1.040323348
(+1, -2)	0.860892237	0.766596403	-2.139007615	-1.058075695
(-2 +4)	1.905480888	-0.338216719	1.133973746	2.10411241
(+1,+4)	1.834714172	0.941739497	1.099792243	2.086360063

From the table above, the simulation created in the following chapter must be able to cover (in terms of normalised values) the following ranges (**Table 4.40**).

Table 4.40: Range of each factor covered by the parameter space outlined earlier – as normalised values

Principal components	Maximum fluid shear rate (s^{-1})	Average fluid shear rate (s^{-1})	Maximum particle shear stress (Pa)	Average particle shear stress (Pa)
Minimum	0.8609	-0.51	-2.139007615	-1.058075695
Maximum	1.9055	0.94	1.133973746	2.10411241

The normalisation is then undone, and gives the following factor values (**Table 4.41**).

Table 4.41: Factor values following the reversal of the normalisation procedure.

Principal components	Maximum fluid shear rate (s^{-1})	Average fluid shear rate (s^{-1})	Maximum particle shear stress (Pa)	Average particle shear stress (Pa)
Minimum	5.98×10^5	8.27×10^2	7.60×10^5	4.80×10^4
Maximum	1.03×10^6	1.21×10^3	9.54×10^5	3.90×10^5

Part 3: Microfluidics and 3D-Printing

Chapter 5

An *in silico* Model of a Microfluidic Device Capable of Mimicking Physiological Fluid Shear Stress.

5.1 Introduction

Previously, in Part 2 of this thesis, a CFD-DEM methodology was developed to simultaneously study fluid and nanoparticle behaviour *in vivo*, then applied to study the fluid and nanoparticle forces present in the immediate aftermath of introducing PLGA nanoparticles into blood flow. Principal component analysis was then used to elucidate further insights into the data through dimensionality reduction. From this, input values for a possible microfluidic device were extrapolated from the PCA values.

In this chapter, a novel microfluidic device will be designed and then modelled *in silico* using the methodology developed earlier to show that physiologically relevant shear stresses can be mimicked and, therefore, it could be used to study polymeric nanoparticles under flow and ascertain the impact these shear forces have on protein corona formation and composition *in vivo*, without need

for animal-based pre-clinical testing. A potentially suitable polymer for 3D printing will also be found via a literature review.

This is the concluding section of the thesis and begins with a literature review where a broad introduction to microfluidics will be covered, including the history of the discipline as well as a review of several potential manufacturing methods. Next, additive manufacturing (with specific reference to fused deposition modelling) will be outlined, as well as attempting to find a suitable polymer for the eventual FDM-based manufacture of this device. This literature review will also determine that PLA is likely to be an appropriate polymer. Next, the design process of the device will be discussed before CFD calculations are undertaken to assess the fluid and nanoparticle behaviour in the device. Finally, comparisons will be made between the values determined *via* PCA in **Chapter 4**, and those obtained *via* simulation (**Figure 5.13**).

5.2 Literature Review

This literature review begins with a brief history of microfluidics before discussing several ways microfluidic devices can be manufactured. Then, the use of CFD with and without machine learning for design analysis and optimisation is considered. Next, additive manufacturing and fused deposition modelling (FDM) are introduced and discussed in detail before the properties influencing the choice of polymer for FDM are reviewed. Finally, examples of 3D-printed microfluidic devices from the literature are explored before the key parameters that determine the design of a microfluidic device are outlined.

5.2.1 An Introduction to Microfluidics

Microfluidics refers to the processes through which small volumes (10^{-9} – 10^{-18} litres) of liquids or gases are manipulated *via* channels between 10-100 μm in diameter.[617,618] Microfluidic devices are typically polymer-based devices with micro- and nano-geometric features to hold and manipulate small fluid volumes.[619] They may sometimes be referred to as lab-on-a-chip devices, but there are slight differences between them. Strictly speaking, lab-on-a-chip devices are a subset of microfluidics, indicating that the chip contains one or more scaled-down laboratory processes. The field has grown significantly over the previous forty years, and a wide range of potential uses (not just within the biological sciences) have been reported within the literature.

5.2.1.1 History of Microfluidic Devices

The field of microfluidics owes much of its development to that of microelectronics, the patenting of photoengraving, which later became the photolithography still in use today for the manufacture of many microfluidic devices, and the development of the integrated circuit in a single silicon crystal.[620]

The earliest reports of microfluidic devices can be found from the early 1960s, with the development of gas chromatography at Stanford and inkjet nozzles at IBM.[621] The first microfluidics device is believed to be a miniaturised version of a gas chromatograph at Stanford in the 1970s.[622] Because of the cost of this device (~$100,000), it was never developed further.[617,621]

1980-1990

The development of 3D printing (stereolithography) by Hull and colleagues in 1986 is another invention which subsequently progressed to affect microfluidics.[623] Stereolithography is a technique by which structures undergo layer-by-layer fabrication. A laser is used to selectively polymerise a photosensitive liquid resin into its solid form; these parts can be fabricated rapidly, but their mechanical properties are often lacking.[624]

LIGA (Lithographie, Galvanoformung, Abformung; German for Lithography, Electroplating, Moulding) is a process that adds an additional electroplating step following lithography to enable the manufacture of reusable moulds that can be used to produce many replicas of the original.[620,625] This technology was initially developed using X-rays from a synchrotron source, but a version utilising Ultraviolet light does exist. This technique is particularly good at creating significantly taller structures than wide ones (high aspect ratio).[625]

At the microscale, electrostatic forces play a far more significant role, and as such, the magnetic values used at the macroscale cannot be used here.[620] The development of miniaturised valves and pumps for microfluidic devices enabled the control and manipulation of small fluid volumes. However, some of their earliest forms were complex in design and challenging to manufacture.[626,627]

1990-2000's

Early in 1990, the term 'micro total analysis systems' (μTAS), now called lab-on-a-chip, was proposed to shrink the entire analytical laboratory to the size of a microfluidic chip. This aim has remained somewhat elusive and is sometimes termed "chip-in-a-lab".[628] One of the earliest reports of "lab-on-a-chip" in the literature is the device manufactured by Manz *et al.* in 1993 for capillary electrophoresis-based separations.[629] Further lab-on-a-chip devices came from the groups of Harrison, Ramsey and Mathies.[630–632] These devices all have one thing in common; they all use glass or silicon as their substrate and are manufactured using techniques adapted from the semiconductor industry – namely etching and photolithography.[617]

In this decade, microfluidics began to take off; its rapid development was fuelled by considerable government funding. Not only were these emerging technologies of interest at the end of the Cold War to the Defence Advanced Research Projects Agency (DARPA) as portable, analytical platforms for the detection of chemical and biological warfare agents, but they also played an important role in the success of the Human Genome Project.[618] The aim of the Human Genome Project was to map the entire human genome within 15 years, but it was rapidly noticed that standard gel electrophoresis techniques did not have adequate throughput to enable this goal to be realised, leading to the development of capillary electrophoresis.[632–635]

Whitesides and colleagues pioneered the novel polymer poly(dimethyl siloxane) (PDMS) in the late 1990s.[617,636,637] Not content to only introduce a novel material, a range of new manufacturing methods were also

developed.[638] These methods are now known as soft lithography – including replica moulding, nanoimprint lithography and microcontact printing (**Section 5.2.1.2**). Finally, the development of the negative photoresist SU-8 by IBM, with its improved aspect ratio, enabled the realisation of many designs for micro-electromechanical systems (MEMS) and lab-on-chip devices that had previously been too difficult to manufacture.[639,640]

2000-2010

A vast range of new techniques had been developed over the previous decade; the turn of the century then brought about rapid expansion in microfluidics research and, consequently, its applications.

Droplet microfluidics (sometimes termed digital microfluidics due to the discrete nature of the droplets themselves) has rapidly been adopted for high-throughput biochemical analysis and reaction screening.[641,642] The droplets are typically formed in an oil-in-water emulsion, and the reactants are captured within each droplet. It is possible for thousands of reactions to happen independently of each other.[620] This technique has also been exploited for the controlled manufacture of liposomes and gold nanoparticles.[643,644]

Surprisingly, it was not until 2007 that Martinez and colleagues developed paper-based microfluidic devices.[645,646] These were initially used to multiplex several biological assays in the same device to analyse microlitre volumes of complex biological fluids (*e.g.,* blood, urine).[645] As predicted by the authors, these paper-based microfluidic devices have been incorporated into a range of point-of-care tests.[647,648]

2010 – Present

More recently, 3D printing has begun to make an impact on microfluidics. Fused deposition modelling is the most commercially successful form of 3D printing. Not only can this technique be used to 3D print masters for microfluidic devices, but the microfluidic device itself can result from 3D printing if a suitable material is selected.[649] Furthermore, a flourishing area of 3D printing includes designing and printing custom laboratory consumables, such as the 3D-printed "Reactionware" by Cronin and colleagues.[650]

One of the most well-researched and rapidly adopted areas of microfluidics is the Organ-on-chip.[651] These systems are microfluidic devices for the 3D culture of cells to better mimic *in vivo* behaviour. The earliest example of an organ-on-chip was designed to capture and copy the organ-level structure of the lung alveolus.[651] Since then, an extensive range of organs-on-chip have been developed, primarily for drug screening applications but also for studying a range of pathological states (*e.g.,* vascular disorders and cancer metastasis).[652–657] Multi-organ-on-chip devices also exist to enable the study of the interactions between organ systems.[658–660] Body-on-chip (also known as human-on-chip) devices have previously been hypothesised by several groups.[659,661,662]

Currently, microfluidics is moving away from the single-function microfluidic chip towards more modular designs.[663,664] Current work towards introducing standards for microfluidics is likely to accelerate this – currently, interoperability of devices is often poor.[663,665,666] Furthermore, the area is moving towards developing technologies that take micro-manufacture out of the cleanroom and into the hands of non-specialists. Particularly useful here is fused deposition modelling (discussed further in **Section 5.2.4.2**). Shin and Choi report an extensive review of the emerging Do-it-Yourself and Open Source paradigms within science and engineering.[667] There are many currently available open-source software and repositories for sharing designs for novel microfluidic devices; one such popular repository has the delightful name of the Thingiverse.[668–672]

5.2.1.2 Manufacturing Microfluidic Devices

A range of methods exist for the manufacture of microscale devices. These methodologies include photolithography, the soft lithographic techniques introduced by Whitesides and colleagues and the more recent application of additive manufacturing (3D printing).

Photolithography

Photolithography is a process by which a photosensitive polymer (a photoresist) is selectively exposed to light through a mask.[673] Light causes the photoresist to undergo a chemical reaction, and depending on the type of resist, this may either cause the polymer to degrade and make this area soluble once the resist is developed (positive photoresist) or cure the polymer, making it insoluble (negative photoresist).[674] Photolithography is frequently used to create the masters, which are then used alongside soft lithographic techniques to develop microfluidic platforms.

Soft Lithography

Various printing methods are used to manufacture microscale devices, which come under the umbrella of soft lithography (**Figure 5.1**).[675] These include microcontact printing, replica moulding, micro-transfer moulding, capillary moulding, solvent-assisted micromoulding, phase-shifting edge lithography, nanotransfer printing, decal transfer lithography and nanoskiving.[675] Only microcontact printing and replica moulding will be discussed in detail; the remainder are outside the scope of this literature review.

Microcontact printing (μCP) is a form of soft lithography which uses a stamp made from PDMS to transfer molecular “inks” onto another surface (**Figure 5.1**). This leads to the formation of self-assembled monolayers (SAMs) on the substrate.[676] These SAMs are often alkanethiols, but examples of other biomolecules, including proteins, can be found within the literature.[676–680] Hager *et al*. have recently explored the possibility of microcontact printing using a PDMS-based stamp and a wide range of polymers as the substrate to develop micropatterned substrates suited for fluorescence microscopy and cellular assays.[678] One stamp can be used to print many devices.[681] Since the stamp is made from PDMS, it can be deformed, either by stretching or

compression, altering the pattern that the stamp reproduces.[676] This property can be exploited to print features of sub-micron size, even though the stamp itself is of much lower resolution.[676] However, if the "ink" includes organic solvents, the PDMS stamp may begin to swell during inking.[676] This swelling causes a deterioration in the fidelity of the pattern produced by the stamp, leading to much larger features in the pattern and smaller gaps between them.[676,681]

Replica moulding is, as its name suggests, the formation of a replica from a master mould (**Figure 5.1**). This method has several advantages over other soft lithography methods, namely, that this technique allows the reproduction of complex 3D structures in a single step.[638] The technique is also simple, reliable, inexpensive and can reproduce patterns with high fidelity.[638] Again, like μCP, the master can repeatedly create many replicas.[638] Using a solid master mould can make the release of small, fragile components of the mould difficult, but this can be overcome by creating the mould from a soft, easily deformable polymer such as PDMS and by using a suitable release agent (*e.g.,* a perfluorosilane).[638]

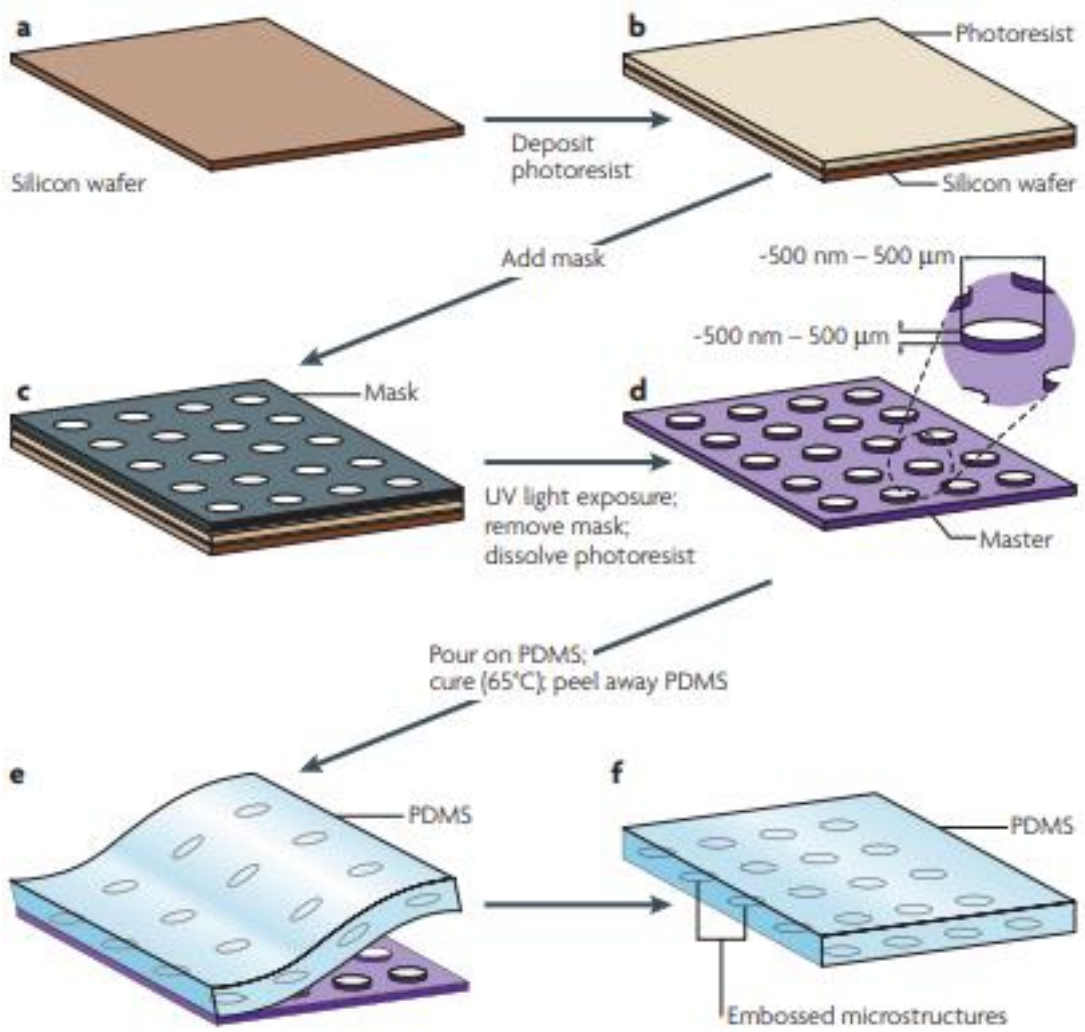

Figure 5.1: A schematic representing the main steps in developing PDMS microfluidic devices. Reproduced with permission from Springer Nature. From [682]. a) The master of the microfluidic device is built on a silicon wafer. b) The photoresist is spin-coated onto the wafer. c) A mask is applied, and the entire assembly is exposed to UV light to cure the photoresist. d) Organic solvent is used to dissolve uncured photoresist. e) PDMS (poly dimethylsiloxane) is poured onto the master, cured thermally, and removed. f) The PDMS layer contains the inverse of the original pattern embossed on the surface of the master.

Additive Manufacturing

Combining additive manufacturing with microfluidics is an emerging technology expected to have considerable influence on the development of organ-on-chip (and, by extension, body-on-chip) devices.[683]

Additive manufacturing (also known as 3D printing, is defined by the ASTM society as “a process of joining materials to make objects from 3D model data, usually layer upon layer, as opposed to subtractive manufacturing methodologies”.[684] Additive manufacturing is therefore an umbrella term that refers to many different techniques, including stereolithography (SLA) and fused deposition modelling (FDM); only FDM is of interest in this work. These techniques have a variety of advantages, including prototypes being quick and often cheap to manufacture compared to traditional methods. Additive manufacturing is discussed in further detail in **Section 5.2.4**.

5.2.1.3 Advantages and Disadvantages of Microfluidic Systems

In recent years, microfluidics has emerged as an incredibly useful tool for bridging the translational gap between animal models and pathological states in humans.[685] They have revolutionised *in vitro* studies, as they afford better mimicry of physiological parameters than previous techniques, enabling novel insights into pathological states to be uncovered.[685] Microfluidic devices can be rapidly and reproducibly manufactured, use significantly smaller volumes of reagents and analytes and give control over a wide range of physiological parameters (*e.g.*, dimensions, surface topology, fluid flow, as well as electrical or mechanical stimuli).[685] Furthermore, a number of compatible substrates and pumping methods have previously been explored.

Speed of Manufacture and Moulds are Reusable

Firstly, through using the soft lithography methods outlined earlier, the devices can be manufactured in a few short hours.[675] Once the master has been created, this can be reused indefinitely if the user is sufficiently careful – particularly if the master mould is made from silicon, as this is known to be fragile, and therefore, the systems are easily reproducible.[617]

Small Sample Volumes

One of the biggest advantages of microfluidic devices is that tiny amounts of reagents or analytes are required. For example, there is the potential for a 10-100-fold decrease in the number of cells needed when such devices are used in comparison to traditional cell culture methods.[686]

Single-cell analysis has also been widely explored through lab-on-a-chip methods, and droplet (digital) microfluidics is a popular choice for microfluidic-assisted high-throughput screening.[687–689] Furthermore, droplet microfluidics has previously been used not only for the synthesis of novel molecules but also for nanoparticles.[650,690,691]

Control Over a Wide Variety of Experimental Parameters

Microfluidic devices are better able to reproduce *in vitro* conditions than static 2D cell culture methods. It is also possible to control a variety of parameters in the system, not just cell parameters but mechanical parameters too (*e.g.,* fluid flow can be under spatial and temporal control). Only the experimental parameters of interest in the context of this project are discussed here. Many other parameters can be controlled, but they are outwith the scope of this thesis. The extra parameters that can be included in microfluidics-based models do not only modify the behaviour of the cell line(s) of interest, but they can also modulate the behaviour of the nanoparticles under test; this includes nanoparticle-cell interactions but also changing how the nanoparticles settle and/or aggregate in solution.[22]

In vivo, nanoparticles are inevitably subject to fluid flow, which impacts not only nanoparticle-cell interactions but also sedimentation and aggregation behaviour.[22,692] Chen *et al.* have recently reported a study on the influence of physiological fluid flow on nanoparticle uptake into endothelial cells.[693] They create a relatively simple microfluidic device for on-chip cell culture, and these

cells are subject to flow prior to nanoparticle introduction to induce the known phenotypic variation as a consequence of flow but appear not to report the co-incubation of the gold nanoparticles in cell culture medium prior to introducing these into the microfluidic chip – counter to the recommendations made by Mahmoudi.[43] Despite this, they state that both time under shear and shear rate influence nanoparticle uptake; the longer the cells are under shear, the fewer nanoparticles are internalised into cells, and the same is true for increasing shear rate.[693] Furthermore, nanoparticle sedimentation and aggregation behaviour have been studied to improve the clinical translation of nanoparticles.[694] Incorporating fluid flow and mechanical forces to better replicate the *in vivo* environment could overcome known issues with nanoparticle sedimentation in static cell culture and how this then alters the perceived cytotoxicity and efficacy.[695]

A Wide Variety of Compatible Substrates

A variety of substrates have been used within the literature to create microfluidic devices for a wide range of different functions. These substrates include PDMS, other polymers (*e.g.,* PLA) and paper.[646,647,650,696]

PDMS is a popular choice of material for the development of microfluidic devices.[636,697] These initial systems were designed to perform capillary electrophoresis.[636] They highlight various properties unique to PDMS, the way in which they reversibly bind to another piece of PDMS so that the device can be opened and the channels cleaned.[636] Additionally, they also show that if the PDMS pieces are treated in an air plasma and subsequently become oxidised, the binding of the PDMS is no longer reversible, irrespective of whether this is to another piece of PDMS or a selection of other substrates, including glass, silicon, and poly(styrene).[636] Many other polymeric materials have also been used as substrates for microfluidic devices. These polymers include poly(lactic acid), poly(propylene) and other thermoplastic polymers.[649,650]

The most well-known or well-recognised biomedical uses of microfluidics are the disposable, paper-based devices. In this context, paper is defined more broadly as any porous membrane that wicks fluid *via* capillary action.[698] The two most commonly used are cellulose-based papers and nitrocellulose-based membranes.[698] The reader will be familiar with the lateral flow assays for SARS-COV-2 (COVID-19). The devices consist of overlapping porous membranes, which include a sample pad, conjugate pad, test line, control line and absorbent pad (

Figure 5.2).[698] To perform a test, the user adds the sample to the sample pad; capillary action then wicks it across the device where it interacts with the labelled conjugate antibody on the conjugate pad.[698] Immobilized capture antibodies are present on both the control and test lines of the device.[698] When the antigen (analyte) is present in the sample, a coloured band forms across the strip as the labelled antibody is retained by the capture antibody via their respective interactions with the antigen.[698] Accumulation of gold nanoparticle

(NP)-antibody conjugates at the test line then gives a visible readout from the assay.[699]

Nishat *et al*. have extensively reviewed paper-based microfluidic devices, particularly their point-of-care applications.[698] Fu *et al.* have developed a paper-based microfluidic device for 3D cell culture.[700] The paper-based wicks exploit capillary action to continually draw up cell-culture medium whilst the cells are cultured on the upper layer.[700]

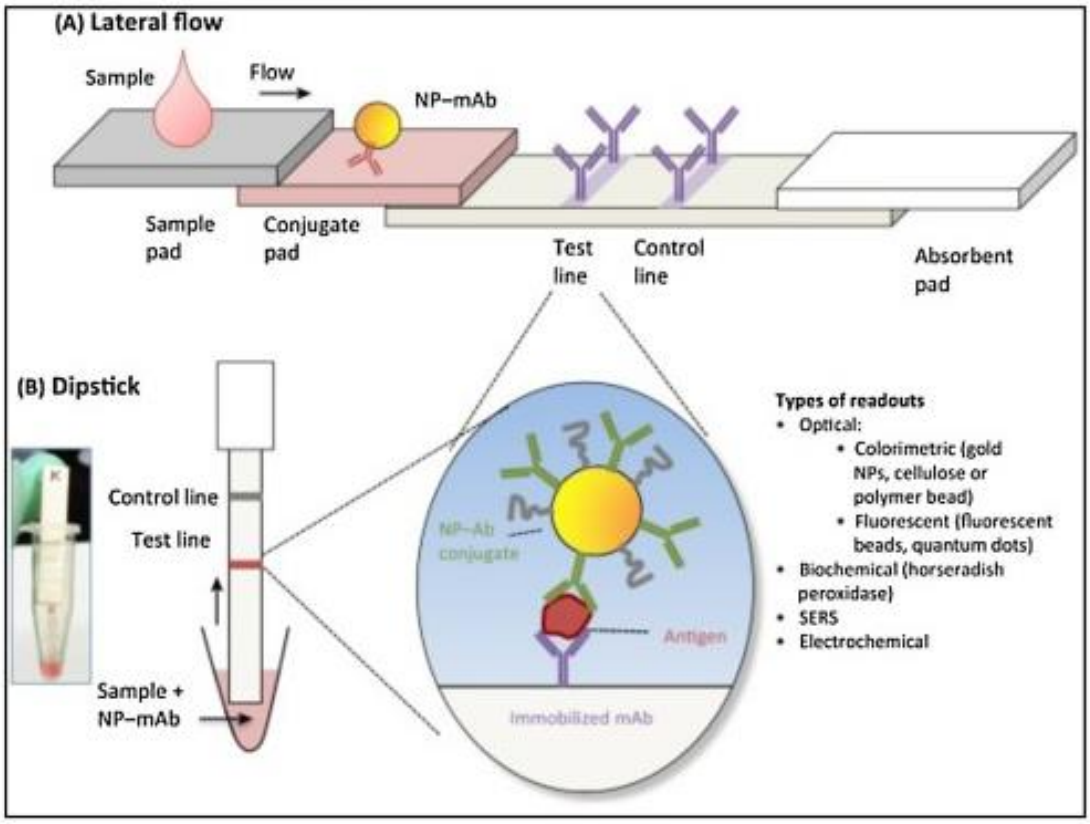

Figure 5.2: Basic Structure of (A) a Lateral Flow Assay (LFA) and (B) a Dipstick Immunoassay. Abbreviations: mAb, monoclonal antibody; NP, nanoparticle; SERS, surface-enhanced Raman spectroscopy. Reproduced with permission from [699]

Range of Pumping Methods

A variety of pumping methods are available.[619] Each has its own advantages and disadvantages, as well as achievable flow rates and flow patterns. These pumping methods can be categorised as passive or active flow (**Table 5.1**). How much control over flow is required is likely to be the deciding factor whether passive flow or mechanically-controlled active flow methods are chosen in the design of microfluidic devices.[619] Passive flow is often much easier to implement, but active flow allows much greater control over the flow rate within the system.[619]

Table 5.1: A summary of pumping methods which have been used with microfluidic devices. From [619]. † represents flow methods which are capable of pulsatile flow, and * represents those where recirculation of media has already been demonstrated within the literature.

Active Flow	Flow rate (µL/min)	Reference	Passive Flow	Flow rate (µL/min	Reference
Syringe pump †*	0.13-0.2	[696,701]	Gravity *	0.008	[702–704]
Vacuum driven †	0.1	[705]	Surface tension-driven	4.2	[686]
Peristaltic pump (general, pneumatic or braille pin) †*	0.03-185.1	[706–708]	Osmosis-driven	0.0025-0.25	[709]
Electric (electro-kinetic, electro-osmotic)	3.6	[710,711]			
Centrifugal	0.6-6000	[712]			

Some of the pumping methods mentioned in **Table 5.1** are capable of recirculating media through the system; therefore, any device using one of these can then perform on-chip perfusion cell culture.[619] Perfusion cell culture describes a system where spent cell culture media is removed at the same rate at which new cell culture medium is added into the system. This is not possible in traditional, static 2D cell culture methods.[619] The number of examples within the literature where microfluidics and perfusion cell culture are combined have rapidly increased since 2019.[693,696,701,703,713,714]

5.2.2 Difficulties with Microfluidics

As explained previously, the manufacture of these devices can be simple, however the design of certainly is not. A variety of parameters must be considered for the results from these devices to be reproducible and applicable to *in vivo* behaviour. These parameters are summarised in **Table 5.2**.

.

Table 5.2: The parameters which must be considering in the design and development of a microfluidic device.

Parameter	Effect on system	Reference(s)
Shear stress & flow rate	If too high (>38 Pa for endothelial cells), can cause cell damage. If too low, cells differentiate in a way which differs from their usual physiological state.	524,619,696
Surface area: volume ratio of microengineered channels	Large surface area: volume ratio may result in significant absorption of active ingredients e.g., signaling factors, components of growth media etc.	715
Substrate stiffness	If too low, cells remain minimally proliferative and prone to apoptosis. If too high, behaviour does not mimic that *in vivo.*	716,717
Identity of substrate	Particularly problematic if the majority of the microengineered device is made of PDMS. PDMS is oxygen-permeable, and this is advantageous if on-chip cell culturing is wanted, but it is also capable of absorbing small hydrophobic chemicals and permits the evaporation of embedded liquids. PDMS also known to not be inert and is capable of leaching silicon into the device.	619,685
Formation of bubbles within the system	Bubbles are known to affect cell perfusion and cell behaviour. Can also cause cell damage.	718
Pumping method	Will determine if perfusion cell culture is possible and if the device needs an electrical supply. Additionally, other mechanical properties such as cell squishing are influenced by the choice of pumping method used with the device.	619
Fundamental characteristics of the biological scenario the device is attempting to mimic	If the most important characteristics are not accurately mimicked in the device, then the results will not be applicable *in vivo*. In this case, the physiological parameters of interest for this device have previously been studied *in silico* in Chapter 4.	715

5.2.3 CFD Studies of Microfluidic Devices

Now, the use of CFD in the design and development of microfluidic devices will be considered. In silico simulations have been extensively used for lab-on-a-chip platforms to simulate fluid flow and transport phenomena.[719] Further, it is often far faster to mock up designs *in silico* and assess necessary parameters than to produce the microfluidic device and determine key parameters *via* experimental methods.[720] These parameters are optimised in one of two ways; extensive examples have been published within the literature where the microfluidic device is optimised with assistance from CFD calculations alone[688,721–723], or CFD is used in conjunction with machine learning – here neural networks seem particularly popular.[724]

Microfluidic devices are often complex, and simulation-based design optimisation and analysis are often necessary as determining key parameters

via experimental parameters is slow, costly, and prone to failure.[720] CFD studies enable a novel design to be rapidly analysed *in silico* before a device is even manufactured. Finite Volume and Finite Element methods are popular for undertaking such studies.[688,721,722]

Additionally, there is an emerging area of such studies that also employ machine learning, and neural networks seem particularly popular.[724–726] As suggested by de Oliveira Maionchi and colleagues, this significantly sped up the identification of the parameters that describe the most efficient microfluidic micromixer.[725] In contrast to running the parameters through a series of CFD simulations manually, which would take nearly a year, the addition of a neural network meant that this took only 40 days.[725]

5.2.4 Additive Manufacturing

In this section, additive manufacturing is introduced before the properties of 3D-printing that make it suited for the fabrication of microfluidic devices are considered. Next, Fused Deposition Modelling is discussed in detail, and then a literature review is undertaken to determine potentially suitable biocompatible polymers for these microfluidic devices. Finally, examples from the literature are given.

5.2.4.1 Introduction to Additive Manufacturing

Additive manufacturing is a computer-controlled process that creates three-dimensional objects by depositing materials, usually in layers, and is often referred to as 3D-printing. The main 3D-printing techniques are stereolithography (SLA), fused deposition modelling (FDM), selective laser sintering (SLS) and direct ink writing.[727] Only Fused Deposition Modelling will be discussed in detail here; the other methods are interesting but fall out of the scope of this thesis. Details of these other methods have been published by Catarino *et al*.[727]

3D-printing fabrication techniques are a nascent area receiving increasing interest as a way to produce microfluidic devices and for a wide variety of other applications.[728–731] These techniques are capable of making devices with complicated designs and do not require the multistep processing necessary with soft lithographic techniques.[728] Furthermore, cleanroom access is not required for most 3D-printing techniques (and is certainly not necessary for FDM); therefore, these technologies are not solely the preserve of researchers at the world's best-funded institutions. These microfluidic devices are often far cheaper to manufacture and often faster too. Saggiomo has written a detailed review of the applications of fused deposition modelling within a chemistry laboratory.[729] Here, they particularly highlight not only the expansive range of laboratory objects and other trinkets already available for 3D-printing but that if such objects have not been previously wanted, designed and uploaded to a repository, these items can often easily be made. This idea of "if I can't find it, I'll make it myself" is then echoed repeatedly within the literature – Ioannidis *et al.* "hacked" a commercially available FDM printer such that it could print a cell-laden alginate-based bioink.[732,733]

5.2.4.2 Introducing Fused Deposition Modelling (FDM)

In this section, Fused deposition modelling (FDM) will be discussed in detail. This technique is what is thought of when 3D-printing is discussed.

Fused deposition modelling is one of the simplest 3D-printing methods and prints layers of thermoplastic polymer through a heated nozzle.[728,734] On printing, this polymer is just above its melting point and, therefore, solidifies immediately once printed. Once this layer is complete, the next layer is printed until the entire model is complete.[734]

Advantages of FDM include that it is a cheap and rapid technique to fabricate prototypes, and furthermore, it is capable of processing almost all types of thermoplastic polymers.[727,734] Disadvantages of FDM generally centre around surface roughness, aspect ratio, and the minimum size of features is currently around 100-200 μm.[734,735]

5.2.4.3 Choosing a Suitable Polymer

Now, the literature will be reviewed to explore the types of polymers that are known to be compatible with FDM. Many polymers have been used previously for FDM. These include the commonly used acrylonitrile butadiene styrene (ABS), polystyrene (PS) and polycarbonate (PC). There is also a wide range of biocompatible polymers, including polycaprolactone (PCL), polylactic acid (PLA), polybutylene terephthalate (PBT) and polyglycolic acid (PGA).[731,734,736–738]

Biocompatible synthetic polymers for tissue engineering applications have been extensively reviewed by several groups.[737] Here, a polymer that is both compatible with FDM and is suitable for tissue engineering (and therefore would support cell growth) needs to be identified. Polylactic acid (PLA) is potentially one such polymer. It is known to be compatible with FDM, and many examples exist of it being used in tissue engineering.[737,739–741] As mentioned previously, its crystalline form takes an extended period of dissolve. Wurm and colleagues looked at cell proliferation, viability, and cell morphology on FDM-manufactured PLA in comparison to titanium and PS.[739] These parameters were found to be acceptable.[739] Similar studies have been performed by Guidoin *et al.*, as well as Gregor and co-workers, and it has not been reported that L-PLA has much influence on cell viability and proliferation.[741,742]

On the other hand, if a completely transparent polymer is required, then polyethylene terephthalate glycol (PETG) is likely to be suitable. It is already used for sterile, single-use, disposable laboratory plasticware for cell culture – therefore, it is clearly not cytotoxic. Furthermore, this polymer has also been explored for its utility in manufacturing 3D-printed microfluidic devices for on-chip cell culture.[743,744]

5.2.4.4 Examples of 3D-printed Microfluidic Devices.

The use of 3D printing in the manufacture of microfluidic devices can be broadly split into two categories: either the master is 3D-printed, and the device

itself is often made in PDMS, or the microfluidic device itself is manufactured *via* 3D-printing.[745]

Where the masters are 3D-printed, this is often termed sacrificial moulding, and soluble polymers are useful here.[746,747] Goh and Hashimoto reported a method to print 2- and 3D microchannels using PVA as a sacrificial mould as this polymer is water soluble.[746] Bazaz *et al.*, however, optimised the use of a novel resin and used this to 3D print a master. This novel methacrylated resin can be removed from cured PDMS far more easily.[748]

3D-printed Devices

Fully 3D-printed microfluidic devices are still novel, but a handful of examples can be found within the literature. They were extensively reviewed by Au and colleagues, but their prediction that 3D-printed microfluidics would replace those manufactured by soft lithographic techniques and PDMS is yet to be fully realised.[749] A range of polymers have been used, including PLA, PS and PMMA.[735,750,751] These 3D-printed microfluidic devices can, like those made from PDMS, be interfaced with electronic sensors. Gaal and colleagues 3D-printed a microfluidic device using PLA, that interfaced with several electronic sensors to create what they term an “electronic tongue”.[751]

5.2.5 Designing a Microfluidic Device

Currently, most microfluidic devices are monolithic chips – that is, they only have one specific, pre-defined purpose.[752] Work towards modular microfluidics, where each module has a single purpose but can be combined in a multitude of ways with others, is currently ongoing.[664]

Low and colleagues report a series of parameters that must be considered in the design of a microfluidic device.[752] These parameters include sample volume, mean fluid velocity, fabrication complexity, Reynolds number and uniformity of flow.[752] In this work, mean fluid velocity and relatedly, shear rate are the two key parameters that will influence the dimensions of the microfluidic channel designed in this chapter. Furthermore, design complexity will dictate the ease with which the chip is manufactured; the simpler the design the better. Also, the 3D-printing method (here FDM) will also influence what it is possible to create by providing minimum channel sizes (not less than 200 μm).[734] Channels are generally rectangular in shape, as these give easily predicted flow and laminar flow is maintained if Reynolds number (R_e) is <200.[752]

5.3 Aims and Objectives

By the end of this chapter, the results obtained in **Chapter 4** will have been used to guide the development of a microfluidic device capable of mimicking physiologically relevant fluid flow. The device would then subject polymeric nanoparticles to the same forces they experience *in vivo*, enabling the impact of fluid behaviour on protein corona physicochemical characteristics and composition to be studied without the need for *in vitro* experimentation.

The objectives of this final project are as follows:

1. To consider which (if any) polymer compatible with Fused Deposition modelling would be suitable for this microfluidic device in lieu of poly(dimethylsiloxane) (PDMS) and standard soft lithography techniques.

This objective will be completed by undertaking a literature review to identify the polymers that are both biocompatible and suited for FDM.

2. To design a microfluidic device capable of replicating the most important parameters to accurately mimic the physiological conditions nanoparticles are exposed to immediately after being introduced *in vivo via* a vascular access device.

This will be done by using the results obtained in **Chapter 4**. The design will be created in SolidWorks, so it can easily be modified.

3. To computationally model this device before manufacture using computational fluid dynamics to ascertain that the device accurately mimics all the most physiologically important parameters.

The 3D model created in #2 will then be studied using STAR CCM+ and the CFD-DEM methodology developed in **Chapter 3** to determine that the necessary parameters regarding fluid flow and particle behaviour are obtained by the device.

5.4 Materials and Methods

The computational models presented in this chapter were simulated using STARCCM+ (Siemens PLM, Version 2022.1.1), a commercially available CFD solver.

5.4.1 Designing the Microfluidic Device

The microfluidic device was created in SolidWorks 2023 (Dassault Systemes/ SolidWorks Corporation) before being imported into STARCCM+. .stl file suitable for 3D printing is available *via* GitHub.

5.4.2 Computational Fluid Dynamics Simulations

The setup is broadly like that defined within Part 2 of this thesis. Since the methodology has been repeatedly confirmed to successfully represent both fluid and particle behaviour, the iterative approach outlined previously is not used in this chapter. A single CFD-DEM simulation will be built and analysed.

5.4.2.1 Mesh Development

Mesh convergence studies were used to confirm that the meshing parameters were appropriate to create a mesh of sufficient quality for further analysis. Cell quality, skewness angle of the cells themselves and the degree by which the volume of one cell differs from its neighbours were assessed. These mesh parameters are summarised in **Table 5.3**.

Table 5.3: Final meshing parameters used to create the volume mesh following mesh convergence studies.

Group	**Mesher**
Surface mesher	Surface remesher
Core volume mesher	Polyhedral mesher
Optional boundary layer mesher	Prism layer mesher
Surface Wrapper	
Base size	1.0×10^{-4} m
Number of prism layers	6
Prism layer stretching	1.5
Prism layer total thickness	33.33 (relative to base)
Automated Mesh	
Base size	1.0×10^{-4} m
Number of prism layers	6
Prism layer stretching	1.5
Prism layer total thickness	33.33 (relative to base)

Coupling CFD and DEM

Once a suitable mesh had been generated, the CFD-DEM methodology developed previously in this thesis was applied to the simulation (

Table 5.4).

Table 5.4: Physics continua for the coupled CFD-DEM model.

Group box	Physics model
Space	Three dimensional
Time	Implicit unsteady
Material	Multi-component liquid
Reaction regime	Non-reacting
Flow	Coupled flow Coupled species (selected automatically) Gradients (selected automatically)
Viscous regime	Laminar
Optional models	Lagrangian multiphase Discrete element model

Defining the Lagrangian Phase

Next, physics models and material properties of the nanoparticulate matter were defined (**Table 5.5**).

Table 5.5: Input parameters to define the solid phase of the coupled CFD-DEM model.

Group box		Physics model	
Particle type		DEM particles Pressure gradient force (selected automatically)	
Particle shape		Spherical particles	
Material		Solid	
Equation of state		Constant density	
Optional particle forces		Drag force	
Optional Models		Two-way Coupling	
Input Parameters – Lagrangian Phase			
Nanoparticles (PLGA) – material properties			Ref
	Density	1062 kg m^3	
	Poisson's ratio	0.4	
	Young's modulus	2.43 kPa	[543,544]
Microfluidic device (PLA) – material properties	Density	1240 kg m^3	[753]
	Poisson's ratio	0.35	[754]
	Young's modulus	3.5G Pa	[755]

5.4.2.2 Multiphase Interactions

Multiphase interactions are interactions between two or more phases. Here, the interactions can be classified as being between two liquid phases or between two solid phases.

Defining Interactions Between the Liquid Phases

Interactions between blood and 0.9 % saline or 5 % glucose are managed automatically by STARCCM+.

Defining Interactions Between the Solid Phases

Interactions are defined between nanoparticles, and the interaction between nanoparticle and walls of the microfluidic channel is also defined (**Table 5.6**).

Table 5.6: Defining multiphase interactions for solid phase in the CFD-DEM model. * applies to nanoparticle-nanoparticle interaction only.

Group box	Physics model
Phase interaction topology	DEM Phase Topology
DEM Contact model	Hertz-Mindlin Rolling resistance (selected automatically)
Optional models	Artificial viscosity Linear cohesion Parallel bonds* Passive Scalar Transfer* Particle-Wall link model

5.4.2.3 Defining the Sources of Particles

Finally, the source of nanoparticles is defined by using injectors. In this case, the PLGA nanoparticles are introduced at one of the two inlets to the geometry.

Table 5.7: Using injectors to introduce PLGA nanoparticles into the simulation.

Properties	Values
Lagrangian phase	PLGA Nanoparticle
Type	Part Injector
Inputs	Inlet
Input parameters	
Retain injected particles	Enabled
Particle diameter	$1x10^{-6}$ m
Point Inclusion Probability	0.1
Particle flow rate	1000 /s

5.5 Results and Discussion

First, a detailed walkthrough of the design of the microfluidic device in SolidWorks is given before a fully referenced technical drawing is discussed. Next, this 3D model will be used to perform a mesh independence study to determine the fidelity of the mesh necessary to accurately resolve fluid (and therefore particle) behaviour within the device, then the quality of this chosen mesh will be assessed (**Appendix B**). CFD calculations then follow to determine that the device accurately mimics *in vivo* conditions.

5.5.1 Design of the Microfluidic Device

It was initially envisaged that fluid flow in this device would come from a syringe pump, since these are often cheap and capable of pulsatile flow (although this property is not exploited here, it would be useful later, *e.g.,* on-chip cell culture). The recirculation of media using this method has already been reported in the literature [696,701] However, a set of calculations were undertaken (**Appendix A**) to confirm the syringe pump and desired size of microfluidic channel were likely to meet the necessary parameters *i.e.,* generate the required fluid velocity and therefore necessary forces to mimic *in vivo* conditions. These calculations found that the use of a syringe pump would not be compatible with the desired use of the device. However, the volumetric flow rates required for the microfluidic device are within the range of a peristaltic pump. Where fluid channels are 1000 μm in height/ width, the values fall slightly outwith the range of a peristaltic pump, as such, it was chosen that the channels would be made smaller (750 μm).

This design uses two freely available CAD templates; one for a standard microscope slide-sized microfluidic device (**Figure 5.3**) and another for a Luer connector (**Figure 5.8**) from Parallelfluidics.com.[756]

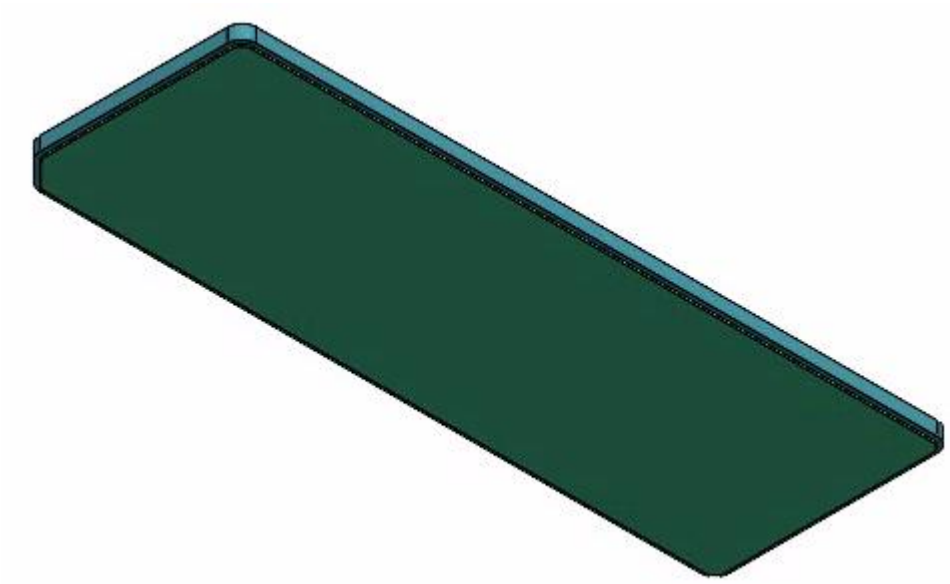

Figure 5.3: The microscope-slide-sized CAD template, as it originally appears in Solidworks, prior to the microfluidic device being created. The fluidic layer is blue (above) whilst the capping layer is green. From [756].

This template consists of two parts: a fluidic layer (blue), in which the microfluidic device is to be designed, and a capping layer (green) to seal the device. During the design process, the capping layer is deliberately hidden so that it is not accidentally selected, and the channel created on or within this layer.

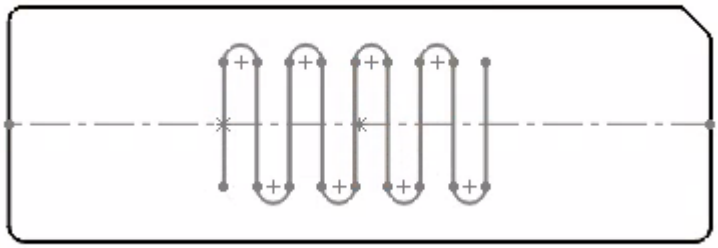

Figure 5.4: The microfluidic device following application of a midline to centre the design on the layer, and the beginnings of the serpentine channel.

Step one of the design involves applying a midline (dot-dash pattern) to the fluidic layer which is used to help centre the design of the serpentine channel (**Figure 5.4**).

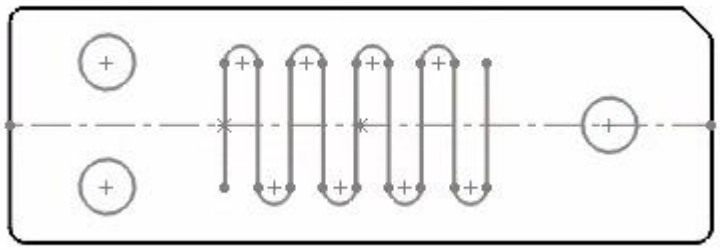

Figure 5.5:The microfluidic device after the diameter of the Luer connectors has been added to the fluidic layer. These show the amount of space each connector will occupy on the device.

In another sketch, the position of the Luer connectors for inlet and outlet ports were added (**Figure 5.5**), before completing the serpentine channel, and connecting the inlet and outlet ports (**Figure 5.6**).

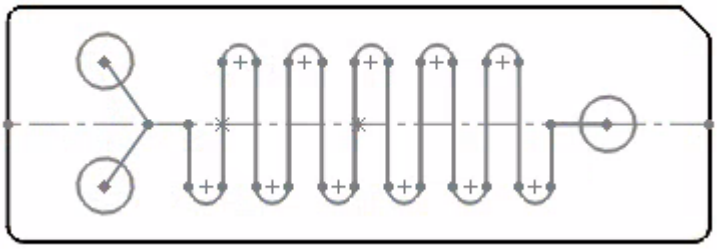

Figure 5.6: Much of the fluidic channel has now been designed. Only minor adjustments are made beyond this point.

Next, the microfluidic channel is cut into the fluidic layer (**Figure 5.7**). rise to the square-shaped microfluidic channel commonly seen in such devices. However, several areas of the design contain sharp edges, and these corners are undesirable. Therefore, the fillet feature is used within SolidWorks to round the corners of the fluidic channel. 0.5 mm fillet on the internal corners and a 0.7 mm fillet on the external corners so that the channel stays a consistent width.

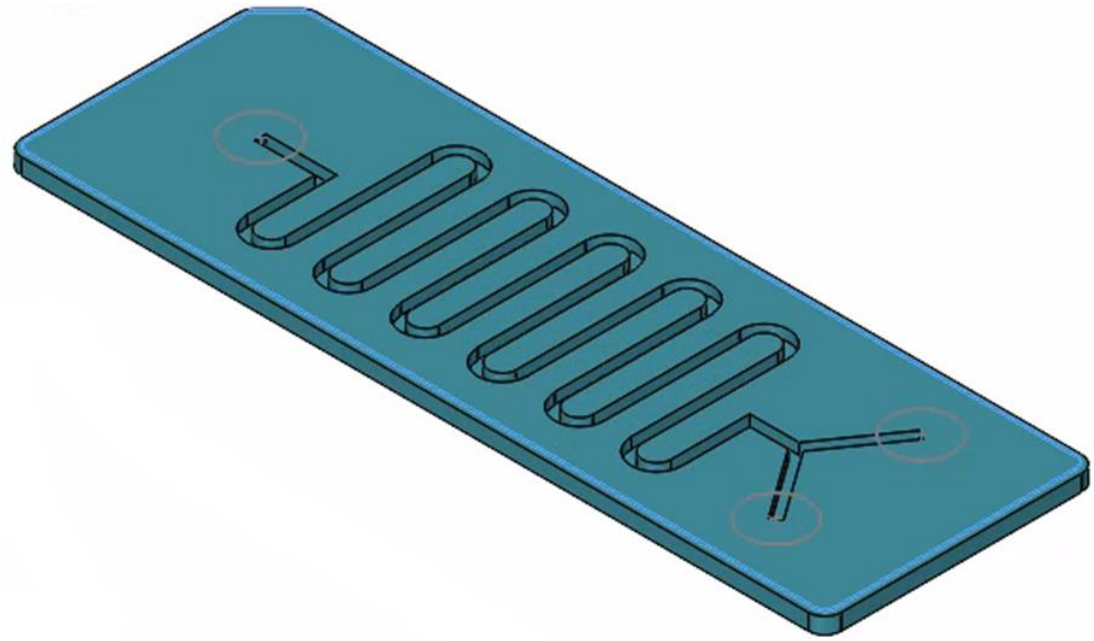

Figure 5.7:The microfluidic device following the channel having been cut into the fluidic layer, the final positions of the inlet/outlet ports are also visible.

Holes are made through the fluidic layer to accommodate the connectors (**Figure 5.8**). The connectors are then aligned by creating an assembly and using the mate tool to align them in X, Y and Z directions. The design of the device is now complete.

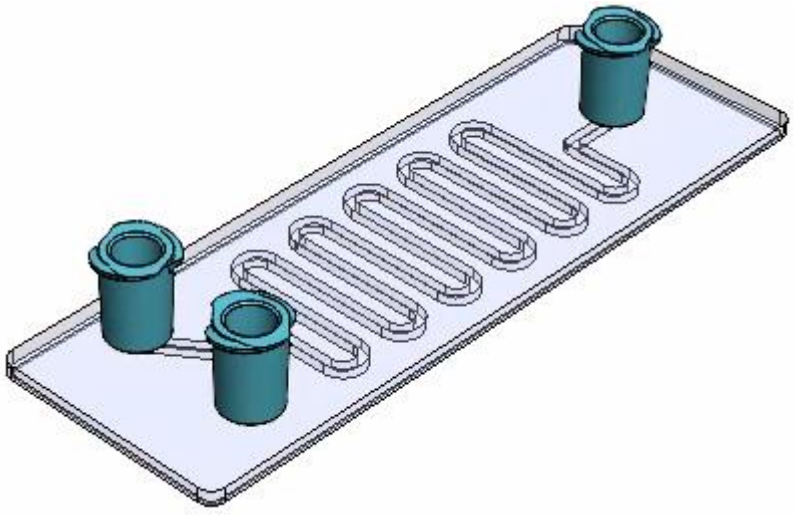

Figure 5.8: The final microfluidic device, with attached Luer connectors. The top face hidden to enable the fluidic channel underneath to be seen.

5.5.2 Proposed Microfluidic Device

Here, the fully referenced technical drawing will be discussed; particularly to determine why certain features were included in the design and the size and aspect ratio of these features (**Figure 5.9**).

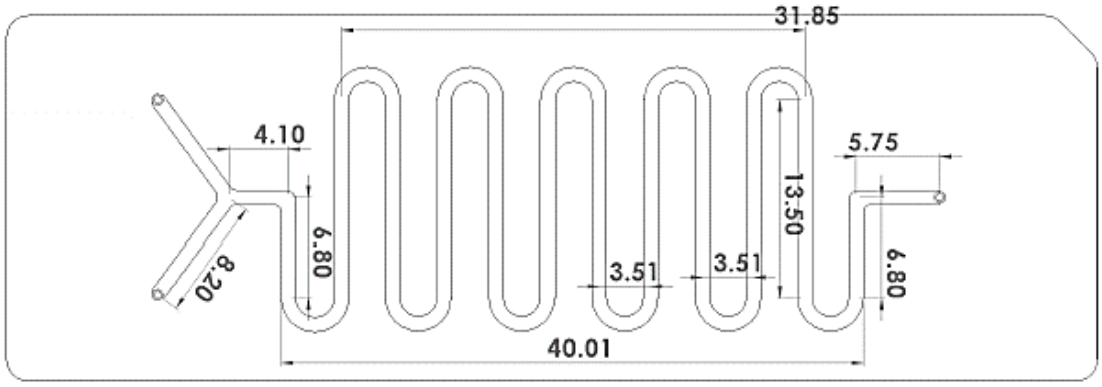

Figure 5.9: Not shown in this view, holes are 0.5mm in diameter and the channel is 0.75 mm deep.

Channel depth was chosen as 0.75 mm (750 µm) because the 3D printing method of interest here limits minimum channel width to 200 µm, and the calculations in **Appendix A** show this size of channel was one of the largest to comfortably fit within the volumetric flow rates possible *via* a peristaltic pump.[734] Furthermore, Zhao and colleagues have undertaken a study to ascertain the relationship between device thickness and accuracy of rheological modelling within microfluidic devices.[757] They report that unexpected changes in shear rate were observed where device thickness is < 50 µm.[757] This result is particularly important here, as shear rate is one of the key attributes of interest in this work. Channel depth is kept consistent throughout the device to facilitate manufacture.

The aspect ratio (in this context) is calculated as the ratio between the width and the height of the fluidic channel. The aspect ratio of the channel here is 1, as the height and width of the channel are identical.

Serpentine channels are a popular component within microfluidics and have been used to accomplish various tasks, including mixing fluids and cell separation.[758,759] An advantage of this geometry is that they are particularly robust in terms of clogging[760] – this was a distinct challenge of the MEMS chip within Archimedes, used for the resonant mass measurement in **Chapter 2**. Furthermore, they are a straightforward way to increase the length of any fluidic channel in such a limited space – here, the device footprint mimics that of a standard microscope slide; this was chosen to enable microscopy work to be done later (*e.g.,* assessment of biofouling or any specific interest in cell or nanoparticle behaviour). This serpentine channel then increases the time under shear stress, but since it is one fixed width throughout it's length, only one shear rate can be applied to the nanoparticles within the device. To better replicate the multiple shear rates the nanoparticles would experience *in vivo*,

as a consequence of bifurcations within blood vessels, a number of narrower segments could be included within this serpentine channel.

The decision to use the fillet tool within SolidWorks to remove sharp edges arose because of the known influence of sharp turns in fluidic channels on fluid behaviour. They tend to create dead zones and/or generate bubbles within the device.[752] It has previously been discussed (**Section 5.2.2**) why bubbles are unwanted in a microfluidic device, particularly where it will (or may later be) used for on-chip cell culture.

5.5.3 CFD Analysis of Microfluidic Device

In this section, CFD analysis of the microfluidic device is studied in detail to confirm that key physiological parameters determined by the PCA analysis undertaken previously can be achieved. CFD analysis of a novel microfluidic device is a common step in the design pathway for such items since it is far faster to optimise the design theoretically (*via* simulation).[720,725] First, the target parameter ranges obtained in the previous chapter will be reproduced before the key parameters (fluid velocity, fluid shear stress and particle shear stresses will be studied and discussed in detail. Only the two simulations that give rise to the minimum and maximum parameter values will be presented. Finally, all the parameters determined *via* PCA and simulation will briefly be compared before further PCA analysis is undertaken to confirm that both extreme configurations broadly replicate the hydrodynamic environment of the VADs studied in the previous chapter.

From **Chapter 4**, the target parameters predicted by PCA for the microfluidic device are as follows (**Table 5.8**); not all of these will be discussed in this chapter. It is interesting to note that despite input velocity more than trebling between the minimum and maximum configurations, not all the parameters for the device vary in this way *e.g.,* average fluid shear covers a much smaller range.

Table 5.8: Target values obtained from PCA in **Chapter 4**.

Design Parameter	Minimum	Maximum
Input Velocity (m s^{-1})	0.24	1.32
Maximum Velocity (m s^{-1})	1.45	3.14
Average Velocity (m s^{-1})	0.22	0.49
Maximum fluid shear rate (s^{-1})	598424.95	1025553.34
Average fluid shear rate (s^{-1})	826.88	1214.00
Maximum Wall shear stress (Pa)	6601.80	45633.18
Average Wall shear stress (Pa)	3763.83	5280.88
Minimum residence time (s)	0.28	0.09
Maximum particle velocity (m s^{-1})	0.57	1.24
Average Particle velocity (m s^{-1})	0.15	0.45
Maximum particle shear stress (Pa)	760169.85	954035.38
Average particle shear stress (Pa)	48023.40	389590.10

CFD analysis was undertaken to confirm key hydrodynamic parameters can be reproduced in this device. The following parameters will be discussed: fluid velocity, average and maximum fluid shear rate, and average and maximum particle shear stress.

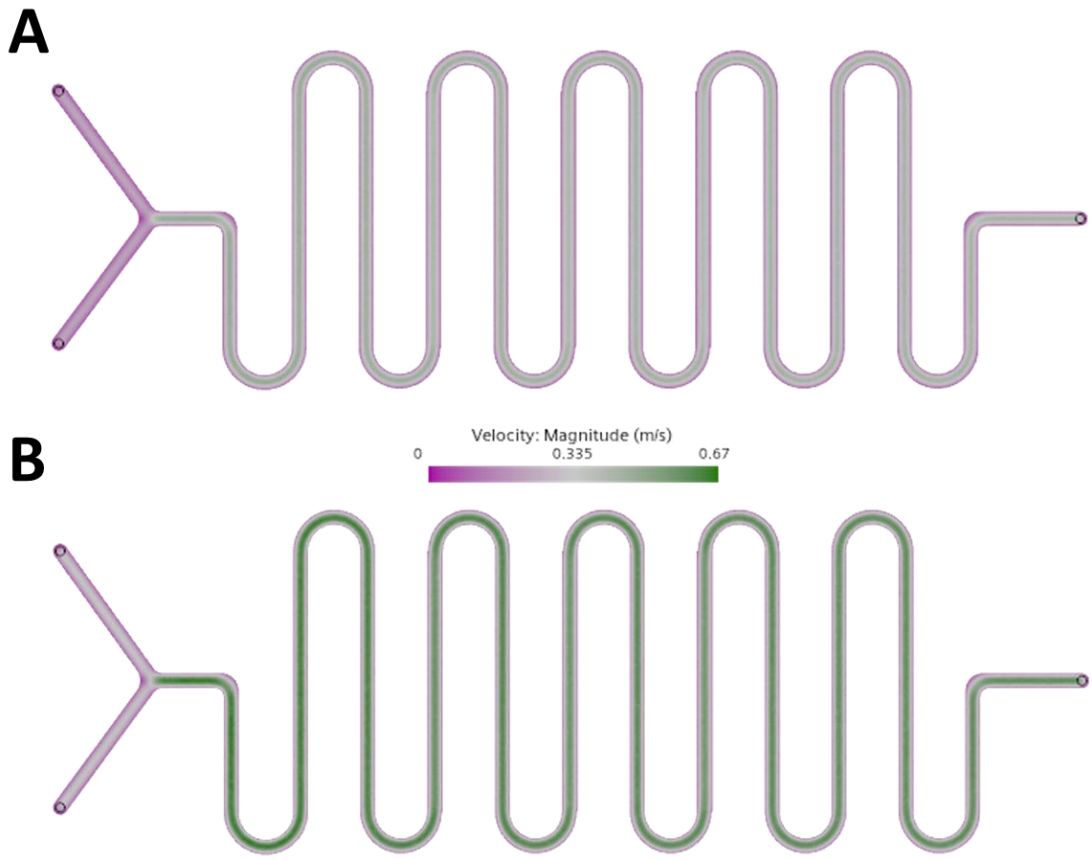

Figure 5.10: Fluid velocity for the minimum configuration (A) and maximum (B) of the microfluidic device designed in this chapter.

In **Figure 5.10**, the entrance length for the geometry can be seen, this is the region of comparatively lower fluid velocity at the inlets of the device. Through the serpentine channel and outlet, the fluid velocity remains constant at 0.48 and 0.67 m s^{-1} for each of the respective configurations.

Fluid shear is a measure of the frictional forces that are present between layers of fluid particles. The fluid shear is shown to vary across the geometry because of the square channels used in the microfluidic device (**Figure 5.11**). For a given geometry, the fluid shear is greater when the top (or bottom) face is studied, compared to a planar section through the middle of the device.

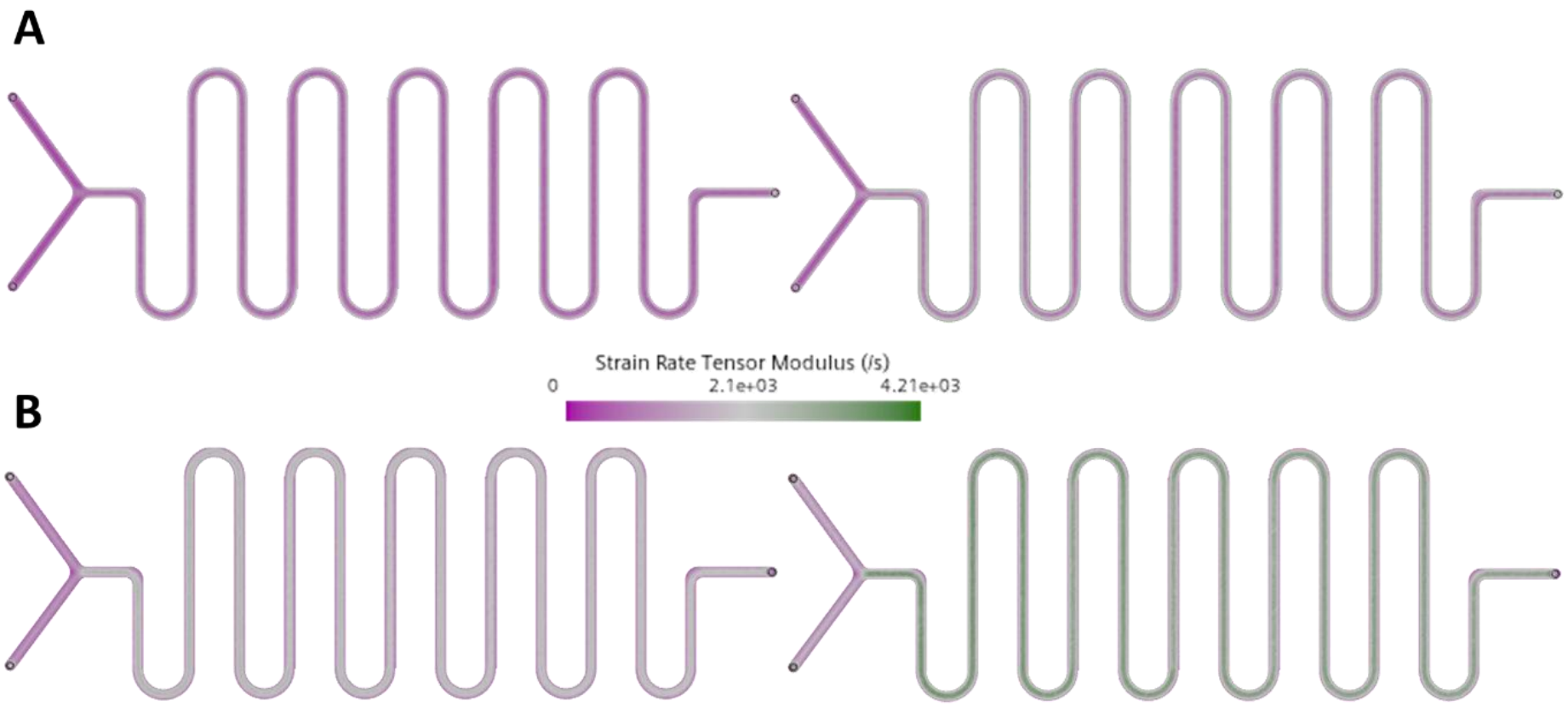

Figure 5.11: As a consequence of channel geometry, fluid shear stress varies across the domain. Left: minimum configuration; Right: maximum configuration. A) fluid shear stress in the centre of the channels as shown by a midplane slice in the X direction. B) fluid shear at the top (and bottom) faces of the channels.Particle shear stress is a measure of (primarily) friction between the fluid and the particles suspended within it. This force is believed to alter the composition of the protein corona around nanoparticles. In **Figure 5.12**,the maximum and average particle shear stresses for both configurations are plotted and is seen to vary as a function of time. The significant and rapid increase in value earlier than 0.05s corresponds to the particles being introduced *via* one inlet into the device and passing through the region identified in **Figure 5.10** as being the entrance length where fluid velocity (and, therefore, particle shear stress) evolves rapidly. Once the particles reach the serpentine channel, particle shear stress values are much more stable.

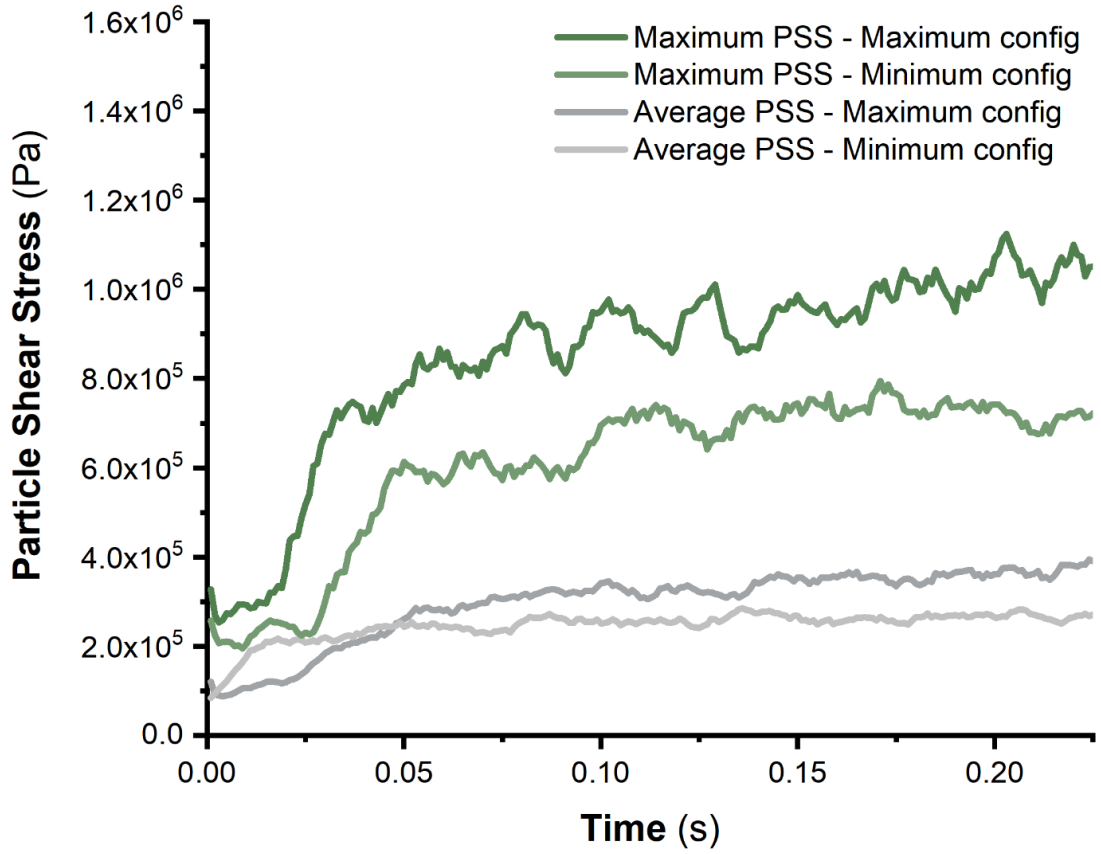

Figure 5.12: Particle shear stress. Plotted as rolling averages of 10 points to smooth the oscillations in value, enabling the trend to be identified easier.

There is good agreement between the values found *via* PCA in **Chapter 4** and the minimum and maximum configurations developed within this chapter (**Figure 5.13**). A few input parameters do not precisely match predictions, but for most of these, reasonable explanations can be given. It was expected that the input velocity of these microfluidic devices would not match that proposed *via* PCA. The significant change in the shape of the geometry impacts the necessary input velocity for the device. Consequently, this alters maximum velocity, and since these channels are square rather than the cylindrical ones studied in **Chapter 4**, it also leads to variation in wall shear stress. Furthermore, it was considered that maximum values might not necessarily be representative of the entire geometry. Therefore, more importance was placed on average values being accurately replicated within the device, even if that resulted in a mismatch between maximum values predicated *via* PCA and those calculated from simulation.

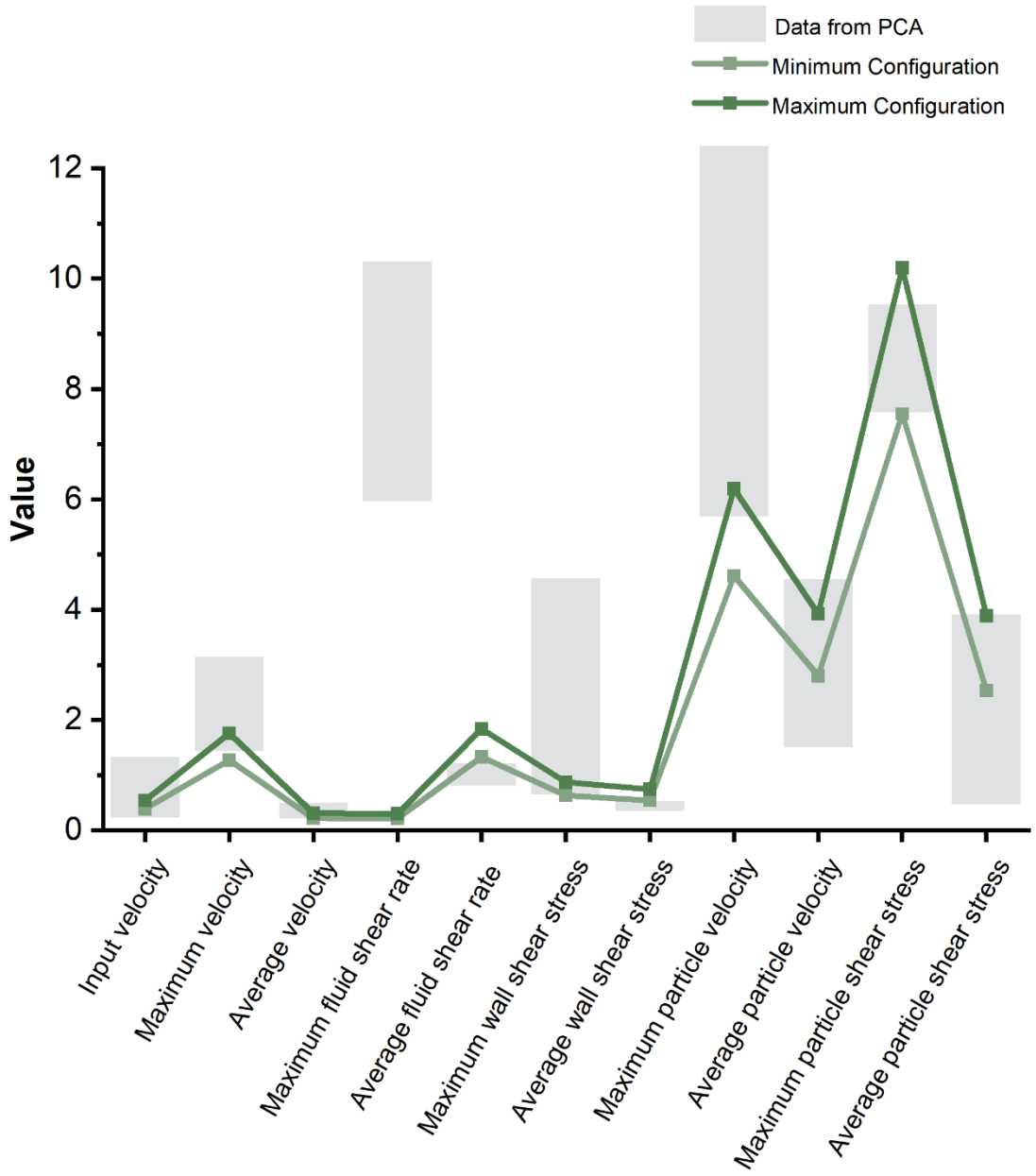

Figure 5.13: A comparison of the desired parameters found via PCA and those obtained for the min/max configurations of the microfluidic device.**N.B., all values have been scaled so it is possible to plot them all on the same axes.** Unscaled values can be found in **Appendix C**

Finally, observing how both simulated configurations fit into the PCA analysis in **Chapter 4** was of interest (**Figure 5.14**). Unlike **Figure 5.13**, this analysis enables the hydrodynamic environment to be assessed, since it is the principal components under study, and the principal components are linear combinations of all the measured features for the device.

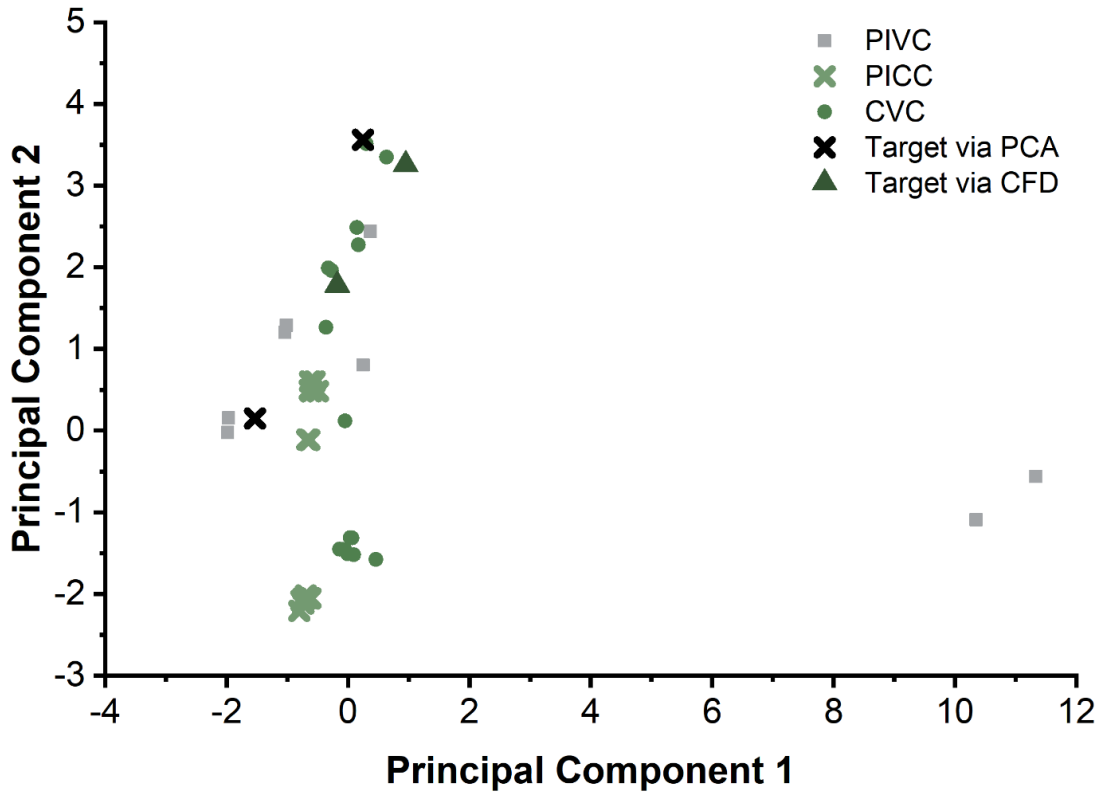

Figure 5.14: Following PCA analysis, both the minimum and maximum configurations fall within the cluster previously determined for the VADs studied in the previous chapter. This indicates the hydrodynamic environment is similar.

In **Figure 5.14**, the final PCA analysis from **Chapter 4** is duplicated, and the points for both the minimum and maximum configurations are added (green triangles). If the points associated with the two configurations simulated in this chapter were far away from where the points cluster for the VADs studied previously (*e.g.,* PIVC saline/ glucose flush simulations), then this would indicate the hydrodynamic environment being quite different. It is shown that both configurations fall within that cluster; therefore, the hydrodynamic environment replicated within the microfluidic device and those simulated previously in **Chapter 4** are similar. Interestingly, when all the parameters are considered *via* PCA, the configurations selected for both minimum and maximum configurations differ from those identified through the previous PCA analysis. This is mostly due to the differences between PCA prediction and simulation for wall shear stress if this parameter is ignored, the distances between target values through PCA and CFD are reduced, indicating increasing similarity.

5.6 Conclusions

In this chapter, the CFD-DEM methodology and the input values extrapolated from the PCA results presented in Part 2 of this thesis have been used in the design and computational simulation of a microfluidic device capable of subjecting nanoparticles to physiologically-relevant fluid shear to enable the study of protein corona formation under dynamic conditions, without the need for *in vitro* experimentation.

This aim has been achieved by first undertaking a literature review to identify polymers known to be compatible with FDM before considering which (if any) were known to be biologically compatible and ideally optically transparent, such that the device could later be used for on-chip nanoparticle uptake experiments. It has been found that poly (lactic acid) is both biologically compatible and sufficiently clear. It was also discussed that if a completely transparent polymer was desired, then polyethylene terephthalate glycol (PETG) could instead be used.[743,744] Next, using the input parameters discovered *via* PCA in the previous chapter, a microfluidic device capable of replicating important parameters to mimic the studied physiological conditions accurately was designed. This design was modelled using CFD to confirm the key parameters could be mimicked in the device. Of particular interest was fluid shear rate, alongside particle shear stress, since these were already known to influence protein corona composition under dynamic conditions. However, little study so far has been conducted on polymeric nanoparticles.[11,52] The results from CFD simulations and further PCA analysis show the design is capable of meeting the target fluid- and particle-related forces outlined previously in this work, and therefore, it can accurately mimic *in vivo* conditions. However, using a search algorithm to further refine the input velocity and output parameters for the minimum configuration outlined in this chapter may be worthwhile. Taken together, these results show that not only could the device be manufactured *via* fused deposition modelling, but the resulting device could be used to study protein corona formation under dynamic conditions

5.7 Appendices

A. Determining Channel Size

From **Chapter 4**, minimum and maximum fluid velocities were calculated as follows:

Minimum: 1.04 m s^{-1}

Maximum 3.12 m s^{-1}

$$Q = \nu A$$

Volumetric flow rate (Q). Where ν is fluid velocity and A is cross sectional area.

Assuming the hydrodynamic cross section of the square channel is 1000 μm^2, this gives from the equation above, the volumetric flow rates below (**Table 5.9**). These values are slightly outwith the range of the pumping methods discussed previously. Consequently, several different sized channels were trialled, being mindful of the limits imposed by the printing method.

Table 5.9: Volumetric flow rate for a range of channel widths for the minimum and maximum input velocities predicted by PCA.

Hydrodynamic diameter	Min (mL min^{-1})	Max (mL min^{-1})
1000	0.0624	0.1872
750	0.0468	0.1404
500	0.0312	0.0936
300	0.01872	0.05616

B. Mesh Independence Study for Initial Microfluidic Device

Here, all faces other than those that make up the microfluidic channel itself, and the face of the capping layer that directly contacts the fluidic layer and therefore seals the fluidic channel have been removed (**Figure 5.15**).

Figure 5.15: Simplified device geometry used for meshing and subsequent simulations.

This has been done to simplify the geometry that needs to be meshed, but also significantly decreases the number of cells within the mesh, therefore reduces computational demand and the amount of time it will take for calculations to complete.

Here, the mesh independence study only considers the mesh density of the inlets, outlet and of the fluidic channel itself. Increased mesh density of the rest of the microfluidic chip is unnecessary. Input velocity arbitrarily chosen as 0.1 m s^{-1} at both inlets.

Table 5.10: Results from mesh independence study for the microfluidic device

Base size (m)	No. of cells	Fluid velocity(m s^{-1})	Continuity
$1x10^{-3}$	1146	0.244	$7.659089x10^{-2}$
$5x10^{-4}$	3473	0.0251	$3.810161x10^{-2}$
$4x10^{-4}$	5125	0.0513	$1.712569x10^{-2}$
$3x10^{-4}$	9502	0.0526	$1.789270x10^{-2}$
$2x10^{-4}$	25956	0.0807	$1.789323x10^{-2}$
$1x10^{-4}$	119049	0.104	$1.874324x10^{-2}$
$5x10^{-5}$	600640	0.119	$1.545575x10^{-2}$
$4x10^{-5}$	1122881	0.121	$1.296927x10^{-2}$

In summary, the results reported above show that a base size of 0.002 m is adequate for the meshing of the bulk of the device and a base size of $1x10^{-5}$ m is appropriate for the meshing of the microfluidic channel and its inlets/outlet.

Cell Quality

Cell quality measures how uniform the cells that make up the mesh are (Error! Reference source not found.). A perfect cell has a cell quality of 1.0. Ideally, the bulk of the cells within the mesh should have a cell quality rating of 0.5 or more.[535] Bad cells are those where quality is less than $1.0x10^{-5}$.[535] Such cell quality values suggest that the cells within the mesh vary significantly in size, shape, and volume.

Table 5.11: Cell quality measures the uniformity of a simulated mesh. Cell quality for the microfluidic model used within this chapter. All cells are seen to have a cell quality > 0.5.

Cell quality	Number of cells
≤ 0.50	0
≤ 0.60	0
≤ 0.70	0
≤ 0.80	0
≤ 0.90	0
≤ 0.95	0
≤ 1.00	118985

Skewness Angle

The skewness angle measures the angle between a face normal and the vector that connects the centre of two neighbouring cells (Error! Reference source not found.).[535] This shows whether the cells on either side are formed such that diffusion of quantities is possible without the quantities becoming unbounded.[535] A perfectly orthogonal mesh will have a skewness angle of 0°. Bad cells are those with a skewness angle greater than 85°, and skewness angles > 90° lead to issues with solution convergence.[535]

Table 5.12: Maximum skewness angles for each geometry part within the PIVC geometry.

Geometry part	Maximum skewness angle (°)
Inlet 1	31.16
Inlet 2	41.90
Outlet	29.57
Fluidic channel	80.09

Volume Change

Volume change describes the ratio of the volume of a cell compared to that of its largest neighbour (**Table 5.13**).[535] A value of 1 is a good cell, as this shows that the cell concerned has a volume equal to or larger than that of its neighbours.[535] Cells where the volume change is < 0.01 are considered bad cells – large increases in volume from one cell to another may lead to inaccuracies in results and instability in the solvers.[535]

Table 5.13: Volume change of cells within a mesh is a proxy measure of the accuracy of the results it will generate. All cells within this mesh have a volume change > 0.01.

Volume change	Number of cells
<0.001	0
<0.01	0
<0.1	4626
≤1	114359

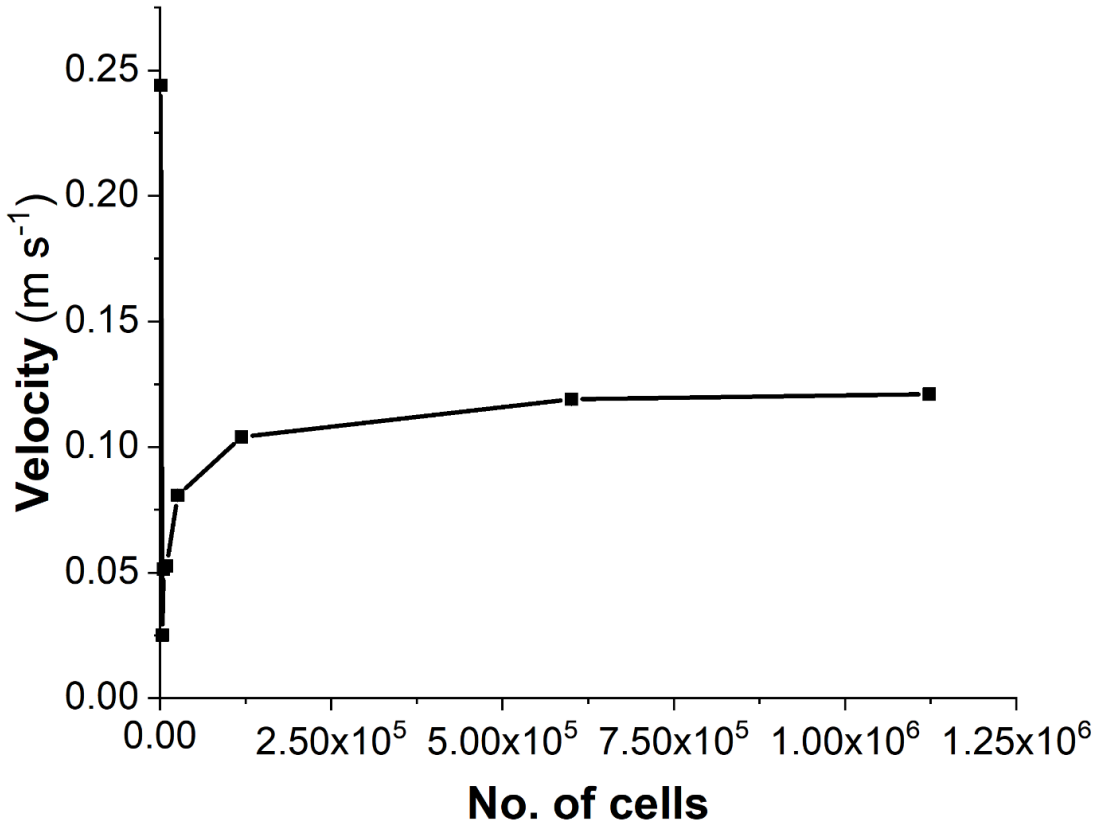

Mesh independence studies enable the least dense (and therefore computationally least intense) mesh to be chosen that does not compromise the accuracy of the result. Results of mesh convergence study for the microfluidic device in this chapter are shown.

C. Unscaled Values for Minimum and Maximum Configuration

The values displayed in **Figure 5.13** have been scaled so they all fall within the same range. However, in reality, the values obtained for the minimum and maximum configurations of the microfluidic device vary by several orders of magnitude. The raw values determined via CFD simulations are presented here (**Table 5.14**).

Table 5.14: Raw values for each parameter for both the minimum and maximum configuration of the microfluidic device studied in this chapter.

Design Parameter	Minimum	Maximum
Input Velocity (m s^{-1})	0.39	0.54
Maximum Velocity (m s^{-1})	1.27	1.76
Average Velocity (m s^{-1})	0.22	0.31
Maximum fluid shear rate (s^{-1})	21645.36	29967.61
Average fluid shear rate (s^{-1})	1327.85	1839.94
Maximum Wall shear stress (Pa)	63258.90	87605.35
Average Wall shear stress (Pa)	5456.25	7470.60
Maximum particle velocity (m s^{-1})	0.46	0.62
Average Particle velocity (m s^{-1})	0.28	0.39
Maximum particle shear stress (Pa)	754795.70	1015299.00
Average particle shear stress (Pa)	252923.90	389205.60

“Space: the final frontier. These are the voyages of the Starship Enterprise. Its continuing mission: to explore strange new worlds. To seek out new life and new civilizations. To boldly go where no one has gone before!”

Captain Jean-Luc Picard, Star Trek: The Next Generation

Chapter 6 Conclusions and Further Work

6.1 Introduction

Here, the thesis will be drawn to a close by summarising the research question, aims and objectives set within this thesis, before taking a broader overview of the conclusions made at the end of each chapter in this work; explaining the significance and implications of these findings, with reference to the strategic aims of the National Centre for the Replacement, Refinement and Reduction of Animals in Research (NC3R). and clearly defining the contribution to knowledge that this research makes. The limitations of this work will be reviewed, before a number of possible avenues for further research are outlined.

6.2 Research Aims and Objectives

This thesis has attempted to develop further understanding regarding the phenomenon of protein corona formation around poly(lactic-co-glycolic acid) (PLGA) nanoparticles following exposure to protein-rich media. Much of this thesis has explored particle shear stress and fluid behaviour *in vivo*, since number of groups believe that the impact of fluid flow and fluid shear on nanoparticles plays a significant role in influencing physicochemical attributes of the formed protein corona.[11,34,51–54] Later work then considered the development of a microfluidic device to replicate these forces *ex vivo*, as a potential method for replacing pre-clinical animal studies.

Several aims were set for this thesis, these include:

- Understand and analyse the effects of protein corona formation on nanoparticle physicochemical characteristics
- Develop a coupled finite-volume discrete element methodology for the study of fluid and nanoparticle behaviour *in vivo*
- Design and consider the possibility of 3D-printing a microfluidic device using a biocompatible polymer.

To address these aims, several objectives for each chapter were developed. In **Chapter 2**, protocols were developed and optimised to evaluate the use of Resonant Mass Measurement (RMM) and Particle Tracking Analysis (PTA) for the *in situ* measurement of protein corona effects on nanoparticle size under conditions where protein concentrations are biologically relevant (*e.g.* cell culture studies where media is supplemented with 10% FBS). A series of timepoint experiments were performed using PLGA/PLGA-PEG nanoparticles to understand the influence of incubation time, temperature, serum origin and impact of PEGylation on protein corona formation. The physicochemical characteristics were analysed *via* RMM, PTA and DLS as appropriate.

In **Chapter 3** and **4**, a literature review was initially undertaken to gather the necessary parameters for the development of physiologically-relevant models. A combined CFD-DEM methodology was developed using an iterative approach to simultaneously model fluid and nanoparticulate behaviour, and this was shown to be robust, and accurately replicate previously published work. This CFD-DEM methodology was then applied to modelling fluid and nanoparticle behaviour to a small set of commonly used vascular access devices, so that their impact on fluid shear could be studied.

In **Chapter 5**, a literature review was undertaken to identify the subset of polymers that are biologically compatible and suited for printing *via* Fused Deposition Modelling. The results from **Chapter 4** were then used to guide the design of a microfluidic device capable of replicating the physiological fluid behaviour seen previously *via* simulation. Computational models were then built using computational fluid dynamics to ascertain that all the most physiologically important parameters are accurately mimicked by the device.

6.3 Significance and Limitations of Research Findings

The spontaneous process of protein (biomolecular) corona formation around nanoparticles is known to influence nanoparticle biological fate, however, the clinical translation of promising novel nanotherapeutics has been limited, even despite the rapid clinical development of two liposomal mRNA-based vaccines for SARS-COV-2 in 2020.[11,16,21,29,30] A number of factors have been implicated in these challenges, including the incomplete translational applicability of *in vitro* cell uptake studies, as they frequently lack the complex chemical, physical and biological cues necessary to accurately capture their 3D structure and behaviours *in vivo.*[22,23] Additionally, a number of common animal models have been discussed in detail in **Chapter 2** (**Section 2.2.9.1**), including zebrafish and murine studies, but these each have their own challenges in replicating

the response in humans and this is often driven by differences in their immune system.[384,385,402,761] As a consequence of these challenges, non-animal methods for pre-clinical testing of novel therapeutics are of interest. Furthermore, predicting the composition of the protein corona *in vivo* from first principles when the identity and physicochemical characteristics of the 'naked' nanoparticle are known, is also challenging and limited prior work exists considering the impact of fluid flow on protein corona formation.[11,34,51–54,762]

The work presented in this thesis shows that the comparatively understudied protein corona around PLGA nanoparticles can be studied *in situ* using the novel analytical techniques of RMM and PTA, enabling further data to be obtained about an understudied system, and its *in situ* nature also allowing the easily disturbed soft corona to be probed. Using a combined CFD-DEM technique means fluid and particle shear forces *in vivo* can be investigated in detail. It has been noted that experimental confirmation of these computational studies needs to be undertaken, and very limited numbers of currently published papers consider particle shear when novel vascular access devices are modelled. Finally, the development of a microfluidic device enables nanoparticles to be subjected to physiologically relevant shear stresses, without need for animal-based pre-clinical studies.

In this work, a novel methodology for the high-resolution analysis of submicron polymeric nanoparticles pre- and post-protein corona formation has been developed and is outlined in **Chapter 2**. Further, this work shows that a combined CFD-DEM methodology can be used to undertake CFD calculations of a number of vascular access devices to simultaneously study fluid and nanoparticle behaviour and the forces acting on both the fluid and PLGA nanoparticles, and that Principal Component Analysis is a useful method to find the key parameters for the design of a microfluidic device. The final section of this thesis then shows that PLA is likely to be a polymer that could satisfactorily be 3D-printed, have sufficient optical clarity to be used with an optical microscope and the polymer itself would support on-chip cell culture; furthermore, the microfluidic device designed in this work will accurately mimic physiological fluid flow. The stage has been set for the rational data-driven design of novel nanotherapeutics, furthers nanoinformatics, as well as makes steps towards the replacement of animals (particularly mice, as these are commonly used for *in vivo* studies[24]) in pre-clinical testing, in line with the aims of the NC3Rs.[763]

These are a number of limitations in this work. Firstly, only PLGA nanoparticles have been considered, since these are the ones most likely to find clinical use – PLGA is known to be biocompatible.[205] However, the *in situ* analytical methods developed here, and the combined CFD-DEM methodology used in the simulations should work with any chosen nanoparticle. The author notes here that the simulations are likely to be significantly more demanding of computational power and/or time, if the nanoparticles are not spherical.[****]

[****] Since the calculations need to additionally consider the orientation of the nanoparticle.

Moreover, the *in situ* analytical method may need further work before it is truly compatible with protein-rich and consequently turbid biological fluids *e.g.,* 100% human serum, whole blood. Also, the CFD simulations do not consider the blood vessel as being in motion nor do they perfectly capture the shape; they are modelled as static, perfectly cylindrical objects. In short, idealised geometries have been used, so results obtained here may well vary from *in vivo*. Discussed later is the possibility of adapting these for personalised simulations.

6.4 Summary

In conclusion, this thesis shows that RMM and PTA are suitable methods for the analysis of protein corona formation around polymeric nanoparticles in protein-rich media. A combined finite volume-DEM methodology can be used to simultaneously study fluid and particle behaviour and a microfluidic device can be designed to subject polymeric nanoparticles to physiologically-relevant fluid shear. A suitable polymer has been found *via* literature review, therefore this device is likely to be suitable for 3D printing, as well as on-chip cell culture. As a consequence of the work undertaken in this thesis, more understanding could be developed, using these methodologies, of protein corona formation under dynamic conditions *e.g.,* polymeric nanoparticles could be subject to physiologically-relevant fluid shear in this device and then protein corona physicochemical characteristics analysed through the methodologies developed within **Chapter 2** of this thesis. What that work would then do, is give the information around protein corona formation under dynamic conditions that the literature currently lacks for many nanoparticles, including PLGA.

6.5 Further Work

This thesis covers several different areas of research: particle metrology for the analysis of novel nanotherapeutics, computational fluid dynamics to study fluid and nanoparticle behaviour, as well as the consideration of using 3D printing and microfluidics. Consequently, the potential directions for further work from this thesis are equally broad and wide-reaching. The directions for further work from the thesis as a whole will be discussed first, followed by a detailed discussion of the directions arising from each individual part of this work.

This work clearly makes the case for a paradigm-shift into the data-driven design of novel nanotherapeutics. Quantitative-Structure Activity Relationship models are needed to predict biomolecular corona composition, and determine eventual biological fate of nanoparticles.[11,762] However, the field currently considers this to be a nascent area, with many issues to be overcome before their use would be common practice, however this certainly could be done.[43,764,765] In the past year alone, a number of machine and deep-learning approaches have been used within other areas of chemistry to develop previously unknown understanding.[766–769] Neural networks appear to be particularly popular.[766,767] Furthermore, the use of machine learning within pharmaceutics, and specifically for the crystallisation of active pharmaceutical ingredients is well studied and has been in use for a long time.[591,765,770,771]

Several issues make the implementation of machine learning into studying the bio-nano interface particularly challenging. Firstly, the multitude of methodologies by which nanoparticle protein corona studies are undertaken and the comparatively recent introduction of the standardised reporting guidelines MIRIBEL and MINBE.[143,326,772] There has additionally been repeated calls by a number of groups including Mahmoudi *et al.*, for standardised methodologies for the incubation of nanoparticles with biological fluids (and the work herein develops a novel orthogonal method of the *in situ* analysis of nanoparticles following protein corona formation (see **Chapter 2**).[43] Additionally, standardised methods for nanoparticle recovery from biofluids are still yet to be implemented. This leads to challenges arising with *in vitro* data that has limited *in vivo* relevance, as well as the potential for the generation of data sets where information regarding the experimental approach is limited and as such replication is difficult, if not impossible. The poor quality of biocorona data has previously been noted by Maojo *et al.,* as well as in the meta-analysis undertaken more recently by Hajipour *et al.*[143,246] Further, the nanoparticles most-likely to be suited for clinical use are the biocompatible polymeric nanoparticles that are comparatively understudied, currently few papers consider the formation and composition of the protein corona around PLGA nanoparticles, and even fewer considering the influence of fluid flow on protein corona physiochemical characteristics.[51,53,54,61,236] Another issue that impairs the implementation of machine learning in this discipline is the selective publication of data. Negative results and/or those that are not statistically significant are generally not published, however this is useful data to feed into a machine learning algorithm; the algorithm would explicitly be taught that parameter X has little to no influence of the composition and characteristics of the protein corona.[773] Finally, deep learning approaches require large quantities of data for their training sets, acquiring enough reproducible data is also challenging. High throughput and/or data mining approaches are likely to be required.[765] Therefore, these issues fundamentally limit the quality of the data we have available for any sort of machine learning (or if the resulting data set is large enough - Deep Learning) approaches that we wish to implement in the rational, data-driven design of novel nanotherapeutics. For these aims to be met, it is likely that there needs to be the development of a consensus in the discipline with regards to methodology and how these approaches are implemented within the laboratory, rigid adherence to data reporting frameworks *e.g.,* MIRIBEL and MINBE to enable facile replication of published studies, and also the development of a data warehouse for such work, which would eventually hold the extensive data sets required by more complex forms of machine learning.

Further work specifically from part one of this thesis can be split into 3 distinct groups: looking further at protein corona composition and its influence on eventual biological fate *in vivo*, the degradation behaviour of polymeric nanoparticles, and the implications these results have on the development of future cell-uptake studies or those where probing the bio-nano interface is of interest.[43,774] In short, they consider how larger volumes of, and more accurate

data could be generated. The orthogonal approach outlined here could be used alongside other protein identification methods, (*e.g.,* ELISA) to identify the composition of the protein corona around nanoparticles *in situ*, uncovering insights into the evolution of its composition as a function of time and therefore potential predictors into eventual biological fate *in vivo.* Resonant Mass Measurement can track both protein corona formation and particle aggregation and agglomeration over time when dry mass is considered. It is expected that this method could be adapted to also enable the degradation behaviour of biocompatible nanoparticles to be studied. The design of future cell culture experiments is also impacted by the results discussed within this chapter. It highlights the need for pre-screening of nanoparticles in both buffer and protein containing media to assess both nanoparticle size distribution and colloidal stability before *in vivo* and *in vitro* studies. Protein corona formation is known to affect efficacy of cell uptake and the pathway by which this occurs.[230,775,776] When these studies are undertaken, it then permits changes in nanoparticle physicochemical properties to be correlated with altered biological interactions and cellular trafficking mechanisms.[777]

Part Two of the thesis considered the use of computational fluid dynamics to understand fluid behaviour *in vivo* and the development of a combined CFD-DEM methodology to simultaneously study fluid and nanoparticle behaviour when subject to physiological fluid flow. There are several ways by which this work could be further developed or otherwise extended. These include: the development of a microfluidic device to replicate the fluid shear calculated by the simulations in this chapter; the development of personalised, patient-specific models as well applying the methodology outlined here to other veins and/ or vascular access devices. Furthermore, there is interest in studying the effect of scaling the input geometry on computational demand and calculation length (*i.e.,* how much RAM and how long (in real time) do these simulations require, and could they be made to run faster or otherwise be less computationally demanding) Finally, the results presented here suggest that VADs could be redesigned to make them stay patent (functional) for extended periods of time.

There are many reasons why microfluidic devices are particularly useful, not only do they require smaller volumes of analytes, they are considered one of the key ways in which pre-clinical testing will move away from animal studies. Here, the microfluidic device is designed to subject the nanoparticles to physiologically relevant fluid shear stresses, so that their developing protein corona is more like that which develops *in vivo*.[52,282] This work towards the development of a suitable microfluidic device was presented in **Chapter 5**. Additionally, this work could move towards personalised, patient-specific models *i.e.,* personalised medicine. The necessary parameters can easily be derived from several commonly used imaging methods including computed tomography. This would likely be excessive for most patients, and unnecessary where PIVC use is considered. However, this could well be useful in the context of central lines (PICC or CVC) which are indwelling for significantly longer, and used with patients who are very unwell, or for whom

peripheral IV access is unavailable. These studies could be used to match the specific type of central line to the patient such that it remains patent for as long as possible. The CFD-DEM methodology developed here could also be applied to different regions of vasculature, or to different VADs – only a small subset of those in clinical use have been modelled here. The effect of scaling input geometry on computational demand and calculation length could also be studied in more detail. Initial studies have shown that the 10x scaling used here significantly reduces total number of cells within a given mesh, (~300,000 vs. 98,000) and thus simulations complete much faster. Furthermore, these studies suggest that the limiting step is the speed at which the calculations can be done, rather than dependent on total number of available processors. Rathmayer *et al.* suggest that there may be a threshold beyond which additional processors afford no additional increase in speed.[778] Initial results (4 vs 64 processors) would certainly support this. Finally, work could also consider possible methods of modifying PIVC design to prevent the component parts of Virchow's triad, therefore making the cannula remain patent for longer.[523,524] It is common for PIVC to be moved (resited) after a maximum of 72 hours.

The most obvious route for further work for part 3 of this thesis would be to 3D print the device and confirm it is suitable for its intended purpose. Further, Kotz *et al.*, and Mader *et al.*, have both previously reported that the transparency of the microfluidic device is improved when the device is printed onto a layer of the corresponding polymer, rather than directly onto the print bed.[735,750] Therefore, this would enable the optical properties of the microfluidic device to be assessed. If the polymer is found to be suitably clear, then several other directions can be undertaken. These directions include: assessing the resistance to biofouling of the device *via* the infusion of fluorescent nanoparticles – 100 nm fluorescent PLGA nanoparticles are commercially available.[779] Low autofluorescence of the polymer is required for the nanoparticles to be seen, which may influence the choice of polymer from which the device is manufactured. In this context, biofouling refers to the non-specific binding of proteins at the interface between fluid and solid *i.e.,* the microfluidic channel. This biofouling potentially prevents the reuse of the device.[780] Studying cell culture on the microfluidic device to understand influence of 3D polymeric structure on cell growth and behaviour, as well as the nanoparticle uptake into cells since this is known to be influenced by fluid shear. Finally, it would be interesting to see if the device could be used for inline analysis with PTA and/or RMM, to undertake the analysis outlined previously in **Chapter 2**, and therefore see the influence of physiological fluid shear on physicochemical characteristics of protein corona formation.

Bibliography

(1) Payton, R. L. *Dynamic and Interactive Scientific Posters: Visualising 3D Models and Simulation Data Using AR*; EGU2020-19037; Copernicus Meetings, 2020.

(2) Quintero, J.; Baldiris, S.; Rubira, R.; Cerón, J.; Velez, G. Augmented Reality in Educational Inclusion. A Systematic Review on the Last Decade. *Front. Psychol.* **2019**, *10*.

(3) Chatterjee, S.; Moon, S.; Rowlands, A.; Chin, F.; Seeberger, P. H.; Merbouh, N.; Gilmore, K. Click, Zoom, Explore: Interactive 3D (i-3D) Figures in Standard Teaching Materials (PDFs). *J. Chem. Educ.* **2021**, *98* (11), 3470–3475.

(4) Mathur, M.; Brozovich, J. M.; Rausch, M. K. A Brief Note on Building Augmented Reality Models for Scientific Visualization. *Finite Elem. Anal. Des.* **2023**, *213*, 103851.

(5) Eriksen, K.; Nielsen, B. E.; Pittelkow, M. Visualizing 3D Molecular Structures Using an Augmented Reality App. *J. Chem. Educ.* **2020**, *97* (5), 1487–1490.

(6) Garzón, J. An Overview of Twenty-Five Years of Augmented Reality in Education. *Multimodal Technol. Interact.* **2021**, *5* (7), 37.

(7) Ard, T.; Bienkowski, M. S.; Liew, S.-L.; Sepehrband, F.; Yan, L.; Toga, A. W. Integrating Data Directly into Publications with Augmented Reality and Web-Based Technologies – Schol-AR. *Sci. Data* **2022**, *9* (1), 298.

(8) *The Physical Properties of Image-Based Targets | VuforiaLibrary*. https://library.vuforia.com/objects/physical-properties-image-based-targets (accessed 2022-11-17).

(9) Silvio, D. D.; Rigby, N.; Bajka, B.; Mayes, A.; Mackie, A.; Bombelli, F. B. Technical Tip: High-Resolution Isolation of Nanoparticle–Protein Corona Complexes from Physiological Fluids. *Nanoscale* **2015**, *7* (28), 11980–11990.

(10) Xiao, W.; Gao, H. The Impact of Protein Corona on the Behavior and Targeting Capability of Nanoparticle-Based Delivery System. *Int. J. Pharm.* **2018**, *552* (1), 328–339.

(11) Berrecoso, G.; Crecente-Campo, J.; Alonso, M. J. Unveiling the Pitfalls of the Protein Corona of Polymeric Drug Nanocarriers. *Drug Deliv. Transl. Res.* **2020**, *10* (3), 730–750.

(12) Salvati, A.; Pitek, A. S.; Monopoli, M. P.; Prapainop, K.; Bombelli, F. B.; Hristov, D. R.; Kelly, P. M.; Åberg, C.; Mahon, E.; Dawson, K. A. Transferrin-Functionalized Nanoparticles Lose Their Targeting Capabilities When a Biomolecule Corona Adsorbs on the Surface. *Nat. Nanotechnol.* **2013**, *8* (2), 137–143.

(13) Dobrovolskaia, M. A.; Aggarwal, P.; Hall, J. B.; McNeil, S. E. Preclinical Studies to Understand Nanoparticle Interaction with the Immune System and Its Potential Effects on Nanoparticle Biodistribution. *Mol. Pharm.* **2008**, *5* (4), 487–495.

(14) Aggarwal, P.; Hall, J. B.; McLeland, C. B.; Dobrovolskaia, M. A.; McNeil, S. E. Nanoparticle Interaction with Plasma Proteins as It Relates to Particle Biodistribution, Biocompatibility and Therapeutic Efficacy. *Adv. Drug Deliv. Rev.* **2009**, *61* (6), 428–437.

(15) Al-Ahmady, Z. S.; Hadjidemetriou, M.; Gubbins, J.; Kostarelos, K. Formation of Protein Corona in Vivo Affects Drug Release from Temperature-Sensitive Liposomes. *J. Control. Release Off. J. Control. Release Soc.* **2018**, *276*, 157–167.

(16) Ju, Y.; Kelly, H. G.; Dagley, L. F.; Reynaldi, A.; Schlub, T. E.; Spall, S. K.; Bell, C. A.; Cui, J.; Mitchell, A. J.; Lin, Z.; Wheatley, A. K.; Thurecht, K. J.; Davenport, M. P.; Webb, A. I.; Caruso, F.; Kent, S. J. Person-Specific

Biomolecular Coronas Modulate Nanoparticle Interactions with Immune Cells in Human Blood. *ACS Nano* **2020**, *14* (11), 15723–15737.
(17) Kihara, S.; Ghosh, S.; McDougall, D. R.; Whitten, A. E.; Mata, J. P.; Köper, I.; McGillivray, D. J. Structure of Soft and Hard Protein Corona around Polystyrene Nanoplastics—Particle Size and Protein Types. *Biointerphases* **2020**, *15* (5), 051002.
(18) Mohammad-Beigi, H.; Hayashi, Y.; Zeuthen, C. M.; Eskandari, H.; Scavenius, C.; Juul-Madsen, K.; Vorup-Jensen, T.; Enghild, J. J.; Sutherland, D. S. *Mapping and Identification of Soft Corona Proteins at Nanoparticles and Their Impact on Cellular Association*; preprint; Pharmacology and Toxicology, 2020.
(19) Obst, K.; Yealland, G.; Balzus, B.; Miceli, E.; Dimde, M.; Weise, C.; Eravci, M.; Bodmeier, R.; Haag, R.; Calderón, M.; Charbaji, N.; Hedtrich, S. Protein Corona Formation on Colloidal Polymeric Nanoparticles and Polymeric Nanogels: Impact on Cellular Uptake, Toxicity, Immunogenicity, and Drug Release Properties. *Biomacromolecules* **2017**, *18* (6), 1762–1771.
(20) Weber, C.; Simon, J.; Mailänder, V.; Morsbach, S.; Landfester, K. Preservation of the Soft Protein Corona in Distinct Flow Allows Identification of Weakly Bound Proteins. *Acta Biomater.* **2018**, *76*, 217–224.
(21) Monopoli, M. P.; Walczyk, D.; Campbell, A.; Elia, G.; Lynch, I.; Baldelli Bombelli, F.; Dawson, K. A. Physical−Chemical Aspects of Protein Corona: Relevance to in Vitro and in Vivo Biological Impacts of Nanoparticles. *J. Am. Chem. Soc.* **2011**, *133* (8), 2525–2534.
(22) He, Z.; Ranganathan, N.; Li, P. Evaluating Nanomedicine with Microfluidics. *Nanotechnology* **2018**, *29* (49), 492001.
(23) Pal, M.; Chen, H.; Lee, B. H.; Lee, J. Y. H.; Yip, Y. S.; Tan, N. S.; Tan, L. P. Epithelial-Mesenchymal Transition of Cancer Cells Using Bioengineered Hybrid Scaffold Composed of Hydrogel/3D-Fibrous Framework. *Sci. Rep.* **2019**, *9* (1), 1–11.
(24) Atkins, J. T.; George, G. C.; Hess, K.; Marcelo-Lewis, K. L.; Yuan, Y.; Borthakur, G.; Khozin, S.; LoRusso, P.; Hong, D. S. Pre-Clinical Animal Models Are Poor Predictors of Human Toxicities in Phase 1 Oncology Clinical Trials. *Br. J. Cancer* **2020**, *123* (10), 1496–1501.
(25) Barenholz, Y. Doxil®--the First FDA-Approved Nano-Drug: Lessons Learned. *J. Control. Release Off. J. Control. Release Soc.* **2012**, *160* (2), 117–134.
(26) Anselmo, A. C.; Mitragotri, S. Nanoparticles in the Clinic. *Bioeng. Transl. Med.* **2016**, *1* (1), 10–29.
(27) Anselmo, A. C.; Mitragotri, S. Nanoparticles in the Clinic: An Update. *Bioeng. Transl. Med.* **2019**, *4* (3), e10143.
(28) Anselmo, A. C.; Mitragotri, S. Nanoparticles in the Clinic: An Update Post COVID-19 Vaccines. *Bioeng. Transl. Med.* **2021**, *6* (3), e10246.
(29) Polack, F. P.; Thomas, S. J.; Kitchin, N.; Absalon, J.; Gurtman, A.; Lockhart, S.; Perez, J. L.; Pérez Marc, G.; Moreira, E. D.; Zerbini, C.; Bailey, R.; Swanson, K. A.; Roychoudhury, S.; Koury, K.; Li, P.; Kalina, W. V.; Cooper, D.; Frenck, R. W.; Hammitt, L. L.; Türeci, Ö.; Nell, H.; Schaefer, A.; Ünal, S.; Tresnan, D. B.; Mather, S.; Dormitzer, P. R.; Şahin, U.; Jansen, K. U.; Gruber, W. C.; C4591001 Clinical Trial Group. Safety and Efficacy of the BNT162b2 mRNA Covid-19 Vaccine. *N. Engl. J. Med.* **2020**, *383* (27), 2603–2615.
(30) CZARSKA-THORLEY, D. *Spikevax (previously COVID-19 Vaccine Moderna)*. European Medicines Agency. https://www.ema.europa.eu/en/medicines/human/EPAR/spikevax (accessed 2021-10-11).
(31) Russell, W. M. S.; Burch, R. L. *The Principles of Humane Experimental Technique.*; Methuen & Co. Ltd.: London, 1959.
(32) Vroman, L. Effect of Adsorbed Proteins on the Wettability of Hydrophilic and Hydrophobic Solids. *Nature* **1962**, *196* (4853), 476–477.

(33) Cedervall, T.; Lynch, I.; Lindman, S.; Berggard, T.; Thulin, E.; Nilsson, H.; Dawson, K. A.; Linse, S. Understanding the Nanoparticle-Protein Corona Using Methods to Quantify Exchange Rates and Affinities of Proteins for Nanoparticles. *Proc. Natl. Acad. Sci.* **2007**, *104* (7), 2050–2055.
(34) Lundqvist, M.; Cedervall, T. Three Decades of Research about the Corona Around Nanoparticles: Lessons Learned and Where to Go Now. *Small* **2020**, *16* (46), 2000892.
(35) Lima, T.; Bernfur, K.; Vilanova, M.; Cedervall, T. Understanding the Lipid and Protein Corona Formation on Different Sized Polymeric Nanoparticles. *Sci. Rep.* **2020**, *10* (1), 1129.
(36) Müller, J.; Prozeller, D.; Ghazaryan, A.; Kokkinopoulou, M.; Mailänder, V.; Morsbach, S.; Landfester, K. Beyond the Protein Corona – Lipids Matter for Biological Response of Nanocarriers. *Acta Biomater.* **2018**, *71*, 420–431.
(37) Corbo, C.; Molinaro, R.; Parodi, A.; Toledano Furman, N. E.; Salvatore, F.; Tasciotti, E. The Impact of Nanoparticle Protein Corona on Cytotoxicity, Immunotoxicity and Target Drug Delivery. *Nanomed.* **2015**, *11* (1), 81–100.
(38) Di Silvio, D.; Maccarini, M.; Parker, R.; Mackie, A.; Fragneto, G.; Baldelli Bombelli, F. The Effect of the Protein Corona on the Interaction between Nanoparticles and Lipid Bilayers. *J. Colloid Interface Sci.* **2017**, *504*, 741–750.
(39) Ndumiso, M.; Buchtová, N.; Husselmann, L.; Mohamed, G.; Klein, A.; Aucamp, M.; Canevet, D.; D'Souza, S.; Maphasa, R. E.; Boury, F.; Dube, A. Comparative Whole Corona Fingerprinting and Protein Adsorption Thermodynamics of PLGA and PCL Nanoparticles in Human Serum. *Colloids Surf. B Biointerfaces* **2020**, *188*, 110816.
(40) Zhang, Y.; Wu, J. L. Y.; Lazarovits, J.; Chan, W. C. W. An Analysis of the Binding Function and Structural Organization of the Protein Corona. *J. Am. Chem. Soc.* **2020**, *142* (19), 8827–8836.
(41) Kari, O. K.; Ndika, J.; Parkkila, P.; Louna, A.; Lajunen, T.; Puustinen, A.; Viitala, T.; Alenius, H.; Urtti, A. In Situ Analysis of Liposome Hard and Soft Protein Corona Structure and Composition in a Single Label-Free Workflow. *Nanoscale* **2020**, *12* (3), 1728–1741.
(42) Walkey, C. D.; Chan, W. C. W. Understanding and Controlling the Interaction of Nanomaterials with Proteins in a Physiological Environment. *Chem. Soc. Rev.* **2012**, *41* (7), 2780–2799.
(43) Mahmoudi, M. Debugging Nano–Bio Interfaces: Systematic Strategies to Accelerate Clinical Translation of Nanotechnologies. *Trends Biotechnol.* **2018**, *36* (8), 755–769.
(44) Mahmoudi, M.; Bertrand, N.; Zope, H.; Farokhzad, O. C. Emerging Understanding of the Protein Corona at the Nano-Bio Interfaces. *Nano Today* **2016**, *11* (6), 817–832.
(45) Domingues, C.; Santos, A.; Alvarez-Lorenzo, C.; Concheiro, A.; Jarak, I.; Veiga, F.; Barbosa, I.; Dourado, M.; Figueiras, A. Where Is Nano Today and Where Is It Headed? A Review of Nanomedicine and the Dilemma of Nanotoxicology. *ACS Nano* **2022**, *16* (7), 9994–10041.
(46) Hajipour, M. J.; Laurent, S.; Aghaie, A.; Rezaee, F.; Mahmoudi, M. Personalized Protein Coronas: A "Key" Factor at the Nanobiointerface. *Biomater. Sci.* **2014**, *2* (9), 1210–1221.
(47) Corbo, C.; Molinaro, R.; Tabatabaei, M.; Farokhzad, O. C.; Mahmoudi, M. Personalized Protein Corona on Nanoparticles and Its Clinical Implications. *Biomater. Sci.* **2017**, *5* (3), 378–387.
(48) Kamali Shahri, S. M.; Sharifi, S.; Mahmoudi, M. Interdependency of Influential Parameters in Therapeutic Nanomedicine. *Expert Opin. Drug Deliv.* **2021**, *18* (10), 1379–1394.
(49) Rahman, M.; Laurent, S.; Tawil, N.; Yahia, L.; Mahmoudi, M. Nanoparticle and Protein Corona. In *Protein-Nanoparticle Interactions: The Bio-Nano*

Interface; Rahman, M., Laurent, S., Tawil, N., Yahia, L., Mahmoudi, M., Eds.; Springer Series in Biophysics; Springer: Berlin, Heidelberg, 2013; pp 21–44.
(50) Dolci, M.; Wang, Y.; Nooteboom, S. W.; Rodriguez, P. E. D. S.; Sanchez, S.; Albertazzi, L.; Zijlstra, P. Real-Time Optical Tracking of Protein Corona Formation on Single Nanoparticles in Serum. ChemRxiv September 18, 2023.
(51) Braun, N. J.; DeBrosse, M. C.; Hussain, S. M.; Comfort, K. K. Modification of the Protein Corona–Nanoparticle Complex by Physiological Factors. *Mater. Sci. Eng. C* **2016**, *64*, 34–42.
(52) Jayaram, D. T.; Pustulka, S. M.; Mannino, R. G.; Lam, W. A.; Payne, C. K. Protein Corona in Response to Flow: Effect on Protein Concentration and Structure. *Biophys. J.* **2018**, *115* (2), 209–216.
(53) Pozzi, D.; Caracciolo, G.; Digiacomo, L.; Colapicchioni, V.; Palchetti, S.; Capriotti, A. L.; Cavaliere, C.; Zenezini Chiozzi, R.; Puglisi, A.; Laganà, A. The Biomolecular Corona of Nanoparticles in Circulating Biological Media. *Nanoscale* **2015**, *7* (33), 13958–13966.
(54) Palchetti, S.; Pozzi, D.; Capriotti, A. L.; Barbera, G. L.; Chiozzi, R. Z.; Digiacomo, L.; Peruzzi, G.; Caracciolo, G.; Laganà, A. Influence of Dynamic Flow Environment on Nanoparticle-Protein Corona: From Protein Patterns to Uptake in Cancer Cells. *Colloids Surf. B Biointerfaces* **2017**, *153*, 263–271.
(55) Amici, A.; Caracciolo, G.; Digiacomo, L.; Gambini, V.; Marchini, C.; Tilio, M.; Capriotti, A. L.; Colapicchioni, V.; Matassa, R.; Familiari, G.; Palchetti, S.; Pozzi, D.; Mahmoudi, M.; Laganà, A. In Vivo Protein Corona Patterns of Lipid Nanoparticles. *RSC Adv.* **2017**, *7* (2), 1137–1145.
(56) Wang, W.; Sedykh, A.; Sun, H.; Zhao, L.; Russo, D. P.; Zhou, H.; Yan, B.; Zhu, H. Predicting Nano–Bio Interactions by Integrating Nanoparticle Libraries and Quantitative Nanostructure Activity Relationship Modeling. *ACS Nano* **2017**, *11* (12), 12641–12649.
(57) Ich-Guideline-S9-Non-Clinical-Evaluation-Anticancer-Pharmaceuticals-Step-5_en.Pdf. https://www.ema.europa.eu/en/documents/scientific-guideline/ich-guideline-s9-non-clinical-evaluation-anticancer-pharmaceuticals-step-5_en.pdf (accessed 2023-03-20).
(58) Ich-S6r1-Preclinical-Safety-Evaluation-Biotechnology-Derived-Pharmaceuticals-Step-5_en.Pdf. https://www.ema.europa.eu/en/documents/scientific-guideline/ich-s6r1-preclinical-safety-evaluation-biotechnology-derived-pharmaceuticals-step-5_en.pdf (accessed 2023-03-20).
(59) Ich-Guideline-M3r2-Non-Clinical-Safety-Studies-Conduct-Human-Clinical-Trials-Marketing-Authorisation_en.Pdf. https://www.ema.europa.eu/en/documents/scientific-guideline/ich-guideline-m3r2-non-clinical-safety-studies-conduct-human-clinical-trials-marketing-authorisation_en.pdf (accessed 2023-03-20).
(60) Van Norman, G. A. Limitations of Animal Studies for Predicting Toxicity in Clinical Trials. *JACC Basic Transl. Sci.* **2020**, *5* (4), 387–397.
(61) Palchetti, S.; Colapicchioni, V.; Digiacomo, L.; Caracciolo, G.; Pozzi, D.; Capriotti, A. L.; La Barbera, G.; Laganà, A. The Protein Corona of Circulating PEGylated Liposomes. *Biochim. Biophys. Acta BBA - Biomembr.* **2016**, *1858* (2), 189–196.
(62) *What is nanomedicine?* | *ETPN*. https://etp-nanomedicine.eu/about-nanomedicine/what-is-nanomedicine/ (accessed 2019-10-04).
(63) *What is Nanotechnology?* | *Nano*. https://www.nano.gov/nanotech-101/what/definition (accessed 2019-10-04).
(64) Etheridge, M. L.; Campbell, S. A.; Erdman, A. G.; Haynes, C. L.; Wolf, S. M.; McCullough, J. The Big Picture on Nanomedicine: The State of Investigational and Approved Nanomedicine Products. *Nanomedicine Nanotechnol. Biol. Med.* **2013**, *9* (1), 1–14.

(65) Litzinger, D. C.; Buiting, A. M. J.; van Rooijen, N.; Huang, L. Effect of Liposome Size on the Circulation Time and Intraorgan Distribution of Amphipathic Poly(Ethylene Glycol)-Containing Liposomes. *Biochim. Biophys. Acta BBA - Biomembr.* **1994**, *1190* (1), 99–107.
(66) O'Neal, D. P.; Hirsch, L. R.; Halas, N. J.; Payne, J. D.; West, J. L. Photo-Thermal Tumor Ablation in Mice Using near Infrared-Absorbing Nanoparticles. *Cancer Lett.* **2004**, *209* (2), 171–176.
(67) Webster, T. J. Nanomedicine: What's in a Definition? *Int. J. Nanomedicine* **2006**, *1* (2), 115–116.
(68) Foulkes, R.; Man, E.; Thind, J.; Yeung, S.; Joy, A.; Hoskins, C. The Regulation of Nanomaterials and Nanomedicines for Clinical Application: Current and Future Perspectives. *Biomater. Sci.* **2020**, *8* (17), 4653–4664.
(69) Nanomedicine_01.Pdf. http://archives.esf.org/fileadmin/Public_documents/Publications/Nanomedicine_01.pdf (accessed 2023-02-20).
(70) Ventola, C. L. Progress in Nanomedicine: Approved and Investigational Nanodrugs. *Pharm. Ther.* **2017**, *42* (12), 742–755.
(71) Namiot, E. D.; Sokolov, A. V.; Chubarev, V. N.; Tarasov, V. V.; Schiöth, H. B. Nanoparticles in Clinical Trials: Analysis of Clinical Trials, FDA Approvals and Use for COVID-19 Vaccines. *Int. J. Mol. Sci.* **2023**, *24* (1), 787.
(72) Jackson, L. A.; Anderson, E. J.; Rouphael, N. G.; Roberts, P. C.; Makhene, M.; Coler, R. N.; McCullough, M. P.; Chappell, J. D.; Denison, M. R.; Stevens, L. J.; Pruijssers, A. J.; McDermott, A.; Flach, B.; Doria-Rose, N. A.; Corbett, K. S.; Morabito, K. M.; O'Dell, S.; Schmidt, S. D.; Swanson, P. A.; Padilla, M.; Mascola, J. R.; Neuzil, K. M.; Bennett, H.; Sun, W.; Peters, E.; Makowski, M.; Albert, J.; Cross, K.; Buchanan, W.; Pikaart-Tautges, R.; Ledgerwood, J. E.; Graham, B. S.; Beigel, J. H.; mRNA-1273 Study Group. An mRNA Vaccine against SARS-CoV-2 - Preliminary Report. *N. Engl. J. Med.* **2020**, *383* (20), 1920–1931.
(73) Bertrand, N.; Wu, J.; Xu, X.; Kamaly, N.; Farokhzad, O. C. Cancer Nanotechnology: The Impact of Passive and Active Targeting in the Era of Modern Cancer Biology. *Adv. Drug Deliv. Rev.* **2014**, *66*, 2–25.
(74) Yang, J.; Wang, X.; Wang, B.; Park, K.; Wooley, K.; Zhang, S. Challenging the Fundamental Conjectures in Nanoparticle Drug Delivery for Chemotherapy Treatment of Solid Cancers. *Adv. Drug Deliv. Rev.* **2022**, *190*, 114525.
(75) Kim, E.; Yang, J.; Park, S.; Shin, K. Factors Affecting Success of New Drug Clinical Trials. *Ther. Innov. Regul. Sci.* **2023**, *57* (4), 737–750.
(76) Germain, M.; Caputo, F.; Metcalfe, S.; Tosi, G.; Spring, K.; Åslund, A. K. O.; Pottier, A.; Schiffelers, R.; Ceccaldi, A.; Schmid, R. Delivering the Power of Nanomedicine to Patients Today. *J. Control. Release Off. J. Control. Release Soc.* **2020**, *326*, 164–171.
(77) Cabral, H.; Li, J.; Miyata, K.; Kataoka, K. Controlling the Biodistribution and Clearance of Nanomedicines. *Nat. Rev. Bioeng.* **2023**, 1–19.
(78) Maeda, H.; Matsumura, Y. A New Concept for Macromolecular Therapeutics in Cancer Chemotherapy: Mechanism of Tumoritropic Accumulation of Proteins and the Antitumor Agent Smancs | Cancer Research. *Am. Assoc. Cancer Res.* **1986**, *46* (12), 6387–6392.
(79) Peer, D.; Karp, J. M.; Hong, S.; Farokhzad, O. C.; Margalit, R.; Langer, R. Nanocarriers as an Emerging Platform for Cancer Therapy. *Nat. Nanotechnol.* **2007**, *2* (12), 751–760.
(80) Wang, M.; Thanou, M. Targeting Nanoparticles to Cancer. *Pharmacol. Res.* **2010**, *62* (2), 90–99.
(81) Hashizume, H.; Baluk, P.; Morikawa, S.; McLean, J. W.; Thurston, G.; Roberge, S.; Jain, R. K.; McDonald, D. M. Openings between Defective

Endothelial Cells Explain Tumor Vessel Leakiness. *Am. J. Pathol.* **2000**, *156* (4), 1363–1380.
(82) Hobbs, S. K.; Monsky, W. L.; Yuan, F.; Roberts, W. G.; Griffith, L.; Torchilin, V. P.; Jain, R. K. Regulation of Transport Pathways in Tumor Vessels: Role of Tumor Type and Microenvironment. *Proc. Natl. Acad. Sci. U. S. A.* **1998**, *95* (8), 4607–4612.
(83) Skinner, S. A.; Tutton, P. J.; O'Brien, P. E. Microvascular Architecture of Experimental Colon Tumors in the Rat. *Cancer Res.* **1990**, *50* (8), 2411–2417.
(84) Kingston, B. R.; Lin, Z. P.; Ouyang, B.; MacMillan, P.; Ngai, J.; Syed, A. M.; Sindhwani, S.; Chan, W. C. W. Specific Endothelial Cells Govern Nanoparticle Entry into Solid Tumors. *ACS Nano* **2021**, *15* (9), 14080–14094.
(85) Sindhwani, S.; Syed, A. M.; Ngai, J.; Kingston, B. R.; Maiorino, L.; Rothschild, J.; MacMillan, P.; Zhang, Y.; Rajesh, N. U.; Hoang, T.; Wu, J. L. Y.; Wilhelm, S.; Zilman, A.; Gadde, S.; Sulaiman, A.; Ouyang, B.; Lin, Z.; Wang, L.; Egeblad, M.; Chan, W. C. W. The Entry of Nanoparticles into Solid Tumours. *Nat. Mater.* **2020**, *19* (5), 566–575.
(86) Nichols, J. W.; Bae, Y. H. EPR: Evidence and Fallacy. *J. Control. Release Off. J. Control. Release Soc.* **2014**, *190*, 451–464.
(87) Shi, Y.; van der Meel, R.; Chen, X.; Lammers, T. The EPR Effect and beyond: Strategies to Improve Tumor Targeting and Cancer Nanomedicine Treatment Efficacy. *Theranostics* **2020**, *10* (17), 7921–7924.
(88) Nguyen, L. N. M.; Ngo, W.; Lin, Z. P.; Sindhwani, S.; MacMillan, P.; Mladjenovic, S. M.; Chan, W. C. W. The Mechanisms of Nanoparticle Delivery to Solid Tumours. *Nat. Rev. Bioeng.* **2024**, 1–13.
(89) Byrne, J. D.; Betancourt, T.; Brannon-Peppas, L. Active Targeting Schemes for Nanoparticle Systems in Cancer Therapeutics. *Adv. Drug Deliv. Rev.* **2008**, *60* (15), 1615–1626.
(90) Ran, S.; Downes, A.; Thorpe, P. E. Increased Exposure of Anionic Phospholipids on the Surface of Tumor Blood Vessels1. *Cancer Res.* **2002**, *62* (21), 6132–6140.
(91) Krasnici, S.; Werner, A.; Eichhorn, M. E.; Schmitt-Sody, M.; Pahernik, S. A.; Sauer, B.; Schulze, B.; Teifel, M.; Michaelis, U.; Naujoks, K.; Dellian, M. Effect of the Surface Charge of Liposomes on Their Uptake by Angiogenic Tumor Vessels. *Int. J. Cancer* **2003**, *105* (4), 561–567.
(92) Yuan, Y.; Cai, T.; Xia, X.; Zhang, R.; Chiba, P.; Cai, Y. Nanoparticle Delivery of Anticancer Drugs Overcomes Multidrug Resistance in Breast Cancer. *Drug Deliv.* **2016**, *23* (9), 3350–3357.
(93) Zhao, Y.; Adjei, A. A. Targeting Angiogenesis in Cancer Therapy: Moving Beyond Vascular Endothelial Growth Factor. *The Oncologist* **2015**, *20* (6), 660–673.
(94) Shi, S.; Zhou, M.; Li, X.; Hu, M.; Li, C.; Li, M.; Sheng, F.; Li, Z.; Wu, G.; Luo, M.; Cui, H.; Li, Z.; Fu, R.; Xiang, M.; Xu, J.; Zhang, Q.; Lu, L. Synergistic Active Targeting of Dually Integrin Avβ3/CD44-Targeted Nanoparticles to B16F10 Tumors Located at Different Sites of Mouse Bodies. *J. Control. Release Off. J. Control. Release Soc.* **2016**, *235*, 1–13.
(95) Liu, Z.; Wang, F.; Chen, X. Integrin Avβ3-Targeted Cancer Therapy. *Drug Dev. Res.* **2008**, *69* (6), 329–339.
(96) Eck, S. M.; Blackburn, J. S.; Schmucker, A. C.; Burrage, P. S.; Brinckerhoff, C. E. Matrix Metalloproteinase and G Protein Coupled Receptors: Co-Conspirators in the Pathogenesis of Autoimmune Disease and Cancer. *J. Autoimmun.* **2009**, *33* (3–4), 214–221.
(97) Kumar, S.; Li, C. Targeting of Vasculature in Cancer and Other Angiogenic Diseases. *Trends Immunol.* **2001**, *22* (3), 129.

(98) Seshacharyulu, P.; Ponnusamy, M. P.; Haridas, D.; Jain, M.; Ganti, AparK.; Batra, S. K. Targeting the EGFR Signaling Pathway in Cancer Therapy. *Expert Opin. Ther. Targets* **2012**, *16* (1), 15–31.
(99) Ennis, B. W.; Lippman, M. E.; Dickson, R. B. The EGF Receptor System as a Target for Antitumor Therapy. *Cancer Invest.* **1991**, *9* (5), 553–562.
(100) Mendelsohn, J. The Epidermal Growth Factor Receptor as a Target for Cancer Therapy. *Endocr. Relat. Cancer* **2001**, *8* (1), 3–9.
(101) Gorain, B.; Bhattamishra, S. K.; Choudhury, H.; Nandi, U.; Pandey, M.; Kesharwani, P. Chapter 3 - Overexpressed Receptors and Proteins in Lung Cancer. In *Nanotechnology-Based Targeted Drug Delivery Systems for Lung Cancer*; Kesharwani, P., Ed.; Academic Press, 2019; pp 39–75.
(102) Guillon, A.; Gueugnon, F.; Mavridis, K.; Dalloneau, E.; Jouan, Y.; Diot, P.; Heuzé-Vourc'h, N.; Courty, Y.; Si-Tahar, M. Interleukin-22 Receptor Is Overexpressed in Nonsmall Cell Lung Cancer and Portends a Poor Prognosis. *Eur. Respir. J.* **2016**, *47* (4), 1277–1280.
(103) Lal, N.; Willcox, C. R.; Beggs, A.; Taniere, P.; Shikotra, A.; Bradding, P.; Adams, R.; Fisher, D.; Middleton, G.; Tselepis, C.; Willcox, B. E. Endothelial Protein C Receptor Is Overexpressed in Colorectal Cancer as a Result of Amplification and Hypomethylation of Chromosome 20q. *J. Pathol. Clin. Res.* **2017**, *3* (3), 155–170.
(104) Felton, J.; Hu, S.; Raufman, J.-P. Targeting M3 Muscarinic Receptors for Colon Cancer Therapy. *Curr. Mol. Pharmacol.* **2018**, *11* (3), 184–190.
(105) Kübler, E.; Albrecht, H. Large Set Data Mining Reveals Overexpressed GPCRs in Prostate and Breast Cancer: Potential for Active Targeting with Engineered Anti-Cancer Nanomedicines. *Oncotarget* **2018**, *9* (38), 24882–24897.
(106) Ceña, V.; Játiva, P. Nanoparticle Crossing of Blood–Brain Barrier: A Road to New Therapeutic Approaches to Central Nervous System Diseases. *Nanomed.* **2018**, *13* (13), 1513–1516.
(107) Rahman, M. F.; Wang, J.; Patterson, T. A.; Saini, U. T.; Robinson, B. L.; Newport, G. D.; Murdock, R. C.; Schlager, J. J.; Hussain, S. M.; Ali, S. F. Expression of Genes Related to Oxidative Stress in the Mouse Brain after Exposure to Silver-25 Nanoparticles. *Toxicol. Lett.* **2009**, *187* (1), 15–21.
(108) Finkel (PharmD.), R.; Clark, M. A.; Cubeddu, L. X. *Pharmacology*; Lippincott Williams & Wilkins, 2009.
(109) Wolfram, J.; Zhu, M.; Yang, Y.; Shen, J.; Gentile, E.; Paolino, D.; Fresta, M.; Nie, G.; Chen, C.; Shen, H.; Ferrari, M.; Zhao, Y. Safety of Nanoparticles in Medicine. *Curr. Drug Targets* **2015**, *16* (14), 1671–1681.
(110) Hua, S.; de Matos, M. B. C.; Metselaar, J. M.; Storm, G. Current Trends and Challenges in the Clinical Translation of Nanoparticulate Nanomedicines: Pathways for Translational Development and Commercialization. *Front. Pharmacol.* **2018**, *9*.
(111) Sangtani, A.; Petryayeva, E.; Susumu, K.; Oh, E.; Huston, A. L.; Lasarte-Aragones, G.; Medintz, I. L.; Algar, W. R.; Delehanty, J. B. Nanoparticle–Peptide–Drug Bioconjugates for Unassisted Defeat of Multidrug Resistance in a Model Cancer Cell Line. *Bioconjug. Chem.* **2019**, *30* (3), 525–530.
(112) Rice, L. B. Federal Funding for the Study of Antimicrobial Resistance in Nosocomial Pathogens: No ESKAPE. *J. Infect. Dis.* **2008**, *197* (8), 1079–1081.
(113) Wang, Z.-H.; Peng, W.-B.; Zhang, P.; Yang, X.-P.; Zhou, Q. Lactate in the Tumour Microenvironment: From Immune Modulation to Therapy. *eBioMedicine* **2021**, *73*.
(114) Michael, M.; Doherty, M. M. Tumoral Drug Metabolism: Overview and Its Implications for Cancer Therapy. *J. Clin. Oncol. Off. J. Am. Soc. Clin. Oncol.* **2005**, *23* (1), 205–229.

(115) Mansoori, B.; Mohammadi, A.; Davudian, S.; Shirjang, S.; Baradaran, B. The Different Mechanisms of Cancer Drug Resistance: A Brief Review. *Adv. Pharm. Bull.* **2017**, *7* (3), 339–348.
(116) Yuan, H.; Xia, P.; Sun, X.; Ma, J.; Xu, X.; Fu, C.; Zhou, H.; Guan, Y.; Li, Z.; Zhao, S.; Wang, H.; Dai, L.; Xu, C.; Dong, S.; Geng, Q.; Li, Z.; Wang, J. Photothermal Nanozymatic Nanoparticles Induce Ferroptosis and Apoptosis through Tumor Microenvironment Manipulation for Cancer Therapy. *Small* **2022**, *18* (41), 2202161.
(117) Delou, J. M. A.; Souza, A. S. O.; Souza, L. C. M.; Borges, H. L. Highlights in Resistance Mechanism Pathways for Combination Therapy. *Cells* **2019**, *8* (9).
(118) Li, J.; Yuan, J. Caspases in Apoptosis and Beyond. *Oncogene* **2008**, *27* (48), 6194–6206.
(119) Longley, D.; Johnston, P. Molecular Mechanisms of Drug Resistance. *J. Pathol.* **2005**, *205* (2), 275–292.
(120) Ozaki, T.; Nakagawara, A. Role of P53 in Cell Death and Human Cancers. *Cancers* **2011**, *3* (1), 994–1013.
(121) Rivlin, N.; Brosh, R.; Oren, M.; Rotter, V. Mutations in the P53 Tumor Suppressor Gene. *Genes Cancer* **2011**, *2* (4), 466–474.
(122) Safa, A. R. Roles of C-FLIP in Apoptosis, Necroptosis, and Autophagy. *J. Carcinog. Mutagen.* **2013**, *Suppl 6*.
(123) Wang, S.-W.; Lee, C.-H.; Lin, M.-S.; Chi, C.-W.; Chen, Y.-J.; Wang, G.-S.; Liao, K.-W.; Chiu, L.-P.; Wu, S.-H.; Huang, D.-M.; Chen, L.; Shen, Y.-S. ZnO Nanoparticles Induced Caspase-Dependent Apoptosis in Gingival Squamous Cell Carcinoma through Mitochondrial Dysfunction and p70S6K Signaling Pathway. *Int. J. Mol. Sci.* **2020**, *21* (5), 1612.
(124) Locher, K. P. Mechanistic Diversity in ATP-Binding Cassette (ABC) Transporters. *Nat. Struct. Mol. Biol.* **2016**, *23* (6), 487–493.
(125) Robey, R. W.; Pluchino, K. M.; Hall, M. D.; Fojo, A. T.; Bates, S. E.; Gottesman, M. M. Revisiting the Role of ABC Transporters in Multidrug-Resistant Cancer. *Nat. Rev. Cancer* **2018**, *18* (7), 452–464.
(126) Dean, M.; Rzhetsky, A.; Allikmets, R. The Human ATP-Binding Cassette (ABC) Transporter Superfamily. *Genome Res.* **2001**, *11* (7), 1156–1166.
(127) Gupta, D.; Singh, A.; Khan, A. U. Nanoparticles as Efflux Pump and Biofilm Inhibitor to Rejuvenate Bactericidal Effect of Conventional Antibiotics. *Nanoscale Res. Lett.* **2017**, *12* (1), 454.
(128) Brown, S. D.; Nativo, P.; Smith, J.-A.; Stirling, D.; Edwards, P. R.; Venugopal, B.; Flint, D. J.; Plumb, J. A.; Graham, D.; Wheate, N. J. Gold Nanoparticles for the Improved Anticancer Drug Delivery of the Active Component of Oxaliplatin. *J. Am. Chem. Soc.* **2010**, *132* (13), 4678–4684.
(129) Ge, C.; Du, J.; Zhao, L.; Wang, L.; Liu, Y.; Li, D.; Yang, Y.; Zhou, R.; Zhao, Y.; Chai, Z.; Chen, C. Binding of Blood Proteins to Carbon Nanotubes Reduces Cytotoxicity. *Proc. Natl. Acad. Sci.* **2011**, *108* (41), 16968–16973.
(130) Duncan, R.; Izzo, L. Dendrimer Biocompatibility and Toxicity. *Adv. Drug Deliv. Rev.* **2005**, *57* (15), 2215–2237.
(131) Svenson, S. The Dendrimer Paradox – High Medical Expectations but Poor Clinical Translation. *Chem. Soc. Rev.* **2015**, *44* (12), 4131–4144.
(132) Thornalley, K. A.; Laurini, E.; Pricl, S.; Smith, D. K. Enantiomeric and Diastereomeric Self-Assembled Multivalent Nanostructures: Understanding the Effects of Chirality on Binding to Polyanionic Heparin and DNA. *Angew. Chem. Int. Ed.* **2018**, *57* (28), 8530–8534.
(133) Chan, C. W.; Laurini, E.; Posocco, P.; Pricl, S.; Smith, D. K. Chiral Recognition at Self-Assembled Multivalent (SAMul) Nanoscale Interfaces – Enantioselectivity in Polyanion Binding. *Chem. Commun.* **2016**, *52* (69), 10540–10543.

(134) Bromfield, S. M.; Posocco, P.; Chan, C. W.; Calderon, M.; Guimond, S. E.; Turnbull, J. E.; Pricl, S.; Smith, D. K. Nanoscale Self-Assembled Multivalent (SAMul) Heparin Binders in Highly Competitive, Biologically Relevant, Aqueous Media. *Chem. Sci.* **2014**, *5* (4), 1484–1492.
(135) Lasic, D. D.; Frederik, P. M.; Stuart, M. C.; Barenholz, Y.; McIntosh, T. J. Gelation of Liposome Interior. A Novel Method for Drug Encapsulation. *FEBS Lett.* **1992**, *312* (2–3), 255–258.
(136) Xiaohu Gao; Gui, Y.; Levenson, R. M.; Chung, L. W. K.; Nie, S. In Vivo Cancer Targeting and Imaging with Semiconductor Quantum Dots. *Nat. Biotechnol.* **2004**, *22* (8), 969–976.
(137) Cao, M.; Sun, Y.; Xiao, M.; Li, L.; Liu, X.; Jin, H.; Pei, H. Multivalent Aptamer-Modified DNA Origami as Drug Delivery System for Targeted Cancer Therapy. *Chem. Res. Chin. Univ.* **2020**, *36* (2), 254–260.
(138) Wang, S.-T.; Gray, M. A.; Xuan, S.; Lin, Y.; Byrnes, J.; Nguyen, A. I.; Todorova, N.; Stevens, M. M.; Bertozzi, C. R.; Zuckermann, R. N.; Gang, O. DNA Origami Protection and Molecular Interfacing through Engineered Sequence-Defined Peptoids. *Proc. Natl. Acad. Sci.* **2020**, *117* (12), 6339–6348.
(139) García-López, V.; Chen, F.; Nilewski, L. G.; Duret, G.; Aliyan, A.; Kolomeisky, A. B.; Robinson, J. T.; Wang, G.; Pal, R.; Tour, J. M. Molecular Machines Open Cell Membranes. *Nature* **2017**, *548* (7669), 567–572.
(140) Liu, D.; García-López, V.; Gunasekera, R. S.; Greer Nilewski, L.; Alemany, L. B.; Aliyan, A.; Jin, T.; Wang, G.; Tour, J. M.; Pal, R. Near-Infrared Light Activates Molecular Nanomachines to Drill into and Kill Cells. *ACS Nano* **2019**, *13* (6), 6813–6823.
(141) Yoo, J.; Tang, S.; Gao, W. Micro- and Nanorobots for Biomedical Applications in the Brain. *Nat. Rev. Bioeng.* **2023**, *1* (5), 308–310.
(142) Farjadian, F.; Ghasemi, A.; Gohari, O.; Roointan, A.; Karimi, M.; Hamblin, M. R. Nanopharmaceuticals and Nanomedicines Currently on the Market: Challenges and Opportunities. *Nanomed.* **2018**, *14* (1), 93–126.
(143) Hajipour, M. J.; Safavi-Sohi, R.; Sharifi, S.; Mahmoud, N.; Ashkarran, A. A.; Voke, E.; Serpooshan, V.; Ramezankhani, M.; Milani, A. S.; Landry, M. P.; Mahmoudi, M. An Overview of Nanoparticle Protein Corona Literature. *Small* **2023**, *19* (36), 2301838.
(144) Yeh, Y.-C.; Creran, B.; Rotello, V. M. Gold Nanoparticles: Preparation, Properties, and Applications in Bionanotechnology. *Nanoscale* **2012**, *4* (6), 1871–1880.
(145) Ghosh, P.; Han, G.; De, M.; Kim, C. K.; Rotello, V. M. Gold Nanoparticles in Delivery Applications. *Adv. Drug Deliv. Rev.* **2008**, *60* (11), 1307–1315.
(146) Cheng, M. M.-C.; Cuda, G.; Bunimovich, Y. L.; Gaspari, M.; Heath, J. R.; Hill, H. D.; Mirkin, C. A.; Nijdam, A. J.; Terracciano, R.; Thundat, T.; Ferrari, M. Nanotechnologies for Biomolecular Detection and Medical Diagnostics. *Curr. Opin. Chem. Biol.* **2006**, *10* (1), 11–19.
(147) Parolo, C.; Merkoçi, A. Paper-Based Nanobiosensors for Diagnostics. *Chem. Soc. Rev.* **2013**, *42* (2), 450–457.
(148) Zhou, J.; Ralston, J.; Sedev, R.; Beattie, D. A. Functionalized Gold Nanoparticles: Synthesis, Structure and Colloid Stability. *J. Colloid Interface Sci.* **2009**, *331* (2), 251–262.
(149) Tiwari, P. M.; Vig, K.; Dennis, V. A.; Singh, S. R. Functionalized Gold Nanoparticles and Their Biomedical Applications. *Nanomaterials* **2011**, *1* (1), 31–63.
(150) Liu, J.; Yu, M.; Zhou, C.; Zheng, J. Renal Clearable Inorganic Nanoparticles: A New Frontier of Bionanotechnology. *Mater. Today* **2013**, *16* (12), 477–486.

(151) Xie, X.; Liao, J.; Shao, X.; Li, Q.; Lin, Y. The Effect of Shape on Cellular Uptake of Gold Nanoparticles in the Forms of Stars, Rods, and Triangles. *Sci. Rep.* **2017**, *7* (1), 1–9.
(152) Nehl, C. L.; Liao, H.; Hafner, J. H. Optical Properties of Star-Shaped Gold Nanoparticles. *Nano Lett.* **2006**, *6* (4), 683–688.
(153) Hu, J.; Wang, Z.; Li, J. Gold Nanoparticles With Special Shapes: Controlled Synthesis, Surface-Enhanced Raman Scattering, and The Application in Biodetection. *Sensors* **2007**, *7* (12), 3299–3311.
(154) Singh, P.; Pandit, S.; Mokkapati, V. R. S. S.; Garg, A.; Ravikumar, V.; Mijakovic, I. Gold Nanoparticles in Diagnostics and Therapeutics for Human Cancer. *Int. J. Mol. Sci.* **2018**, *19* (7).
(155) Burdușel, A.-C.; Gherasim, O.; Grumezescu, A. M.; Mogoantă, L.; Ficai, A.; Andronescu, E. Biomedical Applications of Silver Nanoparticles: An Up-to-Date Overview. *Nanomaterials* **2018**, *8* (9).
(156) Turkevich, J.; Stevenson, P. C.; Hillier, J. A Study of the Nucleation and Growth Processes in the Synthesis of Colloidal Gold. *Discuss. Faraday Soc.* **1951**, *11* (0), 55–75.
(157) Frens, G. Controlled Nucleation for the Regulation of the Particle Size in Monodisperse Gold Suspensions. *Nat. Phys. Sci.* **1973**, *241* (105), 20–22.
(158) Elbert, K. C.; Lee, J. D.; Wu, Y.; Murray, C. B. Improved Chemical and Colloidal Stability of Gold Nanoparticles through Dendron Capping. *Langmuir* **2018**, *34* (44), 13333–13338.
(159) Ladj, R.; Bitar, A.; Eissa, M.; Mugnier, Y.; Dantec, R. L.; Fessi, H.; Elaissari, A. Individual Inorganic Nanoparticles: Preparation, Functionalization and in Vitro Biomedical Diagnostic Applications. *J. Mater. Chem. B* **2013**, *1* (10), 1381–1396.
(160) Munasinghe, E.; Aththapaththu, M.; Jayarathne, L. Magnetic and Quantum Dot Nanoparticles for Drug Delivery and Diagnostic Systems. *Colloid Sci. Pharm. Nanotechnol.* **2019**.
(161) Gupta, A. K.; Wells, S. Surface-Modified Superparamagnetic Nanoparticles for Drug Delivery: Preparation, Characterization, and Cytotoxicity Studies. *IEEE Trans. Nanobioscience* **2004**, *3* (1), 66–73.
(162) Dadfar, S. M.; Roemhild, K.; Drude, N. I.; von Stillfried, S.; Knüchel, R.; Kiessling, F.; Lammers, T. Iron Oxide Nanoparticles: Diagnostic, Therapeutic and Theranostic Applications. *Adv. Drug Deliv. Rev.* **2019**, *138*, 302–325.
(163) Parenteral Iron. In *BNF: British National Formulary*; BMJ Group and Pharmaceutical Press: London, 2014; pp 633–635.
(164) Arias, L. S.; Pessan, J. P.; Vieira, A. P. M.; de Lima, T. M. T.; Delbem, A. C. B.; Monteiro, D. R. Iron Oxide Nanoparticles for Biomedical Applications: A Perspective on Synthesis, Drugs, Antimicrobial Activity, and Toxicity. *Antibiotics* **2018**, *7* (2).
(165) Mashhadi Malekzadeh, A.; Ramazani, A.; Tabatabaei Rezaei, S. J.; Niknejad, H. Design and Construction of Multifunctional Hyperbranched Polymers Coated Magnetite Nanoparticles for Both Targeting Magnetic Resonance Imaging and Cancer Therapy. *J. Colloid Interface Sci.* **2017**, *490*, 64–73.
(166) Bulte, J. W. M. Superparamagnetic Iron Oxides as MPI Tracers: A Primer and Review of Early Applications. *Adv. Drug Deliv. Rev.* **2019**, *138*, 293–301.
(167) Bauer, L. M.; Situ, S. F.; Griswold, M. A.; Samia, A. C. S. Magnetic Particle Imaging Tracers: State-of-the-Art and Future Directions. *J. Phys. Chem. Lett.* **2015**, *6* (13), 2509–2517.
(168) Silva, A. C.; Oliveira, T. R.; Mamani, J. B.; Malheiros, S. M.; Malavolta, L.; Pavon, L. F.; Sibov, T. T.; Amaro, E.; Tannús, A.; Vidoto, E. L.; Martins, M. J.; Santos, R. S.; Gamarra, L. F. Application of Hyperthermia Induced by Superparamagnetic Iron Oxide Nanoparticles in Glioma Treatment. *Int. J. Nanomedicine* **2011**, *6*, 591–603.

(169) Zuvin, M.; Koçak, M.; Ünal, Ö.; Akkoç, Y.; Kutlu, Ö.; Yağci Acar, H.; Gözüaçik, D.; Koşar, A. Nanoparticle Based Induction Heating at Low Magnitudes of Magnetic Field Strengths for Breast Cancer Therapy. *J. Magn. Magn. Mater.* **2019**, *483*, 169–177.
(170) Hervault, A.; Kim Thanh, N. T. Magnetic Nanoparticle-Based Therapeutic Agents for Thermo-Chemotherapy Treatment of Cancer. *Nanoscale* **2014**, *6* (20), 11553–11573.
(171) Chastellain, M.; Petri, A.; Hofmann, H. Particle Size Investigations of a Multistep Synthesis of PVA Coated Superparamagnetic Nanoparticles. *J. Colloid Interface Sci.* **2004**, *278* (2), 353–360.
(172) Ziolo, R. F.; Giannelis, E. P.; Weinstein, B. A.; O'Horo, M. P.; Ganguly, B. N.; Mehrotra, V.; Russell, M. W.; Huffman, D. R. Matrix-Mediated Synthesis of Nanocrystalline γ-Fe2O3: A New Optically Transparent Magnetic Material. *Science* **1992**, *257* (5067), 219–223.
(173) Güney, G.; Genç, L.; Dikmen, G. Use of Nanocarrier Systems in Cancer Therapy. *J. Mater. Sci. Eng. B* **2011**, No. 5, 577–582.
(174) *Medical Applications of Liposomes - 1st Edition*, 1st ed.; Lasic, D. D., Papahadjopoulos, D., Eds.; Elsevier: Amsterdam, 1998.
(175) Rudramurthy, S. M.; Jatana, M.; Singh, R.; Chakrabarti, A. In Vitro Antifungal Activity of Indian Liposomal Amphotericin B against Clinical Isolates of Emerging Species of Yeast and Moulds, and Its Comparison with Amphotericin B Deoxycholate, Voriconazole, Itraconazole and Fluconazole. *Mycoses* **2013**, *56* (1), 39–46.
(176) Ventola, C. L. The Nanomedicine Revolution. *Pharm. Ther.* **2012**, *37* (9), 512–525.
(177) Simões, S.; Moreira, J. N.; Fonseca, C.; Düzgüneş, N.; Pedroso de Lima, M. C. On the Formulation of pH-Sensitive Liposomes with Long Circulation Times. *Adv. Drug Deliv. Rev.* **2004**, *56* (7), 947–965.
(178) Mozafari, M. R.; Zareie, M. H.; Piskin, E.; Hasirci, V. Formation of Supramolecular Structures by Negatively Charged Liposomes in the Presence of Nucleic Acids and Divalent Cations. *Drug Deliv.* **1998**, *5* (2), 135–141.
(179) Akbarzadeh, A.; Rezaei-Sadabady, R.; Davaran, S.; Joo, S. W.; Zarghami, N.; Hanifehpour, Y.; Samiei, M.; Kouhi, M.; Nejati-Koshki, K. Liposome: Classification, Preparation, and Applications. *Nanoscale Res. Lett.* **2013**, *8* (1), 102.
(180) Kammari, R.; Das, N. G.; Das, S. K. Chapter 6 - Nanoparticulate Systems for Therapeutic and Diagnostic Applications. In *Emerging Nanotechnologies for Diagnostics, Drug Delivery and Medical Devices*; Mitra, A. K., Cholkar, K., Mandal, A., Eds.; Micro and Nano Technologies; Elsevier: Boston, 2017; pp 105–144.
(181) Akbari, J.; Saeedi, M.; Ahmadi, F.; Hashemi, S. M. H.; Babaei, A.; Yaddollahi, S.; Rostamkalaei, S. S.; Asare-Addo, K.; Nokhodchi, A. Solid Lipid Nanoparticles and Nanostructured Lipid Carriers: A Review of the Methods of Manufacture and Routes of Administration. *Pharm. Dev. Technol.* **2022**, *27* (5), 525–544.
(182) Mukherjee, S.; Ray, S.; Thakur, R. S. Solid Lipid Nanoparticles: A Modern Formulation Approach in Drug Delivery System. *Indian J. Pharm. Sci.* **2009**, *71* (4), 349–358.
(183) Chauhan, I.; Yasir, M.; Verma, M.; Singh, A. P. Nanostructured Lipid Carriers: A Groundbreaking Approach for Transdermal Drug Delivery. *Adv. Pharm. Bull.* **2020**, *10* (2), 150.
(184) Bayón-Cordero, L.; Alkorta, I.; Arana, L. Application of Solid Lipid Nanoparticles to Improve the Efficiency of Anticancer Drugs. *Nanomaterials* **2019**, *9* (3).

(185) Jain, A.; Kesharwani, P.; Garg, N. K.; Jain, A.; Jain, S. A.; Jain, A. K.; Nirbhavane, P.; Ghanghoria, R.; Tyagi, R. K.; Katare, O. P. Galactose Engineered Solid Lipid Nanoparticles for Targeted Delivery of Doxorubicin. *Colloids Surf. B Biointerfaces* **2015**, *134*, 47–58.
(186) Ma, L.; Yang, D.; Li, Z.; Zhang, X.; Pu, L. Co-Delivery of Paclitaxel and Tanespimycin in Lipid Nanoparticles Enhanced Anti-Gastric-Tumor Effect in Vitro and in Vivo. *Artif. Cells Nanomedicine Biotechnol.* **2018**, *46* (sup2), 904–911.
(187) Liu, B.; Han, L.; Liu, J.; Han, S.; Chen, Z.; Jiang, L. Co-Delivery of Paclitaxel and TOS-Cisplatin via TAT-Targeted Solid Lipid Nanoparticles with Synergistic Antitumor Activity against Cervical Cancer. *Int. J. Nanomedicine* **2017**, *12*, 955–968.
(188) Ghasemiyeh, P.; Mohammadi-Samani, S. Solid Lipid Nanoparticles and Nanostructured Lipid Carriers as Novel Drug Delivery Systems: Applications, Advantages and Disadvantages. *Res. Pharm. Sci.* **2018**, *13* (4), 288–303.
(189) Mishra, V.; Bansal, K. K.; Verma, A.; Yadav, N.; Thakur, S.; Sudhakar, K.; Rosenholm, J. M. Solid Lipid Nanoparticles: Emerging Colloidal Nano Drug Delivery Systems. *Pharmaceutics* **2018**, *10* (4), 191.
(190) Mendonça, M. C. P.; Radaic, A.; Fossa, F. G.; Cruz-Höfling, M. A.; Jesus, M. B. de. Toxicity of Cationic Solid Lipid Nanoparticles in Rats. *J. Phys. Conf. Ser.* **2019**, *1323*, 012016.
(191) Bartnikowski, M.; Dargaville, T. R.; Ivanovski, S.; Hutmacher, D. W. Degradation Mechanisms of Polycaprolactone in the Context of Chemistry, Geometry and Environment. *Prog. Polym. Sci.* **2019**, *96*, 1–20.
(192) Betancourt, T.; Byrne, J. D.; Sunaryo, N.; Crowder, S. W.; Kadapakkam, M.; Patel, S.; Casciato, S.; Brannon-Peppas, L. PEGylation Strategies for Active Targeting of PLA/PLGA Nanoparticles. *J. Biomed. Mater. Res. A* **2009**, *91A* (1), 263–276.
(193) Essa, S.; Louhichi, F.; Raymond, M.; Hildgen, P. Improved Antifungal Activity of Itraconazole-Loaded PEG/PLA Nanoparticles. *J. Microencapsul.* **2013**, *30* (3), 205–217.
(194) Singhvi, M. S.; Zinjarde, S. S.; Gokhale, D. V. Polylactic Acid: Synthesis and Biomedical Applications. *J. Appl. Microbiol.* **2019**, *127* (6), 1612–1626.
(195) Dalzon, B.; Lebas, C.; Jimenez, G.; Gutjahr, A.; Terrat, C.; Exposito, J.-Y.; Verrier, B.; Lethias, C. Poly(Lactic Acid) Nanoparticles Targeting A5β1 Integrin as Vaccine Delivery Vehicle, a Prospective Study. *PLOS ONE* **2016**, *11* (12), e0167663.
(196) da Luz, C. M.; Boyles, M. S. P.; Falagan-Lotsch, P.; Pereira, M. R.; Tutumi, H. R.; de Oliveira Santos, E.; Martins, N. B.; Himly, M.; Sommer, A.; Foissner, I.; Duschl, A.; Granjeiro, J. M.; Leite, P. E. C. Poly-Lactic Acid Nanoparticles (PLA-NP) Promote Physiological Modifications in Lung Epithelial Cells and Are Internalized by Clathrin-Coated Pits and Lipid Rafts. *J. Nanobiotechnology* **2017**, *15* (1), 11.
(197) Alexis, F. Factors Affecting the Degradation and Drug-Release Mechanism of Poly(Lactic Acid) and Poly[(Lactic Acid)-Co-(Glycolic Acid)]. *Polym. Int.* **2005**, *54* (1), 36–46.
(198) Casalini, T.; Rossi, F.; Castrovinci, A.; Perale, G. A Perspective on Polylactic Acid-Based Polymers Use for Nanoparticles Synthesis and Applications. *Front. Bioeng. Biotechnol.* **2019**, *7*.
(199) Lee, B. K.; Yun, Y.; Park, K. PLA Micro- and Nano-Particles. *Adv. Drug Deliv. Rev.* **2016**, *107*, 176–191.
(200) Varan, C.; Bilensoy, E. Cationic PEGylated Polycaprolactone Nanoparticles Carrying Post-Operation Docetaxel for Glioma Treatment. *Beilstein J. Nanotechnol.* **2017**, *8* (1), 1446–1456.

(201) Guarino, V.; Gentile, G.; Sorrentino, L.; Ambrosio, L. Polycaprolactone: Synthesis, Properties, and Applications. In *Encyclopedia of Polymer Science and Technology*; American Cancer Society, 2017; pp 1–36.
(202) Goldberg, D. A Review of the Biodegradability and Utility of Poly(Caprolactone). *J. Environ. Polym. Degrad.* **1995**, *3* (2), 61–67.
(203) Kumari, A.; Yadav, S. K.; Yadav, S. C. Biodegradable Polymeric Nanoparticles Based Drug Delivery Systems. *Colloids Surf. B Biointerfaces* **2010**, *75* (1), 1–18.
(204) Mclauchlin, A. R.; Thomas, N. L. 13 - Biodegradable Polymer Nanocomposites. In *Advances in Polymer Nanocomposites*; Gao, F., Ed.; Woodhead Publishing, 2012; pp 398–430.
(205) Hines, D. J.; Kaplan, D. L. Poly (Lactic-Co-Glycolic Acid) Controlled Release Systems: Experimental and Modeling Insights. *Crit. Rev. Ther. Drug Carrier Syst.* **2013**, *30* (3), 257–276.
(206) Jain, R. A. The Manufacturing Techniques of Various Drug Loaded Biodegradable Poly(Lactide-Co-Glycolide) (PLGA) Devices. *Biomaterials* **2000**, *21* (23), 2475–2490.
(207) Lü, J.-M.; Wang, X.; Marin-Muller, C.; Wang, H.; Lin, P. H.; Yao, Q.; Chen, C. Current Advances in Research and Clinical Applications of PLGA-Based Nanotechnology. *Expert Rev. Mol. Diagn.* **2009**, *9* (4), 325–341.
(208) NICE. *Leuprorelin acetate*. https://bnf.nice.org.uk/drug/leuprorelin-acetate.html#drugAction (accessed 2020-05-02).
(209) Budhian, A.; Siegel, S. J.; Winey, K. I. Production of Haloperidol-Loaded PLGA Nanoparticles for Extended Controlled Drug Release of Haloperidol. *J. Microencapsul.* **2005**, *22* (7), 773–785.
(210) Danhier, F.; Lecouturier, N.; Vroman, B.; Jérôme, C.; Marchand-Brynaert, J.; Feron, O.; Préat, V. Paclitaxel-Loaded PEGylated PLGA-Based Nanoparticles: In Vitro and in Vivo Evaluation. *J. Controlled Release* **2009**, *133* (1), 11–17.
(211) Makadia, H. K.; Siegel, S. J. Poly Lactic-Co-Glycolic Acid (PLGA) as Biodegradable Controlled Drug Delivery Carrier. *Polymers* **2011**, *3* (3), 1377–1397.
(212) Danhier, F.; Ansorena, E.; Silva, J. M.; Coco, R.; Le Breton, A.; Préat, V. PLGA-Based Nanoparticles: An Overview of Biomedical Applications. *J. Controlled Release* **2012**, *161* (2), 505–522.
(213) Ansary, R. H.; Awang, M. B.; Rahman, M. M. Biodegradable Poly(D,L-Lactic-Co-Glycolic Acid)-Based Micro/Nanoparticles for Sustained Release of Protein Drugs - A Review. *Trop. J. Pharm. Res.* **2014**, *13* (7), 1179–1190.
(214) Qi, F.; Wu, J.; Li, H.; Ma, G. Recent Research and Development of PLGA/PLA Microspheres/Nanoparticles: A Review in Scientific and Industrial Aspects. *Front. Chem. Sci. Eng.* **2019**, *13* (1), 14–27.
(215) Sah, E.; Sah, H. *Recent Trends in Preparation of Poly(lactide-co-glycolide) Nanoparticles by Mixing Polymeric Organic Solution with Antisolvent*. Journal of Nanomaterials.
(216) Nath, S. D.; Son, S.; Sadiasa, A.; Min, Y. K.; Lee, B. T. Preparation and Characterization of PLGA Microspheres by the Electrospraying Method for Delivering Simvastatin for Bone Regeneration. *Int. J. Pharm.* **2013**, *443* (1), 87–94.
(217) Roces, C. B.; Christensen, D.; Perrie, Y. Translating the Fabrication of Protein-Loaded Poly(Lactic-Co-Glycolic Acid) Nanoparticles from Bench to Scale-Independent Production Using Microfluidics. *Drug Deliv. Transl. Res.* **2020**, *10* (3), 582–593.
(218) Barrero, A.; Loscertales, I. G. Micro- and Nanoparticles via Capillary Flows. *Annu. Rev. Fluid Mech.* **2007**, *39* (1), 89–106.

(219) Garg, S. M.; Thomas, A.; Heuck, G.; Armstead, A.; Singh, J.; Leaver, T. J.; Wild, A. W.; Ip, S.; Taylor, R. J.; Ramsay, E. C. *Reproducible Production of Sub-100 Nm PLGA Nanoparticles Using the NanoAssemblr® Microfluidic Platform*; PLGA nanoparticles; Precision NanoSystems Inc.: Vancouver, BC, Canada, 2017. https://www.precisionnanosystems.com/resource-center/application-notes/ (accessed 2020-06-28).
(220) *BNF: British National Formulary - Risperidone*. https://bnf.nice.org.uk/medicinal-forms/risperidone.html (accessed 2020-07-01).
(221) Barichello, J. M.; Morishita, M.; Takayama, K.; Nagai, T. Encapsulation of Hydrophilic and Lipophilic Drugs in PLGA Nanoparticles by the Nanoprecipitation Method. *Drug Dev. Ind. Pharm.* **1999**, *25* (4), 471–476.
(222) Pieper, S.; Langer, K. Doxorubicin-Loaded PLGA Nanoparticles - a Systematic Evaluation of Preparation Techniques and Parameters∗. *Mater. Today Proc.* **2017**, *4*, S188–S192.
(223) Budhian, A.; Siegel, S. J.; Winey, K. I. Controlling the in Vitro Release Profiles for a System of Haloperidol-Loaded PLGA Nanoparticles. *Int. J. Pharm.* **2008**, *346* (1), 151–159.
(224) Ji, Y.; Lesniak, A. K.; Prudic, A.; Paus, R.; Sadowski, G. Drug Release Kinetics and Mechanism from PLGA Formulations. *AIChE J.* **2016**, *62* (11), 4055–4065.
(225) Samkange, T.; D'Souza, S.; Obikeze, K.; Dube, A. Influence of PEGylation on PLGA Nanoparticle Properties, Hydrophobic Drug Release and Interactions with Human Serum Albumin. *J. Pharm. Pharmacol.* **2019**, *71* (10), 1497–1507.
(226) Pourtalebi Jahromi, L.; Ghazali, M.; Ashrafi, H.; Azadi, A. A Comparison of Models for the Analysis of the Kinetics of Drug Release from PLGA-Based Nanoparticles. *Heliyon* **2020**, *6* (2), e03451.
(227) Wang, N.; Wu, X. S. Synthesis, Characterization, Biodegradation, and Drug Delivery Application of Biodegradable Lactic/Glycolic Acid Oligomers: Part II. Biodegradation and Drug Delivery Application. *J. Biomater. Sci. Polym. Ed.* **1997**, *9* (1), 75–87.
(228) Wang, N.; Qiu, J. S.; Wu, X. S. Biodegradation of Lactic-Glycolic Acid Oligomers. In *Tailored Polymeric Materials for Controlled Delivery Systems*; McCulloch, I., Shalaby, S. W., Eds.; ACS Symposium Series; American Chemical Society: Washington, DC, 1998; Vol. 709, pp 242–253.
(229) Agrawal, C. M.; McKinney, J. S.; Lanctot, D.; Athanasiou, K. A. Effects of Fluid Flow on the in Vitro Degradation Kinetics of Biodegradable Scaffolds for Tissue Engineering. *Biomaterials* **2000**, *21* (23), 2443–2452.
(230) Cheng, X.; Tian, X.; Wu, A.; Li, J.; Tian, J.; Chong, Y.; Chai, Z.; Zhao, Y.; Chen, C.; Ge, C. Protein Corona Influences Cellular Uptake of Gold Nanoparticles by Phagocytic and Nonphagocytic Cells in a Size-Dependent Manner. *ACS Appl. Mater. Interfaces* **2015**, *7* (37), 20568–20575.
(231) Behzadi, S.; Serpooshan, V.; Sakhtianchi, R.; Müller, B.; Landfester, K.; Crespy, D.; Mahmoudi, M. Protein Corona Change the Drug Release Profile of Nanocarriers: The "Overlooked" Factor at the Nanobio Interface. *Colloids Surf. B Biointerfaces* **2014**, *123*, 143–149.
(232) Tenzer, S.; Docter, D.; Kuharev, J.; Musyanovych, A.; Fetz, V.; Hecht, R.; Schlenk, F.; Fischer, D.; Kiouptsi, K.; Reinhardt, C.; Landfester, K.; Schild, H.; Maskos, M.; Knauer, S. K.; Stauber, R. H. Rapid Formation of Plasma Protein Corona Critically Affects Nanoparticle Pathophysiology. *Nat. Nanotechnol.* **2013**, *8* (10), 772–781.
(233) Docter, D.; Westmeier, D.; Markiewicz, M.; Stolte, S.; Knauer, S. K.; Stauber, R. H. The Nanoparticle Biomolecule Corona: Lessons Learned – Challenge Accepted? *Chem. Soc. Rev.* **2015**, *44* (17), 6094–6121.

(234) Lundqvist, M.; Stigler, J.; Cedervall, T.; Berggård, T.; Flanagan, M. B.; Lynch, I.; Elia, G.; Dawson, K. The Evolution of the Protein Corona around Nanoparticles: A Test Study. *ACS Nano* **2011**, *5* (9), 7503–7509.
(235) Vilanova, O.; Mittag, J. J.; Kelly, P. M.; Milani, S.; Dawson, K. A.; Rädler, J. O.; Franzese, G. Understanding the Kinetics of Protein–Nanoparticle Corona Formation. *ACS Nano* **2016**, *10* (12), 10842–10850.
(236) Luby, A. O.; Breitner, E. K.; Comfort, K. K. Preliminary Protein Corona Formation Stabilizes Gold Nanoparticles and Improves Deposition Efficiency. *Appl. Nanosci.* **2016**, *6* (6), 827–836.
(237) Bertrand, N.; Grenier, P.; Mahmoudi, M.; Lima, E. M.; Appel, E. A.; Dormont, F.; Lim, J.-M.; Karnik, R.; Langer, R.; Farokhzad, O. C. Mechanistic Understanding of in Vivo Protein Corona Formation on Polymeric Nanoparticles and Impact on Pharmacokinetics. *Nat. Commun.* **2017**, *8* (1), 777.
(238) Kokkinopoulou, M.; Simon, J.; Landfester, K.; Mailänder, V.; Lieberwirth, I. Visualization of the Protein Corona: Towards a Biomolecular Understanding of Nanoparticle-Cell-Interactions. *Nanoscale* **2017**, *9* (25), 8858–8870.
(239) Kharazian, B.; Hadipour, N. L.; Ejtehadi, M. R. Understanding the Nanoparticle–Protein Corona Complexes Using Computational and Experimental Methods. *Int. J. Biochem. Cell Biol.* **2016**, *75*, 162–174.
(240) Sahneh, F. D.; Scoglio, C.; Riviere, J. Dynamics of Nanoparticle-Protein Corona Complex Formation: Analytical Results from Population Balance Equations. *PLOS ONE* **2013**, *8* (5), e64690.
(241) Di Felice, R.; Corni, S. Simulation of Peptide–Surface Recognition. *J. Phys. Chem. Lett.* **2011**, *2* (13), 1510–1519.
(242) Dell'Orco, D.; Lundqvist, M.; Oslakovic, C.; Cedervall, T.; Linse, S. Modeling the Time Evolution of the Nanoparticle-Protein Corona in a Body Fluid. *PLOS ONE* **2010**, *5* (6), e10949.
(243) Skakauskas, V.; Katauskis, P. Modeling of a Single Nanoparticle Interaction with the Human Blood Plasma Proteins. *J. Biol. Phys.* **2018**, *44* (4), 605–617.
(244) Vilaseca, P.; Dawson, K. A.; Franzese, G. Understanding and Modulating the Competitive Surface-Adsorption of Proteins through Coarse-Grained Molecular Dynamics Simulations. *Soft Matter* **2013**, *9* (29), 6978–6985.
(245) Lazarovits, J.; Sindhwani, S.; Tavares, A. J.; Zhang, Y.; Song, F.; Audet, J.; Krieger, J. R.; Syed, A. M.; Stordy, B.; Chan, W. C. W. Supervised Learning and Mass Spectrometry Predicts the in Vivo Fate of Nanomaterials. *ACS Nano* **2019**, *13* (7), 8023–8034.
(246) Maojo, V.; Fritts, M.; Iglesia, D. de la; Cachau, R. E.; Garcia-Remesal, M.; Mitchell, J. A.; Kulikowski, C. Nanoinformatics: A New Area of Research in Nanomedicine. *Int. J. Nanomedicine* **2012**, *7*, 3867–3890.
(247) Brown, K. A.; Brittman, S.; Maccaferri, N.; Jariwala, D.; Celano, U. Machine Learning in Nanoscience: Big Data at Small Scales. *Nano Lett.* **2020**, *20* (1), 2–10.
(248) Lavanya, B.; Sasipriya, G. Study on Emerging Machine Learning Trends on Nanoparticles—Nanoinformatics. In *International Conference on Innovative Computing and Communications*; Khanna, A., Gupta, D., Bhattacharyya, S., Hassanien, A. E., Anand, S., Jaiswal, A., Eds.; Advances in Intelligent Systems and Computing; Springer: Singapore, 2022; pp 443–458.
(249) Mahmoudi, M.; Abdelmonem, A. M.; Behzadi, S.; Clement, J. H.; Dutz, S.; Ejtehadi, M. R.; Hartmann, R.; Kantner, K.; Linne, U.; Maffre, P.; Metzler, S.; Moghadam, M. K.; Pfeiffer, C.; Rezaei, M.; Ruiz-Lozano, P.; Serpooshan, V.; Shokrgozar, M. A.; Nienhaus, G. U.; Parak, W. J. Temperature: The "Ignored" Factor at the NanoBio Interface. *ACS Nano* **2013**, *7* (8), 6555–6562.

(250) Partikel, K.; Korte, R.; Mulac, D.; Humpf, H.-U.; Langer, K. Serum Type and Concentration Both Affect the Protein-Corona Composition of PLGA Nanoparticles. *Beilstein J. Nanotechnol.* **2019**, *10* (1), 1002–1015.
(251) Somarathne, R. P.; Amarasekara, D. L.; Kariyawasam, C. S.; Robertson, H. A.; Mayatt, R.; Fitzkee, N. C. Protein Binding Leads to Reduced Stability and Solvated Disorder in the Polystyrene Nanoparticle Corona. bioRxiv July 7, 2023, p 2023.07.06.548033.
(252) Nguyen, V. H.; Lee, B.-J. *Protein corona: a new approach for nanomedicine design*. International Journal of Nanomedicine.
(253) The Influence of Nanostructured Materials on Biointerfacial Interactions. *Adv. Drug Deliv. Rev.* **2012**, *64* (15), 1820–1839.
(254) Patel, P.; Kumar, A. CHAPTER 3:Factors Affecting a Nanoparticle's Protein Corona Formation. In *Nanoparticle–Protein Corona: Biophysics to Biology*; Issues in toxicology; Royal Society of Chemistry: London, UK, 2019; pp 61–79.
(255) Falahati, M.; Attar, F.; Sharifi, M.; Haertlé, T.; Berret, J.-F.; Khan, R. H.; Saboury, A. A. A Health Concern Regarding the Protein Corona, Aggregation and Disaggregation. *Biochim. Biophys. Acta Gen. Subj.* **2019**, *1863* (5), 971–991.
(256) Wang, H.; Ma, R.; Nienhaus, K.; Nienhaus, G. U. Formation of a Monolayer Protein Corona around Polystyrene Nanoparticles and Implications for Nanoparticle Agglomeration. *Small* **2019**, *15* (22), 1900974.
(257) Gebauer, J. S.; Malissek, M.; Simon, S.; Knauer, S. K.; Maskos, M.; Stauber, R. H.; Peukert, W.; Treuel, L. Impact of the Nanoparticle–Protein Corona on Colloidal Stability and Protein Structure. *Langmuir* **2012**, *28* (25), 9673–9679.
(258) Ferreira, L. F.; Picco, A. S.; Galdino, F. E.; Albuquerque, L. J. C.; Berret, J.-F.; Cardoso, M. B. Nanoparticle-Protein Interaction: Demystifying the Correlation between Protein Corona and Aggregation Phenomena. *ACS Appl. Mater. Interfaces* **2022**, *14* (25), 28559–28569.
(259) Lück, M.; Pistel, K. F.; Li, Y. X.; Blunk, T.; Müller, R. H.; Kissel, T. Plasma Protein Adsorption on Biodegradable Microspheres Consisting of Poly(D,L-Lactide-Co-Glycolide), Poly(L-Lactide) or ABA Triblock Copolymers Containing Poly(Oxyethylene). Influence of Production Method and Polymer Composition. *J. Control. Release Off. J. Control. Release Soc.* **1998**, *55* (2–3), 107–120.
(260) Partikel, K.; Korte, R.; Stein, N. C.; Mulac, D.; Herrmann, F. C.; Humpf, H.-U.; Langer, K. Effect of Nanoparticle Size and PEGylation on the Protein Corona of PLGA Nanoparticles. *Eur. J. Pharm. Biopharm.* **2019**, *141*, 70–80.
(261) Hamadani, C. M.; Goetz, M. J.; Mitragotri, S.; Tanner, E. E. L. Protein-Avoidant Ionic Liquid (PAIL)–Coated Nanoparticles to Increase Bloodstream Circulation and Drive Biodistribution. *Sci. Adv.* **2020**, *6* (48), eabd7563.
(262) Kurtz-Chalot, A.; Villiers, C.; Pourchez, J.; Boudard, D.; Martini, M.; Marche, P. N.; Cottier, M.; Forest, V. Impact of Silica Nanoparticle Surface Chemistry on Protein Corona Formation and Consequential Interactions with Biological Cells. *Mater. Sci. Eng. C* **2017**, *75*, 16–24.
(263) Dai, Q.; Bertleff-Zieschang, N.; Braunger, J. A.; Björnmalm, M.; Cortez-Jugo, C.; Caruso, F. Particle Targeting in Complex Biological Media. *Adv. Healthc. Mater.* **2019**, 1700575.
(264) Lundqvist, M.; Stigler, J.; Elia, G.; Lynch, I.; Cedervall, T.; Dawson, K. A. Nanoparticle Size and Surface Properties Determine the Protein Corona with Possible Implications for Biological Impacts. *Proc. Natl. Acad. Sci.* **2008**, *105* (38), 14265–14270.
(265) Gessner, A.; Lieske, A.; Paulke, B. R.; Müller, R. H. Influence of Surface Charge Density on Protein Adsorption on Polymeric Nanoparticles: Analysis

by Two-Dimensional Electrophoresis. *Eur. J. Pharm. Biopharm.* **2002**, *54* (2), 165–170.
(266) Gessner, A.; Waicz, R.; Lieske, A.; Paulke, B.-R.; Mäder, K.; Müller, R. H. Nanoparticles with Decreasing Surface Hydrophobicities: Influence on Plasma Protein Adsorption. *Int. J. Pharm.* **2000**, *196* (2), 245–249.
(267) Petru, J.; Zamostny, P. Analysis of Drug Release from Different Agglomerates Using a Mathmatical Model. *Dissolution Technol.* **2014**, *21* (4), 40–47.
(268) Barrán-Berdón, A. L.; Pozzi, D.; Caracciolo, G.; Capriotti, A. L.; Caruso, G.; Cavaliere, C.; Riccioli, A.; Palchetti, S.; Laganà, A. Time Evolution of Nanoparticle–Protein Corona in Human Plasma: Relevance for Targeted Drug Delivery. *Langmuir* **2013**, *29* (21), 6485–6494.
(269) Hoang, K. N. L.; Wheeler, K. E.; Murphy, C. J. Isolation Methods Influence the Protein Corona Composition on Gold-Coated Iron Oxide Nanoparticles. *Anal. Chem.* **2022**, *94* (11), 4737–4746.
(270) Faserl, K.; Chetwynd, A. J.; Lynch, I.; Thorn, J. A.; Lindner, H. H. Corona Isolation Method Matters: Capillary Electrophoresis Mass Spectrometry Based Comparison of Protein Corona Compositions Following On-Particle versus In-Solution or In-Gel Digestion. *Nanomaterials* **2019**, *9* (6), 898.
(271) Liu, G.; Zhao, Y.; Angeles, A.; Hamuro, L. L.; Arnold, M. E.; Shen, J. X. A Novel and Cost Effective Method of Removing Excess Albumin from Plasma/Serum Samples and Its Impacts on LC-MS/MS Bioanalysis of Therapeutic Proteins. *Anal. Chem.* **2014**, *86* (16), 8336–8343.
(272) Wiig, H.; Tenstad, O.; Iversen, P. O.; Kalluri, R.; Bjerkvig, R. Interstitial Fluid: The Overlooked Component of the Tumor Microenvironment? *Fibrogenesis Tissue Repair* **2010**, *3* (1), 12.
(273) Leeman, M.; Choi, J.; Hansson, S.; Storm, M. U.; Nilsson, L. Proteins and Antibodies in Serum, Plasma, and Whole Blood—Size Characterization Using Asymmetrical Flow Field-Flow Fractionation (AF4). *Anal. Bioanal. Chem.* **2018**, *410* (20), 4867–4873.
(274) Lundqvist, M.; Augustsson, C.; Lilja, M.; Lundkvist, K.; Dahlbäck, B.; Linse, S.; Cedervall, T. The Nanoparticle Protein Corona Formed in Human Blood or Human Blood Fractions. *PLOS ONE* **2017**, *12* (4), e0175871.
(275) Schöttler, S.; Klein, K.; Landfester, K.; Mailänder, V. Protein Source and Choice of Anticoagulant Decisively Affect Nanoparticle Protein Corona and Cellular Uptake. *Nanoscale* **2016**, *8* (10), 5526–5536.
(276) *α₂-Macroglobulin from human plasma M6159*. Sigma-Aldrich. https://www.sigmaaldrich.com/catalog/product/sigma/m6159 (accessed 2020-07-14).
(277) Chiodi, F.; Sidén, Å.; Ösby, E. Isoelectric Focusing of Monoclonal Immunoglobulin G, A and M Followed by Detection with the Avidin-Biotin System. *ELECTROPHORESIS* **1985**, *6* (3), 124–128.
(278) Quagliarini, E.; Di Santo, R.; Pozzi, D.; Caracciolo, G. Protein Corona-Enabled Serological Tests for Early Stage Cancer Detection. *Sens. Int.* **2020**, *1*, 100025.
(279) Laurent, S.; Burtea, C.; Thirifays, C.; Rezaee, F.; Mahmoudi, M. Significance of Cell “Observer” and Protein Source in Nanobiosciences. *J. Colloid Interface Sci.* **2013**, *392*, 431–445.
(280) Whitwell, H.; Mackay, R.-M.; Elgy, C.; Morgan, C.; Griffiths, M.; Clark, H.; Skipp, P.; Madsen, J. Nanoparticles in the Lung and Their Protein Corona: The Few Proteins That Count. *Nanotoxicology* **2016**, *10* (9), 1385–1394.
(281) Monopoli, M. P.; Åberg, C.; Salvati, A.; Dawson, K. A. Biomolecular Coronas Provide the Biological Identity of Nanosized Materials. *Nat. Nanotechnol.* **2012**, *7* (12), 779–786.

(282) Zhang, T.; Dong, C.; Ren, J. Probing the Protein Corona of Nanoparticles in a Fluid Flow by Single-Particle Differenced Resonance Light Scattering Correlation Spectroscopy. *Anal. Chem.* **2023**, *95* (3), 2029–2038.
(283) Docter, D.; Distler, U.; Storck, W.; Kuharev, J.; Wünsch, D.; Hahlbrock, A.; Knauer, S. K.; Tenzer, S.; Stauber, R. H. Quantitative Profiling of the Protein Coronas That Form around Nanoparticles. *Nat. Protoc.* **2014**, *9* (9), 2030–2044.
(284) Digiacomo, L.; Giulimondi, F.; Capriotti, A. L.; Piovesana, S.; Montone, C. M.; Chiozzi, R. Z.; Laganà, A.; Mahmoudi, M.; Pozzi, D.; Caracciolo, G. Optimal Centrifugal Isolating of Liposome–Protein Complexes from Human Plasma. *Nanoscale Adv.* **2021**, *3* (13), 3824–3834.
(285) Münter, R.; Simonsen, J. B. Comment on “Optimal Centrifugal Isolating of Liposome–Protein Complexes from Human Plasma” by L. Digiacomo, F. Giulimondi, A. L. Capriotti, S. Piovesana, C. M. Montone, R. Z. Chiozzi, A. Laganá, M. Mahmoudi, D. Pozzi and G. Caracciolo, Nanoscale Adv., 2021, 3, 3824. *Nanoscale Adv.* **2022**, *5* (1), 290–299.
(286) Berger, S.; Berger, M.; Bantz, C.; Maskos, M.; Wagner, E. Performance of Nanoparticles for Biomedical Applications: The in Vitro/in Vivo Discrepancy. *Biophys. Rev.* **2022**, *3* (1), 011303.
(287) Rahman, M.; Laurent, S.; Tawil, N.; Yahia, L.; Mahmoudi, M. Analytical Methods for Corona Evaluations. In *Protein-Nanoparticle Interactions: The Bio-Nano Interface*; Rahman, M., Laurent, S., Tawil, N., Yahia, L., Mahmoudi, M., Eds.; Springer Series in Biophysics; Springer: Berlin, Heidelberg, 2013; pp 65–82.
(288) Tadjiki, S.; Sharifi, S.; Lavasanifar, A.; Mahmoudi, M. Advancing In Situ Analysis of Biomolecular Corona: Opportunities and Challenges in Utilizing Field-Flow Fractionation. *ACS Bio Med Chem Au* **2024**, *4* (2), 77–85.
(289) Latreille, P.-L.; Rabanel, J.-M.; Le Goas, M.; Salimi, S.; Arlt, J.; Patten, S. A.; Ramassamy, C.; Hildgen, P.; Martinez, V. A.; Banquy, X. In Situ Characterization of the Protein Corona of Nanoparticles In Vitro and In Vivo. *Adv. Mater.* **2022**, *34* (38), 2203354.
(290) Blancher, C.; Jones, A. SDS -PAGE and Western Blotting Techniques. In *Metastasis Research Protocols: Volume I: Analysis of Cells and Tissues*; Brooks, S. A., Schumacher, U., Eds.; Methods in Molecular Medicine; Humana Press: Totowa, NJ, 2001; pp 145–162.
(291) Wong, C.; Sridhara, S.; Bardwell, J. C.; Jakob, U. Heating Greatly Speeds Coomassie Blue Staining and Destaining. *BioTechniques* **2000**, *28* (3), 426–428, 430, 432.
(292) *Chemiluminescent Western Blot Detection - UK*. https://www.thermofisher.com/uk/en/home/life-science/protein-biology/protein-assays-analysis/western-blotting/detect-proteins-western-blot/western-blot-detection-reagents/chemiluminescent-western-blot-detection.html (accessed 2020-07-09).
(293) Mahmood, T.; Yang, P.-C. Western Blot: Technique, Theory, and Trouble Shooting. *North Am. J. Med. Sci.* **2012**, *4* (9), 429–434.
(294) *Liquid Chromatography Tandem Mass Spectrometry | AACC.org*. https://www.aacc.org/publications/cln/articles/2015/july/liquid-chromatography-tandem-mass-spectrometry (accessed 2019-12-09).
(295) Brosch, M.; Yu, L.; Hubbard, T.; Choudhary, J. Accurate and Sensitive Peptide Identification with Mascot Percolator. *J. Proteome Res.* **2009**, *8* (6), 3176–3181.
(296) Ashkarran, A. A.; Gharibi, H.; Voke, E.; Landry, M. P.; Saei, A. A.; Mahmoudi, M. Measurements of Heterogeneity in Proteomics Analysis of the Nanoparticle Protein Corona across Core Facilities. *Nat. Commun.* **2022**, *13* (1), 6610.

(297) Duff, M. R.; Grubbs, J.; Howell, E. E. Isothermal Titration Calorimetry for Measuring Macromolecule-Ligand Affinity. *J. Vis. Exp. JoVE* **2011**, No. 55.
(298) Velazquez-Campoy, A.; Leavitt, S. A.; Freire, E. Characterization of Protein-Protein Interactions by Isothermal Titration Calorimetry. *Methods Mol. Biol. Clifton NJ* **2004**, *261*, 35–54.
(299) Jelesarov, I.; Bosshard, H. R. Isothermal Titration Calorimetry and Differential Scanning Calorimetry as Complementary Tools to Investigate the Energetics of Biomolecular Recognition. *J. Mol. Recognit. JMR* **1999**, *12* (1), 3–18.
(300) Mori, S.; Barth, H. G. *Size Exclusion Chromatography*; Springer Laboratory; Springer-Verlag: Berlin Heidelberg, 1999.
(301) Hamrang, Z.; Rattray, N. J. W.; Pluen, A. Proteins Behaving Badly: Emerging Technologies in Profiling Biopharmaceutical Aggregation. *Trends Biotechnol.* **2013**, *31* (8), 448–458.
(302) Carpenter, J. F.; Randolph, T. W.; Jiskoot, W.; Crommelin, D. J. A.; Middaugh, C. R.; Winter, G. Potential Inaccurate Quantitation and Sizing of Protein Aggregates by Size Exclusion Chromatography: Essential Need to Use Orthogonal Methods to Assure the Quality of Therapeutic Protein Products. *J. Pharm. Sci.* **2010**, *99* (5), 2200–2208.
(303) Hong, P.; Koza, S.; Bouvier, E. S. P. Size-Exclusion Chromatography for the Analysis of Protein Biotherapeutics and Their Aggregates. *J. Liq. Chromatogr. Relat. Technol.* **2012**, *35* (20), 2923–2950.
(304) Stetefeld, J.; McKenna, S. A.; Patel, T. R. Dynamic Light Scattering: A Practical Guide and Applications in Biomedical Sciences. *Biophys. Rev.* **2016**, *8* (4), 409–427.
(305) Schäffler, M.; Semmler-Behnke, M.; Sarioglu, H.; Takenaka, S.; Wenk, A.; Schleh, C.; Hauck, S. M.; Johnston, B. D.; Kreyling, W. G. Serum Protein Identification and Quantification of the Corona of 5, 15 and 80 Nm Gold Nanoparticles. *Nanotechnology* **2013**, *24* (26), 265103.
(306) Fischer, K.; Schmidt, M. Pitfalls and Novel Applications of Particle Sizing by Dynamic Light Scattering. *Biomaterials* **2016**, *98*, 79–91.
(307) Galdino, F. E.; Picco, A. S.; Capeletti, L. B.; Bettini, J.; Cardoso, M. B. Inside the Protein Corona: From Binding Parameters to Unstained Hard and Soft Coronas Visualization. *Nano Lett.* **2021**, *21* (19), 8250–8257.
(308) *Nanoparticle Tracking Analysis NTA | Malvern Panalytical*. https://www.malvernpanalytical.com/en/products/technology/light-scattering/nanoparticle-tracking-analysis (accessed 2020-05-07).
(309) *Archimedes User Manual (English) | Malvern Panalytical*. https://www.malvernpanalytical.com/en/learn/knowledge-center/user-manuals/MAN0580EN (accessed 2020-07-08).
(310) Nejadnik, M. R.; Jiskoot, W. Measurement of the Average Mass of Proteins Adsorbed to a Nanoparticle by Using a Suspended Microchannel Resonator. *J. Pharm. Sci.* **2015**, *104* (2), 698–704.
(311) Gross, J.; Sayle, S.; Karow, A. R.; Bakowsky, U.; Garidel, P. Nanoparticle Tracking Analysis of Particle Size and Concentration Detection in Suspensions of Polymer and Protein Samples: Influence of Experimental and Data Evaluation Parameters. *Eur. J. Pharm. Biopharm.* **2016**, *104*, 30–41.
(312) Luxenhofer, R. Polymers and Nanomedicine: Considerations on Variability and Reproducibility When Combining Complex Systems. *Nanomed.* **2015**, *10* (20), 3109–3119.
(313) Operti, M. C.; Bernhardt, A.; Grimm, S.; Engel, A.; Figdor, C. G.; Tagit, O. PLGA-Based Nanomedicines Manufacturing: Technologies Overview and Challenges in Industrial Scale-Up. *Int. J. Pharm.* **2021**, *605*, 120807.
(314) Hernández-Giottonini, K. Y.; Rodríguez-Córdova, R. J.; Gutiérrez-Valenzuela, C. A.; Peñuñuri-Miranda, O.; Zavala-Rivera, P.; Guerrero-Germán, P.; Lucero-Acuña, A. PLGA Nanoparticle Preparations by Emulsification and

Nanoprecipitation Techniques: Effects of Formulation Parameters. *RSC Adv.* **2020**, *10* (8), 4218–4231.
(315) Wan, B.; Bao, Q.; Burgess, D. Long-Acting PLGA Microspheres: Advances in Excipient and Product Analysis toward Improved Product Understanding. *Adv. Drug Deliv. Rev.* **2023**, *198*, 114857.
(316) Taha, M. S.; Padmakumar, S.; Singh, A.; Amiji, M. M. Critical Quality Attributes in the Development of Therapeutic Nanomedicines toward Clinical Translation. *Drug Deliv. Transl. Res.* **2020**, *10* (3), 766–790.
(317) Holzer, M.; Vogel, V.; Mäntele, W.; Schwartz, D.; Haase, W.; Langer, K. Physico-Chemical Characterisation of PLGA Nanoparticles after Freeze-Drying and Storage. *Eur. J. Pharm. Biopharm.* **2009**, *72* (2), 428–437.
(318) Mosmann, T. Rapid Colorimetric Assay for Cellular Growth and Survival: Application to Proliferation and Cytotoxicity Assays. *J. Immunol. Methods* **1983**, *65* (1), 55–63.
(319) Ostling, O.; Johanson, K. J. Microelectrophoretic Study of Radiation-Induced DNA Damages in Individual Mammalian Cells. *Biochem. Biophys. Res. Commun.* **1984**, *123* (1), 291–298.
(320) Krug, H. F.; Wick, P. Nanotoxicology: An Interdisciplinary Challenge. *Angew. Chem. Int. Ed.* **2011**, *50* (6), 1260–1278.
(321) Azhdarzadeh, M.; Saei, A. A.; Sharifi, S.; Hajipour, M. J.; Alkilany, A. M.; Sharifzadeh, M.; Ramazani, F.; Laurent, S.; Mashaghi, A.; Mahmoudi, M. Nanotoxicology: Advances and Pitfalls in Research Methodology. *Nanomed.* **2015**, *10* (18), 2931–2952.
(322) Ong, K. J.; MacCormack, T. J.; Clark, R. J.; Ede, J. D.; Ortega, V. A.; Felix, L. C.; Dang, M. K. M.; Ma, G.; Fenniri, H.; Veinot, J. G. C.; Goss, G. G. Widespread Nanoparticle-Assay Interference: Implications for Nanotoxicity Testing. *PLOS ONE* **2014**, *9* (3), e90650.
(323) Piret, J.-P.; Bondarenko, O. M.; Boyles, M. S. P.; Himly, M.; Ribeiro, A. R.; Benetti, F.; Smal, C.; Lima, B.; Potthoff, A.; Simion, M.; Dumortier, E.; Leite, P. E. C.; Balottin, L. B.; Granjeiro, J. M.; Ivask, A.; Kahru, A.; Radauer-Preiml, I.; Tischler, U.; Duschl, A.; Saout, C.; Anguissola, S.; Haase, A.; Jacobs, A.; Nelissen, I.; Misra, S. K.; Toussaint, O. Pan-European Inter-Laboratory Studies on a Panel of in Vitro Cytotoxicity and pro-Inflammation Assays for Nanoparticles. *Arch. Toxicol.* **2017**, *91* (6), 2315–2330.
(324) Desai, N. Challenges in Development of Nanoparticle-Based Therapeutics. *AAPS J.* **2012**, *14* (2), 282–295.
(325) Faria, M.; Björnmalm, M.; Thurecht, K. J.; Kent, S. J.; Parton, R. G.; Kavallaris, M.; Johnston, A. P. R.; Gooding, J. J.; Corrie, S. R.; Boyd, B. J.; Thordarson, P.; Whittaker, A. K.; Stevens, M. M.; Prestidge, C. A.; Porter, C. J. H.; Parak, W. J.; Davis, T. P.; Crampin, E. J.; Caruso, F. Minimum Information Reporting in Bio–Nano Experimental Literature. *Nat. Nanotechnol.* **2018**, *13* (9), 777–785.
(326) Chetwynd, A. J.; Wheeler, K. E.; Lynch, I. Best Practice in Reporting Corona Studies: Minimum Information about Nanomaterial Biocorona Experiments (MINBE). *Nano Today* **2019**, *28*, 100758.
(327) Wheeler, K.; Chetwynd, A.; Lynch, I. MINBE. **2019**.
(328) Montoro Bustos, A. R.; Petersen, E. J.; Possolo, A.; Winchester, M. R. Post Hoc Interlaboratory Comparison of Single Particle ICP-MS Size Measurements of NIST Gold Nanoparticle Reference Materials. *Anal. Chem.* **2015**, *87* (17), 8809–8817.
(329) *ISO 19430:2016(en), Particle size analysis — Particle tracking analysis (PTA) method*. https://www.iso.org/obp/ui#iso:std:iso:19430:ed-1:v1:en:fn:2 (accessed 2023-03-07).
(330) Hackley, V.; Clogston, J. NIST - NCL Joint Assay Protocol, PCC-1, 2020.

(331) *ISO/TR 22814:2020(en), Good practice for dynamic light scattering (DLS) measurements*. https://www.iso.org/obp/ui#iso:std:iso:tr:22814:ed-1:v1:en (accessed 2023-03-07).
(332) Hole, P.; Sillence, K.; Hannell, C.; Maguire, C. M.; Roesslein, M.; Suarez, G.; Capracotta, S.; Magdolenova, Z.; Horev-Azaria, L.; Dybowska, A.; Cooke, L.; Haase, A.; Contal, S.; Manø, S.; Vennemann, A.; Sauvain, J.-J.; Staunton, K. C.; Anguissola, S.; Luch, A.; Dusinska, M.; Korenstein, R.; Gutleb, A. C.; Wiemann, M.; Prina-Mello, A.; Riediker, M.; Wick, P. Interlaboratory Comparison of Size Measurements on Nanoparticles Using Nanoparticle Tracking Analysis (NTA). *J. Nanoparticle Res.* **2013**, *15* (12).
(333) Krueger, A. B.; Hadley, J.; Cheney, P. P.; Markova, N.; Carpenter, J. F.; Fradkin, A. H. Application of a Best Practice Approach Using Resonant Mass Measurement for Biotherapeutic Product Characterization. *J. Pharm. Sci.* **2019**, *108* (5), 1675–1685.
(334) Benkstein, K. D.; Balakrishnan, G.; Bhirde, A.; Chalus, P.; Das, T. K.; Do, N.; Duewer, D. L.; Filonov, N.; Cheong, F. C.; Garidel, P.; Gill, N. S.; Grabarek, A. D.; Grier, D. G.; Hadley, J.; Hollingsworth, A. D.; Howard, W. W.; Jarzębski, M.; Jiskoot, W.; Kar, S. R.; Kestens, V.; Khasa, H.; Kim, Y. J.; Koulov, A.; Matter, A.; Philips, L. A.; Probst, C.; Ramaye, Y.; Randolph, T. W.; Ripple, D. C.; Romeijn, S.; Saggu, M.; Schleinzer, F.; Snell, J. R.; Tatarkiewicz, J. "Kuba"; Wright, H. A.; Yang, D. T. An Interlaboratory Comparison on the Characterization of a Sub-Micrometer Polydisperse Particle Dispersion. *J. Pharm. Sci.* **2022**, *111* (3), 699–709.
(335) Solorio-Rodríguez, A.; Escamilla-Rivera, V.; Uribe-Ramírez, M.; Chagolla, A.; Winkler, R.; García-Cuellar, C. M.; Vizcaya-Ruiz, A. D. A Comparison of the Human and Mouse Protein Corona Profiles of Functionalized SiO2 Nanocarriers. *Nanoscale* **2017**, *9* (36), 13651–13660.
(336) Pandey, K. B.; Mishra, N.; Rizvi, S. I. Protein Oxidation Biomarkers in Plasma of Type 2 Diabetic Patients. *Clin. Biochem.* **2010**, *43* (4–5), 508–511.
(337) Kelly-Spratt, K. S.; Pitteri, S. J.; Gurley, K. E.; Liggitt, D.; Chin, A.; Kennedy, J.; Wong, C.-H.; Zhang, Q.; Buson, T. B.; Wang, H.; Hanash, S. M.; Kemp, C. J. Plasma Proteome Profiles Associated with Inflammation, Angiogenesis, and Cancer. *PLoS ONE* **2011**, *6* (5), e19721.
(338) Chu, N.-F.; Chang, J.-B.; Shieh, S.-M. Plasma C-Reactive Protein Concentrations in Relation to 5-Year Body Weight Change among Children: The Taipei Children Heart Study. *Int. J. Obes.* **2003**, *27* (6), 735–739.
(339) Digiacomo, L.; Caputo, D.; Coppola, R.; Cascone, C.; Giulimondi, F.; Palchetti, S.; Pozzi, D.; Caracciolo, G. Efficient Pancreatic Cancer Detection through Personalized Protein Corona of Gold Nanoparticles. *Biointerphases* **2021**, *16* (1), 011010.
(340) Kozlov, M. FDA to Require Diversity Plan for Clinical Trials. *Nature* **2023**.
(341) Liu, K.; Salvati, A.; Sabirsh, A. Physiology, Pathology and the Biomolecular Corona: The Confounding Factors in Nanomedicine Design. *Nanoscale* **2022**, *14* (6), 2136–2154.
(342) Thummel, K. E.; Lin, Y. S. Sources of Interindividual Variability. *Methods Mol. Biol. Clifton NJ* **2014**, *1113*, 363–415.
(343) Bloemen, S.; Huskens, D.; Konings, J.; Kremers, R. M.; Miszta, A.; Laat, B. de; Kelchtermans, H. Interindividual Variability and Normal Ranges of Whole Blood and Plasma Thrombin Generation. *J. Appl. Lab. Med.* **2017**, *2* (2), 150–164.
(344) Nicolas, J.-M.; Espie, P.; Molimard, M. Gender and Interindividual Variability in Pharmacokinetics. *Drug Metab. Rev.* **2009**, *41* (3), 408–421.
(345) Li, Y.; Oosting, M.; Deelen, P.; Ricaño-Ponce, I.; Smeekens, S.; Jaeger, M.; Matzaraki, V.; Swertz, M. A.; Xavier, R. J.; Franke, L.; Wijmenga, C.; Joosten, L. A. B.; Kumar, V.; Netea, M. G. Inter-Individual Variability and Genetic

Influences on Cytokine Responses to Bacteria and Fungi. *Nat. Med.* **2016**, *22* (8), 952–960.
(346) Chiba, K.; Shimizu, K.; Kato, M.; Miyazaki, T.; Nishibayashi, T.; Terada, K.; Sugiyama, Y. Estimation of Interindividual Variability of Pharmacokinetics of CYP2C9 Substrates in Humans. *J. Pharm. Sci.* **2017**, *106* (9), 2695–2703.
(347) Tracy, T. S.; Chaudhry, A. S.; Prasad, B.; Thummel, K. E.; Schuetz, E. G.; Zhong, X.; Tien, Y.-C.; Jeong, H.; Pan, X.; Shireman, L. M.; Tay-Sontheimer, J.; Lin, Y. S. Interindividual Variability in Cytochrome P450–Mediated Drug Metabolism. *Drug Metab. Dispos.* **2016**, *44* (3), 343–351.
(348) Goh, B.-C.; Lee, S.-C.; Wang, L.-Z.; Fan, L.; Guo, J.-Y.; Lamba, J.; Schuetz, E.; Lim, R.; Lim, H.-L.; Ong, A.-B.; Lee, H.-S. Explaining Interindividual Variability of Docetaxel Pharmacokinetics and Pharmacodynamics in Asians Through Phenotyping and Genotyping Strategies. *J. Clin. Oncol.* **2002**, *20* (17), 3683–3690.
(349) Brodin, P.; Davis, M. M. Human Immune System Variation. *Nat. Rev. Immunol.* **2017**, *17* (1), 21–29.
(350) Cortez-Jugo, C.; Czuba-Wojnilowicz, E.; Tan, A.; Caruso, F. A Focus on “Bio” in Bio–Nanoscience: The Impact of Biological Factors on Nanomaterial Interactions. *Adv. Healthc. Mater.* **2021**, *10* (16), 2100574.
(351) Mahmoudi, M.; Saeedi-Eslami, S. N.; Shokrgozar, M. A.; Azadmanesh, K.; Hassanlou, M.; Kalhor, H. R.; Burtea, C.; Rothen-Rutishauser, B.; Laurent, S.; Sheibani, S.; Vali, H. Cell “Vision”: Complementary Factor of Protein Corona in Nanotoxicology. *Nanoscale* **2012**, *4* (17), 5461–5468.
(352) *Exploring the Biological Contributions to Human Health: Does Sex Matter?*; National Academies Press: Washington, D.C., 2001; p 10028.
(353) Miller, L. R.; Marks, C.; Becker, J. B.; Hurn, P. D.; Chen, W.; Woodruff, T.; McCarthy, M. M.; Sohrabji, F.; Schiebinger, L.; Wetherington, C. L.; Makris, S.; Arnold, A. P.; Einstein, G.; Miller, V. M.; Sandberg, K.; Maier, S.; Cornelison, T. L.; Clayton, J. A. Considering Sex as a Biological Variable in Preclinical Research. *FASEB J.* **2017**, *31* (1), 29–34.
(354) Clayton, J. A.; Collins, F. S. Policy: NIH to Balance Sex in Cell and Animal Studies. *Nature* **2014**, *509* (7500), 282–283.
(355) O’Grady, C. Sex and Gender Missing in COVID-19 Data. *Science* **2021**.
(356) *Use of both sexes to be default in laboratory experimental design*. https://www.ukri.org/news/use-of-both-sexes-to-be-default-in-laboratory-experimental-design/ (accessed 2023-03-06).
(357) *NOT-OD-15-102: Consideration of Sex as a Biological Variable in NIH-funded Research*. https://grants.nih.gov/grants/guide/notice-files/not-od-15-102.html (accessed 2023-03-06).
(358) Chen, J.; Jie Chen; Wang, H.; Wang, H.; Long, W.; Shen, X.; Wu, D.; Wu, D.; Song, S.-S.; Sun, Y.-M.; Liu, P.-X.; Fan, S.; Fan, S.; Fan, F.; Zhang, X. Sex Differences in the Toxicity of Polyethylene Glycol-Coated Gold Nanoparticles in Mice. *Int. J. Nanomedicine* **2013**, *8* (1), 2409–2419.
(359) You, D. J.; Lee, H. Y.; Taylor-Just, A. J.; Linder, K. E.; Bonner, J. C. Sex Differences in the Acute and Subchronic Lung Inflammatory Responses of Mice to Nickel Nanoparticles. *Nanotoxicology* **2020**, *14* (8), 1058–1081.
(360) Lovaković, B. T.; Barbir, R.; Pem, B.; Goessler, W.; Ćurlin, M.; Micek, V.; Debeljak, Ž.; Lucija Božičević; Božičević, L.; Ilić, K.; Pavičić, I.; Gorup, D.; Vrček, I. V. Sex-Related Response in Mice after Sub-Acute Intraperitoneal Exposure to Silver Nanoparticles. *NanoImpact* **2021**, *23*, 100340.
(361) Mahdieh, Z.; Britten Postma; Lou A. Herritt; Hamilton, R. F.; Jack R. Harkema; Holian, A. Hyperspectral Microscopy of Subcutaneously Released Silver Nanoparticles Reveals Sex Differences in Drug Distribution. *Micron* **2021**, 103193–103193.

(362) Tarudji, A. W.; Miller, H. A.; Curtis, E. T.; Porter, C. L.; Madsen, G. L.; Kievit, F. M. Sex-Based Differences of Antioxidant Enzyme Nanoparticle Effects Following Traumatic Brain Injury. *J. Controlled Release* **2023**, *355*, 149–159.
(363) Lin, Z.; Jiwani, Z.; Serpooshan, V.; Aghaverdi, H.; Yang, Phillip. C.; Aguirre, A.; Wu, Joseph. C.; Mahmoudi, M. Sex Influences the Safety and Therapeutic Efficacy of Cardiac Nanomedicine Technologies. *Small n/a* (n/a), 2305940.
(364) Hajipour, M. J.; Aghaverdi, H.; Serpooshan, V.; Vali, H.; Sheibani, S.; Mahmoudi, M. Sex as an Important Factor in Nanomedicine. *Nat. Commun.* **2021**, *12* (1), 2984.
(365) Campisi, J. The Biology of Replicative Senescence. *Eur. J. Cancer Oxf. Engl. 1990* **1997**, *33* (5), 703–709.
(366) Hayflick, L. The Cell Biology of Aging. *Clin. Geriatr. Med.* **1985**, *1* (1), 15–27.
(367) Hughes, P.; Marshall, D.; Reid, Y.; Parkes, H.; Gelber, C. The Costs of Using Unauthenticated, over-Passaged Cell Lines: How Much More Data Do We Need? *BioTechniques* **2007**, *43* (5), 575–586.
(368) Panet, E.; Mashriki, T.; Lahmi, R.; Jacob, A.; Ozer, E.; Vecsler, M.; Lazar, I.; Tzur, A. The Interface of Nanoparticles with Proliferating Mammalian Cells. *Nat. Nanotechnol.* **2017**, *12* (7), 598–600.
(369) Kim, J. A.; Åberg, C.; Salvati, A.; Dawson, K. A. Role of Cell Cycle on the Cellular Uptake and Dilution of Nanoparticles in a Cell Population. *Nat. Nanotechnol.* **2012**, *7* (1), 62–68.
(370) Åberg, C.; Kim, J. A.; Salvati, A.; Dawson, K. A. Reply to “The Interface of Nanoparticles with Proliferating Mammalian Cells.” *Nat. Nanotechnol.* **2017**, *12* (7), 600–603.
(371) Rees, P.; Wills, J. W.; Brown, M. R.; Barnes, C. M.; Summers, H. D. The Origin of Heterogeneous Nanoparticle Uptake by Cells. *Nat. Commun.* **2019**, *10* (1), 2341.
(372) Mahmoudi, M.; Azadmanesh, K.; Shokrgozar, M. A.; Journeay, W. S.; Laurent, S. Effect of Nanoparticles on the Cell Life Cycle. *Chem. Rev.* **2011**, *111* (5), 3407–3432.
(373) Bjornson-Hooper, Z. B.; Fragiadakis, G. K.; Spitzer, M. H.; Chen, H.; Madhireddy, D.; Hu, K.; Lundsten, K.; McIlwain, D. R.; Nolan, G. P. A Comprehensive Atlas of Immunological Differences Between Humans, Mice, and Non-Human Primates. *Front. Immunol.* **2022**, *13*.
(374) Prior, H.; Baldrick, P.; Beken, S.; Booler, H.; Bower, N.; Brooker, P.; Brown, P.; Burlinson, B.; Burns-Naas, L. A.; Casey, W.; Chapman, M.; Clarke, D.; de Haan, L.; Doehr, O.; Downes, N.; Flaherty, M.; Gellatly, N.; Moesgaard, S. G.; Harris, J.; Holbrook, M.; Hui, J.; Jones, D.; Jones, K.; Kedar, H.; Mahl, A.; Manninen, A.; McGuire, A.; Mortimer-Cassen, E.; Peraza, M.; Pugsley, M. K.; Richard, J.; Roberts, R.; Roosen, W.; Rothfuss, A.; Schoenmakers, A.; Sewell, F.; Weaver, R.; Weir, L.; Wolfreys, A.; Kimber, I. Opportunities for Use of One Species for Longer-Term Toxicology Testing during Drug Development: A Cross-Industry Evaluation. *Regul. Toxicol. Pharmacol.* **2020**, *113*, 104624.
(375) Participation, E. *Animals (Scientific Procedures) Act 1986*. https://www.legislation.gov.uk/ukpga/1986/14/section/1 (accessed 2023-03-20).
(376) Streisinger, G.; Walker, C.; Dower, N.; Knauber, D.; Singer, F. Production of Clones of Homozygous Diploid Zebra Fish (Brachydanio Rerio). *Nature* **1981**, *291* (5813), 293–296.
(377) van der Vaart, M.; Spaink, H. P.; Meijer, A. H. *Pathogen Recognition and Activation of the Innate Immune Response in Zebrafish*. Advances in Hematology.

(378) Saleem, S.; Kannan, R. R. Zebrafish: An Emerging Real-Time Model System to Study Alzheimer's Disease and Neurospecific Drug Discovery. *Cell Death Discov.* **2018**, *4* (1), 1–13.
(379) Yan, C.; Brunson, D. C.; Tang, Q.; Do, D.; Iftimia, N. A.; Moore, J. C.; Hayes, M. N.; Welker, A. M.; Garcia, E. G.; Dubash, T. D.; Hong, X.; Drapkin, B. J.; Myers, D. T.; Phat, S.; Volorio, A.; Marvin, D. L.; Ligorio, M.; Dershowitz, L.; McCarthy, K. M.; Karabacak, M. N.; Fletcher, J. A.; Sgroi, D. C.; Iafrate, J. A.; Maheswaran, S.; Dyson, N. J.; Haber, D. A.; Rawls, J. F.; Langenau, D. M. Visualizing Engrafted Human Cancer and Therapy Responses in Immunodeficient Zebrafish. *Cell* **2019**, *177* (7), 1903-1914.e14.
(380) Stockhammer, O. W.; Zakrzewska, A.; Hegedûs, Z.; Spaink, H. P.; Meijer, A. H. Transcriptome Profiling and Functional Analyses of the Zebrafish Embryonic Innate Immune Response to Salmonella Infection. *J. Immunol.* **2009**, *182* (9), 5641–5653.
(381) Novoa, B.; Figueras, A. Zebrafish: Model for the Study of Inflammation and the Innate Immune Response to Infectious Diseases. *Adv. Exp. Med. Biol.* **2012**, *946*, 253–275.
(382) Liu, S.; Leach, S. D. Zebrafish Models for Cancer. *Annu. Rev. Pathol. Mech. Dis.* **2011**, *6* (1), 71–93.
(383) Ceol, C. J.; Houvras, Y.; Jane-Valbuena, J.; Bilodeau, S.; Orlando, D. A.; Battisti, V.; Fritsch, L.; Lin, W. M.; Hollmann, T. J.; Ferré, F.; Bourque, C.; Burke, C. J.; Turner, L.; Uong, A.; Johnson, L. A.; Beroukhim, R.; Mermel, C. H.; Loda, M.; Ait-Si-Ali, S.; Garraway, L. A.; Young, R. A.; Zon, L. I. The Histone Methyltransferase SETDB1 Is Recurrently Amplified in Melanoma and Accelerates Its Onset. *Nature* **2011**, *471* (7339), 513–517.
(384) Mestas, J.; Hughes, C. C. W. Of Mice and Not Men: Differences between Mouse and Human Immunology. *J. Immunol.* **2004**, *172* (5), 2731–2738.
(385) Zschaler, J.; Schlorke, D.; Arnhold, J. Differences in Innate Immune Response between Man and Mouse. *Crit. Rev. Immunol.* **2014**, *34* (5), 433–454.
(386) Wagar, L. E.; DiFazio, R. M.; Davis, M. M. Advanced Model Systems and Tools for Basic and Translational Human Immunology. *Genome Med.* **2018**, *10* (1), 73.
(387) Sellers, R. S. Translating Mouse Models: Immune Variation and Efficacy Testing. *Toxicol. Pathol.* **2017**, *45* (1), 134–145.
(388) Fujiwara, S. Humanized Mice: A Brief Overview on Their Diverse Applications in Biomedical Research. *J. Cell. Physiol.* **2018**, *233* (4), 2889–2901.
(389) Bosma, G. C.; Custer, R. P.; Bosma, M. J. A Severe Combined Immunodeficiency Mutation in the Mouse. *Nature* **1983**, *301* (5900), 527–530.
(390) McCune, J. M.; Namikawa, R.; Kaneshima, H.; Shultz, L. D.; Lieberman, M.; Weissman, I. L. The SCID-Hu Mouse: Murine Model for the Analysis of Human Hematolymphoid Differentiation and Function. *Science* **1988**, *241* (4873), 1632–1639.
(391) Allen, T. M.; Brehm, M. A.; Bridges, S.; Ferguson, S.; Kumar, P.; Mirochnitchenko, O.; Palucka, K.; Pelanda, R.; Sanders-Beer, B.; Shultz, L. D.; Su, L.; PrabhuDas, M. Humanized Immune System Mouse Models: Progress, Challenges and Opportunities. *Nat. Immunol.* **2019**, *20* (7), 770–774.
(392) Tian, H.; Lyu, Y.; Yang, Y.-G.; Hu, Z. Humanized Rodent Models for Cancer Research. *Front. Oncol.* **2020**, *10*.
(393) Kopetz, S.; Lemos, R.; Powis, G. The Promise of Patient-Derived Xenografts: The Best Laid Plans of Mice and Men. *Clin. Cancer Res.* **2012**, *18* (19), 5160–5162.
(394) Julien, S.; Merino-Trigo, A.; Lacroix, L.; Pocard, M.; Goéré, D.; Mariani, P.; Landron, S.; Bigot, L.; Nemati, F.; Dartigues, P.; Weiswald, L.-B.; Lantuas, D.;

Morgand, L.; Pham, E.; Gonin, P.; Dangles-Marie, V.; Job, B.; Dessen, P.; Bruno, A.; Pierré, A.; De Thé, H.; Soliman, H.; Nunes, M.; Lardier, G.; Calvet, L.; Demers, B.; Prévost, G.; Vrignaud, P.; Roman-Roman, S.; Duchamp, O.; Berthet, C. Characterization of a Large Panel of Patient-Derived Tumor Xenografts Representing the Clinical Heterogeneity of Human Colorectal Cancer. *Clin. Cancer Res.* **2012**, *18* (19), 5314–5328.

(395) Weroha, S. J.; Becker, M. A.; Enderica-Gonzalez, S.; Harrington, S. C.; Oberg, A. L.; Maurer, M. J.; Perkins, S. E.; AlHilli, M.; Butler, K. A.; McKinstry, S.; Fink, S.; Jenkins, R. B.; Hou, X.; Kalli, K. R.; Goodman, K. M.; Sarkaria, J. N.; Karlan, B. Y.; Kumar, A.; Kaufmann, S. H.; Hartmann, L. C.; Haluska, P. Tumorgrafts as In Vivo Surrogates for Women with Ovarian Cancer. *Clin. Cancer Res.* **2014**, *20* (5), 1288–1297.

(396) Jackson, S. J.; Thomas, G. J. Human Tissue Models in Cancer Research: Looking beyond the Mouse. *Dis. Model. Mech.* **2017**, *10* (8), 939–942.

(397) Zhao, X.; Liu, Z.; Yu, L.; Zhang, Y.; Baxter, P.; Voicu, H.; Gurusiddappa, S.; Luan, J.; Su, J. M.; Leung, H. E.; Li, X.-N. Global Gene Expression Profiling Confirms the Molecular Fidelity of Primary Tumor-Based Orthotopic Xenograft Mouse Models of Medulloblastoma. *Neuro-Oncol.* **2012**, *14* (5), 574–583.

(398) Sasamura, T.; Nakamura, S.; Iida, Y.; Fujii, H.; Murata, J.; Saiki, I.; Nojima, H.; Kuraishi, Y. Morphine Analgesia Suppresses Tumor Growth and Metastasis in a Mouse Model of Cancer Pain Produced by Orthotopic Tumor Inoculation. *Eur. J. Pharmacol.* **2002**, *441* (3), 185–191.

(399) Murphy, W. J. Of Mice and Men. *Biol. Blood Marrow Transplant. J. Am. Soc. Blood Marrow Transplant.* **2013**, *19* (8), 1140–1141.

(400) Bouchlaka, M. N.; Murphy, W. J. Impact of Aging in Cancer Immunotherapy: The Importance of Using Accurate Preclinical Models. *Oncoimmunology* **2013**, *2* (12), e27186.

(401) Academy of Medical Sciences. *The Use of Non-Human Primates in Research*; Academy of Medical Sciences: London, 2006. https://acmedsci.ac.uk/file-download/34785-nhpdownl.pdf (accessed 2019-12-13).

(402) Phillips, K. A.; Bales, K. L.; Capitanio, J. P.; Conley, A.; Czoty, P. W.; 't Hart, B. A.; Hopkins, W. D.; Hu, S.-L.; Miller, L. A.; Nader, M. A.; Nathanielsz, P. W.; Rogers, J.; Shively, C. A.; Voytko, M. L. Why Primate Models Matter. *Am. J. Primatol.* **2014**, *76* (9), 801–827.

(403) The Nuremberg Code (1947). *BMJ* **1996**, *313* (7070), 1448.

(404) *Directive 2010/63/EU of the European Parliament and of the Council of 22 September 2010 on the Protection of Animals Used for Scientific Purposes Text with EEA Relevance*; 2010; Vol. 276. http://data.europa.eu/eli/dir/2010/63/oj/eng (accessed 2023-03-20).

(405) Messaoudi, I.; Estep, R.; Robinson, B.; Wong, S. W. Nonhuman Primate Models of Human Immunology. *Antioxid. Redox Signal.* **2011**, *14* (2), 261–273.

(406) Estes, J. D.; Wong, S. W.; Brenchley, J. M. Nonhuman Primate Models of Human Viral Infections. *Nat. Rev. Immunol.* **2018**, *18* (6), 390–404.

(407) Barreiro, L. B.; Marioni, J. C.; Blekhman, R.; Stephens, M.; Gilad, Y. Functional Comparison of Innate Immune Signaling Pathways in Primates. *PLOS Genet.* **2010**, *6* (12), e1001249.

(408) Knapp, L. A.; Torosin, N. S. The Primate Immune System. In *A Companion to Anthropological Genetics*; John Wiley & Sons, Ltd, 2019; pp 309–326.

(409) Shen, S.; Pyo, C.-W.; Vu, Q.; Wang, R.; Geraghty, D. E. The Essential Detail: The Genetics and Genomics of the Primate Immune Response. *ILAR J.* **2013**, *54* (2), 181–195.

(410) Puente, X. S.; Velasco, G.; Gutiérrez-Fernández, A.; Bertranpetit, J.; King, M.-C.; López-Otín, C. Comparative Analysis of Cancer Genes in the Human and Chimpanzee Genomes. *BMC Genomics* **2006**, *7* (1), 15.
(411) Brown, S. L.; Anderson, D. C.; Dick, E. J.; Guardado-Mendoza, R.; Garcia, A. P.; Hubbard, G. B. Neoplasia in the Chimpanzee (Pan Spp.). *J. Med. Primatol.* **2009**, *38* (2), 137–144.
(412) Park, J. S.; Withers, S. S.; Modiano, J. F.; Kent, M. S.; Chen, M.; Luna, J. I.; Culp, W. T. N.; Sparger, E. E.; Rebhun, R. B.; Monjazeb, A. M.; Murphy, W. J.; Canter, R. J. Canine Cancer Immunotherapy Studies: Linking Mouse and Human. *J. Immunother. Cancer* **2016**, *4* (1), 97.
(413) Moreno, L.; Pearson, A. D. How Can Attrition Rates Be Reduced in Cancer Drug Discovery? *Expert Opin. Drug Discov.* **2013**, *8* (4), 363–368.
(414) Chaikin, P. The Bial 10-2474 Phase 1 Study-A Drug Development Perspective and Recommendations for Future First-in-Human Trials. *J. Clin. Pharmacol.* **2017**, *57* (6), 690–703.
(415) *Rabbit pyrogen test to be replaced by European Pharmacopoeia*. European Pharmaceutical Review. https://www.europeanpharmaceuticalreview.com/news/158259/rabbit-pyrogen-test-to-be-replaced-by-european-pharmacopoeia/ (accessed 2023-03-16).
(416) FDA No Longer Needs to Require Animal Tests before Human Drug Trials, 2023.
(417) Soares, S.; Sousa, J.; Pais, A.; Vitorino, C. Nanomedicine: Principles, Properties, and Regulatory Issues. *Front. Chem.* **2018**, *6*.
(418) Paradise, J. Regulating Nanomedicine at the Food and Drug Administration. *AMA J. Ethics* **2019**, *21* (4), 347–355.
(419) *Drug Products, Including Biological Products, that Contain Nanomaterials - Guidance for Industry*. U.S. Food and Drug Administration. http://www.fda.gov/regulatory-information/search-fda-guidance-documents/drug-products-including-biological-products-contain-nanomaterials-guidance-industry (accessed 2019-12-18).
(420) *FEDERAL FOOD, DRUG, AND COSMETIC ACT*; 2015; Vol. 21, pp 152–153. https://www.govinfo.gov/app/details/USCODE-2011-title21/USCODE-2011-title21-chap9-subchapV-partA-sec353/context.
(421) European-Medicines-Agency-Reflection-Paper-Development-Block-Copolymer-Micelle-Medicinal-Products_en.Pdf. https://www.ema.europa.eu/en/documents/scientific-guideline/joint-ministry-health-labour-welfare/european-medicines-agency-reflection-paper-development-block-copolymer-micelle-medicinal-products_en.pdf (accessed 2023-03-16).
(422) Reflection-Paper-Data-Requirements-Intravenous-Liposomal-Products-Developed-Reference-Innovator_en.Pdf. https://www.ema.europa.eu/en/documents/scientific-guideline/reflection-paper-data-requirements-intravenous-liposomal-products-developed-reference-innovator_en.pdf (accessed 2023-03-16).
(423) Reflection-Paper-Non-Clinical-Studies-Generic-Nanoparticle-Iron-Medicinal-Product-Applications_en.Pdf. https://www.ema.europa.eu/en/documents/scientific-guideline/reflection-paper-non-clinical-studies-generic-nanoparticle-iron-medicinal-product-applications_en.pdf (accessed 2023-03-16).
(424) Reflection-Paper-Surface-Coatings-General-Issues-Consideration-Regarding-Parenteral-Administration_en.Pdf. https://www.ema.europa.eu/en/documents/scientific-guideline/reflection-paper-surface-coatings-general-issues-consideration-regarding-parenteral-administration_en.pdf (accessed 2023-03-16).

(425) Ehmann, F.; Sakai-Kato, K.; Duncan, R.; Pérez de la Ossa, D. H.; Pita, R.; Vidal, J.-M.; Kohli, A.; Tothfalusi, L.; Sanh, A.; Tinton, S.; Robert, J.-L.; Silva Lima, B.; Amati, M. P. Next-Generation Nanomedicines and Nanosimilars: EU Regulators' Initiatives Relating to the Development and Evaluation of Nanomedicines. *Nanomed.* **2013**, *8* (5), 849–856.
(426) *Pierce Detergent Compatible Bradford Assay Kit*. https://www.thermofisher.com/document-connect/document-connect.html?url=https%3A%2F%2Fassets.thermofisher.com%2FTFS-Assets%2FLSG%2Fmanuals%2F23246_23246S_deter_compat_bradford_UG.pdf (accessed 2022-04-25).
(427) *Assay Cascade Protocols | Nanotechnology Characterization Lab (NCL)*. https://ncl.cancer.gov/resources/assay-cascade-protocols (accessed 2020-06-09).
(428) Albanese, A.; Tang, P. S.; Chan, W. C. W. The Effect of Nanoparticle Size, Shape, and Surface Chemistry on Biological Systems. *Annu. Rev. Biomed. Eng.* **2012**, *14* (1), 1–16.
(429) Abdelwahed, W.; Degobert, G.; Stainmesse, S.; Fessi, H. Freeze-Drying of Nanoparticles: Formulation, Process and Storage Considerations. *Adv. Drug Deliv. Rev.* **2006**, *58* (15), 1688–1713.
(430) Shah, J.; Singh, S. CHAPTER 1 Nanoparticle–Protein Corona Complex: Composition, Kinetics, Physico–Chemical Characterization, and Impact on Biomedical Applications. **2019**, 1–30.
(431) Frost, R.; Langhammer, C.; Cedervall, T. Real-Time in Situ Analysis of Biocorona Formation and Evolution on Silica Nanoparticles in Defined and Complex Biological Environments. *Nanoscale* **2017**, *9* (10), 3620–3628.
(432) De, S.; Robinson, D. H. Particle Size and Temperature Effect on the Physical Stability of PLGA Nanospheres and Microspheres Containing Bodipy. *AAPS PharmSciTech* **2004**, *5* (4), 18–24.
(433) Hickey, J. W.; Santos, J. L.; Williford, J.-M.; Mao, H.-Q. Control of Polymeric Nanoparticle Size to Improve Therapeutic Delivery. *J. Control. Release Off. J. Control. Release Soc.* **2015**, *219*, 536–547.
(434) Yu, Z.; Kastenmüller, G.; He, Y.; Belcredi, P.; Möller, G.; Prehn, C.; Mendes, J.; Wahl, S.; Roemisch-Margl, W.; Ceglarek, U.; Polonikov, A.; Dahmen, N.; Prokisch, H.; Xie, L.; Li, Y.; Wichmann, H.-E.; Peters, A.; Kronenberg, F.; Suhre, K.; Adamski, J.; Illig, T.; Wang-Sattler, R. Differences between Human Plasma and Serum Metabolite Profiles. *PLoS ONE* **2011**, *6* (7), e21230.
(435) Bannon, M. S.; López Ruiz, A.; Corrotea Reyes, K.; Marquez, M.; Wallizadeh, Z.; Savarmand, M.; LaPres, C. A.; Lahann, J.; McEnnis, K. Nanoparticle Tracking Analysis of Polymer Nanoparticles in Blood Plasma. *Part. Part. Syst. Charact.* **2021**, *38* (6), 2100016.
(436) Panchal, J.; Kotarek, J.; Marszal, E.; Topp, E. M. Analyzing Subvisible Particles in Protein Drug Products: A Comparison of Dynamic Light Scattering (DLS) and Resonant Mass Measurement (RMM). *AAPS J.* **2014**, *16* (3), 440–451.
(437) Bélteky, P.; Rónavári, A.; Igaz, N.; Szerencsés, B.; Tóth, I. Y.; Pfeiffer, I.; Kiricsi, M.; Kónya, Z. <p>Silver Nanoparticles: Aggregation Behavior in Biorelevant Conditions and Its Impact on Biological Activity</P>. *Int. J. Nanomedicine* **2019**, *14*, 667–687.
(438) Ehrenberg, M. S.; Friedman, A. E.; Finkelstein, J. N.; Oberdörster, G.; McGrath, J. L. The Influence of Protein Adsorption on Nanoparticle Association with Cultured Endothelial Cells. *Biomaterials* **2009**, *30* (4), 603–610.
(439) *Assay Cascade*. http://www.euncl.eu/about-us/assay-cascade/ (accessed 2020-06-09).

(440) Ripple, D. C.; Montgomery, C. B.; Hu, Z. An Interlaboratory Comparison of Sizing and Counting of Subvisible Particles Mimicking Protein Aggregates. *J. Pharm. Sci.* **2015**, *104* (2), 666–677.
(441) Immunogenicity Assessment for Therapeutic Protein Products 1. In *Immune Aspects of Biopharmaceuticals and Nanomedicines*; Bawa, R., Szebeni, J., Webster, T. J., Audette, G. F., Eds.; Jenny Stanford Publishing, 2019; pp 537–583.
(442) Vessely, C.; Fradkin, A. H.; Carpenter, J. F. Meeting Biopharmaceutical Analytical Requirements for Subvisible Particle Sizing and Counting. *Eur. Pharm. Rev.* **2015**, *20* (5), 71–75.
(443) EMA. *Development, production, characterisation and specifications for monoclonal antibodies related products*. European Medicines Agency. https://www.ema.europa.eu/en/development-production-characterisation-specifications-monoclonal-antibodies-related-products (accessed 2022-03-23).
(444) Gräfe, C.; Weidner, A.; Lühe, M. v. d.; Bergemann, C.; Schacher, F. H.; Clement, J. H.; Dutz, S. Intentional Formation of a Protein Corona on Nanoparticles: Serum Concentration Affects Protein Corona Mass, Surface Charge, and Nanoparticle–Cell Interaction. *Int. J. Biochem. Cell Biol.* **2016**, *75*, 196–202.
(445) Tan, J.; Shah, S.; Thomas, A.; Ou-Yang, H. D.; Liu, Y. The Influence of Size, Shape and Vessel Geometry on Nanoparticle Distribution. *Microfluid. Nanofluidics* **2013**, *14* (1–2), 77–87.
(446) Barber, J. O.; Alberding, J. P.; Restrepo, J. M.; Secomb, T. W. Simulated Two-Dimensional Red Blood Cell Motion, Deformation, and Partitioning in Microvessel Bifurcations. *Ann. Biomed. Eng.* **2008**, *36* (10), 1690–1698.
(447) Sherwood, L. *Human Physiology: From Cells to Systems*, 9th edition.; Cengage Learning: Boston, MA, USA, 2015.
(448) Jarvis, S. Vascular System 1: Anatomy and Physiology. *Nurs. Times* **2018**, *114* (4), 40–44.
(449) Leloup, A. J. A.; Van Hove, C. E.; Heykers, A.; Schrijvers, D. M.; De Meyer, G. R. Y.; Fransen, P. Elastic and Muscular Arteries Differ in Structure, Basal NO Production and Voltage-Gated Ca2+-Channels. *Front. Physiol.* **2015**, *6*, 375–384.
(450) Potter, R. F.; Groom, A. C. Capillary Diameter and Geometry in Cardiac and Skeletal Muscle Studied by Means of Corrosion Casts. *Microvasc. Res.* **1983**, *25* (1), 68–84.
(451) Sonavane, S. K.; Milner, D. M.; Singh, S. P.; Abdel, A. K.; Shahir, K. S.; Chaturvedi, A. Comprehensive Imaging Review of the Superior Vena Cava. *RadioGraphics* **2015**, *35* (7), 1873–1892.
(452) Robertson, A. M.; Watton, P. N. Chapter 8 - Mechanobiology of the Arterial Wall. In *Transport in Biological Media*; Becker, S. M., Kuznetsov, A. V., Eds.; Elsevier: Boston, 2013; pp 275–347.
(453) Sangiorgi, S.; Manelli, A.; Dell'Orbo, C.; Congiu, T. A New Method for the Joint Visualization of Vascular Structures and Connective Tissues: Corrosion Casting and 1 N NaOH Maceration. *Microsc. Res. Tech.* **2006**, *69* (11), 919–923.
(454) Munoz, C. J.; Lucas, A.; Williams, A. T.; Cabrales, P. A Review on Microvascular Hemodynamics. *Crit. Care Clin.* **2020**, *36* (2), 293–305.
(455) Christensen, A. M.; Passalacqua, N. V.; Bartelink, E. J. Chapter 2 - Human Osteology and Odontology. In *Forensic Anthropology (Second Edition)*; Christensen, A. M., Passalacqua, N. V., Bartelink, E. J., Eds.; Academic Press, 2019; pp 33–76.
(456) Gregory, P.; Mursell, I. Chapter 13 - Venous Access Devices. In *Manual of Clinical Paramedic Procedures*; John Wiley & Sons, 2013.

(457) Dougherty, L. Peripheral Cannulation. *Nurs. Stand.* **2008**, *22* (52), 49–56.
(458) *Soft-tissue disorders*. Soft-tissue disorders ¦ Treatment summary. https://bnf.nice.org.uk/treatment-summary/soft-tissue-disorders.html (accessed 2021-05-27).
(459) van Loon, F. H. J.; van Hooff, L. W. E.; de Boer, H. D.; Koopman, S. S. H. A.; Buise, M. P.; Korsten, H. H. M.; Dierick-van Daele, A. T. M.; Bouwman, A. R. A. The Modified A-DIVA Scale as a Predictive Tool for Prospective Identification of Adult Patients at Risk of a Difficult Intravenous Access: A Multicenter Validation Study. *J. Clin. Med.* **2019**, *8* (2), 144.
(460) Robertson, L. *NHSGGC Vascular Access Procedure and Practice Guideline Version 1*; NHS Greater Glasgow and Clyde: Glasgow, 2017. https://www.clinicalguidelines.scot.nhs.uk/media/1515/vascular-access-procedure-and-practice-guidelines.pdf (accessed 2021-05-17).
(461) Hawthorn, A.; Bulmer, A. C.; Mosawy, S.; Keogh, S. Implications for Maintaining Vascular Access Device Patency and Performance: Application of Science to Practice. *J. Vasc. Access* **2019**, *20* (5), 461–470.
(462) Kovačič, A. P. M.; Caprnda, M.; Mrhar, A.; Kubatka, P.; Locatelli, I.; Zolakova, B.; Gaspar, L.; Prosecky, R.; Kruzliak, P.; Staffa, R.; Rodrigo, L.; Radonak, J.; Petrovič, D. Impact of Drugs on Venous Thromboembolism Risk in Surgical Patients. *Eur. J. Clin. Pharmacol.* **2019**, *75* (6), 751–767.
(463) Helms, C. C.; Marvel, M.; Zhao, W.; Stahle, M.; Vest, R.; Kato, G. J.; Lee, J. S.; Christ, G.; Gladwin, M. T.; Hantgan, R. R.; Kim-Shapiro, D. B. Mechanisms of Hemolysis-Associated Platelet Activation. *J. Thromb. Haemost. JTH* **2013**, *11* (12), 2148–2154.
(464) Koupenova, M.; Kehrel, B. E.; Corkrey, H. A.; Freedman, J. E. Thrombosis and Platelets: An Update. *Eur. Heart J.* **2017**, *38* (11), 785–791.
(465) Packham, M. A. Role of Platelets in Thrombosis and Hemostasis. *Can. J. Physiol. Pharmacol.* **1994**, *72* (3), 278–284.
(466) Sangkuhl, K.; Shuldiner, A. R.; Klein, T. E.; Altman, R. B. Platelet Aggregation Pathway. *Pharmacogenet. Genomics* **2011**, *21* (8), 516–521.
(467) Luo, S.; Hu, D.; Wang, M.; Zipfel, P. F.; Hu, Y. Complement in Hemolysis- and Thrombosis- Related Diseases. *Front. Immunol.* **2020**, *11*.
(468) Gomez-Garcia, M. J.; Doiron, A. L.; Steele, R. R. M.; Labouta, H. I.; Vafadar, B.; Shepherd, R. D.; Gates, I. D.; Cramb, D. T.; Childs, S. J.; Rinker, K. D. Nanoparticle Localization in Blood Vessels: Dependence on Fluid Shear Stress, Flow Disturbances, and Flow-Induced Changes in Endothelial Physiology. *Nanoscale* **2018**, *10* (32), 15249–15261.
(469) Stephanou, P. S. Elucidating the Rheological Implications of Adding Particles in Blood. *Rheol. Acta* **2021**, *60* (10), 603–616.
(470) Müller, K.; Fedosov, D. A.; Gompper, G. Understanding Particle Margination in Blood Flow - A Step toward Optimized Drug Delivery Systems. *Med. Eng. Phys.* **2016**, *38* (1), 2–10.
(471) Prina-Mello, A.; Samuel; Jain; O'Dowd; Paul; Kashanin; Gerard; Gun'ko; Volkov. Multifactorial Determinants That Govern Nanoparticle Uptake by Human Endothelial Cells under Flow. *Int. J. Nanomedicine* **2012**, 2943.
(472) Fede, C.; Albertin, G.; Petrelli, L.; De Caro, R.; Fortunati, I.; Weber, V.; Ferrante, C. Influence of Shear Stress and Size on Viability of Endothelial Cells Exposed to Gold Nanoparticles. *J. Nanoparticle Res.* **2017**, *19* (9), 316.
(473) Zukerman, H.; Khoury, M.; Shammay, Y.; Sznitman, J.; Lotan, N.; Korin, N. Targeting Functionalized Nanoparticles to Activated Endothelial Cells under High Wall Shear Stress. *Bioeng. Transl. Med.* **2020**, *5* (2), e10151.
(474) L.F Willis. The Effects of Flow on Therapeutic Protein Aggregation. PhD, University of Leeds, Leeds, 2018. https://etheses.whiterose.ac.uk/21963/1/Willis_LF_Molecular%20and%20Cellular%20Biology_PhD_2018.pdf.

(475) Freese, C.; Schreiner, D.; Anspach, L.; Bantz, C.; Maskos, M.; Unger, R. E.; Kirkpatrick, C. J. In Vitro Investigation of Silica Nanoparticle Uptake into Human Endothelial Cells under Physiological Cyclic Stretch. *Part. Fibre Toxicol.* **2014**, *11* (1), 68.
(476) Buxton, G. A. The Fate of a Polymer Nanoparticle Subject to Flow-Induced Shear Stresses. *Europhys. Lett.* **2008**, *84* (2), 26006.
(477) Park, C.; Bae, J.; Choi, Y.; Park, W. Shear Stress-Triggered Deformation of Microparticles in a Tapered Microchannel. *Polymers* **2021**, *13* (1), 55.
(478) Zhu, X.; Braatz, R. D. A Mechanistic Model for Drug Release in PLGA Biodegradable Stent Coatings Coupled with Polymer Degradation and Erosion. *J. Biomed. Mater. Res. A* **2015**, *103* (7), 2269–2279.
(479) Qiao, Y.; Wang, Y.; Chen, Y.; Luo, K.; Fan, J. Mathematical Modeling of Shear-Activated Targeted Nanoparticle Drug Delivery for the Treatment of Aortic Diseases. *Biomech. Model. Mechanobiol.* **2022**, *21* (1), 221–230.
(480) Klein, D. M.; Poortinga, A.; Verhoeven, F. M.; Bonn, D.; Bonnet, S.; van Rijn, C. J. M. Degradation of Lipid Based Drug Delivery Formulations during Nebulization. *Chem. Phys.* **2021**, *547*, 111192.
(481) Beard, D.; Litman, M.; Azarpeykan, S.; Uzun, O.; Bhatta, D.; Buchan, A. M.; Spratt, N.; Ingber, D. Abstract 81: Shear-Activated Nanoparticle Aggregates Containing Nitroglycerin Selectively Increase Collateral Perfusion During Experimental Ischemic Stroke. *Stroke* **2022**, *53* (Suppl_1), A81–A81.
(482) *NanoRx: Mechanically-Activated Drug Targeting*. Wyss Institute. https://wyss.harvard.edu/technology/nanorx-mechanically-activated-drug-targeting/ (accessed 2023-04-27).
(483) Saha, D.; Kumar, S.; Ray, D.; Mata, J.; Aswal, V. K. Structure and Stability of Biodegradable Polymer Nanoparticles in Electrolyte Solution. *Mater. Lett. X* **2021**, *10*, 100066.
(484) Fletcher, C. A. J. Computational Fluid Dynamics: An Introduction. In *Computational Techniques for Fluid Dynamics 1: Fundamental and General Techniques*; Fletcher, C. A. J., Ed.; Springer Series in Computational Physics; Springer: Berlin, Heidelberg, 1988; pp 1–16.
(485) Hu, H. H. Chapter 10 - Computational Fluid Dynamics. In *Fluid Mechanics*; Kundu, P. K., Cohen, I. M., Dowling, D. R., Eds.; Academic Press: Boston, 2012; pp 421–472.
(486) Smyth, T. A. G. A Review of Computational Fluid Dynamics (CFD) Airflow Modelling over Aeolian Landforms. *Aeolian Res.* **2016**, *22*, 153–164.
(487) Mariam; Magar, A.; Joshi, M.; Rajagopal, P. S.; Khan, A.; Rao, M. M.; Sapra, B. K. CFD Simulation of the Airborne Transmission of COVID-19 Vectors Emitted during Respiratory Mechanisms: Revisiting the Concept of Safe Distance. *ACS Omega* **2021**, *6* (26), 16876–16889.
(488) Mohamadi, F.; Fazeli, A. A Review on Applications of CFD Modeling in COVID-19 Pandemic. *Arch. Comput. Methods Eng.* **2022**, 1–20.
(489) Mirzaie, M.; Lakzian, E.; Khan, A.; Warkiani, M. E.; Mahian, O.; Ahmadi, G. COVID-19 Spread in a Classroom Equipped with Partition – A CFD Approach. *J. Hazard. Mater.* **2021**, *420*, 126587.
(490) Yan, S.; Tang, G.; Zhou, C. Q.; Guo, X. Computational Fluid Dynamics Modeling of Combustion Characteristics of a CH4/O2 Combustor in a Copper Anode Furnace. *ACS Omega* **2019**, *4* (7), 12449–12458.
(491) Blazek, J. Chapter 1 - Introduction. In *Computational Fluid Dynamics: Principles and Applications*; Blazek, J., Ed.; Elsevier Science: Oxford, 2005; pp 1–4.
(492) Karmonik, C.; Bismuth, J.; Davies, M. G.; Lumsden, A. B. Computational Fluid Dynamics as a Tool for Visualizing Hemodynamic Flow Patterns. *Methodist DeBakey Cardiovasc. J.* **2009**, *5* (3), 26–33.

(493) Tu, J.; Inthavong, K.; Wong, K. K. L. Computational Haemodynamics—An Introduction. In *Computational Hemodynamics – Theory, Modelling and Applications*; Tu, J., Inthavong, K., Wong, K. K. L., Eds.; Biological and Medical Physics, Biomedical Engineering; Springer Netherlands: Dordrecht, 2015; pp 1–19.
(494) Cundall, P. A. A Computer Model for Simulating Progressive, Large-Scale Movement in Blocky Rock System. In *Proceedings of the International Symposium on Rock Mechanics, 1971*; 1971.
(495) Cundall, P. A.; Strack, O. D. L. A Discrete Numerical Model for Granular Assemblies. *Géotechnique* **1979**, *29* (1), 47–65.
(496) Yeom, S. B.; Ha, E.-S.; Kim, M.-S.; Jeong, S. H.; Hwang, S.-J.; Choi, D. H. Application of the Discrete Element Method for Manufacturing Process Simulation in the Pharmaceutical Industry. *Pharmaceutics* **2019**, *11* (8), 414.
(497) Endres, S. C.; Ciacchi, L. C.; Mädler, L. A Review of Contact Force Models between Nanoparticles in Agglomerates, Aggregates, and Films. *J. Aerosol Sci.* **2021**, *153*, 105719.
(498) Thornton, C.; Yin, K. K.; Adams, M. J. Numerical Simulation of the Impact Fracture and Fragmentation of Agglomerates. *J. Phys. Appl. Phys.* **1996**, *29* (2), 424–435.
(499) Bharadwaj, R.; Khambekar, J.; Orlando, A.; Gao, Z.; Shen, H.; Helenbrook, B.; Royal, T. A.; Weitzman, P.; El-Genk, M. S. A Comparison of Discrete Element Modeling, Finite Element Analysis, and Physical Experiment of Granular Material Systems in a Direct Shear Cell. In *AIP Conference Proceedings*; AIP: Albuquerque (New Mexico), 2008; Vol. 969, pp 221–228.
(500) Liu, W.; Wu, C.-Y. Modelling Complex Particle–Fluid Flow with a Discrete Element Method Coupled with Lattice Boltzmann Methods (DEM-LBM). *ChemEngineering* **2020**, *4* (4), 55.
(501) Zhao, J.; Shan, T. Coupled CFD–DEM Simulation of Fluid–Particle Interaction in Geomechanics. *Powder Technol.* **2013**, *239*, 248–258.
(502) Rapp, B. E. Chapter 31 - Finite Volume Method. In *Microfluidics: Modelling, Mechanics and Mathematics*; Rapp, B. E., Ed.; Micro and Nano Technologies; Elsevier: Oxford, 2017; pp 633–654.
(503) McDonald, P. W. The Computation of Transonic Flow Through Two-Dimensional Gas Turbine Cascades. In *ASME 1971 International Gas Turbine Conference and Products Show*; American Society of Mechanical Engineers: Houston, Texas, USA, 1971; p V001T01A089.
(504) Lopes, D.; Agujetas, R.; Puga, H.; Teixeira, J.; Lima, R.; Alejo, J. P.; Ferrera, C. Analysis of Finite Element and Finite Volume Methods for Fluid-Structure Interaction Simulation of Blood Flow in a Real Stenosed Artery. *Int. J. Mech. Sci.* **2021**, *207*, 106650.
(505) Devarampally, D. R. Development of Two-Way Coupled CFD – DEM Model for Top Spray Fluid Bed Granulator Using Star CCM+. MSc, Rutgers University, New Brunswick, 2017.
(506) An, H.; Song, Y.; Liu, H.; Han, H. Combined Finite-Discrete Element Modelling of Dynamic Rock Fracture and Fragmentation during Mining Production Process by Blast. *Shock Vib.* **2021**, *2021*, e6622926.
(507) Feistauer, M.; Felcman, J.; Lukáčová-Medvid'ová, M. Combined Finite Element-Finite Volume Solution of Compressible Flow. *J. Comput. Appl. Math.* **1995**, *63* (1), 179–199.
(508) Smuts, E. M. A Methodology for Coupled CFD-DEM Modeling of Particulate Suspension Rheology. PhD, University of Cape Town, Cape Town, South Africa, 2015. https://open.uct.ac.za/handle/11427/16782 (accessed 2021-07-09).

(509) Kloss, C.; Goniva, C.; Hager, A.; Amberger, S.; Pirker, S. Models, Algorithms and Validation for Opensource DEM and CFD–DEM. *Prog. Comput. Fluid Dyn. Int. J.* **2012**, *12* (2–3), 140–152.
(510) Ponzini, R.; Da Vià, R.; Bnà, S.; Cottini, C.; Benassi, A. Coupled CFD-DEM Model for Dry Powder Inhalers Simulation: Validation and Sensitivity Analysis for the Main Model Parameters. *Powder Technol.* **2021**, *385*, 199–226.
(511) Hardy, J.; Pomeau, Y.; de Pazzis, O. Time Evolution of a Two-Dimensional Classical Lattice System. *Phys. Rev. Lett.* **1973**, *31* (5), 276–279.
(512) Hardy, J.; de Pazzis, O.; Pomeau, Y. Molecular Dynamics of a Classical Lattice Gas: Transport Properties and Time Correlation Functions. *Phys. Rev. A* **1976**, *13* (5), 1949–1961.
(513) Frisch, U.; Hasslacher, B.; Pomeau, Y. Lattice-Gas Automata for the Navier-Stokes Equation. *Phys. Rev. Lett.* **1986**, *56* (14), 1505–1508.
(514) Chen, S.; Doolen, G. D. Lattice Boltzmann Method for Fluid Flows. *Annu. Rev. Fluid Mech.* **1998**, *30* (1), 329–364.
(515) Đukić, T.; Filipovic, N. Chapter 10 - Numerical Modeling of Cell Separation in Microfluidic Chips. In *Computational Modeling in Bioengineering and Bioinformatics*; Filipovic, N., Ed.; Academic Press, 2020; pp 321–352.
(516) Smagorinsky, J. GENERAL CIRCULATION EXPERIMENTS WITH THE PRIMITIVE EQUATIONS: I. THE BASIC EXPERIMENT. *Mon. Weather Rev.* **1963**, *91* (3), 99–164.
(517) Moin, P. Advances in Large Eddy Simulation Methodology for Complex Flows. *Int. J. Heat Fluid Flow* **2002**, *23* (5), 710–720.
(518) *Population Balance Modelling | OpenFOAM*. https://openfoam.org/guides/population-balance-modelling/ (accessed 2023-04-28).
(519) Lehnigk, R.; Bainbridge, W.; Liao, Y.; Lucas, D.; Niemi, T.; Peltola, J.; Schlegel, F. An Open-Source Population Balance Modeling Framework for the Simulation of Polydisperse Multiphase Flows. *AIChE J.* **2022**, *68* (3), e17539.
(520) Unit 5 - Kinematics of Fluids. In *MST326 Mathematical methods and fluid mechanics*; The Open University: Milton Keynes, 2009.
(521) Reid, L. An Introduction to Biomedical Computational Fluid Dynamics. *Adv. Exp. Med. Biol.* **2021**, *1334*, 205–222.
(522) Wheeler, M. L.; Oyen, M. L. Bioengineering Approaches for Placental Research. *Ann. Biomed. Eng.* **2021**, *49* (8), 1805–1818.
(523) Doyle, B. J.; Kelsey, L. J.; Shelverton, C.; Abbate, G.; Ainola, C.; Sato, N.; Livingstone, S.; Bouquet, M.; Passmore, M. R.; Wilson, E. S.; Colombo, S.; Sato, K.; Liu, K.; Heinsar, S.; Wildi, K.; Carr, P. J.; Suen, J.; Fraser, J.; Li Bassi, G.; Keogh, S. *Design, Development, and Preliminary Assessment of a Novel Peripheral Intravenous Catheter Aimed at Reducing Early Failure Rates*; preprint; Bioengineering, 2022.
(524) Piper, R.; Carr, P. J.; Kelsey, L. J.; Bulmer, A. C.; Keogh, S.; Doyle, B. J. The Mechanistic Causes of Peripheral Intravenous Catheter Failure Based on a Parametric Computational Study. *Sci. Rep.* **2018**, *8* (1), 3441.
(525) Nifong, T. P.; McDevitt, T. J. The Effect of Catheter to Vein Ratio on Blood Flow Rates in a Simulated Model of Peripherally Inserted Central Venous Catheters. *CHEST* **2011**, *140* (1), 48–53.
(526) Jayroe, H.; Foley, K. Arteriovenous Fistula. In *StatPearls*; StatPearls Publishing: Treasure Island (FL), 2023.
(527) Shiu, Y.-T.; Rotmans, J. I.; Geelhoed, W. J.; Pike, D. B.; Lee, T. Arteriovenous Conduits for Hemodialysis: How to Better Modulate the Pathophysiological Vascular Response to Optimize Vascular Access Durability. *Am. J. Physiol.-Ren. Physiol.* **2019**, *316* (5), F794–F806.

(528) Clark, T. W. I.; Van Canneyt, K.; Verdonck, P. Computational Flow Dynamics and Preclinical Assessment of a Novel Hemodialysis Catheter. *Semin. Dial.* **2012**, *25* (5), 574–581.
(529) Owen, D. G.; Oliveira, D. C. de; Qian, S.; Green, N. C.; Shepherd, D. E. T.; Espino, D. M. Impact of Side-Hole Geometry on the Performance of Hemodialysis Catheter Tips: A Computational Fluid Dynamics Assessment. *PLOS ONE* **2020**, *15* (8), e0236946.
(530) Clark, T. W. I.; Isu, G.; Gallo, D.; Verdonck, P.; Morbiducci, U. Comparison of Symmetric Hemodialysis Catheters Using Computational Fluid Dynamics. *J. Vasc. Interv. Radiol.* **2015**, *26* (2), 252-259.e2.
(531) Reneman, R. S.; Hoeks, A. P. G. Wall Shear Stress as Measured in Vivo: Consequences for the Design of the Arterial System. *Med. Biol. Eng. Comput.* **2008**, *46* (5), 499–507.
(532) Sahin, A.; Esendagli, G.; Yerlikaya, F.; Caban-Toktas, S.; Yoyen-Ermis, D.; Horzum, U.; Aktas, Y.; Khan, M.; Couvreur, P.; Capan, Y. A Small Variation in Average Particle Size of PLGA Nanoparticles Prepared by Nanoprecipitation Leads to Considerable Change in Nanoparticles' Characteristics and Efficacy of Intracellular Delivery. *Artif. Cells Nanomedicine Biotechnol.* **2017**, *45* (8), 1657–1664.
(533) Stromberg, Z. R.; Lisa Phipps, M.; Magurudeniya, H. D.; Pedersen, C. A.; Rajale, T.; Sheehan, C. J.; Courtney, S. J.; Bradfute, S. B.; Hraber, P.; Rush, M. N.; Kubicek-Sutherland, J. Z.; Martinez, J. S. Formulation of Stabilizer-Free, Nontoxic PLGA and Elastin-PLGA Nanoparticle Delivery Systems. *Int. J. Pharm.* **2021**, *597*, 120340.
(534) Hammes, M.; Boghosian, M.; Cassel, K.; Watson, S.; Funaki, B.; Doshi, T.; Mahmoudzadeh Akherat, S. M. J.; Hines, J.; Coe, F. Increased Inlet Blood Flow Velocity Predicts Low Wall Shear Stress in the Cephalic Arch of Patients with Brachiocephalic Fistula Access. *PLOS ONE* **2016**, *11* (4), e0152873.
(535) STARCCM+ User Guide.
(536) Kumar, N.; Abdul Khader, S. M.; Pai, R. B.; Kyriacou, P.; Khan, S.; Prakashini, K.; Srikanth Rao, D. Effect of Newtonian and Non-Newtonian Flow in Subject Specific Carotid Artery. *J. Eng. Sci. Technol.* **2020**, *15* (4), 2746–2763.
(537) *Doxorubicin Solution for Injection - Summary of Product Characteristics (SmPC) - (emc)*. https://www.medicines.org.uk/emc/product/6184/smpc (accessed 2021-08-16).
(538) Mross, K.; Niemann, B.; Massing, U.; Drevs, J.; Unger, C.; Bhamra, R.; Swenson, C. E. Pharmacokinetics of Liposomal Doxorubicin (TLC-D99; Myocet) in Patients with Solid Tumors: An Open-Label, Single-Dose Study. *Cancer Chemother. Pharmacol.* **2004**, *54* (6), 514–524.
(539) Chang, H.-I.; Yeh, M.-K. Clinical Development of Liposome-Based Drugs: Formulation, Characterization, and Therapeutic Efficacy. *Int. J. Nanomedicine* **2012**, *7*, 49–60.
(540) Link, J. M.; Godlieb, W.; Tripp, P.; Deen, N. G.; Heinrich, S.; Kuipers, J. A. M.; Schönherr, M.; Peglow, M. Comparison of Fibre Optical Measurements and Discrete Element Simulations for the Study of Granulation in a Spout Fluidized Bed. *Powder Technol.* **2009**, *189* (2), 202–217.
(541) Börner, M.; Bück, A.; Tsotsas, E. DEM-CFD Investigation of Particle Residence Time Distribution in Top-Spray Fluidised Bed Granulation. *Chem. Eng. Sci.* **2017**, *161*, 187–197.
(542) Washino, K.; Hsu, C.; Kawaguchi, T.; Tsuji, Y. Similarity Model for DEM Simulation of Fluidized Bed. *J. Soc. Powder Technol. Jpn.* **2007**, *44* (3), 198–205.
(543) Pannuzzo, M.; Horta, B. A. C.; La Rosa, C.; Decuzzi, P. Predicting the Miscibility and Rigidity of Poly(Lactic-Co-Glycolic Acid)/Polyethylene Glycol

Blends via Molecular Dynamics Simulations. *Macromolecules* **2020**, *53* (10), 3643–3654.
(544) Usune, S.; Kubo, M.; Tsukada, T.; Koike, O.; Tatsumi, R.; Fujita, M.; Takami, S.; Adschiri, T. Numerical Simulations of Dispersion and Aggregation Behavior of Surface-Modified Nanoparticles under Shear Flow. *Powder Technol.* **2019**, *343*, 113–121.
(545) Jahangiri, M.; Saghafian, M.; Sadeghi, M. R. Numerical Study of Turbulent Pulsatile Blood Flow through Stenosed Artery Using Fluid-Solid Interaction. *Comput. Math. Methods Med.* **2015**, *2015*, 1–10.
(546) Mindlin, R. D.; Deresiewicz, H. Elastic Spheres in Contact Under Varying Oblique Forces. *J. Appl. Mech.* **1953**, *20* (3), 327–344.
(547) Ai, J.; Chen, J.-F.; Rotter, J. M.; Ooi, J. Y. Assessment of Rolling Resistance Models in Discrete Element Simulations. *Powder Technol.* **2011**, *206* (3), 269–282.
(548) Liu, D.; Tang, C.; Ding, S.; Fu, B. CFD-DEM Simulation for Distribution and Motion Feature of Crystal Particles in Centrifugal Pump. *Int. J. Fluid Mach. Syst.* **2017**, *10* (4), 378–384.
(549) Hasan, M. K.; Ahamed, M. S.; Alam, M. S.; Hossain, M. B. An Implicit Method for Numerical Solution of Singular and Stiff Initial Value Problems. *J. Comput. Eng.* **2013**, *2013*, 1–5.
(550) Courant, R.; Friedrichs, K.; Lewy, H. über die partiellen Differenzengleichungen der mathematischen Physik. *Math. Ann.* **1928**, *100* (1), 32–74.
(551) DEM Implementation. In *Coupled CFD-DEM Modeling*; John Wiley & Sons, Ltd: Chichester, UK, 2016; pp 68–151.
(552) Norouzi, H. R.; Zarghami, R.; Sotudeh-Gharebagh, R.; Mostoufi, N. Introduction. In *Coupled CFD-DEM Modeling: Formulation, Implementation and Application to Multiphase Flows*; John Wiley & Sons, Ltd: Chichester, UK, 2016; pp 1–13.
(553) Guha, A.; Pradhan, K. Secondary Motion in Three-Dimensional Branching Networks. *Phys. Fluids* **2017**, *29* (6), 063602.
(554) Lee, S. J.; Choi, W.; Seo, E.; Yeom, E. Association of Early Atherosclerosis with Vascular Wall Shear Stress in Hypercholesterolemic Zebrafish. *PLOS ONE* **2015**, *10* (11), e0142945.
(555) Silva, T.; Sequeira, A.; Santos, R. F.; Tiago, J. Mathematical Modeling of Atherosclerotic Plaque Formation Coupled with a Non-Newtonian Model of Blood Flow. *Conf. Pap. Math.* **2013**, *2013*, e405914.
(556) Yu, L. X.; Amidon, G.; Khan, M. A.; Hoag, S. W.; Polli, J.; Raju, G. K.; Woodcock, J. Understanding Pharmaceutical Quality by Design. *AAPS J.* **2014**, *16* (4), 771–783.
(557) Selen, A.; Cruañes, M. T.; Müllertz, A.; Dickinson, P. A.; Cook, J. A.; Polli, J. E.; Kesisoglou, F.; Crison, J.; Johnson, K. C.; Muirhead, G. T.; Schofield, T.; Tsong, Y. Meeting Report: Applied Biopharmaceutics and Quality by Design for Dissolution/Release Specification Setting: Product Quality for Patient Benefit. *AAPS J.* **2010**, *12* (3), 465–472.
(558) *ICH Harmonised Tripartite Guideline: Pharmaceutical Development Q8 (R2)*. http://www.ich.org/fileadmin/Public_Web_Site/ICH_Products/Guidelines/Quality/Q8_R1.
(559) Grimsrud, K. N.; Sherwin, C. M. T.; Constance, J. E.; Tak, C.; Zuppa, A. F.; Spigarelli, M. G.; Mihalopoulos, N. L. Special Population Considerations and Regulatory Affairs for Clinical Research. *Clin. Res. Regul. Aff.* **2015**, *32* (2), 47–56.
(560) Faber, J. E.; Stouffer, G. A. Introduction to Basic Hemodynamic Principles. In *Cardiovascular Hemodynamics for the Clinician*; John Wiley & Sons Ltd: Hoboken, NJ, 2017; pp 1–16.

(561) Wu, S. P.; Ringgaard, S.; Oyre, S.; Hansen, M. S.; Rasmus, S.; Pedersen, E. M. Wall Shear Rates Differ between the Normal Carotid, Femoral, and Brachial Arteries: An in Vivo MRI Study. *J. Magn. Reson. Imaging* **2004**, *19* (2), 188–193.
(562) Katritsis, D.; Kaiktsis, L.; Chaniotis, A.; Pantos, J.; Efstathopoulos, E. P.; Marmarelis, V. Wall Shear Stress: Theoretical Considerations and Methods of Measurement. *Prog. Cardiovasc. Dis.* **2007**, *49* (5), 307–329.
(563) Day, M. A. The No-Slip Condition of Fluid Dynamics. *Erkenntnis* **1990**, *33* (3), 285–296.
(564) Prabhakara, S.; Deshpande, M. D. The No-Slip Boundary Condition in Fluid Mechanics: 1. The Riddle of Fluid Sticking to the Wall in Flow. *Resonance* **2004**, *9* (4), 50–60.
(565) Ben-Dov, G.; Cohen, J. Critical Reynolds Number for a Natural Transition to Turbulence in Pipe Flows. *Phys. Rev. Lett.* **2007**, *98* (6), 064503.
(566) Saqr, K. M.; Tupin, S.; Rashad, S.; Endo, T.; Niizuma, K.; Tominaga, T.; Ohta, M. Physiologic Blood Flow Is Turbulent. *Sci. Rep.* **2020**, *10* (1), 1–12.
(567) Kapinos, V. M.; Tarasov, A. I. Determination of Wall Shear Stress from Velocity Profile Measurement in the Outer Part of the Boundary Layer. *J. Eng. Phys.* **1981**, *40* (5), 473–477.
(568) Li, H.; Li, Y.; Huang, B.; Xu, T. Flow Characteristics of the Entrance Region with Roughness Effect within Rectangular Microchannels. *Micromachines* **2020**, *11* (1), 30.
(569) Everts, M.; Meyer, J. P. Laminar Hydrodynamic and Thermal Entrance Lengths for Simultaneously Hydrodynamically and Thermally Developing Forced and Mixed Convective Flows in Horizontal Tubes. *Exp. Therm. Fluid Sci.* **2020**, *118*, 110153.
(570) Gersten, K. Fully Developed Turbulent Pipe Flow. In *Fluid Mechanics of Flow Metering*; Merzkirch, W., Gersten, K., Peters, F., Vasanta Ram, V., von Lavante, E., Hans, V., Merzkirch, W., Eds.; Springer: Berlin, Heidelberg, 2005; pp 1–22.
(571) Štigler, J. Analytical Velocity Profile in Tube for Laminar and Turbulent Flow. *Eng. Mech.* **2014**, *21* (6), 371–379.
(572) Gray, J. D.; Owen, I.; Escudier, M. P. Dynamic Scaling of Unsteady Shear-Thinning Non-Newtonian Fluid Flows in a Large-Scale Model of a Distal Anastomosis. *Exp. Fluids* **2007**, *43* (4), 535–546.
(573) Beier, S.; Ormiston, J. A.; Webster, M. W.; Cater, J. E.; Norris, S. E.; Medrano-Gracia, P.; Young, A. A.; Cowan, B. R. Dynamically Scaled Phantom Phase Contrast MRI Compared to True-Scale Computational Modeling of Coronary Artery Flow. *J. Magn. Reson. Imaging* **2016**, *44* (4), 983–992.
(574) Sedov, L. I.; Volkovets, A. G. *Similarity and Dimensional Methods in Mechanics*, 10th ed.; CRC Press: Boca Raton, 1993.
(575) Donelan, J. M.; Kram, R. Exploring Dynamic Similarity in Human Running Using Simulated Reduced Gravity. *J. Exp. Biol.* **2000**, *203* (16), 2405–2415.
(576) Friedman, M. H.; Kuban, B. D.; Schmalbrock, P.; Smith, K.; Altan, T. Fabrication of Vascular Replicas From Magnetic Resonance Images. *J. Biomech. Eng.* **1995**, *117* (3), 364–366.
(577) Johnson, K.; Sharma, P.; Oshinski, J. Coronary Artery Flow Measurement Using Navigator Echo Gated Phase Contrast Magnetic Resonance Velocity Mapping at 3.0T. *J. Biomech.* **2008**, *41* (3), 595–602.
(578) Zaman, A.; Ali, N.; Bég, O. A. Numerical Study of Unsteady Blood Flow through a Vessel Using Sisko Model. *Eng. Sci. Technol. Int. J.* **2016**, *19* (1), 538–547.

(579) Rubenstein, D. A.; Yin, W.; Frame, M. D. Chapter 14 - In Silico Biofluid Mechanics. In *Biofluid Mechanics (Second Edition)*; Rubenstein, D. A., Yin, W., Frame, M. D., Eds.; Academic Press: Boston, 2015; pp 461–494.
(580) Cheng, Y.-T.; Cheng, C.-M. Scaling, Dimensional Analysis, and Indentation Measurements. *Mater. Sci. Eng. R Rep.* **2004**, *44* (4–5), 91–149.
(581) Takahashi, T.; Shintani, Y.; Murayama, R.; Noguchi, H.; Abe-Doi, M.; Koudounas, S.; Nakagami, G.; Mori, T.; Sanada, H. Ultrasonographic Measurement of Blood Flow of Peripheral Vein in the Upper Limb of Healthy Participants: A Pilot Study. *J. Jpn. Soc. Wound Ostomy Cont. Manag.* **2021**, *25* (3), 576–584.
(582) Shima, H.; Ohno, K.; Michi, K.; Egawa, K.; Takiguchi, R. An Anatomical Study on the Forearm Vascular System. *J. Cranio-Maxillo-fac. Surg. Off. Publ. Eur. Assoc. Cranio-Maxillo-fac. Surg.* **1996**, *24* (5), 293–299.
(583) Peng, L.; Qiu, Y.; Huang, Z.; Xia, C.; Dai, C.; Zheng, T.; Li, Z. Numerical Simulation of Hemodynamic Changes in Central Veins after Tunneled Cuffed Central Venous Catheter Placement in Patients under Hemodialysis. *Sci. Rep.* **2017**, *7* (1), 15955.
(584) Menter, F. R. Two-Equation Eddy-Viscosity Turbulence Models for Engineering Applications. *AIAA J.* **1994**, *32* (8), 1598–1605.
(585) Saline (Medicine). *Wikipedia*; 2024.
(586) Qasem, N. A. A.; Generous, M. M.; Qureshi, B. A.; Zubair, S. M. A Comprehensive Review of Saline Water Correlations and Data: Part II—Thermophysical Properties. *Arab. J. Sci. Eng.* **2021**, *46* (3), 1941–1979.
(587) *Density of Aqueous Solutions of Organic Substances as Sugars and Alcohols*. https://www.engineeringtoolbox.com/density-aqueous-solution-organic-sugar-alcohol-concentration-d_1954.html (accessed 2024-06-21).
(588) *CRC Handbook of Chemistry and Physics: A Ready-Reference Book of Chemical and Physical Data*, 99th edition.; Rumble, J. R., Lide, D. R., Bruno, T. J., Eds.; CRC Press, Taylor & Francis Group: Boca Raton London New York, 2018.
(589) Tecoflex-B40-TPU-Series.Pdf. https://www.lubrizol.com/-/media/Lubrizol/Health/TDS/Tecoflex-B40-TPU-Series.pdf (accessed 2023-08-31).
(590) Kanyanta, V.; Ivankovic, A. Mechanical Characterisation of Polyurethane Elastomer for Biomedical Applications. *J. Mech. Behav. Biomed. Mater.* **2010**, *3* (1), 51–62.
(591) Diaz, L. P.; J. Brown, C.; Ojo, E.; Mustoe, C.; J. Florence, A. Machine Learning Approaches to the Prediction of Powder Flow Behaviour of Pharmaceutical Materials from Physical Properties. *Digit. Discov.* **2023**, *2* (3), 692–701.
(592) *Intravenous Therapy in Nursing Practice*, 2nd ed.; Dougherty, L., Lamb, J., Eds.; Blackwell Pub: Oxford, UK ; Malden, MA, 2008.
(593) Dolan, J. M.; Kolega, J.; Meng, H. High Wall Shear Stress and Spatial Gradients in Vascular Pathology: A Review. *Ann. Biomed. Eng.* **2013**, *41* (7), 1411–1427.
(594) Mackman, N. New Insights into the Mechanisms of Venous Thrombosis. *J. Clin. Invest.* **2012**, *122* (7), 2331–2336.
(595) Yaakobovich, H.; Koren, O.; Chapas, S.; Gohari, S.; Zaretsky, U.; Rotman, O. M.; Weiss, D. Novel Design of Peripheral Infusion Catheter Improves the Kinetics of Intravenous Drug Release. *J Cardiovasc. Transl. Res.* **2021**, *14* (5), 883–893.
(596) Doyle, B.; Kelsey, L.; Carr, P. J.; Bulmer, A.; Keogh, S. Determining an Appropriate To-Keep-Vein-Open (TKVO) Infusion Rate for Peripheral Intravenous Catheter Usage. *J. Assoc. Vasc. Access* **2021**, *26* (2), 13–20.

(597) Fry, D. L. Acute Vascular Endothelial Changes Associated with Increased Blood Velocity Gradients. *Circ. Res.* **1968**, *22* (2), 165–197.
(598) Garon, A.; Farinas, M.-I. Fast Three-Dimensional Numerical Hemolysis Approximation. *Artif. Organs* **2004**, *28* (11), 1016–1025.
(599) *Estimation of Shear Stress-related Blood Damage in Heart Valve Prostheses - in Vitro Comparison of 25 Aortic Valves - M. Giersiepen, L.J. Wurzinger, R. Opitz, H. Reul, 1990*. https://journals.sagepub.com/doi/10.1177/039139889001300507 (accessed 2022-06-21).
(600) Yu, H.; Engel, S.; Janiga, G.; Thévenin, D. A Review of Hemolysis Prediction Models for Computational Fluid Dynamics: A REVIEW OF HEMOLYSIS PREDICTION MODELS. *Artif. Organs* **2017**, *41* (7), 603–621.
(601) Alemu, Y.; Bluestein, D. Flow-Induced Platelet Activation and Damage Accumulation in a Mechanical Heart Valve: Numerical Studies. *Artif. Organs* **2007**, *31* (9), 677–688.
(602) Fraser, K. H.; Zhang, T.; Taskin, M. E.; Griffith, B. P.; Wu, Z. J. A Quantitative Comparison of Mechanical Blood Damage Parameters in Rotary Ventricular Assist Devices: Shear Stress, Exposure Time and Hemolysis Index. *J. Biomech. Eng.* **2012**, *134* (8), 0810021–08100211.
(603) Holder, M. R.; Stutzman, S. E.; Olson, D. M. Impact of Ultrasound on Short Peripheral Intravenous Catheter Placement on Vein Thrombosis Risk. *J. Infus. Nurs.* **2017**, *40* (3), 176.
(604) Schults, J. A.; Kleidon, T.; Petsky, H. L.; Stone, R.; Schoutrop, J.; Ullman, A. J. Peripherally Inserted Central Catheter Design and Material for Reducing Catheter Failure and Complications. *Cochrane Database Syst. Rev.* **2019**, *2019* (7), CD013366.
(605) *Hickman™ / Broviac™ / Leonard™ Central Venous Catheters*. https://www.bd.com/en-us/products-and-solutions/products/product-families/hickman-broviac-leonard-central-venous-catheters (accessed 2023-05-15).
(606) Pandey, N. N.; Taxak, A.; Kumar, S. Normal Pulmonary Venous Anatomy and Non-Anomalous Variations Demonstrated on CT Angiography: What the Radiologist Needs to Know? *Br. J. Radiol.* **2020**, *93* (1116), 20200595.
(607) Demos, T. C.; Posniak, H. V.; Pierce, K. L.; Olson, M. C.; Muscato, M. Venous Anomalies of the Thorax. *Am. J. Roentgenol.* **2004**, *182* (5), 1139–1150.
(608) Chapter 4 Circulation and Vorticity. In *International Geophysics*; Holton, J. R., Ed.; An Introduction to Dynamic Meteorology; Academic Press, 1979; Vol. 23, pp 78–100.
(609) Bro, R.; K. Smilde, A. Principal Component Analysis. *Anal. Methods* **2014**, *6* (9), 2812–2831.
(610) *Proceedings of the Jointly Organised 11th World Congress on Computational Mechanics (WCCM XI) 5th European Conference on Computational Mechanics (ECCM V) ; 6th European Conference on Computational Fluid Dynamics (ECFD VI) ; Barcelona, Spain, July 20 - 25, 2014*, 1. ed.; 2014.
(611) Frungieri, G.; Vanni, M. Shear-Induced Aggregation of Colloidal Particles: A Comparison between Two Different Approaches to the Modelling of Colloidal Interactions. *Can. J. Chem. Eng.* **2017**, *95* (9), 1768–1780.
(612) Krzysko, A. J.; Nakouzi, E.; Zhang, X.; Graham, T. R.; Rosso, K. M.; Schenter, G. K.; Ilavsky, J.; Kuzmenko, I.; Frith, M. G.; Ivory, C. F.; Clark, S. B.; Weston, J. S.; Weigandt, K. M.; De Yoreo, J. J.; Chun, J.; Anovitz, L. M. Correlating Inter-Particle Forces and Particle Shape to Shear-Induced Aggregation/Fragmentation and Rheology for Dilute Anisotropic Particle Suspensions: A Complementary Study via Capillary Rheometry and in-Situ

Small and Ultra-Small Angle X-Ray Scattering. *J. Colloid Interface Sci.* **2020**, *576*, 47–58.
(613) Srinivas Chimmili, ‡; Deepak Doraiswamy, *; Gupta‡, R. K. *Shear-Induced Agglomeration of Particulate Suspensions†*.
(614) *How can I calculate blood damage (haemolysis) in STAR-CCM+?* https://support.sw.siemens.com/en-US/product/226870983/knowledge-base/KB000035941_EN_US.
(615) Wachter, D. S. D.; Verdonck, P. R.; Vos, J. Y. D.; Hombrouckx, R. O. Blood Trauma in Plastic Haemodialysis Cannulae. *Int. J. Artif. Organs* **1997**.
(616) Berman, D. J.; Schiavi, A.; Frank, S. M.; Duarte, S.; Schwengel, D. A.; Miller, C. R. Factors That Influence Flow through Intravascular Catheters: The Clinical Relevance of Poiseuille's Law. *Transfusion (Paris)* **2020**, *60* (7), 1410–1417.
(617) McDonald, J. C.; Duffy, D. C.; Anderson, J. R.; Chiu, D. T.; Wu, H.; Schueller, O. J. A.; Whitesides, G. M. Fabrication of Microfluidic Systems in Poly(Dimethylsiloxane). *ELECTROPHORESIS* **2000**, *21* (1), 27–40.
(618) Whitesides, G. M. The Origins and the Future of Microfluidics. *Nature* **2006**, *442* (7101), 368–373.
(619) Byun, C. K.; Abi-Samra, K.; Cho, Y.-K.; Takayama, S. Pumps for Microfluidic Cell Culture. *ELECTROPHORESIS* **2014**, *35* (2–3), 245–257.
(620) Convery, N.; Gadegaard, N. 30 Years of Microfluidics. *Micro Nano Eng.* **2019**, *2*, 76–91.
(621) Castillo-León, J. Microfluidics and Lab-on-a-Chip Devices: History and Challenges. In *Lab-on-a-Chip Devices and Micro-Total Analysis Systems: A Practical Guide*; Castillo-León, J., Svendsen, W. E., Eds.; Springer International Publishing: Cham, 2015; pp 1–15.
(622) Terry, S. C.; Jerman, J. H.; Angell, J. B. A Gas Chromatographic Air Analyzer Fabricated on a Silicon Wafer. *IEEE Trans. Electron Devices* **1979**, *26* (12), 1880–1886.
(623) Hull, C. W.; Spence, S. T.; Albert, D. J.; Smalley, D. R.; Harlow, R. Methods and Apparatus for Production of Three-Dimensional Objects by Stereolithography. *Pat. NumberUS 5059359* **1991**.
(624) Rohani Shirvan, A.; Nouri, A.; Wen, C. 12 - Structural Polymer Biomaterials. In *Structural biomaterials*; Wen, C., Ed.; Woodhead publishing series in biomaterials; Woodhead Publishing, 2021; pp 395–439.
(625) Backer, E. W.; Ehrfeld, W.; Münchmeyer, D.; Betz, H.; Heuberger, A.; Pongratz, S.; Glashauser, W.; Michel, H. J.; v. Siemens, R. Production of Separation-Nozzle Systems for Uranium Enrichment by a Combination of X-Ray Lithography and Galvanoplastics. *Naturwissenschaften* **1982**, *69* (11), 520–523.
(626) Jerman, H. Electrically-Activated, Micromachined Diaphragm Valves. In *IEEE 4th Technical Digest on Solid-State Sensor and Actuator Workshop*; 1990; pp 65–69.
(627) Tirén, J.; Tenerz, L.; Hök, B. A Batch-Fabricated Non-Reverse Valve with Cantilever Beam Manufactured by Micromachining of Silicon. *Sens. Actuators* **1989**, *18* (3), 389–396.
(628) Mohammed, M. I.; Haswell, S.; Gibson, I. Lab-on-a-Chip or Chip-in-a-Lab: Challenges of Commercialization Lost in Translation. *Procedia Technol.* **2015**, *20*, 54–59.
(629) Harrison, D. J.; Fluri, K.; Seiler, K.; Fan, Z.; Effenhauser, C. S.; Manz, A. Micromachining a Miniaturized Capillary Electrophoresis-Based Chemical Analysis System on a Chip. *Science* **1993**, *261* (5123), 895–897.
(630) Fluri, K.; Fitzpatrick, G.; Chiem, N.; Harrison, D. J. Integrated Capillary Electrophoresis Devices with an Efficient Postcolumn Reactor in Planar Quartz and Glass Chips. *Anal. Chem.* **1996**, *68* (23), 4285–4290.

(631) Jacobson, S. C.; Hergenroder, Roland.; Koutny, L. B.; Ramsey, J. Michael. High-Speed Separations on a Microchip. *Anal. Chem.* **1994**, *66* (7), 1114–1118.
(632) Woolley, A. T.; Mathies, R. A. Ultra-High-Speed DNA Sequencing Using Capillary Electrophoresis Chips. *Anal. Chem.* **1995**, *67* (20), 3676–3680.
(633) Collins, F. S.; Morgan, M.; Patrinos, A. The Human Genome Project: Lessons from Large-Scale Biology. *Science* **2003**, *300* (5617), 286–290.
(634) Woolley, A. T.; Mathies, R. A. Ultra-High-Speed DNA Fragment Separations Using Microfabricated Capillary Array Electrophoresis Chips. *Proc. Natl. Acad. Sci.* **1994**, *91* (24), 11348–11352.
(635) Woolley, A. T.; Sensabaugh, G. F.; Mathies, R. A. High-Speed DNA Genotyping Using Microfabricated Capillary Array Electrophoresis Chips. *Anal. Chem.* **1997**, *69* (11), 2181–2186.
(636) Duffy, D. C.; McDonald, J. C.; Schueller, O. J. A.; Whitesides, G. M. Rapid Prototyping of Microfluidic Systems in Poly(Dimethylsiloxane). *Anal. Chem.* **1998**, *70* (23), 4974–4984.
(637) McDonald, J. C.; Whitesides, G. M. Poly(Dimethylsiloxane) as a Material for Fabricating Microfluidic Devices. *Acc. Chem. Res.* **2002**, *35* (7), 491–499.
(638) Xia, Y.; Whitesides, G. M. SOFT LITHOGRAPHY. *Annu. Rev. Mater. Sci.* **1998**, *28* (1), 153–184.
(639) Lorenz, H.; Despont, M.; Fahrni, N.; Brugger, J.; Vettiger, P.; Renaud, P. High-Aspect-Ratio, Ultrathick, Negative-Tone near-UV Photoresist and Its Applications for MEMS. *Sens. Actuators Phys.* **1998**, *64* (1), 33–39.
(640) Lee, K. Y.; LaBianca, N.; Rishton, S. A.; Zolgharnain, S.; Gelorme, J. D.; Shaw, J.; Chang, T. H. -P. Micromachining Applications of a High Resolution Ultrathick Photoresist. *J. Vac. Sci. Technol. B Microelectron. Nanometer Struct. Process. Meas. Phenom.* **1995**, *13* (6), 3012–3016.
(641) Ai, Y.; Xie, R.; Xiong, J.; Liang, Q. Microfluidics for Biosynthesizing: From Droplets and Vesicles to Artificial Cells. *Small* 1903940.
(642) Kang, D.-K.; Ali, M. M.; Zhang, K.; Huang, S. S.; Peterson, E.; Digman, M. A.; Gratton, E.; Zhao, W. Rapid Detection of Single Bacteria in Unprocessed Blood Using Integrated Comprehensive Droplet Digital Detection. *Nat. Commun.* **2014**, *5*, 5427.
(643) Abalde-Cela, S.; Taladriz-Blanco, P.; de Oliveira, M. G.; Abell, C. Droplet Microfluidics for the Highly Controlled Synthesis of Branched Gold Nanoparticles. *Sci. Rep.* **2018**, *8* (1), 2440.
(644) Tan, Y.-C.; Hettiarachchi, K.; Siu, M.; Pan, Y.-R.; Lee, A. P. Controlled Microfluidic Encapsulation of Cells, Proteins, and Microbeads in Lipid Vesicles. *J. Am. Chem. Soc.* **2006**, *128* (17), 5656–5658.
(645) Martinez, A. W.; Phillips, S. T.; Butte, M. J.; Whitesides, G. M. Patterned Paper as a Platform for Inexpensive, Low-Volume, Portable Bioassays. *Angew. Chem. Int. Ed.* **2007**, *46* (8), 1318–1320.
(646) Carrilho, E.; Martinez, A. W.; Whitesides, G. M. Understanding Wax Printing: A Simple Micropatterning Process for Paper-Based Microfluidics. *Anal. Chem.* **2009**, *81* (16), 7091–7095.
(647) Ozefe, F.; Yildiz, A. A. Fabrication and Development of a Microfluidic Paper-Based Immunosorbent Assay Platform (μPISA) for Colorimetric Detection of Hepatitis C. *Analyst* **2023**, *148* (4), 898–905.
(648) Silva-Neto, H. A.; Arantes, I. V. S.; Ferreira, A. L.; do Nascimento, G. H. M.; Meloni, G. N.; de Araujo, W. R.; Paixão, T. R. L. C.; Coltro, W. K. T. Recent Advances on Paper-Based Microfluidic Devices for Bioanalysis. *TrAC Trends Anal. Chem.* **2023**, *158*, 116893.
(649) Comina, G.; Suska, A.; Filippini, D. Low Cost Lab-on-a-Chip Prototyping with a Consumer Grade 3D Printer. *Lab. Chip* **2014**, *14* (16), 2978–2982.

(650) J. Kitson, P.; H. Rosnes, M.; Sans, V.; Dragone, V.; Cronin, L. Configurable 3D-Printed Millifluidic and Microfluidic 'Lab on a Chip' Reactionware Devices. *Lab. Chip* **2012**, *12* (18), 3267–3271.
(651) Huh, D.; Matthews, B. D.; Mammoto, A.; Montoya-Zavala, M.; Hsin, H. Y.; Ingber, D. E. Reconstituting Organ-Level Lung Functions on a Chip. *Science* **2010**, *328* (5986), 1662–1668.
(652) Huh, D.; Leslie, D. C.; Matthews, B. D.; Fraser, J. P.; Jurek, S.; Hamilton, G. A.; Thorneloe, K. S.; McAlexander, M. A.; Ingber, D. E. A Human Disease Model of Drug Toxicity–Induced Pulmonary Edema in a Lung-on-a-Chip Microdevice. *Sci. Transl. Med.* **2012**, *4* (159), 159ra147-159ra147.
(653) Bang, S.; Jeong, S.; Choi, N.; Kim, H. N. Brain-on-a-Chip: A History of Development and Future Perspective. *Biomicrofluidics* **2019**, *13* (5), 051301.
(654) Esch, E. W.; Bahinski, A.; Huh, D. Organs-on-Chips at the Frontiers of Drug Discovery. *Nat. Rev. Drug Discov.* **2015**, *14* (4), 248–260.
(655) Paoli, R.; Samitier, J. Mimicking the Kidney: A Key Role in Organ-on-Chip Development. *Micromachines* **2016**, *7* (7).
(656) Sances, S.; Ho, R.; Vatine, G.; West, D.; Laperle, A.; Meyer, A.; Godoy, M.; Kay, P. S.; Mandefro, B.; Hatata, S.; Hinojosa, C.; Wen, N.; Sareen, D.; Hamilton, G. A.; Svendsen, C. N. Human iPSC-Derived Endothelial Cells and Microengineered Organ-Chip Enhance Neuronal Development. *Stem Cell Rep.* **2018**, *10* (4), 1222–1236.
(657) Won, Y. B.; Lee, I.; Lee, J. H.; Cho, S.; Chae, H. D.; Lee, B. S.; Choi, Y. S. Hormone Secretion in a Microfluidic Ovary-on-a-Chip Platform Using Engineered Follicles. *Fertil. Steril.* **2019**, *112* (3), e246–e247.
(658) Sasserath, T.; Rumsey, J. W.; McAleer, C. W.; Bridges, L. R.; Long, C. J.; Elbrecht, D.; Schuler, F.; Roth, A.; Bertinetti-LaPatki, C.; Shuler, M. L.; Hickman, J. J. Differential Monocyte Actuation in a Three-Organ Functional Innate Immune System-on-a-Chip. *Adv. Sci.* 2000323.
(659) Chen, H. J.; Miller, P.; Shuler, M. L. A Pumpless Body-on-a-Chip Model Using a Primary Culture of Human Intestinal Cells and a 3D Culture of Liver Cells. *Lab. Chip* **2018**, *18* (14), 2036–2046.
(660) Hübner, J.; Raschke, M.; Rütschle, I.; Gräßle, S.; Hasenberg, T.; Schirrmann, K.; Lorenz, A.; Schnurre, S.; Lauster, R.; Maschmeyer, I.; Steger-Hartmann, T.; Marx, U. Simultaneous Evaluation of Anti-EGFR-Induced Tumour and Adverse Skin Effects in a Microfluidic Human 3D Co-Culture Model. *Sci. Rep.* **2018**, *8* (1), 1–12.
(661) Miller, P. G.; Shuler, M. L. Design and Demonstration of a Pumpless 14 Compartment Microphysiological System. *Biotechnol. Bioeng.* **2016**, *113* (10), 2213–2227.
(662) Moraes, C.; Labuz, J. M.; Leung, B. M.; Inoue, M.; Chun, T.-H.; Takayama, S. On Being the Right Size: Scaling Effects in Designing a Human-on-a-Chip. *Integr. Biol. Quant. Biosci. Nano Macro* **2013**, *5* (9), 1149–1161.
(663) Reyes, D. R.; van Heeren, H. Proceedings of the First Workshop on Standards for Microfluidics. *J. Res. Natl. Inst. Stand. Technol.* **2019**, *124*, 1–22.
(664) Wu, J.; Fang, H.; Zhang, J.; Yan, S. Modular Microfluidics for Life Sciences. *J. Nanobiotechnology* **2023**, *21* (1), 85.
(665) 14:00-17:00. *IWA 23:2016*. ISO. https://www.iso.org/standard/70603.html (accessed 2023-05-23).
(666) 14:00-17:00. *ISO 22916:2022*. ISO. https://www.iso.org/standard/74157.html (accessed 2023-05-23).
(667) Shin, J. H.; Choi, S. Open-Source and Do-It-Yourself Microfluidics. *Sens. Actuators B Chem.* **2021**, *347*, 130624.
(668) DropletKitchen. DropletKitchen/Pumpsn17, 2020. https://github.com/DropletKitchen/pumpsn17 (accessed 2020-06-24).

(669) Kong, D. S.; Thorsen, T. A.; Babb, J.; Wick, S. T.; Gam, J. J.; Weiss, R.; Carr, P. A. Open-Source, Community-Driven Microfluidics with Metafluidics. *Nat. Biotechnol.* **2017**, *35* (6), 523–529.
(670) *Metafluidics – Open Repository for Fluidic Systems*. https://metafluidics.org/ (accessed 2023-05-23).
(671) Wenzel, T. Free and Open Source Microfluidics Research Hardware, 2023. https://github.com/MakerTobey/OpenMicrofluidics (accessed 2023-05-23).
(672) *Thingiverse - Digital Designs for Physical Objects*. https://www.thingiverse.com/ (accessed 2023-05-24).
(673) Tiginyanu, I.; Ursaki, V.; Popa, V. 10 - Nanoimprint Lithography (NIL) and Related Techniques for Electronics Applications. In *Nanocoatings and Ultra-Thin Films*; Makhlouf, A. S. H., Tiginyanu, I., Eds.; Woodhead Publishing Series in Metals and Surface Engineering; Woodhead Publishing, 2011; pp 280–329.
(674) Quero, J. M.; Perdigones, F.; Aracil, C. 11 - Microfabrication Technologies Used for Creating Smart Devices for Industrial Applications. In *Smart Sensors and MEMs (Second Edition)*; Nihtianov, S., Luque, A., Eds.; Woodhead Publishing Series in Electronic and Optical Materials; Woodhead Publishing, 2018; pp 291–311.
(675) Qin, D.; Xia, Y.; Whitesides, G. M. Soft Lithography for Micro- and Nanoscale Patterning. *Nat. Protoc.* **2010**, *5* (3), 491–502.
(676) Ruiz, S. A.; Chen, C. S. Microcontact Printing: A Tool to Pattern. *Soft Matter* **2007**, *3* (2), 168–177.
(677) Shen, K.; Qi, J.; Kam, L. C. Microcontact Printing of Proteins for Cell Biology. *J. Vis. Exp. JoVE* **2008**, No. 22.
(678) Hager, R.; Forsich, C.; Duchoslav, J.; Burgstaller, C.; Stifter, D.; Weghuber, J.; Lanzerstorfer, P. Microcontact Printing of Biomolecules on Various Polymeric Substrates: Limitations and Applicability for Fluorescence Microscopy and Subcellular Micropatterning Assays. *ACS Appl. Polym. Mater.* **2022**, *4* (10), 6887–6896.
(679) Khadpekar, A. J.; Khan, M.; Sose, A.; Majumder, A. Low Cost and Lithography-Free Stamp Fabrication for Microcontact Printing. *Sci. Rep.* **2019**, *9* (1), 1024.
(680) Lange, S. A.; Benes, V.; Kern, D. P.; Hörber, J. K. H.; Bernard, A. Microcontact Printing of DNA Molecules. *Anal. Chem.* **2004**, *76* (6), 1641–1647.
(681) Kim, P.; Kwon, K. W.; Park, M. C.; Lee, S. H.; Kim, S. M.; Suh, K. Y. Soft Lithography for Microfluidics: A Review. *Biochip J.* **2008**, *2* (1), 1–11.
(682) Weibel, D. B.; DiLuzio, W. R.; Whitesides, G. M. Microfabrication Meets Microbiology. *Nat. Rev. Microbiol.* **2007**, *5* (3), 209–218.
(683) Sun, H.; Jia, Y.; Dong, H.; Dong, D.; Zheng, J. Combining Additive Manufacturing with Microfluidics: An Emerging Method for Developing Novel Organs-on-Chips. *Curr. Opin. Chem. Eng.* **2020**, *28*, 1–9.
(684) ASTM, D. F. 2792-09. Standard Terminology for Additive Manufacturing Technologies. *ASTM Int.* **2009**.
(685) Paloschi, V.; Sabater-Lleal, M.; Middelkamp, H.; Vivas, A.; Johansson, S.; van der Meer, A.; Tenje, M.; Maegdefessel, L. Organ-on-a-Chip Technology: A Novel Approach to Investigate Cardiovascular Diseases. *Cardiovasc. Res.* **2021**, *117* (14), 2742–2754.
(686) Meyvantsson, I.; W. Warrick, J.; Hayes, S.; Skoien, A.; J. Beebe, D. Automated Cell Culture in High Density Tubeless Microfluidic Device Arrays. *Lab. Chip* **2008**, *8* (5), 717–724.
(687) Hochstetter, A. Lab-on-a-Chip Technologies for the Single Cell Level: Separation, Analysis, and Diagnostics. *Micromachines* **2020**, *11* (5), 468.

(688) Sinha, N.; Yang, H.; Janse, D.; Hendriks, L.; Rand, U.; Hauser, H.; Köster, M.; Van De Vosse, F. N.; De Greef, T. F. A.; Tel, J. Microfluidic Chip for Precise Trapping of Single Cells and Temporal Analysis of Signaling Dynamics. *Commun. Eng.* **2022**, *1* (1), 18.
(689) Källberg, J.; Xiao, W.; Van Assche, D.; Baret, J.-C.; Taly, V. Frontiers in Single Cell Analysis: Multimodal Technologies and Their Clinical Perspectives. *Lab. Chip* **2022**, *22* (13), 2403–2422.
(690) Theberge, A. B.; Mayot, E.; Harrak, A. E.; Kleinschmidt, F.; Huck, W. T. S.; Griffiths, A. D. Microfluidic Platform for Combinatorial Synthesis in Picolitre Droplets. *Lab. Chip* **2012**, *12* (7), 1320–1326.
(691) Kuehne, A. J. C.; Weitz, D. A. Highly Monodisperse Conjugated Polymer Particles Synthesized with Drop-Based Microfluidics. *Chem. Commun.* **2011**, *47* (45), 12379–12381.
(692) Jain, R. K.; Stylianopoulos, T. Delivering Nanomedicine to Solid Tumors. *Nat. Rev. Clin. Oncol.* **2010**, *7* (11), 653–664.
(693) Chen, Y. Y.; Syed, A. M.; MacMillan, P.; Rocheleau, J. V.; Chan, W. C. W. Flow Rate Affects Nanoparticle Uptake into Endothelial Cells. *Adv. Mater.* **2020**, *32* (24), 1906274.
(694) Valencia, P. M.; Farokhzad, O. C.; Karnik, R.; Langer, R. Microfluidic Technologies for Accelerating the Clinical Translation of Nanoparticles. *Nat. Nanotechnol.* **2012**, *7* (10), 623–629.
(695) Cho, E. C.; Zhang, Q.; Xia, Y. The Effect of Sedimentation and Diffusion on Cellular Uptake of Gold Nanoparticles. *Nat. Nanotechnol.* **2011**, *6* (6), 385–391.
(696) Kim, J. H.; Park, J. Y.; Jin, S.; Yoon, S.; Kwak, J.-Y.; Jeong, Y. H. A Microfluidic Chip Embracing a Nanofiber Scaffold for 3D Cell Culture and Real-Time Monitoring. *Nanomaterials* **2019**, *9* (4), 588.
(697) Qin, D.; Xia, Y.; Whitesides, G. M. Rapid Prototyping of Complex Structures with Feature Sizes Larger than 20 Mm. *Adv. Mater.* **1996**, *8* (11), 917–919.
(698) Nishat, S.; Jafry, A. T.; Martinez, A. W.; Awan, F. R. Paper-Based Microfluidics: Simplified Fabrication and Assay Methods. *Sens. Actuators B Chem.* **2021**, *336*, 129681.
(699) de Puig, H.; Bosch, I.; Gehrke, L.; Hamad-Schifferli, K. Challenges of the Nano–Bio Interface in Lateral Flow and Dipstick Immunoassays. *Trends Biotechnol.* **2017**, *35* (12), 1169–1180.
(700) Fu, S.; Zuo, P.; Ye, B.-C. A Novel Wick-Like Paper-Based Microfluidic Device for 3D Cell Culture and Anti-Cancer Drugs Screening. *Biotechnol. J.* **2021**, *16* (2), 2000126.
(701) Clancy, A.; Chen, D.; Bruns, J.; Nadella, J.; Stealey, S.; Zhang, Y.; Timperman, A.; Zustiak, S. P. Hydrogel-Based Microfluidic Device with Multiplexed 3D in Vitro Cell Culture. *Sci. Rep.* **2022**, *12* (1), 17781.
(702) Sung, J. H.; Kam, C.; Shuler, M. L. A Microfluidic Device for a Pharmacokinetic–Pharmacodynamic (PK–PD) Model on a Chip. *Lab. Chip* **2010**, *10* (4), 446.
(703) Nocera, G. M.; Viscido, G.; Criscuolo, S.; Brillante, S.; Carbone, F.; Staiano, L.; Carrella, S.; di Bernardo, D. The VersaLive Platform Enables Microfluidic Mammalian Cell Culture for Versatile Applications. *Commun. Biol.* **2022**, *5* (1), 1–9.
(704) Busek, M.; Aizenshtadt, A.; Koch, T.; Frank, A.; Delon, L.; Amirola Martinez, M.; Golovin, A.; Dumas, C.; Stokowiec, J.; Gruenzner, S.; Melum, E.; Krauss, S. Pump-Less, Recirculating Organ-on-a-Chip (rOoC) Platform. *Lab. Chip* **2023**, *23* (4), 591–608.
(705) King, K. R.; Wang, S.; Jayaraman, A.; Yarmush, M. L.; Toner, M. Microfluidic Flow-Encoded Switching for Parallel Control of Dynamic Cellular Microenvironments. *Lab Chip* **2008**, *8* (1), 107–116.

(706) Ota, H.; Yamamoto, R.; Deguchi, K.; Tanaka, Y.; Kazoe, Y.; Sato, Y.; Miki, N. Three-Dimensional Spheroid-Forming Lab-on-a-Chip Using Micro-Rotational Flow. *Sens. Actuators B Chem.* **2010**, *147* (1), 359–365.
(707) Balagaddé, F. K.; You, L.; Hansen, C. L.; Arnold, F. H.; Quake, S. R. Long-Term Monitoring of Bacteria Undergoing Programmed Population Control in a Microchemostat. *Science* **2005**, *309* (5731), 137–140.
(708) Gu, W.; Zhu, X.; Futai, N.; Cho, B. S.; Takayama, S. Computerized Microfluidic Cell Culture Using Elastomeric Channels and Braille Displays. *Proc. Natl. Acad. Sci.* **2004**, *101* (45), 15861–15866.
(709) Park, J. Y.; Hwang, C. M.; Lee, S. H.; Lee, S.-H. Gradient Generation by an Osmotic Pump and the Behavior of Human Mesenchymal Stem Cells under the Fetal Bovine Serum Concentration Gradient. *Lab. Chip* **2007**, *7* (12), 1673.
(710) Li, P. C. H.; Harrison, D. J. Transport, Manipulation, and Reaction of Biological Cells On-Chip Using Electrokinetic Effects. *Anal. Chem.* **1997**, *69* (8), 1564–1568.
(711) Glawdel, T.; Ren, C. L. Electro-Osmotic Flow Control for Living Cell Analysis in Microfluidic PDMS Chips. *Mech. Res. Commun.* **2009**, *36* (1), 75–81.
(712) Rhee, S. W.; Taylor, A. M.; Cribbs, D. H.; Cotman, C. W.; Jeon, N. L. External Force-Assisted Cell Positioning inside Microfluidic Devices. *Biomed. Microdevices* **2007**, *9* (1), 15–23.
(713) Lee, D. W.; Choi, N.; Sung, J. H. A Microfluidic Chip with Gravity-Induced Unidirectional Flow for Perfusion Cell Culture. *Biotechnol. Prog.* **2019**, *35* (1), UNSP e2701.
(714) M. Condelipes, P. G.; Mendes Fontes, P.; Godinho-Santos, A.; S. Brás, E. J.; Marques, V.; B. Afonso, M.; P. Rodrigues, C. M.; Chu, V.; Gonçalves, J.; Pedro Conde, J. Towards Personalized Antibody Cancer Therapy: Development of a Microfluidic Cell Culture Device for Antibody Selection. *Lab. Chip* **2022**, *22* (23), 4717–4728.
(715) Kshitiz, .; Kim, D.-H.; Beebe, D. J.; Levchenko, A. Micro- and Nanoengineering for Stem Cell Biology: The Promise with a Caution. *Trends Biotechnol.* **2011**, *29* (8), 399–408.
(716) Wells, R. G. The Role of Matrix Stiffness in Regulating Cell Behavior. *Hepatology* **2008**, *47* (4), 1394–1400.
(717) Augustine, R.; Dan, P.; Hasan, A.; Khalaf, I. M.; Prasad, P.; Ghosal, K.; Gentile, C.; McClements, L.; Maureira, P. Stem Cell-Based Approaches in Cardiac Tissue Engineering: Controlling the Microenvironment for Autologous Cells. *Biomed. Pharmacother.* **2021**, *138*, 111425.
(718) Sung, J. H.; Shuler, M. L. Prevention of Air Bubble Formation in a Microfluidic Perfusion Cell Culture System Using a Microscale Bubble Trap. *Biomed. Microdevices* **2009**, *11* (4), 731–738.
(719) Kheiri, S.; Kumacheva, E.; Young, E. W. K. Computational Modelling and Big Data Analysis of Flow and Drug Transport in Microfluidic Systems: A Spheroid-on-a-Chip Study. *Front. Bioeng. Biotechnol.* **2021**, *9*.
(720) Krishnamoorthy, S.; Bedekar, A. S.; Feng, J. J.; Sundaram, S. Need for Simulation-Based Design Analysis and Optimization. *JALA J. Assoc. Lab. Autom.* **2006**, *11* (3), 118–127.
(721) Rosenauer, M.; Vellekoop, M. J. A Novel Microfluidic System for Fluorescent Sample Analysis Fabricated by Rapid Prototyping. In *2008 IEEE SENSORS*; 2008; pp 134–137.
(722) Ahmed, F.; Yoshida, Y.; Wang, J.; Sakai, K.; Kiwa, T. Design and Validation of Microfluidic Parameters of a Microfluidic Chip Using Fluid Dynamics. *AIP Adv.* **2021**, *11* (7), 075224.

(723) O'Connor, J.; Day, P.; Mandal, P.; Revell, A. Computational Fluid Dynamics in the Microcirculation and Microfluidics: What Role Can the Lattice Boltzmann Method Play? *Integr. Biol.* **2016**, *8* (5), 589–602.
(724) McIntyre, D.; Lashkaripour, A.; Fordyce, P.; Densmore, D. Machine Learning for Microfluidic Design and Control. *Lab. Chip* **2022**, *22* (16), 2925–2937.
(725) Maionchi, D. de O.; Ainstein, L.; Santos, F. P. dos; Júnior, M. B. de S. Computational Fluid Dynamics and Machine Learning as Tools for Optimization of Micromixers Geometry. arXiv March 4, 2022. http://arxiv.org/abs/2203.02498 (accessed 2023-06-03).
(726) Hamad, H. S.; Kapur, N.; Khatir, Z.; Querin, O. M.; Thompson, H. M.; Wang, Y.; Wilson, M. C. T. Computational Fluid Dynamics Analysis and Optimisation of Polymerase Chain Reaction Thermal Flow Systems. *Appl. Therm. Eng.* **2021**, *183*, 116122.
(727) Catarino, S. O.; Rodrigues, R. O.; Pinho, D.; Miranda, J. M.; Minas, G.; Lima, R. Blood Cells Separation and Sorting Techniques of Passive Microfluidic Devices: From Fabrication to Applications. *Micromachines* **2019**, *10* (9), 593.
(728) Nasiri, R.; Shamloo, A.; Ahadian, S.; Amirifar, L.; Akbari, J.; Goudie, M. J.; Lee, K.; Ashammakhi, N.; Dokmeci, M. R.; Di Carlo, D.; Khademhosseini, A. Microfluidic-Based Approaches in Targeted Cell/Particle Separation Based on Physical Properties: Fundamentals and Applications. *Small* **2020**, *16* (29), 2000171.
(729) Saggiomo, V. A 3D Printer in the Lab: Not Only a Toy. *Adv. Sci.* **2022**, *9* (27), 2202610.
(730) Symes, M. D.; Kitson, P. J.; Yan, J.; Richmond, C. J.; Cooper, G. J. T.; Bowman, R. W.; Vilbrandt, T.; Cronin, L. Integrated 3D-Printed Reactionware for Chemical Synthesis and Analysis. *Nat. Chem.* **2012**, *4* (5), 349–354.
(731) Di Luca, M.; Hoskins, C.; Corduas, F.; Onchuru, R.; Oluwasanmi, A.; Mariotti, D.; Conti, B.; Lamprou, D. A. 3D Printed Biodegradable Multifunctional Implants for Effective Breast Cancer Treatment. *Int. J. Pharm.* **2022**, *629*, 122363.
(732) Ioannidis, K.; Danalatos, R. I.; Champeris Tsaniras, S.; Kaplani, K.; Lokka, G.; Kanellou, A.; Papachristou, D. J.; Bokias, G.; Lygerou, Z.; Taraviras, S. A Custom Ultra-Low-Cost 3D Bioprinter Supports Cell Growth and Differentiation. *Front. Bioeng. Biotechnol.* **2020**, *8*.
(733) Haque, M. E.; Marriott, L.; Naeem, N.; Henry, T.; Conde, A. J.; Kersaudy-Kerhoas, M. A Low-Cost, Open-Source Centrifuge Adaptor for Separating Large Volume Clinical Blood Samples. *PLOS ONE* **2022**, *17* (7), e0266769.
(734) Waheed, S.; M. Cabot, J.; P. Macdonald, N.; Lewis, T.; M. Guijt, R.; Paull, B.; C. Breadmore, M. 3D Printed Microfluidic Devices: Enablers and Barriers. *Lab. Chip* **2016**, *16* (11), 1993–2013.
(735) Mader, M.; Rein, C.; Konrat, E.; Meermeyer, S. L.; Lee-Thedieck, C.; Kotz-Helmer, F.; Rapp, B. E. Fused Deposition Modeling of Microfluidic Chips in Transparent Polystyrene. *Micromachines* **2021**, *12* (11), 1348.
(736) Chia, H. N.; Wu, B. M. Recent Advances in 3D Printing of Biomaterials. *J. Biol. Eng.* **2015**, *9*, 4.
(737) Terzopoulou, Z.; Zamboulis, A.; Koumentakou, I.; Michailidou, G.; Noordam, M. J.; Bikiaris, D. N. Biocompatible Synthetic Polymers for Tissue Engineering Purposes. *Biomacromolecules* **2022**, *23* (5), 1841–1863.
(738) Duty, C.; Ajinjeru, C.; Kishore, V.; Compton, B.; Hmeidat, N.; Chen, X.; Liu, P.; Hassen, A. A.; Lindahl, J.; Kunc, V. What Makes a Material Printable? A Viscoelastic Model for Extrusion-Based 3D Printing of Polymers. *J. Manuf. Process.* **2018**, *35*, 526–537.
(739) Wurm, M. C.; Möst, T.; Bergauer, B.; Rietzel, D.; Neukam, F. W.; Cifuentes, S. C.; Wilmowsky, C. von. In-Vitro Evaluation of Polylactic Acid (PLA) Manufactured by Fused Deposition Modeling. *J. Biol. Eng.* **2017**, *11*, 29.

(740) Biagini, G.; Senegaglia, A. C.; Pereira, T.; Berti, L. F.; Marcon, B. H.; Stimamiglio, M. A. 3D Poly(Lactic Acid) Scaffolds Promote Different Behaviors on Endothelial Progenitors and Adipose-Derived Stromal Cells in Comparison With Standard 2D Cultures. *Front. Bioeng. Biotechnol.* **2021**, *9*.
(741) Gregor, A.; Filová, E.; Novák, M.; Kronek, J.; Chlup, H.; Buzgo, M.; Blahnová, V.; Lukášová, V.; Bartoš, M.; Nečas, A.; Hošek, J. Designing of PLA Scaffolds for Bone Tissue Replacement Fabricated by Ordinary Commercial 3D Printer. *J. Biol. Eng.* **2017**, *11* (1), 31.
(742) Guidoin, M.-F.; Guidoin, R.; Frayssinet, P.; Legrand, A. P.; How, T. Poly-L-Lactide Surfaces Subjected to Long-Term Cell Cultures. Cell Proliferation and Polymer Degradation. *Artif. Cells Blood Substit. Biotechnol.* **2005**, *33* (4), 411–422.
(743) Mehta, V.; Vilikkathala Sudhakaran, S.; Rath, S. N. Facile Route for 3D Printing of Transparent PETg-Based Hybrid Biomicrofluidic Devices Promoting Cell Adhesion. *ACS Biomater. Sci. Eng.* **2021**, *7* (8), 3947–3963.
(744) Sölmann, S.; Rattenholl, A.; Blattner, H.; Ehrmann, G.; Gudermann, F.; Lütkemeyer, D.; Ehrmann, A.; Sölmann, S.; Rattenholl, A.; Blattner, H.; Ehrmann, G.; Gudermann, F.; Lütkemeyer, D.; Ehrmann, A. Mammalian Cell Adhesion on Different 3D Printed Polymers with Varying Sterilization Methods and Acidic Treatment. *AIMS Bioeng.* **2021**, *8* (1), 25–35.
(745) Borenstein, J. T.; Cummins, G.; Dutta, A.; Hamad, E.; Hughes, M. P.; Jiang, X.; Lee, H. (Hugh); Lei, K. F.; Tang, X. (Shirley); Zheng, Y.; Chen, J. Bionanotechnology and bioMEMS (BNM): State-of-the-Art Applications, Opportunities, and Challenges. *Lab. Chip* **2023**, *23* (23), 4928–4949.
(746) Goh, W. H.; Hashimoto, M. Fabrication of 3D Microfluidic Channels and In-Channel Features Using 3D Printed, Water-Soluble Sacrificial Mold. *Macromol. Mater. Eng.* **2018**, *303* (3), 1700484.
(747) Saggiomo, V.; Velders, A. H. Simple 3D Printed Scaffold-Removal Method for the Fabrication of Intricate Microfluidic Devices. *Adv. Sci.* **2015**, *2* (9), 1500125.
(748) Razavi Bazaz, S.; Kashaninejad, N.; Azadi, S.; Patel, K.; Asadnia, M.; Jin, D.; Ebrahimi Warkiani, M. Rapid Softlithography Using 3D-Printed Molds. *Adv. Mater. Technol.* **2019**, *4* (10), 1900425.
(749) Au, A. K.; Huynh, W.; Horowitz, L. F.; Folch, A. 3D-Printed Microfluidics. *Angew. Chem. Int. Ed.* **2016**, *55* (12), 3862–3881.
(750) Kotz, F.; Mader, M.; Dellen, N.; Risch, P.; Kick, A.; Helmer, D.; Rapp, B. E. Fused Deposition Modeling of Microfluidic Chips in Polymethylmethacrylate. *Micromachines* **2020**, *11* (9), 873.
(751) Gaal, G.; Mendes, M.; de Almeida, T. P.; Piazzetta, M. H. O.; Gobbi, Â. L.; Riul, A.; Rodrigues, V. Simplified Fabrication of Integrated Microfluidic Devices Using Fused Deposition Modeling 3D Printing. *Sens. Actuators B Chem.* **2017**, *242*, 35–40.
(752) Low, W. S.; Kadri, N. A.; Wan Abas, W. A. B. bin. Computational Fluid Dynamics Modelling of Microfluidic Channel for Dielectrophoretic BioMEMS Application. *Sci. World J.* **2014**, *2014*, e961301.
(753) Gunasekaran, K. N.; Aravinth, V.; Muthu Kumaran, C. B.; Madhankumar, K.; Pradeep Kumar, S. Investigation of Mechanical Properties of PLA Printed Materials under Varying Infill Density. *Mater. Today Proc.* **2021**, *45*, 1849–1856.
(754) Aldosari, F.; Khan, M. A. A.; Asad, M.; Djavanroodi, F. Finite Element Analysis of PolyLactic Acid (PLA) under Tensile and Compressive Loading. *J. Phys. Conf. Ser.* **2023**, *2468* (1), 012094.
(755) Farah, S.; Anderson, D. G.; Langer, R. Physical and Mechanical Properties of PLA, and Their Functions in Widespread Applications - A Comprehensive Review. *Adv. Drug Deliv. Rev.* **2016**, *107*, 367–392.

(756) *Parallel Fluidics | Microfluidic Design Portal | Core Formats*. https://www.parallelfluidics.com/design-portal/core-formats (accessed 2023-06-09).
(757) Zhao, Y. C.; Vatankhah, P.; Goh, T.; Wang, J.; Valeria Chen, X.; Navvab Kashani, M.; Zheng, K.; Li, Z.; Arnold Ju, L. Computational Fluid Dynamics Simulations at Micro-Scale Stenosis for Microfluidic Thrombosis Model Characterization. *Mol. Cell. Biomech.* **2021**, *18* (1), 1–10.
(758) Ning, S.; Liu, S.; Xiao, Y.; Zhang, G.; Cui, W.; Reed, M. A Microfluidic Chip with a Serpentine Channel Enabling High-Throughput Cell Separation Using Surface Acoustic Waves. *Lab. Chip* **2021**, *21* (23), 4608–4617.
(759) Shingte, S. D.; Altenburg, O.; Verheijen, P. J. T.; Kramer, H. J. M.; Eral, H. B. Microfluidic Platform with Serpentine Geometry Providing Chaotic Mixing in Induction Time Experiments. *Cryst. Growth Des.* **2022**, *22* (7), 4072–4085.
(760) Kang, T. G.; Singh, M. K.; Anderson, P. D.; Meijer, H. E. H. A Chaotic Serpentine Mixer Efficient in the Creeping Flow Regime: From Design Concept to Optimization. *Microfluid. Nanofluidics* **2009**, *7* (6), 783.
(761) Sieber, S.; Grossen, P.; Uhl, P.; Detampel, P.; Mier, W.; Witzigmann, D.; Huwyler, J. Zebrafish as a Predictive Screening Model to Assess Macrophage Clearance of Liposomes in Vivo. *Nanomedicine Nanotechnol. Biol. Med.* **2019**, *17*, 82–93.
(762) Youden, B.; Runqing Jiang; Andrew J Carrier; Mark R Servos; Zhang, X. A Nanomedicine Structure–Activity Framework for Research, Development, and Regulation of Future Cancer Therapies. *ACS Nano* **2022**, *16* (11), 17497–17551.
(763) *What we do | NC3Rs*. https://nc3rs.org.uk/who-we-are/what-we-do (accessed 2024-02-05).
(764) Wyrzykowska, E.; Mikolajczyk, A.; Lynch, I.; Jeliazkova, N.; Kochev, N.; Sarimveis, H.; Doganis, P.; Karatzas, P.; Afantitis, A.; Melagraki, G.; Serra, A.; Greco, D.; Subbotina, J.; Lobaskin, V.; Bañares, M. A.; Valsami-Jones, E.; Jagiello, K.; Puzyn, T. Representing and Describing Nanomaterials in Predictive Nanoinformatics. *Nat. Nanotechnol.* **2022**, *17* (9), 924–932.
(765) Richardson, J. J.; Caruso, F. Nanomedicine toward 2040. *Nano Lett.* **2020**, *20* (3), 1481–1482.
(766) Khrabrov, K.; Shenbin, I.; Ryabov, A.; Tsypin, A.; Telepov, A.; Alekseev, A.; Grishin, A.; Strashnov, P.; Zhilyaev, P.; Nikolenko, S.; Kadurin, A. nablaDFT: Large-Scale Conformational Energy and Hamiltonian Prediction Benchmark and Dataset. *Phys. Chem. Chem. Phys.* **2022**, *24* (42), 25853–25863.
(767) Pablo-García, S.; Morandi, S.; Vargas-Hernández, R. A.; Jorner, K.; Ivković, Ž.; López, N.; Aspuru-Guzik, A. Fast Evaluation of the Adsorption Energy of Organic Molecules on Metals via Graph Neural Networks. *Nat. Comput. Sci.* **2023**, *3* (5), 433–442.
(768) Jablonka, K. M.; Rosen, A. S.; Krishnapriyan, A. S.; Smit, B. An Ecosystem for Digital Reticular Chemistry. *ACS Cent. Sci.* **2023**, *9* (4), 563–581.
(769) Burés, J.; Larrosa, I. Organic Reaction Mechanism Classification Using Machine Learning. *Nature* **2023**, *613* (7945), 689–695.
(770) Johnston, A.; F. Johnston, B.; R. Kennedy, A.; J. Florence, A. Targeted Crystallisation of Novel Carbamazepine Solvates Based on a Retrospective Random Forest Classification. *CrystEngComm* **2008**, *10* (1), 23–25.
(771) Florence, A. J.; Johnston, A.; Price, S. L.; Nowell, H.; Kennedy, A. R.; Shankland, N. An Automated Parallel Crystallisation Search for Predicted Crystal Structures and Packing Motifs of Carbamazepine. *J. Pharm. Sci.* **2006**, *95* (9), 1918–1930.
(772) Faria, M.; Bjornmalm, M. MIRIBEL. **2017**.
(773) Ashkarran, A. A.; Swann, J.; Hollis, L.; Mahmoudi, M. The File Drawer Problem in Nanomedicine. *Trends Biotechnol.* **2021**, *39* (5), 425–427.

(774) Mirshafiee, V.; Kim, R.; Mahmoudi, M.; Kraft, M. L. The Importance of Selecting a Proper Biological Milieu for Protein Corona Analysis in Vitro: Human Plasma versus Human Serum. *Int. J. Biochem. Cell Biol.* **2016**, *75*, 188–195.
(775) Ding, L.; Yao, C.; Yin, X.; Li, C.; Huang, Y.; Wu, M.; Wang, B.; Guo, X.; Wang, Y.; Wu, M. Size, Shape, and Protein Corona Determine Cellular Uptake and Removal Mechanisms of Gold Nanoparticles. *Small* **2018**, *14* (42), 1801451.
(776) Bros, M.; Nuhn, L.; Simon, J.; Moll, L.; Mailänder, V.; Landfester, K.; Grabbe, S. The Protein Corona as a Confounding Variable of Nanoparticle-Mediated Targeted Vaccine Delivery. *Front. Immunol.* **2018**, *9*.
(777) Aliyandi, A.; Reker-Smit, C.; Bron, R.; Zuhorn, I. S.; Salvati, A. Correlating Corona Composition and Cell Uptake to Identify Proteins Affecting Nanoparticle Entry into Endothelial Cells. *ACS Biomater. Sci. Eng.* **2021**, *7* (12), 5573–5584.
(778) Rathmayer, S.; Unger, F. Parallelizing CFX-TfC, a State of the Art Industrial CFD Package. In *Advances in Parallel Computing*; D'Hollander, E. H., Peters, F. J., Joubert, G. R., Trottenberg, U., Völpel, R., Eds.; Parallel Computing; North-Holland, 1998; Vol. 12, pp 179–186.
(779) *Green Fluorescent PLGA nanoparticles 100 nm average diameter | Sigma-Aldrich*. http://www.sigmaaldrich.com/ (accessed 2023-10-13).
(780) Lepowsky, E.; Tasoglu, S. Emerging Anti-Fouling Methods: Towards Reusability of 3D-Printed Devices for Biomedical Applications. *Micromachines* **2018**, *9* (4), 196.

So if you care to find me

Look to the western sky

As someone told me lately

"Everyone deserves the chance to fly"

And if I'm flying solo

At least I'm flying free

To those who ground me

Take a message back from me

Tell them how I am defying gravity

I'm flying high, defying gravity

And soon, I'll match them in renown

And nobody in all of Oz

No wizard that there is or was

Is ever gonna bring me down

Defying Gravity, Wicked.